ADVANCED THERANOSTIC NANOMEDICINE IN ONCOLOGY
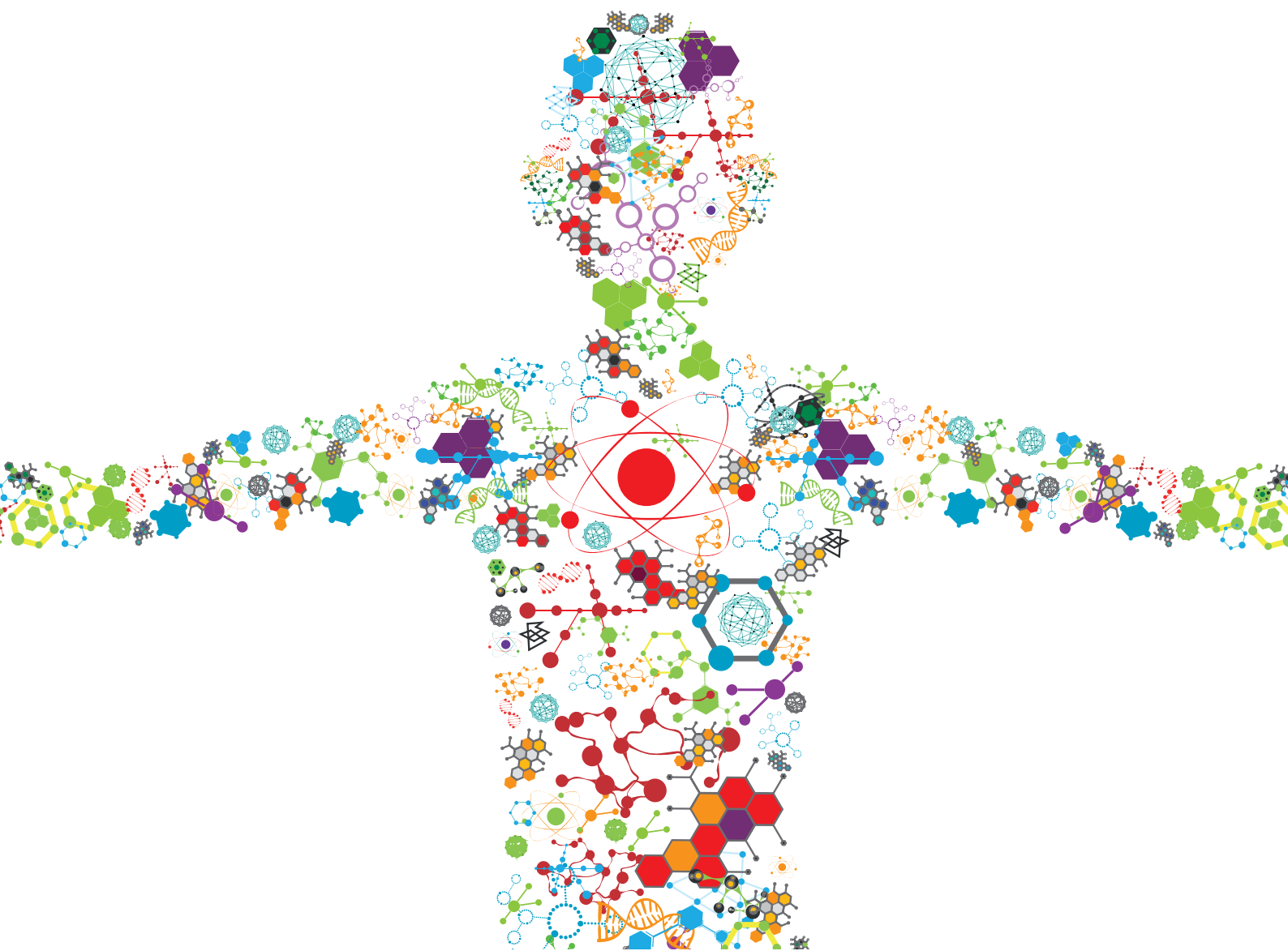
EDITED BY: Gianni Ciofani, Attilio Marino and Christos Tapeinos

frontiers Research Topics

About Frontiers

Frontiers is more than just an open-access publisher of scholarly articles: it is a pioneering approach to the world of academia, radically improving the way scholarly research is managed. The grand vision of Frontiers is a world where all people have an equal opportunity to seek, share and generate knowledge. Frontiers provides immediate and permanent online open access to all its publications, but this alone is not enough to realize our grand goals.

Frontiers Journal Series

The Frontiers Journal Series is a multi-tier and interdisciplinary set of open-access, online journals, promising a paradigm shift from the current review, selection and dissemination processes in academic publishing. All Frontiers journals are driven by researchers for researchers; therefore, they constitute a service to the scholarly community. At the same time, the Frontiers Journal Series operates on a revolutionary invention, the tiered publishing system, initially addressing specific communities of scholars, and gradually climbing up to broader public understanding, thus serving the interests of the lay society, too.

Dedication to Quality

Each Frontiers article is a landmark of the highest quality, thanks to genuinely collaborative interactions between authors and review editors, who include some of the world's best academicians. Research must be certified by peers before entering a stream of knowledge that may eventually reach the public - and shape society; therefore, Frontiers only applies the most rigorous and unbiased reviews.
Frontiers revolutionizes research publishing by freely delivering the most outstanding research, evaluated with no bias from both the academic and social point of view. By applying the most advanced information technologies, Frontiers is catapulting scholarly publishing into a new generation.

What are Frontiers Research Topics?

Frontiers Research Topics are very popular trademarks of the Frontiers Journals Series: they are collections of at least ten articles, all centered on a particular subject. With their unique mix of varied contributions from Original Research to Review Articles, Frontiers Research Topics unify the most influential researchers, the latest key findings and historical advances in a hot research area! Find out more on how to host your own Frontiers Research Topic or contribute to one as an author by contacting the Frontiers Editorial Office: researchtopics@frontiersin.org

ADVANCED THERANOSTIC NANOMEDICINE IN ONCOLOGY

Topic Editors:
Gianni Ciofani, Italian Institute of Technology (IIT), Italy
Attilio Marino, Italian Institute of Technology (IIT), Italy
Christos Tapeinos, Italian Institute of Technology (IIT), Italy

Table of Contents

frontiers
in Bioengineering and Biotechnology

Editorial: Advanced Theranostic Nanomedicine in Oncology

Christos Tapeinos*, Attilio Marino* and Gianni Ciofani*

Smart Bio-Interfaces, Istituto Italiano di Tecnologia, Pisa, Italy

Editorial on the Research Topic

Advanced Theranostic Nanomedicine in Oncology

The Research Topic entitled "Advanced Theranostic Nanomedicine in Oncology" presents a series of articles that describe the latest research updates of biologically-inspired nanostructures used in the field of oncology. In addition, it briefly describes the biological mechanisms of certain cancers and how we can take advantage of these mechanisms to improve the therapeutic efficacy of future nano-therapeutics. With this issue, we aim to raise awareness for the challenges in the common ground between the fields of oncology and biomedical engineering, and also to present up-to-date counter-challenging research achievements. The issue is comprised of 12 selected peer-reviewed manuscripts (8 reviews and 4 original research articles) derived from the fields of (bio)materials science and engineering, chemistry, physics, and biology.

A variety of smart nanomaterials, including carbon-based nanofibers (Sayin et al.), multifunctional liposomes (Formicola et al.), polymeric nano-constructs (Ferreira et al.), and inorganic nanoparticles (Hossain et al.) are presented through original research works. These novel and smart nanomaterials with tailor-made characteristics have been carefully designed, aiming at improving their therapeutic efficacy while in tandem to reduce the side-effects of the chemotherapeutics that they encapsulate.

The first example of these smart nanomaterials is given by polyvinyl alcohol (PVA)-based nanofibers made through electrospinning by Sayin et al.. In this work, the fabricated nanofibers presented excellent biocompatibility and a pH-controlled release of the encapsulated Rose Bengal drug model. The nanofibers also demonstrated an increase in reactive oxygen species (ROS) production that led to the apoptosis of U87 glioblastoma cells.

A different approach to the treatment of glioblastoma is also presented by Formicola et al.. In this study, multifunctional liposomes made of cholesterol/sphingomyelin and surface functionalized with mApoE and chlorotoxin peptides (Mf-LIP) were used as a model nano-vehicle to study the formation of tunneling nanotubes, and the effect of these nanotubes in the delivery of chemotherapeutics. The comparison of the U87 MG cell line with a standard human astrocytic cell line demonstrated that he U87 MG cells form almost exclusively thick and long protrusions, whereas healthy astrocytes formed thinner and shorter tunneling nanotubes. This suggested that nanotubes are potentially useful as drug-delivery channels for cancer therapy especially for isolated tumor niches that cannot be targeted through simple chemotherapeutic diffusion.

Discoidal polymeric nano-constructs consist of a class of nano-theranostic agents with tunable characteristics including high biocompatibility, controllable size, loading capacity, and stimuli-responsive release. In the presented work of Ferreira et al. food and drug administration (FDA)-approved poly (lactic-*co*-glycolic acid) was used for the fabrication of discoidal nano-constructs, which were subsequently optimized to increase their loading efficiencies. Two different loading methodologies (direct vs. absorption) and compound attributes (hydrophobicity and molecular weight) have been studied. *In vitro* (breast cancer cells) and preliminary *in vivo*

studies demonstrated that the properties of these nano-constructs could be finely tuned and improve their overall therapeutic performance.

The final original research presented in this topic by Hossain et al. is related to the investigation of the antibacterial activity of biogenic silver nanoparticles. Despite the fact that this research is not directly related to the field of oncology, it presents valuable data on the fabrication, characterization, and antibacterial activity of biocompatible silver nanoparticles that have already been reported elsewhere as potential anticancer agents.

Besides the original research manuscripts, this topic presents a series of review papers that summarize the recent advances in the fields of nanomedicine and oncology. As a starting example, the application of high-intensity ultrasound as a non-invasive tumor-ablation method, its immunomodulatory action, and its effects in drug delivery are discussed by Tharkar et al.. In continuation, theranostic applications based on gold nanoparticles and their effect depending on the heterogeneity of tumors is discussed by Roma-Rodrigues et al., while a variety of general nano-theranostics for the treatment of pancreatic adenocarcinoma are described by Brachi et al..

The increasing development and the numerous applications of two-dimensional (2D) nanostructures in various fields, including cancer therapy and diagnosis, and more specifically in the field of photodynamic therapy, is presented by Gazzi et al.. Carrying on the field of 2D nanomaterials, the synthesis, the surface modification strategies, the biocompatibility, and the bioapplications of 2D boron nitride nanostructures are reported by Emanet et al.. Theranostic nanomedicine approaches for the treatment of glioblastoma are detailed by d'Angelo et al., while nanomaterials-based combinational chemo-photothermal therapy is introduced by Li et al..

Finally, Natoni et al. elucidate the mechanisms behind sialylation and multiple myeloma, and how the inhibition of sialylation may represent an advanced therapeutic strategy able to overcome the bone marrow-mediated chemotherapy resistance. In addition, different approaches that allow the delivery of sialylation inhibitors to the bone marrow microenvironment are also analyzed.

Summarizing, we hope that this collection of the-state-of-the-art articles and reviews will provide insights into the limitations on the field of nanomedicine, and will promote ideas on how to overcome these limitations for successfully developing enhanced therapeutic strategies. Additionally, we anticipate that this Research Topic will constitute a convenient and beneficial guide toward early-stage and senior researchers in the field of biomedical engineering.

AUTHOR CONTRIBUTIONS

CT wrote the editorial, which was revised, proofed, and accepted by all the authors.

FUNDING

Nanotheranostics Targeting the Tumor Microenvironment

Catarina Roma-Rodrigues, Inês Pombo, Luís Raposo, Pedro Pedrosa, Alexandra R. Fernandes and Pedro V. Baptista*

UCIBIO, Departamento de Ciências da Vida, Faculdade de Ciências e Tecnologia, Universidade NOVA de Lisboa, Costa da Caparica, Portugal

Cancer is considered the most aggressive malignancy to humans, and definitely the major cause of death worldwide. Despite the different and heterogenous presentation of the disease, there are pivotal cell elements involved in proliferation, differentiation, and immortalization, and ultimately the capability to evade treatment strategies. This is of utmost relevance when we are just beginning to grasp the complexity of the tumor environment and the molecular "evolution" within. The tumor micro-environment (TME) is thought to provide for differentiation niches for clonal development that results in tremendous cancer heterogeneity. To date, conventional cancer therapeutic strategies against cancer are failing to tackle the intricate interplay of actors within the TME. Nanomedicine has been proposing innovative strategies to tackle this TME and the cancer cells that simultaneously provide for biodistribution and/or assessment of action. These nanotheranostics systems are usually multi-functional nanosystems capable to carry and deliver active cargo to the site of interest and provide diagnostics capability, enabling early detection, and destruction of cancer cells in a more selective way. Some of the most promising multifunctional nanosystems are based on gold nanoparticles, whose physic-chemical properties have prompt for the development of multifunctional, responsive nanomedicines suitable for combinatory therapy and theranostics. Herein, we shall focus on the recent developments relying on the properties of gold nanoparticles as the basis for nanotheranostics systems against the heterogeneity within the TME.

Keywords: tumor microenvironment, nanomedicine, cancer therapy, diagnostic, gold nanoparticles, nanotheranostics

INTRODUCTION

As the knowledge about cancer development progresses, it highlights the complexity of the disease characterized by inter-tumor and intra-tumor heterogeneity between cancer types of different or the same anatomical region (Mroz and Rocco, 2016; Grzywa et al., 2017; Liu et al., 2018a). This interplay between growing tumor cells and surrounding environment creates a tumor micro-environment (TME), whose arrangement varies according to the anatomical region of the tumor and the genetic and phenotypic traits of cancer cells (Correia and Bissell, 2012; Abadjian et al., 2017). Still, several common features can be found, such as the micro-environment of epithelial tumors is generally composed by tumor cells, the extracellular matrix (ECM), stromal cells, including fibroblasts, mesenchymal stromal cells, cells from the blood and lymphatic systems, and occasionally adipocytes and cells from the immune system, including macrophages, T and B lymphocytes, and natural killer cells.

TME composition and maturation dictates tumor progression, prognosis and the efficacy of chemotherapeutics, where it is becoming more evident that one therapy does not fit all (Netea-Maier et al., 2018). That is why a thorough comprehension of a patient's TME may provide for important clues of the most effective therapeutics. For this, efforts have been made to develop imaging and therapeutic strategies focused on TME for improving the efficacy of treatment (Roma-Rodrigues et al., 2019). Perhaps the most innovative and effective strategies have been put forward by nanomedicine, that offers a vast number of diagnostics and therapeutics, alone or combined into a single platform, in what is known as nanotheranostics. The Medical Standing Committee of the European Science Foundation states that "Nanomedicine is the science and technology of diagnosing, treating, and preventing disease and traumatic injury, of relieving pain, and of preserving and improving human health, using molecular tools, and molecular knowledge of the human body." The last decades have fueled the synthesis and assembly of a plethora of nanomaterials, such as nanoparticles made of noble metals, carbon, heavy metals, etc., in many forms, e.g., spherical or non-spherical nanoparticles, nanowires, nanotubes and nanofilms. These nanomaterials have got unique properties that might be explored for theranostics applications. For example, carbon nanotubes are excellent conductors, with exceptional strength; iron oxide nanoparticles are superparamagnetic; while gold nanoparticles have unique spectral (optical) properties (reviewed in Pedrosa et al., 2015; Elzoghby et al., 2016; Bhise et al., 2017; Bayda et al., 2018).

These nanostructures' primary advantages for biomedical applications are the small size within the same scale than that of biomolecules and an augmented area-to-volume ratio

allowing an increased interphase area in a small mass (Pedrosa et al., 2015; Elzoghby et al., 2016; Bhise et al., 2017; Bayda et al., 2018). One crucial advantage of nanoparticles for cancer therapy is their tendency to naturally accumulate within tumors via enhanced permeability retention (EPR; Nichols and Bae, 2014). The fundamental features of EPR are hyperpermeability of tumor vasculature to large particles (enhanced permeability) and impaired lymphatic drainage, retaining the particles into the interstitial space of the tumor (enhanced retention) (Nichols and Bae, 2014). This way, nanomaterials passively accumulate at tumors' sites where they can then exert their therapeutic/diagnostic effect. In order to extravasate the vasculature and avoid renal filtration and liver capture, nanoparticles should range between 10 and 100 nm and preferably present a neutral or anionic charge (Danhier et al., 2010; Dreaden et al., 2012). Using the EPR to passively accumulate nanoconjugates at the tumor site has been thoroughly described in a general way. However, tumors are heterogeneous, impacting the capacity of nanoparticles to homogeneously penetrate the neoplastic tissue (Danhier, 2016). For example, larger particles (100 nm) have higher retentions times in the tumor (Danhier et al., 2010). Also, the EPR based accumulation varies greatly with the degree of vascularization, which is not always easy to predict (Danhier et al., 2010). There are also several tumor types that do not preset an EPR effect that can be used, such as prostate and pancreatic tumors (Danhier et al., 2010). Another limitation of passive targeting relying solely on EPR is the inability of passive targeting to access necrotic tissue, in the core of the tumor due to the low vascularization (Ngoune et al., 2016). These disadvantages can be overcome with different strategies, for instance, using drugs to modulate vascularization. For example, vasoconstriction drugs cause normal vessels constriction, but tumor vessels do not respond to this effect due to insufficient muscular structure, which leads to an increased uptake of particles by tumor tissues (Maeda, 2012). To overcome limitation imposed by using EPR alone, several strategies include active targeting by means of several moieties (e.g., antibodies or peptides), capable to promote ligand-receptor interactions at the surface of tumor cells, inducing receptor-mediated endocytosis and drug release inside the cell (Kobayashi et al., 2014). Such moieties include, for example, EGFR, TGF-α, folate, or glucose receptors, which are known to be overexpressed in cancer cells. Active targeting has been critical for the development of vectorization systems that enable the nanoparticles to deliver their cargo on tumor site improving the therapeutic effect (Dreaden et al., 2012). Among the variety of nanomaterials, spherical gold nanoparticles (AuNPs) have been extensively studied for cancer diagnosis and treatment, mostly due to their unique optical properties, easy synthesis in aqueous solution, and functionalization with biomolecules, which together have not presented toxicity to the cells and organisms (Conde et al., 2014). AuNPs can be easily functionalized with different moieties, such as drugs, targeting ligand, protein or peptides, nucleic acids, imaging agents, photosensitizers, bioactive/bio-responsive moieties, among others. Targeting ligands bound to the surface of nanoparticles interact with receptors selectively expressed in tumor cells (Haume et al., 2016). By means of

targeting ligands, it is possible to profit from the EPR effect to accumulate the AuNPs in the tumor site and then direct the gold nanoconjugates selectively to cancer cells. This way the anti-tumor effect may be delivered solely (or mostly) to the malignant cells while sparing the healthy tissues, thus with a beneficial impact in decreasing side effects (Guo et al., 2017). In addition, bioactive/bio-responsive moieties can be sensitive to TME and respond to specific stimuli, such as pH or matrix metalloproteinase (MMP; Guo et al., 2017). Chemotherapeutics drugs may also be loaded onto or attached to the surface of nanoparticles, thus functioning as carriers (Singh et al., 2018).

Besides the possible functionalization of AuNPs to a specific TME target, naked AuNPs were found to disrupt the crosstalk between cells within the TME and, consequently, preventing tumor progression. For example, AuNPs were found to influence angiogenesis by diminishing both the tube formation and migration of endothelial cells, through blockage of vascular endothelial growth factor (VEGF) signaling from TME cells to endothelial cells (Zhang Y. et al., 2019). Also, AuNPs have been found to promote tumor vasculature normalization while increasing blood perfusion and reducing hypoxia (Li et al., 2017). These basic AuNP systems may also be used to improve imaging approaches to assist surgeons during tumor resection, by injecting functionalized AuNPs specifically into the tumor it is possible to distinguish between healthy and malignant cells (Singh et al., 2018).

TUMOR MICROENVIRONMENT

Despite the growing knowledge of tumor development and progression, it is virtually impossible to determine cause-effect chain of events, from the initial stage when cells become tumorigenic and initiate uncontrolled proliferation, to a mature high-grade tumor. Sometimes one is tempted to associate one event triggered by proliferating tumor cells to an event occurring within the TME, but this correlation falls far from reality since it is the evolving interplay of all TME components that ultimately will be responsible for tumor modulation and progression (Hanahan and Weinberg, 2011; Netea-Maier et al., 2018). Here we shall focus on each component of the TME separately for simplicity. However, it is crucial to understand that each one of these events, occurring for each component, may be triggered in a different way for a different tumor or tumor type, thus affect all the other TME components differently, and consequently resulting in different outcomes. **Figure 1** and **Table 1** highlight the major events occurring at the TME that contribute for tumor progression.

The rapid proliferation of tumor cells results in a constrain in oxygen and nutrient supply that cannot be sustained by adjacent blood vessels (Hanahan and Weinberg, 2011). The oxygen scarcity experienced by growing tumor cells induce the cellular response to hypoxia, principally via hypoxia-induced factors (HIF) (reviewed in Vaupel and Multhoff, 2018). The HIF family of transcriptional factors is composed by HIF1, HIF2 and HIF3 proteins that activate genes involved in glucose metabolism, angiogenesis, cell proliferation and migration, and

immune system modulation (Huang et al., 2017; Sormendi and Wielockx, 2018; Vaupel and Multhoff, 2018). The HIF response together with high energetic requirements, trigger a metabolic adjustment in tumor cells from oxidative phosphorylation to the aerobic glycolysis, in a process known as the Warburg effect (Gwangwa et al., 2018). This metabolic switch subsists even in the presence of oxygen and results in an increased secretion of lactate to the extracellular space and consequent TME acidification (Lu, 2019). The glycolytic metabolism and intensified proliferation of tumor cells result in an increase of reactive oxygen species (ROS) production, which in turn target cellular components, such as DNA, promoting genomic instability that further alters the cells' characteristics, and also induces the activation of antioxidant defenses (Gwangwa et al., 2018). These events, together with increased expression of efflux pumps for lactic and carbonic acid secretion gives an advantage to tumor cells to survive and thrive in hostile environments, contributing for multidrug resistance (MDR; Tsai et al., 2014). Interestingly, rather than oncogenic promoters in malignant cells, HIF proteins act as tumor suppressors (Mazumdar et al., 2010; Lee et al., 2016; Nakazawa et al., 2016). However, HIF-mediated paracrine communications between tumor cells and neighborhood, including stromal cells, immune system cells, metastases and extracellular matrix modulation, promote tumor development, rendering oncogenic features to HIF proteins at the TME level (reviewed in Huang et al., 2017; Sormendi and Wielockx, 2018).

The secretion of vascular endothelial growth factor A (VEGFA) by TME components, promote the sprouting of adjacent vessels through binding to VEGF receptors (VEGFR) located in endothelial cells (De Palma et al., 2017; Klein, 2018). The high levels of angiogenic signals at the TME, lead to the formation of vessels with defective or discontinuous basement membranes, resulting in the leaking vasculature with chaotic organization unevenly distributed along the tumor, with cancer regions enriched with vessels and cancer regions poorly supplied (Klein, 2018). This restricts the nutrient and oxygen supply to the TME, promoting hypoxia, and difficult the chemotherapeutic agents' distribution throughout the tumor (Klein, 2018). Moreover, the unbalanced distribution of blood vessels results in an altered distribution of cytokines involved in inflammatory and coagulation processes at the TME (Klein, 2018). Nevertheless, it is this less organized leaky vasculature that allows nanomedicines to passively target the tumor site.

The formation of lymphatic vessels at the TME, named tumor-associated lymphangiogenesis, is sustained by VEGF-C and VEGF-D secreted by tumor cells, immune cells, and other stromal cells (Garnier et al., 2019). Then, lymphatic endothelial cells (LECs) form single layer lymph capillaries with minimal basement membrane, that join to collecting lymphatic vessels with a basement membrane and valves that prevent retrograde flow (Garnier et al., 2019). The formation of lymphatic vessels at the TME is correlated with poor prognosis, since it favors metastatic propagation in distal organs (Garnier et al., 2019). On the other side, LECs have a prominent role in immune system modulation at the TME contributing for anti-tumor immunity (reviewed in Farnsworth et al., 2019; Garnier et al., 2019).
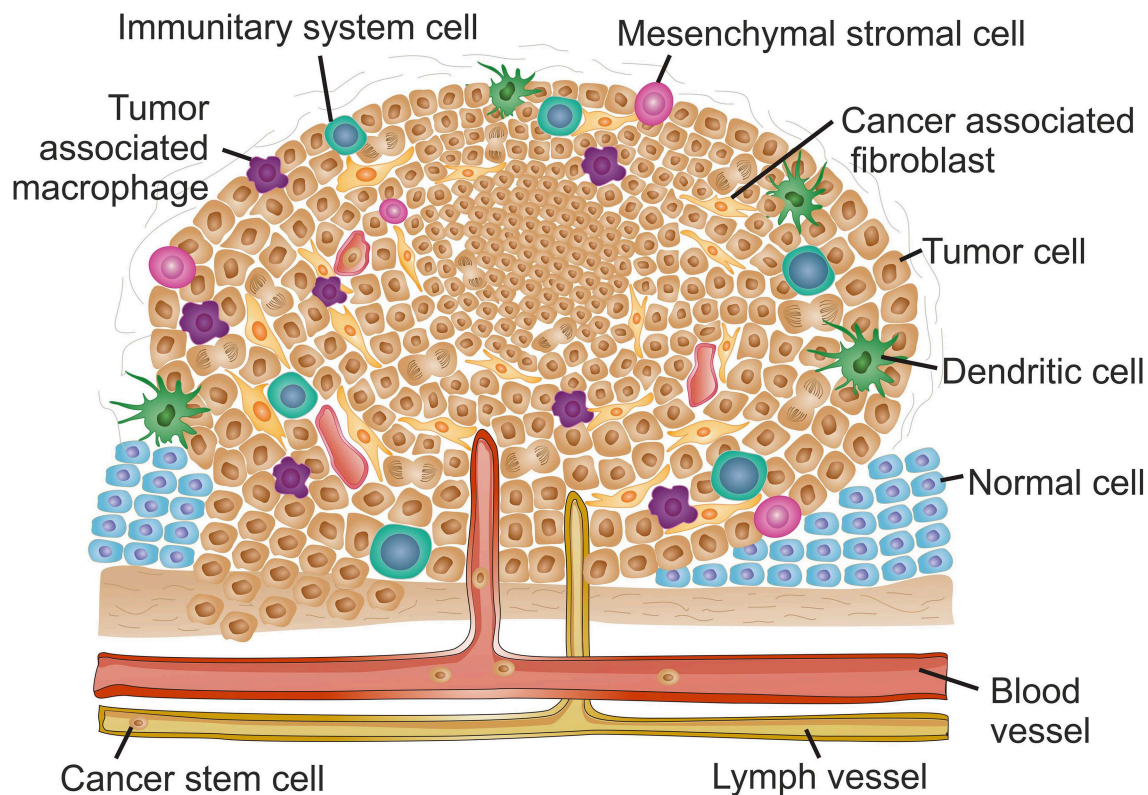
FIGURE 1 | The complex context of tumor microenvironment. Schematic reorientation highlighting the diversity of elements within the tumor micro-environment (TME). The features and composition of a late stage solid TME are extremely heterogeneous with high intra- and inter-tumor variability. Common features include the appearance of hypoxic regions usually at the core of the tumor indicated as a denser cell population. Hypoxia is usually associated to decreased interstitial pH and induces angiogenesis, resulting in an uneven distribution of blood vessels along the TME. Lymphatic vessels are also frequently found in tumor late stages. The increased vasculature at the TME contribute for local invasion, the dissemination of cancer stem cells and formation of metastasis. The inflammatory environment recruits mesenchymal stromal cells and innate system tumor cells. Tumor associated macrophages usually infiltrate the tumor and promote a pro-inflammatory microenvironment contributing for tumor growth and reinforcing input for angiogenesis. Adaptive immune system cells are mainly found at the TME margins. The inflammatory environment stimulates transformation of fibroblasts into cancer associated fibroblasts that, together with an alteration of the extracellular matrix stiffness, contribute for increased desmoplasia at the TME and hence induce metastasis.

Again, the defective lymph drainage assists the accumulation of nanomedicines at the locus via the EPR.

Concerning immune system cells, the TME varies considerably throughout the tumor development and throughout the various types of cancers (Netea-Maier et al., 2018). Due to the continuous changes and adaptations occurring at the TME, different recruitment factors (e.g., cytokines and chemokines) are secreted, resulting in the enrollment of cells from both innate and adaptive immune systems (Chen and Mellman, 2017; Clark, 2018). Importantly, the molecular signals composition of the TME determine the clinical outcome by promoting the tumor escape to immunosurveillance or tumor constrain (Netea-Maier et al., 2018). Once in the TME, monocytes can differentiate into two different types of macrophages depending on the chemical composition at the tumor location, the M1-type macrophages are formed in the presence of interferon gamma (IFN-γ), and the M2-type macrophages when exposed to different interleukins (IL, e.g., IL-4 or IL-10), transforming growth factor beta (TGF-β), Granulocyte-macrophage colony

stimulating factor (GM-CSF), annexin A1 or tumor cell-surface molecules (reviewed in Italiani and Boraschi, 2014; Goswami et al., 2017). This macrophages polarization is crucial for tumor prognosis, as M1-type are correlated with a good prognosis, while tumor associated macrophages (TAMs) generally have the M2 phenotype and contribute for tumor growth, angiogenesis, invasion, and metastasis (Italiani and Boraschi, 2014; Goswami et al., 2017; Jeong et al., 2019; Prenen and Mazzone, 2019). Inflammation is usually displayed in TME, promoted initially by tumor cells (intrinsic pathway) and sustained and/or aggravated by other TME components (reviewed in Mantovani et al., 2019). A pro-inflammatory environment is usually accompanied by a poor prognosis (reviewed in Netea-Maier et al., 2018; Mantovani et al., 2019). The TAMs-mediated secretion of IL-1 cytokines contribute for chronic inflammation and strengthen a pro-tumoral micro-environment (reviewed in Mantovani et al., 2018). The role of the lymphoid lineage cells in tumor progression is also contradictory. While B cells and regulatory T cells create an immunosuppressive microenvironment, innate

TABLE 1 | Tumor microenvironment components and their major effects on tumor development.

TME components	Major effect on tumor development	Disease prognosis	References
Hypoxia	HIF activation	Poorer	Vaupel and Multhoff, 2018
	HIF loss of function	Poorer	Mazumdar et al., 2010; Lee et al., 2016; Nakazawa et al., 2016
	HIF mediated paracrine TME communication	Poorer	Huang et al., 2018; Sormendi and Wielockx, 2018
Aerobic glycolysis (Warburg effect)	TME acidification	Poorer	Lu, 2019
	Reactive Oxygen Species	Poorer	Gwangwa et al., 2018
	Genomic instability	Poorer	Gwangwa et al., 2018
	Activation of antioxidation defenses	Poorer	Gwangwa et al., 2018
Lymphoangiogenesis	VEGF secretion in TME	Poorer	Garnier et al., 2019
	Formation of lymph vessels by LECs	Poorer	Garnier et al., 2019
Activation of the Immune system	Impairment of anti-tumor immunity through LECs loss of function	Poorer	Farnsworth et al., 2019; Garnier et al., 2019
	M1-type monocytes activation through IFN-γ, etc.	Better	Italiani and Boraschi, 2014; Goswami et al., 2017; Jeong et al., 2019; Prenen and Mazzone, 2019
	M2-type monocytes (also known as TAM) activation through IL-4, IL-10, TGF-β, GM-CSF, Annexin A1, etc.	Poorer	Italiani and Boraschi, 2014; Goswami et al., 2017
Inflammation	TAM mediated chronic inflammation in TME	Poorer	Mantovani et al., 2018
	Activation of B and regulatory T lymphocytes	Better	DeNardo et al., 2010; Hui and Chen, 2015; Labiano et al., 2015; Wu, 2017; Steven and Seliger, 2018
	Activation of NK and NK T lymphocytes	Poorer	DeNardo et al., 2010; Hui and Chen, 2015; Labiano et al., 2015; Wu, 2017; Steven and Seliger, 2018
	GM-CSF and VEGF mediated production of MDSCs	Poorer	Schupp et al., 2017; Bruno et al., 2019
Altered ECM	Desmoplasia and metastatic dissemination	Poorer	Pickup et al., 2014; Kai et al., 2019
	Mesenchymal Stem Cells recruitment to TME	Either depending on TME	Trivanovic et al., 2016; Rivera-Cruz et al., 2017
	CAF differentiation through inflammation and TGF-β	Poorer	Liu T. et al., 2019; Sanford-Crane et al., 2019; Yoshida et al., 2019
Desmoplasia	Induction of EMT and the formation of Cancer Stem Cells	Poorer	Kang et al., 2019; Pearson, 2019; Vahidian et al., 2019
	Activation of MMPs in EMT	Poorer	Yao et al., 2018
Exosomes	Autocrine and paracrine communications between tumor cells and TME	Poorer	Hannafon and Ding, 2013; Franzen et al., 2014; Roma-Rodrigues et al., 2014, 2017a
	Autocrine and paracrine communications between normal cells and TME	Better	Hannafon and Ding, 2013; Franzen et al., 2014; Roma-Rodrigues et al., 2014, 2017a

HIF, hypoxia induced factor; TME, tumor microenvironment; VEGF, vascular endothelial growth factor; LECS, lymphatic endothelial cells; IFN, interferon; TAM, tumor associated macrophages; IL, interleukin; TGF, tumor growth factor; GM-CSF, granulocyte-macrophage colony stimulating factor; NK, natural killer; MDSCs, myeloid-derived suppressive cells; CAF, cancer associated fibroblasts; EMT, epithelial to mesenchymal transition.

cytotoxic lymphocytes, natural killer (NK) cells and NKT cells contribute for an immunostimulant TME (DeNardo et al., 2010; Hui and Chen, 2015; Labiano et al., 2015; Wu, 2017; Steven and Seliger, 2018). In different types of cancers, the increased expression of GM-CSF and VEGF induce the production of myeloid-derived suppressive cells (MDSCs) at the bone

marrow that are recruited to the TME where they remain undifferentiated (reviewed in Bruno et al., 2019). The presence of MDSCs is generally correlated with a poor prognosis, as they are involved in angiogenesis, and suppression of NK cells and CD8+ cytotoxic T cells (Schupp et al., 2017; Bruno et al., 2019).

In epithelial cancers, growing tumor cells and TME cell components are supported in an ECM with altered biochemical and biomechanical properties when compared with healthy tissue (reviewed in Pickup et al., 2014; Kai et al., 2019). The low oxygenation and inflammatory environment induce alterations in ECM proteins that result in desmoplasia, characterized by increased stiffness (Pickup et al., 2014; Kai et al., 2019). The ECM major contributors for desmoplasia include collagen types I, III, and IV, fibronectin, laminin, hyaluronic acid (HA) and osteonectin (Whatcott et al., 2011).

Stromal cells are also important for tumor development and prognosis. Mesenchymal stromal cells (MSCs) are recruited to the tumor due to the inflammatory environment and, according to the chemical composition at the TME they may promote or inhibit the tumor progression (reviewed in Trivanovic et al., 2016; Rivera-Cruz et al., 2017). Moreover, the inflammation and consequent secretion of TGF-β at the TME, induce the differentiation of fibroblasts into cancer associated fibroblasts (CAFs) (reviewed in Liu T. et al., 2019; Sanford-Crane et al., 2019; Yoshida et al., 2019). Besides tumor cells, CAFs are the most abundant cell type at the TME and play an important role in increased desmoplasia of the TME (Liu T. et al., 2019; Sanford-Crane et al., 2019; Yoshida et al., 2019).

Hypoxia, increased desmoplasia and the interactions between the several TME players favor the epithelial-to-mesenchymal transition (EMT) of tumor cells resulting in the formation of cancer stem cells (CSC) (reviewed in Kang et al., 2019; Pearson, 2019; Vahidian et al., 2019). EMT results in disruption of intracellular adhesion and loss of cell polarity, conferring migratory ability to CSC that could enter in adjacent blood or lymph vessels at the TME and travel to another anatomical location where they can experience mesenchymal-to-epithelial transition (MET) and potentiate the formation of a metastatic niche (Kang et al., 2019; Pearson, 2019; Vahidian et al., 2019). Matrix metalloproteinases (MMPs) have an important role in EMT, being responsible for the detachment of tumor cells from the ECM promoting CSC formation (Yao et al., 2018).

During the initial stages of tumorigenesis, the genomic profile of tumor cells determines the tumor maturation. As the cancer progresses, the intercellular communication between tumor and neighboring cells dictates TME and tumor progression, contributing for intra- and inter-tumor heterogeneity (Hanahan and Weinberg, 2011; Netea-Maier et al., 2018). Exosomes are pivotal for the cell to cell communication. Exosomes are endosomal pathway derived vesicles with 30–100 nm diameter, composed by a lipid bilayer with membrane proteins, entrapping soluble proteins, signaling molecules, including cytokines, chemokines and growth factors, and nucleic acids including mRNA and miRNA (Roma-Rodrigues et al., 2014). Importantly, exosomes' content depends on the cell of origin, often reflecting the physiological condition of the cell (Hannafon and Ding, 2013). After released to the extracellular milieu, exosomes can

be internalized by secondary cells adjacent to the primary cell or travel through the vascular or lymphatic system to other anatomical location where they can be internalized by local cells. Once internalized, exosomes are able to modify the phenotype of the recipient cell that will adjust to the incoming signals (Franzen et al., 2014; Roma-Rodrigues et al., 2017a). Tumor cells derived exosomes (TCDEs) have an important role in tumor progression, including for example in immune system modulation, contributing in normal to tumoral transition of adjacent cells and preparation of the metastatic niche at a new anatomical location (Chen et al., 2017; Roma-Rodrigues et al., 2017a).

As discussed, TME development is astonishingly similar between types of cancer, exhibiting several common features in composition and organization. However, TME features are also highly dependent on tissue/organ. For example, hematological cancers will show an increased angiogenesis at the TME site in the bone marrow (reviewed in Cheng et al., 2018).

Notwithstanding the growing awareness of the role played by the TME in tumorigenesis, tumor progression and metastasis in the organism, most studies rely on *in vitro* data to build models, simulate conditions, and for the screening of novel drugs. What is more, most of these screenings and assessments are made using traditional cell lines that only resemble the real tumor in the individuals, letting the whole of intra- and inter-tumor heterogeneity at large. One of the most relevant trends in studying the effect novel diagnostics and therapeutic strategies for cancer has prompt for the development of realistic *in vitro* and *ex vivo* models to substitute the expensive and variable *in vivo* studies, thus allowing to speed up research in this critical field.

MODELING THE TME

Despite the amount of data from conventional *in vitro* models that rely on two-dimensional (2D) cell cultures, solid tumors are three-dimensional (3D) entities with cells growing on heterogenous gradients of nutrients and oxygen, suffering from various degrees of different chemical and physical stresses and interacting with different types of cells (LaBarbera et al., 2012; Weiswald et al., 2015). Therefore, promising drugs need to be tested in pre-clinical models mimicking the TME, and recurring to murine models with tumor xenografts, before they can get approval for human trials (Ranga et al., 2014). This is an expensive process that often fails to accurately predict therapeutic responses due to the fundamental differences between animal and human physiology. Only 5% of the compounds deemed promising in the initial evaluations are successful in clinical applications, which highlights the shortcomings of common standard models used for routine drug screening (LaBarbera et al., 2012; Ranga et al., 2014).

For assisting faster and more robust clinical translation, several (cell) models have been proposed. For example, humanized mice (HM) have been increasingly used to reduce the gap between animal and humans. HM are genetically engineered mice with human genes or human cells alongside the tumor xenografts (Morton et al., 2016). Another increasingly used pre-clinical model is patient derived xenografts (PDX) (Hidalgo

et al., 2014). Mice xenografts produced directly from tumor biopsies can be used to more accurately predict how patients will respond to treatment and opens the door to personalized therapeutics (Hidalgo et al., 2014). However, these animal models are too expensive for high throughput screening (HTS) of novel drugs or treatment vectorizations (Rodrigues et al., 2018; Sasmita and Wong, 2018). For a long time, HTS has strongly depended on primary screening made with 2D cultures whose physiological and TME associated limitations have been surpassed by the advent of 3D cell culture models. For instance, cellular signal transduction pathways have been shown not to properly be activated in 2D cultures. Moreover, sensitivity to chemotherapeutic agents and induction of apoptosis are impaired in cell lines grown in 2D monolayers due to the lack of cell-cell and cell-extracellular matrix interactions, that are present in tissues and in 3D models (Kenny et al., 2007; Serebriiskii et al., 2008; Yin et al., 2016; Reynolds et al., 2017; Riedl et al., 2017; Buzzelli et al., 2018). Also, these models made possible the study of angiogenesis within a tumor and the evaluate the importance of the immune system in tumor growth (LaBarbera et al., 2012; Ranga et al., 2014; Buzzelli et al., 2018).

The simplest 3D model are multicellular tumor spheroids, or simply spheroids, obtained when adherent cell lines are grown in non-adherent conditions. The cells form 3D structures similar to *in vivo* tumors and are capable to recapitulate the TME interactions that are crucial for *in vivo* development (Sutherland et al., 1971; LaBarbera et al., 2012; Lancaster and Knoblich, 2014; Ranga et al., 2014). At first, spheroids were grown with only one cell line, however the complex nature of solid tumors led to the development of more intricate systems, with two or more different cell types, and thus able to mimic ECM, inter-cellular signaling and *in vivo* growth (LaBarbera et al., 2012). These more complex spheroids, with at least one tumor cell type, have been called organoids. Although the term was originally developed for spheroids grown from stem cells or organ progenitor cells, that would grow and differentiate into different cell types resulting in a spheroid with spatial auto-organization of different cell types similarly to the organization found *in vivo* for the organ from which they derive (Sung et al., 2008; LaBarbera et al., 2012; Lancaster and Knoblich, 2014). Considering that, in this filed, terminology is not consensual, we shall name spheroids to those multicellular spheroids constituted with only one cell type; multitype spheroids with at least one tumor cell line/type will be named tumor organoids, while the others will be named normal-type organoids.

In order to devise 3D systems that more accurately reflect the molecular diversity of tumors and their respective TME, there was a need for protocols to promote the growth of spheroids and/or tumor organoids derived from cancer biopsies from patients (Song et al., 2018; Vlachogiannis et al., 2018). These patient derived tumor organoids are capable to recapitulate the molecular profile of the patients' tumors and have become a valuable platform for HTS of compounds and for personalization of therapy (van de Wetering et al., 2015; Vlachogiannis et al., 2018). For example, AuNP have already been tested in some of the novel systems constituted by A549, HEG2, S2PV10, HCT116, and MCF7 cancer line spheroids so as to evaluate NP penetration within the tridimensional structure (Huang et al., 2012; England et al., 2013; Rane and Armani, 2016). Also, the potential photothermal therapy effectiveness of AuNPs have been evaluated on HeLa, normal ovarian cells, and human umbilical vein endothelial cells (HUVEC) spheroids, and in HeLa tumor organoids (Lee et al., 2018). Additionally, normal-type organoids have been used to test potential nephrotoxicity of AuNPs (Astashkina et al., 2014).

To further narrow the gap between *in vitro* and *in vivo* models, great efforts have been made to use microfluids platforms to reproduce more accurately TME and normal tissue functions, originating tissue-on-chip and organ-on-chip systems. The first organ-on-a-chip models (OoC) presented cells capable to replicate the physiological functions of the lung and heart within a microfluidic device with appropriate channels, chambers and mechanic movement (Huh et al., 2010; Annabi et al., 2013). The combination of different cell types, from liver and skin, within a multi-organ-chip, proved their potential in therapeutic drug testing (Wagner et al., 2013). The use of cancer cell lines on microfluidic devices led to the construction of tumor-on-a-chip models (ToC), also called cancer-on-a-chip. These systems have been shown to accurately mimic several features observed in tumors, such as pressure, chemical and gas gradients and fluidic shear stress, while being more amenable to HTS than other previous 2D and 3D models (Bhatia and Ingber, 2014; Tsai et al., 2017; Sleeboom et al., 2018; Shang et al., 2019). These ToC have been successfully used to co-culture cancer cells with endothelial cells, thus facilitating the study of the interplay in the TME between vasculature and tumor cells (Sleeboom et al., 2018; Shang et al., 2019). Also, these chip-based platforms have been used to assess nanoparticles' fate and action in more complex models. For example, AuNPs have been tested in an OoC with HUVEC to evaluate how endothelial thermotolerance could affect nanoparticle transport to tumors (Bagley et al., 2015). ToCs incorporating spheroids of MDA-MB-453 and MCF-7 cells were used to study tissue penetration and cellular uptake of AuNPs (Albanese et al., 2013; Kwak et al., 2014). Deeper insights into the EPR effect have also been possible via a tumor-vasculature-on-a-chip developed to study the perfusion of nanoparticles in an *in vitro* model (Wang H. F. et al., 2018).

It is based on these developing 3D complex models, harboring different players from within the TME, that several nanomedicines have been tested and evaluated, aiming at eventually being translated to the clinics and providing additional tools for the fight against cancer. Not surprisingly, these complex 3D and chip models have been crucial for the evaluation of innovative approaches in tacking the TME, which, whole or in part, make use of the one or more of the elements within the TME that modulate tumor growth and development.

TARGETING TME VIA GOLD NANOPARTICLES

Several types of nanomaterials, and nanoparticles in particular, have been proposed as tools to study and/or assist in the fight against cancer. Amongst these nanoparticles, gold has emerged

as a material of choice due to their spectral properties, ease of synthesis and functionalization. Additionally, small (15–60 nm) spherical AuNPs has not been shown to exhibit toxicity, which has prompt for their use as valuable platforms for diagnostics (e.g., imaging) and therapy. The interaction between AuNPs and the TME is, thus, of crucial relevance toward the development of innovative efficacious nanomedicines that could tackle tumors alone or in combinatory approaches with more traditional therapies. **Table 2** summarizes the specific characteristics of the TME to be targeted by AuNPs for diagnostic and/or therapy in cancer.

Tackling the Acidic pH in the TME

Several features of TME can be used to target nanomedicines to the tumor site for improved diagnosis and/or therapy. For example, the acidic microenvironment may be used to trigger responsive nanomedicines that release the cargo upon pH stimuli. In this respect, citraconic amides are moieties sensitive to pH, being hydrolyzed and converted in positively charged primary amines that are suitable to act as pH switches. Interaction with positive and negative charged nanoparticles cause nanoparticle aggregation that could be used for photoacoustic imaging, amplifying the signal and blocking exocytosis. Nanosystems using the aggregation of AuNPs induced by citraconic amides have been used as a diagnostic tool (Song et al., 2016; Li et al., 2019). Song et al. (2016) showed that an agent containing these amides coupled to AuNPs accumulates specifically in cancer cells, leading to an *in vivo* signal amplification that is the double of that non-functionalized NPs (Song et al., 2016). Additional functionalization may be added to the nanoplatform to also carry a suitable chemotherapeutic drug, resulting in a theranostic agent (Song et al., 2016). Li et al. (2019) created AuNPs functionalized with 4-(2-(5-(1,2-dithiolan-3-yl)pentanamido)ethylamino)-2methyl-4-oxobut-2-enoic acid (LSC) that contain the citraconic amide moiety and a cyclic RGDyK peptide conjugated with 16-mercaptohexadecanoic acid (c(RGDyK)MHDA) that allows the active tumor-targeting due to the connection to overexpressed integrin $\alpha v \beta 3$ receptors (Li et al., 2019). Using a tumor-xenograft mouse model, the conjugated molecules, LSC and c(RGDyK), allowed for longer circulation times and enhanced accumulation at the tumoral tissue, which then provided for optimized photoacoustic signals at low concentration. Similar approaches using fluorescence imaging (FL imaging) activated in the TME due to the pH-sensitive structures have also been proposed to assist diagnostics and biodistribution assessment (Lai et al., 2017; Tang et al., 2019).

A similar rational has been used to enhance the efficacy of photodynamic therapy (PDT) and photothermal therapy (PTT). Liu et al. (2018b) used mesoporous silica coated gold nanorods (AuNR@MSN) with 2,3-dimethylmaleic anhydride (DMA)-modified chitosan oligosaccharide-block -poly (ethylene glycol) polymer (CS(DMA)-PEG) as a pH sensitive polymer. In presence of acidic pH, the amide bonds between CS and DMA are broken and the RLA ([RLARLAR]2) peptide is exposed to facilitate cellular internalization and mitochondrial accumulation. In addition, AuNR@MSM is also loaded with

indocyanine green (ICG), a photosensitizer. Since the pH trigger allows for tumor targeting and selective internalization, upon laser irradiation both therapeutic approaches are active: (i) PDT triggers the production of ROS that will hamper cell viability; and (ii) PTT leads to heat generation that kills cancer cells in a selective way. The combination of these two approaches allows an enhanced therapeutic effect and lower side effects due to the guided TME accumulation (Liu et al., 2018b). Other have developed a system relying on self-assembly AuNPs through dithiol-polyethylene glycol (HS-PEG-SH) molecules that allow NP cross-linking. AuNPs are functionalized also with Doxorubicin (DOX), bonded through the hydrazone-thiol group, and an epidermal growth factor (EGF) peptide to act as an active targeting moiety to cancer cells overexpressing the EGF receptor. Once in the TME, the acidic and redox environment disassembles the complexes, and hydrolysis of the hydrazone bonds release the DOX. Using an *in vivo* mouse model the self-assembled AuNPs presented an increased accumulation at the TME when compared to solo AuNPs (Feng et al., 2017).

pH induced aggregation of metal nanoparticles may also be used to enhance the efficacy of photothermal therapy (Li et al., 2014; Dai et al., 2015). Similar to the concept described above, Jung et al. (2013) used citraconic amide moieties to trigger NP aggregation when within the acidic TME that leads to the creation of hot spots for surface-enhanced Raman scattering (SERS) imaging and shifts the absorption to the near infrared (NIR) for concomitant PTT (Jung et al., 2013). Another strategy that is based on TME induced NP aggregation was assayed for simultaneous photoacoustic imaging (PAI) and PTT (Yu et al., 2017). In this work, two types of AuNPs coated with complementary single-strand DNA containing at the pyridine-2-imine end an α-cyclodextrin (α-CD) were used. The acidic TME leads to the protonation of pyridine-2-imine triggering separation of the α-CD and allows aggregation of AuNPs due to complementary base pairing. Aggregation also favors the retention of AuNP at the TME, which can then be used for selective intratumoral PAI and PTT (Yu et al., 2017). Another approach based on the pH within the TME combined PDT and a set of imaging techniques: fluorescence, PAI, and magnetic resonance imaging (MRI) using core-shell gold nanocages@manganese dioxide (AuNC@MnO$_2$) (Liang et al., 2018). The acidic TME triggers degradation of the MnO$_2$ shell, releasing O$_2$ and Mn^{2+}, which causes an enrichment of the environment (including the hypoxic parts) with O$_2$, thus potentiating the PDT. Upon irradiation, the presence of O$_2$, Mn^{2+} and the AuNC itself allows for concomitant use of PDT, PAI, MRI, and FL imaging, in what is a multifunctional nanotheranostics. Besides the effective production of ROS due to the PDT that causes cell death, the events unleashed via this approach cause immunogenic cell death through the damage-associated molecular patterns (DAMPs) liberation and, consequently, dendritic cells maturation, which leads to effector cells activation (e.g., CD8 T cells, CD4 T cells, and NK cells). Once again, the response to the pH stimulus permits selective TME targeting, improving efficacy while decreasing undesired deleterious effects to neighboring healthy tissues.

TABLE 2 | Targeting strategies for AuNPs toward TME.

System name	Nanoparticle (type)	TME component	Diagnostics	Therapeutics	3D in vitro/in vivo model	References
"Smart" AuNPs (SANs)	AuNP	Acidic pH	PAI		Xenograft mouse model	Song et al., 2016
c(RGDyK)-MHDA/LSC@AuNP	AuNP	Acidic pH	PAI		Xenograft mouse model	Li et al., 2019
LGAuNP	AuNP	Acidic pH	FLimaging		Xenograft mouse model	Lai et al., 2017
GNPs-CKL-FA	AuNP	Acidic pH	FLimaging		Xenograft bearing mice model	Tang et al., 2019
AuNR@MSN-RLA/CS(DMA)-PEG	AuNR	Acidic pH		PDT; PTT	Xenograft bearing mice model	Liu et al., 2018b
DOX-EGF-SA-AuNP	AuNP	Acidic pH		DD	Xenograft mouse model	Feng et al., 2017
MC-GNPs	AuNP	Acidic pH		PTT		Li et al., 2014
pH-GSNPs	Gold Shell nanoparticles	Acidic pH		PTT; DD		Dai et al., 2015
MBA/SMART-AuNP	AuNP	Acidic pH	SERS imaging	PTT		Jung et al., 2013
Gold nanomachines	AuNP	Acidic pH	PAI	PTT	Xenograft mouse model	Yu et al., 2017
AuNC@MnO2	AuNC	Acidic pH; Hypoxia; Immunosuppressive tumor microenvironment	FL imaging; PAI; MRI	PDT	Xenograft mouse model	Liang et al., 2018
V7-CMG	AuNR	Acidic pH	MSOT	DD	Xenograft mouse model	Zeiderman et al., 2016
Nanoprobe	AuNP	MMP-2; MMP-7	FLimaging			Wang et al., 2012
MMP-sensitive AuNP probe	AuNP	MMP	NIRF tomographic imaging		Xenograft mouse model	Lee et al., 2008
MMP-GC-AuNPs	AuNP	MMP	CT; FLimaging		Xenograft bearing mice model	Sun et al., 2011
G-AuNPs-DOX-PEG	AuNP	MMP-2 Acidic pH		DD	Xenograft bearing mice model	Ruan et al., 2015a
DOX-GLT/EGCG AuNPs	AuNP	MMP	FLimaging	DD		Tsai et al., 2016
G-AuNPs-DC-RRGD	AuNP	MMP-2; Acidic pH	FLimaging	DD	Xenograft bearing mice model; Spheroid	Ruan et al., 2015b
DOX-substrate/AuNP	AuNP	MMP-2	FLimaging	DD	Xenograft bearing mice model	Chen et al., 2013
CDGM NPs	GNC	MMP-2; Acidic pH	FLimaging	PDT; DD	Xenograft bearing mice model	Xia et al., 2018
Au@BSA-NHA	AuNP	Hypoxia	CT		Xenograft bearing mice model	Shi et al., 2016
Au-PCM-AlDH	AuNC	Hypoxia		PTT; Free Radicals		Shen et al., 2017
DOX-HZN-DTDP @ Au NPs-LA-PEG2000-CAI	AuNP	Hypoxia Acidic pH		DD	Spheroid	Shabana et al., 2018

AuNP, spherical gold nanoparticles; AuNR, gold nanorods; AuNC, gold nanocages; SERS imaging, Surface-enhanced Raman scattering imaging; PTT, photothermal therapy; FLimaging, Fluorescence imaging; MRI, magnetic resonance imaging; PAI, photoacoustic imaging, PDT, photodynamic therapy; MMP, matrix metalloproteinases; MMP-2, matrix metalloproteinases; NIRF tomografic imaging, near infrared fluorescence imaging; CT, computed tomography; DD, drug delivery; DOX, doxorubicin; PCM, phase-change material.

Gold nanorods (AuNR) coated with mesoporous silica capped with chitosan have been used as PAI contrast agent for Multispectral Optoacoustic Tomography (MSOT) after NIR excitation (Zeiderman et al., 2016). For active targeting, these nanoconjugates were grafted with a pH sensitive variant 7 pHLIP peptide that allows specific accumulation at the tumor site. These AuNRs may also convey a cargo of chemotherapy (gemcitabine, a pyrimidine analog), where the TME acidic pH protonates the amino groups of chitosan, causing chitosan swelling (proton sponge) with consequent gemcitabine dissociation and release from the mesoporous silica (Zeiderman et al., 2016).

The Case for the Matrix Metalloproteinases (MMP)

The increased expression of MMPs have an important role in tumor progression and the substrate of these proteinases can be used to selectively target nanomedicines to the TME. For example, these substrates conjugated to dyes coupled to AuNPs have been used as probes for imaging of cancer sites toward diagnostic applications (Wang et al., 2012). Since MMP-2 and MMP-7 are overexpressed in multiple tumors, the authors designed AuNPs functionalized with a peptide spacer that contains an MMP-2 substrate (Gly-Pro-Leu-Gly-Val-Arg-Gly) and an MMP-7 substrate

(Val-Pro-Leu-Ser-Leu-Thr-Met-Gly). The N-terminus of the peptide has attached to a lanthanide complex, BCTOT-EuIII (BCTOT=1,10-bis(5′-chlorosulfo-thiophene-2′-yl)-4,4,5,5,6,6,7,7-octafluorodecane1,3,8,10-tetraone) and the C-terminus has attached to a 7-amino-4-methylcoumarin (AMC), which may be hydrolyzed by one or both MMPs within the TME, and fluorescence emission of dyes occurs. This results in differences in fluorescence emission between cancer and normal cells that may be used for imaging (Wang et al., 2012). Lee et al. (2008) functionalized AuNPs with Cy5.5 dye attached to a peptide (Gly-Pro-Leu-Gly-Val-Arg-Gly-Cys) that contains the substrate for MMP (Pro-LeuGly-Val-Arg). Once in the TME, the substrate is recognized and cleaved by the proteases, causing dequenching of the dye and the near infrared fluorescence (NIRF) signal may be assessed via NIRF tomographic imaging (Lee et al., 2008). Sun et al. (2011) also used Cy5.5 dye linked to the same substrate for MMP but in a different peptide to develop a computed tomography (CT) contrast probe that may simultaneously be assessed by NIRF. The AuNPs were coupled with glycol chitosan polymers, which have shown excellent stability and tumor targeting ability by EPR, and an organic dark quencher. Upon MNP proteolysis, the dye is released and NIR fluorescence emission may be detected. As such, it is possible to obtain CT and NIRF images to provide anatomical and MMP-dependent biological data of the TME (Sun et al., 2011).

Gelatin is another substrate for MMP, particularly for MPP-2. Ruan et al. created a system for drug delivery relying on a gelatin nanoparticle decorated with small AuNPs (Ruan et al., 2015b). The AuNP surface is loaded with DOX linked by hydrazone bonds that are hydrolyzed when in the acidic TME medium. When the G-AuNPs-DOX-PEG nanoconjugate reaches the TME, the gelatin nanoparticles are degraded by the MPP-2, and the AuNPs-DOX-PEG released into the microenvironment. Once free, these smaller nanocarriers may reach deeper into the tumor and, due to the acidic microenvironment, DOX is released leading to a more efficacious anti-tumor effect. In another study, the same system was improved by addition of two components: a tandem peptide, RRGD, and Cy5.5 dye attached by hydrazone bonds to the AuNPs' surface. The RRGD peptide allows the active targeting to overexpressed integrin αvβ3 receptor and enhances the penetration capability of the system. The Cy5.5 is release together with DOX by hydrolyze of the hydrazone bonds in the acidic TME, permitting the visualization via fluorescence imaging. The released small AuNPs are capable of deeper tissue penetration, leading to accumulation at the target and colocalization of Cy5.5 and DOX, in what can be considered a two-stage multifunctional nanotheranostics system (Ruan et al., 2015a).

Relying on the fluorescence emission of DOX, Chen and co-workers developed a nanotheranostics system using AuNPs with DOX attached to the surface via a protease substrate (Ac-Cys-Pro-Leu-Gly-Leu-Ala-Gly-Gly-DOX) (Chen et al., 2013). Within the TME, MMP-2 cleaves the ligation and DOX is released, exerting its cytotoxic effect while proving for fluorescence imaging selectively within the TME. Another nanotheranostics system combining two therapeutic modalities, PDT and chemotherapy, coupled to fluorescence imaging

has been developed using gold nanoclusters conjugated with an MMP-2 substrate (Cys-Pro-Leu-Gly-Val-Arg-Gly-Arg-Gly-Asp-Ser), and DOX bonded to cis-aconitic anhydride and a photosensitizer chlorin e6 (Ce6) (Xia et al., 2018). The MMP-2 substrate acts as active targeting to the TME due to the overexpression of metalloproteinases and the cis-aconityl linkage allows for controlled release of DOX on site due to the tumor acidic hydrolyzed of the bonds. The photosensitizer allows for PDT and imaging through fluorescence. The effect of this nanoconjugate in tumor-bearing mice show great promise, showing an enhanced anti-tumor effect when compared to free DOX and AuNPs without the MMP-2 substrate.

Impact of ECM Components

The increased desmoplasia that frequently occur at the TME may result in poor distribution of AuNPs inside the tumor (Whilhelm et al., 2016). In an attempt of improving drug delivery into the tumor, Abdolahinia et al. analyzed the effect of AuNPs conjugated with collagenase (Col-AuNPs) combined with AuNPs conjugated with metformin (MET-AuNPs). They observed an increased number of apoptotic cells in breast cancer spheroids when simultaneously treated with Col-AuNPs and MET-AuNPs, suggesting increased AuNPs penetration in the spheroid (Abdolahinia et al., 2019). In another interesting study, Han et al. developed gold nanoparticles coated with PEGylated polyethylenimine and conjugated with all-trans retinoic acid (ATRA) and siRNA targeting heat shock protein 47 (HSP47) envisaging the activation of pancreatic stellate cells (PSC). With this pH responsive nanosystem, they were able to induce PSC quiescence (through ATRA) and inhibit ECM desmoplasia (through silencing of HSP47, a collagen-specific molecular chaperone) (Han et al., 2018). Interestingly, a study performed by Zhao et al. revealed that naked AuNPs were effective in decreasing the TME desmoplasia of colorectal cancer xerograft mice, by reducing the production of collagen I and diminishing the expression of profibrotic signals (Zhao et al., 2018).

Hyaluronic acid, a linear anionic polymer found in the connective, epithelial, and neural tissues has been widely used in the clinics for arthritis treatment, ophthalmic surgery, tissue engineering, and even drug delivery (Oh et al., 2010; Kim et al., 2019). Due to the presence of carboxylic acid, hydroxyl and N-acetyl groups, HA is easily combined with other chemicals. Moreover, the selective transfer of HA to the tumor location due to EPR effect, coupled to its connection with TME cellular receptors, including cluster determinant CD44, receptor for HA-mediated motility (RHAMM), and lymphatic vessel endothelial receptor-1 (LYVE-1), makes this molecule suitable for improving targeted nanomedicine (reviewed in Kim et al., 2019 and references therein). More recent reports describe the production of nanoconjugates for combined photothermal therapy (Liu R. et al., 2019; Yang et al., 2019). Liu et al. proposed to use cationic small sized red emission gold nanoclusters coated with BSA and conjugated with indocyanine green as imaging probe for theranostic and HA for increased retention at the tumor location (AuNC@CBSA-ICG@HA) (Liu R. et al., 2019). An in vivo study using mice breast cancer model revealed a suppression of 95% of tumor growth (Liu R. et al., 2019). Yang et al. proposed a

nanotheranostics platform based on gold nanoclusters combined with graphene oxide and conjugated with HA, 5-fluorouracil. The enzymatic degradation of HA at the TME by the hyaluronidases allow the release of 5-fluorouracil, that, together with laser irradiation, enhance the anti-tumor efficacy (Yang et al., 2019).

Making Use of Hypoxia for Selective Targeting to the TME

The hypoxic TME has an active role in tumorigenesis and has been shown to be a crucial factor in the lack of response to some therapies and cancer drug resistance. As such, it may be considered both as a critical element for selective action within the TME and as an important target for therapy and diagnostics. For example, Shi and co-workers presented a gold nanoprobe for CT imaging responsive to hypoxia through the conjugation of nitroimidazole moiety to AuNPs (Shi et al., 2016). Under hypoxia, the nitro group of nitroimidazole is reduced by nitroreductase, an enzyme present at elevated levels in the TME, and the resultant reactive amide group will bind to macromolecules within the TME leading to on site accumulation. The AuNPs are coated with bovine serum albumin (BSA) for increased colloidal stability, water solubility and biocompatibility. This technique enhances the contrast attained in CT imaging allowing for visualization of different intratumoral hypoxic levels which can be helpful to disease prognosis. Others have used AuNCs loaded with 2,2′-azobis[2-(2-imidazolin-2-yl) propane] dihydrochloride (AIPH) coated by a phase-change material, which allows the hypoxic cancer cells death through the oxygen independent production of free-radicals (Shen et al., 2017). After NIR irradiation, the photothermal effect of AuNC triggers the melting of the coating and, consequent AIPH release. Once free, AIPH decomposes due to thermal/irradiation stimulation and alkyl radicals are generated, that in turn cause oxidation of cell components oxidation and increased lipid hydroperoxides, which will induce apoptosis. This concept allows for the destruction of cells in hypoxic tumors and can be applied in combination with photothermal therapy. Shabana et al. took advantage of carbonic anhydrase IX (CA IX) overexpression that occurs in hypoxic TME to develop AuNPs functionalized with DOX and a CA inhibitor ligand, that allows active targeting to hypoxic tumors (Shabana et al., 2018). DOX is grafted to the NPs through a hydrazone group that is cleaved in acidic pH, releasing the drug. This way, it is possible to selectively target the TME to tackle the hypoxia-induced chemoresistance with improved tumor penetration of the drug.

Synergistic Approach With the TME Immune System

Immune cells in the TME play an important role in tumor surveillance and development. The immune system behaves differently within the TME and its differential modulation also modifies the TME itself and can thus be used to improve therapy. Some strategies have been described that use AuNPs to modulate the immune system in the TME. For instance, AuNPs coated with mouse serum albumin (MSA) induce the production of ROS and reactive nitrogen species (RNS) that activate pro-inflammatory

pathways in TAMs (Pal et al., 2016). As a consequence, the production of TNF-α and IL-10 is decreased and the production of the pro-inflammatory cytokine IL-12 increased. These changes triggered by AuNPs lead to a polarization of TAMs from an M2 phenotype to an M1 phenotype (pro-inflammatory). These changes in TAMs were also observed for a gold-manganese oxide nanocomposite stabilized with MSA, where the manganese oxide permits the enhancement of magnetic resonance of the agent and, as a result, allows its use as a contrast agent in magnetic resonance imaging (MRI). In another approach, AuNPs functionalized with tumor necrosis factor-related apoptosis-inducing ligand (TRAIL) that belongs to tumor necrosis factor (TNF) superfamily have also been used to actively target M2 macrophages within the TME (Huang and Hsu, 2017). The AuNPs bind to M2 macrophages due to the binding of TRAIL to the cell surface death receptor 4 (DR4) and death receptor 5 (DR5), which activates a caspase-dependent extrinsic apoptosis pathway and, consequently, cancer cell death in a specific way. AuNPs have also been used as a carrier for tumor-associated self-antigens that elicit the maturation of dendritic cells and T cells proliferation (Ahn et al., 2014; Fogli et al., 2017). Also, galactofuranose-coated AuNPs demonstrated the capability to stimulate the maturation of dendritic cells and, thus, promote a pro-inflammatory response (Chiodo et al., 2014). The modulation of TAMs, dendritic cells and T cells indicate to be suitable strategies to modulate the immune response within the TME against cancer cells so as to hamper tumor progression.

Addressing Angiogenesis

The growth of new blood vessels from preexisting vessels is essential for tumor expansion and to modulate TME, increasing the levels of oxygen, nutrients, and decreasing toxic metabolites (De Palma et al., 2017). In this respect, AuNPs have been shown to be capable not only to disrupt signal transduction from tumor mesenchymal cells to epithelial cells, but also to inhibit angiogenic phenotypes *in vitro* (Zhang Y. et al., 2019). Among the various VEGF subtypes, isoform VEGF165 is a heparin binding protein and perhaps the most potent cytokine in angiogenic process (Mukherjee et al., 2005; Arvizo et al., 2011). By binding to tyrosine kinase receptor VEGFR-2, a signal cascade is initiated, ultimately leading to the proliferation and migration of endothelial cells and resulting in angiogenesis. As such, therapeutic antibodies targeting VEGF165 have been developed and are currently applied in the clinics to inhibit the VEGF165 cascade activation (Ferrara and Kerbel, 2005). Also, non-functionalized AuNPs are capable to inhibit of pro-angiogenic heparin-binding growth factors (HB-GFs), such as VEGF165, basic fibroblast growth factors (bFGFs), and placental growth factor (PlGF) (Ferrara and Kerbel, 2005). The surface of AuNPs inhibits HB-GFs by inducing changes in conformation but, remarkably, AuNPs do not affect the activity of non-HB-GFs, such as VEGF121 and EGF. These observations have been corroborated *in vivo*, where VEGF/vascular permeability factor (VPF) stimulated permeability was inhibited by AuNPs (Mukherjee et al., 2005; Arvizo et al., 2011). AuNPs may also influence angiogenesis by diminishing the tube formation and the migration of endothelial cells through blockage of the VEGF-VEGFR2 signaling in TME cells (Zhang Y. et al., 2019). What

is more, AuNPs have been able to promote tumor vasculature normalization while increasing blood perfusion and reducing hypoxia (Li et al., 2017).

Not only "naked" AuNPs but also AuNP-conjugates have been used as modulators of angiogenesis. Recombinant human endostatin is an anti-angiogenic agent used for tumor treatment that has been coupled to AuNPs to reduce cell migration and tube formation in vitro (HUVECs), induced by anterior gradient 2 (AGR2) (Pan et al., 2017). AGR2 is one of the latent tumor angiogenesis factors, which has been mostly related to tumor cell proliferation, transformation, migration and drug resistance. In vivo metastatic colorectal cancer xenografts have shown that recombinant human endostatin–AuNP are capable to increase pericyte expression while inhibiting VEGFR2 and anterior gradient 2. As such, these nanoconjugates might be used to normalize tumor vessels using AGR2 as an anti-angiogenic tumor target. Additional work by the Kanaras group has demonstrated the enhanced effect of peptides, designed to selectively interact with VEGFR1, for inhibition of angiogenesis when grafted onto AuNPs (Bartczak et al., 2013, 2015; Millar and Kanaras, 2013). This gold-nanoconjugates can influence the extent and morphology of vascular structures, without causing toxicity (Bartczak et al., 2013, 2015; Millar and Kanaras, 2013). By exposing a chicken chorioallantoic membrane to the same AuNP-peptide, the same effect was observed in vivo (Roma-Rodrigues et al., 2016), but could be tremendously enhanced by irradiating the nanoformulation with a green laser, which simultaneously allowed to cauterize emerging blood vessels with extreme spatial precision, and prevented neo-vascularization (Pedrosa et al., 2017). These studies highlighted the role of the VEGFR1 dependent pathways in the process, which were downregulated by the nanoformulation with and without irradiation (Pedrosa et al., 2017). These studies show that AuNPs can be used to alter the expression of anti-angiogenic factors, under biological conditions, and may be a valuable tool to tackle the angiogenesis within the TME.

The Role for TME Derived Exosomes

The role of exosomes in TME maturation combined with their stability in body fluids, have made these nanovesicles as promising agents in cancer management. There have been several studies reporting on the use of AuNPs for therapy and diagnostics (nanotheranostics) (see Roma-Rodrigues et al., 2017b for extended discussion). The developmental and metabolic state of each cell is reflected on exosome production, trafficking and the exosomes' own content. What is more, after entering the circulatory system, TME derived exosomes have been proposed as valuable cancer biomarkers, particularly when referring the use of liquid biopsies. Nevertheless, the direct diagnostics using exosomes, is hampered by the low concentration of circulating tumor cells derived exosomes (TCDEs) in the initial stages of tumor progression. As such, Huang and co-workers designed a dual-signal amplification platform for detection of exosomes derived from leukemia cells (Huang et al., 2018). The detection system consisted in three steps: (i) the high abundance of the tetraspanin CD63 at the exosome membrane was used to capture the vesicles using anti-CD63 antibodies conjugated to magnetic beads; (ii) the highly abundant nucleolin at the

surface of exosomes was used as target to bind the vesicles to a nucleolin-recognition aptamer (AS1411), allowing the initiation of a rolling circle amplification (RCA) reaction; and (iii) the resulting amplified sequences hybridize with AuNPs conjugated with a specific oligonucleotide and a quenched fluorescent dye (FAM), which, via the action of an endonuclease, will result in FAM release and concomitant emission of fluorescence. With this platform, it was possible to detect exosomes in a spiked serum sample with high sensitivity. Others have used a SERS-based biosensors by modifying the surface of gold nanostars@4-mercaptobenzoic acid@nanoshell structures with bivalent cholesterol- labeled DNA anchor (Tian et al., 2018). After capturing exosomes with magnetic beads containing CD-9 antibody, the SERS biosensors were fixed at the exosome surface through hydrophobic interactions between the cholesterol present in the beads and the lipidic membrane of the vesicles. When assembled to the exosomes, a SERS signal could be attained for improved detection. Also focused on SERS, a screening platform using capturing substrates, consisting in gold shell magnetic nanobeads conjugated with aptamers for recognition of CD63 at the surface of exosomes, and in SERS probes with three distinct Raman reporters was proposed (Wang Z. et al., 2018). With this technology, it was possible to detect distinct types of exosomes in blood samples, rendering this methodology as promising for diagnosis of early stage cancer.

Also, one the most important characteristics of exosomes is their role in transport of virus, chemotherapeutic agents, DNA and proteins, making them promising vectors for cancer therapy (reviewed in Srivastava et al., 2016). Recent studies describe the transport of AuNPs by exosomes derived from different types of cells, including macrophages and breast cancer cells (Roma-Rodrigues et al., 2017a; Logozzi et al., 2019). Taking advantage of this feature, Sancho-Albero et al. loaded MSCs with hollow AuNPs and revealed a selective transfer of the exosome-cargo into cells of the same type than that of the cell of origin. It was then proposed to apply this preferential uptake conjugated with light-induced hyperthermia for anti-cancer therapy (Sancho-Albero et al., 2019).

Taking Advantage of Folate Requirements of Tumor Cells for Active Targeting

As already mentioned in section Tumor Microenvironment, the high proliferation rate of tumor cells demands a higher nutritional supply, resulting in the increased expression of nutrient receptors, such as folic acid receptors (or folate) to respond to the high request of folate for DNA synthesis (Farran et al., 2019). The functionalization of AuNPs with folate has showed a great potential for increased AuNPs targeting in cancer (reviewed in Samadian et al., 2016; Beik et al., 2017). Several groups have proposed gold nanostructures functionalized with PEG conjugated with folate for photothermal therapy (Ghaznavi et al., 2018; Wang J. et al., 2018; Majidi et al., 2019). Ghaznavi et al. (2018) developed gold and iron oxide core-shell nanoparticles coated with PEG conjugated with folate (FA-PEG-Au@IONP), Majidi et al. synthesized silica and gold core-shell nanoparticles with folate (FA-SiO$_2$@AuNPs) and Wang et al. proposed a gold nanostars-based nanocomposites conjugated with a fluorescent polypeptide for image-guided therapy. Zeinizade et al. analyzed

the effect of folate conjugated AuNPs. In these four reports, increased apoptosis was observed only when tumor cells were simultaneously treated with nanoconjugates and laser irradiation (Ghaznavi et al., 2018; Wang J. et al., 2018; Zeinizade et al., 2018; Majidi et al., 2019). With the same objective, Wang et al. designed multi-layered single walled carbon nanotubes consisting in single walled carbon nanotubes coated with BSA and functionalized with PEG conjugated with folate and with doxorubicin (SWNT@BSA@Au-S-PEG-FA@DOX). The treatment of mice bearing tumors with nanoconjugates and near infrared laser (808 nm) resulted in complete tumor eradication with negligible damage of normal tissues (Wang D. et al., 2018). Zhao et al. developed gold nanochains with worm like structures as a light-triggered system for photodynamic therapy and multiplex detection. These gold nanochains were synthesized using hyaluronic acid-hydrocaffeic acid conjugates as templates and Raman reporters, photosensitizers and folate for active targeting. They observed that low concentrations of these nanoconjugates result in high selectivity and phototoxicity after laser irradiation (Zhao et al., 2019).

Other groups have proposed gold-based nanocomposites conjugated with folate for imaging purposes. Beik et al. analyzed with detail the effect of AuNPs conjugated with folate for CT with the advantage of using lower dosage and enhanced image contrast (Beik et al., 2018). Kumar et al. used green synthesis to prepare gum kondagogu capped gold nanoparticles coupled to folate and fluorescein isothiocyanate (FITC) and observed a high affinity of nanoconjugates toward folate receptor positive cells (Kumar et al., 2018). In another approach, Zhang et al. synthesized mesoporous carbon-gold hybrid nanozyme nanoprobes stabilized with BSA and folate and loaded with IR780 iodide (OMCAPs@rBSA-FA@IR780). *In vivo* analysis revealed efficient tumor targeting and retention (Zhang A. et al., 2019). Khademi et al. studied the *in vivo* targeting of AuNPs conjugated with folate through cysteamine (FA-Cys-AuNPs) for nasopharyngeal head and neck cancer, which were judged suitable for use as contrast agents in CT scan imaging (Khademi et al., 2019).

CONCLUSIONS

In the past, cancer, and tumor development have been considered alone almost as if a strange body to the host organism. Nowadays, tumorigeneses and development must be considered as an element within a larger context that modulates itself in a continuous process of cell progression and maturation. The tumor micro-environment constitutes that differentiating niche where clonal expansion is possible through a multitude of molecular inputs that are at the basis of cancer heterogeneity. Notwithstanding the exponential development of therapeutic approaches to tackle these niches, there has been a growing need to combine several modes of action and therapy modalities simultaneously to tackle the TME. Nanomedicine has been providing for a plethora of multi-functional platforms capable of conveying different cargos to the site of interest in a selective way, while simultaneously providing for diagnostics, imaging

and/or biodistribution capability, toward earlier detection, and destruction of cancer cells. These nanotheranostics systems have relied heavily on gold nanoparticles due to their chemical versatility, biocompatibility and unique spectral properties. This way, making use of the specific conditions within the TME, it has been possible to develop bio responsive platforms to selectively address this particular cellular context. AuNPs have been engineered so as to tackle and/or profit from particular aspects of the TME toward a more selective targeting of the tumor site, or a focal delivery of the therapeutic cargo, and/or to accumulate the nanoconjugates at a precise location that potentiates the use of photoinduced therapies based on the spectral properties of AuNPs.

Still, there are several issues that need to be addressed. Despite the growing number of *in vitro* modeling systems, these are still not equivalent to the real TME. Usually these *in vitro* models, be it the 3D co-cultures and/or on-chip platforms, do not address more than three to four types of cells embedded in an unchanging support media/scaffold. As such, one only gets a couple of *photograms* from the evolving context of the TME *film*. These photograms provide valuable information to address a particular factor and/or pathway in a hierarchized hypothesis rather than the *whole* TME. Nevertheless, the possibility to link and associate several of these models into more complex and interconnected chip systems may provide for systems that more closely resemble what is happening in the TME *in vivo*, and that researchers only now start to get a deeper understanding of events. These models, despite their actual limitations, have been providing for valuable tools to screen and develop new approaches to study and tackle the TME. Here, innovative nanomedicines have taken the lead in making use of the conditions and characteristics of the TME to deliver therapeutics with increasing precision, while providing for signal outputs that allow to follow their effect in real time—real nanotheranostics platforms.

These nanotheranostics strategies may be combined in approaches that simultaneously profit from distinct features of the TME for potentiating the active targeting, controlled release, and therapy modality coupled to imaging/diagnostics. As such, the combination of these features may provide for valuable tools to tackle the TME, addressing the tumor heterogeneity, decreasing tumor resistance, and bringing more efficacious strategies to the clinics.

AUTHOR CONTRIBUTIONS

FUNDING

REFERENCES

Abadjian, M. Z., Edwards, W. B., and Anderson, C. J. (2017). Imaging the tumor microenvironment. *Adv. Exp. Med. Biol.* 1036, 229–257. doi: 10.1007/978-3-319-67577-0_15

Abdolahinia, E. D., Nadri, S., Rahbarghazi, R., Barar, J., Aghanejad, A., and Omidi, Y. (2019). Enhanced penetration and cytotoxicity of metformin and collagenase conjugated gold nanoparticles in breast cancer spheroids. *Life Sci.* 231:116545. doi: 10.1016/j.lfs.2019.116545

Ahn, S., Lee, I. H., Kang, S., Kim, D., Choi, M., Saw, P. E., et al. (2014). Gold nanoparticles displaying tumor-associated self-antigens as a potential vaccine for cancer immunotherapy. *Adv. Healthc. Mater.* 3, 1194–1199. doi: 10.1002/adhm.201300597

Albanese, A., Lam, A. K., Sykes, E. A., Rocheleau, J. V., and Chan, W. C. (2013). Tumour-on-a-chip provides an optical window into nanoparticle tissue transport. *Nat. Commun.* 4:2718. doi: 10.1038/ncomms3718

Annabi, N., Selimovic, S., Acevedo Cox, J. P., Ribas, J., Afshar Bakooshli, M., Heintze, D., et al. (2013). Hydrogel-coated microfluidic channels for cardiomyocyte culture. *Lab Chip* 13, 3569–3577. doi: 10.1039/c3lc50252j

Arvizo, R. R., Rana, S., Miranda, O. R., Bhattacharya, R., Rotello, V. M., and Mukherjee, P. (2011). Mechanism of anti-angiogenic property of gold nanoparticles: role of nanoparticle size and surface charge. *Nanomedicine* 7, 580–587. doi: 10.1016/j.nano.2011.01.011

Astashkina, A. I., Jones, C. F., Thiagarajan, G., Kurtzeborn, K., Ghandehari, H., Brooks, B. D., et al. (2014). Nanoparticle toxicity assessment using an *in vitro* 3-D kidney organoid culture model. *Biomaterials* 35, 6323–6331. doi: 10.1016/j.biomaterials.2014.04.060

Bagley, A. F., Scherz-Shouval, R., Galie, P. A., Zhang, A. Q., Wyckoff, J., Whitesell, L., et al. (2015). Endothelial thermotolerance impairs nanoparticle transport in tumors. *Cancer Res.* 75, 3255–3267. doi: 10.1158/0008-5472.CAN-15-0325

Bartczak, D., Muskens, O. L., Nitti, S., Millar, T. M., and Kanaras, A. G. (2015). Nanoparticles for inhibition of *in vitro* tumour angiogenesis: synergistic actions of ligand function and laser irradiation. *Biomater. Sci.* 3, 733–741. doi: 10.1039/c5bm00053j

Bartczak, D., Muskens, O. L., Sanchez-Elsner, T., Kanaras, A. G., and Millar, T. M. (2013). Manipulation of *in vitro* angiogenesis using peptide-coated gold nanoparticles. *ACS Nano* 7, 5628–5636. doi: 10.1021/nn402111z

Bayda, S., Hadla, M., Palazzolo, S., Riello, P., Corona, G., Toffoli, G., et al. (2018). Inorganic nanoparticles for cancer therapy: a transition from lab to clinic. *Curr. Med. Chem.* 25, 4269–4303. doi: 10.2174/0929867325666171229141156

Beik, J., Jafariyan, M., Montazerabadi, A., Ghadimi-Daresajini, A., Tarighi, P., Mahmoudabadi, A., et al. (2018). The benefits of folic acid-modified gold nanoparticles in CT-based molecular imaging: radiation dose reduction and image contrast enhancement. *Artif. Cells Nanomed. Biotechnol.* 46, 1993–2001. doi: 10.1080/21691401.2017.1408019

Beik, J., Khademi, S., Attaran, N., Sarkar, S., Shakeri-Zadeh, A., Ghaznavi, H., et al. (2017). A nanotechnology-based strategy to increase the efficiency of cancer diagnosis and therapy: folate-conjugated gold nanoparticles. *Curr. Med. Chem.* 24, 4399–4416. doi: 10.2174/0929867324666170810154917

Bhatia, S. N., and Ingber, D. E. (2014). Microfluidic organs-on-chips. *Nat. Biotechnol.* 32, 760–772. doi: 10.1038/nbt.2989

Bhise, K., Sau, S., Alsaab, H., Kashaw, S. K., Tekade, R. K., and Iyer, A. K. (2017). Nanomedicine for cancer diagnosis and therapy: advancement, success and structure-activity relationship. *Ther. Deliv.* 8, 1003–1018. doi: 10.4155/tde-2017-0062

Bruno, A., Mortara, L., Baci, D., Noonan, D. M., and Albini, A. (2019). Myeloid derived suppressor cells interactions with natural killer cells and pro-angiogenic activities: roles in tumor progression. *Front. Immunol.* 10, 771. doi: 10.3389/fimmu.2019.00771

Buzzelli, J. N., Ouaret, D., Brown, G., Allen, P. D., and Muschel, R. J. (2018). Colorectal cancer liver metastases organoids retain characteristics of original tumor and acquire chemotherapy resistance. *Stem Cell Res.* 27, 109–120. doi: 10.1016/j.scr.2018.01.016

Chen, D. S., and Mellman, I. (2017). Elements of cancer immunity and the cancer-immune set point. *Nature* 541, 321–330. doi: 10.1038/nature21349

Chen, W., Jiang, J., Xia, W., and Huang, J. (2017). Tumor-related exosomes contribute to tumor-promoting microenvironment: an immunological perspective. *J Immunol Res* 2017, 1073947. doi: 10.1155/2017/1073947

Chen, W. H., Xu, X. D., Jia, H. Z., Lei, Q., Luo, G. F., Cheng, S. X., et al. (2013). Therapeutic nanomedicine based on dual-intelligent functionalized gold nanoparticles for cancer imaging and therapy *in vivo*. *Biomaterials* 34, 8798–8807. doi: 10.1016/j.biomaterials.2013.07.084

Cheng, H., Sun, G., and Cheng, T. (2018). Hematopoiesis and microenvironment in hematological malignancies. *Cell Regen.* 7, 22–26. doi: 10.1016/j.cr.2018.08.002

Chiodo, F., Marradi, M., Park, J., Ram, A. F., Penades, S., van Die, I., et al. (2014). Galactofuranose-coated gold nanoparticles elicit a pro-inflammatory response in human monocyte-derived dendritic cells and are recognized by DC-SIGN. *ACS Chem. Biol.* 9, 383–389. doi: 10.1021/cb4008265

Clark, D. P. (2018). Biomarkers for immune checkpoint inhibitors: The importance of tumor topography and the challenges to cytopathology. *Cancer Cytopathol.* 126, 11–19. doi: 10.1002/cncy.21951

Conde, J., Larguinho, M., Cordeiro, A., Raposo, L. R., Costa, P. M., Santos, S., et al. (2014). Gold-nanobeacons for gene therapy: evaluation of genotoxicity, cell toxicity and proteome profiling analysis. *Nanotoxicology*, 8, 521–532. doi: 10.3109/17435390.2013.802821

Correia, A. L., and Bissell, M. J. (2012). The tumor microenvironment is a dominant force in multidrug resistance. *Drug Resist. Updat.* 15, 39–49. doi: 10.1016/j.drup.2012.01.006

Dai, J., Li, Q., Liu, W., Lin, S., Hao, Y., Zhang, C., et al. (2015). Synthesis and characterization of cell-microenvironment-sensitive leakage-free gold-shell nanoparticles with the template of interlayer-crosslinked micelles. *Chem. Commun.* 51, 9682–9685. doi: 10.1039/c5cc02556g

Danhier, F. (2016). To exploit the tumor microenvironment: since the EPR effect fails in the clinic, what is the future of nanomedicine? *J. Control. Release* 244, 108–121. doi: 10.1016/j.jconrel.2016.11.015

Danhier, F., Feron, O., and Préat, V. (2010). To exploit the tumor microenvironment: passive and active tumor targeting of nanocarriers for anti-cancer drug delivery. *J. Control. Release* 148, 135–146. doi: 10.1016/j.jconrel.2010.08.027

De Palma, M., Biziato, D., and Petrova, T. V. (2017). Microenvironmental regulation of tumour angiogenesis. *Nat. Rev. Cancer* 17, 457–474. doi: 10.1038/nrc.2017.51

DeNardo, D. G., Andreu, P., and Coussens, L. M. (2010). Interactions between lymphocytes and myeloid cells regulate pro- versus anti-tumor immunity. *Cancer Metastasis Rev.* 29, 309–316. doi: 10.1007/s10555-010-9223-6

Dreaden, E. C., Austin, L. A., Mackey, M. A., and El-Sayed, M. A. (2012). Size matters: gold nanoparticles in targeted cancer drug delivery. *Ther. Deliv.* 3, 457–478. doi: 10.4155/tde.12.21

Elzoghby, A. O., Hemasa, A. L., and Freag, M. S. (2016). Hybrid protein-inorganic nanoparticles: from tumor-targeted drug delivery to cancer imaging. *J. Control. Release* 243, 303–322. doi: 10.1016/j.jconrel.2016.10.023

England, C. G., Priest, T., Zhang, G., Sun, X., Patel, D. N., McNally, L. R., et al. (2013). Enhanced penetration into 3D cell culture using two and three layered gold nanoparticles. *Int. J. Nanomedicine* 8, 3603–3617. doi: 10.2147/IJN.S51668

Farnsworth, R. H., Karnezis, T., Maciburko, S. J., Mueller, S. N., and Stacker, S. A. (2019). The interplay between lymphatic vessels and chemokines. *Front. Immunol.* 10:518. doi: 10.3389/fimmu.2019.00518

Farran, B., Pavitra, E., Kasa, P., Peela, S., Rama Raju, G. S., and Nagaraju, G. P. (2019). Folate-targeted immunotherapies: passive and active strategies for cancer. *Cytokine Growth Factor Rev.* 45, 45–52. doi: 10.1016/j.cytogfr.2019.02.001

Feng, Q., Shen, Y., Fu, Y., Muroski, M. E., Zhang, P., Wang, Q., et al. (2017). Self-assembly of gold nanoparticles shows microenvironment-mediated dynamic switching and enhanced brain tumor targeting. *Theranostics* 7, 1875–1889. doi: 10.7150/thno.18985

Ferrara, N., and Kerbel, R. S. (2005). Angiogenesis as a therapeutic target. *Nature* 438, 967–974. doi: 10.1038/nature04483

Fogli, S., Montis, C., Paccosi, S., Silvano, A., Michelucci, E., Berti, D., et al. (2017). Inorganic nanoparticles as potential regulators of immune response in dendritic cells. *Nanomedicine* 12, 1647–1660. doi: 10.2217/nnm-2017-0061

Franzen, C. A., Simms, P. E., Van Huis, A. F., Foreman, K. E., Kuo, P. C., and Gupta, G. N. (2014). Characterization of uptake and internalization of exosomes by bladder cancer cells. *Biomed. Res. Int.* 2014:619829. doi: 10.1155/2014/619829

Garnier, L., Gkountidi, A.-O., and Hugues, S. (2019). Tumor-associated lymphatic vessel features and immunomodulatory functions. *Front. Immunol.* 10:720. doi: 10.3389/fimmu.2019.00720

Ghaznavi, H., Hosseini-Nami, S., Kamrava, S. K., Irajirad, R., Maleki, S., Shakeri-Zadeh, A., et al. (2018). Folic acid conjugated PEG coated gold-iron oxide core-shell nanocomplex as a potential agent for targeted photothermal therapy of cancer. *Artif. Cells Nanomed. Biotechnol.* 46, 1594–1604. doi: 10.1080/21691401.2017.1384384

Goswami, K. K., Ghosh, T., Ghosh, S., Sarkar, M., Bose, A., and Baral, R. (2017). Tumor promoting role of anti-tumor macrophages in tumor microenvironment. *Cell. Immunol.* 316, 1–10. doi: 10.1016/j.cellimm.2017.04.005

Grzywa, T. M., Paskal, W., and Wlodarski, P. K. (2017). Intratumor and intertumor heterogeneity in melanoma. *Transl. Oncol.* 10, 956–975. doi: 10.1016/j.tranon.2017.09.007

Guo, J., Rahme, K., He, Y., Li, L. L., Holmes, J. D., and O'Driscoll, C. M. (2017). Gold nanoparticles enlighten the future of cancer theranostics. *Int. J. Nanomedicine* 12, 6131–6152. doi: 10.2147/IJN.S140772

Gwangwa, M. V., Joubert, A. M., and Visagie, M. H. (2018). Crosstalk between the Warburg effect, redox regulation and autophagy induction in tumourigenesis. *Cell. Mol. Biol. Lett.* 23:20. doi: 10.1186/s11658-018-0088-y

Han, X., Li, Y., Xu, Y., Zhao, X., Zhang, Y., Yang, X., et al. (2018). Reversal of pancreatic desmoplasia by re-educating stellate cells with a tumour microenvironment-activated nanosystem. *Nat. Commun.* 9:3390. doi: 10.1038/s41467-018-05906-x

Hanahan, D., and Weinberg, R. A. (2011). Hallmarks of cancer: the next generation. *Cell* 144, 646–674. doi: 10.1016/j.cell.2011.02.013

Hannafon, B. N., and Ding, W. Q. (2013). Intercellular communication by exosome-derived microRNAs in cancer. *Int. J. Mol. Sci.* 14, 14240–14269. doi: 10.3390/ijms140714240

Haume, K., Rosa, S., Grellet, S., Smialek, M. A., Butterworth, K. T., Solov'yov, A. V., et al. (2016). Gold nanoparticles for cancer radiotherapy: a review. *Cancer Nanotechnol.* 7:8. doi: 10.1186/s12645-016-0021-x

Hidalgo, M., Amant, F., Biankin, A. V., Budinska, E., Byrne, A. T., Caldas, C., et al. (2014). Patient-derived xenograft models: an emerging platform for translational cancer research. *Cancer Discov.* 4, 998–1013. doi: 10.1158/2159-8290.CD-14-0001

Huang, K., Ma, H., Liu, J., Huo, S., Kumar, A., Wei, T., et al. (2012). Size-dependent localization and penetration of ultrasmall gold nanoparticles in cancer cells, multicellular spheroids, and tumors *in vivo*. *ACS Nano* 6, 4483–4493. doi: 10.1021/nn301282m

Huang, L., Wang, D. B., Singh, N., Yang, F., Gu, N., and Zhang, X. E. (2018). A dual-signal amplification platform for sensitive fluorescence biosensing of leukemia-derived exosomes. *Nanoscale* 10, 20289–20295. doi: 10.1039/c8nr07720g

Huang, Y., Lin, D., and Taniguchi, C. M. (2017). Hypoxia inducible factor (HIF) in the tumor microenvironment: friend or foe? *Sci. China Life Sci.* 60, 1114–1124. doi: 10.1007/s11427-017-9178-y

Huang, Y. J., and Hsu, S. H. (2017). TRAIL-functionalized gold nanoparticles selectively trigger apoptosis in polarized macrophages. *Nanotheranostics* 1, 326–337. doi: 10.7150/ntno.20233

Huh, D., Matthews, B. D., Mammoto, A., Montoya-Zavala, M., Hsin, H. Y., and Ingber, D. E. (2010). Reconstituting organ-level lung functions on a chip. *Science* 328, 1662–1668. doi: 10.1126/science.1188302

Hui, L., and Chen, Y. (2015). Tumor microenvironment: Sanctuary of the devil. *Cancer Lett.* 368, 7–13. doi: 10.1016/j.canlet.2015.07.039

Italiani, P., and Boraschi, D. (2014). From monocytes to M1/M2 macrophages: phenotypical vs. *Functional Differentiation. Front. Immunol.* 5:514. doi: 10.3389/fimmu.2014.00514

Jeong, H., Kim, S., Hong, B. J., Lee, C. J., Kim, Y. E., Bok, S., et al. (2019). Tumor-associated macrophages enhance tumor hypoxia and aerobic glycolysis. *Cancer Res.* 79, 795–806. doi: 10.1158/0008-5472.CAN-18-2545

Jung, S., Nam, J., Hwang, S., Park, J., Hur, J., Im, K., et al. (2013). Theragnostic pH-sensitive gold nanoparticles for the selective surface enhanced Raman scattering and photothermal cancer therapy. *Anal. Chem.* 85, 7674–7681. doi: 10.1021/ac401390m

Kai, F., Drain, A. P., and Weaver, V. M. (2019). The extracellular matrix modulates the metastatic journey. *Dev. Cell* 49, 332–346. doi: 10.1016/j.devcel.2019.03.026

Kang, H., Kim, H., Lee, S., Youn, H., and Youn, B. (2019). Role of metabolic reprogramming in Epithelial(-)Mesenchymal Transition (EMT). *Int. J. Mol. Sci.* 20:2042. doi: 10.3390/ijms20082042

Kenny, P. A., Lee, G. Y., Myers, C. A., Neve, R. M., Semeiks, J. R., Spellman, P. T., et al. (2007). The morphologies of breast cancer cell lines in three-dimensional assays correlate with their profiles of gene expression. *Mol. Oncol.* 1, 84–96. doi: 10.1016/j.molonc.2007.02.004

Khademi, S., Sarkar, S., Shakeri-Zadeh, A., Attaran, N., Kharrazi, S., Ay, M. R., et al. (2019). Targeted gold nanoparticles enable molecular CT imaging of head and neck cancer: an *in vivo* study. *Int. J. Biochem. Cell Biol.* 114:105554. doi: 10.1016/j.biocel.2019.06.002

Kim, K., Choi, H., Choi, E. S., Park, M. H., and Ryu, J. H. (2019). Hyaluronic acid-coated nanomedicine for targeted cancer therapy. *Pharmaceutics* 11:e301. doi: 10.3390/pharmaceutics11070301

Klein, D. (2018). The tumor vascular endothelium as decision maker in cancer therapy. *Front. Oncol.* 8:367. doi: 10.3389/fonc.2018.00367

Kobayashi, H., Watanabe, R., and Choyke, P. L. (2014). Improving conventional enhanced permeability and retention (EPR) effects; what is the appropriate target? *Theranostics* 4, 81–89. doi: 10.7150/thno.7193

Kumar, S. S. D., Mahesh, A., Antoniraj, M. G., Rathore, H. S., Houreld, N. N., and Kandasamy, R. (2018). Cellular imaging and folate receptor targeting delivery of gum kondagogu capped gold nanoparticles in cancer cells. *Int. J. Biol. Macromol.* 109, 220–230. doi: 10.1016/j.ijbiomac.2017.12.069

Kwak, B., Ozcelikkale, A., Shin, C. S., Park, K., and Han, B. (2014). Simulation of complex transport of nanoparticles around a tumor using tumor-microenvironment-on-chip. *J. Control. Release* 194, 157–167. doi: 10.1016/j.jconrel.2014.08.027

LaBarbera, D. V., Reid, B. G., and Yoo, B. H. (2012). The multicellular tumor spheroid model for high-throughput cancer drug discovery. *Expert Opin. Drug Discov.* 7, 819–830. doi: 10.1517/17460441.2012.708334

Labiano, S., Palazon, A., and Melero, I. (2015). Immune response regulation in the tumor microenvironment by hypoxia. *Semin. Oncol.* 42, 378–386. doi: 10.1053/j.seminoncol.2015.02.009

Lai, X., Tan, L., Deng, X., Liu, J., Li, A., Liu, J., et al. (2017). Coordinatively self-assembled luminescent gold nanoparticles: fluorescence turn-on system for high-efficiency passive tumor imaging. *ACS Appl. Mater. Interfaces* 9, 5118–5127. doi: 10.1021/acsami.6b14681

Lancaster, M. A., and Knoblich, J. A. (2014). Organogenesis in a dish: modeling development and disease using organoid technologies. *Science* 345:1247125. doi: 10.1126/science.1247125

Lee, J. M., Park, D. Y., Yang, L., Kim, E. J., Ahrberg, C. D., Lee, K. B., et al. (2018). Generation of uniform-sized multicellular tumor spheroids using hydrogel microwells for advanced drug screening. *Sci. Rep.* 8:17145. doi: 10.1038/s41598-018-35216-7

Lee, K. E., Spata, M., Bayne, L. J., Buza, E. L., Durham, A. C., Allman, D., et al. (2016). Hif1a deletion reveals pro-neoplastic function of B cells in pancreatic neoplasia. *Cancer Discov.* 6, 256–269. doi: 10.1158/2159-8290.CD-15-0822

Lee, S., Cha, E. J., Park, K., Lee, S. Y., Hong, J. K., Sun, I. C., et al. (2008). A near-infrared-fluorescence-quenched gold-nanoparticle imaging probe for *in vivo* drug screening and protease activity determination. *Angew. Chem. Int. Ed Engl.* 47, 2804–2807. doi: 10.1002/anie.200705240

Li, H., Liu, X., Huang, N., Ren, K., Jin, Q., and Ji, J. (2014). "Mixed-charge self-assembled monolayers" as a facile method to design pH-induced aggregation of large gold nanoparticles for near-infrared photothermal cancer therapy. *ACS Appl. Mater. Interfaces* 6, 18930–18937. doi: 10.1021/am504813f

Li, S., Lui, K.-H., Tsoi, T.-H., Lo, W.-S., Li, X., Hu, X., et al. (2019). pH-responsive targeted gold nanoparticles for *in vivo* photoacoustic imaging of tumor microenvironments. *Nanoscale Adv.* 1, 554–564. doi: 10.1039/c8na00190a

Li, W., Li, X., Liu, S., Yang, W., Pan, F., Yang, X. Y., et al. (2017). Gold nanoparticles attenuate metastasis by tumor vasculature normalization and epithelial-mesenchymal transition inhibition. *Int. J. Nanomedicine* 12, 3509–3520. doi: 10.2147/IJN.S128802

Liang, R., Liu, L., He, H., Chen, Z., Han, Z., Luo, Z., et al. (2018). Oxygen-boosted immunogenic photodynamic therapy with gold nanocages@manganese dioxide to inhibit tumor growth and metastases. *Biomaterials* 177, 149–160. doi: 10.1016/j.biomaterials.2018.05.051

Liu, J., Dang, H., and Wang, X. W. (2018a). The significance of intertumor and intratumor heterogeneity in liver cancer. *Exp. Mol. Med.* 50:e416. doi: 10.1038/emm.2017.165

Liu, J., Liang, H., Li, M., Luo, Z., Zhang, J., Guo, X., et al. (2018b). Tumor acidity activating multifunctional nanoplatform for NIR-mediated multiple enhanced photodynamic and photothermal tumor therapy. *Biomaterials* 157, 107–124. doi: 10.1016/j.biomaterials.2017.12.003

Liu, R., Hu, C., Yang, Y., Zhang, J., and Gao, H. (2019). Theranostic nanoparticles with tumor-specific enzyme-triggered size reduction and drug release to perform photothermal therapy for breast cancer treatment. *Acta Pharm Sin. B.* 9, 410–420. doi: 10.1016/j.apsb.2018.09.001

Liu, T., Zhou, L., Li, D., Andl, T., and Zhang, Y. (2019). Cancer-associated fibroblasts build and secure the tumor microenvironment. *Front. Cell Dev. Biol.* 7:60. doi: 10.3389/fcell.2019.00060

Logozzi, M., Mizzoni, D., Bocca, B., Di Raimo, R., Petrucci, F., Caimi, S., et al. (2019). Human primary macrophages scavenge AuNPs and eliminate it through exosomes. A natural shuttling for nanomaterials. *Eur. J. Pharm. Biopharm.* 137, 23–36. doi: 10.1016/j.ejpb.2019.02.014

Lu, J. (2019). The Warburg metabolism fuels tumor metastasis. *Cancer Metastasis Rev.* 38, 157–164. doi: 10.1007/s10555-019-09794-5

Maeda, H. (2012). Macromolecular therapeutics in cancer treatment: the EPR effect and beyond. *J. Control. Release* 164, 138–144. doi: 10.1016/j.jconrel.2012.04.038

Majidi, F. S., Mohammadi, E., Mehravi, B., Nouri, S., Ashtari, K., and Neshasteh-Riz, A. (2019). Investigating the effect of near infrared photo thermal therapy folic acid conjugated gold nano shell on melanoma cancer cell line A375. *Artif. Cells Nanomed. Biotechnol.* 47, 2161–2170. doi: 10.1080/21691401.2019.1593188

Mantovani, A., Barajon, I., and Garlanda, C. (2018). IL-1 and IL-1 regulatory pathways in cancer progression and therapy. *Immunol. Rev.* 281, 57–61. doi: 10.1111/imr.12614

Mantovani, A., Ponzetta, A., Inforzato, A., and Jaillon, S. (2019). Innate immunity, inflammation and tumour progression: double-edged swords. *J. Intern. Med.* 285, 524–532. doi: 10.1111/joim.12886

Mazumdar, J., Hickey, M. M., Pant, D. K., Durham, A. C., Sweet-Cordero, A., Vachani, A., et al. (2010). HIF-2alpha deletion promotes Kras-driven lung tumor development. *Proc. Natl. Acad. Sci. U.S.A.* 107, 14182–14187. doi: 10.1073/pnas.1001296107

Millar, T. M., and Kanaras, A. G. (2013). Nanoparticulate drugs for the manipulation of angiogenesis. *Ther. Deliv.* 4, 1217–1219. doi: 10.4155/tde.13.96

Morton, J. J., Bird, G., Refaeli, Y., and Jimeno, A. (2016). Humanized mouse xenograft models: narrowing the tumor-microenvironment gap. *Cancer Res.* 76, 6153–6158. doi: 10.1158/0008-5472.CAN-16-1260

Mroz, E. A., and Rocco, J. W. (2016). Intra-tumor heterogeneity in head and neck cancer and its clinical implications. *World J. Otorhinolaryngol. Head Neck Surg.* 2, 60–67. doi: 10.1016/j.wjorl.2016.05.007

Mukherjee, P., Bhattacharya, R., Wang, P., Wang, L., Basu, S., Nagy, J. A., et al. (2005). Antiangiogenic properties of gold nanoparticles. *Clin. Cancer Res.* 11, 3530–3534. doi: 10.1158/1078-0432.CCR-04-2482

Nakazawa, M. S., Eisinger-Mathason, T. S., Sadri, N., Ochocki, J. D., Gade, T. P., Amin, R. K., et al. (2016). Epigenetic re-expression of HIF-2alpha suppresses soft tissue sarcoma growth. *Nat. Commun.* 7:10539. doi: 10.1038/ncomms10539

Netea-Maier, R. T., Smit, J. W. A., and Netea, M. G. (2018). Metabolic changes in tumor cells and tumor-associated macrophages: a mutual relationship. *Cancer Lett.* 413, 102–109. doi: 10.1016/j.canlet.2017.10.037

Ngoune, R., Peters, A., von Elverfeldt, D., Winkler, K., and Pütz, G. (2016). Accumulating nanoparticles by EPR: a route of no return. *J. Control. Release* 238, 58–70. doi: 10.1016/j.jconrel.2016.07.028

Nichols, J. W., and Bae, Y. H. (2014). EPR: evidence and fallacy. *J. Control. Release* 190, 451–464. doi: 10.1016/j.jconrel.2014.03.057

Oh, E. J., Park, K., Kim, K. S., Yang, J. A., Kong, J. H., Lee, M. Y., et al. (2010). Target specific and long-acting delivery of protein, peptide, and nucleotide therapeutics using hyaluronic acid derivatives. *J. Control. Release* 141, 2–12. doi: 10.1016/j.jconrel.2009.09.010

Pal, R., Chakraborty, B., Nath, A., Singh, L. M., Ali, M., Rahman, D. S., et al. (2016). Noble metal nanoparticle-induced oxidative stress modulates tumor associated macrophages (TAMs) from an M2 to M1 phenotype: an *in vitro* approach. *Int. Immunopharmacol.* 38, 332–341. doi: 10.1016/j.intimp.2016.06.006

Pan, F., Yang, W., Li, W., Yang, X. Y., Liu, S., Li, X., et al. (2017). Conjugation of gold nanoparticles and recombinant human endostatin modulates vascular normalization via interruption of anterior gradient 2-mediated angiogenesis. *Tumour Biol.* 39:1010428317708547. doi: 10.1177/1010428317708547

Pearson, G. W. (2019). Control of Invasion by epithelial-to-mesenchymal transition programs during metastasis. *J. Clin. Med.* 8:E646. doi: 10.3390/jcm8050646

Pedrosa, P., Heuer-Jungemann, A., Kanaras, A. G., Fernandes, A. R., and Baptista, P. V. (2017). Potentiating angiogenesis arrest *in vivo* via laser irradiation of peptide functionalised gold nanoparticles. *J. Nanobiotechnol.* 15:85. doi: 10.1186/s12951-017-0321-2

Pedrosa, P., Vinhas, R., Fernandes, A., and Baptista, P. V. (2015). Gold nanotheranostics: proof-of-concept or clinical tool? *Nanomaterials* 5, 1853–1879. doi: 10.3390/nano5041853

Pickup, M. W., Mouw, J. K., and Weaver, V. M. (2014). The extracellular matrix modulates the hallmarks of cancer. *EMBO Rep.* 15, 1243–1253. doi: 10.15252/embr.201439246

Prenen, H., and Mazzone, M. (2019). Tumor-associated macrophages: a short compendium. *Cell. Mol. Life Sci.* 76, 1447–1458. doi: 10.1007/s00018-018-2997-3

Rane, T. D., and Armani, A. M. (2016). Two-photon microscopy analysis of gold nanoparticle uptake in 3D cell spheroids. *PLoS ONE* 11:e0167548. doi: 10.1371/journal.pone.0167548

Ranga, A., Gjorevski, N., and Lutolf, M. P. (2014). Drug discovery through stem cell-based organoid models. *Adv. Drug Deliv. Rev.* 69–70, 19–28. doi: 10.1016/j.addr.2014.02.006

Reynolds, D. S., Tevis, K. M., Blessing, W. A., Colson, Y. L., Zaman, M. H., and Grinstaff, M. W. (2017). Breast cancer spheroids reveal a differential cancer stem cell response to chemotherapeutic treatment. *Sci. Rep.* 7:10382. doi: 10.1038/s41598-017-10863-4

Riedl, A., Schlederer, M., Pudelko, K., Stadler, M., Walter, S., Unterleuthner, D., et al. (2017). Comparison of cancer cells in 2D vs 3D culture reveals differences in AKT–mTOR–S6K signaling and drug responses. *J. Cell Sci.* 130, 203–218. doi: 10.1242/jcs.188102

Rivera-Cruz, C. M., Shearer, J. J., Figueiredo Neto, M., and Figueiredo, M. L. (2017). The immunomodulatory effects of mesenchymal stem cell polarization within the tumor microenvironment niche. *Stem Cells Int.* 2017:4015039. doi: 10.1155/2017/4015039

Rodrigues, T., Kundu, B., Silva-Correia, J., Kundu, S. C., Oliveira, J. M., Reis, R. L., et al. (2018). Emerging tumor spheroids technologies for 3D *in vitro* cancer modeling. *Pharmacol. Ther.* 184, 201–211. doi: 10.1016/j.pharmthera.2017.10.018

Roma-Rodrigues, C., Fernandes, A. R., and Baptista, P. V. (2014). Exosome in tumour microenvironment: overview of the crosstalk between normal and cancer cells. *Biomed Res. Int.* 2014:179486. doi: 10.1155/2014/179486

Roma-Rodrigues, C., Heuer-Jungemann, A., Fernandes, A. R., Kanaras, A. G., and Baptista, P. V. (2016). Peptide-coated gold nanoparticles for modulation of angiogenesis *in vivo*. *Int. J. Nanomedicine* 11, 2633–2639. doi: 10.2147/IJN.S108661

Roma-Rodrigues, C., Mendes, R., Baptista, P. V., and Fernandes, A. R. (2019). Targeting tumor microenvironment for cancer therapy. *Int. J. Mol. Sci.* 20:E840. doi: 10.3390/ijms20040840

Roma-Rodrigues, C., Pereira, F., Alves de Matos, A. P., Fernandes, M., Baptista, P. V., and Fernandes, A. R. (2017a). Smuggling gold nanoparticles across cell types - a new role for exosomes in gene silencing. *Nanomedicine* 13, 1389–1398. doi: 10.1016/j.nano.2017.01.013

Roma-Rodrigues, C., Raposo, L. R., Cabral, R., Paradinha, F., Baptista, P. V., and Fernandes, A. R. (2017b). Tumor microenvironment modulation via gold nanoparticles targeting malicious exosomes: implications for cancer diagnostics and therapy. *Int. J. Mol. Sci.* 18:162. doi: 10.3390/ijms18010162

Ruan, S., Cao, X., Cun, X., Hu, G., Zhou, Y., Zhang, Y., et al. (2015a). Matrix metalloproteinase-sensitive size-shrinkable nanoparticles for deep tumor penetration and pH triggered doxorubicin release. *Biomaterials* 60, 100–110. doi: 10.1016/j.biomaterials.2015.05.006

Ruan, S., He, Q., and Gao, H. (2015b). Matrix metalloproteinase triggered size-shrinkable gelatin-gold fabricated nanoparticles for tumor microenvironment sensitive penetration and diagnosis of glioma. *Nanoscale* 7, 9487–9496. doi: 10.1039/c5nr01408e

Samadian, H., Hosseini-Nami, S., Kamrava, S. K., and Ghaznavi, H. (2016). Folate-conjugated gold nanoparticle as a new nanoplatform for targeted cancer therapy. *J. Cancer Res. Clin. Oncol.* 142, 2217–2229. doi: 10.1007/s00432-016-2179-3

Sancho-Albero, M., Navascues, N., Mendoza, G., Sebastian, V., Arruebo, M., Martin-Duque, P., et al. (2019). Exosome origin determines cell targeting and the transfer of therapeutic nanoparticles towards target cells. *J. Nanobiotechnol.* 17:16. doi: 10.1186/s12951-018-0437-z

Sanford-Crane, H., Abrego, J., and Sherman, M. H. (2019). Fibroblasts as modulators of local and systemic cancer metabolism. *Cancers* 11:E619. doi: 10.3390/cancers11050619

Sasmita, A. O., and Wong, Y. P. (2018). Organoids as reliable breast cancer study models: an update. *Int. J. Oncol. Res.* 1:008. doi: 10.23937/ijor-2017/1710008

Schupp, J., Krebs, F. K., Zimmer, N., Trzeciak, E., Schuppan, D., and Tuettenberg, A. (2017). Targeting myeloid cells in the tumor sustaining microenvironment. *Cell Immunol.* doi: 10.1016/j.cellimm.2017.10.013. [Epub ahead of print].

Serebriiskii, I., Castello-Cros, R., Lamb, A., Golemis, E. A., and Cukierman, E. (2008). Fibroblast-derived 3D matrix differentially regulates the growth and drug-responsiveness of human cancer cells. *Matrix Biol.* 27, 573–585. doi: 10.1016/j.matbio.2008.02.008

Shabana, A. M., Mondal, U. K., Alam, M. R., Spoon, T., Ross, C. A., Madesh, M., et al. (2018). pH-sensitive multiligand gold nanoplatform targeting carbonic anhydrase IX enhances the delivery of doxorubicin to hypoxic tumor spheroids and overcomes the hypoxia-induced chemoresistance. *ACS Appl. Mater. Interfaces* 10, 17792–17808. doi: 10.1021/acsami.8b05607

Shang, M., Soon, R. H., Lim, C. T., Khoo, B. L., and Han, J. (2019). Microfluidic modelling of the tumor microenvironment for anti-cancer drug development. *Lab Chip* 19, 369–386. doi: 10.1039/c8lc00970h

Shen, S., Zhu, C., Huo, D., Yang, M., Xue, J., and Xia, Y. (2017). A hybrid nanomaterial for the controlled generation of free radicals and oxidative destruction of hypoxic cancer cells. *Angew. Chem. Int. Ed Engl.* 56, 8801–8804. doi: 10.1002/anie.201702898

Shi, H., Wang, Z., Huang, C., Gu, X., Jia, T., Zhang, A., et al. (2016). A functional CT contrast agent for *in vivo* imaging of tumor hypoxia. *Small* 12, 3995–4006. doi: 10.1002/smll.201601029

Singh, P., Pandit, S., Mokkapati, V., Garg, A., Ravikumar, V., and Mijakovic, I. (2018). Gold nanoparticles in diagnostics and therapeutics for human cancer. *Int. J. Mol. Sci.* 19:E1979. doi: 10.3390/ijms19071979

Sleeboom, J. J. F., Eslami Amirabadi, H., Nair, P., Sahlgren, C. M., and den Toonder, J. M. J. (2018). Metastasis in context: modeling the tumor microenvironment with cancer-on-a-chip approaches. *Dis. Model. Mech.* 11:dmm03310. doi: 10.1242/dmm.033100

Song, J., Kim, J., Hwang, S., Jeon, M., Jeong, S., Kim, C., et al. (2016). "Smart" gold nanoparticles for photoacoustic imaging: an imaging contrast agent responsive to the cancer microenvironment and signal amplification via pH-induced aggregation. *Chem. Commun.* 52, 8287–8290. doi: 10.1039/c6cc03100e

Song, Y., Kim, J. S., Kim, S. H., Park, Y. K., Yu, E., Kim, K. H., et al. (2018). Patient-derived multicellular tumor spheroids towards optimized treatment for patients with hepatocellular carcinoma. *J. Exp. Clin. Cancer Res.* 37:109. doi: 10.1186/s13046-018-0752-0

Sormendi, S., and Wielockx, B. (2018). Hypoxia pathway proteins as central mediators of metabolism in the tumor cells and their microenvironment. *Front. Immunol.* 9:40. doi: 10.3389/fimmu.2018.00040

Srivastava, A., Babu, A., Filant, J., Moxley, K. M., Ruskin, R., Dhanasekaran, D., et al. (2016). Exploitation of exosomes as nanocarriers for gene-, chemo-, and immune-therapy of cancer. *J. Biomed. Nanotechnol.* 12, 1159–1173. doi: 10.1166/jbn.2016.2205

Steven, A., and Seliger, B. (2018). The role of immune escape and immune cell infiltration in breast cancer. *Breast Care* 13, 16–21. doi: 10.1159/000486585

Sun, I. C., Eun, D. K., Koo, H., Ko, C. Y., Kim, H. S., Yi, D. K., et al. (2011). Tumor-targeting gold particles for dual computed tomography/optical cancer imaging. *Angew. Chem. Int. Ed Engl.* 50, 9348–9351. doi: 10.1002/anie.201102892

Sung, S. Y., Hsieh, C. L., Law, A., Zhau, H. E., Pathak, S., Multani, A. S., et al. (2008). Coevolution of prostate cancer and bone stroma in three-dimensional coculture: implications for cancer growth and metastasis. *Cancer Res.* 68, 9996–10003. doi: 10.1158/0008-5472.CAN-08-2492

Sutherland, R. M., McCredie, J. A., and Inch, W. R. (1971). Growth of multicell spheroids in tissue culture as a model of nodular carcinomas. *J. Nat. Cancer Inst.* 46, 113–120.

Tang, Y., Shi, H., Cheng, D., Zhang, J., Lin, Y., Xu, Y., et al. (2019). pH-Activatable tumor-targeting gold nanoprobe for near-infrared fluorescence/CT dual-modal imaging *in vivo*. *Colloids Surf. B Biointerfaces* 179, 56–65. doi: 10.1016/j.colsurfb.2019.03.049

Tian, Y. F., Ning, C. F., He, F., Yin, B. C., and Ye, B. C. (2018). Highly sensitive detection of exosomes by SERS using gold nanostar@Raman reporter@nanoshell structures modified with a bivalent cholesterol-labeled DNA anchor. *Analyst* 143, 4915–4922. doi: 10.1039/c8an01041b

Trivanovic, D., Krstic, J., Djordjevic, I. O., Mojsilovic, S., Santibanez, J. F., Bugarski, D., et al. (2016). The roles of mesenchymal stromal/stem cells in tumor microenvironment associated with inflammation. *Mediators Inflamm.* 2016:7314016. doi: 10.1155/2016/7314016

Tsai, H. F., Trubelja, A., Shen, A. Q., and Bao, G. (2017). Tumour-on-a-chip: microfluidic models of tumour morphology, growth and microenvironment. *J. R. Soc. Interface* 14:20170137. doi: 10.1098/rsif.2017.0137

Tsai, L. C., Hsieh, H. Y., Lu, K. Y., Wang, S. Y., and Mi, F. L. (2016). EGCG/gelatin-doxorubicin gold nanoparticles enhance therapeutic efficacy of doxorubicin for prostate cancer treatment. *Nanomedicine* 11, 9–30. doi: 10.2217/nnm.15.183

Tsai, M. J., Chang, W. A., Huang, M. S., and Kuo, P. L. (2014). Tumor microenvironment: a new treatment target for cancer. *ISRN Biochem.* 2014:351959. doi: 10.1155/2014/351959

Vahidian, F., Duijf, P. H. G., Safarzadeh, E., Derakhshani, A., Baghbanzadeh, A., and Baradaran, B. (2019). Interactions between cancer stem cells, immune system and some environmental components: friends or foes? *Immunol. Lett.* 208, 19–29. doi: 10.1016/j.imlet.2019.03.004

van de Wetering, M., Francies, H. E., Francis, J. M., Bounova, G., Iorio, F., Pronk, A., et al. (2015). Prospective derivation of a living organoid biobank of colorectal cancer patients. *Cell* 161, 933–945. doi: 10.1016/j.cell.2015.03.053

Vaupel, P., and Multhoff, G. (2018). Hypoxia-/HIF-1alpha-driven factors of the tumor microenvironment impeding antitumor immune responses and promoting malignant progression. *Adv. Exp. Med. Biol.* 1072, 171–175. doi: 10.1007/978-3-319-91287-5_27

Vlachogiannis, G., Hedayat, S., Vatsiou, A., Jamin, Y., Fernandez-Mateos, J., Khan, K., et al. (2018). Patient-derived organoids model treatment response of metastatic gastrointestinal cancers. *Science* 359, 920–926. doi: 10.1126/science.aao2774

Wagner, I., Materne, E. M., Brincker, S., Sussbier, U., Fradrich, C., Busek, M., et al. (2013). A dynamic multi-organ-chip for long-term cultivation and substance testing proven by 3D human liver and skin tissue co-culture. *Lab Chip* 13, 3538–3547. doi: 10.1039/c3lc50234a

Wang, D., Meng, L., Fei, Z., Hou, C., Long, J., Zeng, L., et al. (2018). Multi-layered tumor-targeting photothermal-doxorubicin releasing nanotubes eradicate tumors *in vivo* with negligible systemic toxicity. *Nanoscale*. 10, 8536–8546. doi: 10.1039/c8nr00663f

Wang, H. F., Ran, R., Liu, Y., Hui, Y., Zeng, B., Chen, D., et al. (2018). Tumor-vasculature-on-a-chip for investigating nanoparticle extravasation and tumor accumulation. *ACS Nano* 12, 11600–11609. doi: 10.1021/acsnano.8b06846

Wang, J., Zhou, Z., Zhang, F., Xu, H., Chen, W., and Jiang, T. (2018). A novel nanocomposite based on fluorescent turn-on gold nanostars for near-infrared photothermal therapy and self-theranostic caspase-3 imaging of glioblastoma tumor cell. *Colloids Surf. B Biointerfaces* 170, 303–311. doi: 10.1016/j.colsurfb.2018.06.021

Wang, X., Xia, Y., Liu, Y., Qi, W., Sun, Q., Zhao, Q., et al. (2012). Dual-luminophore-labeled gold nanoparticles with completely resolved emission for the simultaneous imaging of MMP-2 and MMP-7 in living cells under single wavelength excitation. *Chemistry* 18, 7189–7195. doi: 10.1002/chem.201200227

Wang, Z., Zong, S., Wang, Y., Li, N., Li, L., Lu, J., et al. (2018). Screening and multiple detection of cancer exosomes using an SERS-based method. *Nanoscale* 10, 9053–9062. doi: 10.1039/c7nr09162a

Weiswald, L. B., Bellet, D., and Dangles-Marie, V. (2015). Spherical cancer models in tumor biology. *Neoplasia* 17, 1–15. doi: 10.1016/j.neo.2014.12.004

Whatcott, C. J., Han, H., Posner, R. G., Hostetter, G., and Von Hoff, D. D. (2011). Targeting the tumor microenvironment in cancer: why hyaluronidase deserves a second look. *Cancer Discov.* 1, 291–296. doi: 10.1158/2159-8290

Whilhelm, S., Tavares, A. J., Dai, Q., Ohta, S., Audet, J., Dvorak, H. F., et al. (2016). Analysis of nanoparticle delivery to tumours. *Nat. Rev. Mat.* 1:16014. doi: 10.1038/natrevmats.2016.14

Wu, D. (2017). Innate and adaptive immune cell metabolism in tumor microenvironment. *Adv. Exp. Med. Biol.* 1011, 211–223. doi: 10.1007/978-94-024-1170-6_7

Xia, F., Hou, W., Liu, Y., Wang, W., Han, Y., Yang, M., et al. (2018). Cytokine induced killer cells-assisted delivery of chlorin e6 mediated self-assembled gold nanoclusters to tumors for imaging and immuno-photodynamic therapy. *Biomaterials* 170, 1–11. doi: 10.1016/j.biomaterials.2018.03.048

Yang, Y., Wang, S., Wang, C., Tian, C., Shen, Y., and Zhu, M. (2019). Engineered targeted hyaluronic acid-glutathione-stabilized gold nanoclusters/graphene oxide 5-fluorouracil as a smart theranostic platform for stimulus-controlled fluorescence imaging-assisted synergetic chemo/phototherapy. *Chem Asian J.* 14, 1418–1423. doi: 10.1002/asia.201900153

Yao, Q., Kou, L., Tu, Y., and Zhu, L. (2018). MMP-responsive 'Smart' drug delivery and tumor targeting. *Trends Pharmacol. Sci.* 39, 766–781. doi: 10.1016/j.tips.2018.06.003

Yin, X., Mead, B. E., Safaee, H., Langer, R., Karp, J. M., and Levy, O. (2016). Engineering stem cell organoids. *Cell Stem Cell* 18, 25–38. doi: 10.1016/j.stem.2015.12.005

Yoshida, G. J., Azuma, A., Miura, Y., and Orimo, A. (2019). Activated fibroblast program orchestrates tumor initiation and progression; molecular mechanisms and the associated therapeutic strategies. *Int. J. Mol. Sci.* 20:2256. doi: 10.3390/ijms20092256

Yu, Z., Wang, M., Pan, W., Wang, H., Li, N., and Tang, B. (2017). Tumor microenvironment-triggered fabrication of gold nanomachines for tumor-specific photoacoustic imaging and photothermal therapy. *Chem. Sci.* 8, 4896–4903. doi: 10.1039/c7sc00700k

Zeiderman, M. R., Morgan, D. E., Christein, J. D., Grizzle, W. E., McMasters, K. M., and McNally, L. R. (2016). Acidic pH-targeted chitosan capped mesoporous silica coated gold nanorods facilitate detection of pancreatic tumors via multispectral optoacoustic tomography. *ACS Biomater Sci. Eng.* 2, 1108–1120. doi: 10.1021/acsbiomaterials.6b00111

Zeinizade, E., Tabei, M., Shakeri-Zadeh, A., Ghaznavi, H., Attaran, N., Komeili, A., et al. (2018). Selective apoptosis induction incancer cells using folate-conjugated gold nanoparticles and controlling the laser irradiation conditions. *Artif. Cells Nanomed. Biotechnol.* 46, 1026–1038. doi: 10.1080/21691401.2018.1443116

Zhang, A., Pan, S., Zhang, Y., Chang, J., Huang, Z., Li, T., et al. (2019). Carbon-gold hybrid nanoprobes for real-time imaging, photothermal/photodynamic and nanozyme oxidative therapy. *Theranostics.* 9, 3443–3458. doi: 10.7150/thno.33266

Zhang, Y., Xiong, X., Huai, Y., Dey, A., Hossen, M. N., Roy, R. V., et al. (2019). Gold nanoparticles disrupt tumor microenvironment - endothelial cell cross talk to inhibit angiogenic phenotypes *in vitro*. *Bioconjug. Chem.* 30, 1724–1733. doi: 10.1021/acs.bioconjchem.9b00262

Zhao, L., Choi, J., Lu, Y., and Kim, S. Y. (2019). Targeted photodynamic therapy activities of surface-enhanced Raman scattering-active theranostic system based on folate/Hyaluronic acid-functionalized gold nanochains. *J. Biomed. Nanotechnol.* 15, 544–554. doi: 10.1166/jbn.2019.2710

Zhao, X., Pan, J., Li, W., Yang, W., Qin, L., and Pan, Y. (2018). Gold nanoparticles enhance cisplatin delivery and potentiate chemotherapy by decompressing colorectal cancer vessels. *Int. J. Nanomedicine.* 13, 6207–6221. doi: 10.2147/IJN.S176928

Check for
updates

Targeted Approaches to Inhibit Sialylation of Multiple Myeloma in the Bone Marrow Microenvironment

Alessandro Natoni[1], Raghvendra Bohara[2], Abhay Pandit[2] and Michael O'Dwyer[1]*

[1] Apoptosis Research Centre, School of Medicine, National University of Ireland, Galway, Ireland, [2] Centre for Research in Medical Devices (CÚRAM), National University of Ireland, Galway, Ireland

Aberrant glycosylation modulates different aspects of tumor biology, and it has long been recognized as a hallmark of cancer. Among the different forms of glycosylation, sialylation, the addition of sialic acid to underlying oligosaccharides, is often dysregulated in cancer. Increased expression of sialylated glycans has been observed in many types of cancer, including multiple myeloma, and often correlates with aggressive metastatic behavior. Myeloma, a cancer of plasma cells, develops in the bone marrow, and colonizes multiple sites of the skeleton including the skull. In myeloma, the bone marrow represents an essential niche where the malignant cells are nurtured by the microenvironment and protected from chemotherapy. Here, we discuss the role of hypersialylation in the metastatic process focusing on multiple myeloma. In particular, we examine how increased sialylation modulates homing of malignant plasma cells into the bone marrow by regulating the activity of molecules important in bone marrow cellular trafficking including selectins and integrins. We also propose that inhibiting sialylation may represent a new therapeutic strategy to overcome bone marrow-mediated chemotherapy resistance and describe different targeted approaches to specifically deliver sialylation inhibitors to the bone marrow microenvironment.

Keywords: multiple myeloma, microenvironment, sialylation, targeted delivery, chemotherapy, ST3GAL6, E-selectin, integrins

INTRODUCTION

The development and progression of human malignancies from the first appearance of benign lesions to the emergence of deadly metastatic clones consist of a multi-step process involving the progressive acquisition of selective alterations that ultimately result in the pathological behavior of cancer cells. Glycosylation represents one of these processes that are often dysregulated in cancer. It is one of the most important co- and post-translational modifications that contributes to and modulates the many diverse functions of glycoconjugates. This extraordinary range of biological functions originates from the complexity and the diversity found within the glycan structure such as carbohydrate composition and linkage, anomeric state, branching, presence of additional modification (sulfation), and linkage to their aglycone part (carrier). As the majority of known glycoconjugates are exposed to the outer surface of the plasma membrane or secreted into the extracellular milieu, they mediate important biological processes such as cell adhesion, migration, immune response, as well as receptor activation and intracellular signaling. During tumor development, the glycan profile undergoes a profound and dynamic alteration that allows

cancer cells to acquire novel traits necessary for tumor progression. These glycosylation changes are not random and involve, among others, *de novo* synthesis of new carbohydrate structures, premature termination of pre-existing glycans, and increased expression of terminal sialylated glycans. Acquisition of sialylated structures represents one of the most important modifications of the glycome during tumor development, and it is often associated with an aggressive metastatic phenotype. However, the study of the role of sialylation in cancer is still in its infancy and strategies to efficiently and safely target this important biological process are still lacking.

MULTIPLE MYELOMA: A METASTATIC DISEASE THAT DEPENDS ON THE BONE MARROW MICROENVIRONMENT

Multiple myeloma (MM) arises from clonal expansion of terminally differentiated plasma cells in the bone marrow (BM). MM is usually preceded by asymptomatic precursor states called Monoclonal Gammopathy of Undetermined Significance (MGUS) and Smoldering MM (SMM). Genetic abnormalities, epigenetic alterations, and microenvironmental factors co-operate in the development of symptomatic MM (Bianchi and Munshi, 2015). The BM microenvironment represents the perfect niche where MM cells proliferate and become resistant to chemotherapeutic drugs (Manier et al., 2012). A combination of soluble growth factors and adhesion molecules mediate these pro-survival and proliferative signaling pathways (Di Marzo et al., 2016). This extreme dependency on the BM suggests that malignant cells could be particularly vulnerable in the circulation where the effective concentration of a chemotherapeutic drug is higher than in the BM and where they are more susceptible to an immune response. Thus, MM cells must have evolved strategies to enhance their survival in the bloodstream such as mechanisms of immune evasion and efficient homing into the BM. Supporting this hypothesis is the evidence that MM is highly metastatic, colonizing different sites of the axial skeleton including the skull (Moschetta et al., 2017). Homing of MM cells into the BM is primarily mediated by stromal cell-derived factor 1α (SDF1α) and its receptor C-X-C chemokine receptor type 4 (CXCR4) (Alsayed et al., 2007). This chemokine also plays a role in adhesion and possibly retention of MM in the BM via α4β1-dependent adhesion on fibronectin and vascular cell adhesion molecule 1 (VCAM-1) (Gazitt and Akay, 2004; Parmo-Cabanas et al., 2004; Menu et al., 2006). Besides SDF1α, other molecules have been shown to be important in homing and adhesion of MM to the BM. These include integrin α4β1, α4/β7, and P-selectin glycoprotein ligand-1 (PSGL-1), all of which are highly expressed on MM cells (Sanz-Rodriguez et al., 1999; Florena et al., 2005; Neri et al., 2011). Notably, these molecules, including SDF1α, are also involved in cell adhesion-mediated drug resistance (CAM-DR) and therefore represent attractive targets for MM therapy (Damiano et al., 1999; Azab et al., 2009; Muz et al., 2015; Waldschmidt et al., 2017). Although these molecules have been shown to be important in regulating critical biological processes involved in the progression and development of MM, little

is known about how post-translational modifications influence their functions. Above all, the role of sialylation in regulating some of the biological functions of these molecules has only been recently recognized. Secretion of extracellular vesicles (EVs) by malignant plasma cells represents another important mechanism of MM dissemination (Colombo et al., 2019). Indeed, MM-EVs have been found both in MM patients' peripheral blood (PB) and BM, and their levels in bloodstream positively correlate with the number of bone lesions (Zhang L. et al., 2019). It has been proposed that EVs have an important role in different steps of the metastatic process (Colombo et al., 2019). Due to their pro-coagulant activity, EVs could lead to platelet activation and polymerization of fibrinogen to fibrin, which in turn would enhance MM dissemination by protecting the malignant plasma cells in the circulation, favoring their seeding to distant sites and pre-conditioning the metastatic niche with platelet-derived cytokines (Labelle et al., 2014; Remiker and Palumbo, 2018; Nielsen et al., 2019). It has also been shown that MM-EVs contribute to neo-angiogenesis by inducing endothelial cell proliferation and formation of new blood vessels (Liu et al., 2014; Wang et al., 2016; Li et al., 2019; Zarfati et al., 2019). Whether MM-EV sialylation status is important for some or all their biological functions is yet to be confirmed. It is also tempting to speculate that MM-EVs could also alter the sialylation status of the metastatic niche favoring MM seeding and homing into the BM. Although this is just a hypothesis, it represents an exciting field for future studies.

SIALYLATION: AN IMPORTANT CO- AND POST-TRANSLATIONAL MODIFICATION IN CANCER BIOLOGY

Sialic acid refers to a group of ∼50 chemical variants of the nine carbon sugar neuraminic acid that are strategically placed at the tip of glycans. At physiological pH, sialic acids confer a negative charge to the underlying glycoproteins and glycolipids, which contribute to their physiological and biophysical functions. Indeed, sialic acids provide charge repulsion on human erythrocytes and other cells, preventing unwanted interactions of cells in the circulation. In the kidneys, sialic acids are critical in maintaining their normal filtering function (Gelberg et al., 1996), and extended polysialic acid chains can affect neuronal plasticity (Rutishauser, 2008). Moreover, sialic acids represent critical determinants of selectin ligands, which contribute to extravasation of immune cells to target organs and sites (Mcever, 2015). Pathologically, sialic acids are involved in many infectious diseases, being the targets for the binding of a large number of pathogenic organisms and their toxins, and in cancer (Varki, 2008). Indeed, aberrant sialylation is observed in many cancers and it seems to be a major contributor of the metastatic phenotype (Schultz et al., 2012).

Sialic acids can be added to the underlying sugars through different linkages: an α2-3- or an α2-6-bond to galactose (Gal); an α2-6-bond to N-acetylgalactosamine (GalNAc) or N-acetylglucosamine (GlcNAc); and an α2-8-bond to another sialic acid, forming polysialic acid. These linkages are elaborated by a

family of 20 sialyltransferases (STs), a class of glycosyltransferases that share the cytosine monophosphate (CMP)–sialic acid as substrate donor, but differ in tissue distribution, in the catalysis of the specific glycosidic linkage and in the recognition of the acceptor oligosaccharide and/or glycoconjugates (Harduin-Lepers et al., 2001). All the STs are highly stereoselective and catalyze the formation of an α-linked sialic acid to a precise hydroxyl group on a specific saccharide residue. The combination of the acceptor saccharide residue and the precise hydroxyl group on this residue can be used to divide the family into four distinct sub-families. For example, ST6Gal enzymes catalyze the transfer of sialic acid to the 6′-hydroxyl group of a Gal residue, ST3Gal enzymes catalyze the transfer of sialic acid to the 3′-hydroxyl group of a Gal residue, ST3GalNAc enzymes catalyze the transfer of sialic acid to the 6′-hydroxyl group of a GalNac, and ST3Sia enzymes catalyze the transfer of sialic acid to the 8′-hydroxyl group of another sialic acid residue. The number of the STs exceeds by far the number of existing sialyl linkages, suggesting a certain degree of redundancy. However, although there are six STs capable of catalyzing the transfer of sialic acid to an underlying Gal residue in an α2-3 linkage, only two of them, namely, ST3GAL4 and ST3GAL6, have been implicated in synthetizing selectin ligands (Rodrigues and Macauley, 2018). Thus, it might be possible that the structure of the underlying glycans together with the protein or lipid backbone dictate the specificity of the different STs.

Aberrant sialylation can arise as a result of different mechanisms including overexpression of STs, dysfunction of the enzymes that controls the synthesis and availability of CPM–sialic acids and downregulation of sialidase, the enzymes that cleave off sialic acids from glycans (Rodrigues and Macauley, 2018). Aberrant sialylation seems to be particularly important in promoting tumor dissemination, survival in the circulation, adhesion on the target endothelium, and extravasation (Schultz et al., 2012). For example, ST6GAL1 has been implicated in many metastatic tumors (Garnham et al., 2019). Physiologically, ST6GAL1 is involved in the generation of CD22 ligands that control B cell functions (Clark and Giltiay, 2018). However, upregulation of ST6GAL1 in cancer leads to enhanced migration and invasiveness by specifically inducing sialylation of the integrin β1 (Seales et al., 2005; Christie et al., 2008; Shaikh et al., 2008). Selectin ligands represent another class of molecules that are regulated by sialylation and are instrumental in directing tumor cell adhesion on the endothelium of target organs during metastatic dissemination (Natoni et al., 2016). Sialyl Lewis (sLe) structures are essential determinants for the function of selectin ligands. These are tetrasaccharide structures composed of a GlcNAc-Gal backbone, an α2-3-linked sialic acid to Gal, and a fucose linked to GlcNAc either with an α1-3 (sLe^x) or an α1-4 linkage (sLe^a). Through selectin ligand/selectin interactions, tumor cells are able to tether and roll on the vascular endothelium in a process that closely mirror leukocyte extravasation during inflammation or homing (Gout et al., 2008). This represents the first step in cancer seeding and colonization of target organs. Notably, the expression of selectin ligands on cancer cells seems to correlate with metastatic phenotype (Fukuoka et al., 1998; Tatsumi et al., 1998; Ben-David et al., 2008; Geng

et al., 2012; Li et al., 2013) and disease progression (Chien et al., 2013; Gakhar et al., 2013) and negatively correlate with patient survival (Amado et al., 1998; Baldus et al., 1998; Grabowski et al., 2000; Woodman et al., 2016).

Aberrant sialylation can indirectly promote metastatic spread by increasing survival of metastatic cells in the circulation. P-selectin ligands on tumor cells interact with P-selectin on platelets, inducing the formation of a platelet cloak that efficiently suppresses the innate immune system and promotes metastasis (Placke et al., 2012; Cluxton et al., 2019). Sialoglycans are also recognized by a class of immunomodulatory receptors named sialic acid-binding immunoglobulin-type lectins (Siglecs), which mainly serve as negative modulators of the immune system (Rodrigues and Macauley, 2018). In this respect, sialoglycans can be considered as self-associated molecular patterns (SAMPs) that can lead to inhibition of immune responses against self. Hypersialylation can also induce immune evasion by interference with the complement system via a "molecular cloaking" mechanism mediated by Factor H sequestration and dampening of the complement-mediated cell lysis and opsonization (Fedarko et al., 2000). Thus, hypersialylation can contribute to the metastatic phenotype of cancer cells with a variety of mechanisms that interfere with different biological processes spanning from immune surveillance to adhesion.

ROLE OF SIALYLATION IN THE BIOLOGY OF MYELOMA

The first evidence of altered sialylation in MM dates back to 1984, when an increase in ST activity was reported in mononuclear cells and serum derived from the PB and BM of MM patients compared to MGUS and healthy individuals (Cohen et al., 1989). However, despite this important observation, there was no functional characterization of this enhanced ST activity. Direct evidence of a role of aberrant sialylation in MM came from the observation that ST3GAL6, a ST responsible for the generation of α2-3-linked sialic acids, was highly expressed in MM and correlated with inferior overall survival (Glavey et al., 2014). In particular, it was shown that ST3GAL6 knock-down reduced MM adhesion on BM stromal cells and transendothelial migration *in vitro* and MM homing into the BM *in vivo*. This study revealed for the first time a functional link between sialylation and homing of MM into the BM and inspired subsequent studies aiming at understanding the underlying molecular mechanism(s). ST3GAL6 contributes to the generation of sialofucosylated structures such as Sle$^{a/x}$ that are recognized by E-selectin (Yang et al., 2012) and may directly participate to the generation of E-selectin ligands on MM cells. Importantly, E-selectin is constitutively expressed on the BM endothelium (Schweitzer et al., 1996; Sipkins et al., 2005) and plays a crucial role in homing of human hematopoietic stem cells (HSC) into the BM (Hidalgo et al., 2002). It has also been shown that E-selectin drives cancer metastasis into the BM (Price et al., 2016; Esposito et al., 2019). Since MM metastasizes into the BM and expresses high levels of ST3GAL6, it is conceivable to hypothesize that E-selectin, together with SDF1α, plays an important role

in MM homing. Indeed, it was recently shown that E-selectin ligands expressed on MM cells played a role in BM homing and possibly retention of the malignant cells in the BM (Martinez-Moreno et al., 2016; Natoni et al., 2017). Notably, it was shown that MM cells enriched for E-selectin ligands recognized by the monoclonal antibody Heca452 (MM$^{Heca452\ Enriched}$) were resistant to bortezomib treatment *in vivo*, and this resistance was reversed by a small glycomimetic molecule, GMI-1271, which inhibits E-selectin/E-selectin ligand interaction (Natoni et al., 2017). The mechanism(s) of this bortezomib resistance displayed *in vivo* by the MM$^{Heca452\ Enriched}$ cells is still not known. An intriguing hypothesis is that the presence of E-selectin ligands on the MM$^{Heca452\ Enriched}$ cells facilitate their homing into the BM, which then provides protection to bortezomib-induced cell death. In this scenario, E-selectin ligands ensure efficient trafficking into the BM, decreasing the time MM$^{Heca452\ Enriched}$ cells are exposed to bortezomib in the circulation. In line with this hypothesis, we found that GMI-1271 treatment induced an accumulation of MM$^{Heca452\ Enriched}$ cells in the peripheral blood where they may be more sensitive to bortezomib. Alternatively, E-selectin may retain the MM$^{Heca452\ Enriched}$ cells into the BM and GMI-1271 induced egress of these cells into the circulation, a mechanism that has been proposed for leukemic stem cells (Winkler et al., 2014). Obviously, a combination of both mechanisms could be possible.

In addition to the generation of selectin ligands, sialylation plays other roles in MM. Indeed, we have recently shown that the sialylation status of the α4 subunit of integrins α4β1 and α4β7 modulates their activity (Natoni et al., 2019). Specifically, we have shown that inhibition of sialylation using 3F$_{ax}$-Neu5Ac, a global inhibitor of the ST family (Rillahan et al., 2012), impaired maturation of the α4 chain, greatly reducing the ability of MM cells to interact with VCAM-1 and mucosal vascular addressin cell adhesion molecule 1 (MADCAM-1). VCAM-1, the counter-receptor for integrin α4β1, is expressed by the BM endothelial and stromal cells (Simmons et al., 1992; Schweitzer et al., 1996) and participates in MM adhesion on BM endothelial cells (Okada et al., 1999; Parmo-Cabanas et al., 2004). MADCAM-1, the counter-receptor for integrin α4β7, is also expressed in the BM and promotes homing of HSCs into the BM (Katayama et al., 2004; Tada et al., 2008; Murakami et al., 2016). Similarly, MADCAM-1 together with E-selectin and SDF1α could facilitate homing of MM into the BM. Thus, global inhibition of sialylation may have a broad impact on MM homing. Indeed, we have shown that using a mouse model identical to our previous study, 3F$_{ax}$-Neu5Ac not only improved survival by enhancing bortezomib sensitivity but also prolonged survival and reduced tumor burden even in the absence of bortezomib, indicating that inhibition of sialylation was beneficial even without the addition of chemotherapy (Natoni et al., 2019).

Sialylation seems to regulate the function of CD147, also known as extracellular matrix metalloproteinase inducer (EMMPRIN). CD147 has been shown to be involved in MM proliferation and metastasis (Zhu et al., 2015). Importantly, sialylation of CD147 is upregulated by IL-6 (Wang et al., 2017). This observation opens the fascinating possibility that sialylation

is also regulated by the microenvironment. Indeed, in the same study, it was shown that IL-6 transcriptionally upregulated several STs, such as *ST3GAL3*, *ST3GAL6*, and *ST6GAL1* through the activation of signal transducer and activator of transcription 3 (STAT3) (Wang et al., 2017). It should be noted that ST6GAL1 has been proposed to be the main ST regulating the sialylation of the integrin subunit β1; thus, it might impact migration, adhesion, and dissemination of MM cells (Seales et al., 2005; Christie et al., 2008; Shaikh et al., 2008).

Another microenvironmental factor that regulates the expression of STs and, in particular, ST3GAL6 is hypoxia (Glavey et al., 2014). MM develops in the BM, which represents an extremely hypoxic niche (Hu et al., 2010), and it has been shown that hypoxia promotes MM dissemination (Azab et al., 2012). Thus, upregulation of STs may represent one of the mechanisms by which hypoxia facilitates metastatic spread of MM cells.

Besides the microenvironment, ST expression in MM can also be regulated by long non-coding RNAs (lncRNAs). Indeed, it has been recently shown that the mRNA levels of *ST3GAL6* are regulated by the lncRNA ST3GAL6-AS1 (Shen et al., 2018a; Vinci et al., 2018). Interestingly, ST3GAL6-AS1 is upregulated in MM, and its mRNA levels directly correlate with those of ST3GAL6 (Shen et al., 2018b; Vinci et al., 2018). Knocking down ST3GAL6-AS1 results in decreased migration, invasion, and adhesion of MM to fibronectin, HUVEC, and collagen type I (Shen et al., 2018a). Although the molecular mechanisms responsible for these phenotypes are still unknown, ST3GAL6-AS1 knock-down causes a decrease in ST3GAL6 levels, suggesting co-regulatory mechanism(s), resulting in impaired sialylation.

It has been recently shown that the monoclonal immunoglobulins secreted by the malignant plasma cells display an aberrant glycosylation pattern (Zhang Z. et al., 2019). In particular, a detailed analysis of the total protein *N*-glycans derived from serum samples of MM patients showed a decrease in the α2-3- and α2-6-linked sialic acids on secreted monoclonal immunoglobulins. Thus, it might be possible that alterations in the ST expression pattern in MM favor an increase in sialylation of the cell surface over secreted proteins, although this needs to be confirmed. Moreover, in the previous study, the *N*-glycans, but not *O*-glycans, were analyzed; thus, a more comprehensive view of the sialylation status of MM secreted proteins is still lacking.

As all these studies point out, aberrant sialylation plays an important role in MM, especially in the metastatic spread of the malignant cells and in their retention into the BM niche. The relevance of sialylation in MM is reinforced by the observation that the expression of ST genes such as *ST3GAL6* and *ST3GAL1*, either alone or in combination with other glycogenes, can identify patients with poor outcome (Glavey et al., 2013; Connolly et al., 2016). While ST3GAL6 has been implicated in the generation of E-selectin ligands (Yang et al., 2012), ST3GAL1 acts predominantly on Core-1 O-glycans, masking the tumor from surrounding immune cells (Burchell et al., 1999). Therefore, sialylation may well-represent an important target for future therapeutic strategies especially in combination with standard and novel chemotherapeutic drugs. However, a major obstacle to clinical development of current

ST inhibitors is their potential to induce nephrotoxicity, which appears to be the major dose-limiting toxicity in *in vivo* studies (Macauley et al., 2014). This is particularly relevant in MM where renal impairment is common. While novel and more specific ST inhibitors may overcome this problem, targeted delivery systems capable of selectively releasing ST inhibitors into the BM microenvironment or the MM cells, could represent an attractive alternative solution. Besides nephrotoxicity, other potential side effects of global sialylation inhibition are those related to the hematopoietic system. Since sialic acid is an important determinant of E-, P-, and L-selectin ligands present on the immune cells (Varki, 1994; Sperandio, 2006; Zarbock et al., 2011), global sialylation inhibition will inevitably affect their biological functions, in particular leukocyte trafficking and extravasation. Elevated levels of α2-3-linked sialic acid together with overexpression of ST3GAL6 have been found in CD133 positive hematopoietic stem and progenitor cells (Hemmoranta et al., 2007). Moreover, it has been shown that expression of E-selectin in the BM is required for HSC homing into the BM (Hidalgo et al., 2002). Thus, sialylation inhibition would probably lead to hematopoietic stem and progenitor cell mobilization and impair their homing into the BM. However, it should be noted that E-selectin inhibition using the specific E-selectin inhibitor

GMI1271 in clinical trials in MM (NCT02811822) and AML (NCT02306291) has not been associated with myelosuppression or other side effects.

LIPOSOME-BASED TARGETED DELIVERY IN MM

Nanomedicine approaches offer the potential of enhanced and more personalized therapeutics in MM with a reduced risk of off-target effects (**Table 1**). Current treatments in MM rely on immunomodulatory drugs such as lenalidomide combined with proteasome inhibitors (PI) such as bortezomib (De La Puente and Azab, 2017). The introduction of PI inhibitors has contributed to major improvements in patient survival, but off-target effects, in particular neurotoxicity, remain a major concern (Richardson et al., 2009). Moreover, the emergence of drug resistance and how to deal with this has become a burning issue of research in MM. The tumor physiology offers a wide range of targeting opportunity, which can be designed or tuned and simultaneously co-delivered with chemotherapeutics for more personalized therapy in MM. Several groups have developed different systems to facilitate targeted delivery of chemotherapeutics in MM

TABLE 1 | Liposome-based targeted treatment available for MM.

References	Nanoparticles	Drug loaded	Targeting moiety	*In vitro* study	*In vivo* study
Ashley et al., 2014	Liposomes	Carfilzomib	VLA-4 targeted	MM1S and NCI-H929 cell	SCID mice injected with NCI-H929 tumors
Braham et al., 2018	Liposomes	Doxorubicin Bortezomib	VLA-4 targeted	BM myeloma multipotent mesenchymal stromal cells, endothelial progenitor cells, and L363, and MM1S cells co-cultured in hydrogel.	N/A
Chang et al., 2016	Liposomes	Paclitaxel	Alendronate and transferrin	MM1S	MM1S GFP+ cells were injected into each mouse via the tail vein to prepare the tumor-bearing model
Lopes De Menezes et al., 2000	Liposomes	Doxorubicin	Anti-CD 19	Heterogeneous mixture of PBMC from MM patients and ARH77 cell	N/A
Maillard et al., 2005	Liposome	Hydroxy-tamoxifen (4-HT) or RU 58668	N/A	RPMI 8226	RPMI 8226 in female nude mice
Swami et al., 2014	PEG PLGA	Bortezomib	Alendronate	MM1S	NOD/SCID mice injected with MM1S GFP+ Luc+ cells
De La Puente et al., 2018	Chitosan	Bortezomib	anti-CD38	MM1S, RPMI 8226, NCI-H929, and U266	MM1S GFP+ Luc+-injected SCID mice
Yang et al., 2015	Fe₃O₄	Paclitaxel	Monoclonal antibody against ABCG2	RPMI 8266 cells and BM mononuclear cells	MM CSCs from human MM RPMI 8226 cells based on the CD138⁻CD34⁻cell phenotypes injected in NOD/SCID
Kotagiri et al., 2018	Nano micelles	Titanocene	VLA-4 targeted	MM1S	MM1S Luc+ cells in SCID mice

ABCG2, ATP binding cassette subfamily g member 2; BM, bone marrow; CSCs, cancer stem cells; HA-P(TMC-co-DTC), HA-b-poly(trimethylene carbonate-co-dithiolane trimethylene carbonate) (HA-P[TMC-co-DTC]); GFP, green fluorescence protein; Luc, Luciferase; NOD, non-obese diabetic; MM, multiple myeloma; N/A, not available; PBMC, peripheral blood mononuclear cells; PEG, polyethylene glycol; PLGA, poly(lactic-co-glycolic acid); SCID, severe combined immunodeficiency; VLA, very late antigen.

(Du et al., 2012). Targeting tumor physiology using antibodies, functional groups, or small molecules seems to be a more rational approach to minimize off-target effects. Kiziltepe et al. have shown that delivering doxorubicin using a lipid-PEG block polymer nano-formulation tagged by the VLA-4 antigen was significantly more cytotoxic to MM cells compared to the free drug (Kiziltepe et al., 2012). Using an alternative approach, Chang et al. developed dioleoyl phosphatidic acid (DOPA)-based paclitaxel (PTX)-loaded liposomes with modifications of alendronate and transferrin, which were able to target the bone microenvironment (Chang et al., 2016). Targeting the CD38 receptor in MM represents an additional attractive approach as CD38 is highly expressed on malignant plasma cells (De La Puente et al., 2018). Azab's group successfully prepared a chitosan nanoparticle formulation tagged with anti-CD38 monoclonal antibodies to deliver bortezomib *in vivo*, improving its therapeutic efficacy and reducing side effects (De La Puente et al., 2018). This formulation showed increased therapeutic activity and reduced off-target effects compared to the free drug. Thus, targeted delivery of chemotherapeutic drugs has proven valuable in MM, and a similar approach could be used to safely deliver $3F_{ax}$-Neu5Ac, avoiding kidney toxicity. Indeed, Büll et al. have shown that encapsulation of $3F_{ax}$-Neu5Ac in poly(lactic-co-glycolic acid) (PLGA)-based nanoparticles (NPs) targeting the melanoma antigen tyrosinase related protein-1 (TRP-1) allowed specific and prolonged blockade of sialic acid expression *in vitro* and precluded metastatic spread *in vivo* (Bull et al., 2015). A similar strategy could be employed using antibodies specific to MM antigens (such as CD38 and BCMA) or by incorporating bisphosphonates into the nanoparticles to target the BM (Swami et al., 2014). Inhibiting sialylation using these approaches could have also beneficial effects on the tumor microenvironment. For instance, it has been recently reported that sialic acid blockade via intra-tumoral injection of $3F_{ax}$-Neu5Ac could suppress tumor growth by enhancing T cell-mediated tumor immunity (Bull et al., 2018). Indeed, ST inhibition increased the number of activated effector immune cells, including $CD8^+$ T cells and natural killer (NK) cells, along with a reduction in regulatory T cells (Tregs) and activation of dendritic cells (DCs).

CONCLUSION

Using different systems, it should be possible to safely target the delivery of $3F_{ax}$-Neu5Ac to the BM to inhibit sialylation in MM. We are currently working on a delivery system that employs $3F_{ax}$-Neu5Ac encapsulated into liposomes functionalized with bisphosphonates for selective delivery into the BM with promising results. This approach has the potential to block homing of MM into the BM and mobilize the malignant cells into the circulation, making them more sensitive to chemotherapeutic drugs. Moreover, release of $3F_{ax}$-Neu5Ac in the BM could have profound effects on the BM microenvironment. Indeed, we have recently shown that BM stromal cells cultured under conditions that mimic the inflammatory BM microenvironment in MM become highly immune suppressive and that this phenotype could be completely reverted by $3F_{ax}$-Neu5Ac (Lynch et al., 2017). Thus, sialylation is a valuable target in both MM cells and the BM microenvironment.

AUTHOR CONTRIBUTIONS

AN and RB conceived and wrote the manuscript. AP and MO'D proofed and approved the final version of the manuscript.

REFERENCES

Alsayed, Y., Ngo, H., Runnels, J., Leleu, X., Singha, U. K., Pitsillides, C. M., et al. (2007). Mechanisms of regulation of CXCR4/SDF-1 (CXCL12)-dependent migration and homing in multiple myeloma. *Blood* 109, 2708–2717. doi: 10.1182/blood-2006-07-035857

Amado, M., Carneiro, F., Seixas, M., Clausen, H., and Sobrinho-Simoes, M. (1998). Dimeric sialyl-Le(x) expression in gastric carcinoma correlates with venous invasion and poor outcome. *Gastroenterology* 114, 462–470. doi: 10.1016/S0016-5085(98)70529-3

Ashley, J. D., Stefanick, J. F., Schroeder, V. A., Suckow, M. A., Alves, N. J., Suzuki, R., et al. (2014). Liposomal carfilzomib nanoparticles effectively target multiple myeloma cells and demonstrate enhanced efficacy *in vivo*. *J. Control. Release* 196, 113–121. doi: 10.1016/j.jconrel.2014.10.005

Azab, A. K., Hu, J., Quang, P., Azab, F., Pitsillides, C., Awwad, R., et al. (2012). Hypoxia promotes dissemination of multiple myeloma through acquisition of epithelial to mesenchymal transition-like features. *Blood* 119, 5782–5794. doi: 10.1182/blood-2011-09-380410

Azab, A. K., Runnels, J. M., Pitsillides, C., Moreau, A. S., Azab, F., Leleu, X., et al. (2009). CXCR4 inhibitor AMD3100 disrupts the interaction of multiple myeloma cells with the bone marrow microenvironment and enhances their sensitivity to therapy. *Blood* 113, 4341–4351. doi: 10.1182/blood-2008-10-186668

Baldus, S. E., Zirbes, T. K., Monig, S. P., Engel, S., Monaca, E., Rafiqpoor, K., et al. (1998). Histopathological subtypes and prognosis of gastric cancer are correlated with the expression of mucin-associated sialylated antigens: Sialosyl-Lewis(a), Sialosyl-Lewis(x) and sialosyl-Tn. *Tumour Biol.* 19, 445–453. doi: 10.1159/000030036

Ben-David, T., Sagi-Assif, O., Meshel, T., Lifshitz, V., Yron, I., and Witz, I. P. (2008). The involvement of the sLe-a selectin ligand in the extravasation of human colorectal carcinoma cells. *Immunol. Lett.* 116, 218–224. doi: 10.1016/j.imlet.2007.11.022

Bianchi, G., and Munshi, N. C. (2015). Pathogenesis beyond the cancer clone(s) in multiple myeloma. *Blood* 125, 3049–3058. doi: 10.1182/blood-2014-11-568881

Braham, M. V., Deshantri, A. K., Minnema, M. C., Oner, F. C., Schiffelers, R. M., Fens, M. H., et al. (2018). Liposomal drug delivery in an *in vitro* 3D bone

marrow model for multiple myeloma. *Int. J. Nanomedicine* 13, 8105–8118. doi: 10.2147/IJN.S184262

Bull, C., Boltje, T. J., Balneger, N., Weischer, S. M., Wassink, M., Van Gemst, J. J., et al. (2018). Sialic acid blockade suppresses tumor growth by enhancing T-cell-mediated tumor immunity. *Cancer Res.* 78, 3574–3588. doi: 10.1158/0008-5472.CAN-17-3376

Bull, C., Boltje, T. J., Van Dinther, E. A., Peters, T., De Graaf, A. M., Leusen, J. H., et al. (2015). Targeted delivery of a sialic acid-blocking glycomimetic to cancer cells inhibits metastatic spread. *ACS Nano* 9, 733–745. doi: 10.1021/nn5061964

Burchell, J., Poulsom, R., Hanby, A., Whitehouse, C., Cooper, L., Clausen, H., et al. (1999). An alpha2,3 sialyltransferase (ST3Gal I) is elevated in primary breast carcinomas. *Glycobiology* 9, 1307–1311. doi: 10.1093/glycob/9.12.1307

Chang, Q., Geng, R., Wang, S., Qu, D., and Kong, X. (2016). DOPA-based paclitaxel-loaded liposomes with modifications of transferrin and alendronate for bone and myeloma targeting. *Drug Deliv.* 23, 3629–3638. doi: 10.1080/10717544.2016.1214989

Chien, S., Haq, S. U., Pawlus, M., Moon, R. T., Estey, E. H., Appelbaum, F. R., et al. (2013). Adhesion of acute myeloid leukemia blasts to E-selectin in the vascular niche enhances their survival by mechanisms such as Wnt activation. *Blood* 122:62.

Christie, D. R., Shaikh, F. M., Lucas, J. A. IV, Lucas, J. A. III, and Bellis, S. L. (2008). ST6Gal-I expression in ovarian cancer cells promotes an invasive phenotype by altering integrin glycosylation and function. *J. Ovarian Res.* 1:3. doi: 10.1186/1757-2215-1-3

Clark, E. A., and Giltiay, N. V. (2018). CD22: a regulator of innate and adaptive B cell responses and autoimmunity. *Front. Immunol.* 9:2235. doi: 10.3389/fimmu.2018.02235

Cluxton, C. D., Spillane, C., O'toole, S. A., Sheils, O., Gardiner, C. M., and O'leary, J. J. (2019). Suppression of natural killer cell NKG2D and CD226 anti-tumour cascades by platelet cloaked cancer cells: implications for the metastatic cascade. *PLoS ONE* 14:e0211538. doi: 10.1371/journal.pone.0211538

Cohen, A. M., Allalouf, D., Bessler, H., Djaldetti, M., Malachi, T., and Levinsky, H. (1989). Sialyltransferase activity and sialic-acid levels in multiple-myeloma and monoclonal gammopathy. *Eur. J. Haematol.* 42, 289–292. doi: 10.1111/j.1600-0609.1989.tb00114.x

Colombo, M., Giannandrea, D., Lesma, E., Basile, A., and Chiaramonte, R. (2019). Extracellular vesicles enhance multiple myeloma metastatic dissemination. *Int. J. Mol. Sci.* 20:E3236. doi: 10.3390/ijms20133236

Connolly, C., Jha, A., Natoni, A., and O'dwyer, M. E. (2016). A 13-glycosylation gene signature in multiple myeloma can predicts survival and identifies candidates for targeted therapy (GiMM13). *Blood* 128:4423.

Damiano, J. S., Cress, A. E., Hazlehurst, L. A., Shtil, A. A., and Dalton, W. S. (1999). Cell adhesion mediated drug resistance (CAM-DR): role of integrins and resistance to apoptosis in human myeloma cell lines. *Blood* 93, 1658–1667.

De La Puente, P., and Azab, A. K. (2017). Nanoparticle delivery systems, general approaches, and their implementation in multiple myeloma. *Eur. J. Haematol.* 98, 529–541. doi: 10.1111/ejh.12870

De La Puente, P., Luderer, M. J., Federico, C., Jin, A., Gilson, R. C., Egbulefu, C., et al. (2018). Enhancing proteasome-inhibitory activity and specificity of bortezomib by CD38 targeted nanoparticles in multiple myeloma. *J. Control. Release* 270, 158–176. doi: 10.1016/j.jconrel.2017.11.045

Di Marzo, L., Desantis, V., Solimando, A. G., Ruggieri, S., Annese, T., Nico, B., et al. (2016). Microenvironment drug resistance in multiple myeloma: emerging new players. *Oncotarget* 7, 60698–60711. doi: 10.18632/oncotarget.10849

Du, B. Y., Song, W., Bai, L., Shen, Y., Miao, S. Y., and Wang, L. F. (2012). Synergistic effects of combination treatment with bortezomib and doxorubicin in human neuroblastoma cell lines. *Chemotherapy* 58, 44–51. doi: 10.1159/000335603

Esposito, M., Mondal, N., Greco, T. M., Wei, Y., Spadazzi, C., Lin, S. C., et al. (2019). Bone vascular niche E-selectin induces mesenchymal–epithelial transition and Wnt activation in cancer cells to promote bone metastasis. *Nat. Cell Biol.* 21, 627–639. doi: 10.1038/s41556-019-0309-2

Fedarko, N. S., Fohr, B., Robey, P. G., Young, M. F., and Fisher, L. W. (2000). Factor H binding to bone sialoprotein and osteopontin enables tumor cell evasion of complement-mediated attack. *J. Biol. Chem.* 275, 16666–16672. doi: 10.1074/jbc.M001123200

Florena, A. M., Tripodo, C., Miceli, L., Ingrao, S., Porcasi, R., and Franco, V. (2005). Identification of CD162 in plasma-cell dyscrasia. *Lancet Oncol.* 6:632. doi: 10.1016/S1470-2045(05)70287-4

Fukuoka, K., Narita, N., and Saijo, N. (1998). Increased expression of sialyl Lewis(x) antigen is associated with distant metastasis in lung cancer patients: immunohistochemical study on bronchofiberscopic biopsy specimens. *Lung Cancer* 20, 109–116. doi: 10.1016/S0169-5002(98)00016-6

Gakhar, G., Navarro, V. N., Jurish, M., Lee, G. Y., Tagawa, S. T., Akhtar, N. H., et al. (2013). Circulating tumor cells from prostate cancer patients interact with E-selectin under physiologic blood flow. *PLoS ONE* 8:e85143. doi: 10.1371/journal.pone.0085143

Garnham, R., Scott, E., Livermore, K. E., and Munkley, J. (2019). ST6GAL1: a key player in cancer. *Oncol. Lett.* 18, 983–989. doi: 10.3892/ol.2019.10458

Gazitt, Y., and Akay, C. (2004). Mobilization of myeloma cells involves SDF-1/CXCR4 signaling and downregulation of VLA-4. *Stem Cells* 22, 65–73. doi: 10.1634/stemcells.22-1-65

Gelberg, H., Healy, L., Whiteley, H., Miller, L. A., and Vimr, E. (1996). *In vivo* enzymatic removal of alpha 2–>6-linked sialic acid from the glomerular filtration barrier results in podocyte charge alteration and glomerular injury. *Lab. Invest.* 74, 907–920.

Geng, Y., Yeh, K., Takatani, T., and King, M. R. (2012). Three to tango: MUC1 as a ligand for both E-selectin and ICAM-1 in the breast cancer metastatic cascade. *Front. Oncol.* 2:76. doi: 10.3389/fonc.2012.00076

Glavey, S., Wu, P., Murillo, L. S., Loughrey, C., Roccaro, A. M., Morgan, G. J., et al. (2013). Low expression of the FUCA1 gene is an adverse prognostic factor in myeloma and combined with high sialyltransferase gene expression identifies patients at increased risk of early disease progression and death. *Blood* 122:1864.

Glavey, S. V., Manier, S., Natoni, A., Sacco, A., Moschetta, M., Reagan, M. R., et al. (2014). The sialyltransferase ST3GAL6 influences homing and survival in multiple myeloma. *Blood* 124, 1765–1776. doi: 10.1182/blood-2014-03-560862

Gout, S., Tremblay, P. L., and Huot, J. (2008). Selectins and selectin ligands in extravasation of cancer cells and organ selectivity of metastasis. *Clin. Exp. Metastasis* 25, 335–344. doi: 10.1007/s10585-007-9096-4

Grabowski, P., Mann, B., Mansmann, U., Lovin, N., Foss, H. D., Berger, G., et al. (2000). Expression of SIALYL-Le(x) antigen defined by MAb AM-3 is an independent prognostic marker in colorectal carcinoma patients. *Int. J. Cancer* 88, 281–286. doi: 10.1002/1097-0215(20001015)88:2<281::AID-IJC21>3.0.CO;2-2

Harduin-Lepers, A., Vallejo-Ruiz, V., Krzewinski-Recchi, M. A., Samyn-Petit, B., Julien, S., and Delannoy, P. (2001). The human sialyltransferase family. *Biochimie* 83, 727–737. doi: 10.1016/S0300-9084(01)01301-3

Hemmoranta, H., Satomaa, T., Blomqvist, M., Heiskanen, A., Aitio, O., Saarinen, J., et al. (2007). N-glycan structures and associated gene expression reflect the characteristic N-glycosylation pattern of human hematopoietic stem and progenitor cells. *Exp. Hematol.* 35, 1279–1292. doi: 10.1016/j.exphem.2007.05.006

Hidalgo, A., Weiss, L. A., and Frenette, P. S. (2002). Functional selectin ligands mediating human CD34(+) cell interactions with bone marrow endothelium are enhanced postnatally. *J. Clin. Invest.* 110, 559–569. doi: 10.1172/JCI0214047

Hu, J., Handisides, D. R., Van Valckenborgh, E., De Raeve, H., Menu, E., Vande Broek, I., et al. (2010). Targeting the multiple myeloma hypoxic niche with TH-302, a hypoxia-activated prodrug. *Blood* 116, 1524–1527. doi: 10.1182/blood-2010-02-269126

Katayama, Y., Hidalgo, A., Peired, A., and Frenette, P. S. (2004). Integrin alpha4beta7 and its counterreceptor MAdCAM-1 contribute to hematopoietic progenitor recruitment into bone marrow following transplantation. *Blood* 104, 2020–2026. doi: 10.1182/blood-2003-12-4157

Kiziltepe, T., Ashley, J. D., Stefanick, J. F., Qi, Y. M., Alves, N. J., Handlogten, M. W., et al. (2012). Rationally engineered nanoparticles target multiple myeloma cells, overcome cell-adhesion-mediated drug resistance, and show enhanced efficacy *in vivo*. *Blood Cancer J.* 2:e64. doi: 10.1038/bcj.2012.10

Kotagiri, N., Cooper, M. L., Rettig, M., Egbulefu, C., Prior, J., Cui, G., et al. (2018). Radionuclides transform chemotherapeutics into phototherapeutics for precise treatment of disseminated cancer. *Nat. Commun.* 9, 275–286. doi: 10.1038/s41467-017-02758-9

Labelle, M., Begum, S., and Hynes, R. O. (2014). Platelets guide the formation of early metastatic niches. *Proc. Natl. Acad. Sci. U.S.A.* 111, E3053–3061. doi: 10.1073/pnas.1411082111

Li, B., Hong, J., Hong, M., Wang, Y., Yu, T., Zang, S., et al. (2019). piRNA-823 delivered by multiple myeloma-derived extracellular vesicles promoted tumorigenesis through re-educating endothelial cells in the tumor environment. *Oncogene* 38, 5227–5238. doi: 10.1038/s41388-019-0788-4

Li, J., Guillebon, A. D., Hsu, J. W., Barthel, S. R., Dimitroff, C. J., Lee, Y. F., et al. (2013). Human fucosyltransferase 6 enables prostate cancer metastasis to bone. *Br. J. Cancer* 109, 3014–3022. doi: 10.1038/bjc.2013.690

Liu, Y., Zhu, X. J., Zeng, C., Wu, P. H., Wang, H. X., Chen, Z. C., et al. (2014). Microvesicles secreted from human multiple myeloma cells promote angiogenesis. *Acta Pharmacol. Sin.* 35, 230–238. doi: 10.1038/aps.2013.141

Lopes De Menezes, D. E., Pilarski, L. M., Belch, A. R., and Allen, T. M. (2000). Selective targeting of immunoliposomal doxorubicin against human multiple myeloma *in vitro* and *ex vivo*. *Biochim. Biophys. Acta* 1466, 205–220. doi: 10.1016/S0005-2736(00)00203-0

Lynch, K., Grace, O. M., Ryan, A., Ritter, T., and O'dwyer, M. (2017). Mesenchymal stromal cell sialylation enhances immune suppression in multiple myeloma. *Blood* 130:124.

Macauley, M. S., Arlian, B. M., Rillahan, C. D., Pang, P. C., Bortell, N., Marcondes, M. C., et al. (2014). Systemic blockade of sialylation in mice with a global inhibitor of sialyltransferases. *J. Biol. Chem.* 289, 35149–35158. doi: 10.1074/jbc.M114.606517

Maillard, S., Ameller, T., Gauduchon, J., Gougelet, A., Gouilleux, F., Legrand, P., et al. (2005). Innovative drug delivery nanosystems improve the anti-tumor activity *in vitro* and *in vivo* of anti-estrogens in human breast cancer and multiple myeloma. *J. Steroid Biochem. Mol. Biol.* 94, 111–121. doi: 10.1016/j.jsbmb.2004.12.023

Manier, S., Sacco, A., Leleu, X., Ghobrial, I. M., and Roccaro, A. M. (2012). Bone marrow microenvironment in multiple myeloma progression. *J. Biomed. Biotechnol.* 2012, 157496–157500. doi: 10.1155/2012/157496

Martinez-Moreno, M., Leiva, M., Aguilera-Montilla, N., Sevilla-Movilla, S., Isern De Val, S., Arellano-Sanchez, N., et al. (2016). *In vivo* adhesion of malignant B cells to bone marrow microvasculature is regulated by α4β1 cytoplasmic-binding proteins. *Leukemia* 30, 861–872. doi: 10.1038/leu.2015.332

Mcever, R. P. (2015). Selectins: initiators of leucocyte adhesion and signalling at the vascular wall. *Cardiovasc. Res.* 107, 331–339. doi: 10.1093/cvr/cvv154

Menu, E., Asosingh, K., Indraccolo, S., De Raeve, H., Van Riet, I., Van Valckenborgh, E., et al. (2006). The involvement of stromal derived factor 1alpha in homing and progression of multiple myeloma in the 5TMM model. *Haematologica* 91, 605–612.

Moschetta, M., Kawano, Y., Sacco, A., Belotti, A., Ribolla, R., Chiarini, M., et al. (2017). Bone marrow stroma and vascular contributions to myeloma bone homing. *Curr. Osteoporos. Rep.* 15, 499–506. doi: 10.1007/s11914-017-0399-3

Murakami, J. L., Xu, B., Franco, C. B., Hu, X., Galli, S. J., Weissman, I. L., et al. (2016). Evidence that β7 integrin regulates hematopoietic stem cell homing and engraftment through interaction with MAdCAM-1. *Stem Cells Dev.* 25, 18–26. doi: 10.1089/scd.2014.0551

Muz, B., Azab, F., De La Puente, P., Rollins, S., Alvarez, R., Kawar, Z., et al. (2015). Inhibition of P-selectin and PSGL-1 using humanized monoclonal antibodies increases the sensitivity of multiple myeloma cells to bortezomib. *Biomed. Res. Int.* 2015, 417586–417593. doi: 10.1155/2015/417586

Natoni, A., Farrell, M. L., Harris, S., Falank, C., Kirkham-Mccarthy, L., Macauley, M. S., et al. (2019). Sialyltransferase inhibition leads to inhibition of tumor cell interactions with E-selectin, VCAM1, and MADCAM1, and improves survival in a human multiple myeloma mouse model. *Haematologica*. haematol.2018.212266. doi: 10.3324/haematol.2018.212266. [Epub ahead of print].

Natoni, A., Macauley, M. S., and O'dwyer, M. E. (2016). Targeting selectins and their ligands in cancer. *Front. Oncol.* 6:93. doi: 10.3389/fonc.2016.00093

Natoni, A., Smith, T. A. G., Keane, N., Mcellistrim, C., Connolly, C., Jha, A., et al. (2017). E-selectin ligands recognised by HECA452 induce drug resistance in myeloma, which is overcome by the E-selectin antagonist, GMI-1271. *Leukemia* 31, 2642–2651. doi: 10.1038/leu.2017.123

Neri, P., Ren, L., Azab, A. K., Brentnall, M., Gratton, K., Klimowicz, A. C., et al. (2011). Integrin β7-mediated regulation of multiple

myeloma cell adhesion, migration, and invasion. *Blood* 117, 6202–6213. doi: 10.1182/blood-2010-06-292243

Nielsen, T., Kristensen, S. R., Gregersen, H., Teodorescu, E. M., Christiansen, G., and Pedersen, S. (2019). Extracellular vesicle-associated procoagulant phospholipid and tissue factor activity in multiple myeloma. *PLoS ONE* 14:e0210835. doi: 10.1371/journal.pone.0210835

Okada, T., Hawley, R. G., Kodaka, M., and Okuno, H. (1999). Significance of VLA-4-VCAM-1 interaction and CD44 for transendothelial invasion in a bone marrow metastatic myeloma model. *Clin. Exp. Metastasis* 17, 623–629. doi: 10.1023/A:1006715504719

Parmo-Cabanas, M., Bartolome, R. A., Wright, N., Hidalgo, A., Drager, A. M., and Teixido, J. (2004). Integrin alpha4beta1 involvement in stromal cell-derived factor-1alpha-promoted myeloma cell transendothelial migration and adhesion: role of cAMP and the actin cytoskeleton in adhesion. *Exp. Cell Res.* 294, 571–580. doi: 10.1016/j.yexcr.2003.12.003

Placke, T., Orgel, M., Schaller, M., Jung, G., Rammensee, H. G., Kopp, H. G., et al. (2012). Platelet-derived MHC class I confers a pseudonormal phenotype to cancer cells that subverts the antitumor reactivity of natural killer immune cells. *Cancer Res.* 72, 440–448. doi: 10.1158/0008-5472.CAN-11-1872

Price, T. T., Burness, M. L., Sivan, A., Warner, M. J., Cheng, R., Lee, C. H., et al. (2016). Dormant breast cancer micrometastases reside in specific bone marrow niches that regulate their transit to and from bone. *Sci. Transl. Med.* 8:340ra373. doi: 10.1126/scitranslmed.aad4059

Remiker, A. S., and Palumbo, J. S. (2018). Mechanisms coupling thrombin to metastasis and tumorigenesis. *Thromb. Res.* 164(Suppl. 1), S29–S33. doi: 10.1016/j.thromres.2017.12.020

Richardson, P. G., Xie, W., Mitsiades, C., Chanan-Khan, A. A., Lonial, S., Hassoun, H., et al. (2009). Single-agent bortezomib in previously untreated multiple myeloma: efficacy, characterization of peripheral neuropathy, and molecular correlations with response and neuropathy. *J. Clin. Oncol.* 27, 3518–3525. doi: 10.1200/JCO.2008.18.3087

Rillahan, C. D., Antonopoulos, A., Lefort, C. T., Sonon, R., Azadi, P., Ley, K., et al. (2012). Global metabolic inhibitors of sialyl- and fucosyltransferases remodel the glycome. *Nat. Chem. Biol.* 8, 661–668. doi: 10.1038/nchembio.999

Rodrigues, E., and Macauley, M. S. (2018). Hypersialylation in cancer: modulation of inflammation and therapeutic opportunities. *Cancers* 10:E207. doi: 10.3390/cancers10060207

Rutishauser, U. (2008). Polysialic acid in the plasticity of the developing and adult vertebrate nervous system. *Nat. Rev. Neurosci.* 9, 26–35. doi: 10.1038/nrn2285

Sanz-Rodriguez, F., Ruiz-Velasco, N., Pascual-Salcedo, D., and Teixido, J. (1999). Characterization of VLA-4-dependent myeloma cell adhesion to fibronectin and VCAM-1. *Br. J. Haematol.* 107, 825–834. doi: 10.1046/j.1365-2141.1999.01762.x

Schultz, M. J., Swindall, A. F., and Bellis, S. L. (2012). Regulation of the metastatic cell phenotype by sialylated glycans. *Cancer Metastasis Rev.* 31, 501–518. doi: 10.1007/s10555-012-9359-7

Schweitzer, K. M., Drager, A. M., Van Der Valk, P., Thijsen, S. F., Zevenbergen, A., Theijsmeijer, A. P., et al. (1996). Constitutive expression of E-selectin and vascular cell adhesion molecule-1 on endothelial cells of hematopoietic tissues. *Am. J. Pathol.* 148, 165–175.

Seales, E. C., Jurado, G. A., Brunson, B. A., Wakefield, J. K., Frost, A. R., and Bellis, S. L. (2005). Hypersialylation of beta1 integrins, observed in colon adenocarcinoma, may contribute to cancer progression by up-regulating cell motility. *Cancer Res.* 65, 4645–4652. doi: 10.1158/0008-5472.CAN-04-3117

Shaikh, F. M., Seales, E. C., Clem, W. C., Hennessy, K. M., Zhuo, Y., and Bellis, S. L. (2008). Tumor cell migration and invasion are regulated by expression of variant integrin glycoforms. *Exp. Cell Res.* 314, 2941–2950. doi: 10.1016/j.yexcr.2008.07.021

Shen, Y., Feng, Y., Chen, H., Jia, Y., Peng, Y., Zhang, R., et al. (2018a). Silencing long non-coding rna st3gal6-as1 inhibits adhesion and migration of myeloma cells *in vitro*. *Blood* 132, 4470–4470. doi: 10.1182/blood-2018-99-114660

Shen, Y., Feng, Y. D., Chen, H. L., Huang, L. J., Wang, F. X., Bai, J., et al. (2018b). Focusing on long non-coding RNA dysregulation in newly diagnosed multiple myeloma. *Life Sci.* 196, 133–142. doi: 10.1016/j.lfs.2018.01.025

Simmons, P. J., Masinovsky, B., Longenecker, B. M., Berenson, R., Torok-Storb, B., and Gallatin, W. M. (1992). Vascular cell adhesion molecule-1 expressed by bone marrow stromal cells mediates the binding of hematopoietic progenitor cells. *Blood* 80, 388–395.

Sipkins, D. A., Wei, X., Wu, J. W., Runnels, J. M., Cote, D., Means, T. K., et al. (2005). *In vivo* imaging of specialized bone marrow endothelial microdomains for tumour engraftment. *Nature* 435, 969–973. doi: 10.1038/nature03703

Sperandio, M. (2006). Selectins and glycosyltransferases in leukocyte rolling *in vivo*. *FEBS J.* 273, 4377–4389. doi: 10.1111/j.1742-4658.2006.05437.x

Swami, A., Reagan, M. R., Basto, P., Mishima, Y., Kamaly, N., Glavey, S., et al. (2014). Engineered nanomedicine for myeloma and bone microenvironment targeting. *Proc. Natl. Acad. Sci. U.S.A.* 111, 10287–10292. doi: 10.1073/pnas.1401337111

Tada, T., Inoue, N., Widayati, D. T., and Fukuta, K. (2008). Role of MAdCAM-1 and its ligand on the homing of transplanted hematopoietic cells in irradiated mice. *Exp. Anim.* 57, 347–356. doi: 10.1538/expanim.57.347

Tatsumi, M., Watanabe, A., Sawada, H., Yamada, Y., Shino, Y., and Nakano, H. (1998). Immunohistochemical expression of the sialyl Lewis x antigen on gastric cancer cells correlates with the presence of liver metastasis. *Clin. Exp. Metastasis* 16, 743–750. doi: 10.1023/A:1006584829246

Varki, A. (1994). Selectin ligands. *Proc. Natl. Acad. Sci. U.S.A.* 91, 7390–7397. doi: 10.1073/pnas.91.16.7390

Varki, A. (2008). Sialic acids in human health and disease. *Trends Mol. Med.* 14, 351–360. doi: 10.1016/j.molmed.2008.06.002

Vinci, C., Taiana, E., Favasuli, V., Ronchetti, D., Agnelli, L., Manzoni, M., et al. (2018). The long non-coding rna st3gal6-as1 deregulated in multiple myeloma. *Haematologica* 103, S23–S23.

Waldschmidt, J. M., Simon, A., Wider, D., Muller, S. J., Follo, M., Ihorst, G., et al. (2017). CXCL12 and CXCR7 are relevant targets to reverse cell adhesion-mediated drug resistance in multiple myeloma. *Br. J. Haematol.* 179, 36–49. doi: 10.1111/bjh.14807

Wang, J., De Veirman, K., Faict, S., Frassanito, M. A., Ribatti, D., Vacca, A., et al. (2016). Multiple myeloma exosomes establish a favourable bone marrow microenvironment with enhanced angiogenesis and immunosuppression. *J. Pathol.* 239, 162–173. doi: 10.1002/path.4712

Wang, Y. M., Fan, R., Lei, L., Wang, A. Y., Wang, X. M., Ying, S., et al. (2017). Interleukin-6 drives multiple myeloma progression through upregulating of CD147/emmprin expression and its sialylation. *Blood* 130:3037.

Winkler, I. G., Barbier, V., Pattabiraman, D. R., Gonda, T. J., Magnani, J. L., and Levesque, J. P. (2014). Vascular niche E-selectin protects acute myeloid leukaemia stem cells from chemotherapy. *Blood* 124, 620.

Woodman, N., Pinder, S. E., Tajadura, V., Le Bourhis, X., Gillett, C., Delannoy, P., et al. (2016). Two E-selectin ligands, BST-2 and LGALS3BP, predict metastasis and poor survival of ER-negative breast cancer. *Int. J. Oncol.* 49, 265–275. doi: 10.3892/ijo.2016.3521

Yang, C., Xiong, F., Dou, J., Xue, J., Zhan, X., Shi, F., et al. (2015). Target therapy of multiple myeloma by PTX-NPs and ABCG2 antibody in a mouse xenograft model. *Oncotarget* 6, 27714–27724. doi: 10.18632/oncotarget.4663

Yang, W. H., Nussbaum, C., Grewal, P. K., Marth, J. D., and Sperandio, M. (2012). Coordinated roles of ST3Gal-VI and ST3Gal-IV sialyltransferases in the synthesis of selectin ligands. *Blood* 120, 1015–1026. doi: 10.1182/blood-2012-04-424366

Zarbock, A., Ley, K., Mcever, R. P., and Hidalgo, A. (2011). Leukocyte ligands for endothelial selectins: specialized glycoconjugates that mediate rolling and signaling under flow. *Blood* 118, 6743–6751. doi: 10.1182/blood-2011-07-343566

Zarfati, M., Avivi, I., Brenner, B., Katz, T., and Aharon, A. (2019). Extracellular vesicles of multiple myeloma cells utilize the proteasome inhibitor mechanism to moderate endothelial angiogenesis. *Angiogenesis* 22, 185–196. doi: 10.1007/s10456-018-9649-y

Zhang, L., Lei, Q., Wang, H., Xu, C., Liu, T., Kong, F., et al. (2019). Tumor-derived extracellular vesicles inhibit osteogenesis and exacerbate myeloma bone disease. *Theranostics* 9, 196–209. doi: 10.7150/thno.27550

Zhang, Z., Westhrin, M., Bondt, A., Wuhrer, M., Standal, T., and Holst, S. (2019). Serum protein N-glycosylation changes in multiple myeloma. *Biochim. Biophys. Acta Gen. Subj.* 1863, 960–970. doi: 10.1016/j.bbagen.2019.03.001

Zhu, D., Wang, Z., Zhao, J. J., Calimeri, T., Meng, J., Hideshima, T., et al. (2015). The cyclophilin A-CD147 complex promotes the proliferation and homing of multiple myeloma cells. *Nat. Med.* 21, 572–580. doi: 10.1038/nm.3867

Check for updates

Investigation of the Antibacterial Activity and *in vivo* Cytotoxicity of Biogenic Silver Nanoparticles as Potent Therapeutics

Md. Monir Hossain[1†], Shakil Ahmed Polash[1†], Masato Takikawa[2], Razib Datta Shubhra[1], Tanushree Saha[3], Zinia Islam[1], Sharif Hossain[1], Md. Ashraful Hasan[4], Shinji Takeoka[2] and Satya Ranjan Sarker[1]*

[1] Department of Biotechnology and Genetic Engineering, Jahangirnagar University, Dhaka, Bangladesh, [2] Department of Advanced Science and Engineering, Graduate School of Advanced Science and Engineering, Waseda University, Tokyo, Japan, [3] Department of Textile Engineering, Dhaka University of Engineering and Technology, Gazipur, Bangladesh, [4] Department of Biochemistry and Molecular Biology, Jahangirnagar University, Dhaka, Bangladesh

Biogenic nanoparticles are the smartest weapons to deal with the multidrug-resistant "superbugs" because of their broad-spectrum antibacterial propensity as well as excellent biocompatibility. The aqueous biogenic silver nanoparticles (Aq-bAgNPs) and ethanolic biogenic silver nanoparticles (Et-bAgNPs) were synthesized using aqueous and ethanolic extracts of *Andrographis paniculata* stem, respectively, as reducing agents. Electron microscopic images confirmed the synthesis of almost spherical shaped biogenic silver nanoparticles (bAgNPs). The zeta potentials of the nanoparticles were negative and were -22 and -26 mV for Aq-bAgNPs and Et-bAgNPs, respectively. The antibacterial activity of bAgNPs was investigated against seven pathogenic (i.e., enteropathogenic *Escherichia coli*, *Salmonella typhi*, *Staphylococcus aureus*, *Vibrio cholerae*, *Enterococcus faecalis*, *Hafnia alvei*, *Acinetobacter baumannii*) and three nonpathogenic (i.e., *E. coli* DH5α, *E. coli* K12, and *Bacillus subtilis*) bacteria at different time points (i.e., 12, 16, 20, and 24 h) in a dose-dependent manner (i.e., 20, 40, and 60 μg) through broth dilution assay, disk diffusion assay, CellTox[TM] Green uptake assay, and trypan blue dye exclusion assay. The lowest minimum inhibitory concentration value for both the bAgNPs was 0.125 μg. Et-bAgNPs showed the highest antibacterial activity against *S. aureus* at 60 μg after 16 h and the diameter of inhibited zone was 28 mm. Lipid peroxidation assay using all the bacterial strains revealed the formation of malondialdehyde–thiobarbituric acid adduct due to the oxidation of cell membrane fatty acids by bAgNPs. The bAgNPs showed excellent hemocompatibility against human as well as rat red blood cells. Furthermore, there was no significant toxicity observed when the levels of rat serum ALT, AST, γ-GT (i.e., liver function biomarkers), and creatinine (i.e., kidney function biomarker) were determined.

Keywords: biogenic silver nanoparticles, antimicrobial activity, pathogenic bacteria, CellTox[TM] green assay, hemocompatibility, biocompatibility, lipid peroxidation, biomarkers

INTRODUCTION

Pathogenic bacteria are the real threat to mankind due to their ability to develop resistance mechanism against the commercially available antibiotics (Aslam et al., 2018). Most of the patients in the post-operative care get infected through multidrug-resistant bacteria (e.g., methicillin-resistant *Staphylococcus aureus* and multidrug-resistant *Salmonella typhimurium*) (Khan et al., 2011; Blair et al., 2015; Ramalingam et al., 2016). Frequent use and abuse of antibiotics have led to the evolution of multidrug-resistant bacteria, also called "superbugs," which are resistant to all the commercially available antibiotics (Wang et al., 2017). Inherent mutations and lateral gene transfer among bacteria have also been contributing to the emergence of superbugs (Wang et al., 2017). On the other hand, the effectiveness of antibiotics remains for a short period of time and, therefore, used for continuous antibacterial treatment (Han et al., 2019). Therefore, it is crucial to develop new antibacterial agents with the ability to kill any pathogenic bacteria and superbugs and with prolonged and broad-spectrum antibacterial activity.

Inorganic nanoparticles including gold (Au) (Ramamurthy et al., 2013; Vijayakumar et al., 2017b), silver (Ag) (Lok et al., 2007; Ramamurthy et al., 2013; Shanthi et al., 2016; Thaya et al., 2016; Malaikozhundan et al., 2017b), graphene oxide (GO) (Rasool et al., 2016), zinc oxide (ZnO) nanoparticles (NPs) (Lu et al., 2008; Malaikozhundan et al., 2017a; Vijayakumar et al., 2017a) have been widely explored as antibacterial agents because of their excellent physical and chemical properties. Among them, silver nanoparticles (AgNPs) have been widely used in pharmaceuticals and cosmetics and in the treatment of water because of their antibacterial propensity against a wide range of bacteria (Ramalingam et al., 2016). However, the chemically synthesized AgNPs are highly unstable and get aggregated because they are prone to easy oxidation (Gondikas et al., 2012; Levard et al., 2012). The aggregated AgNPs lose their antibacterial activity (Gondikas et al., 2012; Levard et al., 2012), and the leakage of Ag^+ from the chemically synthesized AgNPs creates health as well as environmental hazard (Ramalingam et al., 2016). In addition, the chemical synthesis of AgNPs is tedious, expensive, and hazardous for the environment. Recent approaches for the synthesis of AgNPs using plant extract as the source of reducing agents instead of chemicals including $NaHB_4$ (Mehr et al., 2015) and citric acid (Kilin et al., 2008) for the reduction of silver nitrate are easier, more effective, cost-effective, and ecofriendly (Schluesener and Schluesener, 2013; Poulose et al., 2014). There are several plants including *Andrographis paniculata*, *Phyllanthus emblica*, and *Centella asiatica* have medicinal applications (Mondal et al., 2017; Polash et al., 2017; Masum et al., 2019). Because these plants contain various secondary metabolites (e.g., alkaloids, phenols, flavonoids, terpenoids, tannins, andrographolides, and so on), they have antimicrobial, antioxidant, anticancer, and antidiabetic activities (Jain et al., 2019). The reducing potential of the plant extracts is used to reduce $AgNO_3$ into AgNPs (He et al., 2016), which are frequently used for their anti-inflammatory, antimicrobial, antifungal, anti-angiogenesis, antiplatelet (He et al., 2016), and anticancer activities (Tolaymat et al., 2010; Dar et al., 2013).

Silver nanoparticles are not toxic for the human healthy peripheral lymphocytes (Gengan et al., 2013). However, they have high affinity and significant toxicity to bacteria as well as cancer cells (Greulich et al., 2012; Gengan et al., 2013). Recently, AgNPs have been used in cancer theranostics (i.e., diagnosis and treatment) (Ong et al., 2013). They are used as drugs by themselves or targeted delivery vehicles of anticancer drugs or probes for the early detection of cancer (Wei et al., 2012; Locatelli et al., 2014).

In this study, we synthesized two different types of biogenic silver nanoparticles (i.e., Aq-bAgNPs and Et-bAgNPs) using aqueous and ethanolic extract of *A. paniculata* stem. The as-synthesized bAgNPs were characterized by UV-Vis spectroscopy, Fourier transform infrared (FTIR) spectroscopy, energy dispersive X-ray spectroscopy (EDS), powder X-ray diffractometer (XRD), transmission electron microscopy (TEM), scanning electron microscopy (SEM), and a scanning TEM unit with a high-angle annular dark field (HAADF) detector. The hydrodynamic size and zeta potential of the as-synthesized bAgNPs were determined by zeta size analyzer. The antibacterial potential of bAgNPs was investigated against seven pathogenic bacterial strains including enteropathogenic *E. coli* (EPEC), *Salmonella typhi*, *S. aureus*, *Vibrio cholerae*, *Enterococcus faecalis*, *Hafnia alvei*, and *Acinetobacter baumannii*. Food- and water-borne bacteria are the cause of various acute or chronic infections including diarrhea, cholera, salmonellosis, shigellosis, traveler's diarrhea, typhoid fever, pneumonia, and dysentery (Panayidou et al., 2014). Therefore, the pathogenic bacterial strains were used to investigate the antibacterial propensity of our as-synthesized bAgNPs. In addition, three nonpathogenic bacterial strains such as *E. coli* DH5α, *E. coli* K12, and *Bacillus subtilis* RBW were also used in the experiment. The antibacterial potential of bAgNPs was investigated through determination of the diameter (in millimeter) of the zone of inhibition (ZOI) through disk diffusion assay, determination of minimum inhibitory concentration (MIC) value through broth dilution method, CellTox™ green assay, and trypan blue dye exclusion assay. Lipid peroxidation (LPO) assay was performed to investigate the mechanism of antibacterial propensity of bAgNPs. Furthermore, we have investigated the hemocompatibility of bAgNPs against human as well as rat red blood cells (RBCs). The biocompatibility of bAgNPs was investigated *in vivo* using Wister rat model. The effect of bAgNPs on liver and kidneys was investigated through determining the level of serum ALT, AST, and γ-GT as liver function biomarkers and serum creatinine as kidney function biomarker.

MATERIALS AND METHODS

Materials

Silver nitrate ($AgNO_3$), potassium bromide (KBr), EDTA, and absolute ethanol were purchased from Sigma-Aldrich (USA). CellTox™ Green dye was purchased from Promega (USA). Trypan blue dye was collected from Alfa Aesar (United Kingdom). Agar powder was purchased from Titan Biotech Ltd. (India). Peptone, yeast extract, and sodium chloride were collected from Unichem (China). Trichloroacetic acid

(TCA) and thiobarbituric acid (TBA) were purchased from Merck (Germany) and JT Baker (USA), respectively. The biochemical analysis kits for serum AST, ALT, and γ-GT analysis were purchased from Vitro Scient (Egypt) and the serum creatinine determination kit was purchased from Crescent Diagnostics (The Kingdom of Saudi Arabia). Seven pathogenic [i.e., enteropathogenic *Escherichia coli* (ATCC 43887), *S. typhi* (ATCC 14028), *S. aureus* (ATCC 25923), *V. cholerae* (ATCC 55057), *E. faecalis* (ATCC 29212), *H. alvei* (ATCC 51815), and *A. baumannii* (ATCC 17978)] and three nonpathogenic [i.e., *E. coli* DH5α (ATCC 25922), *E. coli* K12 (ATCC 10798), and *B. subtilis* RBW (ATCC 6051)] strains were obtained from the Department of Biotechnology and Genetic Engineering, Jahangirnagar University, Savar, Dhaka 1342, Bangladesh. Thirty Wistar male rats (weighing between 170 and 180 g) were obtained from the Department of Biochemistry and Molecular Biology, Jahangirnagar University, Dhaka, Bangladesh.

Methods

Synthesis of Biogenic Silver Nanoparticles (bAgNPs)

A. paniculata stem extract was used to prepare biogenic silver nanoparticles (bAgNPs) since it is cost effective and has medicinal property. The fresh stem of *A. paniculata* was collected and pulverized, and 10% aqueous as well as 10% ethanolic extracts were prepared according to our previously published protocol (Polash et al., 2017). Briefly, 10 mM AgNO₃ solution was prepared and mixed with the as-prepared aqueous as well as ethanolic stem extracts separately at a ratio of 9:1 (i.e., 36 ml AgNO₃ and 4 ml plant extracts). The mixture of AgNO₃ solution and the extracts was incubated at 30°C for 24 h upon constant stirring in a dark chamber to reduce the photo activation of AgNO₃. Herein, the plant extract was used as a reducing agent and the reduction of Ag^+ to Ag^0 was confirmed by the change of color of the solution from colorless to brown (Ahmed et al., 2016). The reaction mixture was then centrifuged at 16,873 g for 1 h at room temperature to remove the unconjugated plant extract and AgNO₃. The supernatant was aspirated and the bAgNPs generated by aqueous as well as ethanolic extracts were deposited as pellet at the bottom of the tube. Finally, the bAgNPs were washed twice with distilled water and redispersed in distilled water.

Characterization of Biogenic Silver Nanoparticles (bAgNPs)

The as-synthesized biogenic silver nanoparticles (bAgNPs) were characterized using a UV-Vis spectrophotometer (Specord® 205, Analytik Jena, Germany) and FTIR spectroscopy (IRPrestige-21, SHIMADZU, Japan). The hydrodynamic size and zeta potential of bAgNPs were determined with a zeta size analyzer (Nano-ZS90; Spectris PLC, Egham, England) after sonicating for 30 min in a bath-type sonicator. The shape, morphology, and composition of biogenic nanoparticles were analyzed with TEM with a field emission gun (HF-2200; Hitachi, Tokyo, Japan) coupled with energy dispersive X-ray spectroscopy (EDAX Genesis; AMETEK, Pennsylvania, USA) operating at 200 kV. A scanning TEM unit with a HAADF detector and secondary electron (SE) detector were also equipped. The nanoparticles were neither stained with any conventional staining agent nor coated with any conductive metal before observing them under electron microscopy.

The powder X-ray diffraction (XRD) patterns of bAgNPs were obtained using a powder X-ray diffractometer (GNR X-Ray Explorer, Italy) equipped with Cu Kα (0.154 nm) at 25 mA without Ni filter. The XRD spectrum was obtained by scanning the diffraction angle (2θ) region at 30 kV. The diffraction angle was varied in the range of 10–50° and the scanning rate was 5°/s.

Antimicrobial Activity Assay

The antimicrobial activity of the bAgNPs was investigated against seven pathogenic (i.e., Enteropathogenic *E. coli*, *S. typhi*, *S. aureus*, *V. cholerae*, *E. faecalis*, *H. alvei*, and *Acinetobacter*) and three nonpathogenic (i.e., *E. coli* DH5α, *E. coli* K12, and *B. subtilis*) bacterial strains. Among all the bacteria, *S. aureus, E. faecalis,* and *B. subtilis* are Gram-positive, and the remaining bacterial strains are gram negative. The antibacterial activity of bAgNPs was determined in terms of their MIC value, ZOI in millimeters, trypan blue dye exclusion assay, and CellTox™ Green cytotoxicity assay.

Determination of the MIC value

The MIC value was determined to identify the minimum amount of bAgNPs (i.e., Aq-bAgNPs and Et-bAgNPs) required to inhibit the growth of a particular bacterial strain. The MIC value of the as-synthesized bAgNPs was determined according to the broth dilution method (Mondal et al., 2017). Briefly, 990 µl of fresh LB broth was inoculated with 10 µl of overnight grown bacterial culture and incubated at 37°C and 120 rpm for 4 h. After incubation, different amounts (i.e., 0.125, 0.25, 0.5, 1, 2, 3, 4, 5, and 6 µg) of either Aq-bAgNPs or Et-bAgNPs was added to the bacterial culture and incubated at 37°C and 120 rpm overnight. The optical density (OD) of the respective bacterial culture was then measured at 600 nm using UV-Vis spectrophotometer (Optizen, POP, Korea) to determine the MIC values of bAgNPs.

Determination of ZOI

The antimicrobial activity of the as-synthesized Aq-bAgNPs and Et-bAgNPs was determined by disk diffusion method (Polash et al., 2017). Briefly, all the tested bacterial strains were cultured in Luria Bertani (LB) medium at 37°C and 120 rpm overnight. From the respective bacterial culture, 100 µl was spreaded consistently on LB agar plates. Metrical filter paper disks containing different amounts of bAgNPs (i.e., 60, 40, and 20 µg) were placed on the LB agar plates containing uniformly spreaded bacteria. The LB agar plates were then incubated overnight at 37°C for optimum growth of bacteria. The antibacterial activity of Aq-bAgNPs and Et-bAgNPs was determined by the presence of clear zones surrounding the disks that were different with different amounts of bAgNPs (i.e., Aq-bAgNPs and Et-bAgNPs) and confirm the inhibition of the growth of bacteria. After incubation, the diameter of the clear zones was measured using slide calipers at different time points such as 12, 16, 20, and 24 h.

Trypan blue dye exclusion assay

Trypan blue is a negatively charged dye and can't pass through the intact cell wall of bacteria. Therefore, it is used to differentiate cell wall compromised dead bacteria from cell wall intact live bacteria. This is because the dead cells allow the uptake of trypan blue dye through their damaged cell membrane (Tran et al., 2011; Ranjan Sarker et al., 2019). The trypan blue dye exclusion assay was performed according to our previously established protocol with little modifications (Ranjan Sarker et al., 2019). Briefly, 20 μl (1 μg/μl) of Aq-bAgNPs and Et-bAgNPs was mixed separately with 80 μl of overnight grown culture (1 × 10^6 CFU/ml) of the respective bacterial strains (i.e., seven pathogenic and three nonpathogenic bacterial strains) and incubated at 37°C and 120 rpm for 1.5 h. The bacterial cultures treated with bAgNPs were mixed with 0.4% trypan blue solution at a ratio of 1:1 and incubated at room temperature for 15 min before taking images of live and dead bacterial cells using a phase contrast microscope (Olympus BX50 Fluorescence Microscope, Olympus, Japan) at 40× magnification.

CellTox^TM green assay

CellTox^TM Green is a fluorescent dye that penetrates through the disrupted cell membrane and emits green fluorescence upon binding with the DNA (Zhang et al., 1999). Overnight grown bacterial culture was diluted with LB broth and the concentration was set to 1 × 10^7 CFU/ml. Either Aq-bAgNPs or Et-bAgNPs (20 μl; 1 μg/μl) were mixed with 80 μl (1 × 10^7 CFU/ml) of the respective bacterial strains. Then, 900 μl of fresh LB broth was added to bAgNPs containing bacterial culture before incubating at 37°C and 120 rpm for 2 h. After the incubation, 1 μl of CellTox^TM Green reagent (2×) was mixed properly with bAgNPs containing bacterial culture and incubated at room temperature for another 30 min in the dark. Twenty microliters of the CellTox^TM-treated bacterial culture was kept aside to observe the dead cells under fluorescence microscope (Olympus BX50 Fluorescence Microscope, Olympus, Japan). The remaining bacterial suspension was used to measure the fluorescence intensity of the green fluorescent dye treated bacterial cultures using a spectrofluorophotometer (SHIMADZU RF-6000, Japan) at 490 nm. Biogenic AgNPs with control groups (i.e., cells and media) were run without CellTox^TM Green alongside the treatment groups. All experiments were carried out in triplicate.

LPO Assay

The LPO potential of bAgNPs was investigated according to previously established protocol (Singh et al., 2009; Ranjan Sarker et al., 2019). Briefly, 1 ml of each of the bacterial cultures was mixed separately with 200 μl (i.e., 200 μg) of each of the bAgNPs and incubated for 30 min at room temperature. After centrifugation, 2 ml of 10% TCA was mixed with the bAgNP-treated bacterial culture and centrifuged at 10,416 g for 35 min at room temperature to separate the insoluble cellular components. The supernatant was taken out and centrifuged again in the same relative centrifugal force (g) for 20 min to remove any protein precipitates as well as dead cells. Finally, the supernatant containing malondialdehyde was collected in a fresh tube and mixed with freshly prepared 4 ml of 0.67%

TBA solution and incubated in a hot water bath for 10 min to facilitate the formation of malondialdehyde-TBA adduct before cooling down to room temperature. The absorbance of the malondialdehyde-TBA adduct was measured by UV-Vis spectrophotometer (Specord® 205, Analytik Jena, Germany) at 532 nm.

Hemocompatibility Assay

The hemocompatibility of bAgNPs (i.e., Aq-bAgNPs, and Et-bAgNPs) with human as well as rat RBCs was investigated according to previously established protocol with some modification (Li et al., 2014; Ranjan Sarker et al., 2019). Briefly, 6 ml of human blood was collected from the left hand of donor through venipuncture method and collected in a vacutainer blood tube containing 10% EDTA. On the other hand, two rats were anesthetized with 0.3 ml/250 g ketamine/xylazine (100 mg/ml ketamine + 20 mg/ml xylazine) before the collection of blood and ∼6 ml (3 ml from each rat) of blood was drawn from the inferior vena cava and collected in a vacutainer blood tube containing 10% EDTA. RBCs of human as well as rat were separated from serum through centrifugation at 500 g for 10 min at room temperature. The serum was then discarded and RBCs were resuspended in 5 ml of phosphate buffered saline (PBS) and centrifuged again at 500 g for 10 min. The cell suspension was washed twice with 150 mM NaCl solution at 3000 g for 3 min. Finally, 0.1 ml of RBCs solution was mixed with 0.4 ml of different amounts of bAgNPs (i.e., 10, 20, 30, 40, 50, 60, 80, 100, 200, 400, 800, and 1,600 μg) and incubated at 37°C and 150 rpm for 30 min. After incubation, the RBCs and bAgNPs mixtures were centrifuged at 1,377 g for 5 min at room temperature. The supernatant was taken out and the absorbance was measured at 570 nm. Herein, RBCs incubated with PBS and water were considered as negative and positive controls, respectively (Li et al., 2014). All the samples were taken in triplicate. The percentage of hemolysis was calculated using the following formula:

$$\% \text{ of hemolysis} = \left(\frac{\text{Absorbance of sample} - \text{Absorbance of negative control}}{\text{Absorbance of positive control} - \text{Absorbance of negative control}} \right) \times 100$$

(1)

In vivo Cytotoxicity Assay

Intravenous delivery of bAgNPs

Wistar male rats were used for the study and 30 rats were divided into five groups ($n = 6$). The rats were housed in a hygienic environment under controlled temperature ($23 \pm 2°C$) and humidity ($55 \pm 7\%$) with a 12-h day and 12-h night cycle (Lee et al., 2018). The rats were allowed to acclimatize for a week before the delivery of bAgNPs. According to Katarzyna et al., if the size of AgNPs is ∼20 nm, their deposition is higher in the tissues (e.g., liver, spleen, kidney, and brain) when compared to that of the larger nanoparticles (Dziendzikowska et al., 2012; Yang et al., 2017). Since the size of our as-synthesized Aq-bAgNPs and Et-bAgNPs are 24.90 and 25.24, respectively, we fixed the highest

dose as 5 mg/kg of rat body weight. All the rats were anesthetized with 0.3 ml/250 g ketamine/xylazine (100 mg/ml ketamine + 20 mg/ml xylazine) before intravenous delivery of bAgNPs. Two doses (i.e., 2 and 5 mg/kg of rat body weight) of both Aq-bAgNPs and Et-bAgNPs were delivered through intravenous route via tail's vein. After the delivery of bAgNPs, the rats were kept in the cage under the same condition for 7 days. After 7 days, blood (∼3 ml) was drawn from all the rats and centrifuged at 538 g for 10 min at room temperature to separate the serum. The serum samples were stored at −20°C for further biochemical analysis. The experiments in this study were approved by the Biosafety, Biosecurity & Ethical Committee of Jahangirnagar University (BBEC, JU/M 2019(4)1).

Investigation of liver and kidney function biomarkers

To determine whether bAgNPs have any toxic effects to rat tissues, we measured the concentration of several enzymes whose level usually get hiked once there is any damage in the liver and kidneys. We measured the level of serum aspartate aminotransferase (AST), alanine aminotransferase (ALT), gamma-glutamyltransferase (γ-GT), and creatinine of the experimental rats and compared them with that of control rats. The serum AST, ALT, and γ-GT are known as the liver function biomarkers and creatinine is known as the kidney function biomarker. The concentrations of all the biomarkers were measured according to the manual provided with the reagent kits, and the detailed protocol has been added in the supplementary section.

Statistical Analysis

All the data were presented as the mean ± SEM. Data were subjected to statistical analysis using one-way ANOVA with GraphPad Prism 5.0 (GraphPad Software Inc., San Diego, CA). *Post hoc* test was performed using the Dunnett test. The mean values were considered to be statistically significant at $P < 0.05$ (Adeyemi and Adewumi, 2014). All experiments were carried out in triplicate, and the results presented are the average measurements of the runs with standard deviation.

RESULTS AND DISCUSSION

Characterization of bAgNPs

The colorless AgNO$_3$ (10 mM) solution turned brown as soon as *A. paniculata* stem extract was added into it and incubated for ∼24 h (**Figure 1**). When aqueous stem extract was added into AgNO$_3$ solution, the color of the solution turned dark brown when compared to that of brown in the case of ethanolic stem extract. The change of color confirms the reduction of Ag^{1+} to Ag^0 due to the presence of secondary metabolites including flavonoids and different types of andrographolides in *A. paniculata* stem extract (Singh et al., 2018). Flavonoids and andrographolides present in the *A. paniculata* stem extract would bind to the biogenic nanoparticles surface as capping agents. The final yield of both the bAgNPs was 9.1%. The UV-Vis spectra confirm the synthesis of biogenic silver nanoparticles (bAgNPs) because the absorption maximum (λ$_{max}$) for Aq-bAgNPs and Et-AgNPs is ∼412 and ∼418 nm (**Figure 1**), respectively, which
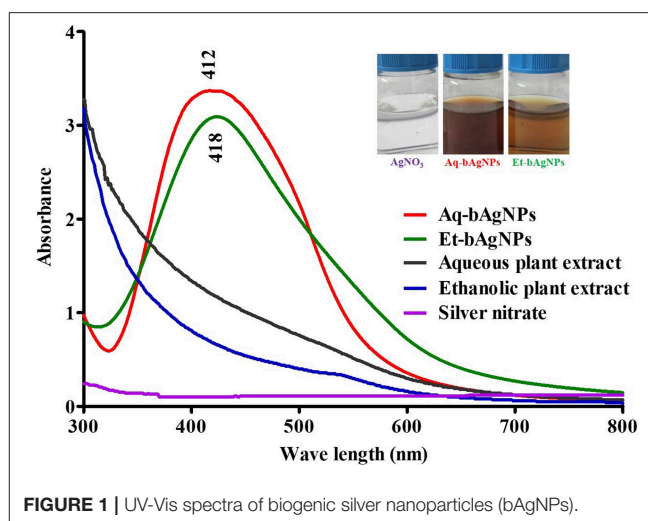
FIGURE 1 | UV-Vis spectra of biogenic silver nanoparticles (bAgNPs).

are almost equal to the surface plasma resonance (SPR) value of AgNPs (i.e., 420 nm) (Ramalingam et al., 2016). At a particular wavelength, electrons on the metal surface undergo a collective oscillation when excited by light resulting in the strong scattering and absorption properties of bAgNPs (Li et al., 2010). Et-bAgNPs derived from the ethanolic extract of *A. paniculata* stem appeared brown due to the presence of higher amount of andrographolides in the ethanolic stem extract that caused greater reduction of Ag^{1+} at room temperature (Daniel et al., 2013). Therefore, a slight red shift was observed in case of Et-bAgNPs.

The analysis of FTIR spectra confirm the presence of various bioactive compounds having different functional groups in the plant extract as well as in the bAgNPs (Alshaye et al., 2017; Elamawi et al., 2018). The spectra of Aq-bAgNPs (**Figure S1**) and aqueous stem extract of *A. paniculata* (**Figure S1**) revealed strong bands at (839 and 797), (1,048 and 1,043), (1,376 and 1,398), (1,615 and 1,650), (2,915 and 2,923), and (3,342 and 3,377 cm^{-1}) that were attributed to aromatic C–H (aryl group), C–OH stretching, C–N stretching, carbonyl stretch, C–H asymmetric stretching, and N–H stretching, respectively (Basseter and Silverstein, 1992). The spectra of Et-bAgNPs (**Figure S1**) and ethanolic stem extract of *A. paniculata* (**Figure S1**) showed strong bands at (804 and 797), (1,034 and 1,055), (1,383 and 1,394), (1,610 and 1,655), (2,916 and 2,930), and (3,321 and 3,398 cm^{-1}) that were due to aromatic C–H (aryl group), C–OH stretching, C–N stretching, carbonyl stretch, C–H asymmetric stretching, and N–H stretching, respectively (Ahmed et al., 2016). The intense band at 1,370 cm^{-1} is characteristic of silver nitrate (Rogachev et al., 2013). The FTIR spectra clearly showed that the hydroxyl group (-OH) and carboxyl group (-COOH) containing bioactive compounds present in *A. paniculata* stem extracts act as capping agents in the synthesis of bAgNPs. The observed peaks were mainly attributed to flavonoids and andrographolides present in the plant extract (Banerjee et al., 2014).

The average hydrodynamic diameter of both bAgNPs was larger than that of their nominal particle size (**Table S1**).

The hydrodynamic diameters of Aq-bAgNPs and Et-bAgNPs were 428.2 ± 197.0 and 190.1 ± 102 nm, respectively. The polydispersity index (PDI) of both the bAgNPs was almost the same (i.e., 0.4). The zeta potentials of Aq-bAgNPs and Et-bAgNPs were −22.1 ± 0.9 and −26.1 ± 1.4 mV, respectively (**Table S1**). The negative zeta potential of bAgNPs is due to the adsorption of bioactive molecules onto the particle surface (Rao and Paria, 2015).

The shape and morphology of biogenic nanoparticles were analyzed using scanning transmission electron microscope (STEM). For both the bAgNPs, STEM images showed that Ag nanoparticles were surrounded with polymers and were not directly observed. In addition, respective TEM or HAADF images also exhibited that Ag nanoparticles were coated with polymers and most of the nanoparticles were spherical in shape (**Figure 2**). The particle size distribution (PSD) graphs (i.e., histogram) were drawn from the TEM images of both Aq-bAgNPs and Et-bAgNPs (**Figures 2D,H**). The average size of Aq-bAgNPs and Et-bAgNPs was 24.90 and 25.24 nm, respectively. The hydrodynamic size of bAgNPs was larger than the size of the same nanoparticles observed under TEM. This is because TEM measures the size of the dried nanoparticles. On the other hand, DLS measures the hydrodynamic size of the particles containing conjugated/adsorbed polymers on the surface. The stability of the nanoparticles depend on the nature of the conjugated polymers as well as the physicochemical properties of solvents used to disperse them (Domingos et al., 2009). If the particles have the tendency to agglomerate, the hydrodynamic size is usually larger. EDS analysis confirmed that nanoparticles are composed of Ag, C, and O (**Figures 3A,B**). The characteristic Ag peak was observed at ∼3 keV. Other peaks, such as Cu and Si, are artifacts used during the analysis by TEM grid and silicon oil for a vacuum pump, respectively. Considering these results in EM observation and EDS analysis, we judged that Ag nanoparticles were coated with bioactive polymers present in *A. paniculata* stem extracts.

Powder XRD analysis was performed to identify the phase, orientation, and grain size of the as-synthesized bAgNPs (i.e., Aq-bAgNPs and Et-bAgNPs). **Figures 3C,D** clearly show the characteristic diffraction peaks associated with the crystalline silver. The Braggs peaks at 2θ degrees were observed at 27.68°, 32.27°, 38.16°, and 46.27° which correspond to the Miller indices (111), (200), (220), and (311) for both the as-synthesized bAgNPs confirming face-centered cubic (fcc) crystalline elemental silver. The obtained results match the JCPDS (Joint Commission of Powder Diffraction Standards) database bearing file no. (04-0783). Furthermore, the crystalline grain size of the as-synthesized bAgNPs was calculated using Scherer's equation: $D = (K\lambda/\beta\cos\theta)$ [where D is the mean crystalline size of the particle, K is the shape factor whose value is 0.9, λ is the wavelength of the X-ray radiation (i.e., 0.154 nm), β is (π/180)*FWMH, and θ is the Bragg angle]. The average size obtained using Scherer's equation was 23.62 and 23.81 nm for Aq-bAgNPs and Et-bAgNPs, respectively (Chauhan and Chauhan, 2014; Nayak et al., 2016b).

Investigation of Antimicrobial Activity
MIC and ZOI

Broth dilution method was used to determine the MIC value of the as-synthesized Aq-bAgNPs and Et-bAgNPs. In case of Aq-bAgNPs, the lowest MIC value was 0.125 μg/ml against *E. coli* DH5α, *S. typhi*, *V. cholerae*, *E coli* K12, and *H. alvei*. On the other hand, the lowest MIC value for Et-bAgNPs was also 0.125 μg/ml against *B. subtilis*, *V. cholerae*, *H. alvei*, and *A. baumannii* (**Table 1**). A clear zone surrounding the metrical filter paper disk confirmed the antibacterial/bactericidal activity of the as-synthesized bAgNPs. The highest antibacterial activity of Aq-bAgNPs and Et-bAgNPs was observed against *S. aureus*, a Gram-positive bacteria, and the ZOI was ∼25 and 28 mm in diameter, respectively (**Table 1**). However, the lowest antibacterial activity of Aq-bAgNPs and Et-bAgNPs was observed against enteropathogenic *E. coli* (i.e., ∼12.25 mm) and *B. subtilis* (i.e., ∼11.75 mm), respectively. Aqueous stem extract, ethanolic stem extract, and silver nitrate were used as control and they showed no significant antibacterial activity against any of the tested microorganisms (**Table 1**). The time-dependent (i.e., 12, 16, 20, and 24 h) as well as dose-dependent (i.e., 20, 40, and 60 μg) antimicrobial activity of our as-synthesized bAgNPs is shown in **Table S2**. The diameter of clear zone (millimeter) surrounding the disk reduced after 16 h of incubation with bAgNPs, plant extracts, and AgNO₃ in case of all the bacteria. The maximum diameter of clear zone (millimeter) surrounding the disk was obtained at 60 μg of bAgNPs, plant extracts, and AgNO₃ in case of all the bacteria, which is larger than the area of clear zone for already reported biogenic silver nanoparticles (Ahmed et al., 2016; Masum et al., 2019).

The phytoconstituents present in *A. paniculata* stem extracts contain various bioactive compounds with long hydrocarbon chain and hydroxyl as well as carboxyl groups that act as the hydrophilic moieties. Hence, the interactions between the bAgNPs and bacteria were mainly through noncovalent (i.e., hydrophobic) interactions. Therefore, the increased uptake of negatively charged Aq-bAgNPs and Et-bAgNPs was due to their higher hydrophobicity compared to plant extract and silver nitrate (Bu et al., 2010; Li et al., 2014). Secondly, the interaction between the bAgNPs and bacteria could also be due to molecular crowding (Arakha et al., 2015). Thirdly, the basic antibacterial mechanism of bAgNPs has been shown to be either due to the release of silver ions or intracellular deposition of bAgNPs (Kim et al., 2016; Hoseinnejad et al., 2018). The detailed mechanism involves the damage of cell membrane, disruption of energy metabolism, generation of oxidative stress due to reactive oxygen species (ROS) generation, and inhibition of gene transcription (Hindi et al., 2009). Silver ions released from bAgNPs interact with sulfur- and phosphorus-containing proteins present in the plasma membrane as well as in the bacterial cell wall through electrostatic interactions (Hindi et al., 2009). This leads to the pore formation in the bacterial cell membrane that executes the outflow of bacterial intracellular contents. As a result, an electrochemical imbalance is generated in the cells resulting in permanent cell damage (Dakal et al., 2016). Both the Aq-bAgNPs and Et-bAgNPs showed better antibacterial activity to

FIGURE 2 | Analysis of the shape, morphology, and size of biogenic Ag nanoparticles (bAgNPs) with scanning transmission electron microscope (STEM). SE images show the formation of Aq-bAgNPs **(A)**. Scanning TEM images **(B)**, high-angle annular dark-field (HAADF) images (Z-contrast images) **(C)**, and histogram for particle size distribution **(D)** show the formation, spherical shape, and size of Aq-bAgNPs. Similarly, SE **(E)**, scanning TEM **(F)**, HAADF images **(G)**, and histogram for particle size distribution **(H)** show the formation spherical shape and size of Et-bAgNPs. Scale bar: 200 nm.
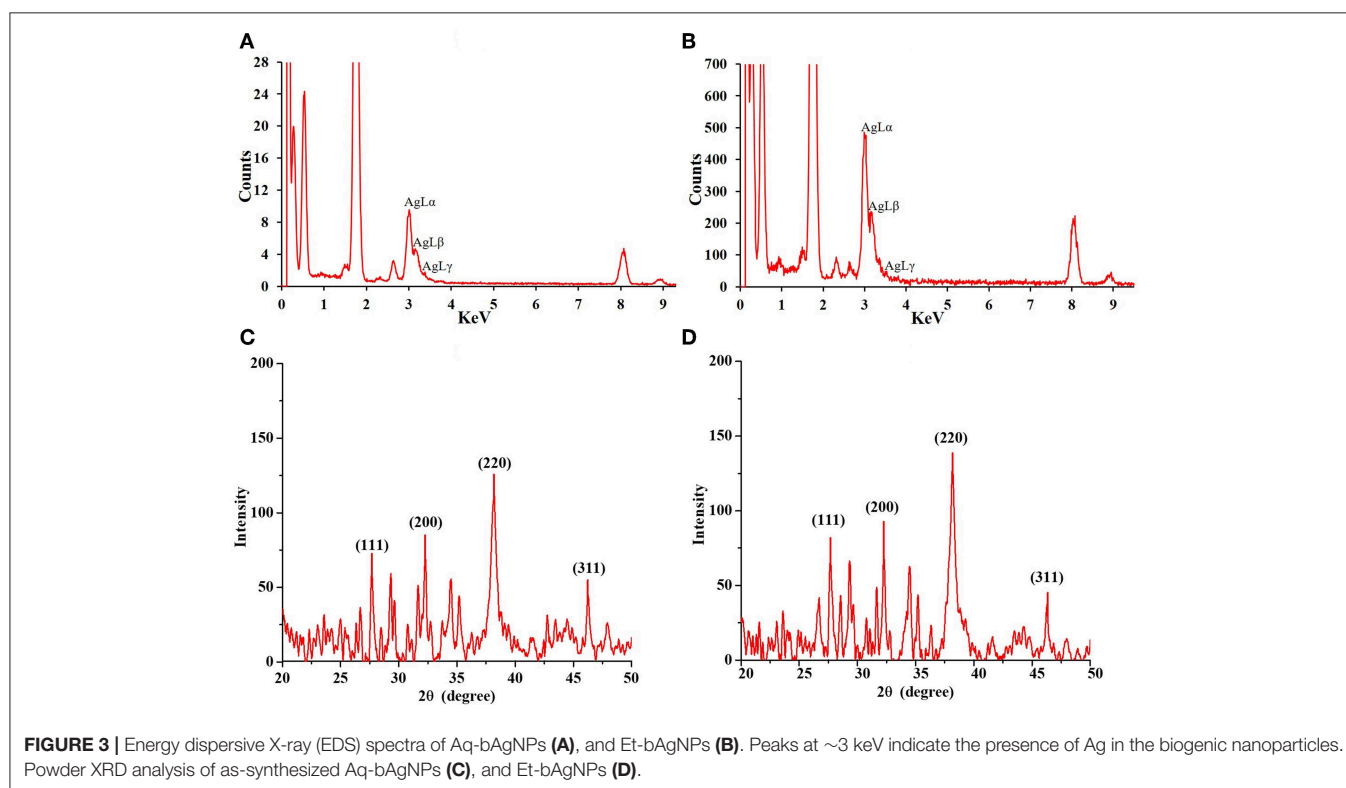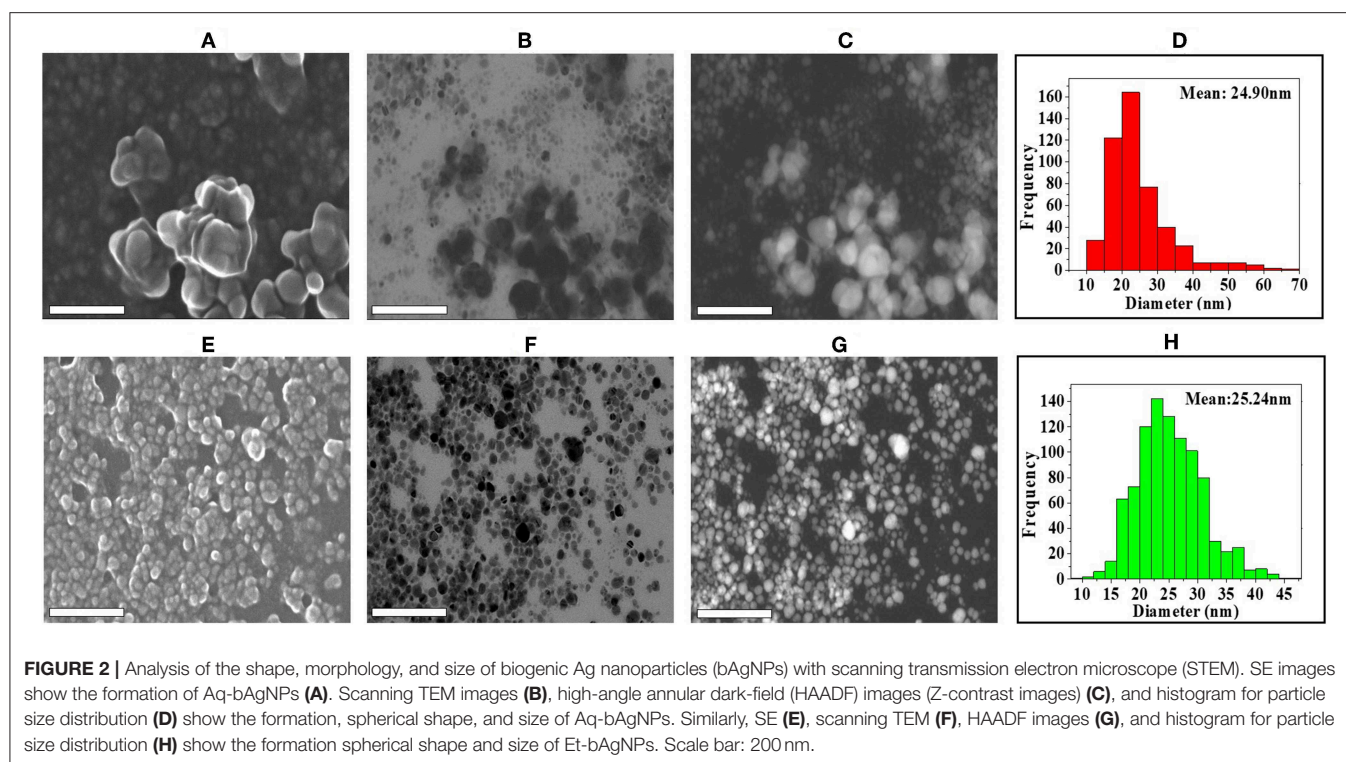

FIGURE 3 | Energy dispersive X-ray (EDS) spectra of Aq-bAgNPs **(A)**, and Et-bAgNPs **(B)**. Peaks at ∼3 keV indicate the presence of Ag in the biogenic nanoparticles. Powder XRD analysis of as-synthesized Aq-bAgNPs **(C)**, and Et-bAgNPs **(D)**.

TABLE 1 | Zone of inhibition and MIC value for bAgNPs against bacteria.

	MIC (µg)		Zone of inhibition (mm)					Pathogenicity
	Aq-bAgNPs	Et-bAgNPs	Aq-bAgNPs (60 µg)	Aqueous plant extract (60 µg)	Et-bAgNPs (60 µg)	Ethanolic plant extract (60 µg)	AgNO$_3$	
B. subtilis	0.250	0.125	17.5 ± 1.0	8.5 ± 0.0	11.8 ± 0.3	7.5 ± 0.00	7.5 ± 0.0	Nonpathogenic
E. coli DH5α	0.125	0.250	14.0 ± 0.5	9.5 ± 0.0	16.5 ± 0.0	7.5 ± 0.0	8.3 ± 1.3	Nonpathogenic
EPEC	0.25	0.250	12.3 ± 0.8	8.0 ± 0.0	12.8 ± 0.3	7.0 ± 0.0	7.0 ± 0.0	Pathogenic
S. typhi	0.125	0.250	17.8 ± 0.8	11.0 ± 0.0	15.5 ± 1.0	10 ± 0.00	7.0 ± 0.0	Pathogenic
S. aureus	0.250	0.250	25.0 ± 0.5	8.0 ± 0.0	28.0 ± 0.0	11.5 ± 0.0	10.3 ± 0.3	Pathogenic
V. cholera	0.125	0.125	17.0 ± 0.0	7.0 ± 0.0	17.5 ± 0.0	7.0 ± 0.0	8.0 ± 0.0	Pathogenic
E. coli K12	0.125	0.25	15.0 ± 0.0	8.0 ± 0.0	16.0 ± 0.0	8.0 ± 00	9.0 ± 0.0	Nonpathogenic
E. faecalis	0.250	0.250	15.8 ± 0.3	8.5 ± 0.0	15.8 ± 0.3	7.0 ± 0.00	7.0 ± 0.00	Pathogenic
H. alvei	0.125	0.125	15.0 ± 0.0	7.5 ± 0.0	15.3 ± 0.3	7.0 ± 0.0	7.0 ± 0.0	Pathogenic
A. baumannii	0.250	0.125	17.8 ± 0.3	7.0 ± 0.0	18.3 ± 0.3	7.5 ± 0.00	11.0 ± 0.0	Pathogenic

Gram-positive bacteria (i.e., *S. aureus*) when compared to Gram-negative bacteria (i.e., EPEC) because the cell wall of Gram-positive bacteria contains a thick layer of peptidoglycan and abundant pores through which external molecules can enter into the cell that brings about membrane damage and cellular death (Bu et al., 2010). The difference of antibacterial activity of bAgNPs against particular bacterial strain could also be different due to the differences in lipid composition, gross composition of the membranes, or even specific protein complexes present in the surface of the bacterial cell wall (Hayden et al., 2012).

CellTox™ Green Assay

CellTox™ Green is a DNA binding dye. It binds to DNA of cell wall compromised bacteria and emits green fluorescence. Since CellTox™ Green is impermeable to intact cell membrane, it is usually used to detect dead cells only. The green fluorescence of CellTox™ Green-treated dead bacteria was quantified using a spectrofluorophotometer (SHIMADZU RF-6000, Japan) at 490 nm. The Et-bAgNP-treated *S. aureus* showed the highest fluorescence intensity followed by Aq-bAgNP-treated *S. aureus* (**Figure 4A**), and the intensities were ∼6.5-fold higher than that of the untreated cells. The data support the ZOI (in millimeters) obtained from the disk diffusion assay. The green fluorescence of bAgNP-treated dead bacteria was also observed under a fluorescence microscope (**Figure 4B** and **Figures S2, S3**). The fluorescence images confirm the damage of bacterial cell membrane after treating them with bAgNPs and the dead bacteria appeared green.

Trypan Blue Dye Exclusion Assay

Trypan blue dye exclusion assay was performed to confirm the damage of bacterial cell wall because of their interactions with bAgNPs. The interaction between bAgNPs and the bacterial cell wall took place through hydrophobic interactions that resulted in damage on the cell wall. This paves the way for the entry of trypan blue dye into the bacterial cytosol from their surroundings. Consequently, the cell wall compromised or nonviable bacteria appeared blue under the phase contrast microscope (**Figures S4–S8**) (Ranjan Sarker et al., 2019).

LPO Assay

LPO assay was performed to investigate the oxidation potential of bacterial cell membrane fatty acids by bAgNPs. The malondialdehyde–thiobarbituric acid (MDA–TBA) adduct was formed when bacteria were treated with both the bAgNPs (i.e., Aq-bAgNPs and Et-bAgNPs) because of the strong hydrophobic interactions between bAgNPs and bacterial cell wall. Among all the bacterial strains, the highest MDA–TBA adduct was formed when *E. coli* K12, a Gram-negative bacterium, was treated with Et-bAgNPs (**Figure 5**). However, *E. faecalis*, a Gram-positive bacterium, showed the highest amount of MDA–TBA adduct among all the bacterial strains treated with Aq-bAgNPs (**Figure 5**). The amount of MDA adduct is different for different bacterial strains, and it is due to the differences in the interaction of bAgNPs with bacteria. The cell wall composition of bacteria differs from species to species. The generation of lipid peroxide (LPO) took place due to the oxidation of bacterial cell membrane fatty acids by bAgNPs.

The generation of ROS is stimulated after exposure of bacterial cell membrane to bAgNPs since transition metals put oxidative stress on fatty acids (Li et al., 2012; Wang et al., 2017). The ROS oxidize the bacterial membrane fatty acids to produce lipid peroxides and the redox balance of cells favor oxidation (Wang et al., 2017). Furthermore, ROS-mediated oxidative stress inhibits the electron transport chain and alters bacterial metabolic reactions (Wang et al., 2017). Thus, it stimulates the expression of apoptotic genes and the oxidative proteins to bring about the apoptosis of the respective bacterial cell (Wang et al., 2017).

Hemocompatibility Assay

Hemolytic potential assay was performed using human as well as rat RBCs to investigate the hemocompatibility of the as-synthesized bAgNPs. Both the bAgNPs showed excellent hemocompatibility to human as well as rat RBCs (**Figure 6**). Hemocompatibility of bAgNPs to human and rat RBCs was performed using different amount (i.e., 10–1,600 µg) of both the nanoparticles (i.e., Aq-bAgNPs and Et-bAgNPs). The HC$_{50}$ values (the amount of nanoparticles required to lyse the 50% of RBCs) of Aq-bAgNPs and Et-bAgNPs to human RBCs were
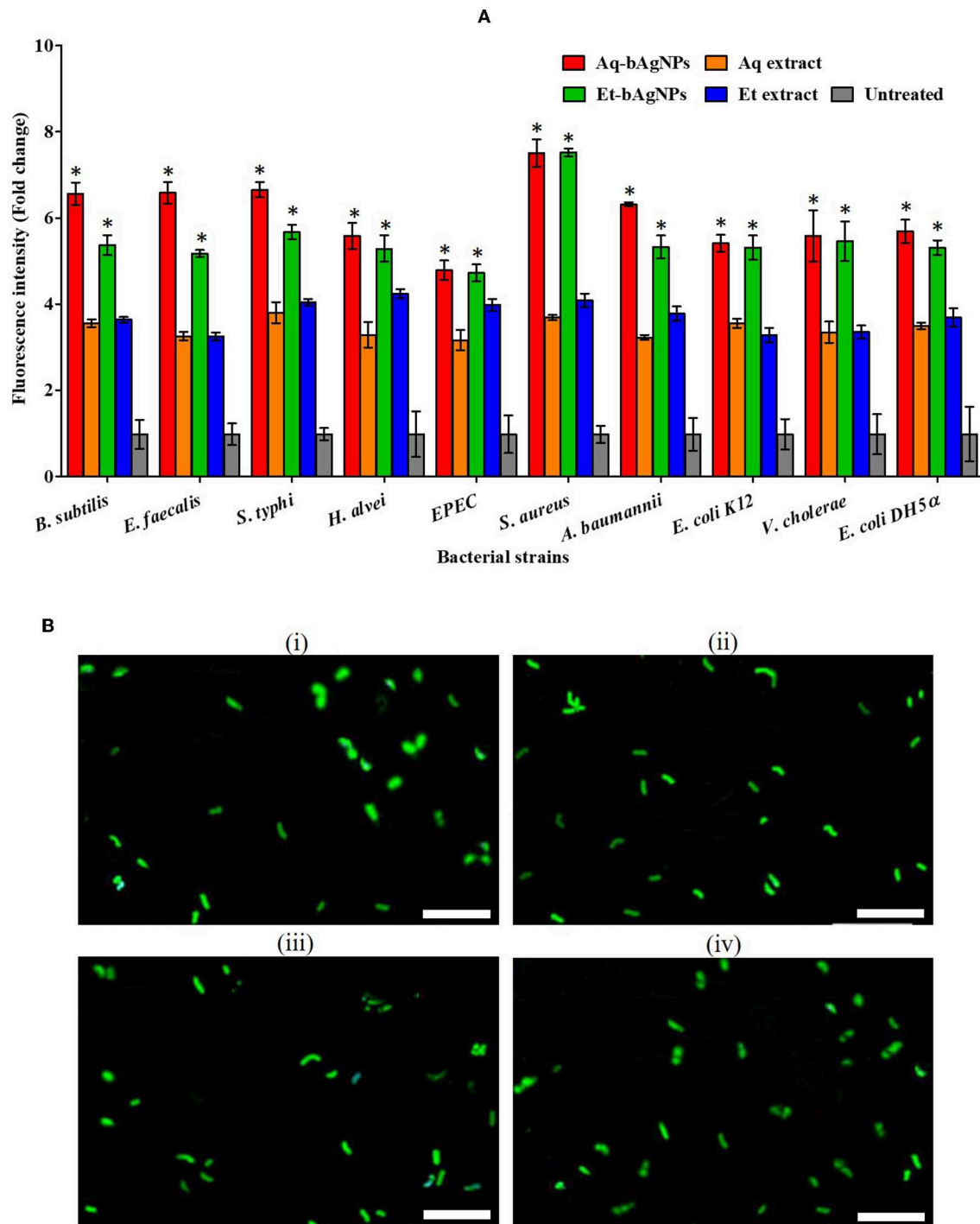
FIGURE 4 | (A) CellTox^{TM} Green uptake assay. The fluorescence intensity of bacteria treated with Aq-bAgNPs and Et-bAgNPs was measured at 490 nm using a spectrofluorometer. The values presented are mean $\pm$ SE of multiple samples ($n = 3$). Data were analyzed using one-way ANOVA followed by Tukey's multiple comparison test. The fluorescence intensity of both bAgNP-treated bacteria was significantly higher than that of the plant extract treated as well as untreated bacteria and $*P < 0.05$. **(B)** CellTox^{TM} Green uptake assay. *B. subtilis* was first treated with Aq-bAgNPs (i) and Et-bAgNPs (ii). The treated bacteria were then incubated with CellTox^{TM} green to stain the cell wall compromised bacterial DNA, and green fluorescence was observed under a fluorescence microscope. The same experiment was also performed for *E. faecalis* after treating them with Aq-bAgNPs (iii) and Et-bAgNPs (iv). Scale bar: 20 μm.
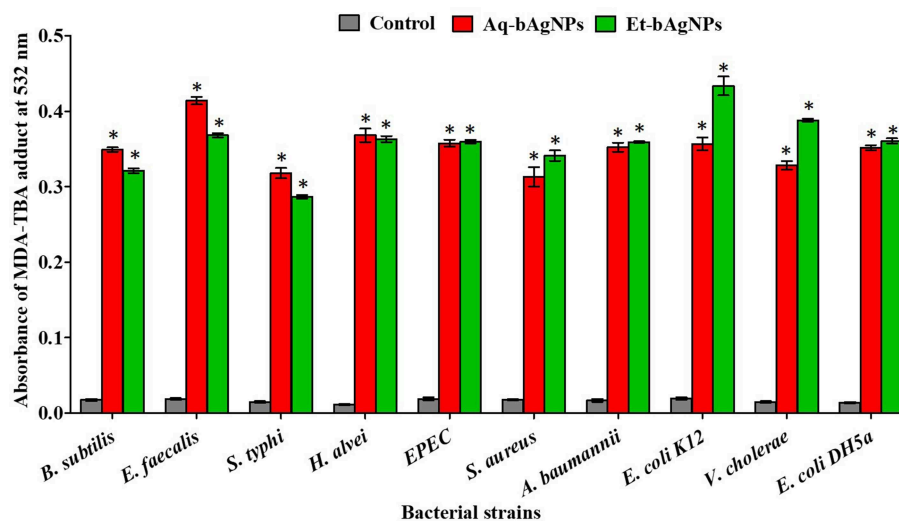
FIGURE 5 | Lipid peroxidation assay. The cell membrane fatty acid oxidation potential of biogenic silver nanoparticles was measured through MDA–TBA adduct assay. The absorbance of MDA–TBA pink adduct was measured at 532 nm (i.e., λ_{max}). The values presented are mean $\pm$ SE of multiple samples ($n = 3$). Data were analyzed using one-way ANOVA followed by Tukey's multiple comparison test. The absorbance of MDA–TBA adduct of bAgNPs treated bacteria were significantly higher than that of the untreated bacteria (i.e., control) and *$P < 0.01$.
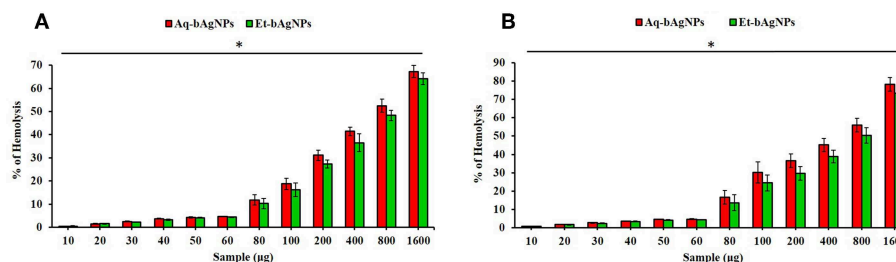
FIGURE 6 | Hemocompatibility of bAgNPs to human (A) and rat (B) red blood cells (RBCs). The HC$_{50}$ values of Aq-bAgNPs and Et-bAgNPs to human RBCs were 700 and 800 μg, respectively. However, the HC$_{50}$ values of Aq-bAgNPs and Et-bAgNPs to rat RBCs were 600 and 800 μg, respectively. The hemocompatibility assay was performed three times on three different days. The values presented are mean $\pm$ SE of multiple samples ($n = 3$) and paired t-test was performed for analyzing significant difference between Aq-bAgNPs and Et-bAgNPs. The hemocompatibility of bAgNPs was significantly different from each other and *$P \leq 0.05$.

700 and 800 μg, respectively. However, the HC$_{50}$ values of Aq-bAgNPs and Et-bAgNPs to rat RBCs were 600 and 800 μg, respectively. The HC$_{50}$ values are more than 10 times higher than that of the amount used for the antibacterial activity assay (i.e., 60 μg) (**Figure 6**). The percentage of hemolysis for 60 μg Et-bAgNPs was 4.33 and 4.35% in the case of human and rat RBCs, respectively. On the other hand, the percentage of hemolysis for 60 μg Aq-bAgNPs was 4.56 and 4.66% in the case of human and rat RBCs, respectively. The slightly higher hemocompatibility of Et-bAgNPs against both human and rat RBCs is due to their greater negative zeta potential (i.e., -26 mV) that results in stronger electrostatic repulsion with the negatively charged RBCs. These low percentage of hemolytic potential is less than that of the acceptable hemolytic value (i.e., 5%), a value that is regarded as critically safe for therapeutic applications of the biomaterials (Sarika et al., 2015; Nayak et al., 2016a). The membrane composition of rat RBCs differ significantly from that of the human RBCs (Da Silveiracavalcante et al., 2015). Therefore,

the hemocompatibility of bAgNPs to human and rat RBCs is different (Da Silveiracavalcante et al., 2015).

Evaluation of Rat Liver and Kidney Function Biomarkers

The bAgNPs (i.e., Aq-bAgNPs and Et-bAgNPs) administered through intravenous route had no significant toxic effect on rat liver and kidneys (**Figure 7**). More specifically, there was no significant difference ($P > 0.05$) of serum ALT, AST, γ-GT, and creatinine level between the control and experimental rats (**Figure 7**). The data showed that neither Aq-bAgNP-treated (2 and 5 mg/kg) nor Et-bAgNP-treated (2 and 5 mg/kg) rat groups had significant influence on the aforementioned biomarkers. Liver is a vital organ of rat and colloidal AgNPs usually get deposited into it (Kim et al., 2007; Ahmad and Zhou, 2017). To determine the toxic effects of bAgNPs, liver function was investigated by measuring the level of serum ALT, AST, and γ-GT enzymes after intravenous delivery of bAgNPs. The level
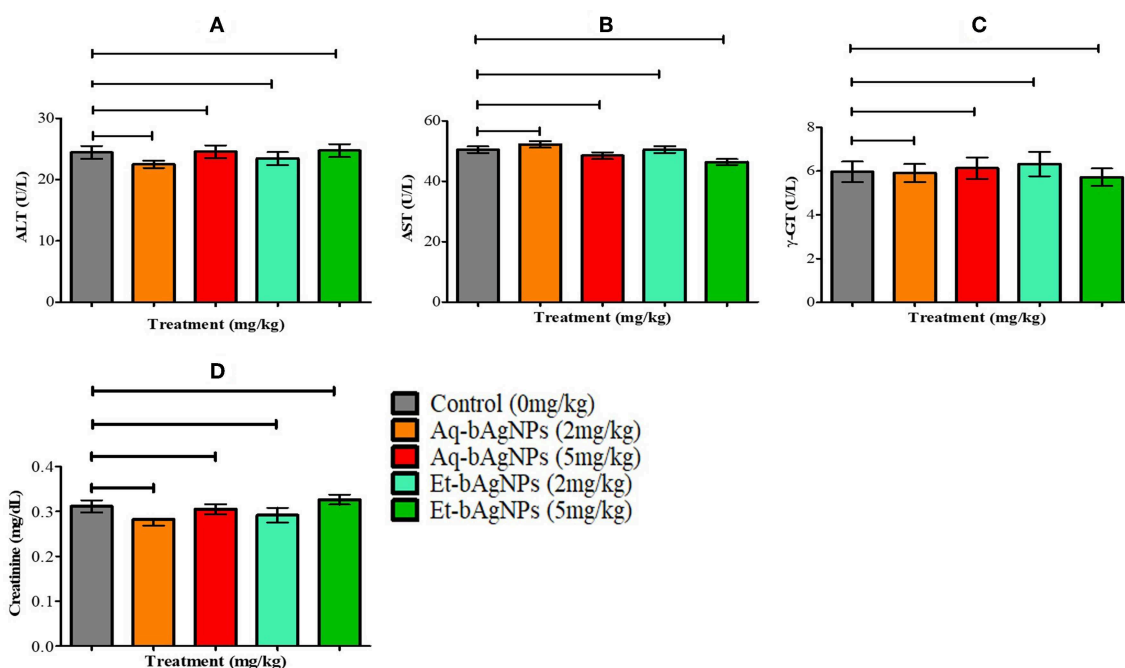
FIGURE 7 | *In vivo* cytotoxicity assay. The effect of bAgNPs on liver function was investigated by measuring the levels of ALT **(A)**, AST **(B)**, and γ-GT **(C)**. The effect of bAgNPs on kidney function was also investigated by measuring the level of serum creatinine **(D)**. The values presented are mean ± SE of multiple samples (six animals per group). Data were analyzed by GraphPad Prism 5.0 (GraphPad software) using one-way ANOVA test. Dunnett test was used for *post hoc* comparison. No significant difference was observed when treatment groups were compared with control and $P > 0.05$.

of ATP, a high-energy phosphate compound, decreases whenever there is any damage in liver. The decreased ATP level provokes the release of enzymes (ALT and AST) in the tissues. Thus, the level of enzymes increase in the serum whenever the liver is damaged (Gupta and Goad, 2000; Ramaiah, 2007). Gamma glutamyltransferase (γ-GT) is an enzyme of the hepatobiliary origin and its activity is minimal in normal hepatic tissues. However, the level of γ-GT rises within hours of cholestasis (impairment of bile flow) by an unknown mechanism (Ramaiah, 2007). Therefore, our data suggest that any dose of bAgNPs (up to 5 mg/kg) is therapeutically safe for liver, since no statistically significant change in the biomarkers was observed. On the other hand, the toxic effect of bAgNPs on kidneys was assessed by determining the level of serum creatinine. The low level of serum creatinine indicates the inability of kidneys to filter the waste products from the blood and excrete them through the urine (Kaur et al., 2012). Intravenous administration of different doses (up to 5 mg/kg) of bAgNPs for 7 days showed no statistically significant difference in the level of serum creatinine. Hence, bAgNPs did not show any toxic effect to kidneys besides their compatibility to liver.

CONCLUSION

We synthesized biogenic silver nanoparticles (bAgNPs) in a cost-effective and ecofriendly manner. The aqueous as well as ethanolic extracts of *A. paniculata* stem were used to synthesize Aq-bAgNPs and Et-bAgNPs, respectively. The synthesis of bAgNPs was confirmed through UV-Vis, FTIR, and EDS spectroscopy, and powder X-ray diffractometer. The as-synthesized bAgNPs were characterized in terms of their size, zeta potential, shape, and morphology. The antimicrobial activity of bAgNPs was investigated against seven pathogenic and three nonpathogenic bacterial strains. Both Et-bAgNPs and Aq-bAgNPs showed the highest antimicrobial activity against pathogenic *S. aureus*, a Gram-positive bacterium. They showed the antibacterial activity through damaging the bacterial cell wall, which was confirmed through CellTox™ Green assay and trypan blue dye exclusion assay. After damaging the bacterial cell wall, bAgNPs oxidize the cell membrane fatty acids to produce lipid peroxides that facilitate the interaction bAgNPs with DNA and other cellular macromolecules to bring about bacterial death. On the other hand, our as-synthesized bAgNPs showed excellent hemocompatibility and did not show any significant toxicity to liver and kidneys at a high dose. Therefore, it can be concluded that our as-synthesized bAgNPs are cost effective, have broad-spectrum antibacterial propensity and excellent biocompatibility, and can be recommended for future therapeutic applications.

DATA AVAILABILITY STATEMENT

All datasets generated for this study are included in the manuscript/**Supplementary Material**.

ETHICS STATEMENT

The animal study was reviewed and approved by Biosafety, Biosecurity, and Ethical Committee of Jahangirnagar University, Dhaka, Bangladesh.

AUTHOR CONTRIBUTIONS

All authors listed have made a substantial, direct and intellectual contribution to the work, and approved it for publication.

FUNDING

ACKNOWLEDGMENTS

SUPPLEMENTARY MATERIAL

The Supplementary Material for this article can be found online at: https://www.frontiersin.org/articles/10.3389/fbioe. 2019.00239/full#supplementary-material

REFERENCES

Adeyemi, O. S., and Adewumi, I. (2014). Biochemical evaluation of silver nanoparticles in wistar rats. *Int. Schol. Res. Notices* 2014:196091. doi: 10.1155/2014/196091

Ahmad, F., and Zhou, Y. (2017). Pitfalls and challenges in nanotoxicology: a case of cobalt ferrite ($CoFe_2O_4$) nanocomposites. *Chem. Res. Toxicol.* 30, 492–507. doi: 10.1021/acs.chemrestox.6b00377

Ahmed, S., Saifullah, Ahmad, M., Swami, B. L., and Ikram, S. (2016). Green synthesis of silver nanoparticles using *Azadirachta indica* aqueous leaf extract. *J. Radiat. Res. Appl. Sci.* 9, 1–7. doi: 10.1016/j.jrras.2015.06.006

Alshaye, N. A., Elobeid, M. M., Alkhalifah, D. H., and Mohammed, A. E. (2017). Characterization of biogenic silver nanoparticles by *Salvadora persica* leaves extract and its application against some MDR pathogens *E. coli* and *S. aureus.* *Res. J. Microbiol.* 12, 74–81. doi: 10.3923/jm.2017.74.81

Arakha, M., Pal, S., Samantarrai, D., Panigrahi, T. K., Mallick, B. C., Pramanik, K., et al. (2015). Antimicrobial activity of iron oxide nanoparticle upon modulation of nanoparticle–bacteria interface. *Sci. Rep.* 5:14813. doi: 10.1038/srep14813

Aslam, B., Wang, W., Arshad, M. I., Khurshid, M., Muzammil, S., Rasool, M. H., et al. (2018). Antibiotic resistance: a rundown of a global crisis. *Infect. Drug Resist.* 11, 1645–1658. doi: 10.2147/IDR.S173867

Banerjee, P., Satapathy, M., Mukhopahayay, A., and Das, P. (2014). Leaf extract mediated green synthesis of silver nanoparticles from widely available Indian plants: synthesis, characterization, antimicrobial property and toxicity analysis. *Bioresour. Bioprocess.* 1:3. doi: 10.1186/s40643-014-0003-y

Basseter, G., and Silverstein, R. (1992). *Spectrophotometric Identification of Organic Compounds.* New York, NY: Wiley.

Blair, J. M., Webber, M. A., Baylay, A. J., Ogbolu, D. O., and Piddock, L. J. (2015). Molecular mechanisms of antibiotic resistance. *Nat. Rev. Microbiol.* 13, 42–51. doi: 10.1038/nrmicro3380

Bu, Q., Yan, G., Deng, P., Peng, F., Lin, H., Xu, Y., et al. (2010). NMR-based metabonomic study of the sub-acute toxicity of titanium dioxide nanoparticles in rats after oral administration. *Nanotechnology.* 21:125105. doi: 10.1088/0957-4484/21/12/125105

Chauhan, A., and Chauhan, P. (2014). Powder XRD technique and its applications in science and technology. *J. Anal. Bioanal. Tech.* 5:212. doi: 10.4172/2155-9872.1000212

Da Silveiracavalcante, L., Acker, J. P., and Holovati, J. L. (2015). Differences in rat and human erythrocytes following blood component manufacturing: the effect of additive solutions. *Transf. Med. Hemother.* 42, 150–157. doi: 10.1159/000371474

Dakal, T. C., Kumar, A., Majumdar, R. S., and Yadav, V. (2016). Mechanistic basis of antimicrobial actions of silver nanoparticles. *Front. Microbiol.* 7:1831. doi: 10.3389/fmicb.2016.01831

Daniel, K., Guevara, S. C., Mahalakshmi, N., Sandhiya, J., Kasi, N., and Muthusamy, S. (2013). Rapid synthesis of Ag nanoparticles using Henna extract for the fabrication of photoabsorption enhanced dye sensitized solar cell (PE-DSSC). *Adv. Mater. Res.* 678, 349–360. doi: 10.4028/www.scientific.net/AMR.678.349

Dar, M. A., Ingle, A., and Rai, M. (2013). Enhanced antimicrobial activity of silver nanoparticles synthesized by *Cryphonectria* sp. evaluated singly and in combination with antibiotics. *Nanomedicine* 9, 105–110. doi: 10.1016/j.nano.2012.04.007

Domingos, R. F., Baalousha, M. A., Ju-Nam, Y., Reid, M. M., Tufenkji, N., Lead, J. R., et al. (2009). Characterizing manufactured nanoparticles in the environment: multimethod determination of particle sizes. *Environ. Sci. Technol.* 43, 7277–7284. doi: 10.1021/es900249m

Dziendzikowska, K., Gromadzka-Ostrowska, J., Lankoff, A., Oczkowski, M., Krawczynska, A., Chwastowska, J., et al. (2012). Time-dependent biodistribution and excretion of silver nanoparticles in male Wistar rats. *J. Appl. Toxicol.* 32, 920–928. doi: 10.1002/jat.2758

Elamawi, R. M., Al-Harbi, R. E., and Hendi, A. A. (2018). Biosynthesis and characterization of silver nanoparticles using *Trichoderma longibrachiatum* and their effect on phytopathogenic fungi. *Egypt. J. Biol. Pest Control* 28:28. doi: 10.1186/s41938-018-0028-1

Gengan, R., Anand, K., Phulukdaree, A., Chuturgoon, A. J. C., and Biointerfaces, S. B. (2013). A549 lung cell line activity of biosynthesized silver nanoparticles using *Albizia adianthifolia* leaf. *Colloids Surf. B Biointerfaces.* 105, 87–91. doi: 10.1016/j.colsurfb.2012.12.044

Gondikas, A. P., Morris, A., Reinsch, B. C., Marinakos, S. M., Lowry, G. V., and Hsu-Kim, H. (2012). Cysteine-induced modifications of zero-valent silver nanomaterials: Implications for particle surface chemistry, aggregation, dissolution, and silver speciation. *Environ. Sci. Technol.* 46, 7037–7045. doi: 10.1021/es3001757

Greulich, C., Braun, D., Peetsch, A., Diendorf, J., Siebers, B., Epple, M., et al. (2012). The toxic effect of silver ions and silver nanoparticles towards bacteria and human cells occurs in the same concentration range. *RSC Adv.* 2, 6981–6987. doi: 10.1039/c2ra20684f

Gupta, R. C., and Goad, J. T. (2000). Role of high-energy phosphates and their metabolites in protection of carbofuran-induced biochemical changes in diaphragm muscle by memantine. *Arch. Toxicol.* 74, 13–20. doi: 10.1007/s002040050646

Han, H., Zhu, J., Wu, D. Q., Li, F. X., Wang, X. L., Yu, J. Y., et al. (2019). Inherent guanidine nanogels with durable antibacterial and bacterially antiadhesive properties. *Adv. Func. Mater.* 29:1806594. doi: 10.1002/adfm.201806594

Hayden, S. C., Zhao, G., Saha, K., Phillips, R. L., Li, X., Miranda, O. R., et al. (2012). Aggregation and interaction of cationic nanoparticles on bacterial surfaces. *J. Am. Chem. Soc.* 134, 6920–6923. doi: 10.1021/ja301167y

He, Y., Du, Z., Ma, S., Liu, Y., Li, D., Huang, H., et al. (2016). Effects of green-synthesized silver nanoparticles on lung cancer cells *in vitro* and grown as xenograft tumors *in vivo*. *Int. J. Nanomed.* 11, 1879–1887. doi: 10.2147/IJN.S103695

Hindi, K. M., Ditto, A. J., Panzner, M. J., Medvetz, D. A., Han, D. S., Hovis, C. E., et al. (2009). The antimicrobial efficacy of sustained release silver–carbene complex-loaded L-tyrosine polyphosphate nanoparticles: characterization, *in vitro* and *in vivo* studies. *Biomaterials* 30, 3771–3779. doi: 10.1016/j.biomaterials.2009.03.044

Hoseinnejad, M., Jafari, S. M., and Katouzian, I. (2018). Inorganic and metal nanoparticles and their antimicrobial activity in food packaging applications. *Crit. Rev. Microbiol.* 44, 161–181. doi: 10.1080/1040841X.2017.1332001

Jain, C., Khatana, S., and Vijayvergia, R. (2019). Bioactivity of secondary metabolites of various plants: a review. *Int. J. Pharm. Sci.* 10, 494–404. doi: 10.13040/IJPSR.0975-8232.10(2).494-04

Kaur, B., Khera, A., and Sandhir, R. (2012). Attenuation of cellular antioxidant defense mechanisms in kidney of rats intoxicated with carbofuran. *J. Biochem. Mol. Toxicol.* 26, 393–398. doi: 10.1002/jbt.21433

Khan, S. A., Singh, A. K., Senapati, D., Fan, Z., and Ray, P. C. (2011). Bio-conjugated popcorn shaped gold nanoparticles for targeted photothermal killing of multiple drug resistant *Salmonella* DT104. *J. Mater. Chem.* 21, 17705–17709. doi: 10.1039/c1jm13320a

Kilin, D. S., Prezhdo, O. V., and Xia, Y. (2008). Shape-controlled synthesis of silver nanoparticles: Ab initio study of preferential surface coordination with citric acid. *Chem. Phys. Lett.* 458, 113–116. doi: 10.1016/j.cplett.2008.04.046

Kim, D.-H., Kim, K.-N., Kim, K.-M., Shim, I.-B., and Lee, Y.-K. (2007). "*In vitro* and *in vivo* toxicity of CoFe$_2$O$_4$ for application to magnetic hyperthermia," in *Technical Proceedings of the 2007 NSTI Nanotechnology Conference and Trade Show, Volume 2* (Santa Clara, CA), 748–751.

Kim, T., Braun, G. B., She, Z. G., Hussain, S., Ruoslahti, E., and Sailor, M. J. (2016). Composite porous silicon–silver nanoparticles as theranostic antibacterial agents. *ACS Appl. Mater. Interfaces* 8, 30449–30457. doi: 10.1021/acsami.6b09518

Lee, J. H., Gulumian, M., Faustman, E. M., Workman, T., Jeon, K., and Yu, I. J. (2018). Blood biochemical and hematological study after subacute intravenous injection of gold and silver nanoparticles and coadministered gold and silver nanoparticles of similar sizes. *BioMed Res. Int.* 2018:8460910. doi: 10.1155/2018/8460910

Levard, C., Hotze, E. M., Lowry, G. V., and Brown, G. E. Jr. (2012). Environmental transformations of silver nanoparticles: impact on stability and toxicity. *Environ. Sci. Technol.* 46, 6900–6914. doi: 10.1021/es2037405

Li, W. R., Xie, X. B., Shi, Q. S., Zeng, H. Y., You-Sheng, O. Y., and Chen, Y. B. (2010). Antibacterial activity and mechanism of silver nanoparticles on *Escherichia coli*. *Appl. Microbiol. Biotechnol.* 85, 1115–1122. doi: 10.1007/s00253-009-2159-5

Li, X., Robinson, S. M., Gupta, A., Saha, K., Jiang, Z., Moyano, D. F., et al. (2014). Functional gold nanoparticles as potent antimicrobial agents against multi-drug-resistant bacteria. *ACS Nano.* 8, 10682–10686. doi: 10.1021/nn5042625

Li, Y., Zhang, W., Niu, J., and Chen, Y. J. (2012). Mechanism of photogenerated reactive oxygen species and correlation with the antibacterial properties of engineered metal-oxide nanoparticles. *ACS Nano.* 6, 5164–5173. doi: 10.1021/nn300934k

Locatelli, E., Naddaka, M., Uboldi, C., Loudos, G., Fragogeorgi, E., Molinari, V., et al. (2014). Targeted delivery of silver nanoparticles and alisertib: *in vitro* and *in vivo* synergistic effect against glioblastoma. *Nanomedicine* 9, 839–849. doi: 10.2217/nnm.14.1

Lok, C. N., Ho, C. M., Chen, R., He, Q. Y., Yu, W. Y., Sun, H., et al. (2007). Silver nanoparticles: partial oxidation and antibacterial activities. *J. Biol. Inorg. Chem.* 12, 527–534. doi: 10.1007/s00775-007-0208-z

Lu, W., Liu, G., Gao, S., Xing, S., and Wang, J. J. N. (2008). Tyrosine-assisted preparation of Ag/ZnO nanocomposites with enhanced photocatalytic performance and synergistic antibacterial activities. *Nanotechnology* 19:445711. doi: 10.1088/0957-4484/19/44/445711

Malaikozhundan, B., Vaseeharan, B., Vijayakumar, S., Pandiselvi, K., Kalanjiam, M. A., Murugan, K., et al. (2017a). Biological therapeutics of *Pongamia pinnata* coated zinc oxide nanoparticles against clinically important pathogenic bacteria, fungi and MCF-7 breast cancer cells. *Microb. Pathog.* 104, 268–277. doi: 10.1016/j.micpath.2017.01.029

Malaikozhundan, B., Vijayakumar, S., Vaseeharan, B., Jenifer, A. A., Chitra, P., Prabhu, N. M., et al. (2017b). Two potential uses for silver nanoparticles coated with *Solanum nigrum* unripe fruit extract: biofilm inhibition

and photodegradation of dye effluent. *Microb. Pathog.* 111, 316–324. doi: 10.1016/j.micpath.2017.08.039

Masum, M. M. I., Siddiqa, M. M., Ali, K. A., Zhang, Y., Abdallah, Y., Ibrahim, E., et al. (2019). Biogenic synthesis of silver nanoparticles using *Phyllanthus emblica* fruit extract and its inhibitory action against the pathogen *Acidovorax oryzae* Strain RS-2 of rice bacterial brown stripe. *Front. Microbiol.* 10:820. doi: 10.3389/fmicb.2019.00820

Mehr, F. P., Khanjani, M., and Vatani, P. (2015). Synthesis of nano-ag particles using sodium borohydride. *Orient. J. Chem.* 31, 1831–1833. doi: 10.13005/ojc/310367

Mondal, R., Polash, S. A., Saha, T., Islam, Z., Sikder, M. M., Alam, N., et al. (2017). Investigation of the phytoconstituents and bioactivity of various parts of wild type and cultivated *Phyllanthus emblica* L. *Adv. Biosci. Biotechnol.* 8, 211–227. doi: 10.4236/abb.2017.87016

Nayak, D., Ashe, S., Rauta, P. R., Kumari, M., Nayak, B. J. M. S., and, C., et al. (2016a). Bark extract mediated green synthesis of silver nanoparticles: evaluation of antimicrobial activity and antiproliferative response against osteosarcoma. *Mater. Sci. Eng.* 58, 44–52. doi: 10.1016/j.msec.2015.08.022

Nayak, D., Kumari, M., Rajachandar, S., Ashe, S., Thathapudi, N. C., and Nayak, B. (2016b). Biofilm impeding AgNPs target skin carcinoma by inducing mitochondrial membrane depolarization mediated through ROS production. *ACS Appl. Mater. Interfaces* 8, 28538–28553. doi: 10.1021/acsami.6b11391

Ong, C., Lim, J., Ng, C., Li, J., Yung, L., and Bay, B. (2013). Silver nanoparticles in cancer: therapeutic efficacy and toxicity. *Curr. Med. Chem.* 20, 772–781. doi: 10.2174/0929867311320060003

Panayidou, S., Ioannidou, E., and Apidianakis, Y. J. V. (2014). Human pathogenic bacteria, fungi, and viruses in *Drosophila*: disease modeling, lessons, and shortcomings. *Virulence* 5, 253–269. doi: 10.4161/viru.27524

Polash, S. A., Saha, T., Hossain, M. S., and Sarker, S. R. (2017). Investigation of the phytochemicals, antioxidant, and antimicrobial activity of the *Andrographis paniculata* leaf and stem extracts. *Adv. Biosci. Biotechnol.* 8, 149–162. doi: 10.4236/abb.2017.85012

Poulose, S., Panda, T., Nair, P. P., and Theodore, T. (2014). Biosynthesis of silver nanoparticles. *J. Nanosci. Nanotechnol.* 14, 2038–2049. doi: 10.1166/jnn.2014.9019

Ramaiah, S. K. (2007). A toxicologist guide to the diagnostic interpretation of hepatic biochemical parameters. *Food Chem. Toxicol.* 45, 1551–1557. doi: 10.1016/j.fct.2007.06.007

Ramalingam, B., Parandhaman, T., and Das, S. K. (2016). Antibacterial effects of biosynthesized silver nanoparticles on surface ultrastructure and nanomechanical properties of gram-negative bacteria viz. *Escherichia coli* and *Pseudomonas aeruginosa*. *ACS Appl. Mater. Interfaces* 8, 4963–4976. doi: 10.1021/acsami.6b00161

Ramamurthy, C., Padma, M., Mareeswaran, R., Suyavaran, A., Kumar, M. S., Premkumar, K., et al. (2013). The extra cellular synthesis of gold and silver nanoparticles and their free radical scavenging and antibacterial properties. *Colloids Surf. B Biointerfaces* 102, 808–815. doi: 10.1016/j.colsurfb.2012.09.025

Ranjan Sarker, S., Polash, S. A., Boath, J., Kandjani, A. E., Poddar, A., Dekiwadia, C., et al. (2019). Functionalization of elongated tetrahexahedral Au nanoparticles and their antimicrobial activity assay. *ACS Appl. Mater. Interfaces* 11, 13450–13459. doi: 10.1021/acsami.9b02279

Rao, K. J., and Paria, S. (2015). Aegle marmelos leaf extract and plant surfactants mediated green synthesis of Au and Ag nanoparticles by optimizing process parameters using Taguchi method. *ACS Sustainable Chem. Eng.* 3, 483–491. doi: 10.1021/acssuschemeng.5b00022

Rasool, K., Helal, M., Ali, A., Ren, C. E., Gogotsi, Y., Mahmoud, K., et al. (2016). Antibacterial activity of Ti3C2T x MXene. *ACS Nano.* 10, 3674–3684. doi: 10.1021/acsnano.6b00181

Rogachev, A., Yarmolenko, M., Rogachou, A., Tapalski, D., Liu, X., and Gorbachev, D. (2013). Morphology and structure of antibacterial nanocomposite organic–polymer and metal–polymer coatings deposited from active gas phase. *RSC Adv.* 3, 11226–11233. doi: 10.1039/c3ra23284k

Sarika, P., Kumar, P. A., Raj, D. K., and James, N. R. (2015). Nanogels based on alginic aldehyde and gelatin by inverse miniemulsion technique: synthesis and characterization. *Carbohydr. Polym.* 119, 118–125. doi: 10.1016/j.carbpol.2014.11.037

Schluesener, J. K., and Schluesener, H. (2013). Nanosilver: application and novel aspects of toxicology. *Arch. Toxicol.* 87, 569–576. doi: 10.1007/s00204-012-1007-z

Shanthi, S., Jayaseelan, B. D., Velusamy, P., Vijayakumar, S., Chih, C. T., and Vaseeharan, B. J. M. P. (2016). Biosynthesis of silver nanoparticles using a probiotic *Bacillus licheniformis* Dahb1 and their antibiofilm activity and toxicity effects in *Ceriodaphnia cornuta*. *Microb. Pathog.* 93, 70–77. doi: 10.1016/j.micpath.2016.01.014

Singh, P., Garg, A., Pandit, S., Mokkapati, V., and Mijakovic, I. (2018). Antimicrobial effects of biogenic nanoparticles. *Nanomaterials* 8:1009. doi: 10.3390/nano8121009

Singh, S., Patel, P., Jaiswal, S., Prabhune, A., Ramana, C., and Prasad, B. (2009). A direct method for the preparation of glycolipid–metal nanoparticle conjugates: sophorolipids as reducing and capping agents for the synthesis of water re-dispersible silver nanoparticles and their antibacterial activity. *N. J. Chem.* 33, 646–652. doi: 10.1039/B811829A

Thaya, R., Malaikozhundan, B., Vijayakumar, S., Sivakamavalli, J., Jeyasekar, R., Shanthi, S., et al. (2016). Chitosan coated Ag/ZnO nanocomposite and their antibiofilm, antifungal and cytotoxic effects on murine macrophages. *Microb. Pathog.* 100, 124–132. doi: 10.1016/j.micpath.2016.09.010

Tolaymat, T. M., El Badawy, A. M., Genaidy, A., Scheckel, K. G., Luxton, T. P., and Suidan, M. (2010). An evidence-based environmental perspective of manufactured silver nanoparticle in syntheses and applications: a systematic review and critical appraisal of peer-reviewed scientific papers. *Sci. Total Environ.* 2010 408, 999–1006. doi: 10.1016/j.scitotenv.2009.11.003

Tran, S.-L., Puhar, A., Ngo-Camus, M., and Ramarao, N. (2011). Trypan blue dye enters viable cells incubated with the pore-forming toxin HlyII of *Bacillus cereus*. *PLoS ONE* 6:e22876. doi: 10.1371/journal.pone.0022876

Vijayakumar, S., Malaikozhundan, B., Shanthi, S., Vaseeharan, B., and Thajuddin, N. (2017a). Control of biofilm forming clinically important bacteria by green synthesized ZnO nanoparticles and its ecotoxicity on *Ceriodaphnia cornuta*. *Microb. Pathog.* 107, 88–97. doi: 10.1016/j.micpath.2017.03.019

Vijayakumar, S., Vaseeharan, B., Malaikozhundan, B., Gopi, N., Ekambaram, P., Pachaiappan, R., et al. (2017b). Therapeutic effects of gold nanoparticles synthesized using *Musa paradisiaca* peel extract against multiple antibiotic resistant *Enterococcus faecalis* biofilms and human lung cancer cells (A549). *Microb. Pathog.* 102, 173–183. doi: 10.1016/j.micpath.2016.11.029

Wang, L., Hu, C., and Shao, L. (2017). The antimicrobial activity of nanoparticles: Present situation and prospects for the future. *Int. J. Nanomed.* 12:1227. doi: 10.2147/IJN.S121956

Wei, X., Li, H., Li, Z., Vuki, M., Fan, Y., Zhong, W., et al. (2012). Metal-enhanced fluorescent probes based on silver nanoparticles and its application in IgE detection. *Anal. Bioanal. Chem.* 402, 1057–1063. doi: 10.1007/s00216-011-5591-1

Yang, L., Kuang, H., Zhang, W., Aguilar, Z. P., Wei, H., and Xu, H. (2017). Comparisons of the biodistribution and toxicological examinations after repeated intravenous administration of silver and gold nanoparticles in mice. *Sci. Rep.* 7:3303. doi: 10.1038/s41598-017-03015-1

Zhang, J.-H., Chung, T. D., and Oldenburg, K. R. (1999). A simple statistical parameter for use in evaluation and validation of high throughput screening assays. *J. Biomol. Screen.* 4, 67–73. doi: 10.1177/108705719900400206

Recent Advances in Nanomaterials-Based Chemo-Photothermal Combination Therapy for Improving Cancer Treatment

Zuhong Li[1†], Yangjun Chen[2*†], Ya Yang[1], Yan Yu[3], Yanhong Zhang[1], Danhua Zhu[1], Xiaopeng Yu[1], Xiaoxi Ouyang[1], Zhongyang Xie[1], Yalei Zhao[1] and Lanjuan Li[1*]

[1] State Key Laboratory for Diagnosis and Treatment of Infectious Diseases, Collaborative Innovation Centre for Diagnosis and Treatment of Infectious Diseases, The First Affiliated Hospital, Zhejiang University School of Medicine, Hangzhou, China, [2] School of Ophthalmology & Optometry, Eye Hospital, Wenzhou Medical University, Wenzhou, China, [3] Department of Gynecologic Oncology, Women's Hospital, Zhejiang University School of Medicine, Hangzhou, China

Conventional chemotherapy for cancer treatment is usually compromised by shortcomings such as insufficient therapeutic outcome and undesired side effects. The past decade has witnessed the rapid development of combination therapy by integrating chemotherapy with hyperthermia for enhanced therapeutic efficacy. Near-infrared (NIR) light-mediated photothermal therapy, which has advantages such as great capacity of heat ablation and minimally invasive manner, has emerged as a powerful approach for cancer treatment. A variety of nanomaterials absorbing NIR light to generate heat have been developed to simultaneously act as carriers for chemotherapeutic drugs, contributing as heat trigger for drug release and/or inducing hyperthermia for synergistic effects. This review aims to summarize the recent development of advanced nanomaterials in chemo-photothermal combination therapy, including metal-, carbon-based nanomaterials and particularly organic nanomaterials. The potential challenges and perspectives for the future development of nanomaterials-based chemo-photothermal therapy were also discussed.

Keywords: cancer, nanomaterials, NIR responsive, chemo-photothermal therapy, synergistic effect

INTRODUCTION

Traditional chemotherapy, typically the main treatment for late stage cancer or adjunct method for surgery in early stage cancer, usually suffers severe systemic toxicity due to the unspecific cytotoxicity of chemotherapeutic drugs for both cancerous and normal cells (Cobley et al., 2010; Mahmoudi et al., 2011; DeSantis et al., 2014). As a result, the outcome of chemotherapy is often limited by safe dosage, generating insufficient drug concentration in tumor site. Moreover, drug resistance is possibly developed to further hamper the overall efficacy during the treatment course (Holohan et al., 2013). Thus, it is urgent to improve specific delivery to reduce side effects, and optimize the therapeutic efficacy at a lower tolerance dose.

Hyperthermia as cancer therapy refers to the treatment of cancer through heating and has been used in various forms since the original study pioneered by Coley in the end of nineteenth

century (Mallory et al., 2016). Although it can be used alone, hyperthermia is most often used in combination with other therapeutic modalities including chemotherapy and radiation therapy. Hyperthermia typically falls under three categories: local hyperthermia, regional hyperthermia, and whole-body hyperthermia. Clinical application of heat can be induced by radiofrequency, microwave, ultrasound, or perfusion methods (Falk and Issels, 2001). While these methods heat tissues efficiently, they also cause either a risk of systemic toxicity from whole-body hyperthermia exposure, require invasive surgery or probe, or may damage normal tissues due to non-targeted heating in local region (Wust et al., 2002). Thus, photothermal therapy has been proposed as a promising modality for hyperthermia treatment. Compared with other methods, light is an ideal external stimulus as it is easily regulated, focused, and remotely controlled. The ease of control and focus enables better targeted treatments and leads to less damage in healthy tissues.

NIR photothermal therapy as an emerging strategy, utilizing NIR laser-generated heat to conduct cancer treatment, has gained increasing attentions (Peng et al., 2011; Wu et al., 2013; Yue et al., 2013). In NIR window, NIR light is minimally absorbed by endogenous absorbers in tissues, which offers deeper tissue penetration *in vivo* (Weissleder, 2001; Weissleder and Ntziachristos, 2003). Besides the heat ablation for direct cell killing in tumor, NIR light-induced mild hyperthermia can increase vascular permeability in tumor tissues with newly formed immature blood vessels, which brings specific drug accumulation and enhanced cytotoxicity (Hauck et al., 2008; Park et al., 2009). Various kinds of nano-structured materials, including both organic and inorganic nanomaterials, have been designed and applied for photothermal therapy as shown in several excellent reviews (Jung et al., 2018; Khafaji et al., 2019; Vines et al., 2019). However, due to the non-uniform heat distribution and restricted laser power to avoid normal tissue damage, the photothermal therapy alone is unlikely to eradicate tumor completely (Wang H. et al., 2013; Luo et al., 2017).

To address these issues, nanomaterials-based combination of chemotherapy and hyperthermia has exhibited the effectiveness in optimizing the efficacy for cancer treatment (You et al., 2012; Zheng et al., 2013; Wang L. M. et al., 2014). It is well-known that nanomedicines can preferentially accumulate in tumor site through passive targeting via enhanced permeability and retention (EPR) effect, or active targeting via surface-conjugated molecules (Jain and Stylianopoulos, 2010; Kratz and Warnecke, 2012). Their unique physicochemical properties also offer different pharmacokinetics and *in vivo* distribution for loaded chemotherapeutic agents (Ernsting et al., 2013). In another hand, nanomaterials-mediated NIR photothermal therapy is finely localized inside the tumor region, and the hyperthermia is tunable simply by controlling the timing and intensity of the extrinsic energy source (Kim et al., 2016). It has been widely accepted that combined chemo-photothermal therapy based on nanomaterials exhibits remarkable advantages over single cancer treatment. Generally, co-delivery of cytotoxic drugs and hyperthermia can simultaneously exert two benefits to improve cancer treatments, and combined chemo-photothermal therapy usually generates synergistic effect. Photothermal

ablation coupled with targeted drug delivery can synergistically enhance therapeutic index via different manner: (i) elevating cell membrane permeability; (ii) augmenting drug cytotoxicity (Hahn et al., 1975; Overgaard, 1976); (iii) triggering drug release at target region. This can be especially significant in treating cancers with multidrug resistance (MDR) (Wang L. M. et al., 2014). So far, there have been several related reviews published, reporting either organic or inorganic nanomaterials for chemo-photothermal combination therapy (Zhang et al., 2013; Zhang A. et al., 2018; Khafaji et al., 2019). Considering the rapid development of this research area, we believe it is highly desirable and important to systematically summarize the recent advances in combined chemo-photothermal therapy based on both organic and inorganic nanomaterials.

Herein, we will review the recent efforts to design and construct nanomaterials for cancer chemo-photothermal therapy. This topic will be presented based on the properties and classifications of nanomaterials applied as photothermal agents and nanocarriers. Upon briefly elaborating new progress in metal and carbon nanomaterials mediated chemo-photothermal therapy, organic nanomaterials-based combination therapy was discussed in particular. Material design and formulations for integrated drug delivery and NIR-responsive hyperthermia are highlighted on the background of their potential capacity in optimizing efficacy of cancer treatment.

METAL NANOMATERIALS-BASED CHEMO-PHOTOTHERMAL THERAPY

Gold Nanoparticles

As is well-known, gold nanoparticles (AuNPs) have been widely investigated in biomedical fields due to their unique size- and shape-dependent optical and photothermal properties, originating from localized surface plasmon resonance (LSPR) where collective oscillation of electrons occurs on the surface of AuNPs after light absorption at a certain frequency (Cobley et al., 2011; Dreaden et al., 2012; Saha et al., 2012). Following excitation of LSPR by NIR laser, the attenuation of resonance energy can occur through radiative and non-radiative relaxation, generating localized heat to surrounding medium. The heat converted from absorbed NIR light can be used to perform hyperthermia or trigger drug release in delivery systems (Hu et al., 2006; Dykman and Khlebtsov, 2012; Llevot and Astruc, 2012). AuNPs also exhibit chemical inertness and good biocompatibility in biological tissues (Khlebtsov and Dykman, 2011). All these properties make AuNPs a promising candidate for effective chemo-photothermal combination therapy (**Figure 1**). The synthesis of AuNPs with controlled size and morphology has obtained various nanostructures such as gold nanorods (Xiao et al., 2012; Ren et al., 2013; Shen et al., 2013; Manivasagan et al., 2019), gold nanoshells (Lee et al., 2010; Liu et al., 2011), hollow gold nanospheres (You et al., 2010, 2012), gold nanocages (Yavuz et al., 2009; Shi et al., 2012; Feng et al., 2019), and gold nanostar (Li M. et al., 2016; Zhang L. et al., 2016), whose LSPR absorption features can be finely tuned to NIR region. However, weak interactions between anticancer drugs and naked Au surface
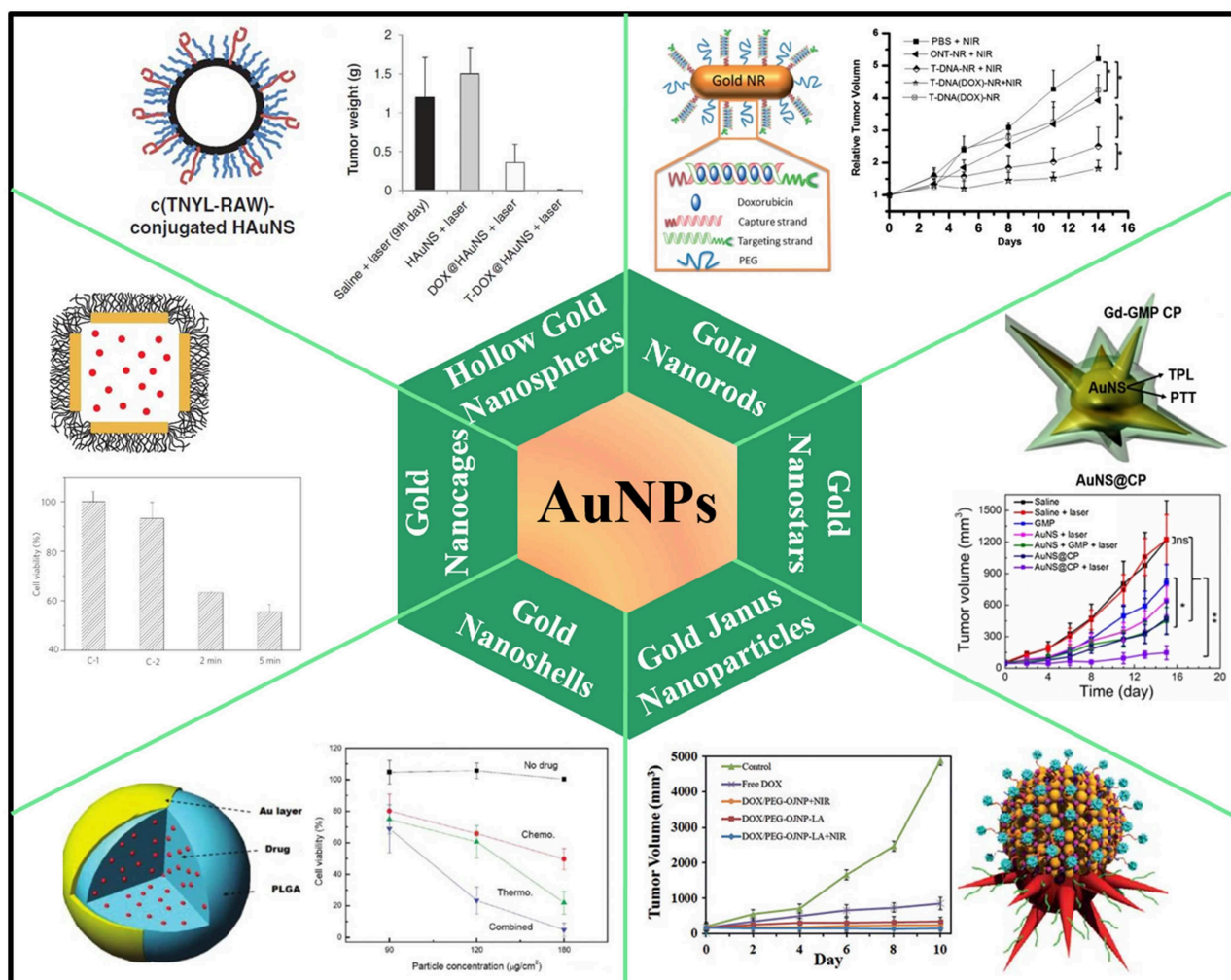
FIGURE 1 | AuNPs-based nanoplatforms for NIR light-responsive chemo-photothermal therapy. Hollow gold nanospheres, reproduced with permission from You et al. (2012); Gold nanorods, reproduced with permission from Xiao et al. (2012); Gold nanocages, reproduced with permission from Yavuz et al. (2009); Gold nanstars, reproduced with permission from Li M. et al. (2016); Gold nanoshells, reproduced with permission from Park et al. (2009); Gold Janus nanoparticles, reproduced with permission from Zhang L. et al. (2016).

make them hardly attach to AuNPs for *in vitro* or *in vivo* co-delivery application. Thus, extra outer/inner layer for molecule absorption or pore-blocking strategy have been widely developed to load drug molecules for chemo-photothermal therapy. For example, thermo-sensitive amphiphilic block polymer, lipoic acid conjugated poly(ethylene glycol)-*b*-poly(ε-caprolactone), was employed to coat AuNRs surface for DOX loading via hydrophobic interactions. Light-triggered drug release after NIR irradiation was achieved due to the phase transition of poly(ε-caprolactone) on the AuNRs surface (Zhong et al., 2013). Mesoporous silica has also been widely explored to decorate AuNPs for drug delivery. High surface area, tunable pore size, and good biocompatibility make them suitable to augment drug loading capacity. For instance, mesoporous silica-coated AuNRs were developed to encapsulate DOX for chemo-photothermal therapy, exhibiting light-controlled drug release

under low-intensity NIR laser irradiation (Zhang et al., 2012). DNA molecules can also serve as capping agents on the surface of AuNPs to realize drug encapsulation and release. DNA duplex strands, consisting of sequential CG base pairs, provide DOX loading sites on the AuNRs surface. Photothermal effects trigger de-hybridization of double-strand DNA by raising temperature higher than melting temperature to release DOX under light-controlled mode (Xiao et al., 2012). Hollow gold nanospheres and gold nanocages themselves could be employed as nano-carriers to load drugs into both outer and inner space. A well-known AuNC-based system was fabricated by coating AuNC surface with thermo-sensitive polymer [poly-(N-isopropylacrylamide), pNIPAAm] as pore blockers. Following temperature rise above a certain threshold, pNIPAAm layer collapsed and the pores on nanocages were exposed for interior drug release (Yavuz et al., 2009). The state of the art of AuNPs-based chemo-photothermal

FIGURE 2 | Different copper chalcogenides nanocrystals mediated chemo-photothermal therapy. **(A)** Schematic illustration and TEM image of PEG-Fol-Cu$_2$S nanoparticles, and photoexcitation mediated drug release. Reproduced with permission from Poulose et al. (2015). **(B)** Schematic illustration and TEM image of Cu$_{2-x}$Se@mSiO$_2$-PEG nanoparticles, and synergistic effects on cell viability and tumor volume. Reproduced with permission from Liu et al. (2014). **(C)** TEM image of PEG-Cu$_{2-x}$Te nanocubes and effects of chemo-photothermal treatment on cell viability and cellular apoptosis. Reproduced with permission from Poulose et al. (2016).

therapy has been wonderfully summarized in some review articles (Wang H. et al., 2013; Zhang et al., 2013; Ai et al., 2016; Kim et al., 2016).

Despite the tremendous attentions and encouraging results on AuNPs, some important issues should be addressed before further applications. On the one hand, AuNPs are subject to deformation upon high-power laser irradiation, leading to loss of LSPR absorption in the NIR region (Opletal et al., 2011; Young et al., 2012). On the other hand, the *in vivo* long-term toxicity and clearance pathways of AuNPs are still uncertain and require further study. To date, some studies have unveiled potential factors that have effect on AuNPs cytotoxicity. It is believed that surface charge and particle size are likely to be the most influential factors. It was reported that half the dose of positively charged 5 nm AuNPs were excreted after 5 days, while only about 10% of the dose of negatively or neutrally charged 5 nm particles were excreted (Balogh et al., 2007). Most of AuNPs accumulations occur within liver and spleen after

intravenous injection of PEG-coated AuNRs (Glenn et al., 2010). Moreover, chronic inflammation was observed in tissues around these AuNPs, despite the unclear long-term consequence under this type of chronic inflammation. *In vivo* observation of AuNPs only take place up to 6 months in animal models, leaving unanswered questions about the potential influence on health over long time course.

Palladium Nanosheets and Copper Chalcogenides Nanocrystals

Another noble metal-based nanostructure, Pd nanosheets, has also been developed to conduct chemo-photothermal therapy. Pd nanosheets exhibit tunable LSPR peaks in the NIR region, as well as photothermal stability, thermal transformation efficiency and biocompatibility (Huang et al., 2011). To facilitate the hyperthermia-assisted chemotherapy, Pd nanosheets were deposited onto hollow mesoporous silica particles or coated with a mesoporous silica layer to achieve drug release under

NIR irradiation and low pH (Fang et al., 2012a,b). Besides noble metal-based nanomaterials, copper chalcogenides nanocrystals have been supposed to be a promising photothermal agent in biomedical applications. Being p-type semiconductors, copper chalcogenides nanocrystals provide composition-dependent LSPR in NIR region and high photothermal conversion efficiency (Hessel et al., 2011; Lie et al., 2014). Kumar et al. decorated Cu_2S nanocrystals with polyethylene glycol (PEG) and folate (PEG-Fol-Cu_2S) to physically absorb doxorubicin (DOX) for multimodal therapeutics against brain cancer cells (Poulose et al., 2015). The folate targeted photothermal ablation in synergism with photo-responsive DOX release proved to be a rapid precision guided cancer-killing module (**Figure 2A**). Hu et al. reported a low-toxic di-functional nanoplatform based on $Cu_{2-x}Se@mSiO_2$-PEG core-shell nanoparticles for cancer treatment (Liu et al., 2014). DOX was loaded into mesoporous silica shell, and the release of DOX can be triggered by pH and NIR laser, resulting in a synergistic effect in anti-tumor therapy. The chemo-photothermal therapy driven by NIR radiation with safe power density significantly improved the therapeutic efficacy (**Figure 2B**). In another work, DOX loaded PEG-Cu_{2-x}Te nanocubes were developed for treatment of hypermethylated breast cancer cells (Poulose et al., 2016). PEG-Cu_{2-x}Te/DOX nanocubes conducted highly effective chemo-photothermal-photodynamic therapy to overcome hypermethylated cancer cells resisting to chemotherapeutic drugs (**Figure 2C**).

Two-Dimensional Transition Metal Dichalcogenides

In recent years, a class of two-dimensional transition metal dichalcogenides (2D TMDCs) has attracted tremendous attention. 2D TMDCs are typically made up of a layer of transition metal atomssandwiched between two layers of chalcogen atoms. Their generalized formula is MX_2, where M is a transition metal of groups 4-10 (Mo, W, Ti, Ta, Zr, V, Nb, etc.) and X is a chalcogen (Chhowalla et al., 2013). Single-layered 2D TMDCs exhibit superior properties, such as strong NIR absorbance, high photothermal conversion efficiency as well as good photothermal stability, offering the possibility to be excellent photothermal agents (Wang C. et al., 2016; Zhu et al., 2017). Moreover, the ultra-high surface area of 2D TMDCs endows themselves with efficient cargo loading ability as drug carriers for chemotherapy.

Meng et al. prepared aptamer conjugated PEG-MoS_2/$Cu_{1.8}S$ nanosheets (ATPMC) as multifunctional platforms for chemo-photothermal therapy (Meng et al., 2017). ATPMC nanoplatform possessed superb photothermal conversion efficiency due to the interactions of MoS_2/$Cu_{1.8}S$ nanocomposites. DOX loaded ATPMC displayed NIR laser-induced programmed chemotherapy and advanced photothermal therapy, and the targeted chemo-photothermal therapy presented excellent antitumor efficiency (**Figure 3A**). In another work, flower-like MoS_2 nanoparticles coated with bovine serum albumin (BSA) were successfully fabricated to load DOX for cancer treatment (Chen L. et al., 2016). Fabricated MoS_2@BSA-DOX exhibited high photothermal conversion efficiency as well as intelligent

drug release. Combination of DOX release and photothermal treatment displayed better therapeutic efficacy than single photothermal therapy or chemotherapy (**Figure 3B**). Kim et al. reported a photothermally controllable DOX-MoS_2@SiO_2-PEG nanoplate as functional drug delivery carrier (Lee et al., 2016). DOX release was facilitated by external NIR laser irradiation under acidic pH. Enhanced anticancer effect of DOX-MoS_2@SiO_2-PEG was achieved by the combination of heat damage and enhanced DOX release as well as endosomal escape (**Figure 3C**).

Beside MoS_2 nanosheetes, other 2D TMDCs have also been studied for the application of chemo-photothermal therapy (Wang Y. et al., 2019). Jiang et al. successfully prepared $MoSe_2$@PDA-DOX to be applicable for multi-modal chemo-photothermal therapy (Wang C. et al., 2016). $MoSe_2$@PDA-DOX nanocomposites showed high loading efficiency and NIR-responsive DOX release. Synergistic therapy significantly inhibited cancer cell viability, and suppressed *in vivo* tumor growth (**Figure 3D**). In addition, Liu et al. fabricated WS_2nanosheets with iron oxide (IO) nanoparticles on surface, subsequently coated with mesoporous silica shell and PEG (Yang G. B. et al., 2015). The obtained WS_2-IO@MS-PEG nanocomposites exhibited high NIR light and X-ray absorbance as well as NIR-responsive DOX release. Chemo-photothermal therapy based on WS_2-IO@MS-PEG/DOX achieved a remarkable synergistic effect superior to the respective mono-therapies (**Figure 3E**).

As other metal nanomaterials, biosafety is one of the most concerning issues for 2D TMDCs in biomedical applications, while the knowledge about toxicity for 2D TMDCs is very limited. Till now, only a few 2D TMDCs have been tested for their *in vitro* and *in vivo* cytotoxicity, and further studies should be systematically carried out to examine their acute and long-term cytotoxicity.

CARBON-BASED CHEMO-PHOTOTHERMAL THERAPY

Over the past few decades, a range of carbon nanoallotropes with surprising properties and diverse potential applications have been discovered, such as carbon nanotubes (Iijima, 1991), graphene (Novoselov et al., 2004), carbon dots (Xu et al., 2004), fullerene (Kroto et al., 1985), and nanodiamonds (Niwase et al., 1995). The majority of the interest in carbon nanomaterials for biomedical applications relates to bio-imaging and cancer treatment because of their extraordinary photon-to-thermal conversion efficiency and ultrahigh surface area (Lim et al., 2014), as well as the ability to integrate different biomolecules and drugs on a nanoscale platform, generating advanced hybrid delivery systems.

Graphene/Graphene Oxide

Graphene is a two-dimension shaped carbon nanoallotrope, in which carbon atoms are arranged in a single atom thick sheet packed into a honeycomb lattice (Novoselov et al., 2004). The unique feature of graphene provide tremendous tunable surface

FIGURE 3 | 2D TMDCs for combined chemo-photothermal therapy. **(A)** Schematic illustration of DOX loaded ATPMC for NIR-laser irradiation-induced chemotherapy. TEM image of MoS$_2$/Cu$_{1.8}$S nanosheets and tumor volume change with different treatments (*P < 0.01 compared with control group; #P < 0.01 compared with ATPMCD group). Reproduced with permission from Meng et al. (2017). **(B)** FESEM image of MoS$_2$@BSA nanoparticles and combined therapeutic efficacy of MoS$_2$@BSA-DOX in 4T1 cells (**P < 0.01 compared with MoS$_2$@BSA-DOX + NIR group). Reproduced with permission from Chen L. et al. (2016). **(C)** TEM image of MoS$_2$@SiO$_2$-NH$_2$ nanoplates and NIR-induced cytotoxicity of DOX-MoS$_2$@SiO$_2$-PEG against HepG2 cells (**P < 0.01). Reproduced with permission from Lee et al. (2016). **(D)** TEM image of MoSe$_2$@PDA nanocomposites and tumor growth curves of different treatments. Reproduced with permission from Wang C. et al. (2016). **(E)** TEM image of WS$_2$-IO@MS-PEG and growth of 4T1 tumors in different groups of mice after various treatments (***P < 0.001, *P < 0.05). Reproduced with permission from Yang G. B. et al. (2015).

with great mechanical Young's modulus, fracture strength, electrical, thermal and optical properties (Yang et al., 2010; Feng and Liu, 2011). Graphene oxide (GO) is a highly oxidized form of graphene that is comprised of single atom carbon sheet with carboxylate groups on the border areas, and hydroxyl, epoxide groups on the basal surface. Carboxylate groups provide negatively charged surface and colloidal stability, whereas basal planes offer π-π interaction for the absorption of drug molecules. Like other nanomaterials-based photothermal agents, PEGylated GO and reduced GO exhibit high NIR absorbance and capacity in photothermal treatment (Robinson et al., 2011; Yang et al., 2012a; Zaharie-Butucel et al., 2019). Meanwhile, due to the ultrahigh surface area and delocalized π electron, many anticancer agents such as camptothecin (CPT), DOX, and 7-ethyl-10-hydroxycamptothecin (SN38) have been successfully loaded onto the GO surface (Li et al., 2006; Zhang et al., 2010; Bao et al., 2011; Pan et al., 2011). The works concerning on nano-graphene based chemo-photothermal therapy have been well-reviewed (Yang et al., 2013; Orecchioni et al., 2015; Rahman et al., 2015; Yang K. et al., 2015). For biomedical application of nano-graphene,

one of the critical issues is still the potential long-term toxicity in biological systems (Kiew et al., 2016). It is urgent to figure out that whether and how nano-graphene would be gradually degraded in living body, which is essentially unclear at present and needs a lot more efforts in future studies.

Carbon Dots and Mesoporous Carbon Nanoparticles

Carbon dots (C-dots) are quasi-spherical carbon nanoparticles with diameters of 2–10 nm, and consist of oxygen, nitrogen elements and other doped heteroatoms (Baker and Baker, 2010). Due to their high quantum yield, superior chemical and photostability, low cytotoxicity and low cost, C-dots are generally regarded as a promising candidate in cancer therapeutic applications (Zhao et al., 2015; Zheng et al., 2015; Wang and Qiu, 2016). Gomes et al. prepared PEG$_{2000}$ passivated nitrogen-doped C-dots (CND-P) to remotely initiate the delivery of DOX in 3D cultured MCF-7 cells (Ardekani et al., 2017). CND-P possessed high drug loading capacity with the ability to release DOX under two-photon excitation. CND-P/DOX

FIGURE 4 | C-dots- and MCNs-based chemo-photothermal therapy. **(A)** Schematic illustration of CND-P and cell viability with different treatments. Reproduced with permission from Ardekani et al. (2017). **(B)** Schematic illustration of GdN@CQDs/GP and relative tumor volume of tumor-bearing mice after various treatments. Reproduced with permission from Zhang et al. (2017a). **(C)** Schematic illustration of MCNs, and cytotoxicity assays of MDA-MB-231 cells under different treatments. Reproduced with permission from Zhou et al. (2015). **(D)** Schematic illustration of FPC-NCs and *in vitro* cytotoxicity after various treatments. Reproduced with permission from Wang H. et al. (2015).

mediated chemo-photothermal treatment was superior to single treatment of CND-P or DOX in killing efficiency (**Figure 4A**). Moreover, magnetofluorescent C-dots were also reported as chemo-photothermal therapeutic agents (Zhang et al., 2017a,b). For example, Zhou et al. prepared Gd doped magnetofluorescent C-dots (GdN@CQDs) as drug carriers, followed with cross-linking by genipin to form multifunctional delivery system (GdN@CQDs/GP-DOX) with pH- and NIR-triggered drug release (Zhang et al., 2017a). GdN@CQDs/GP demonstrated strong NIR absorption and high photothermal conversion efficiency. Upon laser irradiation, GdN@CQDs/GP-DOX has the ability to achieve synergistic therapeutic effect (**Figure 4B**).

Recently, mesoporous carbon nanoparticles (MCNs) have received considerable attention in the family of carbon-nanomaterials (Fang et al., 2010). This growing interest stems from their intrinsic properties, such as high surface areas, large pore volumes, and well-defined surface properties, offering significant advantages as drug carrier on the basis of higher loading capacity and biologic inertness without cytotoxicity (Karavasili et al., 2013). Furthermore, MCNs could also be used as NIR-absorbing nanomaterials with high photothermal conversion efficacy (Dong et al., 2016; Wang X. et al., 2019). Qu et al. developed hyaluronic acid surface-modified MCNs (MCNs-HA) as nanocarriers for effective dual-triggered synergistic cancer therapy (Zhou et al., 2015). This system was sensitive to both intracellular hyaluronidase-1 and GSH level to release loaded DOX. In combination with photothermal therapy, DOX-MCNs-HA showed effective therapeutic efficiency toward target

cells (**Figure 4C**). In another study, hollow porous carbon nanoparticles with C-dots embedded in carbon shell (FPC-NCs) were fabricated (Wang H. et al., 2015). Such prepared FPC-NCs demonstrated great potential to combine multiple functions for simultaneous two-photon cell imaging, responsive drug delivery, and photothermal therapy. DOX-loaded FPC-NCs manifested NIR-responsive drug release and combined chemo-photothermal therapy (**Figure 4D**).

ORGANIC NANOMATERIALS-BASED CHEMO-PHOTOTHERMAL THERAPY

In spite of the excellent photothermal conversion efficiency, the poor biodegradability and potential long-term toxicity of inorganic nanoparticles are still major obstacles for their clinical applications in the future (Jung et al., 2018). In this regard, organic nanoparticles usually exhibit optimized biodegradability and biocompatibility as an alternative approach for combined chemo-photothermal therapy in cancer treatment (Shi et al., 2017; Pierini et al., 2018). Additionally, organic nanoparticles have other attractive advantages such as facile preparation under mild conditions, desirable photothermal features based on easily tuning molecular structures, and satisfactory drug loading efficiency (Yue et al., 2017). In this section, we will mainly talk about small molecular NIR dyes, conjugated polymers and melanin-like polydopamine based organic nano-systems and their applications in synergistic chemo-photothermal therapy.

Small Molecular NIR Dyes

Over the past few years, small molecular NIR dyes have attracted lots of attention mainly due to their excellent performance in fluorescent imaging and the ease of tuning photothermal features through elaborate chemical design and synthesis. In principle, these organic dyes with strong NIR absorbance can serve as photothermal agents as well (Song et al., 2015). Therefore, nano-systems containing NIR dyes can be easily designed as a nano-platform for multifunctional theranostics. To date, the well-studied NIR dyes include porphyrin, cyanine derivatives, borondipyrromethane dyes, diketopyrrolopyrrole derivatives and so on (Cai et al., 2018). Direct use of NIR dyes is mainly hindered by the rapid blood clearance following with undesired aggregation caused by the poor aqueous solubility/stability and non-specific protein adsorption (Chen Y. J. et al., 2016). From this point of view, NIR dyes are similar to many anticancer drugs which usually need to be administrated in the form of nano-formulations to improve therapeutic efficacy. Therefore, rational design of nano-systems with drugs/NIR dyes either encapsulated or conjugated is of great significance to achieve favorable synergistic outcomes of chemo-photothermal therapy.
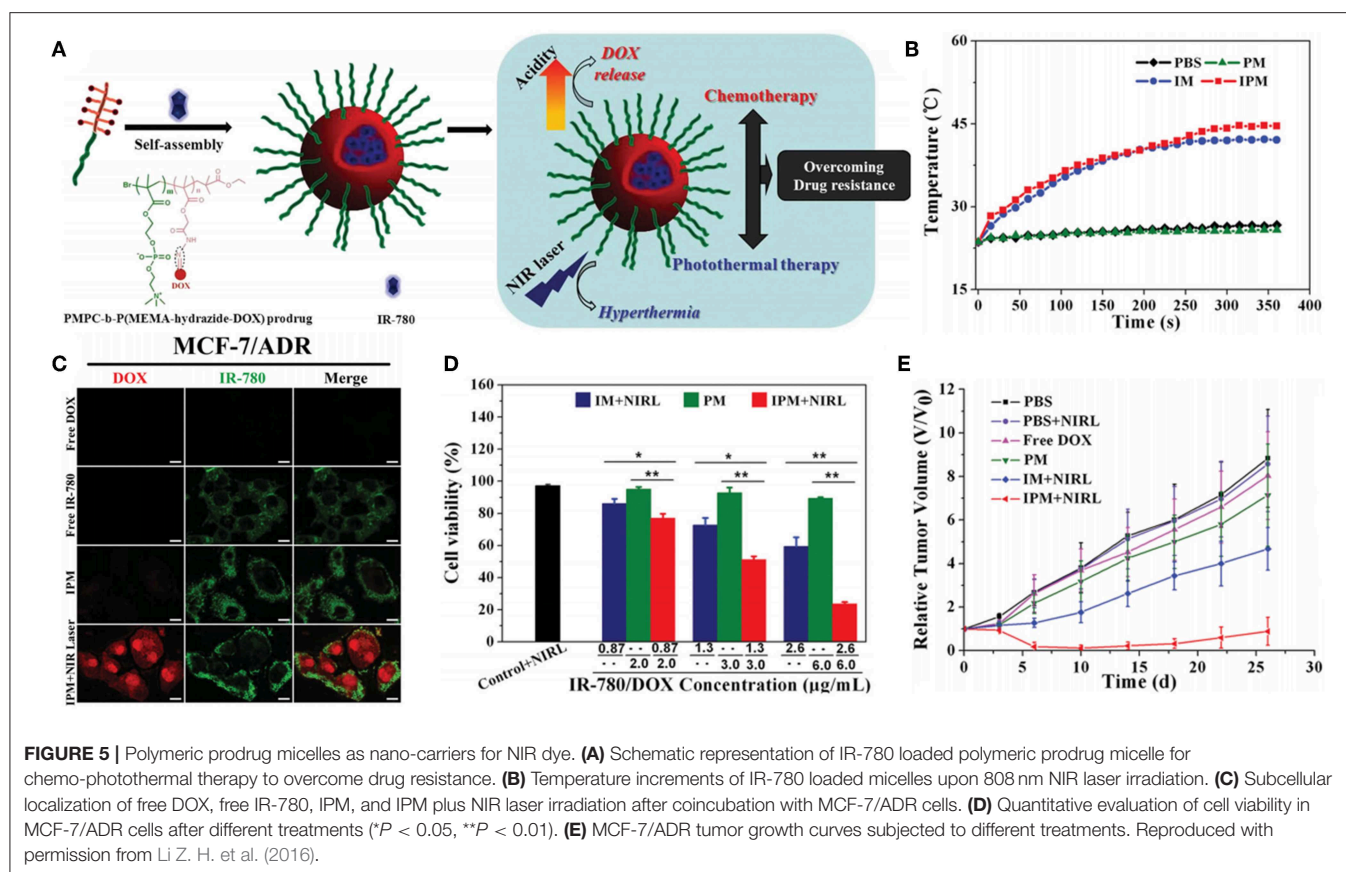
The simplest way to combine NIR dyes and chemotherapeutic drugs is co-encapsulation in one nanoparticle by physical interactions. Cai et al. prepared poly(lactic-co-glycolic acid) (PLGA)-lecithin-PEG nanoparticles (DINPs) containing both DOX and indocyanine green (ICG) by a single-step sonication method (Zheng et al., 2013). ICG is the quintessential NIR dye and has been approved by US Food and Drug Administration (FDA) for several clinical applications (Sheng et al., 2013; Porcu et al., 2016). The stability of ICG was significantly improved by encapsulation in DINPs, thus generating higher localized temperature than free ICG under NIR laser irradiation and facilitating DOX release and cellular uptake. Encouragingly, combined chemo-photothermal therapy realized successful suppression of MCF-7 and DOX-resistant MCF-7/ADR tumor growth as well as prevention of tumor recurrence *in vivo*. Similarly, many other attempts have been made to co-encapsulate various NIR dyes and drugs in different kinds of nano-carriers like liposomes (Li et al., 2015; Feng et al., 2016; Yan et al., 2016; Gao et al., 2018; Mu et al., 2019), polymeric nanoparticles (Su et al., 2015; Zhu et al., 2015; Chen Y. et al., 2017; Wang et al., 2017; Deng et al., 2018; He H. Z. et al., 2018; Yao et al., 2018; Tan et al., 2019; Zhang et al., 2019), protein nanoparticles (Chen et al., 2015; Lin and Shieh, 2018; Gao et al., 2019; Pei et al., 2019), and cell membranes (Sun et al., 2015; Li X. et al., 2018; Wan et al., 2018; Zhang N. et al., 2018; Ye et al., 2019). For example, Liu et al. developed "Abraxane-like" nanodrug through self-assembly of human serum albumin (HSA), paclitaxel (PTX), and ICG in a simple mixing manner (Chen et al., 2015). The nanodrug remarkably improved solubility of both PTX and ICG, achieving prolonged blood circulation time and high tumor accumulation. The combined chemo-photothermal therapy completely destructed subcutaneous tumors and exhibited great therapeutic benefit in treating lung metastasis. The excellent therapeutic effect and FDA-approved components endow this

"Abraxane-like" nanodrug with great potential for clinical use in the future.

The simple processing method of physically co-encapsulated nano-formulations is usually preferred for clinical translation. However, undesirable premature leakage of drugs and NIR dyes during administration can happen and lead to insufficient tumor accumulation and potential adverse effects as well. Covalent conjugation of drugs and/or NIR dyes to nano-carriers is believed to potently address this issue. Polymeric prodrugs with therapeutic molecules reversibly linked to polymer chains have already been extensively studied for their longer blood circulation time, higher tumor accumulation and better therapeutic effect but lower systemic toxicity (Duncan, 2006; Larson and Ghandehari, 2012; Delplace et al., 2014). Therefore, polymeric prodrug assemblies can serve as a good platform for co-loading of NIR dyes to perform combined chemo-photothermal therapy. Ji et al. prepared IR-780 loaded polymeric prodrug micelles (IPM) for overcoming multidrug resistance by combination of chemo-photothermal therapy (**Figure 5**; Li Z. H. et al., 2016). Zwitterionic polymer with DOX conjugated by acid-cleavable hydrazone bonds can self-assemble into polymeric prodrug micelles, simultaneously encapsulating lipophilic IR-780 dye in the hydrophobic micellar core. The prodrug micelles kept remarkable stability at pH 7.4 while exhibited accelerated DOX release at pH 5.0 which mimics the acidic endosome/lysosome environment. Interestingly, IPM combined with NIR laser irradiation can dramatically increase DOX accumulation in cytoplasm of MCF-7/ADR cells, which should be attributed to hyperthermia-induced enhanced cytoplasm permeability. Significant suppression of MCF-7/ADR tumor growth can be achieved by localized NIR laser irradiation post-intravenous injection of IPM. Recently, several similar strategies have been reported by encapsulating various NIR dyes in different kinds of polymeric prodrug nanoparticles (Zhang Y. Y. et al., 2016a,b, 2018; Chen et al., 2018; Wang W. H. et al., 2018). For example, Hu and Xing et al. prepared smart nanoplatforms by loading ICG in enzyme-responsive cisplatin polyprodrug amphiphiles for cascade photo-chemotherapy (Wang W. H. et al., 2018). Zhao et al. utilized host-guest supramolecular chemistry to fabricate reduction-sensitive CPT prodrug nanoparticles, which can further incorporate IR825 dye to achieve simultaneous chemo-photothermal therapy (Zhang Y. Y. et al., 2018).

Nano-systems with both drugs and NIR dyes covalently conjugated, however, have rarely been reported. The multiple steps that are usually necessary for conjugating two or more molecules in one single system may be the major obstacle. One of the very few examples is P-DOX/P-cypate hybrid micelles, which were composed of enzyme-responsive DOX polymeric prodrugsandcypate-linked polymers (Yu et al., 2015). Hyperthermia effect of the hydride micelles upon NIR irradiation significantly enhanced tumor penetration and cytosol release of DOX, further inducing high therapeutic efficacy in combating DOX resistance in MCF-7/ADR breast cancer.

Considering the tremendous benefits of NIR dyes-based nano-systems whereas few applications so far, further efforts are needed to simplify the synthesis procedures and precisely control the loading ratios of chemical drugs and NIR dyes, thus enabling

FIGURE 5 | Polymeric prodrug micelles as nano-carriers for NIR dye. **(A)** Schematic representation of IR-780 loaded polymeric prodrug micelle for chemo-photothermal therapy to overcome drug resistance. **(B)** Temperature increments of IR-780 loaded micelles upon 808 nm NIR laser irradiation. **(C)** Subcellular localization of free DOX, free IR-780, IPM, and IPM plus NIR laser irradiation after coincubation with MCF-7/ADR cells. **(D)** Quantitative evaluation of cell viability in MCF-7/ADR cells after different treatments (*$P < 0.05$, **$P < 0.01$). **(E)** MCF-7/ADR tumor growth curves subjected to different treatments. Reproduced with permission from Li Z. H. et al. (2016).

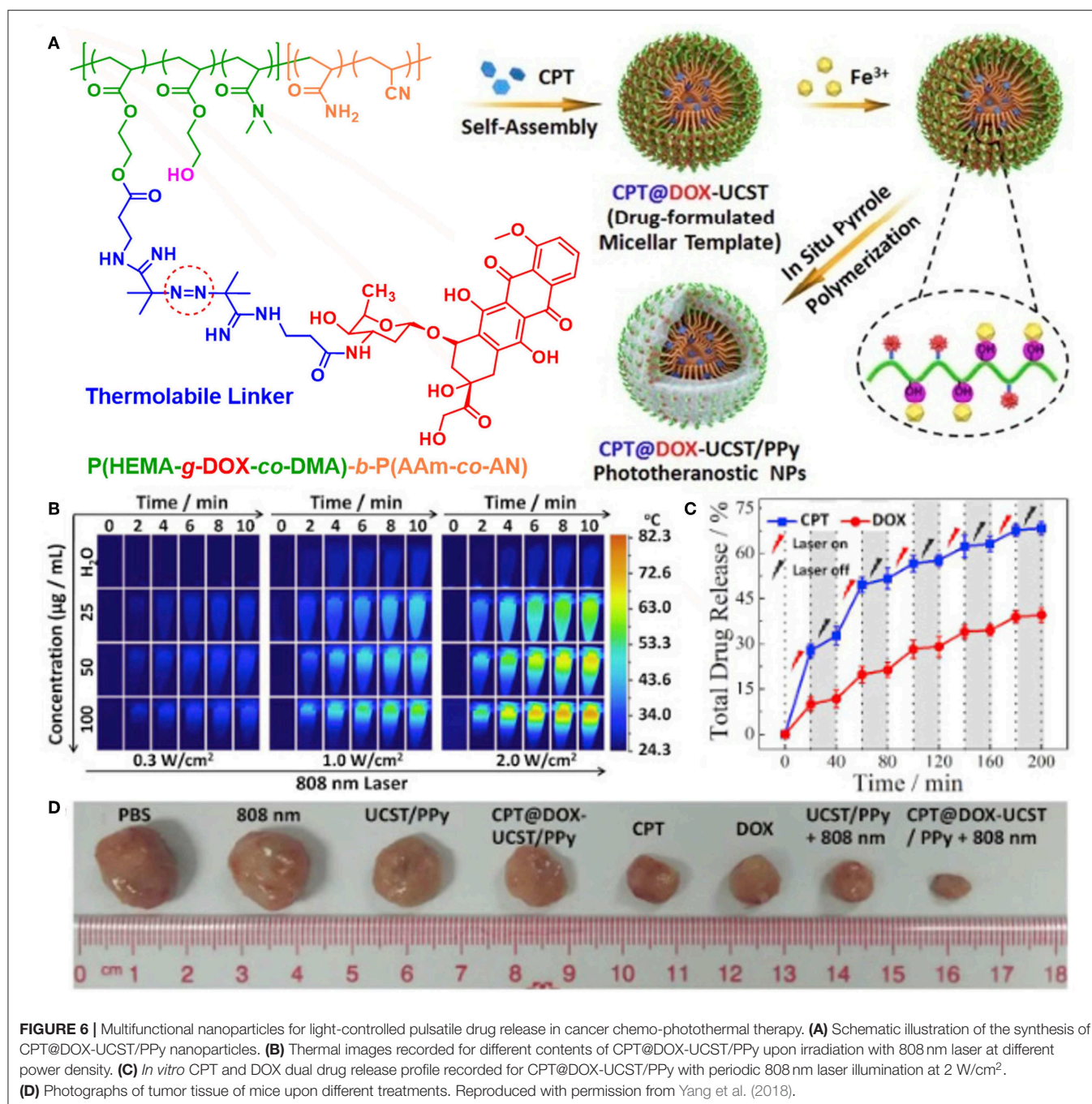ease of availability and optimizing the synergistic effect of chemo-photothermal therapy.

Conjugated Polymers

Conjugated polymers are well-known for their fantastic photoelectric properties due to the existence of large π-conjugated backbones. For a long time in the past, conjugated polymers were extensively studied in the areas like organic semiconductors and solar cells, but not biomedicine. It was not until the year of 2011–2012 that two kinds of very commonly used conjugated polymers, polyaniline (PANI) and polypyrrole (PPy), were successfully developed as photothermal agents for the first time (Yang et al., 2011, 2012b). Later on, lots of semiconducting polymers were further explored for fluorescent imaging and phototherapy (Li J. C. et al., 2018; Zhu et al., 2018). Benefiting from the unique chemical structures, conjugated polymers hold the advantages of excellent photostability and high photothermal conversion efficiency. Several excellent reviews have summarized the applications of conjugated polymers in fluorescent imaging and phototherapy (Xu et al., 2014; Qian et al., 2017; Li J. C. et al., 2018; Sun et al., 2018). Conjugated polymers are generally hydrophobic organic molecules, therefore, nano-stabilizing methods like encapsulation in amphiphiles or covalent grafting of hydrophilic polymers are usually necessary prior to their use *in vitro* and *in vivo*. By further incorporation of chemical drugs, conjugated

polymers based nanomaterials can be utilized for combined chemo-photothermal therapy.

PANI nanoparticles were firstly reported to serve as a photothermal agent for *in vitro* treatment of epithelial cancer in 2011 (Yang et al., 2011). Li et al. further prepared F127 stabilized PANI nanoparticles for *in vivo* tumor ablation with no tumor regrowth observed (Zhou et al., 2013). Chemotherapeutic drugs were encapsulated within PANI nanoparticles to perform the combination of chemo- and photothermal therapy. For example, Kim and Yong et al. prepared multifunctional hybrid polymeric nanoparticles (denoted as LT-MTX/PANI NPs) by incorporation of methotrexate (MTX) and PANI together and further conjugation with Lanreotide (LT) for cancer targeting (Nguyen et al., 2018). The hybrid NPs showed burst release of MTX upon NIR light irradiation due to heat generation by PANI. Enhanced cell apoptosis *in vitro* as well as improved tumor suppression *in vivo* were observed by treatment of LT-MTX/PANI NPs with NIR light irradiation.

In 2012, Liu's group firstly reported poly(vinyl alcohol) (PVA)-stabilized PPy nanoparticles for photothermal therapy (Yang et al., 2012b). Then, they fabricated core-shell structured Fe_3O_4@PPy-PEG-DOX nanocomposite by oxidative polymerization of pyrrole on the surface of Fe_3O_4 nanoclusters and subsequent surface modification and drug loading (Wang C. et al., 2013). The Fe_3O_4 core can be used for MRI to monitor the therapeutic effect, while the PPy shell can generate

FIGURE 6 | Multifunctional nanoparticles for light-controlled pulsatile drug release in cancer chemo-photothermal therapy. **(A)** Schematic illustration of the synthesis of CPT@DOX-UCST/PPy nanoparticles. **(B)** Thermal images recorded for different contents of CPT@DOX-UCST/PPy upon irradiation with 808 nm laser at different power density. **(C)** *In vitro* CPT and DOX dual drug release profile recorded for CPT@DOX-UCST/PPy with periodic 808 nm laser illumination at 2 W/cm². **(D)** Photographs of tumor tissue of mice upon different treatments. Reproduced with permission from Yang et al. (2018).

mild hyperthermia to enhance intracellular delivery of DOX. Remarkable anticancer effect *in vivo* was achieved by combined chemo-photothermal therapy. Other groups also designed various nano-platforms for combined chemo-photothermal therapy by loading drugs in PPy-based nanomaterials, mainly by physical interactions (Wang Y. et al., 2014; Wang J. et al., 2015; Wang K. et al., 2016; Zhu et al., 2016; Chen X. J. et al., 2017; Yao et al., 2017). Very recently, Hu et al. prepared multifunctional PPy/micelle hybrid nanoparticles (denoted as CPT@DOX-UCST/PPy) by polymerizing pyrrole in the shell

of polymeric micelles with upper critical solution temperature (UCST) feature (**Figure 6**; Yang et al., 2018). The polymeric micelles are exquisitely designed by tethering thermo-cleavable DOX prodrug in the corona and encapsulating hydrophobic CPT in the UCST micellar core. CPT@DOX-UCST/PPy had multiple synergistic effects upon NIR light irradiation, which showed great potential to kill three birds with one stone. First, PPy shell can generate heat for photothermal therapy. Second, DOX can be released by cleavage of the thermo-labile linker. Third, CPT can also be released following micellar swelling
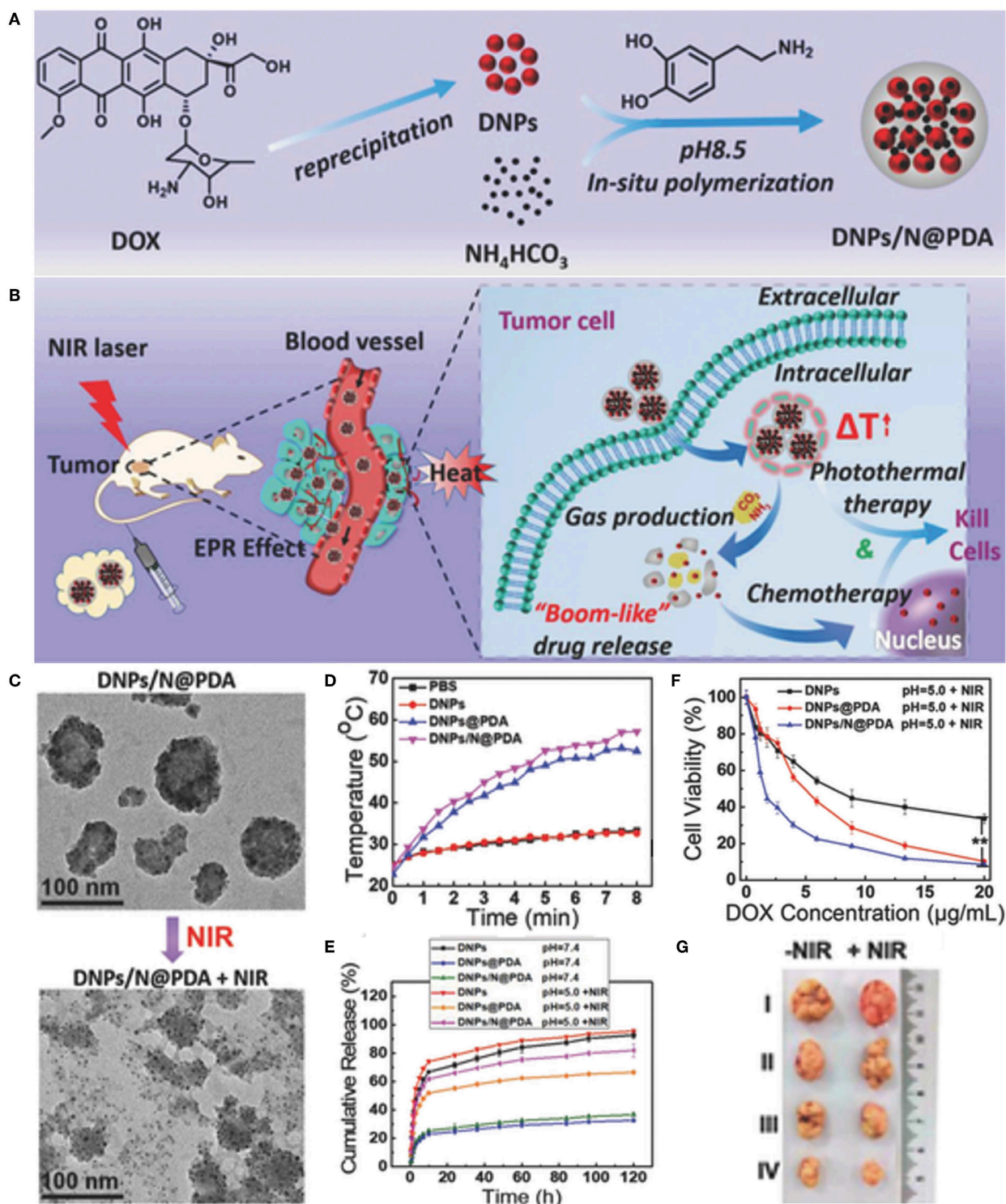
FIGURE 7 | Carrier-free "Nanobomb" for on demand drug release and enhanced chemo-photothermal therapy. **(A)** Schematic illustration of the preparation of DNPs/N@PDA. **(B)** Schematic illustration of the stable blood circulation of DNPs/N@PDA and on demand "bomb-like" drug release and enhanced chemo-photothermal therapy triggered by NIR irradiation. **(C)** TEM images of DNPs/N@PDA before and after NIR laser irradiation (808 nm, 5 W/cm^2) for 5 min. **(D)** Temperature increase profiles of PBS, DNPs, DNPs@PDA, and DNPs/N@PDA with NIR laser irradiation of 808 nm (5 W/cm^2, 8 min). **(E)** Cumulative release profiles of DOX from DNPs, DNPs@PDA, and DNPs/N@PDA in PBS with different pHs without or with NIR irradiation (808 nm, 5 W/cm^2). **(F)** In vitro cytotoxicity of DNPs, DNPs@PDA, and DNPs/N@PDA at pH 5.0 with NIR laser irradiation (808 nm) of 5 W/cm^2 for 1 min at different DOX concentrations on HeLa cells after 48 h incubation (**p < vs. DNPs/N@PDA group with NIR irradiation). **(G)** Representative photos of excised tumors 21 d after treatments. Reproduced with permission from Li M. H. et al. (2018).

triggered by phase transition of the UCST core. Together with the photoacoustic (PA) imaging module, CPT@DOX-UCST/PPy can serve as a multifunctional nano-platform for combined chemo-photothermal therapy and theranostics.

Poly(3,4-ethylenedioxythiophene):poly(4-styrenesulfonate) (PEDOT:PSS), commonly used in organic electronics, was developed by Liu's group for photothermal therapy in 2012 (Gong et al., 2013). PEDOT:PSS-PEG nanoparticles were prepared through layer-by-layer coating of charged polymers followed by conjugating with branched PEG. In another work of the same group, chemotherapeutic drugs like DOX and SN38, as well as photodynamic agent Ce6, were encapsulated within PEDOT:PSS-PEG nanoparticles through π-π stacking and hydrophobic interaction. The photothermal effect of PEDOT:PSS-PEG promoted intracellular delivery of DOX, obtaining integrated chemo-photothermal therapy with synergistic effect.

To achieve higher photothermal conversion efficiency, conjugated polymers with narrow energy band gap are highly desired as they are expected to have sharper adsorption peaks to get greater heat generation (He Y. L. et al., 2018). The concept of donor-acceptor (D-A) has been widely applied for designing conjugated polymer-based field-effect transistors and organic photovoltaics. In 2013, Levi-Polyachenko et al. reported for the first time the use of D-A conjugated polymer nanoparticles with low band gap for photothermal ablation of cancer cells in vitro (MacNeill et al., 2013). Since then, lots of D-A conjugated polymers have been synthesized for photothermal therapy by proper design of the donor and acceptor structures (Sun et al., 2018). Chemotherapeutic drugs can be co-loaded with hydrophobic D-A conjugated polymers in liposomes or polymeric micelles, or encapsulated in micelles formed with PEG-modified D-A conjugated polymers. These nano-formulations can thus gain significant synergistic effect of combined chemo-photothermal therapy upon NIR light irradiation. For example, Yang's group reported a D-A conjugated polymer PBIBDF-BT with alternating isoindigo derivative bis(2-oxoindolin-3-ylidene)-benzodifuran-dione (BIBDF) and bithiophene (BT) units (Li D. D. et al., 2016). Hydrophobic PBIBDF-BT together with anticancer drug DOX were simultaneously encapsulated in micelles formed by an amphiphilic copolymer poly(ethylene glycol)-block-poly(hexyl ethylene phosphate) (mPEG-b-PHEP). DOX-loaded PBIBDF-BT@NPPPE nanoparticles exhibited NIR-triggered intracellular drug release and synergistic anticancer treatment. Liu and coworkers prepared poly[9,9-bis(4-(2-ethylhexyl)phenyl)fluorene-alt-co-6,7-bis(4-(hexyloxy)phenyl)-4,9-di(thiophen-2-yl)thiadiazolo-quinoxaline] (PFTTQ) with strong absorption in the NIR region (Yuan et al., 2015). An amphiphilic brush copolymer, decorated with 2-diazo-1,2-naphthoquinones (DNQ) moieties and cyclic arginine-glycine-aspartic acid (cRGD), was used to encapsulate hydrophobic PFTTQ and DOX (forming T-PFTTQ/DOX). Upon NIR laser irradiation, the DNQ moieties could undergo hydrophobic-hydrophilic transformation, inducing disassembly of the micelles and subsequent DOX release. At the same time, hyperthermia generated by PFTTQ further contributed to the efficient killing

of cancer cells. The combination index was calculated to be 0.48, indicating the synergistic effect of T-PFTTQ/DOX for combined chemo-photothermal therapy. Pu's group synthesized an amphiphilic PEG-grafted poly(cyclopentadithiophene-alt-benzothiadiazole) (PEG-PCB), which could self-assemble into homogenous nanoparticles and simultaneously load anticancer drug DOX via strong hydrophobic and π-π interactions (Jiang et al., 2017). Drug-loaded PEG-PCB (DSPN) could serve as a multifunctional theranosticnanoagent for NIR fluorescence/PA imaging guided chemo-photothermal therapy. Both in vitro and in vivo results confirmed the superior antitumor efficacy by the synergistic treatment. Similarly, Li et al. prepared several theranosticnanosystems by co-encapsulating diketopyrrolopyrrole-based D-A polymers with anticancer drugs like DOX or curcumin in polymeric micelles or thermosensitive liposomes (Cao et al., 2017a,b). These nanoparticles also exhibited excellent PA imaging-guided chemo-photothermal combined cancer therapy.

Polydopamine-Based Nanoparticles

Polydopamine (PDA), a melanin-like polymer, can be easily obtained by self-polymerization of dopamine under mild conditions. PDA was introduced by Lee and Messersmith for the first time as a simple and powerful surface functionalization method in 2007 (Lee et al., 2007). Lu's group reported the first application of PDA nanoparticles (PDA-NPs) for in vivo photothermal ablation of tumors in 2013 (Liu et al., 2013). PDA-NPs are well-evaluated to have advantages such as strong NIR light absorption, high photothermal conversion efficiency as well as remarkable biocompatibility and biodegradability. Moreover, the surface of PDA-NPs remains high reactive activity for further functional modification. Thiol- and amino-terminated molecules, such as hydrophilic PEG and cancer targeting moieties, can be covalently attached onto PDA nano-surface via Michael addition or Schiff base reactions (Park et al., 2014).

So far, PDA-NPs have been extensively utilized as drug delivery systems for combined chemo-photothermal therapy (Ambekar and Kandasubramanian, 2019; Farokhi et al., 2019). Cheng et al. synthesized PEGylated PDA-NPs (PDA-PEG) to encapsulate anticancer drugs such as DOX and SN38 (Wang X. Y. et al., 2016). Remarkable photothermal effect of PDA-PEG was observed upon 808 nm NIR light irradiation along with enhanced drug release. Drug-loaded PDA-PEG was proved to have synergetic effect on cancer cell killing in vitro and tumor suppression in vivo. Then, alendronate (ALN)-anchored and SN38-loaded polydopamine nanoparticles (PDA-ALN/SN38) were prepared by the same group, successfully regressing bone tumor and osteolysis by combined chemo-photothermaltherapy (Wang Y. T. et al., 2018). Lu's group prepared PDA nanocomplex (PDA@CP$_x$, x = 3,6,9) by encapsulating biodegradable coordination polymer (CP) on iron-chelated PDA nanosurface via layer-by-layer method (Chen Y. et al., 2016). DOX loaded PDA@CP$_3$ noncomplex was developed for T1/T2 dual mode MRI together with synergistic chemo-photothermal therapy both in vitro and in vivo, which showed great potential for theranositc nanomedicine.

TABLE 1 | Photothermal conversion efficiency of various nanomaterials applied in chemo-phototermal therapy.

Nanomaterials	Photothermal conversion efficiency (%)	NIR light (nm)	References
Gold nanorods	16.92	808	Manivasagan et al., 2019
Gold Janus nanoparticles	49.5	808	Zhang L. et al., 2016
$Cu_{2-x}Te$ nanocubes	25.68	808	Poulose et al., 2016
Cu_2S nanocrystals	25.3	800	Poulose et al., 2015
$MoS_2/Cu_{1.8}S$ nanosheets	32.5	980	Meng et al., 2017
$MoSe_2$ nanosheets	32.8	808	Wang C. et al., 2016
$MoSe_2/Bi_2Se_3$ nanosheets	59.3	808	Wang Y. et al., 2019
Bamboo charcoal nanoparticles	29.42	808	Dong et al., 2016
Mesoporous carbon nanoparticles	27.4	808	Wang X. et al., 2019
IR780-HSA NPs	10	808	Pei et al., 2019
IR780-CSOSA	33.5	808	Tan et al., 2019
Aza-BODIPY prodrug NPs	38.3	660	Chen et al., 2018
PPy	40	808	Chen X. J. et al., 2017
PEGylated poly-(diketopyrrolopyrrole-thiophene)	76	808	Yao et al., 2017
PBIBDF-BT@NP$_{PPE}$	46.7	808	Li D. D. et al., 2016
PEG grafted poly(cyclopentadithiophene-alt-benz othiadiazole)	30.8	808	Jiang et al., 2017
PDA	40	808	Liu et al., 2013
PDA	33.7	808	Ding et al., 2019

Benefiting from the excellent surface adhesive capability of PDA, core-shell structured nanocomposites consisting of drug-loaded polymeric core and PDA coated shell were developed for combined chemo-photothermal therapy. Xu et al. reported tumor targeting PLGA/PDA core-shell nanocomposites by coating PDA on DOX loaded PLGA nanoparticles, followed by surface PEGylation and anchoring of Anti-EGFR antibody (He et al., 2017). The PDA shell here not only offered reactive sites for surface decoration but also generated hyperthermia under NIR light irradiation for both photothermal therapy and triggering drug release to improve the synergistic chemotherapy. Nie et al. prepared polymer/PDA nanocomposites by coating PDA on nanoparticles formed from a thermo-sensitive block copolymer P(MEO$_2$MA-co-OEGMA-co-DMAEMA)-b-PLGA (Ding et al., 2017). DOX, PTX, and small interfering RNAs were simultaneously loaded within these nanocomposites, generating accurately drug release in response to photothermal effect. These multifunctional nanocomposites integrating photothermal, chemo-, and gene therapy successfully caused regression in triple-negative breast cancer with negligible side effects. Very recently, Dong et al. reported a novel polypeptide nanocomposite PNOC-PDA/DOX by coating PDA on micelles formed by S-nitroso (SNO, a kind of heatsensitive NO donor) conjugated polypeptide copolymer and further loading with DOX (Ding et al., 2019). Upon NIR light irradiation, NO gas was released due to heat-induced S-NO cleavage. The mild hyperthermia together with NO gas therapy were proved to overcome MDR and maximize chemotherapy. The triple chemo-NO-photothermal therapies completely eradicated MCF-7/ADR tumors without skin damage, scarring, and tumor recurrence within 30 days, indicating excellent synergistic effects for reversing MDR in tumors.

Carrier-free nanoparticles with high drug loading and on-demand drug release have attracted increasing attention. Liu and coworkers introduced a novel carrier-free "nanobomb" with drug loading efficiency as high as 85.8% (Li M. H. et al., 2018). The "nanobomb" was prepared by two simple steps: the first is making DOX nano-precipitates (DNPs) of ca. 5 nm, and the second is surface deposition of PDA which further induced secondary aggregation of small DNPs to form nanodrugs with an average size of around 70 nm (**Figure 7**). When exposed to NIR laser, the PDA shell generated enough heat to produce CO_2 and NH_3 gases from the encapsulated NH_4HCO_3. PDA film outside the DNPs was thus broken up to facilitate *in situ* release of DOX for enhanced chemotherapy. The synergistic photothermal and chemotherapy of the NIR responsive "nanobomb" achieved excellent anticancer activity both *in vitro* and *in vivo*. Recently, Dong's group synthesized high drug-loading PDA-chlorambucil conjugate nanoparticles by direct polymerizing dopamine with a novel pH and reduction-responsive dopamine-chloroambucil prodrug (Du et al., 2019). The PDA-chlorambucil prodrug nanoparticles exhibited triple pH/reduction/NIR light responsive drug release profile *in vitro* and achieved traceless and complete ablation of MCF-7 tumors without recurrence within 50 days by combined chemotherapy and mild hyperthermia.

CONCLUSION AND OUTLOOK

In this review, we summarized recent advances in NIR light responsive nanomaterials for combined chemo-photothermal cancer therapy. Metal-, carbon-based and organic nanomaterials were included to discuss their design, preparation and application in combined therapy for improving cancer treatment. The combined chemo-photothermal therapy has

been widely evaluated to show synergistic anticancer effect in a "1+1>2" manner. On the one hand, hyperthermia induced by photothermal agents upon specific NIR laser irradiation in the tumor region can not only kill cancer cells directly, but also serve as heat trigger to stimulate drug release in a controlled manner and facilitate cell membrane permeability to enhance drug uptake. On the other hand, optimized chemotherapy by systematic administration of anticancer drugs can help to completely eradicate tumors together with photothermal therapy. The combined chemo-photothermal therapy has also shown excellent performance in overcoming MDR and lung metastasis.

In spite of the rapid development and promising potential of nanomaterials for chemo-photothermal therapy, there still exist several critical issues that need to be addressed. Firstly, the photothermal conversion efficiency, which will significantly influence the dosage of photothermal agents and NIR light intensity/irradiation time for efficient heat generation, differs among various nanomaterials concerned in this review. Photothermal conversion efficiencies of several kinds of nanomaterials are summarized in **Table 1**. More efforts are needed to be put into the creation of novel nanomaterials with favorable photothermal conversion efficiency in order to achieve satisfactory photothermal outcome and reduce the administration dose of nanomaterials. Secondly, though NIR laser can reach deeper tumor tissues, the penetrated depth is still limited. Therefore, the non-invasive photothermal therapy seems mostly feasible for superficial tumors. For internal organ tumors, efficient photothermal therapy can be conducted with minimal intervention by the development of novel invasive medical devices. Thirdly, long-term cytotoxicity of these nanomaterials, especially those with poor biodegradability such as carbon-based nanomaterials, remains uncertain and deserves more attention in future studies. In this regard, organic photothermal agents-based nanomaterials exhibit better performance in biodegradability and biocompatibility. For example, nano-formulations containing FDA-approved ICG are very promising for future clinical utilization. Another concern of cytotoxicity comes from the loaded chemotherapeutic drugs. Though excellent anticancer efficacy can be obtained in a lower dosage with the assistance of hyperthermia, the systematic distribution may still induce undesired side effects. Covalently conjugated prodrugs can significantly decrease premature release of drugs during blood circulation before linker cleavage under

tumor physiological environment. Surface tailoring through conjugation of targeting moieties on nanomaterials can further enhance tumor accumulation via specific nano-cell interactions, consequently enhancing anticancer efficacy, and reducing side effects. Lastly, the mechanism of synergistic effect for combined chemo-photothermal therapy needs deeper investigation in the future. Hyperthermia has been reported to increase vascular permeability within tumor tissues, thus promoting drug enrichment and enhancing therapeutic outcome of chemotherapy. Multidrug resistance is one of the major obstacles against efficient cancer treatment by single chemotherapy. Photothermal therapy has been proved to significantly reduce drug efflux by inhibiting P-glycoprotein expression with augmentation of drug sensitivity to cancer cells. Nevertheless, molecular mechanisms beneath chemo-photothermal therapy, involving multiple signaling pathways in cancer cells, are still rarely to be explored. Certainly, studies on tumor biology will help us to have better understanding about intrinsic mechanism for drug resistance, facilitating the design of novel nanomaterials for precise and efficient cancer treatments.

Regardless of the existing challenges, chemo-photothermal combination therapy has shown promising results in many experiments. With the rapid development of nanoscience, material chemistry, and tumor biology, we believe that successful clinical applications of nanomaterials for chemo-photothermal cancer treatment can be expected in the future.

AUTHOR CONTRIBUTIONS

LL conceived and coordinated this project. ZL and YC wrote this paper. YYa and YYu collected and summarized literatures. YZhan, DZ, and XY edited pictures in this paper. XO, ZX, and YZhao revised this paper.

FUNDING

REFERENCES

Ai, X. Z., Mu, J., and Xing, B. G. (2016). Recent advances of light-mediated theranostics. *Theranostics* 6, 2439–2457. doi: 10.7150/thno.16088

Ambekar, R. S., and Kandasubramanian, B. (2019). A polydopamine-based platform for anti-cancer drug delivery. *Biomater. Sci.* 7, 1776–1793. doi: 10.1039/C8BM01642A

Ardekani, S. M., Dehghani, A., Hassan, M., Kianinia, M., Aharonovich, I., and Gomes, V. G. (2017). Two-photon excitation triggers combined chemo-photothermal therapy via doped carbon nanohybrid dots for effective breast cancer treatment. *Chem. Eng. J.* 330, 651–662. doi: 10.1016/j.cej.2017.07.165

Baker, S. N., and Baker, G. A. (2010). Luminescent carbon nanodots: emergent nanolights. *Angew. Chem. Int. Ed.* 49, 6726–6744. doi: 10.1002/anie.200906623

Balogh, L., Nigavekar, S. S., Nair, B. M., Lesniak, W., Zhang, C., Sung, L. Y., et al. (2007). Significant effect of size on the *in vivo* biodistribution of gold composite nanodevices in mouse tumor models. *Nanomed Nanotechnol.* 3, 281–296. doi: 10.1016/j.nano.2007.09.001

Bao, H., Pan, Y., Ping, Y., Sahoo, N., Wu, T., Li, L., et al. (2011). Chitosan-functionalized graphene oxide as a nanocarrier for drug and gene delivery. *Small* 7, 1569–1578. doi: 10.1002/smll.201100191

Cai, Y., Si, W., Huang, W., Chen, P., Shao, J., and Dong, X. (2018). Organic dye based nanoparticles for cancer phototheranostics. *Small* 14:1704247. doi: 10.1002/smll.201704247

Cao, Y., Wu, Y. N., Wang, G. N., Yi, J. W., Yu, C. L., Huang, Y. X. et al. (2017a). Near-infrared conjugated polymers for photoacoustic imaging-guided photothermal/chemo combination therapy. *J. Mater. Chem. B* 5, 5479–5487. doi: 10.1039/C7TB01264K

Cao, Y., Yi, J., Yang, X., Liu, L., Yu, C., Huang, Y. et al. (2017b). Efficient cancer regression by a thermosensitive liposome for photoacoustic imaging-guided photothermal/chemo combinatorial therapy. *Biomacromolecules* 18, 2306–2314. doi: 10.1021/acs.biomac.7b00464

Chen, D., Tang, Q., Zou, J., Yang, X., Huang, W., Zhang, Q., et al. (2018). pH-responsive PEG-doxorubicin-encapsulated aza-BODIPY nanotheranostic agent for imaging-guided synergistic cancer therapy. *Adv. Funct. Mater.* 7:1701272. doi: 10.1002/adhm.201701272

Chen, L., Feng, W., Zhou, X. J., Qiu, K. X., Miao, Y. K., Zhang, Q. Q. et al. (2016). Facile synthesis of novel albumin-functionalized flower-like MoS$_2$ nanoparticles for *in vitro* chemo-photothermal synergistic therapy. *RSC Adv.* 6, 13040–13049. doi: 10.1039/C5RA27822H

Chen, Q., Liang, C., Wang, C., and Liu, Z. (2015). An imagable and photothermal "Abraxane-like" nanodrug for combination cancer therapy to treat subcutaneous and metastatic breast tumors. *Adv. Mater.* 27, 903–910. doi: 10.1002/adma.201404308

Chen, X. J., Zhang, M. J., Li, S. N., Li, L., Zhang, L. Y., Wang, T. T. et al. (2017). Facile synthesis of polypyrrole@metal-organic framework core-shell nanocomposites for dual-mode imaging and synergistic chemo-photothermal therapy of cancer cells. *J. Mater. Chem. B* 5, 1772–1778. doi: 10.1039/C6TB03218D

Chen, Y., Ai, K., Liu, J., Ren, X., Jiang, C., and Lu, L. (2016). Polydopamine-based coordination nanocomplex for T1/T2 dual mode magnetic resonance imaging-guided chemo-photothermal synergistic therapy. *Biomaterials* 77, 198–206. doi: 10.1016/j.biomaterials.2015.11.010

Chen, Y., Li, H., Deng, Y., Sun, H., Ke, X., and Ci, T. (2017). Near-infrared light triggered drug delivery system for higher efficacy of combined chemo-photothermal treatment. *Acta Biomater.* 51, 374–392. doi: 10.1016/j.actbio.2016.12.004

Chen, Y., Li, Z., Wang, H., Wang, Y., Han, H., Jin, Q. et al. (2016). IR-780 loaded phospholipid mimicking homopolymeric micelles for near-IR imaging and photothermal therapy of pancreatic cancer. *ACS Appl. Mater. Inter.* 8, 6852–6858. doi: 10.1021/acsami.6b00251

Chhowalla, M., Shin, H. S., Eda, G., Li, L. J., Loh, K. P., and Zhang, H. (2013). The chemistry of two-dimensional layered transition metal dichalcogenide nanosheets. *Nat. Chem.* 5, 263–275. doi: 10.1038/nchem.1589

Cobley, C. M., Au, L., Chen, J., and Xia, Y. (2010). Targeting gold nanocages to cancer cells for photothermal destruction and drug delivery. *Expert Opin. Drug Deliv.* 7, 577–587. doi: 10.1517/17425240903571614

Cobley, C. M., Chen, J. Y., Cho, E. C., Wang, L. V., and Xia, Y. N. (2011). Gold nanostructures: a class of multifunctional materials for biomedical applications. *Chem. Soc. Rev.* 40, 44–56. doi: 10.1039/B821763G

Delplace, V., Couvreur, P., and Nicolas, J. (2014). Recent trends in the design of anticancer polymer prodrug nanocarriers. *Polym. Chem.* 5, 1529–1544. doi: 10.1039/C3PY01384G

Deng, Y. Y., Käfer, F., Chen, T. T., Jin, Q., Ji, J., and Agarwal, S. (2018). Let there be light: polymeric micelles with upper critical solution temperature as light-triggered heat nanogenerators for combating drug-resistant cancer. *Small* 14:1802420. doi: 10.1002/smll.201802420

DeSantis, C. E., Lin, C. C., Mariotto, A. B., Siegel, R. L., Stein, K. D., Kramer, J. L., et al. (2014). Cancer treatment and survivorship statistics, 2014. *CA Cancer J. Clin.* 64, 252–271. doi: 10.3322/caac.21235

Ding, Y., Du, C., Qian, J., and Dong, C.-M. (2019). NIR-responsive polypeptide aanocomposite generates NO gas, mild photothermia, and chemotherapy to reverse multidrug-resistant cancer. *Nano Lett.* 19, 4362–4370. doi: 10.1021/acs.nanolett.9b00975

Ding, Y., Su, S. S., Zhang, R., Shao, L., Zhang, Y., Wang, B. et al. (2017). Precision combination therapy for triple negative breast cancer via biomimetic polydopamine polymer core-shell nanostructures. *Biomaterials* 113, 243–252. doi: 10.1016/j.biomaterials.2016.10.053

Dong, X., Yin, W., Yu, J., Dou, R., Bao, T., Zhang, X., et al. (2016). Mesoporous bamboo charcoal nanoparticles as a new near-infrared responsive drug carrier for imaging-guided chemotherapy/photothermal synergistic therapy of tumor. *Adv. Healthc. Mater.* 5, 1627–1637. doi: 10.1002/adhm.201600287

Dreaden, E. C., Alkilany, A. M., Huang, X. H., Murphy, C. J., and El-Sayed, M. A. (2012). The golden age: gold nanoparticles for biomedicine. *Chem. Soc. Rev.* 41, 2740–2779. doi: 10.1039/C1CS15237H

Du, C., Ding, Y., Qian, J., Zhang, R., and Dong, C.-M. (2019). Achieving traceless ablation of solid tumors without recurrence by mild photothermal-chemotherapy of triple stimuli-responsive polymer-drug conjugate nanoparticles. *J. Mater. Chem. B* 7, 415–432. doi: 10.1039/C8TB02432D

Duncan, R. (2006). Polymer conjugates as anticancer nanomedicines. *Nat. Rev. Cancer* 6, 688–701. doi: 10.1038/nrc1958

Dykman, L., and Khlebtsov, N. (2012). Gold nanoparticles in biomedical applications: recent advances and perspectives. *Chem. Soc. Rev.* 41, 2256–2282. doi: 10.1039/C1CS15166E

Ernsting, M. J., Murakami, M., Roy, A., and Li, S. D. (2013). Factors controlling the pharmacokinetics, biodistribution and intratumoral penetration of nanoparticles. *J. Control. Release* 172, 782–794. doi: 10.1016/j.jconrel.2013.09.013

Falk, M. H., and Issels, R. D. (2001). Hyperthermia in oncology. *Int. J. Hyperthermia* 17, 1–18. doi: 10.1080/02656730150201552

Fang, W. J., Tang, S. H., Liu, P. X., Fang, X. L., Gong, J. W., and Zheng, N. F. (2012a). Pd nanosheet-covered hollow mesoporous silica nanoparticles as a platform for the chemo-photothermal treatment of cancer cells. *Small* 8, 3816–3822. doi: 10.1002/smll.201200962

Fang, W. J., Yang, J., Gong, J. W., and Zheng, N. F. (2012b). Photo- and pH-triggered release of anticancer drugs from mesoporous silica-coated Pd@Ag nanoparticles. *Adv. Funct. Mater.* 22, 842–848. doi: 10.1002/adfm.201101960

Fang, Y., Gu, D., Zou, Y., Wu, Z., Li, F., Che, R. et al. (2010). A low-concentration hydrothermal synthesis of biocompatible ordered mesoporous carbon nanospheres with tunable and uniform size. *Angew. Chem. Int. Ed.* 49, 7987–7991. doi: 10.1002/anie.201002849

Farokhi, M., Mottaghitalab, F., Saeb, M. R., and Thomas, S. (2019). Functionalized theranostic nanocarriers with bio-inspired polydopamine for tumor imaging and chemo-photothermal therapy. *J. Control. Release* 309, 203–219. doi: 10.1016/j.jconrel.2019.07.036

Feng, L. Z., Gao, M., Tao, D. L., Chen, Q., Wang, H. R., Dong, Z. L. et al. (2016). Cisplatin-prodrug-constructed liposomes as a versatile theranostic nanoplatform for bimodal imaging guided combination cancer therapy. *Adv. Funct. Mater.* 26, 2207–2217. doi: 10.1002/adfm.201504899

Feng, L., and Liu, Z. (2011). Graphene in biomedicine: opportunities and challenges. *Nanomedicine* 6, 317–324. doi: 10.2217/nnm.10.158

Feng, Y., Cheng, Y., Chang, Y., Jian, H., Zheng, R., Wu, X. et al. (2019). Time-staggered delivery of erlotinib and doxorubicin by gold nanocages with two smart polymers for reprogrammable release and synergistic with photothermal therapy. *Biomaterials* 217:119327. doi: 10.1016/j.biomaterials.2019.119327

Gao, C., Liang, X., Mo, S., Zhang, N., Sun, D., and Dai, Z. (2018). Near-infrared cyanine-loaded liposome-like nanocapsules of camptothecin floxuridine conjugate for enhanced chemophotothermal combination cancer therapy. *ACS Appl. Mater. Inter.* 10, 3219–3228. doi: 10.1021/acsami.7b14125

Gao, G., Jiang, Y. W., Sun, W., Guo, Y., Jia, H. R., Yu, X. W. et al. (2019). Molecular targeting-mediated mild-temperature photothermal therapy with a smart albumin-based nanodrug. *Small* 15:e1900501. doi: 10.1002/smll.201900501

Glenn, P. G., LiLi, B., Kelly, L. G. S., Krystina, L. S., James, C. W., and Payne, J. D. (2010). Photothermal therapy in a murine colon cancer model using near-infrared absorbing gold nanorods. *J. Biomed. Opt.* 15:018001. doi: 10.1117/1.3290817

Gong, H., Cheng, L., Xiang, J., Xu, H., Feng, L. Z., Shi, X. Z. et al. (2013). Near-infrared absorbing polymeric nanoparticles as a versatile drug carrier for cancer combination therapy. *Adv. Funct. Mater.* 23, 6059–6067. doi: 10.1002/adfm.201301555

Hahn, G. M., Braun, J., and Harkedar, I. (1975). Thermochemotherapy-synergism between hyperthermia (42-43 degrees) and adriamycin (or bleomycin) in mammalian-cell inactivation. *Proc. Natl. Acad. Sci. U.S.A.* 72, 937–940. doi: 10.1073/pnas.72.3.937

Hauck, T. S., Jennings, T. L., Yatsenko, T., Kumaradas, J. C., and Chan, W. C. W. (2008). Enhancing the toxicity of cancer chemotherapeutics with gold nanorod hyperthermia. *Adv. Mater.* 20, 3832–3838. doi: 10.1002/adma.200800921

He, H., Markoutsa, E., Zhan, Y., Zhang, J., and Xu, P. (2017). Mussel-inspired PLGA/polydopamine core-shell nanoparticle for light

induced cancer thermochemotherapy. *Acta Biomater.* 59, 181–191. doi: 10.1016/j.actbio.2017.07.005

He, H. Z., Zhou, J. L., Liu, Y. J., Liu, S., Xie, Z. G., Yu, M. et al. (2018). Near-infrared-light-induced morphology transition of poly(ether amine) nanoparticles for supersensitive drug release. *ACS Appl. Mater. Inter.* 10, 7413–7421. doi: 10.1021/acsami.8b00194

He, Y. L., Cao, Y. Y., and Wang, Y. P. (2018). Progress on photothermal conversion in the second NIR window based on conjugated polymers. *Asian J. Org. Chem.* 7, 2201–2212. doi: 10.1002/ajoc.201800450

Hessel, C. M., Pattani, V. P., Rasch, M., Panthani, M. G., Koo, B., Tunnell, J. W. et al. (2011). Copper selenide nanocrystals for photothermal therapy. *Nano Lett.* 11, 2560–2566. doi: 10.1021/nl201400z

Holohan, C., Van Schaeybroeck, S., Longley, D. B., and Johnston, P. G. (2013). Cancer drug resistance: an evolving paradigm. *Nat. Rev. Cancer* 13, 714–726. doi: 10.1038/nrc3599

Hu, M., Chen, J. Y., Li, Z. Y., Au, L., Hartland, G. V., Li, X. D. et al. (2006). Gold nanostructures: engineering their plasmonic properties for biomedical applications. *Chem. Soc. Rev.* 35, 1084–1094. doi: 10.1039/b517615h

Huang, X., Tang, S. H., Mu, X., Dai, Y., Chen, G., Zhou, Z., et al. (2011). Freestanding palladium nanosheets with plasmonic and catalytic properties. *Nat. Nanotechnol.* 6, 28–32. doi: 10.1038/nnano.2010.235

Iijima, S. (1991). Helical microtubules of graphitic carbon. *Nature* 354, 56–58. doi: 10.1038/354056a0

Jain, R. K., and Stylianopoulos, T. (2010). Delivering nanomedicine to solid tumors. *Nat. Rev. Clin. Oncol.* 7, 653–664. doi: 10.1038/nrclinonc.2010.139

Jiang, Y., Cui, D., Fang, Y., Zhen, X., Upputuri, P. K., Pramanik, M. et al. (2017). Amphiphilic semiconducting polymer as multifunctional nanocarrier for fluorescence/photoacoustic imaging guided chemo-photothermal therapy. *Biomaterials* 145, 168–177. doi: 10.1016/j.biomaterials.2017.08.037

Jung, H. S., Verwilst, P., Sharma, A., Shin, J., Sessler, J. L., and Kim, J. S. (2018). Organic molecule-based photothermal agents: an expanding photothermal therapy universe. *Chem. Soc. Rev.* 47, 2280–2297. doi: 10.1039/C7CS00522A

Karavasili, C., Amanatiadou, E. P., Sygellou, L., Giasafaki, D. K., Steriotis, T. A., Charalambopoulou, G. C., et al. (2013). Development of new drug delivery system based on ordered mesoporous carbons: characterisation and cytocompatibility studies. *J. Mater. Chem. B* 1, 3167–3174. doi: 10.1039/c3tb20304b

Khafaji, M., Zamani, M., Golizadeh, M., and Bavi, O. (2019). Inorganic nanomaterials for chemo/photothermal therapy: a promising horizon on effective cancer treatment. *Biophys. Rev.* 11, 335–352. doi: 10.1007/s12551-019-00532-3

Khlebtsov, N., and Dykman, L. (2011). Biodistribution and toxicity of engineered gold nanoparticles: a review of *in vitro* and *in vivo* studies. *Chem. Soc. Rev.* 40, 1647–1671. doi: 10.1039/C0CS00018C

Kiew, S. F., Kiew, L. V., Lee, H. B., Imae, T., and Chung, L. Y. (2016). Assessing biocompatibility of graphene oxide-based nanocarriers: a review. *J. Control. Release* 226, 217–228. doi: 10.1016/j.jconrel.2016.02.015

Kim, H., Chung, K., Lee, S., Kim, D. H., and Lee, H. (2016). Near-infrared light-responsive nanomaterials for cancer theranostics. *Wiley Interdiscip. Rev. Nanomed. Nanobiotechnol.* 8, 23–45. doi: 10.1002/wnan.1347

Kratz, F., and Warnecke, A. (2012). Finding the optimal balance: challenges of improving conventional cancer chemotherapy using suitable combinations with nano-sized drug delivery systems. *J. Control. Release* 164, 221–235. doi: 10.1016/j.jconrel.2012.05.045

Kroto, H. W., Heath, J. R., Obrien, S. C., Curl, R. F., and Smalley, R. E. (1985). C-60 - Buckminsterfullerene. *Nature* 318, 162–163. doi: 10.1038/318162a0

Larson, N., and Ghandehari, H. (2012). Polymeric conjugates for drug delivery. *Chem. Mater.* 24, 840–853. doi: 10.1021/cm2031569

Lee, H., Dellatore, S. M., Miller, W. M., and Messersmith, P. B. (2007). Mussel-inspired surface chemistry for multifunctional coatings. *Science* 318, 426–430. doi: 10.1126/science.1147241

Lee, J., Kim, J., and Kim, W. J. (2016). Photothermally controllable cytosolic drug delivery based on core-shell MoS$_2$-porous silica nanoplates. *Chem. Mater.* 28, 6417–6424. doi: 10.1021/acs.chemmater.6b02944

Lee, S. M., Park, H., and Yoo, K. H. (2010). Synergistic cancer therapeutic effects of locally delivered drug and heat using multifunctional nanoparticles. *Adv. Mater.* 22, 4049–4053. doi: 10.1002/adma.201001040

Li, D. D., Wang, J. X., Ma, Y., Qian, H. S., Wang, D., Wang, L., et al. (2016). A donor-acceptor conjugated polymer with alternating isoindigo derivative and bithiophene units for near-infrared modulated cancer thermo-chemotherapy. *ACS Appl. Mater. Inter.* 8, 19312–19320.

Li, J. C., Rao, J. H., and Pu, K. Y. (2018). Recent progress on semiconducting polymer nanoparticles for molecular imaging and cancer phototherapy. *Biomaterials* 155, 217–235. doi: 10.1016/j.biomaterials.2017.11.025

Li, M., Li, L., Zhan, C., and Kohane, D. S. (2016). Core-shell nanostars for multimodal therapy and imaging. *Theranostics* 6, 2306–2313. doi: 10.7150/thno.15843

Li, M., Sun, X., Zhang, N., Wang, W., Yang, Y., Jia, H., et al. (2018). NIR-activated polydopamine-coated carrier-free "nanobomb" for *in situ* on-demand drug release. *Adv. Sci.* 5:1800155. doi: 10.1002/advs.201800155

Li, M. H., Teh, C., Ang, C. Y., Tan, S. Y., Luo, Z., Qu, Q. Y., et al. (2015). Near-infrared light-absorptive stealth liposomes for localized photothermal ablation of tumors combined with chemotherapy. *Adv. Funct. Mater.* 25, 5602–5610. doi: 10.1002/adfm.201502469

Li, Q. Y., Zu, Y. G., Shi, R. Z., and Yao, L. P. (2006). Review camptothecin: current perspectives. *Curr. Med. Chem.* 13, 2021–2039. doi: 10.2174/092986706777585004

Li, X., Zhao, X., Pardhi, D., Wu, Q., Zheng, Y., Zhu, H., et al. (2018). Folic acid modified cell membrane capsules encapsulating doxorubicin and indocyanine green for highly effective combinational therapy *in vivo*. *Acta Biomater.* 74, 374–384. doi: 10.1016/j.actbio.2018.05.006

Li, Z. H., Wang, H. B., Chen, Y. J., Wang, Y., Li, H., Han, H. J., et al. (2016). pH- and NIR light-responsive polymeric prodrug micelles for hyperthermia-assisted site-specific chemotherapy to reverse drug resistance in cancer treatment. *Small* 12, 2731–2740. doi: 10.1002/smll.201600365

Lie, S. Q., Wang, D. M., Gao, M. X., and Huang, C. Z. (2014). Controllable copper deficiency in Cu$_{2-x}$Se nanocrystals with tunable localized surface plasmon resonance and enhanced chemiluminescence. *Nanoscale* 6, 10289–10296. doi: 10.1039/C4NR02294G

Lim, D. J., Sim, M., Oh, L., Lim, K., and Park, H. (2014). Carbon-based drug delivery carriers for cancer therapy. *Arch. Pharm. Res.* 37, 43–52. doi: 10.1007/s12272-013-0277-1

Lin, C. Y., and Shieh, M. J. (2018). Near-infrared fluorescent dye-decorated nanocages to form grenade-like nanoparticles with dual control release for photothermal theranostics and chemotherapy. *Bioconjug. Chem.* 29, 1384–1398. doi: 10.1021/acs.bioconjchem.8b00088

Liu, H. Y., Chen, D., Li, L. L., Liu, T. L., Tan, L. F., Wu, X. L., et al. (2011). Multifunctional gold nanoshells on silica nanorattles: a platform for the combination of photothermal therapy and chemotherapy with low systemic toxicity. *Angew. Chem. Int. Ed.* 50, 891–895. doi: 10.1002/anie.201002820

Liu, X. J., Wang, Q., Li, C., Zou, R. J., Li, B., Song, G. S., et al. (2014). Cu$_{2-x}$Se@mSiO$_2$-PEG core-shell nanoparticles: a low-toxic and efficient difunctional nanoplatform for chemo-photothermal therapy under near infrared light radiation with a safe power density. *Nanoscale* 6, 4361–4370. doi: 10.1039/C3NR06160D

Liu, Y. L., Ai, K. L., Liu, J. H., Deng, M., He, Y. Y., and Lu, L. H. (2013). Dopamine-melanin colloidal nanospheres: an efficient near-infrared photothermal therapeutic agent for *in vivo* cancer therapy. *Adv. Mater.* 25, 1353–1359. doi: 10.1002/adma.201204683

Llevot, A., and Astruc, D. (2012). Applications of vectorized gold nanoparticles to the diagnosis and therapy of cancer. *Chem. Soc. Rev.* 41, 242–257. doi: 10.1039/C1CS15080D

Luo, D., Carter, K. A., Miranda, D., and Lovell, J. F. (2017). Chemophototherapy: an emerging treatment option for solid tumors. *Adv. Sci.* 4:1600106. doi: 10.1002/advs.201600106

MacNeill, C. M., Coffin, R. C., Carroll, D. L., and Levi-Polyachenko, N. H. (2013). Low band gap donor-acceptor conjugated polymer nanoparticles and their NIR-mediated thermal ablation of cancer cells. *Macromol. Biosci.* 13, 28–34. doi: 10.1002/mabi.201200241

Mahmoudi, M., Sant, S., Wang, B., Laurent, S., and Sen, T. (2011). Superparamagnetic iron oxide nanoparticles (SPIONs): development, surface modification and applications in chemotherapy. *Adv. Drug Deliv. Rev.* 63, 24–46. doi: 10.1016/j.addr.2010.05.006

Mallory, M., Gogineni, E., Jones, G. C., Greer, L., and Simone, C. B. II. (2016). Therapeutic hyperthermia: the old, the new, and the upcoming. *Crit. Rev. Oncol. Hematol.* 97, 56–64. doi: 10.1016/j.critrevonc.2015.08.003

Manivasagan, P., Jun, S. W., Nguyen, V. T., Truong, N. T. P., Hoang, G., Mondal, S., et al. (2019). A multifunctional near-infrared laser-triggered drug delivery system using folic acid conjugated chitosan oligosaccharide encapsulated gold nanorods for targeted chemo-photothermal therapy. *J. Mater. Chem. B* 7, 3811–3825. doi: 10.1039/C8TB02823K

Meng, X. D., Liu, Z. Q., Cao, Y., Dai, W. H., Zhang, K., Dong, H. F., et al. (2017). Fabricating aptamer-conjugated PEGylated-MoS$_2$/Cu$_{1.8}$S theranostic nanoplatform for multiplexed imaging diagnosis and chemo-photothermal therapy of cancer. *Adv. Funct. Mater.* 27:1605592. doi: 10.1002/adfm.201605592

Mu, W., Jiang, D., Mu, S., Liang, S., Liu, Y., and Zhang, N. (2019). Promoting early diagnosis and precise therapy of hepatocellular carcinoma by glypican-3-targeted synergistic chemo-photothermal theranostics. *ACS Appl. Mater. Inter.* 11, 23591–23604. doi: 10.1021/acsami.9b05526

Nguyen, H. T., Phung, C. D., Thapa, R. K., Pham, T. T., Tran, T. H., Jeong, J. H., et al. (2018). Multifunctional nanoparticles as somatostatin receptor-targeting delivery system of polyaniline and methotrexate for combined chemo-photothermal therapy. *Acta Biomater.* 68, 154–167. doi: 10.1016/j.actbio.2017.12.033

Niwase, K., Tanaka, T., Kakimoto, Y., Ishihara, K. N., and Shingu, P. H. (1995). Raman-spectra of graphite and diamond mechanically milled with agate or stainless-steel ball-mill. *Mater. Trans. JIM* 36, 282–288. doi: 10.2320/matertrans1989.36.282

Novoselov, K. S., Geim, A. K., Morozov, S. V., Jiang, D., Zhang, Y., Dubonos, S. V., et al. (2004). Electric field effect in atomically thin carbon films. *Science* 306, 666–669. doi: 10.1126/science.1102896

Opletal, G., Grochola, G., Chui, Y. H., Snook, I. K., and Russo, S. P. (2011). Stability and transformations of heated gold nanorods. *J. Phys. Chem. C* 115, 4375–4380. doi: 10.1021/jp1074913

Orecchioni, M., Cabizza, R., Bianco, A., and Delogu, L. G. (2015). Graphene as cancer theranostic tool: progress and future challenges. *Theranostics* 5, 710–723. doi: 10.7150/thno.11387

Overgaard, J. (1976). Combined adriamycin and hyperthermia treatment of a murine mammary-carcinoma *in vivo. Cancer Res.* 36, 3077–3081.

Pan, Y. Z., Bao, H. Q., Sahoo, N. G., Wu, T. F., and Li, L. (2011). Water-soluble poly(N-isopropylacrylamide)-graphene sheets synthesized via click chemistry for drug delivery. *Adv. Funct. Mater.* 21, 2754–2763. doi: 10.1002/adfm.201100078

Park, H., Yang, J., Lee, J., Haam, S., Choi, I. H., and Yoo, K. H. (2009). Multifunctional nanoparticles for combined doxorubicin and photothermal treatments. *ACS Nano* 3, 2919–2926. doi: 10.1021/nn900215k

Park, J., Brust, T. F., Lee, H. J., Lee, S. C., Watts, V. J., and Yeo, Y. (2014). Polydopamine-based simple and versatile surface modification of polymeric nano drug carriers. *ACS Nano* 8, 3347–3356. doi: 10.1021/nn405809c

Pei, Q., Hu, X., Zheng, X., Xia, R., Liu, S., Xie, Z., et al. (2019). Albumin-bound paclitaxel dimeric prodrug nanoparticles with tumor redox heterogeneity-triggered drug release for synergistic photothermal/chemotherapy. *Nano Res.* 12, 877–887. doi: 10.1007/s12274-019-2318-7

Peng, C. L., Shih, Y. H., Lee, P. C., Hsieh, T. M., Luo, T. Y., and Shieh, M. J. (2011). Multimodal image-guided photothermal therapy mediated by [188]Re-labeled micelles containing a cyanine-type photosensitizer. *ACS Nano* 5, 5594–5607. doi: 10.1021/nn201100m

Pierini, F., Nakielski, P., Urbanek, O., Pawlowska, S., Lanzi, M., De Sio, L., et al. (2018). Polymer-based nanomaterials for photothermal therapy: from light-responsive to multifunctional nanoplatforms for synergistically combined technologies. *Biomacromolecules* 19, 4147–4167. doi: 10.1021/acs.biomac.8b01138

Porcu, E. P., Salis, A., Gavini, E., Rassu, G., Maestri, M., and Giunchedi, P. (2016). Indocyanine green delivery systems for tumour detection and treatments. *Biotechnol. Adv.* 34, 768–789. doi: 10.1016/j.biotechadv.2016.04.001

Poulose, A. C., Veeranarayanan, S., Mohamed, M. S., Aburto, R. R., Mitcham, T., Bouchard, R. R., et al. (2016). Multifunctional Cu$_{2-x}$Te nanocubes mediated combination therapy for multi-drug resistant MDA MB 453. *Sci. Rep.* 6:35961. doi: 10.1038/srep35961

Poulose, A. C., Veeranarayanan, S., Mohamed, M. S., Nagaoka, Y., Aburto, R. R., Mitcham, T., et al. (2015). Multi-stimuli responsive Cu$_2$S nanocrystals

as trimodal imaging and synergistic chemo-photothermal therapy agents. *Nanoscale* 7, 8378–8388. doi: 10.1039/C4NR07139E

Qian, C. G., Chen, Y. L., Feng, P. J., Xiao, X. Z., Dong, M., Yu, J. C., et al. (2017). Conjugated polymer nanomaterials for theranostics. *Acta Pharmacol. Sin.* 38, 764–781. doi: 10.1038/aps.2017.42

Rahman, M., Akhter, S., Ahmad, M. Z., Ahmad, J., Addo, R. T., Ahmad, F. J., et al. (2015). Emerging advances in cancer nanotheranostics with graphene nanocomposites: opportunities and challenges. *Nanomedicine* 10, 2405–2422. doi: 10.2217/nnm.15.68

Ren, F., Bhana, S., Norman, D. D., Johnson, J., Xu, L. J., Baker, D. L., et al. (2013). Gold nanorods carrying paclitaxel for photothermal-chemotherapy of cancer. *Bioconjug. Chem.* 24, 376–386. doi: 10.1021/bc300442d

Robinson, J. T., Tabakman, S. M., Liang, Y. Y., Wang, H. L., Casalongue, H. S., Vinh, D., et al. (2011). Ultrasmall reduced graphene oxide with high near-infrared absorbance for photothermal therapy. *J. Am. Chem. Soc.* 133, 6825–6831. doi: 10.1021/ja2010175

Saha, K., Agasti, S. S., Kim, C., Li, X. N., and Rotello, V. M. (2012). Gold nanoparticles in chemical and biological sensing. *Chem. Rev.* 112, 2739–2779. doi: 10.1021/cr2001178

Shen, S., Tang, H. Y., Zhang, X. T., Ren, J. F., Pang, Z. Q., Wang, D. G., et al. (2013). Targeting mesoporous silica-encapsulated gold nanorods for chemo-photothermal therapy with near-infrared radiation. *Biomaterials* 34, 3150–3158. doi: 10.1016/j.biomaterials.2013.01.051

Sheng, Z. H., Hu, D. H., Xue, M. M., He, M., Gong, P., and Cai, L. T. (2013). Indocyanine green nanoparticles for theranostic applications. *Nanomicro Lett.* 5, 145–150. doi: 10.1007/BF03353743

Shi, P., Qu, K. G., Wang, J. S., Li, M., Ren, J. S., and Qu, X. G. (2012). pH-responsive NIR enhanced drug release from gold nanocages possesses high potency against cancer cells. *Chem. Commun.* 48, 7640–7642. doi: 10.1039/c2cc33543c

Shi, Y. G., Liu, M. Y., Deng, F. J., Zeng, G. J., Wan, Q., Zhang, X. Y., et al. (2017). Recent progress and development on polymeric nanomaterials for photothermal therapy: a brief overview. *J. Mater. Chem. B* 5, 194–206. doi: 10.1039/C6TB02249A

Song, X. J., Chen, Q., and Liu, Z. (2015). Recent advances in the development of organic photothermal nano-agents. *Nano Res.* 8, 340–354. doi: 10.1007/s12274-014-0620-y

Su, S. S., Tian, Y. H., Li, Y. Y., Ding, Y. P., Ji, T. J., Wu, M. Y., et al. (2015). "Triple-punch" strategy for triple negative breast cancer therapy with minimized drug dosage and improved antitumor efficacy. *ACS Nano* 9, 1367–1378. doi: 10.1021/nn505729m

Sun, H., Lv, F., Liu, L., Gu, Q., and Wang, S. (2018). Conjugated polymer materials for photothermal therapy. *Adv. Ther.* 1:1800057. doi: 10.1002/adtp.201800057

Sun, X. Q., Wang, C., Gao, M., Hu, A. Y., and Liu, Z. (2015). Remotely controlled red blood cell carriers for cancer targeting and near-infrared light-triggered drug release in combined photothermal-chemotherapy. *Adv. Funct. Mater.* 25, 2386–2394. doi: 10.1002/adfm.201500061

Tan, Y., Zhu, Y., Wen, L., Yang, X., Liu, X., Meng, T., et al. (2019). Mitochondria-responsive drug release along with heat shock mediated by multifunctional glycolipid micelles for precise cancer chemo-photothermy. *Theranostics* 9, 691–707. doi: 10.7150/thno.31022

Vines, J. B., Yoon, J. H., Ryu, N. E., Lim, D. J., and Park, H. (2019). Gold nanoparticles for photothermal cancer therapy. *Front. Chem.* 7:167. doi: 10.3389/fchem.2019.00167

Wan, G. Y., Chen, B. W., Li, L., Wang, D., Shi, S. R., Zhang, T., et al. (2018). Nanoscaled red blood cells facilitate breast cancer treatment by combining photothermal/photodynamic therapy and chemotherapy. *Biomaterials* 155, 25–40. doi: 10.1016/j.biomaterials.2017.11.002

Wang, C., Bai, J., Liu, Y. W., Jia, X. D., and Jiang, X. (2016). Polydopamine coated selenide molybdenum: a new photothermal nanocarrier for highly effective chemo-photothermal synergistic therapy. *ACS Biomater. Sci. Eng.* 2, 2011–2017. doi: 10.1021/acsbiomaterials.6b00416

Wang, C., Xu, H., Liang, C., Liu, Y., Li, Z., Yang, G., et al. (2013). Iron oxide@polypyrrole nanoparticles as a multifunctional drug carrier for remotely controlled cancer therapy with synergistic antitumor effect. *ACS Nano* 7, 6782–6795. doi: 10.1021/nn4017179

Wang, H., Sun, Y. B., Yi, J. H., Fu, J. P., Di, J., Alonso, A. D., et al. (2015). Fluorescent porous carbon nanocapsules for two-photon imaging, NIR/pH

dual-responsive drug carrier, and photothermal therapy. *Biomaterials* 53, 117–126. doi: 10.1016/j.biomaterials.2015.02.087

Wang, H., Zhao, Y. L., and Nie, G. J. (2013). Multifunctional nanoparticle systems for combined chemo- and photothermal cancer therapy. *Front. Mater. Sci.* 7, 118–128. doi: 10.1007/s11706-013-0207-7

Wang, J., Lin, F. X., Chen, J. X., Wang, M. Z., and Ge, X. W. (2015). The preparation, drug loading and *in vitro* NIR photothermal-controlled release behavior of raspberry-like hollow polypyrrole microspheres. *J. Mater. Chem. B* 3, 9186–9193. doi: 10.1039/C5TB01314C

Wang, J. L., and Qiu, J. J. (2016). A review of carbon dots in biological applications. *J. Mater. Sci.* 51, 4728–4738. doi: 10.1007/s10853-016-9797-7

Wang, K., Fan, X., Zhao, L., Zhang, X., Zhang, X., Li, Z., et al. (2016). Aggregation induced emission fluorogens based nanotheranostics for targeted and imaging-guided chemo-photothermal combination therapy. *Small* 12, 6568–6575. doi: 10.1002/smll.201601473

Wang, L. M., Lin, X. Y., Wang, J., Hu, Z. J., Ji, Y. L., Hou, S., et al. (2014). Novel insights into combating cancer chemotherapy resistance using a plasmonic nanocarrier: enhancing drug sensitiveness and accumulation simultaneously with localized mild photothermal stimulus of femtosecond pulsed laser. *Adv. Funct. Mater.* 24, 4229–4239. doi: 10.1002/adfm.201400015

Wang, W. H., Liang, G. H., Zhang, W. J., Xing, D., and Hu, X. L. (2018). Cascade-promoted photo-chemotherapy against resistant cancers by enzyme-responsive polyprodrug nanoplatforms. *Chem. Mater.* 30, 3486–3498. doi: 10.1021/acs.chemmater.8b01149

Wang, X., Li, X., Mao, Y., Wang, D., Zhao, Q., and Wang, S. (2019). Multi-stimuli responsive nanosystem modified by tumor-targeted carbon dots for chemophototherapy synergistic therapy. *J. Colloid Interface Sci.* 552, 639–650. doi: 10.1016/j.jcis.2019.05.085

Wang, X. Y., Zhang, J. S., Wang, Y. T., Wang, C. P., Xiao, J. R., Zhang, Q., et al. (2016). Multi-responsive photothermal-chemotherapy with drug-loaded melanin-like nanoparticles for synergetic tumor ablation. *Biomaterials* 81, 114–124. doi: 10.1016/j.biomaterials.2015.11.037

Wang, Y., Xiao, Y., and Tang, R. K. (2014). Spindle-like polypyrrole hollow nanocapsules as multifunctional platforms for highly effective chemo-photothermal combination therapy of cancer cells *in vivo*. *Chemistry* 20, 11826–11834. doi: 10.1002/chem.201403480

Wang, Y., Zhao, J., Chen, Z., Zhang, F., Wang, Q., Guo, W., et al. (2019). Construct of MoSe$_2$/Bi$_2$Se$_3$ nanoheterostructure: multimodal CT/PT imaging-guided PTT/PDT/chemotherapy for cancer treating. *Biomaterials* 217:119282. doi: 10.1016/j.biomaterials.2019.119282

Wang, Y. T., Huang, Q., He, X., Chen, H., Zou, Y., Li, Y. W., et al. (2018). Multifunctional melanin-like nanoparticles for bone-targeted chemo-photothermal therapy of malignant bone tumors and osteolysis. *Biomaterials* 183, 10–19. doi: 10.1016/j.biomaterials.2018.08.033

Wang, Y. Y., Deng, Y. B., Luo, H. H., Zhu, A. J., Ke, H. T., Yang, H., et al. (2017). Light-responsive nanoparticles for highly efficient cytoplasmic delivery of anticancer agents. *ACS Nano* 11, 12134–12144. doi: 10.1021/acsnano.7b05214

Weissleder, R. (2001). A clearer vision for *in vivo* imaging. *Nat. Biotechnol.* 19, 316–317. doi: 10.1038/86684

Weissleder, R., and Ntziachristos, V. (2003). Shedding light onto live molecular targets. *Nat. Med.* 9, 123–128. doi: 10.1038/nm0103-123

Wu, L., Fang, S., Shi, S., Deng, J., Liu, B., and Cai, L. (2013). Hybrid polypeptide micelles loading indocyanine green for tumor imaging and photothermal effect study. *Biomacromolecules* 14, 3027–3033. doi: 10.1021/bm400839b

Wust, P., Hildebrandt, B., Sreenivasa, G., Rau, B., Gellermann, J., Riess, H., et al. (2002). Hyperthermia in combined treatment of cancer. *Lancet Oncol.* 3, 487–497. doi: 10.1016/S1470-2045(02)00818-5

Xiao, Z. Y., Ji, C. W., Shi, J. J., Pridgen, E. M., Frieder, J., Wu, J., et al. (2012). DNA self-assembly of targeted near-infrared-responsive gold nanoparticles for cancer thermo-chemotherapy. *Angew. Chem. Int. Ed.* 51, 11853–11857. doi: 10.1002/anie.201204018

Xu, L. G., Cheng, L., Wang, C., Peng, R., and Liu, Z. (2014). Conjugated polymers for photothermal therapy of cancer. *Polym. Chem.* 5, 1573–1580. doi: 10.1039/C3PY01196H

Xu, X. Y., Ray, R., Gu, Y. L., Ploehn, H. J., Gearheart, L., Raker, K., et al. (2004). Electrophoretic analysis and purification of fluorescent single-walled carbon nanotube fragments. *J. Am. Chem. Soc.* 126, 12736–12737. doi: 10.1021/ja040082h

Yan, F., Duan, W. L., Li, Y. K., Wu, H., Zhou, Y. L., Pan, M., et al. (2016). NIR-laser-controlled drug release from DOX/IR-780-loaded temperature-sensitive-liposomes for chemo-photothermal synergistic tumor therapy. *Theranostics* 6, 2337–2351. doi: 10.7150/thno.14937

Yang, G. B., Gong, H., Liu, T., Sun, X. Q., Cheng, L., and Liu, Z. (2015). Two-dimensional magnetic WS$_2$@Fe$_3$O$_4$ nanocomposite with mesoporous silica coating for drug delivery and imaging-guided therapy of cancer. *Biomaterials* 60, 62–71. doi: 10.1016/j.biomaterials.2015.04.053

Yang, J., Choi, J., Bang, D., Kim, E., Lim, E. K., Park, H., et al. (2011). Convertible organic nanoparticles for near-infrared photothermal ablation of cancer cells. *Angew. Chem. Int. Ed.* 50, 441–444. doi: 10.1002/anie.201005075

Yang, J., Zhai, S., Qin, H., Yan, H., Xing, D., and Hu, X. (2018). NIR-controlled morphology transformation and pulsatile drug delivery based on multifunctional phototheranostic nanoparticles for photoacoustic imaging-guided photothermal-chemotherapy. *Biomaterials* 176, 1–12. doi: 10.1016/j.biomaterials.2018.05.033

Yang, K., Feng, L. Z., and Liu, Z. (2015). The advancing uses of nano-graphene in drug delivery. *Expert Opin. Drug Deliv.* 12, 601–612. doi: 10.1517/17425247.2015.978760

Yang, K., Feng, L. Z., Shi, X. Z., and Liu, Z. (2013). Nano-graphene in biomedicine: theranostic applications. *Chem. Soc. Rev.* 42, 530–547. doi: 10.1039/C2CS35342C

Yang, K., Wan, J. M., Zhang, S., Tian, B., Zhang, Y. J., and Liu, Z. (2012a). The influence of surface chemistry and size of nanoscale graphene oxide on photothermal therapy of cancer using ultra-low laser power. *Biomaterials* 33, 2206–2214. doi: 10.1016/j.biomaterials.2011.11.064

Yang, K., Xu, H., Cheng, L., Sun, C. Y., Wang, J., and Liu, Z. (2012b). *In vitro* and *in vivo* near-infrared photothermal therapy of cancer using polypyrrole organic nanoparticles. *Adv. Mater.* 24, 5586–5592. doi: 10.1002/adma.201202625

Yang, K., Zhang, S. A., Zhang, G. X., Sun, X. M., Lee, S. T., and Liu, Z. A. (2010). Graphene in mice: ultrahigh *in vivo* tumor uptake and efficient photothermal therapy. *Nano Lett.* 10, 3318–3323. doi: 10.1021/nl100996u

Yao, J., Kang, S., Zhang, J., Du, J., Zhang, Z., and Li, M. (2017). Amphiphilic near-infrared conjugated polymer for photothermal and chemo combination therapy. *ACS Biomater. Sci. Eng.* 3, 2230–2234. doi: 10.1021/acsbiomaterials.7b00344

Yao, M. Q., Ma, Y. C., Liu, H., Khan, M. I., Shen, S., Li, S. Y., et al. (2018). Enzyme degradable hyperbranched polyphosphoester micellar nanomedicines for NIR imaging-guided chemo-photothermal therapy of drug-resistant cancers. *Biomacromolecules* 19, 1130–1141. doi: 10.1021/acs.biomac.7b01793

Yavuz, M. S., Cheng, Y. Y., Chen, J. Y., Cobley, C. M., Zhang, Q., Rycenga, M., et al. (2009). Gold nanocages covered by smart polymers for controlled release with near-infrared light. *Nat. Mater.* 8, 935–939. doi: 10.1038/nmat2564

Ye, S., Wang, F., Fan, Z., Zhu, Q., Tian, H., Zhang, Y., et al. (2019). Light/pH-triggered biomimetic red blood cell membranes camouflaged small molecular drug assemblies for imaging-guided combinational chemo-photothermal therapy. *ACS Appl. Mater. Inter.* 11, 15262–15275. doi: 10.1021/acsami.9b00897

You, J., Zhang, G. D., and Li, C. (2010). Exceptionally high payload of doxorubicin in hollow gold nanospheres for near-infrared light-triggered drug release. *ACS Nano* 4, 1033–1041. doi: 10.1021/nn901181c

You, J., Zhang, R., Xiong, C. Y., Zhong, M., Melancon, M., Gupta, S., et al. (2012). Effective photothermal chemotherapy using doxorubicin-loaded gold nanospheres that target EphB4 receptors in tumors. *Cancer Res.* 72, 4777–4786. doi: 10.1158/0008-5472.CAN-12-1003

Young, J. K., Figueroa, E. R., and Drezek, R. A. (2012). Tunable nanostructures as photothermal theranostic agents. *Angew. Chem. Int. Ed.* 40, 1206–1208. doi: 10.1007/s10439-011-0472-5

Yu, H. J., Cui, Z. R., Yu, P. C., Guo, C. Y., Feng, B., Jiang, T. Y., et al. (2015). pH- and NIR light-responsive micelles with hyperthermia-triggered tumor penetration and cytoplasm drug release to reverse doxorubicin resistance in breast cancer. *Adv. Funct. Mater.* 25, 2489–2500. doi: 10.1002/adfm.201404484

Yuan, Y., Wang, Z., Cai, P., Liu, J., Liao, L. D., Hong, M., et al. (2015). Conjugated polymer and drug co-encapsulated nanoparticles for chemo- and photo-thermal combination therapy with two-photon regulated fast drug release. *Nanoscale* 7, 3067–3076. doi: 10.1039/C4NR06420H

Yue, C., Liu, P., Zheng, M., Zhao, P., Wang, Y., Ma, Y., et al. (2013). IR-780 dye loaded tumor targeting theranostic nanoparticles for

NIR imaging and photothermal therapy. *Biomaterials* 34, 6853–6861. doi: 10.1016/j.biomaterials.2013.05.071

Yue, X. L., Zhang, Q., and Dai, Z. F. (2017). Near-infrared light-activatable polymeric nanoformulations for combined therapy and imaging of cancer. *Adv. Drug Deliv. Rev.* 115, 155–170. doi: 10.1016/j.addr.2017.04.007

Zaharie-Butucel, D., Potara, M., Suarasan, S., Licarete, E., and Astilean, S. (2019). Efficient combined near-infrared-triggered therapy: phototherapy over chemotherapy in chitosan-reduced graphene oxide-IR820 dye-doxorubicin nanoplatforms. *J. Colloid Interface Sci.* 552, 218–229. doi: 10.1016/j.jcis.2019.05.050

Zhang, A., Li, A., Zhao, W., and Liu, J. (2018). Recent advances in functional polymer decorated two-dimensional transition-metal dichalcogenides nanomaterials for chemo-photothermal therapy. *Chem. Eur. J.* 24, 4215–4227. doi: 10.1002/chem.201704197

Zhang, J., Qiao, Z., Liu, H. Y., Song, J., and Yin, J. (2019). Positively charged helical chain-modified stimuli-responsive nanoassembly capable of targeted drug delivery and photoacoustic imaging-guided chemo-photothermal synergistic therapy. *Biomater. Sci.* 7, 2050–2060. doi: 10.1039/C9BM00055K

Zhang, L., Chen, Y., Li, Z., Li, L., Saint-Cricq, P., Li, C., et al. (2016). Tailored synthesis of octopus-type Janus nanoparticles for synergistic actively-targeted and chemo-photothermal therapy. *Angew. Chem. Int. Ed.* 55, 2118–2121. doi: 10.1002/anie.201510409

Zhang, L. M., Xia, J. G., Zhao, Q. H., Liu, L. W., and Zhang, Z. J. (2010). Functional graphene oxide as a nanocarrier for controlled loading and targeted delivery of mixed anticancer drugs. *Small* 6, 537–544. doi: 10.1002/smll.200901680

Zhang, M., Wang, J., Wang, W. T., Zhang, J., and Zhou, N. L. (2017a). Magnetofluorescent photothermal micelles packaged with GdN@CQDs as photothermal and chemical dual-modal therapeutic agents. *Chem. Eng. J.* 330, 442–452. doi: 10.1016/j.cej.2017.07.138

Zhang, M., Wang, W. T., Zhou, N. L., Yuan, P., Su, Y. T., Shao, M. N., et al. (2017b). Near-infrared light triggered photo-therapy, in combination with chemotherapy using magnetofluorescent carbon quantum dots for effective cancer treating. *Carbon N. Y.* 118, 752–764. doi: 10.1016/j.carbon.2017.03.085

Zhang, N., Li, M. H., Sun, X. T., Jia, H. Z., and Liu, W. G. (2018). NIR-responsive cancer cytomembrane-cloaked carrier-free nanosystems for highly efficient and self-targeted tumor drug delivery. *Biomaterials* 159, 25–36. doi: 10.1016/j.biomaterials.2018.01.007

Zhang, Y. Y., Ang, C. Y., Li, M. H., Tan, S. Y., Qu, Q. Y., and Zhao, Y. L. (2016a). Polymeric prodrug grafted hollow mesoporous silica nanoparticles encapsulating near-infrared absorbing dye for potent combined photothermal-chemotherapy. *ACS Appl. Mater. Inter.* 8, 6869–6879. doi: 10.1021/acsami.6b00376

Zhang, Y. Y., Teh, C., Li, M. H., Ang, C. Y., Tan, S. Y., Qu, Q. Y., et al. (2016b). Acid-responsive polymeric doxorubicin prodrug nanoparticles encapsulating a near-infrared dye for combined photothermal-chemotherapy. *Chem. Mater.* 28, 7039–7050. doi: 10.1021/acs.chemmater.6b02896

Zhang, Y. Y., Yang, D., Chen, H. Z., Lim, W. Q., Phua, F. S. Z., An, G. H., et al. (2018). Reduction-sensitive fluorescence enhanced polymeric prodrug nanoparticles for combinational photothermal-chemotherapy. *Biomaterials* 163, 14–24. doi: 10.1016/j.biomaterials.2018.02.023

Zhang, Z., Wang, L., Wang, J., Jiang, X., Li, X., Hu, Z., et al. (2012). Mesoporous silica-coated gold nanorods as a light-mediated multifunctional theranostic platform for cancer treatment. *Adv. Mater.* 24, 1418–1423. doi: 10.1002/adma.201104714

Zhang, Z. J., Wang, J., and Chen, C. H. (2013). Near-infrared light-mediated nanoplatforms for cancer thermo-chemotherapy and optical imaging. *Adv. Mater.* 25, 3869–3880. doi: 10.1002/adma.201301890

Zhao, A. D., Chen, Z. W., Zhao, C. Q., Gao, N., Ren, J. S., and Qu, X. G. (2015). Recent advances in bioapplications of C-dots. *Carbon N. Y.* 85, 309–327. doi: 10.1016/j.carbon.2014.12.045

Zheng, M., Yue, C., Ma, Y., Gong, P., Zhao, P., Zheng, C. et al. (2013). Single-step assembly of DOX/ICG loaded lipid-polymer nanoparticles for highly effective chemo-photothermal combination therapy. *ACS Nano* 7, 2056–2067. doi: 10.1021/nn400334y

Zheng, X. T., Ananthanarayanan, A., Luo, K. Q., and Chen, P. (2015). Glowing graphene quantum dots and carbon dots: properties, syntheses, and biological applications. *Small* 11, 1620–1636. doi: 10.1002/smll.201402648

Zhong, Y., Wang, C., Cheng, L., Meng, F., Zhong, Z., and Liu, Z. (2013). Gold nanorod-cored biodegradable micelles as a robust and remotely controllable doxorubicin release system for potent inhibition of drug-sensitive and -resistant cancer cells. *Biomacromolecules* 14, 2411–2419. doi: 10.1021/bm400530d

Zhou, J., Lu, Z., Zhu, X., Wang, X., Liao, Y., Ma, Z. et al. (2013). NIR photothermal therapy using polyaniline nanoparticles. *Biomaterials* 34, 9584–9592. doi: 10.1016/j.biomaterials.2013.08.075

Zhou, L., Dong, K., Chen, Z. W., Ren, J. S., and Qu, X. G. (2015). Near-infrared absorbing mesoporous carbon nanoparticle as an intelligent drug carrier for dual-triggered synergistic cancer therapy. *Carbon N. Y.* 82, 479–488. doi: 10.1016/j.carbon.2014.10.091

Zhu, A., Miao, K., Deng, Y., Ke, H., He, H., Yang, T., et al. (2015). Dually pH/reduction-responsive vesicles for ultrahigh-contrast fluorescence imaging and thermo-chemotherapy-synergized tumor ablation. *ACS Nano* 9, 7874–7885. doi: 10.1021/acsnano.5b02843

Zhu, H., Cheng, P., Chen, P., and Pu, K. (2018). Recent progress in the development of near-infrared organic photothermal and photodynamic nanotherapeutics. *Biomater. Sci.* 6, 746–765. doi: 10.1039/C7BM01210A

Zhu, H. J., Lai, Z. C., Fang, Y., Zhen, X., Tan, C. L., Qi, X. Y., et al. (2017). Ternary chalcogenide nanosheets with ultrahigh photothermal conversion efficiency for photoacoustic theranostics. *Small* 13:1604139. doi: 10.1002/smll.201604139

Zhu, Y. D., Chen, S. P., Zhao, H., Yang, Y., Chen, X. Q., Sun, J. et al. (2016). PPy@MIL-100 nanoparticles as a pH- and near-IR-irradiation-responsive drug carrier for simultaneous photothermal therapy and chemotherapy of cancer cells. *ACS Appl. Mater. Inter.* 8, 34209–34217. doi: 10.1021/acsami.6b11378

Photodynamic Therapy Based on Graphene and MXene in Cancer Theranostics

Arianna Gazzi[1,2], Laura Fusco[1,2,3], Anooshay Khan[4], Davide Bedognetti[3], Barbara Zavan[5,6], Flavia Vitale[7,8*], Acelya Yilmazer[4,9*] and Lucia Gemma Delogu[2,10*]

[1] Department of Chemical and Pharmaceutical Sciences, University of Trieste, Trieste, Italy, [2] Fondazione Istituto di Ricerca Pediatrica Città della Speranza, Padua, Italy, [3] Sidra Medical and Research Center, Doha, Qatar, [4] Department of Biomedical Engineering, University of Ankara, Ankara, Turkey, [5] Department of Medical Sciences, University of Ferrara, Ferrara, Italy, [6] Maria Cecilia Hospital, GVM Care & Research, Ravenna, Italy, [7] Department of Neurology, Bioengineering, Physical Medicine & Rehabilitation, Center for Neuroengineering and Therapeutics, University of Pennsylvania, Philadelphia, PA, United States, [8] Center for Neurotrauma, Neurodegeneration, and Restoration, Corporal Michael J. Crescenz Veterans Affairs Medical Center, Philadelphia, PA, United States, [9] Stem Cell Institute, University of Ankara, Ankara, Turkey, [10] Department of Biomedical Sciences, University of Padua, Padua, Italy

Cancer is one of the leading causes of death in the world. Therefore, the development of new advanced and targeted strategies in cancer research for early diagnosis and treatment has become essential to improve diagnosis outcomes and reduce therapy side effects. Graphene and more recently, MXene, are the main representatives of the family of two-dimensional (2D) materials and are widely studied as multimodal nanoplatforms for cancer diagnostics and treatment, in particular leveraging their potentialities as photodynamic therapeutic agents. Indeed, due to their irreplaceable physicochemical properties, they are virtuous allies for photodynamic therapy (PDT) in combination with bioimaging, photothermal therapy, as well as drug and gene delivery. In this review, the rapidly progressing literature related to the use of these promising 2D materials for cancer theranostics is described in detail, highlighting all their possible future advances in PDT.

Keywords: photodynamic therapy, theranostics, graphene, MXene, nanomedicine

INTRODUCTION

Photodynamic therapy (PDT) is a form of phototherapy aimed at achieving cell death via the generation of cytotoxic reactive oxygen species (ROS). Although PDT is still an emerging therapeutic modality, it has already been established as a clinically approved method for the treatment of various malignant diseases, including cancer (Agostinis et al., 2011).

Clinically, PDT is usually used in conjunction with other forms of treatments, such as surgery, radiotherapy (RT), and chemotherapy (CT). Due to its local activation and limited tissue penetration, PDT has relatively low invasiveness, and in many cases, good cosmetic results. Therefore, this therapy is particularly suitable for the treatment of exposed skin and sensitive areas, like the head and neck. Moreover, even though it may induce prolonged periods of skin photosensitivity, during which patients need to avoid light, it lacks the serious adverse events (AE) seen in RT and systemic CT. Surgery represents the first-choice treatment and, for the majority of tumor types, the only curative intervention for early diagnosed cancer. However, since most patients are usually diagnosed at late stages, treatments such CT and RT are then preferred. In case of inoperable disease and failure or refusal of other

treatments, PDT can potentially be used as a standalone treatment or in combination with other therapies due to the absence of systemic effects and its ability to preserve the organ function. Furthermore, unlike RT, PDT mechanisms of action allow its use also for repeated treatments.

Currently, there are 563 registered clinical trials for PDT, of which almost 60% are directed against cancer (www.clinicaltrials.gov). Among the drug-device combination products, PDT was the first one approved by the Food and Drug Administration (FDA), being now under investigation in preclinical studies to improve its efficacy and safety (Ferreira Dos Santos et al., 2019). The PDT procedure requires three main components: a photosensitizer (PS), a light source (laser), and molecular tissue oxygen. In the context of cancer treatment, the PS is administered locally or systemically, being accumulated in the tumor site. Subsequently, the patient is locally irradiated with light of a proper wavelength, with the aim to activate the PS in the presence of molecular oxygen (Dolmans et al., 2003).

Following administration, PSs can be internalized by both cancer and normal cells. While healthy tissues can eliminate the PS over time, this is not possible for tumor cells due to the lymphatic inadequacy. The resulting PS retention in tumor tissues, together with the localized activation by irradiation, makes PDT a selective treatment for cancer.
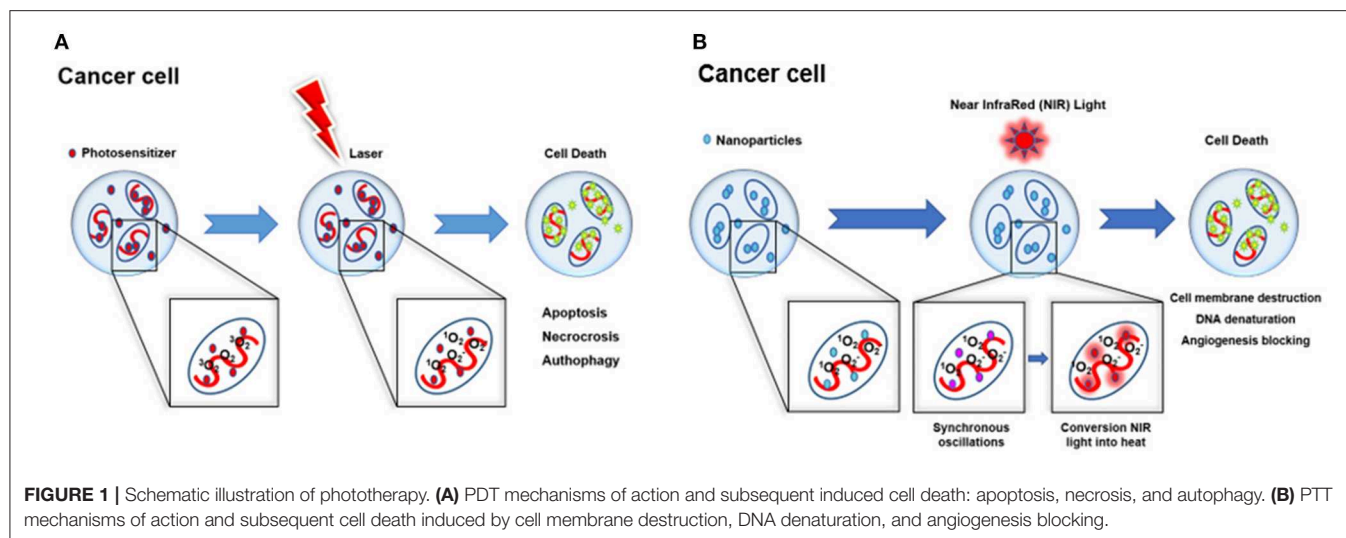
The treatment will result in localized oxidative photodamage, consisting in the oxidation of a large range of cellular biomolecules, including nucleic acids, lipids, and proteins. Consequently, the process will lead to selective cytotoxicity, mainly due to a severe alteration in cell signaling cascades and gene expression regulation. The cellular response to photodamage is closed related to several factors. Due to its characteristics, a PS will usually accumulate toward different cellular organelles (e.g., mitochondria and lysosomes), plasma membrane, Golgi apparatus, or endoplasmic reticulum (ER). Generally, three main mechanisms of photodamage-induced cell death have been described: apoptosis, necrosis and autophagy at the tumor site (Bacellar et al., 2015; Ferreira Dos Santos et al., 2019). This process is also accompanied by the induction of an acute local inflammatory reaction that participates in the removal of dead cells, restoration of normal tissue homeostasis and development of systemic immunity (Henderson et al., 2004; Korbelik, 2006). This ability of PDT to activate multiple cell death pathways enables circumvention of apoptosis-resistance in cancer cells, one of the main problems for anticancer approaches.

The superoxide anions released in type I reactions do not pose particular harm to biological systems directly but contribute to the production of hydrogen peroxide, resulting in lipid peroxidation, ultimately leading to the disruption of cellular membranes. Thanks to the short singlet oxygen ($^1O_2$) lifetime of ∼40 ns and its short-range action (maximum action radius of about 20 nm), together with the localized PS light-induced activation, PDT is a highly controllable and specific therapy. PS localization can also modulate the subcellular site of action of PDT. Extensive cell damages could also affect apoptotic pathway components, and therefore apoptosis may not be properly executed. Thanks to the autophagy process, cells have the ability to recycle damaged cytoplasmic components

and organelles trough the creation of the "autophagosome," a double membrane structure that after the engulfment of the damaged particles fuses with lysosomes in order to degrade its contents. This autophagic process is not only considered to be a cytoprotective mechanism, being observed also as a cell death mechanism in response to PDT. When the apoptotic mechanism is compromised, cell death mainly occurs through autophagy. This seems to be also correlated with PDT dose, since autophagy can serve as a protective mechanism or initiate the autophagic cell-death, when using low or high doses, respectively (**Figures 1A,B**). Several preclinical studies have been performed to improve the safety and efficacy of PDT, as well as to extend the number of the different types of diseased tissues that can be treated, thanks to the use of next-generation PSs. The design of second-generation PSs was aimed to develop new agents with higher absorption wavelengths, enabling deeper organs to be targeted thanks to enhanced penetration of light (Lou et al., 2004; Agostinis et al., 2011; Story et al., 2013). Later, the introduction of third-generation PSs allowed improving targeting strategies, such as antibody-directed PS and PS-loaded nanocarriers (Agostinis et al., 2011; Yoon et al., 2013).

Thanks to the progress of nanotechnology, the improvement of PDT using theranostic two-dimensional (2D) nanomaterials (NMs) is attracting growing attention. Therapeutic strategies were combined with imaging modalities for a theranostic aim in order to monitor the biodistribution of therapeutic agents and to identify and/or localize the tumor mass and its growth (Cho et al., 2013; Wang et al., 2013; Ge et al., 2014; Gollavelli and Ling, 2014; Rong et al., 2014; Kim et al., 2015; Wu et al., 2015; Yan et al., 2015b; Guan et al., 2016; Kalluru et al., 2016; Luo et al., 2016; Gulzar et al., 2018).

Currently, multiple combinations of various therapeutic and diagnostic modalities are adopted to achieve a theranostic effect (Orecchioni et al., 2015; Ji et al., 2019), and can be further improved and expanded thanks to the development of NM-based theranostic nanoplatforms. Among 2D NMs suitable for this purpose, graphene and graphene-based materials (GBMs), including few layer graphene (FLG), graphene oxide (GO), reduced graphene oxide (rGO), nano-graphene oxide (NGO), and graphene quantum dots (GQDs), bring the technological innovations needed to the current societal and industrial challenges (Boukhvalov and Katsnelson, 2008; Park and Ruoff, 2009; Gao et al., 2010; Kuila et al., 2012; Mao et al., 2012; James and Tour, 2013; Quintana et al., 2013; Yang et al., 2013a; Roppolo et al., 2014; Sechi et al., 2014; Servant et al., 2014; Kim et al., 2016; Shin et al., 2016; McManus et al., 2017; Park et al., 2017). Graphene, consisting of a single layer of carbon atoms arranged in a honeycomb structure, exhibits a unique combination of physiochemical properties, including high surface area (2,630 m^2 g^{-1}), optimal thermal conductivity (∼5,000 Wm K^{-1}), remarkable optical transparency (single layer graphene absorbs ∼2.3% of visible light), strong mechanical strength (Young's modulus of ∼1 TPa), and room temperature quantum hall effect for electrons and holes (Novoselov et al., 2012). Its 2D plane sp^2 hybridization results in delocalized out of plane π bonds providing an outstanding carrier mobility (ranging from ∼ 200,000 to ∼500,000 cm^2 V^{-1} s^{-1}, in case of

FIGURE 1 | Schematic illustration of phototherapy. **(A)** PDT mechanisms of action and subsequent induced cell death: apoptosis, necrosis, and autophagy. **(B)** PTT mechanisms of action and subsequent cell death induced by cell membrane destruction, DNA denaturation, and angiogenesis blocking.

suspended graphene or graphene-based field effect transistors, respectively). Due to its characteristics, graphene offers new fascinating perspectives in nanomedicine for the development of new therapeutic delivery approaches, imaging strategies, as well as biosensor-based diagnostic tools (Yang et al., 2013b; Orecchioni et al., 2014, 2015, 2016b; Avitabile et al., 2018; Fadeel et al., 2018b).

Recently, other promising 2D NMs have attracted attention for their possible applications in various fields, including biomedical sciences (Chen et al., 2015; Luo et al., 2018). One of the most recently discovered 2D materials is MXene, which was first introduced by Gogotsi et al. in 2011 (Naguib et al., 2011). Since then, more than 20 species of MXenes have been successfully synthesized, and the structure/properties of more than 70 have been predicted *in silico*. MXenes are composed of early-transition-metal carbides, carbonitrides, and nitrides with structural formula Mn + 1Xn, where M is an early transition metal, X stands for carbon, nitrogen, or both, and $n = 1$–3. MXenes are synthesized through selectively etching the A-group element from the precursor ternary-layered carbides of MAX phases, where A represents a group of 12–16 periodic table elements. As a consequence of the selectively etching of the A group with -F containing etchants, such as HF, the resulting MXenes will be characterized by abundant surface-terminating functional groups, e.g., hydroxyl (–OH), oxygen (–O), or fluorine (–F), endowing their hydrophilic nature and allowing their flexible surface modification and functionalization. Thanks to the production scalability, the rich surface chemistry, the metallic conductivity, the excellent mechanical/thermal properties, and ease of processability, MXenes have attracted increasing attention for a number of different applications, such as energy storage (Lukatskaya et al., 2017), electromagnetic interference shielding (Shahzad et al., 2016), electrocatalysts (Seh et al., 2016), electrochemical supercapacitors (Ghidiu et al., 2015), and Li-ion batteries (Er et al., 2014; Anasori et al., 2017), just to name a few.

In recent years, MXenes have also been explored for their applications in biomedicine, especially as building-blocks in nano-biotechnology platforms. From the topological perspective,

MXenes share all the advantages of other classes of 2D NMs, stemming from their impressive properties, such as extreme thinness, high surface-to-volume ratio, and mechanical toughness. Additionally, the rich chemistry on the surface of MXenes provides abundant reactive sites for enzyme or drug functionalization, while their volumetric capacitance and metallic conductivity are highly desirable for low-noise and high-fidelity biosensors (Driscoll et al., 2018). MXenes exhibit strong absorption in the near-infrared (NIR) region, both in the first (650–950 nm) and second biological window (1,000–1,350 nm), where the low scattering and energy absorption allow maximum penetration of the radiation through the tissue.

The suitability of GBMs for multiple cancer theranostic applications is due to their unique intrinsic physicochemical properties, making them superior nanotools compared to the existing materials and devices used for this purpose, such as optical transparency, high surface area, easy surface functionalization, and low-cost production. In this contest, the use of GBMs and MXenes has been proposed to enhance PDT efficiency. For example, these promising materials are able to correct some of the limits showed by the conventional PSs required for this medical technique. Those are mainly represented by porphyrin-based molecules, such as Chlorin e6 (Ce6), which are characterized by low solubility, photostability, difficulties in delivery efficiency, and inability to be absorbed in regions where the skin is the most transparent (Detty et al., 2004; Huang, 2005). Besides providing a superior biocompatibility, 2D NMs, and in particular GO, can endow them with higher water dispersibility (Gao et al., 2004; Michalet et al., 2005; Resch-Genger et al., 2008), photostability, cytotoxicity, and ROS-generation efficiency (Ge et al., 2014; Pelin et al., 2018). Other materials, such as GQDs, are able to perform better than conventional PDT agents due to their extremely high $^1O_2$ quantum yield, GQDs (Ge et al., 2014).

Moreover, the particular nanostructure and the large surface area of these 2D NMs facilitate the loading of PSs and other targeting moieties or drugs, allowing a specific release of the treatment and selectivity for cancer cells. Indeed, the presence of the 2D surface characterized by delocalized π electrons and,
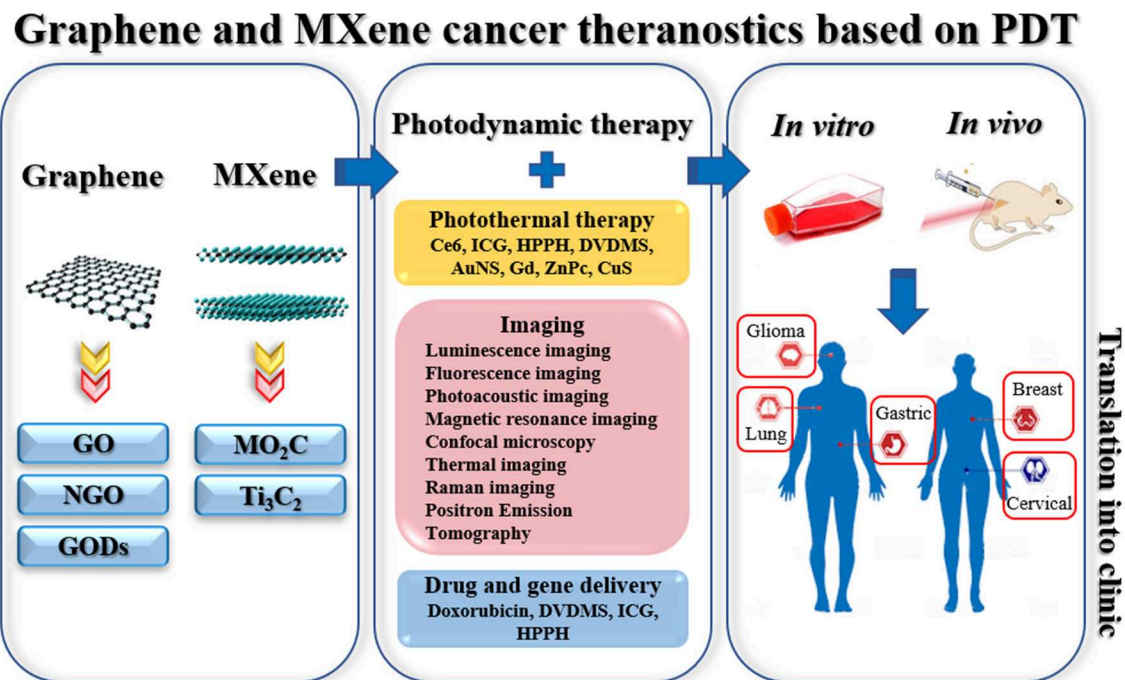
FIGURE 2 | Schematic representation of the current applications in PDT for cancer theranostics based on graphene and MXene. Left panel: representation of graphene and MXene. Middle panel: combined applications with PDT, types of conjugated molecules (for PTT), types of imaging, and examples of conjugated drugs (for drug delivery). Right panel: types of cancer investigated *in vitro* and *in vivo*.

in particular for GO, the existence of polar functionalities (e.g., epoxide, carbonyl, carboxyl, and hydroxyl groups), allows high drug loading ratios to be reached simply, even of poorly soluble chemotherapeutic drugs, based on electrostatic or hydrophobic interactions and π-π stacking capability, which can even achieve 200 wt% (Augustine et al., 2017). In addition, thanks to the high surface-to-volume ratio, it is possible to reach a superior bio-functionalization, which allows several drugs and molecules to be added, including such fluorescent probes, genes, and targeting moieties to specifically recognize cancer cells, making it possible to achieve their guided and controlled release to the targeted cells.

Furthermore, thanks to the intrinsic NIR absorption properties, GO is a suitable tool for both PDT and photothermal therapy (PTT), obtaining a higher therapeutic efficiency through both *in situ* production of ROS and tumor ablation under NIR irradiation. Together with PDT, PTT represents an alternative anticancer therapy thanks to the selectivity of the hyperthermic process toward cancer cells, sparing healthy tissues. Irradiation of plasmonic NPs accumulated in the tumor with a light of appropriate wavelength leads the NP conduction band electrons to undergo synchronized oscillations, allowing the conversion of NIR light into heat. There are three mechanisms that lead to cell death: cell membrane damage, denaturation of DNA, and angiogenesis blocking (**Figure 1B**). The investigation of MXenes as PSs for PDT is still in its infancy and, as of June 2019, most of the published works have reported on different MXene species as photothermal conversion agents (PTAs) for PTT (Lin et al., 2016, 2017; Dai et al., 2017; Han et al., 2018; Feng et al., 2019). Indeed, MXenes show higher photothermal effect compared to GO; thus,

they appear particularly suitable as PTA for cancer therapy and imaging (Lin et al., 2016, 2018).

In light of this consideration, in this review, we aim to discuss the current state of the art of PDT in cancer theranostics based on GBMs and MXenes, alone or in combination with other therapies (i.e., PTT and drug delivery). A literature mining protocol was developed to present an overview of the literature in this context, focusing on the different types of models, cancer, functionalization, and combined approaches. A schematic representation of graphene- and MXene-based PDT for cancer theranostic applications is shown in **Figure 2**. We then have analyzed the future trends in PDT related to graphene and MXene, identifying different knowledge gaps in the field.

GRAPHENE AND MXene LITERATURE SURFING

A systematic review of the literature on graphene and MXene, studied in biomedicine as nanotools for cancer theranostic applications based on PDT, was performed with no time restriction, according to the Preferred Reporting Items for Systematic Reviews and Meta-Analyses (PRISMA) guidelines. The electronic databases (PubMed, Scopus, and ToxLine) were used as data sources, via the following keywords in several different combinations: graphene, GBMs, FLG, GO, rGO, NGO, GQDs, MXene, theranostic, and PDT. To help the reader, **Table 1** shows all the acronyms used in the text. As an additional tool, high-impact review articles were also considered. The list of reported studies includes all the retrieved publications from 2008

to January 2019. The adopted inclusion criteria were as follows: (1) studies published in English; (2) full text articles; and (3) the use of PDT in combination with other graphene/MXene applications. A total of 20 eligible studies were identified through the literature review for inclusion in the current review, 1 for MXenes and 19 for GBMs. The latter are summarized in **Table 2** based on the different types of cancer, combined applications, species of investigation, model, and material used in the respective study. The trend from 2011 to 2018 displays a remarkable growing interest in graphene and GBMs for cancer PDT.

A search on clinical trials was performed using the same criteria; however, although there are currently 325 clinical trials based on PDT for cancer therapy (www.clinicaltrials.gov), none of them involves GBMs or MXenes. This result highlights that the research on 2D nanomaterials for PDT, despite promising results obtained *in vitro* and *in vivo*, is still at a very early stage for a clinical translation.

The 19 manuscripts on graphene-based PDT in cancer theranostics were analyzed with respect to type of applications combined with PDT, model used for the study (*in vivo* or *in vitro*), and type of cancer studied (**Figure 3**). Focusing on the association of other cancer theranostic applications, it emerged that PDT was often applied together with one or multiple therapies and imaging modalities: the majority of the studies (58%) concerned the simultaneous application of PDT, imaging, and PTT, drug delivery or other therapies, followed by the combination of PDT with PTT, drug delivery or other therapies (32%), while only 10% of the works used PTD associated with imaging alone (**Figure 3A**). In particular, PDT was used in combination with different imaging techniques, such as luminescence imaging (CLI), fluorescence imaging, photoacoustic imaging (PAI), magnetic resonance imaging (MRI), confocal microscopy (CLSM), thermal imaging (IRT), Raman imaging, and positron emission tomography (PET). From the analysis of the model used in the works, it emerged that most studies were carried out both *in vitro* and *in vivo* (48%), a large number (47%) using only *in vitro* models consisting of different kinds of cancer cells, while only 5% tested these materials exclusively *in vivo* (**Figure 3B**).

Finally, we focused on the different types of tumors studied (**Figure 3C**), identifying cervical cancer as the most investigated (32% of publications). Indeed, according to the World Health Organization (WHO)[1], cervical cancer is the fourth most common type of tumor in women and the eighth most frequently occurring overall; rising with 570,000 new cases in 2018 and representing 6.6% of all female cancers (from world health organization www.who.int). The second largest portion comprises works focusing on lung cancer (23%), followed by publications concerning breast cancer (18%) and gastric cancer (9%). Papers investigating other kinds of tumors, such as skin, brain, liver cancer, and papilloma, make up the remainder (5%).

---

[1]WHO. *Cervical Cancer WHO*. Available online at: http://www.who.int/cancer/ prevention/diagnosis-screening/cervical-cancer/en/ (accessed July 4, 2019).

TABLE 1 | List of abbreviations.

ABBREVIATIONS	
AE	Adverse events
Ce6	Chlorin e6
CLI	Cerenkov luminescence imaging
CLSM	Confocal laser scanning microscopy
CT	Chemotherapy
DOX	Doxorubicin
DPBF	1,3-diphenyli-sobenzofuran
DVDMS	Sinoporphyrin sodium
EPR	Enhanced permeability and retention
ER	Endoplasmic reticulum
FDA	Federal Drug Administration
GBMs	Graphene based materials
GO	Graphene Oxide
GQDs	Graphene quantum dots
HA	Hyaluronic acid
HB	Hypocrellin B
hMPO	human myeloperoxidase
HPPH	3-(1′-hexyloxyethyl)-3-devinyl pyropheophorbide-a
H_2O_2	Hydrogen peroxide
ICG	Indocyanine green
IRT	Infrared thermal imaging
LSPR	Localized Surface plasmon resonance
MIRIBEL	Minimum Information Reporting in Bio–Nano Experimental Literature
miRNA	MicroRNA
MRI	Magnetic resonance imaging
NGO	Nanographene oxide
NIR	Near infrared
NMs	Nanomaterials
$^1O_2$	Singlet oxigen
PAI	Photoacoustic imaging
PDT	Photodynamic therapy
PEG	Polyethylene glycol
PEI	Polyethylenimine
PET	Positron emission tomography
PRISMA	Preferred Reporting Items for Systematic Reviews and Meta-Analyses
PS	Photosensitizer
PTA	Photothermal conversion agents
PTT	Photothermal therapy
rGO	Reduced graphene oxide
RT	Radiotherapy
siRNA	Short interfering RNA
UCL imaging	Upconversion Luminescence Imaging
UCNPs	Upconversion nanoparticles
WHO	World health organization
ZnPc	Phthalocyanine

PROGRESS IN PHOTODYNAMIC THERAPY IN GRAPHENE- AND MXENE-MEDIATED THERANOSTICS

GBMs have attracted attention for PDT exploiting their optical loading properties (Avitabile et al., 2018; Viseu et al.,

TABLE 2 | Table showing all the studies using GBMs for PDT theranostic applications.

References	Type of cancer	Type of applications	Model	Drug/PS	Imaging	Material
Tian et al. (2011)	Cervical cancer	PDT and drug delivery	*In vitro*	Chlorin e6	–	GO-PEG
Huang et al. (2011)	Gastric carcinoma	PDT and drug delivery	*In vitro*	Chlorin e6	–	FA-GO-Ce6
Zhou et al. (2012)	Lung cancer	PDT and drug delivery	*In vitro*	Hypocrellin A and Camptothecin	–	rGO
Wang et al. (2013)	Papilloma, cervical cancer	Imaging, PDT, and PTT	*In vitro and in vivo*	Doxorubicin	CLSM and MRI	UCNPs-NGO/ZnPc
Sahu et al. (2013)	Cervical cancer	PDT and PTT	*In vitro and in vivo*	Methylene blue	–	GO
Cho et al. (2013)	Lung cancer	Imaging, PDT, and PTT	*In vitro*	Chlorin e6	NIR fluorescence imaging	GO–HA–Ce6
Rong et al. (2014)	Breast cancer	Imaging and PDT	*In vitro, in vivo, and ex vivo*	HPPH	PET imaging, (NIR) fluorescence imaging	GO-PEG-HPPH
Zhou et al. (2014)	Lung cancer	PDT and drug delivery	*In vitro*	Hypocrellin A and Camptothecin	–	HA/SN-38/GO
Gollavelli and Ling (2014)	Cervical cancer	Imaging, PDT, and PTT	*In vitro*	–	Fluorescence imaging and MRI	MFG (magnetic and fluorescent graphene)
Ge et al. (2014)	Cervical, breast cancer	Imaging and PDT	*In vitro and in vivo*	–	Fluorescence imaging	NGs-QDs
Yan et al. (2015a)	Lung cancer	Imaging, PDT, and PTT	*In vitro and in vivo*	DVDMS	Fluorescence imaging and PAI	GO-PEG-DVDMS
Wu et al. (2015)	Breast cancer	Imaging, PDT, PTT, and drug delivery	*In vitro*	Indocyanine green	NIR fluorescence imaging	pGO-CuS/ICG
Yan et al. (2015b)	Brain cancer	Imaging, PDT and drug delivery	*In vitro, in vivo, and ex vivo*	DVDMS	Fluorescence imaging	GO-PEG-DVDMS
Kim et al. (2015)	Cervical cancer	Imaging, PDT, and PTT	*In vitro*	Au	Raman Bioimaging	PEG-Au@GON NPs
Luo et al. (2016)	Lung cancer	Imaging, PDT, and PTT	*In vitro and in vivo*	–	Fluorescence confocal microscope NIR fluorescence and thermal imaging	NGO-808
Kalluru et al. (2016)	Melanoma	Imaging, PDT and PTT	*In vivo*	–	Fluorescence imaging	GO-PEG-folate
Wo et al. (2016)	Esophageal squamous carcinoma	PDT, PTT, drug delivery, and magneto-mechanical therapy	*In vitro*	Doxorubicin	–	HMNS/SiO2/GQDs-DOX
Wu et al. (2017)	Breast cancer	Imaging, PDT, and PTT	*In vitro and in vivo*	Chlorin e6	CLSM, thermal/PT imaging	GO/AuNS-PEG and GO/AuNS-PEG/Ce6
Gulzar et al. (2018)	Liver and cervical cancer	Imaging, PDT, and PTT	*In vitro, in vivo, and ex vivo*	Chlorin e6	UCL imaging	NGO-UCNP-Ce6 (NUC)

The 19 selected studies were characterized on the basis of different type of cancer, application, model, drug/PS, imaging method and material.

2018). Studies in the field of theranostics started by using GBMs as delivery vehicles for both PS and imaging agent (Sahu et al., 2013; Gollavelli and Ling, 2014), paving the way to the following research for a more detailed exploration of nanotechnology-based PDT in cancer theranostics. Graphene has been shown to adsorb light in the near infrared (NIR) region, allowing its potential application for cancer phototherapy to be evaluated both *in vivo* and *in vitro* (Cho et al., 2013; Sahu et al., 2013; Wang et al., 2013; Gollavelli and Ling, 2014; Rong et al., 2014; Kim et al., 2015; Wu et al.,

2015, 2017; Yan et al., 2015a; Kalluru et al., 2016; Luo et al., 2016; Wo et al., 2016; Gulzar et al., 2018).

Moreover, it has been demonstrated, both in cell and animal models, that GBMs exhibit several advantages for drug delivery, giving the possibility of high drug loading efficiency, controlled drug release and tumor-targeted drug delivery (Bitounis et al., 2013; Yang et al., 2016; Zhang et al., 2016, 2017). Indeed, different biomolecules, such as DNA, microRNA (miRNA), short interfering RNA (siRNA), and chemotherapeutic drugs can be loaded onto the surface of these materials for gene transfection

FIGURE 3 | Overview of graphene-based PDT theranostics. Percentages of manuscripts (19 papers) on the basis of **(A)** type of applications combined with PDT, **(B)** model used for the study (*in vivo* or *in vitro*), **(C)** type of cancer studied.
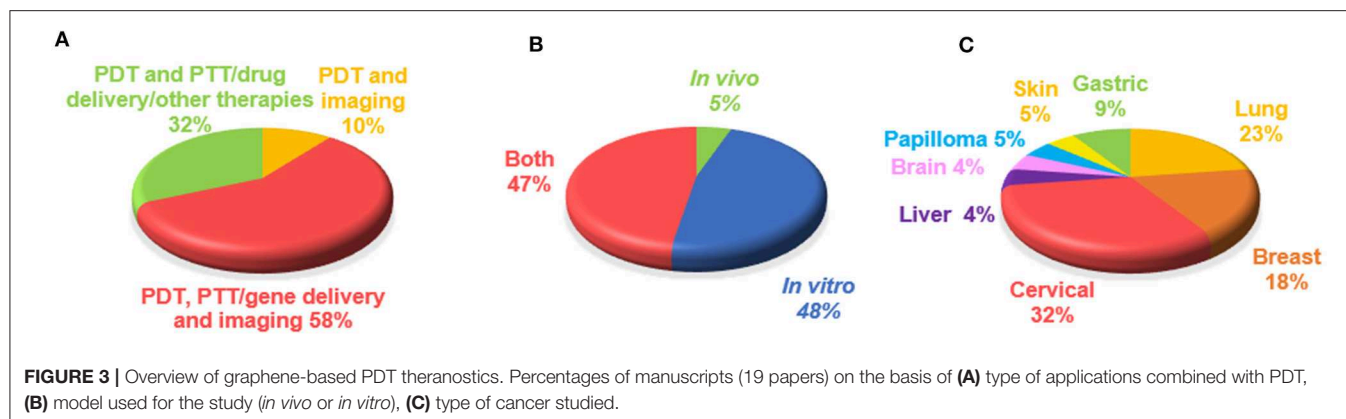
and drug delivery (Huang et al., 2011; Tian et al., 2011; Zhou et al., 2014; Yan et al., 2015b; Wo et al., 2016; Wu et al., 2017). GBMs and MXenes are also suitable for imaging purposes. In particular, GO-based nanoplatforms show great potential exploitable for imaging purposes, thanks not only to the efficient quenching properties of GO toward several fluorescent moieties, including dyes, quantum dots, and conjugated polymers, but also to its ability to improve their stability, distribution, biocompatibility, and photodynamic efficiency (Yan et al., 2015b). Other materials, such as NGO sheets, have a photoluminescent emission in the visible and infrared regions (Sun et al., 2008). This intrinsic photoluminescence (PL) can be exploited for little background-NIR live cell imaging (Sun et al., 2008). GQDs exhibit multiple properties, ranging from their broad absorption in the visible and NIR light range, their good aqueous dispersibility, deep-red emission, high pH and photo-stability up to their positive biocompatibility. In addition, GQDs display a relevant $^1O_2$ generation yield, beyond 1.3 (almost double compared to the other PDT agents studied in literature). Among the various unique properties, GQDs also present an up-conversion PL (Zhu et al., 2012a,b; Feng et al., 2017), ranging from blue to yellow colors (Li et al., 2013). Due to all their properties, GQDs are able to behave as a multifunctional nanoplatform for the theranostic combination of imaging and highly efficient *in vivo* PDT (Ge et al., 2014).

For these reasons, scientists attempted to exploit these therapeutic and imaging potentialities of GBMs in cancer theranostics to achieve targeted cancer cell killing as well as less impairment of healthy cells. An example of PDT based on graphene for combined applications in cancer theranostic is reported in **Figure 4**.

Combined Therapy: PDT and Drug Delivery/PTT

The development of outstanding nanoplatforms leveraging PDT and synergistic therapies, based on drug delivery and PTT, is currently being extensively investigated for cancer treatment. In one of the earliest works showing the promise of GBMs in PDT, in 2011, Tian et al. loaded polyethylene glycol (PEG)-functionalized GO with the PS Ce6 *via* supramolecular π-π stacking (Tian et al., 2011). The material was taken up by cervical

cancer cells and resulted in the formation of ROS under light excitation. Anti-cancer activity of the GO-PEG-Ce6-mediated PDT protocol was more pronounced compared to free Ce6. Also, Huang et al. proposed to use GO as a delivery platform for Ce6 (Huang et al., 2011). Like the above studies, Ce6 was loaded onto folic acid targeted GO through π-π stacking and hydrophobic interactions. The system was shown to kill MGC803 gastric cancer cells upon irradiation. Later, Zhou et al. efficiently loaded GO with the PS hypocrellin B (HB) through π-π stacking interaction. They showed that the material was able to generate $^1O_2$ upon irradiation (Zhou et al., 2012). The same group later reported that the efficiency of PS-loaded GO anticancer activity could be even improved through its combination with chemotherapy (Zhou et al., 2014). In particular, in this study, hypocrellin A and 7-ethyl-10-hydroxycamptothecin were co-loaded on GO and the resulting system induced higher cell death in a lung cancer cell line model when exposed to light, demonstrating that chemotherapy and PDT can work synergistically (Zhou et al., 2012).

Later, in another study, functionalized nano-graphene oxide (NGO) was complexed with a PS methylene blue in order to achieve combined PTT/PDT of cancer (Sahu et al., 2013). Due to the pluronic functionalization, material showed great stability in biological fluids. Authors reported that the nanocomplex was efficiently taken up by cancer cells and able to release methylene blue in a pH-dependent manner. Only when exposed to light did the system showed anti-cancer activity *in vitro*. Following its systemic administration in tumor bearing mice, nanocomplex was shown to accumulate in tumor. When mice were irradiated with NIR light, it caused total ablation of tumor tissue through the combined action of photodynamic and photothermal effects.

These studies suggested the possibility of exploiting the properties of GBMs and MXene to perform an improved PDT in multimodal nanosystems for cancer treatment and paved the way up for future theranostic works.

Theranostics: Imaging and PDT

GBMs can be used not only in PDT protocols and other combined therapies, but also for imaging purpose, allowing the development of new theranostic nanoplatforms for cancer diagnosis and treatment. For example, in 2014, Ge et al.
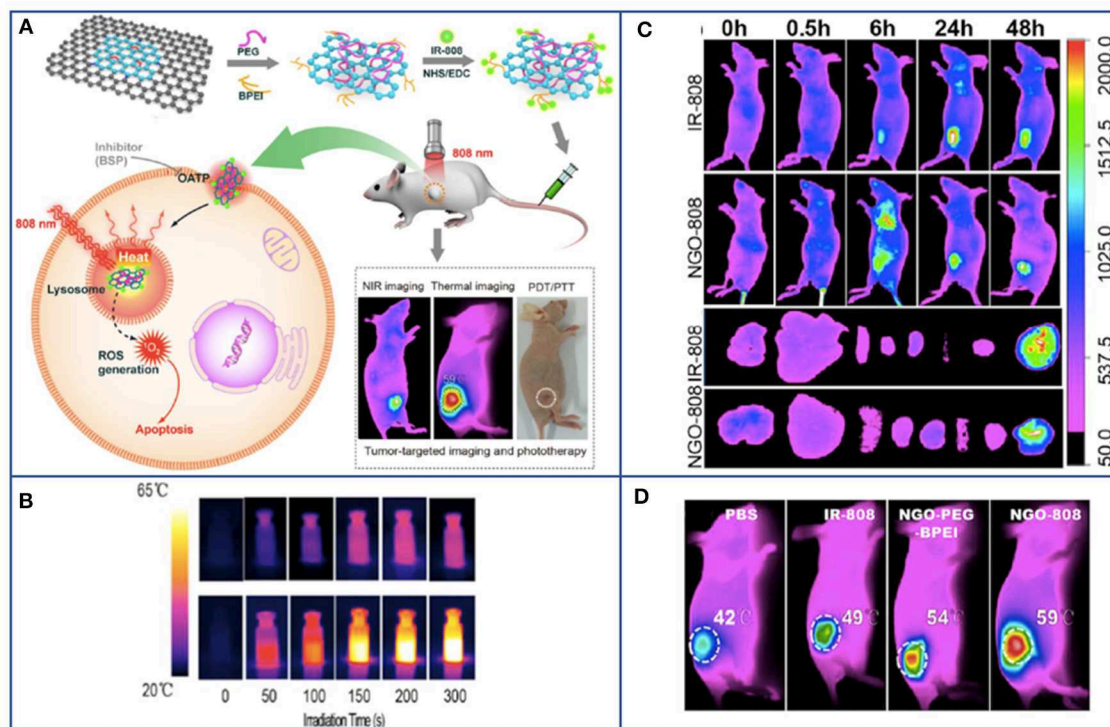
FIGURE 4 | Example of PDT based on graphene for combined and multimodal applications in cancer theranostic. **(A)** Schematic illustration of NGO-808 preparation and combined A549 tumor xenografts-targeted NIR imaging and synergistic phototherapy (PDT and PTT). **(B)** Thermal images showing the higher heat generation of NGO-808 (bottom row) compared to that in blank phosphate-buffered saline (upper row) during 5 min 808 nm laser irradiation. **(C)** *In vivo* NIR imaging of NGO-808 on A549 tumor xenografts. **(D)** *In vivo* combined PDT and PTT on A549 tumor xenografts treated with NGO-808. Adapted with permission from Luo et al. (2016), copyright 2016 American Chemical Society.

exploited the intrinsic properties of graphene quantum dots (GQDs), such as the broad absorption from the visible to the NIR, high pH- and photo-stability, and biocompatibility for imaging purposes (Ge et al., 2014). In this study, GQDs exhibited a massive $^1O_2$ generation yield, making them efficient multifunctional nanoplatforms for *in vivo* simultaneous imaging and extremely efficient PDT of different types of cancer, including skin melanoma and tumors located near the skin. During the same year, Rong et al. identified PEG-functionalized GO as a suitable nanoplatform to increase PDT efficacy and improve long-term survival after treatment (Rong et al., 2014). This was obtained mainly thanks to the ability of the GO-based nanotool to serve as a carrier for the PS agent HPPH, increasing its accumulation to the cancer site. In their *in vivo* studies, the distribution and delivery were traced through fluorescent imaging and positron emission tomography (PET) by the ^{64}Cu radiolabeling of HPPH. Compared to free HPPH, GO-PEG-HPPH enhanced the photodynamic cancer cell killing ability thanks to HPPH's improved tumor delivery.

Theranostics: Imaging, PDT, and Drug Delivery

In a study directed against lung cancer, a novel photo-theranostic platform based on sinoporphyrin sodium (DVDMS) loaded on

PEGylated GO was investigated (Yan et al., 2015a). The GO-PEG carrier improved the loaded PS DVDMS fluorescence through intramolecular charge transfer and facilitated tumor accumulation efficiency of DVDMS by enhanced permeability and retention effect. The NIR absorption of GO was enhanced by DVDMS, leading to improved photoacoustic imaging and PTT. The *in vivo* intravenous injection of low doses of GO-PEG (1 mg/kg) and of DVDMS (2 mg/kg) resulted in 100% tumor eradication.

Theranostics: Imaging, PDT, and PTT

New advances have been made in cancer treatment to establish a targeted protocol that covers the simultaneous application of imaging methods for diagnosis and PTT or PDT for its care. The theranostic progress made by the early studies led to the development of new combined protocols involving graphene nanoplatforms for a simultaneous imaging, PTT, and PDT approach. Wang et al. developed a promising integrated probe for UCL image-guided conjunctional PDT/PTT of cancer (Wang et al., 2013). This multifunctional nanoplatform (UCNPs-NGO/ZnPc) was composed of covalently grafted core–shell structured upconversion nanoparticles (UCNPs) with nanographene oxide (NGO) via bifunctional PEG loaded with phthalocyanine (ZnPc). Authors suggested that this

nanoplatform could be used as UCL high contrast imaging probing of cells and whole-body for diagnosis, as well as for PDT causing the formation of cytotoxic $^1O_2$ under light excitation and for PTT, by converting the 808 nm laser energy into thermal energy (Wang et al., 2013). Another promising platform for combined PTT/PDT directed for lung cancer was realized by combining biocompatible HA-conjugated Ce6 with GO (Cho et al., 2013). This dual PTT/PDT enzyme-activatable GO–PS nanoplatform (GO–HA–Ce6) acts as a biologically tunable agent, exploitable for NIR fluorescence imaging and photo-induced cancer therapy (Cho et al., 2013). Another incredible example of graphene-based combined multimodal nanosystem for simultaneous imaging, NIR-induced PTT and PDT was presented by Wu et al. (2017). In this research, all the promising applications of graphene/Au-based nanohybrids have been summed up into one single nanoplatform. They formulated a graphene-Au nanostar hybrid NM (GO/AuNS-PEG) activated by a single wavelength laser-mediated phototheranostic design, based on the loading of Ce6 (GO/AuNS-PEG/Ce6) (Sahu et al., 2013). Gollavelli et al. developed a superparamagnetic graphene-based nanoplatform, so-called MFG-SiNc4, carrying the hydrophobic silicon napthalocyanine bis (trihexylsilyloxide) (SiNc4) PS (Gollavelli and Ling, 2014). The graphene used in the study showed a wide range for NIR absorption (600–1,200 nm). Therefore, the presence of SiNc4, working at any wavelength within this range, facilitated the possibility of single light induced phototherapy. *In vitro* and *in vivo* results have shown that the simultaneous dual modal imaging and PTT/PDT abilities of magnetic fluorescent graphene MFGeSiNc4 achieved a significant cell killing efficacy which was a synergistic effect of PDT and PTT. In 2016, Kalluru et al. reported for the first time that NGO showed single-photon excitation wavelength-dependent photoluminescence in the visible and short NIR region, which could be exploitable for *in vivo* multi-color fluorescence imaging (Kalluru et al., 2016). NGO induced the formation of $^1O_2$ both *in vitro* and *in vivo* for combined PDT and PTT in melanoma. When mice with B16F0 melanoma tumors were irradiated with NIR light at ultra-low doses, their average half-life span was improved. In another study, with the introduction of PS (IR-808) on nanoGO, authors were able to combine NIR imaging synergistically with enhanced PDT and PTT (Luo et al., 2016). Tumors were treated with PEG- and PEI-functionalized NGO-808 and irradiated; apoptosis and necrosis occurred, obtaining as result the complete ablation of the tumor. Moreover, no recurrence was observed after 60 days post-irradiation.
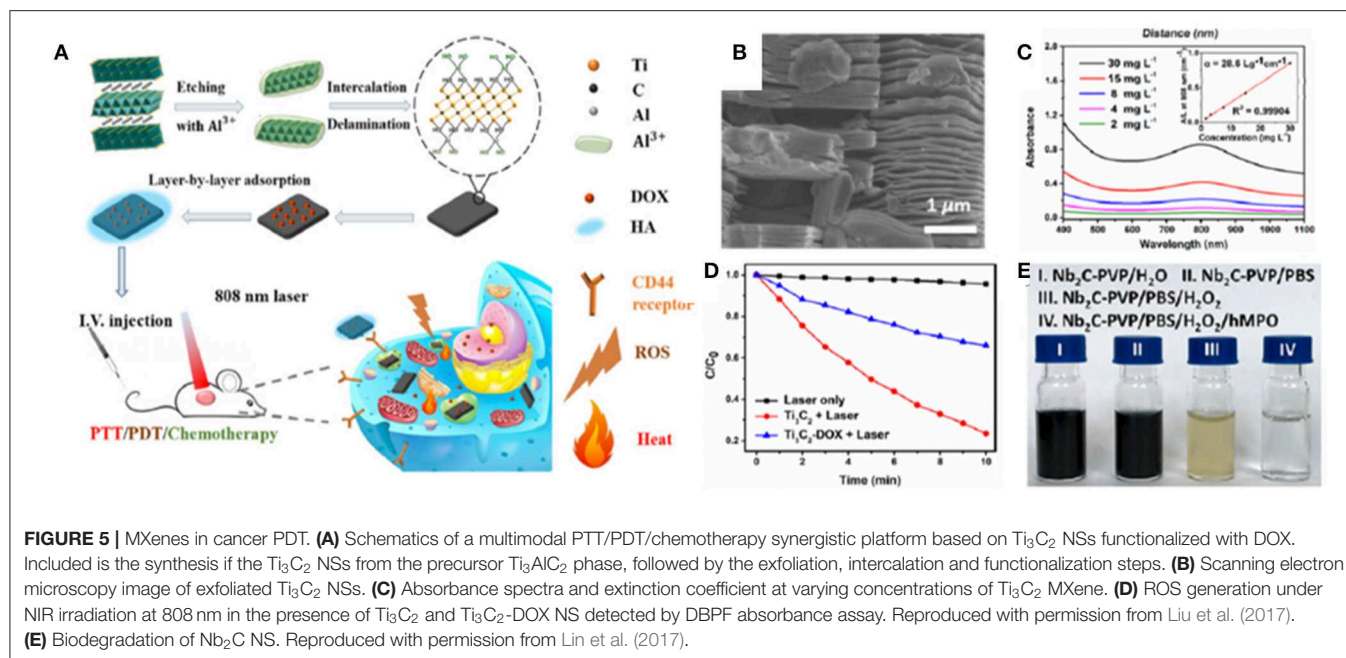
In various studies, PEG was combined with the graphene-based nanoplatforms to improve PDT efficacy or the material biodistribution. For example, in 2015, Kim et al. studied the effects of PEGylated graphene-gold nanoparticles (ZnPc-PEG-Au@GON NPs) that, beside possessing a photothermal effect, positively displayed multiple roles as Raman imaging agents, delivery vehicle of ZnPc, and PS for enhanced combined imaging, PTT, and PDT diagnosis and therapy (Kim et al., 2015). A simultaneous and synergistic combination of PDT and PTT was achieved as well as thermal and fluorescence imaging. GO/AuNS-PEG composite demonstrated to produce

a high photothermal conversion efficiency due to the graphene and gold nanostars enhanced optical absorbance in the NIR range. The PS-assembled graphene/gold nanostar hybrid completely eliminated the EMT6 xenografted tumors thanks to the synergistic *in vivo* cancer cell killing of parallel PDT and PTT under a single NIR laser irradiation (660 nm). Indeed, this study further inspires new graphene-Au nanostar hybrid applications as biocompatible nanoplatforms for imaging-guided (fluorescence/thermal/photoacoustic imaging) multimodal breast cancer therapy (PDT/PTT/chemotherapy/sonodynamic therapy) (Wu et al., 2017).

More recently, Zhang et al. (2019) proposed Mo_2C MXene *ad hoc* synthesized in the nanosphere (NSph) topology as a theranostic nanoagent for combined cancer dual therapy (PTT and PDT) and imaging (photoacoustic and computerized tomography). Also in this work, the ROS generation capability was characterized by the modulation of DPBF absorbance at 420 nm under NIR irradiation at 1,064 nm and confirmed by the inhibition of DPBF degradation upon addition of the ROS quencher NaN_3. In addition, synergistic PTT and PDT on human liver carcinoma cells (HepG2) *in vitro* revealed more than 80% of apoptotic cells in a dose-dependent manner, confirming the critical contribution of ROS generation to the efficacy of the Mo_2C-mediated PTT/PDT synergistic therapy. *In vivo* antitumor efficacy tested 14 days post-treatment in HepG2 tumor bearing mice showed complete tumor ablation and lack of regrowth after 10-min NIR exposure in the presence of Mo_2C pre-injected into the tumor, whereas control animals, either non-irradiated or irradiated without Mo_2C, showed a 4-fold increase in tumor volume. Hematologic, body weight, and post-mortem histological analysis of explanted organ tissue supported the safety of Mo_2C NSph as an injectable PTA for cancer theranostics.

Theranostics: Imaging, PDT, Drug Delivery, and PTT

A low number of studies were carried to evaluate the use of GBMs and MXenes for simultaneous imaging, PDT, drug delivery, and PTT. In 2015, a NIR photo-triggered drug delivery system pGO-CuS/IndoCyanine Green (ICG) exhibited high efficacy of photothermal conversion, being a perfect candidate for highly efficient controlled theranostic applications (i.e., bimodal PDT and PTT therapy plus NIR imaging for a broad range of deep-seated cancer tissues) (Wu et al., 2015). This promising nanoplatform displayed optimal stability, high loading efficiency of ICG, good photon energy conversion to heat and significant $^1O_2$ generation yield under NIR laser treatment. It is able, via passive transmembrane pathway, to readily reach the cellular inner cytoplasm as a potent synergic platform for PDT and PTT, killing specifically cancer cells by the appropriate tuning the two NIR light irradiations (Wu et al., 2015). Later, Wo et al. developed a multimodal system which was able to enclose four different synergetic anti-cancer activities: photodynamic toxicity, photothermal damage, chemotherapy, and magnetic field-mediated mechanical stimulation (Wo et al., 2016). The authors formed liposome-stabilized doxorubicin (DOX)-loaded

FIGURE 5 | MXenes in cancer PDT. **(A)** Schematics of a multimodal PTT/PDT/chemotherapy synergistic platform based on Ti_3C_2 NSs functionalized with DOX. Included is the synthesis if the Ti_3C_2 NSs from the precursor Ti_3AlC_2 phase, followed by the exfoliation, intercalation and functionalization steps. **(B)** Scanning electron microscopy image of exfoliated Ti_3C_2 NSs. **(C)** Absorbance spectra and extinction coefficient at varying concentrations of Ti_3C_2 MXene. **(D)** ROS generation under NIR irradiation at 808 nm in the presence of Ti_3C_2 and Ti_3C_2-DOX NS detected by DBPF absorbance assay. Reproduced with permission from Liu et al. (2017). **(E)** Biodegradation of Nb_2C NS. Reproduced with permission from Lin et al. (2017).

magnetic nanospheres, aimed at enhancing anti-cancer activity through magnetic field-mediated mechanical force and NIR laser irradiation.

Liu et al. (2017) first demonstrated the feasibility of Ti_3C_2 MXene nanosheets (NSs) as PSs for PDT in a PTT/PDT/chemo-synergistic platform (**Figures 5A–C**). ROS generation in the presence of Ti_3C_2 NSs in aqueous suspensions was investigated using 1,3-diphenyli-sobenzofuran (DPBF) as the singlet $^1O_2$ detector. Upon NIR irradiation of Ti_3C_2 NSs at 808 nm for 10 min, DPBF showed a ∼80% decrease in absorbance at 420 nm, consequently revealing the generation of $^1O_2$ (**Figure 5D**). Similar ROS generation capability, although less pronounced, was observed when Ti_3C_2 functionalized with DOX was exposed to the same irradiation protocol, thus enabling the development of combined PDT/chemotherapeutics. The exact mechanism of $^1O_2$ generation in Ti_3C_2 is still unclear and warrants further investigations. The authors attribute it to the energy transfer of photoexcited electrons from Ti_3C_2 to triplet oxygen (ground state oxygen, $^3O_2$), a mechanism similar to the photodynamic behavior of GQDs (Ge et al., 2014) and black phosphorous (Wang et al., 2015). The localized surface plasmonic resonance (LSPR) effect might also play a role similar to what has been reported for metals, like gold nanoparticles. In these systems, the efficiency of energy transfer is enhanced when the particles are in the aggregated state. Thus, the high surface area of Ti_3C_2 might be particularly favorable for LSPR. Compared to the individual therapeutic modalities, synergistic PTT/PDT/chemotherapy with Ti_3C_2-DOX led to significant improvements in therapeutic efficacy and recurrence outcomes against human colon carcinoma (HCT-116) *in vivo* in tumor-bearing mice. The abundant surface termination in the Ti_3C_2 NSs also enables specific functionalization to selectively target

species in the tumor microenvironment. For example, coating Ti_3C_2-DOX with hyaluronic acid increased colloidal stability and actively targeted the surface protein CD44$^+$ overexpressed in breast cancer cells.

Theranostic Outcomes of the *in vivo* Studies

By analyzing the *in vivo* outcomes, it is possible to conclude that all the studies presented very promising results for the use of these materials in cancer theranostics, achieving a significant (Kalluru et al., 2016; Gulzar et al., 2018) or even total cancer ablation without tumor recurrence (Sahu et al., 2013; Wang et al., 2013; Ge et al., 2014; Rong et al., 2014; Yan et al., 2015a,b; Luo et al., 2016; Wu et al., 2017), as shown in **Table 3**. Among all the materials, GO-based nanoplatforms were the most investigated (5 *in vivo* studies out of 9), followed by NGO and GQDs (3 and 1 studies out of 9, respectively). Since GO and NGO can act both as a photothermal agent and a delivery carrier for PSs, most the works exploited its theranostic potential for combined PDT and PTT. This strategy led to total cancer ablation between 14 and 21 days.

Thanks to the to the quantum confinement effect related to their small dimensions, NGO and GQDs possess non-blinking photoluminescence and photostability. Therefore, these materials have been explored mainly for PDT in association with UCL imaging (Luo et al., 2016; Gulzar et al., 2018) or fluorescence imaging (Ge et al., 2014; Luo et al., 2016). In particular, two studies investigated NGO for imaging-guided PDT in combination with PTT (Luo et al., 2016; Gulzar et al., 2018), achieving significant (Gulzar et al., 2018) or even total (Luo et al., 2016) cancer ablation between 14 and 16 days.

TABLE 3 | Comparison of nanomaterials and laser powers used for PDT-based cancer theranostic applications and relative outcomes *in vivo*.

References	Tumor	Laser wavelength	Laser power intensity	Irradiation time	Starting material	Combined therapy	Outcome (number of days after the treatment)
Sahu et al. (2013)	Cervical cancer	650 nm	0.1 W/cm^2	10 min (one time)	NGO	PTT	Total ablation (15 days)
Ge et al. (2014)	Cervical, breast cancer	400–800 nm	0.1 W/cm^2	10 min (two times)	GQDs	–	Total ablation (17 days)
Rong et al. (2014)	Breast cancer	671 nm	90.0 W/cm^2, 0.1 W/cm^2	20 min (one time)	GO	–	Total ablation (60 days)
Yan et al. (2015a)	Lung cancer	630 nm	16.0 W/cm^2	5 min (one time)	GO	PTT	Total ablation (14 days)
Yan et al. (2015b)	Brain cancer	630 nm	156.0 W/cm^2	– (one time)	GO	Drug delivery	Total ablation (10 days)
Luo et al. (2016)	Lung cancer	808 nm	1.0 W/cm^2	5 min (one time)	NGO	PTT	Total ablation (16 days)
Wu et al. (2017)	Breast cancer	660 nm	0.8, 1.2 and 2.0 W/cm^2	10 min (one time)	GO	PTT	Total ablation (21 days)
Gulzar et al. (2018)	Liver and cervical cancer	808 nm	0.7 W/cm^2	10 min (one time)	NGO	PTT	Partial ablation (14 days)
Kalluru et al. (2016)	Melanoma	808 nm	0.2 W/cm^2	8–10 min (every day)	GO	PTT	Partial ablation (14 days)

Finally, only one study evaluated the suitability of GQDs for PDT-based cancer theranostics based on PDT (Ge et al., 2014). The main advantage of GQDs is represented by their ability to serve as imaging tools and perform better than conventional PDT agents in terms of $^1O_2$ quantum yield. However, since this result is achieved in the visible light region, the suitability of these tools appears to be limited to superficial tumors, such as skin cancer.

FUTURE PERSPECTIVES

Following its discovery, graphene has attracted attention of the society in general with several expectations from the public in the context of nanomedicine (Sechi et al., 2014), and the turn of MXene is already on the stage.

Thanks to their chemical, physical and biological properties, graphene and MXene have shown to be powerful tools for PDT in cancer theranostics. Both 2D nanosystems allow the simultaneous application of non-invasive bioimaging and therapeutic strategies that can be associated with PDT, including photothermal therapy, magnetic therapy, and remotely controlled chemotherapy by drug and gene delivery.

The suitability of these promising materials as photothermal agents for tumor therapy and imaging is due to their ability to adsorb light in the NIR region. Moreover, the easy functionalization capability, thanks to their high surface-to-volume ratio, allows the loading of photosensitizer agents on these nanoplatforms, enhancing the targeting and efficiency, resulting in a more localized action, characterized by reduced side effects and improved therapy.

In addition, the combination with chemotherapeutic drugs loaded on these 2D NMs can work synergistically with PDT, leading to an improved anticancer activity. Furthermore, the

functionalization with other agents, such as Au, endows them with a high photothermal conversion efficiency that can further enhance their optical absorbance in the NIR range. Beside the therapeutic efficiency of these nanoplatforms, their stability in aqueous matrix can also be improved thanks to their ability to be loaded with hydrophilic molecules, such as PEG. This aspect is of great interest in view of their intravenous administration, since most PSs are hydrophobic and could easily aggregate in biological fluids, with a consequent decrease in their quantum yield and increase in immune responses (Sibani et al., 2008; Kashef et al., 2017).

However, despite the encouraging promising results, there is still an extensive work to be accomplished to further clarify and prove the potentialities of GBM- and MXene-based PDT for cancer theranostics. First of all, for the translation of these 2D materials into clinical application, the assessment of their long-term toxicity is required to fully characterize their safety profile.

The potential widespread use of graphene and MXene-based materials for commercial purposes will favor their interactions with biological and environmental components. Therefore, several studies have been carried out to define the cyto- and bio-compatibility of these nanomaterials *in vitro* and *in vivo* (Fadeel et al., 2018a; Lin et al., 2018). These studies, particularly for graphene, state that the toxicity depends on the complex interaction of several physiochemical properties, such as shape, size, functional groups, oxidative state, dispersion state, synthesis methods, exposure times, as well as route and dose of administration. Moreover, graphene can contain several chemical contaminants and impurities coming from synthesis (Liao et al., 2018) and post-synthesis processing steps that can lead to graphene structure disruption and smaller carbonaceous debris production. Therefore, these confounding aspects may elicit variable toxicity responses (Li and Boraschi, 2016).

In this view, various studies have been performed to better understand and predict GBM toxicity and their potential impact on the immune system which governs every aspect of our health, including the way we react to therapies in cancer (Orecchioni et al., 2014, 2016a,b, 2017; Russier et al., 2017; Fadeel et al., 2018b). The obtained results have highlighted the importance of material characterization as a key element for hazard assessment as well as bio and immune compatibility. Therefore, biomedical scientists should not consider graphene as a single material but as a complex class of materials, taking into account the role of physicochemical properties (e.g., lateral dimension, carbon oxygen ratio and number of layers) while assessing the biological effects (Fadeel et al., 2018a). Concerning MXene, preliminary evaluations of Ti_3C_2 MXene biocompatibility have not evidenced apoptosis or signs of cytotoxicity in vitro in cancer cells (Dai et al., 2017; Lin et al., 2017; Liu et al., 2017; Han et al., 2018) and neurons (Driscoll et al., 2018). Ti_3C_2 NSs injected in vivo in the blood stream appear to be either excreted in the urine via physiologic renal clearance pathways or retained in the tumor site via the enhanced permeability and retention (EPR) effect, without accumulating in the major organs. Similar findings have been reported for the cyto-biocompatibility and systemic safety of Ta_4C_3 (Dai et al., 2017; Liu et al., 2018) and Nb_2C MXenes (Lin et al., 2017). Despite all these data on MXene biocompatibility, the assessment of its potential toxicity is still at a very early stage. For both types of materials, new studies on their biomedical application should take into consideration general requirements with respect to Minimum Information Reporting in Bio–Nano Experimental Literature (MIRIBEL) and other key considerations on the issue of transparency and reproducibility in nanomedicine, such as that the choice of material physical-chemical characteristics should be tailored for their intended use (Faria et al., 2018; Leong et al., 2019). That consideration is even more valid in the context of cancer theranostics were the starting properties of the material can make the difference in the successful application of new 2D material-based cancer treatment. Another key point is related to the materials' fine characterization and reproducibility, which should be considered in every work based on engineered nanomaterials as a key aspect to avoid hype around the potential translation into clinic (DeLoid et al., 2017).

Beyond the toxicity context and physical-chemical material choice, other knowledge gaps need to be filled to shed light on the actual potentialities of these 2D NMs for cancer theranostics and PDT in particular. Indeed, the understanding of these aspects cannot overlook the elucidation of fundamental mechanisms underlying the ROS generation elicited by these materials, which is at the basis of PDT. Moreover, more efforts should be directed into a deeper understanding of the nanoparticle-tumor interaction, the possibility of a scaled-up synthesis, and the development of regulatory theranostic protocols in order to determine a personalized therapy framework.

Finally, controlling the lifetime of the nanoagents in the body and mitigating the risks related to retention of NMs and their byproducts could significantly advance NM-based theranostic platforms in the translational pipeline (Orecchioni et al., 2015). The complete clearance from the body, along with the biodegradation of 2D nanostructures needs to be assessed for these materials in order to be translated into clinical settings (Andón et al., 2013; Bhattacharya et al., 2013; Farrera et al., 2014; Kurapati et al., 2018; Mukherjee et al., 2018; Martín et al., 2019). Although GBMs can be considered structurally persistent, it has been proved that oxidative enzymes (i.e., peroxidases) are capable of catalyzing the GO degradation in vitro and in vivo (Bai et al., 2014; Kurapati et al., 2018; Mukherjee et al., 2018). Nb_2C MXene NSs can be engineered to degrade through an active biodegradation scheme that leverages human myeloperoxidase (hMPO), a free-radical species generating enzyme expressed by neutrophils to carry out their antimicrobial activity (Lin et al., 2017). In the presence of hydrogen peroxide (H_2O_2), hMPO generates hypochlorous acid and reactive radical intermediates, which degrade polymers and carbon-based materials. The incubation of Nb_2C NSs in hMPO and H_2O_2 enriched medium for 24 h has been reported to cause the complete degradation and disappearance of NSs, thus demonstrating in vitro the feasibility of this enzyme-triggered degradation route for MXenes (**Figures 5D,E**).

Overall, this review has shown that significant advances in the theranostic use of graphene-based materials and MXenes have been made. However, three main aspects should be carefully taken more into account: (i) the potential not-targeted toxicity, (ii) a choice of physical-chemical material characteristics prior their assessment for cancer therapy, (iii) a fine characterization, and (iv) the assessment of their potential biodegradability. Despite that knowledge gaps in the field still need to be filled, virtuous perspectives for GBMs and MXene were evidenced from over 30 works here analyzed, standing out as the most promising 2D NMs intended to change the patterns of conventional cancer theranostics, guaranteeing new protocols for personalized therapies.

AUTHOR CONTRIBUTIONS

LD proposed the topic of the review and designed and coordinated the work. LD, AY, and FV wrote the manuscript with the help from AG, LF, and AK. AG, LF, and AK investigated the literature and prepared the figures with the help of LD, AY, and FV. DB and BZ critically revised the manuscript. All authors discussed and revised the manuscript.

ACKNOWLEDGMENTS

REFERENCES

Agostinis, P., Berg, K., Cengel, K. A., Foster, T. H., Girotti, A. W., Gollnick, S. O., et al. (2011). Photodynamic therapy of cancer: an update. *CA Cancer J. Clin.* 61, 250–281. doi: 10.3322/caac.20114

Anasori, B., Lukatskaya, M. R., and Gogotsi, Y. (2017). 2D metal carbides and nitrides (MXenes) for energy storage. *Nat. Rev. Mater.* 2:16098. doi: 10.1038/natrevmats.2016.98

Andón, F. T., Kapralov, A. A., Yanamala, N., Feng, W., Baygan, A., Chambers, B. J., et al. (2013). Biodegradation of single-walled carbon nanotubes by eosinophil peroxidase. *Small* 9, 2721–2729, 2720. doi: 10.1002/smll.201202508

Augustine, S., Singh, J., Srivastava, M., Sharma, M., Das, A., and Malhotra, B. D. (2017). Recent advances in carbon based nanosystems for cancer theranostics. *Biomater. Sci.* 5, 901–952. doi: 10.1039/C7BM00008A

Avitabile, E., Bedognetti, D., Ciofani, G., Bianco, A., and Delogu, L. G. (2018). How can nanotechnology help the fight against breast cancer? *Nanoscale* 10, 11719–11731. doi: 10.1039/C8NR02796J

Bacellar, I. O. L., Tsubone, T. M., Pavani, C., and Baptista, M. S. (2015). Photodynamic efficiency: from molecular photochemistry to cell death. *Int. J. Mol. Sci.* 16, 20523–20559. doi: 10.3390/ijms160920523

Bai, H., Jiang, W., Kotchey, G. P., Saidi, W. A., Bythell, B. J., Jarvis, J. M., et al. (2014). Insight into the mechanism of graphene oxide degradation via the photo-fenton reaction. *J. Phys. Chem. C* 118, 10519–10529. doi: 10.1021/jp503413s

Bhattacharya, K., Andón, F. T., El-Sayed, R., and Fadeel, B. (2013). Mechanisms of carbon nanotube-induced toxicity: focus on pulmonary inflammation. *Adv. Drug Deliv. Rev.* 65, 2087–2097. doi: 10.1016/j.addr.2013.05.012

Bitounis, D., Ali-Boucetta, H., Hong, B. H., Min, D.-H., and Kostarelos, K. (2013). Prospects and challenges of graphene in biomedical applications. *Adv. Mater. Weinheim* 25, 2258–2268. doi: 10.1002/adma.201203700

Boukhvalov, D. W., and Katsnelson, M. I. (2008). Chemical functionalization of graphene with defects. *Nano Lett.* 8, 4373–4379. doi: 10.1021/nl802234n

Chen, Y., Tan, C., Zhang, H., and Wang, L. (2015). Two-dimensional graphene analogues for biomedical applications. *Chem. Soc. Rev.* 44, 2681–2701. doi: 10.1039/C4CS00300D

Cho, Y., Kim, H., and Choi, Y. (2013). A graphene oxide–photosensitizer complex as an enzyme-activatable theranostic agent. *Chem. Commun.* 49, 1202–1204. doi: 10.1039/c2cc36297j

Dai, C., Chen, Y., Jing, X., Xiang, L., Yang, D., Lin, H., et al. (2017). Two-dimensional tantalum carbide (MXenes) composite nanosheets for multiple imaging-guided photothermal tumor ablation. *ACS Nano* 11, 12696–12712. doi: 10.1021/acsnano.7b07241

DeLoid, G. M., Cohen, J. M., Pyrgiotakis, G., and Demokritou, P. (2017). Preparation, characterization, and *in vitro* dosimetry of dispersed, engineered nanomaterials. *Nat. Protoc.* 12, 355–371. doi: 10.1038/nprot.2016.172

Detty, M. R., Gibson, S. L., and Wagner, S. J. (2004). Current clinical and preclinical photosensitizers for use in photodynamic therapy. *J. Med. Chem.* 47, 3897–3915. doi: 10.1021/jm040074b

Dolmans, D. E. J. G. J., Fukumura, D., and Jain, R. K. (2003). Photodynamic therapy for cancer. *Nat. Rev. Cancer* 3:380. doi: 10.1038/nrc1071

Driscoll, N., Richardson, A. G., Maleski, K., Anasori, B., Adewole, O., Lelyukh, P., et al. (2018). Two-dimensional Ti3C2 MXene for high-resolution neural interfaces. *ACS Nano* 12, 10419–10429. doi: 10.1021/acsnano.8b06014

Er, D., Li, J., Naguib, M., Gogotsi, Y., and Shenoy, V. B. (2014). Ti3C2 MXene as a high capacity electrode material for metal (Li, Na, K, Ca) ion batteries. *ACS Appl. Mater. Interfaces* 6, 11173–11179. doi: 10.1021/am501144q

Fadeel, B., Bussy, C., Merino, S., Vázquez, E., Flahaut, E., Mouchet, F., et al. (2018a). Safety assessment of graphene-based materials: focus on human health and the environment. *ACS Nano* 12, 10582–10620. doi: 10.1021/acsnano.8b04758

Fadeel, B., Farcal, L., Hardy, B., Vázquez-Campos, S., Hristozov, D., Marcomini, A., et al. (2018b). Advanced tools for the safety assessment of nanomaterials. *Nat. Nanotechnol.* 13, 537–543. doi: 10.1038/s41565-018-0185-0

Faria, M., Björnmalm, M., Thurecht, K. J., Kent, S. J., Parton, R. G., Kavallaris, M., et al. (2018). Minimum information reporting in bio–nano experimental literature. *Nat. Nanotechnol.* 13:777. doi: 10.1038/s41565-018-0246-4

Farrera, C., Bhattacharya, K., Lazzaretto, B., Andón, F. T., Hultenby, K., Kotchey, G. P., et al. (2014). Extracellular entrapment and degradation of single-walled carbon nanotubes. *Nanoscale* 6, 6974–6983. doi: 10.1039/c3nr06047k

Feng, L., Wu, Y.-X., Zhang, D.-L., Hu, X., Zhang, J., Wang, P., et al. (2017). A near infrared graphene quantum dots-based two-photon nanoprobe for direct bioimaging of endogenous ascorbic acid in living cells. *Anal. Chem.* 89, 4077–4084. doi: 10.1021/acs.analchem.6b04943

Feng, W., Wang, R., Zhou, Y., Ding, L., Gao, X., Zhou, B., et al. (2019). Ultrathin molybdenum carbide MXene with fast biodegradability for highly efficient theory-oriented photonic tumor hyperthermia. *Adv. Funct. Mater.* 1901942, 1–15. doi: 10.1002/adfm.201901942

Ferreira Dos Santos, A., Raquel Queiroz De Almeida, D., Ferreira Terra, L., Baptista, M., and Labriola, L. (2019). Photodynamic therapy in cancer treatment–an update review. *J. Cancer Metast. Treat.* 5:25. doi: 10.20517/2394-4722.2018.83

Gao, X., Cui, Y., Levenson, R. M., Chung, L. W. K., and Nie, S. (2004). *In vivo* cancer targeting and imaging with semiconductor quantum dots. *Nat. Biotechnol.* 22, 969–976. doi: 10.1038/nbt994

Gao, X., Jang, J., and Nagase, S. (2010). Hydrazine and thermal reduction of graphene oxide: reaction mechanisms, product structures, and reaction design. *J. Phys. Chem. C* 114, 832–842. doi: 10.1021/jp909284g

Ge, J., Lan, M., Zhou, B., Liu, W., Guo, L., Wang, H., et al. (2014). A graphene quantum dot photodynamic therapy agent with high singlet oxygen generation. *Nat. Commun.* 5:4596. doi: 10.1038/ncomms5596

Ghidiu, M., Lukatskaya, M. R., Zhao, M. Q., Gogotsi, Y., and Barsoum, M. W. (2015). Conductive two-dimensional titanium carbide "clay" with high volumetric capacitance. *Nature* 516, 78–81. doi: 10.1038/nature13970

Gollavelli, G., and Ling, Y. C. (2014). Magnetic and fluorescent graphene for dual modal imaging and single light induced photothermal and photodynamic therapy of cancer cells. *Biomaterials* 35, 4499–4507. doi: 10.1016/j.biomaterials.2014.02.011

Guan, M., Li, J., Jia, Q., Ge, J., Chen, D., Zhou, Y., et al. (2016). A versatile and clearable nanocarbon theranostic based on carbon dots and gadolinium metallofullerene nanocrystals. *Adv. Healthc. Mater.* 5, 2283–2294. doi: 10.1002/adhm.201600402

Gulzar, A., Xu, J., Yang, D., Xu, L., He, F., Gai, S., et al. (2018). Nano-graphene oxide-UCNP-Ce6 covalently constructed nanocomposites for NIR-mediated bioimaging and PTT/PDT combinatorial therapy. *Dalton Trans.* 47, 3931–3939. doi: 10.1039/C7DT04141A

Han, X., Huang, J., Lin, H., Wang, Z., Li, P., and Chen, Y. (2018). 2D ultrathin MXene-based drug-delivery nanoplatform for synergistic photothermal ablation and chemotherapy of cancer. *Adv. Healthc. Mater.* 306, 1701313–1701394. doi: 10.1002/adhm.201701394

Henderson, B. W., Gollnick, S. O., Snyder, J. W., Busch, T. M., Kousis, P. C., Cheney, R. T., et al. (2004). Choice of oxygen-conserving treatment regimen determines the inflammatory response and outcome of photodynamic therapy of tumors. *Cancer Res.* 64, 2120–2126. doi: 10.1158/0008-5472.CAN-03-3513

Huang, P., Xu, C., Lin, J., Wang, C., Wang, X., Zhang, C., et al. (2011). Folic acid-conjugated graphene oxide loaded with photosensitizers for targeting photodynamic therapy. *Theranostics* 1, 240–250. doi: 10.7150/thno/v01p0240

Huang, Z. (2005). A review of progress in clinical photodynamic therapy. *Technol. Cancer Res. Treat.* 4, 283–293. doi: 10.1177/153303460500400308

James, D. K., and Tour, J. M. (2013). Graphene: powder, flakes, ribbons, and sheets. *Acc. Chem. Res.* 46, 2307–2318. doi: 10.1021/ar300127r

Ji, D.-K., Ménard-Moyon, C., and Bianco, A. (2019). Physically-triggered nanosystems based on two-dimensional materials for cancer theranostics. *Adv. Drug Deliv. Rev.* 138, 211–232. doi: 10.1016/j.addr.2018.08.010

Kalluru, P., Vankayala, R., Chiang, C.-S., and Hwang, K. C. (2016). Nano-graphene oxide-mediated *in vivo* fluorescence imaging and bimodal photodynamic and photothermal destruction of tumors. *Biomaterials* 95, 1–10. doi: 10.1016/j.biomaterials.2016.04.006

Kashef, N., Huang, Y.-Y., and Hamblin, M. R. (2017). Advances in antimicrobial photodynamic inactivation at the nanoscale. *Nanophotonics* 6, 853–879. doi: 10.1515/nanoph-2016-0189

Kim, J., Lee, J., Son, D., Choi, M. K., and Kim, D.-H. (2016). Deformable devices with integrated functional nanomaterials for wearable electronics. *Nano Converg.* 3:4. doi: 10.1186/s40580-016-0062-1

Kim, Y.-K., Na, H.-K., Kim, S., Jang, H., Chang, S.-J., and Min, D.-H. (2015). One-pot synthesis of multifunctional Au@graphene oxide nanocolloid core@shell nanoparticles for Raman bioimaging, photothermal, and photodynamic therapy. *Small* 11, 2527–2535. doi: 10.1002/smll.201402269

Korbelik, M. (2006). PDT-associated host response and its role in the therapy outcome. *Lasers Surg. Med.* 38, 500–508. doi: 10.1002/lsm.20337

Kuila, T., Bose, S., Mishra, A., Khanra, P., Kim, N. H., and Lee, J. (2012). Chemical functionalization of graphene and its applications. *Prog. Mater. Sci.* 57, 1061–1105. doi: 10.1016/j.pmatsci.2012.03.002

Kurapati, R., Mukherjee, S. P., Martín, C., Bepete, G., Vázquez, E., Pénicaud, A., et al. (2018). Degradation of single-layer and few-layer graphene by neutrophil myeloperoxidase. *Angew. Chem. Int. Ed. Engl.* 57, 11722–11727. doi: 10.1002/anie.201806906

Leong, H. S., Butler, K. S., Brinker, C. J., Azzawi, M., Conlan, S., Dufés, C., et al. (2019). On the issue of transparency and reproducibility in nanomedicine. *Nat. Nanotechnol.* 14, 629–635. doi: 10.1038/s41565-019-0496-9

Li, L., Wu, G., Yang, G., Peng, J., Zhao, J., and Zhu, J.-J. (2013). Focusing on luminescent graphene quantum dots: current status and future perspectives. *Nanoscale* 5, 4015–4039. doi: 10.1039/c3nr33849e

Li, Y., and Boraschi, D. (2016). Endotoxin contamination: a key element in the interpretation of nanosafety studies. *Nanomedicine (Lond).* 11, 269–287. doi: 10.2217/nnm.15.196

Liao, C., Li, Y., and Tjong, S. C. (2018). Graphene nanomaterials: synthesis, biocompatibility, and cytotoxicity. *Int. J. Mol. Sci.* 19:E3564. doi: 10.3390/ijms19113564

Lin, H., Chen, Y., and Shi, J. (2018). Insights into 2D MXenes for versatile biomedical applications: current advances and challenges ahead. *Adv. Sci.* 5:1800518. doi: 10.1002/advs.201800518

Lin, H., Gao, S., Dai, C., Chen, Y., and Shi, J. (2017). A two-dimensional biodegradable niobium carbide (MXene) for photothermal tumor eradication in NIR-I and NIR-II biowindows. *J. Am. Chem. Soc.* 139, 16235–16247. doi: 10.1021/jacs.7b07818

Lin, H., Wang, X., Yu, L., Chen, Y., and Shi, J. (2016). Two-dimensional ultrathin MXene ceramic nanosheets for photothermal conversion. *Nano Lett.* 17, 384–391. doi: 10.1021/acs.nanolett.6b04339

Liu, G., Zou, J., Tang, Q., Yang, X., Zhang, Y., Zhang, Q., et al. (2017). Surface modified Ti3C2 MXene nanosheets for tumor targeting photothermal/photodynamic/chemo synergistic therapy. *ACS Appl. Mater. Interfaces* 9, 40077–40086. doi: 10.1021/acsami.7b13421

Liu, Z., Lin, H., Zhao, M., Dai, C., Zhang, S., Peng, W., et al. (2018). 2D superparamagnetic tantalum carbide composite MXenes for efficient breast-cancer theranostics. *Theranostics* 8, 1648–1664. doi: 10.7150/thno.23369

Lou, P.-J., Jäger, H. R., Jones, L., Theodossy, T., Bown, S. G., and Hopper, C. (2004). Interstitial photodynamic therapy as salvage treatment for recurrent head and neck cancer. *Br. J. Cancer* 91, 441–446. doi: 10.1038/sj.bjc.6601993

Lukatskaya, M. R., Kota, S., Lin, Z., Zhao, M.-Q., Shpigel, N., Levi, M. D., et al. (2017). Ultra-high-rate pseudocapacitive energy storage in two-dimensional transition metal carbides. *Nat. Energy* 2:17105. doi: 10.1038/nenergy.2017.105

Luo, S., Yang, Z., Tan, X., Wang, Y., Zeng, Y., Wang, Y., et al. (2016). Multifunctional photosensitizer grafted on polyethylene glycol and polyethylenimine dual-functionalized nanographene oxide for cancer-targeted near-infrared imaging and synergistic phototherapy. *ACS Appl. Mater. Interfaces* 8, 17176–17186. doi: 10.1021/acsami.6b05383

Luo, Y., Li, Z., Zhu, C., Cai, X., Qu, L., Du, D., et al. (2018). Graphene-like metal-free 2D nanosheets for cancer imaging and theranostics. *Trends Biotechnol.* 36, 1145–1156. doi: 10.1016/j.tibtech.2018.05.012

Mao, S., Pu, H., and Chen, J. (2012). Graphene oxide and its reduction: modeling and experimental progress. *RSC Adv.* 2, 2643–2662. doi: 10.1039/c2ra00663d

Martín, C., Kostarelos, K., Prato, M., and Bianco, A. (2019). Biocompatibility and biodegradability of 2D materials: graphene and beyond. *Chem. Commun.* 55, 5540–5546. doi: 10.1039/C9CC01205B

McManus, D., Vranic, S., Withers, F., Sanchez-Romaguera, V., Macucci, M., Yang, H., et al. (2017). Water-based and biocompatible 2D crystal inks for all-inkjet-printed heterostructures. *Nat. Nanotechnol.* 12, 343–350. doi: 10.1038/nnano.2016.281

Michalet, X., Pinaud, F. F., Bentolila, L. A., Tsay, J. M., Doose, S., Li, J. J., et al. (2005). Quantum dots for live cells, *in vivo* imaging, and diagnostics. *Science* 307, 538–544. doi: 10.1126/science.1104274

Mukherjee, S. P., Gliga, A. R., Lazzaretto, B., Brandner, B., Fielden, M., Vogt, C., et al. (2018). Graphene oxide is degraded by neutrophils and the degradation products are non-genotoxic. *Nanoscale* 10, 1180–1188. doi: 10.1039/C7NR03552G

Naguib, M., Kurtoglu, M., Presser, V., Lu, J., Niu, J., Heon, M., et al. (2011). Two-dimensional nanocrystals produced by exfoliation of Ti3AlC2. *Adv. Mater.* 23, 4248–4253. doi: 10.1002/chin.201152200

Novoselov, K. S., Fal′ko, V. I., Colombo, L., Gellert, P. R., Schwab, M. G., and Kim, K. (2012). A roadmap for graphene. *Nature* 490, 192–200. doi: 10.1038/nature11458

Orecchioni, M., Bedognetti, D., Newman, L., Fuoco, C., Spada, F., Hendrickx, W., et al. (2017). Single-cell mass cytometry and transcriptome profiling reveal the impact of graphene on human immune cells. *Nat. Commun.* 8:1109. doi: 10.1038/s41467-017-01015-3

Orecchioni, M., Bedognetti, D., Sgarrella, F., Marincola, F. M., Bianco, A., and Delogu, L. G. (2014). Impact of carbon nanotubes and graphene on immune cells. *J. Transl. Med.* 12:138. doi: 10.1186/1479-5876-12-138

Orecchioni, M., Cabizza, R., Bianco, A., and Delogu, L. G. (2015). Graphene as cancer theranostic tool: progress and future challenges. *Theranostics* 5, 710–723. doi: 10.7150/thno.11387

Orecchioni, M., Jasim, D. A., Pescatori, M., Manetti, R., Fozza, C., Sgarrella, F., et al. (2016a). Molecular and genomic impact of large and small lateral dimension graphene oxide sheets on human immune cells from healthy donors. *Adv. Healthc. Mater.* 5, 276–287. doi: 10.1002/adhm.201500606

Orecchioni, M., Ménard-Moyon, C., Delogu, L. G., and Bianco, A. (2016b). Graphene and the immune system: challenges and potentiality. *Adv. Drug Deliv. Rev.* 105, 163–175. doi: 10.1016/j.addr.2016.05.014

Park, M. V. D. Z., Bleeker, E. A. J., Brand, W., Cassee, F. R., van Elk, M., Gosens, I., et al. (2017). Considerations for safe innovation: the case of graphene. *ACS Nano* 11, 9574–9593. doi: 10.1021/acsnano.7b04120

Park, S., and Ruoff, R. S. (2009). Chemical methods for the production of graphenes. *Nat. Nanotechnol.* 4, 217–224. doi: 10.1038/nnano.2009.58

Pelin, M., Fusco, L., Martín, C., Sosa, S., Frontiñán-Rubio, J., Miguel González-Domínguez, J., et al. (2018). Graphene and graphene oxide induce ROS production in human HaCaT skin keratinocytes: the role of xanthine oxidase and NADH dehydrogenase. *Nanoscale* 10, 11820–11830. doi: 10.1039/C8NR02933D

Quintana, M., Vazquez, E., and Prato, M. (2013). Organic functionalization of graphene in dispersions. *Acc. Chem. Res.* 46, 138–148. doi: 10.1021/ar300138e

Resch-Genger, U., Grabolle, M., Cavaliere-Jaricot, S., Nitschke, R., and Nann, T. (2008). Quantum dots versus organic dyes as fluorescent labels. *Nat. Methods* 5, 763–775. doi: 10.1038/nmeth.1248

Rong, P., Yang, K., Srivastan, A., Kiesewetter, D. O., Yue, X., Wang, F., et al. (2014). Photosensitizer loaded nano-graphene for multimodality imaging guided tumor photodynamic therapy. *Theranostics* 4, 229–239. doi: 10.7150/thno.8070

Roppolo, I., Chiappone, A., Bejtka, K., Celasco, E., Chiodoni, A., Giorgis, F., et al. (2014). A powerful tool for graphene functionalization: Benzophenone mediated UV-grafting. *Carbon* 77, 226–235. doi: 10.1016/j.carbon.2014.05.025

Russier, J., León, V., Orecchioni, M., Hirata, E., Virdis, P., Fozza, C., et al. (2017). Few-layer graphene kills selectively tumor cells from myelomonocytic leukemia patients. *Angew. Chem. Int. Ed. Engl.* 56, 3014–3019. doi: 10.1002/anie.201700078

Sahu, A., Choi, W. I., Lee, J. H., and Tae, G. (2013). Graphene oxide mediated delivery of methylene blue for combined photodynamic and photothermal therapy. *Biomaterials* 34, 6239–6248. doi: 10.1016/j.biomaterials.2013.04.066

Sechi, G., Bedognetti, D., Sgarrella, F., Van Eperen, L., Marincola, F. M., Bianco, A., et al. (2014). The perception of nanotechnology and nanomedicine: a worldwide social media study. *Nanomedicine (Lond).* 9, 1475–1486. doi: 10.2217/nnm.14.78

Seh, Z. W., Fredrickson, K. D., Anasori, B., Kibsgaard, J., Strickler, A. L., Lukatskaya, M. R., et al. (2016). Two-dimensional molybdenum carbide (MXene) as an efficient electrocatalyst for hydrogen evolution. *ACS Energy Lett.* 3, 589–594. doi: 10.1021/acsenergylett.6b00247

Servant, A., Bianco, A., Prato, M., and Kostarelos, K. (2014). Graphene for multi-functional synthetic biology: the last "zeitgeist" in nanomedicine. *Bioorg. Med. Chem. Lett.* 24, 1638–1649. doi: 10.1016/j.bmcl.2014.01.051

Shahzad, F., Alhabeb, M., Hatter, C. B., Anasori, B., Hong, S. M., Koo, C. M., et al. (2016). Electromagnetic interference shielding with 2D transition metal carbides (MXenes). *Science* 353, 1137–1140. doi: 10.1126/science.aag2421

Shin, S. R., Li, Y.-C., Jang, H. L., Khoshakhlagh, P., Akbari, M., Nasajpour, A., et al. (2016). Graphene-based materials for tissue engineering. *Adv. Drug Deliv. Rev.* 105, 255–274. doi: 10.1016/j.addr.2016.03.007

Sibani, S. A., McCarron, P. A., Woolfson, A. D., and Donnelly, R. F. (2008). Photosensitiser delivery for photodynamic therapy. Part 2: systemic carrier platforms. *Expert Opin. Drug Deliv.* 5, 1241–1254. doi: 10.1517/17425240802444673

Story, W., Sultan, A. A., Bottini, G., Vaz, F., Lee, G., and Hopper, C. (2013). Strategies of airway management for head and neck photo-dynamic therapy. *Lasers Surg. Med.* 45, 370–376. doi: 10.1002/lsm.22149

Sun, X., Liu, Z., Welsher, K., Robinson, J. T., Goodwin, A., Zaric, S., et al. (2008). Nano-graphene oxide for cellular imaging and drug delivery. *Nano Res.* 1, 203–212. doi: 10.1007/s12274-008-8021-8

Tian, B., Wang, C., Zhang, S., Feng, L., and Liu, Z. (2011). Photothermally enhanced photodynamic therapy delivered by nano-graphene oxide. *ACS Nano* 5, 7000–7009. doi: 10.1021/nn201560b

Viseu, T., Lopes, C. M., Fernandes, E., Real Oliveira, M. E. C. D., and Lúcio, M. (2018). A systematic review and critical analysis of the role of graphene-based nanomaterials in cancer theranostics. *Pharmaceutics* 10:282. doi: 10.3390/pharmaceutics10040282

Wang, H., Yang, X., Shao, W., Chen, S., Xie, J., Zhang, X., et al. (2015). Ultrathin black phosphorus nanosheets for efficient singlet oxygen generation. *J. Am. Chem. Soc.* 137, 11376–11382. doi: 10.1021/jacs.5b06025

Wang, Y., Wang, H., Liu, D., Song, S., Wang, X., and Zhang, H. (2013). Graphene oxide covalently grafted upconversion nanoparticles for combined NIR mediated imaging and photothermal/photodynamic cancer therapy. *Biomaterials* 34, 7715–7724. doi: 10.1016/j.biomaterials.2013.06.045

Wo, F., Xu, R., Shao, Y., Zhang, Z., Chu, M., Shi, D., et al. (2016). A multimodal system with synergistic effects of magneto-mechanical, photothermal, photodynamic and chemo therapies of cancer in graphene-quantum dot-coated hollow magnetic nanospheres. *Theranostics* 6, 485–500. doi: 10.7150/thno.13411

Wu, C., Li, D., Wang, L., Guan, X., Tian, Y., Yang, H., et al. (2017). Single wavelength light-mediated, synergistic bimodal cancer photoablation and amplified photothermal performance by graphene/gold nanostar/photosensitizer theranostics. *Acta Biomater.* 53, 631–642. doi: 10.1016/j.actbio.2017.01.078

Wu, C., Zhu, A., Li, D., Wang, L., Yang, H., Zeng, H., et al. (2015). Photosensitizer-assembled PEGylated graphene-copper sulfide nanohybrids as a synergistic near-infrared phototherapeutic agent. *Expert Opin. Drug Deliv.* 13, 155–165. doi: 10.1517/17425247.2016.1118049

Yan, X., Hu, H., Lin, J., Jin, A. J., Niu, G., Zhang, S., et al. (2015a). Optical and photoacoustic dual-modality imaging guided synergistic photodynamic/photothermal therapies. *Nanoscale* 7, 2520–2526. doi: 10.1039/C4NR06868H

Yan, X., Niu, G., Lin, J., Jin, A. J., Hu, H., Tang, Y., et al. (2015b). Enhanced fluorescence imaging guided photodynamic therapy of sinoporphyrin sodium loaded graphene oxide. *Biomaterials* 42, 94–102. doi: 10.1016/j.biomaterials.2014.11.040

Yang, K., Feng, L., Hong, H., Cai, W., and Liu, Z. (2013a). Preparation and functionalization of graphene nanocomposites for biomedical applications. *Nat. Protoc.* 8, 2392–2403. doi: 10.1038/nprot.2013.146

Yang, K., Feng, L., and Liu, Z. (2016). Stimuli responsive drug delivery systems based on nano-graphene for cancer therapy. *Adv. Drug Deliv. Rev.* 105, 228–241. doi: 10.1016/j.addr.2016.05.015

Yang, Y., Asiri, A. M., Tang, Z., Du, D., and Lin, Y. (2013b). Graphene based materials for biomedical applications. *Materials Today* 16, 365–373. doi: 10.1016/j.mattod.2013.09.004

Yoon, I., Li, J. Z., and Shim, Y. K. (2013). Advance in photosensitizers and light delivery for photodynamic therapy. *Clin. Endosc.* 46, 7–23. doi: 10.5946/ce.2013.46.1.7

Zhang, B., Wang, Y., and Zhai, G. (2016). Biomedical applications of the graphene-based materials. *Mater. Sci. Eng. C Mater. Biol. Appl.* 61, 953–964. doi: 10.1016/j.msec.2015.12.073

Zhang, Q., Huang, W., Yang, C., Wang, F., Song, C., Gao, Y., et al. (2019). The theranostic nanoagent Mo_2C for multi-modal imaging-guided cancer synergistic phototherapy. *Biomater. Sci.* 7, 2729–2739. doi: 10.1039/C9BM00239A

Zhang, Q., Wu, Z., Li, N., Pu, Y., Wang, B., Zhang, T., et al. (2017). Advanced review of graphene-based nanomaterials in drug delivery systems: synthesis, modification, toxicity and application. *Mater. Sci. Eng. C Mater. Biol. Appl.* 77, 1363–1375. doi: 10.1016/j.msec.2017.03.196

Zhou, L., Jiang, H., Wei, S., Ge, X., Zhou, J., and Shen, J. (2012). High-efficiency loading of hypocrellin B on graphene oxide for photodynamic therapy. *Carbon* 50, 5594–5604. doi: 10.1016/j.carbon.2012.08.013

Zhou, L., Zhou, L., Wei, S., Ge, X., Zhou, J., Jiang, H., et al. (2014). Combination of chemotherapy and photodynamic therapy using graphene oxide as drug delivery system. *J. Photochem. Photobiol. B Biol.* 135, 7–16. doi: 10.1016/j.jphotobiol.2014.04.010

Zhu, S., Zhang, J., Liu, X., Li, B., Wang, X., Tang, S., et al. (2012a). Graphene quantum dots with controllable surface oxidation, tunable fluorescence and up-conversion emission. *RSC Adv.* 2, 2717–2720. doi: 10.1039/c2ra20182h

Zhu, S., Zhang, J., Tang, S., Qiao, C., Wang, L., Wang, H., et al. (2012b). Surface chemistry routes to modulate the photoluminescence of graphene quantum dots: from fluorescence mechanism to up-conversion bioimaging applications. *Adv. Funct. Mater.* 22, 4732–4740. doi: 10.1002/adfm.201201499

Nanomedicine for Imaging and Therapy of Pancreatic Adenocarcinoma

Giulia Brachi[1], Federico Bussolino[2,3], Gianluca Ciardelli[1]* and Clara Mattu[1]*

[1] Politecnico di Torino, DIMEAS, Turin, Italy, [2] Department of Oncology, University of Torino, Turin, Italy, [3] Candiolo Cancer Institute -IRCCS-FPO, Candiolo, Italy

Pancreatic adenocarcinoma has the worst outcome among all cancer types, with a 5-year survival rate as low as 10%. The lethal nature of this cancer is a result of its silent onset, resistance to therapies, and rapid spreading. As a result, most patients remain asymptomatic and present at diagnosis with an already infiltrating and incurable disease. The tumor microenvironment, composed of a dense stroma and of disorganized blood vessels, coupled with the dysfunctional signal pathways in tumor cells, creates a set of physical and biological barriers that make this tumor extremely hard-to-treat with traditional chemotherapy. Nanomedicine has great potential in pancreatic adenocarcinoma, because of the ability of nano-formulated drugs to overcome biological barriers and to enhance drug accumulation at the target site. Moreover, monitoring of disease progression can be achieved by combining drug delivery with imaging probes, resulting in early detection of metastatic patterns. This review describes the latest development of theranostic formulations designed to concomitantly treat and image pancreatic cancer, with a specific focus on their interaction with physical and biological barriers.

Keywords: nanomedicine, pancreatic cancer, nanoparticle, theranostics, biological barriers

INTRODUCTION

Pancreatic ductal adenocarcinoma (PDAC) is the fourth leading cause of cancer death in Europe and in the US (Siegel et al., 2018). The 1-year overall survival is limited to a discouraging 29%, while the overall survival at 5-year post-diagnosis is <10% (Siegel et al., 2018). The major problem is that most patients remain asymptomatic until late in their course and present at diagnosis with an already infiltrating and incurable disease (Smith et al., 2015). For the small percent of patients (19%) who present at diagnosis with local, partly resectable disease the 5-year survival reaches 27%, a prognosis that still remains dismal (Garrido-Laguna and Hidalgo, 2015).

PDAC evolves from early precursor lesions, including pancreatic intraepithelial neoplasia (PanIN), intraductal papillary mucinous neoplasms (IPMN) and mucinous cystic neoplasia (MCN), a highly invasive neosplasms characterized by an ovarian-type stroma and a mucin-producing epithelium (Hruban et al., 2007; Distler et al., 2014; Pusateri and Krishna, 2018). While PanIN often occurs as a progressive multifocal disease with hardly detectable small lesions (Bardeesy and DePinho, 2002; Makohon-Moore and Iacobuzio-Donahue, 2016), IPMNs mostly localize in the main pancreatic duct and in its related branches (Torisu et al., 2019).

Several signaling pathways, such as RAS, PI3K, and Hedgehog (Hh) are known to play a role in supporting tumorigenesis and progression (Morris et al., 2010; Cowan and Maitra, 2014). In spite of the extensive research that led to significant improvement in the understanding of the evolution of this disease, little advancement has been made toward more efficient therapeutic and early detection options for PDAC (Matsubayashi et al., 2019). The lack of indicative clinical signs and of disease-specific biomarkers, makes early detection extremely difficult (Adiseshaiah et al., 2016). In addition, pharmacological treatments remain largely ineffective, due to the difficulty in penetrating the tumor microenvironment (Conroy et al., 2011; Zhao et al., 2018). PDAC is characterized by a dense, desmoplastic stroma consisting of different cellular and acellular components (e.g., collagen and fibrin), which impedes efficient drug delivery, generates solid stress and increases interstitial fluid pressure (IFP), resulting in blood vessels collapse and in the generation of a hypoxic tumor microenvironment (Rucki, 2014; Xie and Xie, 2015; Dougan, 2017).

Nanomedicine formulations, e.g., formulation of drugs into nano-size delivery vehicles, such as liposomes and polymer nanoparticles (NPs), represent a valuable option in PDAC treatment by virtue of their ability to overcome biological barriers, protect their payload from degradation, and to achieve targeted delivery (El-Zahaby et al., 2019). Depending on their size, shape and surface charge, NPs have been shown to passively accumulate into tumors through the enhanced permeability and retention (EPR) effect (Maeda, 2001) and to actively interact with cancer cells after surface-modification with specific ligands (Yu et al., 2009), thereby enhancing selectivity and reducing undesired side effects of chemotherapy.

Although the EPR effect is not relevant in PDAC due to blood vessel collapse and to the presence of a dense desmoplastic stroma (Tanaka and Kano, 2018), several nanomedicine-based strategies have been designed and tested for the treatment of this disease (Adiseshaiah et al., 2016; Meng and Nel, 2018). For instance, conjugation of Gemcitabine (GEM) to the natural lipid squalene (SQ-GEM) to form self-assembled nanoparticles of 130 nm in size has been shown to enhance the stability of GEM and to reduce its de-activation by cytidine deaminase (Couvreur et al., 2008). SQ-GEM significantly reduced metastatic colonization and enhanced survival of mice bearing orthotopic Panc1 pancreatic tumors, compared to equivalent doses of free GEM (Réjiba et al., 2011). Another example is the liposomal formulation of Irinotecan (MM-398), which in combination with 5-fluoruracil and leucovorin (5-FU/LV) is currently recommended as second line therapy after failure of GEM treatment (Ko et al., 2013; Wang-Gillam et al., 2019; Woo et al., 2019).

In spite of these promising results, cell intrinsic (e.g., drug resistance) and cell extrinsic (e.g., tumor microenvironment) barriers should be overcome to facilitate drug accumulation in pancreatic tumors, coupled with better diagnostic and imaging modalities (Yang et al., 2012; Meng and Nel, 2018). A new class of theranostic nanomedicines that combines imaging and therapeutic options in a single platform may address this need.

Herein, we discuss the recent advancement in the design of nanosystems to improve imaging and treatment of PDAC.

PHYSICAL AND BIOLOGICAL BARRIERS IN PDAC

PDAC is characterized by a thick desmoplastic stroma, composed of several cell types (including endothelial and immune cells), embedded in a dense matrix composed of fibrin, collagen, hyaluronan, and fibronectin (Cowan and Maitra, 2014; Rucki, 2014). Neoplastic cells account for <20% of the tumor mass, while the stromal volume covers up to 70% of the total tumor volume (Yang et al., 2012).

During PDAC progression, secretion of pro-inflammatory cytokines by tumor cells stimulates extracellular matrix (ECM) deposition by fibroblasts and stellate stromal cells (Hwang et al., 2008; von Ahrens et al., 2017). The continuous generation of a dense stroma generates solid stress which, together with the collapse of the lymphatic drainage in the center of the tumor, contributes to the increased intratumoral IFP and the consequent vessel compression, reduced perfusion, and generation of a hypoxic environment (Adiseshaiah et al., 2016; Meng and Nel, 2018). As a result, approximately 80% of blood vessels in PDAC are non-functional, poorly fenestrated, and surrounded by a thick layer of pericytes, that impede efficient accumulation of nanomedicines into the tumor. Moreover, pancreatic stellate cells secrete cytokines and growth factors that generate an immune-suppressive microenvironment (Thind et al., 2017). This feature of stellate cells is further amplified during tumor progression, because cancer cells induce their differentiation in two subtypes of cancer-associated fibroblasts, respectively showing a pro-inflammatory or a pro-fibrogenic phenotype (Öhlund et al., 2017). This concept has been further reinforced by single cell transcriptome analysis (Ligorio et al., 2018) performed on human PDAC underscoring a wider fibroblast heterogeneity, which locally influences the proliferative and metastatic potential of cancer cells.

MODULATION OF PDAC MICROENVIRONMENT WITH NANOMEDICINE

As summarized in **Table 1**, several strategies have been implemented to design nanomedicines that can negotiate with the microenvironmental barriers in PDAC through alleviation of the stroma burden (Thompson et al., 2010; Provenzano et al., 2012; Bhaw-Luximon and Jhurry, 2015), normalization of tumor blood vessels, or by eliciting nanoparticle-mediated immunogenic cell death (Zhao et al., 2016), as thoroughly discussed by Adiseshaiah et al. (2016) and by Meng and Nel (2018).

Stroma depletion through delivery of pegylated hyaluronidase (PEGPH2O) was shown to enhance accumulation of high molecular weight tracers into pancreatic tumors (Jacobetz et al., 2013). Tested in combination with Abraxane and GEM in clinical trials with patients whose tumors had high

TABLE 1 | Nanomedicines for imaging and/or treatment of PDAC.

Therapeutic strategy	Nanocarrier	Encapsulated agents	Achieved results
Stromal depletion via hyaluronan accumulation	Pegylated hyaluronidase	Abraxane + GEM	45% Response rate 11.5 months median overall survival (Jacobetz et al., 2013)
Stromal depletion via hedgehog inhibition	Polymer NPs	Paclitaxel + cyclopamine	63% higher inhibition of tumor growth (Hingorani et al., 2018)
Stromal homeostasis via PSC reprogramming	Pegylated gold NPs	Retinoic acid + HSP47-siRNA+GEM	Suppressive effect in sub-cutaneous and orthotopic tumor model (Catenacci et al., 2015)
Reduction of hypoxic microenvironment	Polymer NPs	HIF1α-siRNA + GEM	Significant reduction of tumor size and metastasis prevention (Jaster et al., 2003)
Sensitization to radiotherapy via ROS	Cerium Oxide NPs	Cerium oxide	Significant reduction in tumor weight and volume (Zhao et al., 2015)
Targeted pH-driven gene silencing	Polymer NPs	GEM + GDC 0449	Selective internalization and enhanced intratumor accumulation (Vassie et al., 2017)
Temperature-triggered drug release	Hybrid NPs	GEM	4.4-fold decreased tumor weight and reduction of tumor size (Zeiderman et al., 2016)
Targeted intracellular hyperthermia	Gold NPs	Cetuximab or PAM4	Significant reduction of tumor size after 6 weeks of combined therapy (Ray et al., 2019)
Targeted chemotherapy + MRI	Iron oxide NPs	Doxorubicin/iron oxide NPs	66.6% Inhibition of tumor growth (Mattheolabakis et al., 2015)
Targeted Enzyme Responsive Drug Release + MRI	Iron oxide NPs	GEM/iron oxide NPs	Improved intracellular release and tumor growth inhibition up to 50% (Tummers et al., 2018)
Magnetic hyperthermia + chemotherapy + MRI	Polymer NPs	GEM/fluorescent iron oxide NPs	Significant tumor regression and MRI contrast enhancement (Hoogstins et al., 2018)
Image-guided targeted photothermal therapy	Carbon nanotubes	Cyanine 7	Dynamic disease monitoring and improved median survival time (Rosenberger et al., 2015)
Targeted intra-operative fluorescent imaging	Polymer NPs	Indocyanine green	Early detection of primary tumor and splenic metastases (Handgraaf et al., 2014)
Targeted multi-modal Imaging	Polymer NPs	Iron oxide NPs + FITC	Selective tumor accumulation and active disease monitoring (Vahrmeijer et al., 2013)

hyaluronan content, an objective response rate of 45 vs. 31% and a median overall survival of 11.5 vs. 8.5 months was achieved in comparison with Abraxane/GEM therapy (Hingorani et al., 2018). Inhibition of signal pathways involved in stroma deposition, such as Hh, was implemented to facilitate accumulation of NPs to PDAC tumor models. Zhang et al. (2016) showed that oral administration of cyclopamine, a Hh inhibitor, reduced fibronectin content and enhanced tumor vascularization, resulting in a significantly higher accumulation of NPs in subcutaneous Capan-2 xenografts. Using paclitaxel (PTX)-loaded NPs combined with cyclopamine, they achieved a 63% increased inhibition of tumor growth (Zhang et al., 2016). In spite of these results, the Hh inhibitor Vismodegib combined with GEM failed to produce significant clinical benefit to patients with metastatic PDAC. No significant improvement in the overall survival or in the disease free progression was observed in comparison to standard treatment with GEM alone (Catenacci et al., 2015).

In addition to these discouraging results, other reports have shown that stroma depletion may facilitate cell proliferation and worsen the metastatic spreading, thus reducing the potential applicability of these therapies in PDAC treatment (Kiesslich et al., 2012; Özdemir et al., 2014; Adiseshaiah et al., 2016).

As an alternative to stromal depletion, Han et al. (2018) proposed to restore the fibrotic stromal homeostasis in PDAC by reprogramming pancreatic stellate cells (PSCs). They reported on the design of pH-responsive pegylated gold nanoparticles co-loaded with all-*trans* retinoic acid (ATRA) and heat shock protein 47(HSP47)-small interfering RNA (siRNA). ATRA is involved in maintaining PSCs homeostasis and quiescence, while silencing of HSP47 has the potential to reduce collagen accumulation and, consequently, to normalize the desmoplastic stroma (Jaster et al., 2003; Masamune and Shimosegawa, 2009). Combined with GEM treatment, these particles showed significant tumor suppressive effect in both, sub-cutaneous and orthotopic, PSC/PANC-1 xenografts in mice.

Knockdown of target genes involved in drug resistance, and in tumor invasion by RNA interference, is another possible strategy to modulate PDAC microenvironment (Burnett and Rossi, 2012). NPs have demonstrated to improve the biodistribution and to reduce clearance of siRNAs and micro-RNAs (miRNAs) and have been used in combination with cytotoxic drugs, such as GEM or Doxorubicin (Zhao et al., 2015; Gibori et al., 2018; Chen et al., 2019).

As an example, inhibition of the hypoxia inducible transcription factor HIF1α through siRNA combined with

GEM release was proposed by Zhao et al. (2015). The hypoxic microenvironment in PDAC is responsible for the activation of genes that regulate invasion, angiogenesis, resistance to treatment and proliferation, driven mostly by the secretion of HIFs (Feig et al., 2012). GEM-loaded, lipid-coated polymer NPs, where siRNA was complexed to positively charged polylysine residues on the surface of NPs, significantly delayed the growth of subcutaneous PANC-1 tumor xenografts, demonstrating a synergistic effect between HIF1α down-regulation and GEM. Moreover, the combination therapy significantly reduced tumor size in an orthotopic PDAC model, as compared to un-encapsulated siRNA and GEM, or with particles loaded with GEM only. In addition, no peritoneal metastases were observed in the group treated with the combination therapy, while all other animals had signs of liver and peritoneal secondary tumors.

Since PDAC microenvironment generates resistance to chemo and radiotherapy (RT), Wason et al. proposed the delivery of cerium oxide nanoparticles (CONPs) to modulate production of reactive oxygen species (ROS) that sensitized PDAC cells to radiotherapy (RT) (Wason et al., 2013; Vassie et al., 2017). CONPs-based pretreatment limited tumor growth in an orthotopic L3.6pl tumor model in athymic nude mice, leading to a significant reduction in tumor weight ($P = 0.0112$) and volume ($P = 0.0006$) as compared to RT alone.

SMART NANOMEDICINES IN PDAC TREATMENT

Smart NPs are designed respond to environmental or external stimuli to trigger drug release after passive or active tumor accumulation, as schematized in **Figure 1** (Zeiderman et al., 2016; Mattu et al., 2018).

Ray et al. (2019) proposed a pH-responsive platform based on block co-polymers of PEG-b-poly (carbonate) loaded with GEM and the Hh inhibitor GDC 0449. These NPs respond to the low pH of the extra- (pH 6.9–6.5) and intra-cellular compartments (pH 5.5–4.5) in PDAC, by virtue of the presence of tertiary amine side chains that promote disassembly of NPs under acidic conditions. To facilitate NPs accumulation in PDAC, the surface was modified with an iRGD peptide that selectively targets neuropilin and integrin receptors over-expressed by tumor cells. Successful accumulation was achieved and NPs were detected into BxPC-3 tumor xenografts up to 6 hours post systemic administration (Ray et al., 2019).

Temperature-triggered drug release was proposed by Oluwasanmi et al. (2017) after passive accumulation of NPs into PDAC xenografts, followed by external laser irradiation. They designed thermo-responsive hybrid NPs (HNPs) and linked GEM through a thermosensitive linker containing the Diels–Alder adducts, that are cleaved upon heat generation, thus triggering GEM release at the tumor site (Gregoritza and Brandl, 2015). When administered *in vivo* to BxPC-3 xenografts, the formulation showed enhanced anti-cancer activity, demonstrated by a 4.4-fold decreased tumor weight and reduction of tumor size when compared to GEM-loaded HNPs without laser irradiation.

Gold NPs (Au NPs) stimulated with external radio frequency (RF) irradiation have also been proposed for the non-invasive intracellular hyperthermia of PDAC (Glazer et al., 2010). Au NPs conjugated with Cetuximab or PAM4, for active targeting of epidermal growth factor receptor1 (EGFR-1) and mucine-1 (MUC-1), were intraperitoneally administered to mice bearing PANC-1 or Capan-1 xenografts. PAM4-conjugated Au NPs exhibited the highest tumor internalization. When combined with RF in the first 2 weeks of treatment, these NPs produced a significantly higher reduction of tumor size with minimal side effects, compared to unconjugated NPs or to conjugated NPs in absence of the external RF.

THERANOSTIC NANOPARTICLES

Theranostic NPs have the potential to localize imaging agents together with therapies at the tumor site (Handgraaf et al., 2014). Early detection and surgical resection have been shown to increase the mean 5-year survival of PDAC patients up to 31.7 ± 3.6 months (Cleary et al., 2004), highlighting the possibility to exploit the tumor-accumulation ability of NPs to deliver imaging agents for early recognition of PDAC (Vahrmeijer et al., 2013).

Qi et al. (2018) designed a near infrared fluorescent probe by encapsulating indocyanine green (ICG) into hyaluronic acid (HA) NPs (NanoICG). The fluorescence emission of ICG could be detected to a depth of 8 mm in tissues and was exploited to facilitate visualization of the infiltrating tumor tissue. The affinity of HA for the membrane receptor CD44 over-expressed by pancreatic cancer cells was exploited to enhance NPs accumulation into PDAC through active recognition mechanisms (Mattheolabakis et al., 2015). High tumor accumulation was achieved after administration to mice bearing a syngeneic orthotopic PDAC model. The fluorescence signal from the encapsulated ICG allowed the detection of the primary tumor as well as the splenic metastases to a much higher extent when compared to free ICG, confirming the targeting-ability of HA NPs toward PDAC.

The disease accumulation properties of NPs could be leveraged to also facilitate disease visualization during surgery (Qi et al., 2018). Recently, high-resolution fluorescent imaging agents coupled to antibodies have been used in small in-patients studies, for the detection of the primary disease or the presence of small metastatic sites during resection surgery (Hoogstins et al., 2018; Tummers et al., 2018). This may facilitate identification of the resection margins and quantification of the residual disease, albeit the clinical benefit still remains to be demonstrated.

Combination of magnetic resonance imaging (MRI) with fluorescence imaging, by co-encapsulation of superparamagnetic iron oxide NPs (IONPs) was also proposed. For instance, IONPs and fluorescein isothiocyanate (FITC) were co-encapsulated into HA NPs to exploit selective recognition of HA by CD44 receptors (Luo et al., 2019), and into NPs modified with tissue plasminogen activator-derived peptides with high affinity toward galectin-1, overexpressed by pancreatic cancer cells (Rosenberger
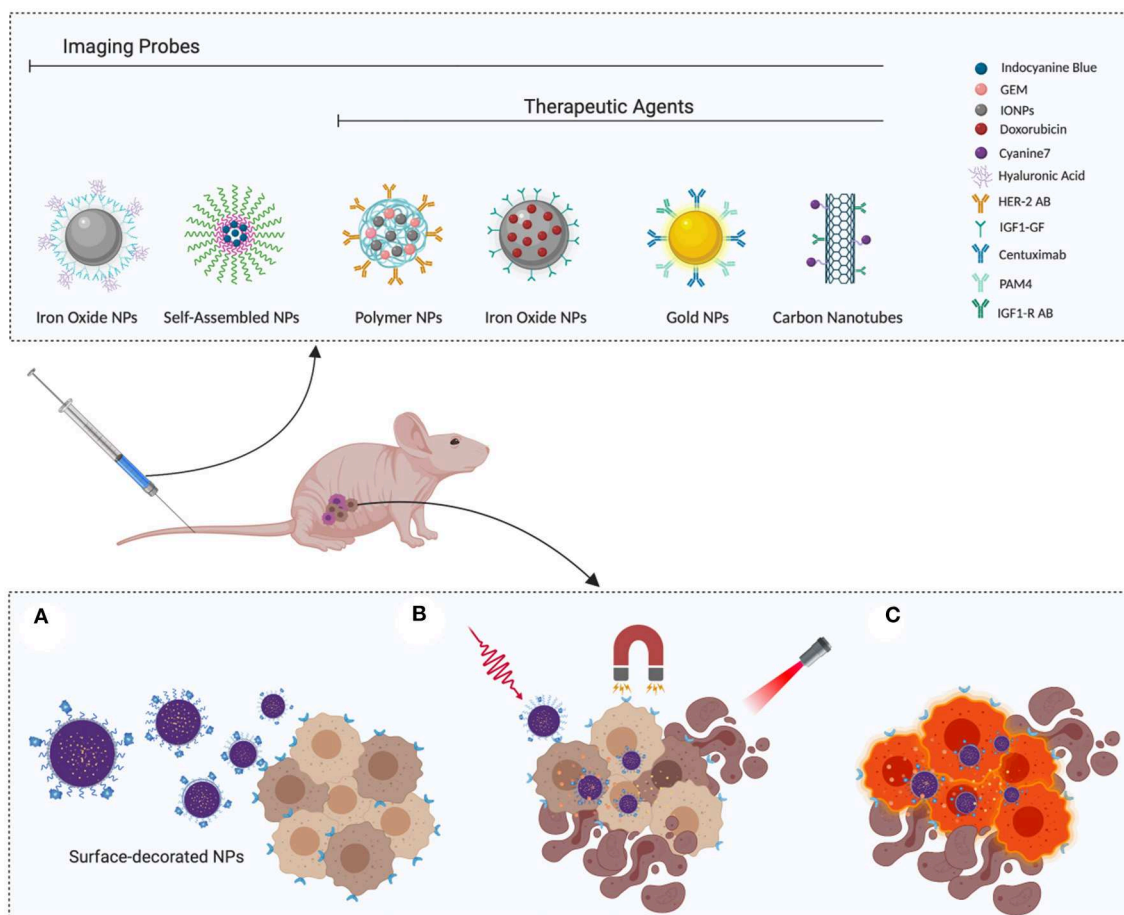
FIGURE 1 | Smart nanoparticles for PDAC theranostic: **(A)** Surface-functionalized nanoparticles actively recognize tumor cells, thereby enhancing selective accumulation. **(B)** Once they reach the target site, release can be triggered by applying external stimuli, such as magnetic field or irradiation. **(C)** Selective recognition of cancer cells can be exploited to enhance their visualization, favoring complete eradication during surgery or disease monitoring with classic diagnostic tools, such as PET or MRI. Image created with Biorender.

et al., 2015). Accurate monitoring of tumor growth with MRI was achieved in both cases, after active accumulation of NPs in tumors.

MRI imaging combined with doxorubicin (Dox) chemotherapy was proposed for PDAC theranostic (Zhou et al., 2015). IONPs were conjugated to human insulin-like growth factor1 (IGF1) that selectively binds to IGF1-receptors in pancreatic cancer cells, and loaded with Dox. IGF1-IONPs exhibited excellent tumor penetration ability after IV administration in an orthotopic patient-derived tumor model. Moreover, when administered intratumorally, these particles led to a significant inhibition of tumor growth (66.6%), compared to treatment with free Dox, non-targeted IONP-Dox, or PBS. Enhanced MRI contrast was obtained for the group treated with IGF1-IONP-Dox, while no significant contrast was observed in non-targeted IONP-Dox, suggesting IGF1R-mediated accumulation.

Lee et al. (2013) designed urokinase plasminogen activator (uPAR)-modified IONPs loaded with GEM via an enzyme-cleavable tetrapeptide linker. They achieved improved endocytosis through active recognition of uPAR receptors, and a consequently higher intracellular release of GEM and MRI contrast. Moreover, inhibition of tumor growth (up to 50%) was obtained in an orthotopic pancreatic cancer model.

IONPs have the potential to generate heat after external irradiation (Jaidev et al., 2017). Jaidev et al. (2017) developed polymeric NPs for MRI, magnetic hyperthermia (MHT) and chemotherapy for application in PDAC. Poly(lactide-co-glycolide) (PLGA)-based NPs encapsulating fluorescent IONPs and GEM were conjugated with anti-human epidermal growth factor receptor 2 (HER-2) antibody. When administered in subcutaneous MIAPaCa-2 tumor models in combination with mild hyperthermia, NPs led to a significant tumor regression; moreover, a remarkable contrast enhancement was observed in T2-MRI images of treated mice.

Single-walled carbon nanotubes (SWNTs) can also convert heat after near infrared (NIR) irradiation, resulting in localized hyperthermia that leads to tumor cells death via ROS production (Singh and Torti, 2013). Lu et al. (2019) formulated anti-IGF-1R antibody functionalized SWNTs for enhanced imaging-guided cytotoxic photothermal therapy (PTT) of PDAC. SWNTs exhibited preferential accumulation into tumors, resulting in dynamic monitoring of the disease. Fluorescence-guided PTT significantly improved the survival of mice bearing an orthotopic PDAC model, compared to groups treated with PBS or only with NIR laser.

CONCLUSIONS AND FUTURE DIRECTIONS

PDAC remains an incurable disease. The dense stroma, the lack of vascular access, and the heterogeneous microenvironment, make PDAC extremely refractory to treatment penetration, requiring the design of smart strategies to by-pass these barriers and to maximize treatment accumulation in the tumor (Gibori et al., 2018).

Late disease detection worsens patient outcome, making surgical resection ineffective. The tumor-accumulation and targeting ability of nanomedicines could be leveraged to improve disease detection at early stage, considerably improving survival and enhancing the extent of surgical resection (Handgraaf et al., 2014). Early stage detection may also result in more efficacious nanomedicine-based treatments, for instance coupled with stroma-depleting agents which would further potentiate disease homing.

Local delivery is an attractive, yet poorly exploited, alternative to treat PDAC. Local administration avoids the stroma protection and overcomes the restricted vascular access, potentially reducing side effects, as demonstrated by the encouraging results of the siG12D-LODER implant (Adiseshaiah et al., 2016). SiG12D-LODER is a biodegradable implant for the local delivery of liposomal-encapsulated anti-KRAS siRNA that is placed near the tumor by means of standard endoscopic surgery (Golan et al., 2015). In a small subset of PDAC patients, stabilization of tumor growth, and partial response was achieved in combination with

chemotherapy, suggesting the potential of this smart delivery method (Schultheis et al., 2014).

As discussed above, extensive research has shown the potential of nanomedicine in PDAC and some formulations, such as albumin-bound paclitaxel (Abraxane) and liposomal irinotecan (MM-398), reached clinical approval (Kalra et al., 2014; Goldstein et al., 2015; von Ahrens et al., 2017). It must be noted that although MM-398 in combination with other cytotoxic agents improved patient survival, it failed to produce similar improvements when used as mono-therapy (Adiseshaiah et al., 2016; Kipps et al., 2017; Wang-Gillam et al., 2019).

Additionally, the different animal models, cell source, tumor location (e.g., heterotopic vs. orthotopic), and nanoparticle design used in pre-clinical research may result in difficult comparison between published research and in the overestimation of the results (Murtaugh, 2014; Adiseshaiah et al., 2016; Leong et al., 2019).

Efforts toward standardization of research and treatment protocols may further improve the potential of nanomedicine in the field.

AUTHOR CONTRIBUTIONS

All authors listed have made a substantial, direct and intellectual contribution to the work, and approved it for publication.

FUNDING

REFERENCES

Adiseshaiah, P. P., Crist, R. M., Hook, S. S., and McNeil, S. E. (2016). Nanomedicine strategies to overcome the pathophysiological barriers of pancreatic cancer. *Nat. Rev. Clin. Oncol.* 13, 750–765. doi: 10.1038/nrclinonc.2016.119

Bardeesy, N., and DePinho, R. A. (2002). Pancreatic cancer biology and genetics. *Nat. Rev. Cancer* 2, 897–909. doi: 10.1038/nrc949

Bhaw-Luximon, A., and Jhurry, D. (2015). New avenues for improving pancreatic ductal adenocarcinoma (PDAC) Treatment: selective stroma depletion combined with nano drug delivery. *Cancer Lett.* 369, 266–273. doi: 10.1016/j.canlet.2015.09.007

Burnett, J. C., and Rossi, J. J. (2012). RNA-based therapeutics: current progress and future prospects. *Chem. Biol.* 19, 60–71. doi: 10.1016/j.chembiol.2011.12.008

Catenacci, D. V. T., Junttila, M. R., Karrison, T., Bahary, N., Horiba, M. N., Nattam, S. R., et al. (2015). Randomized phase Ib/II study of gemcitabine plus placebo

or vismodegib, a hedgehog pathway inhibitor, in patients with metastatic pancreatic cancer. *J. Clin. Oncol.* 33, 4284–4292. doi: 10.1200/JCO.2015.62.8719

Chen, W., Zhou, Y., Zhi, X., Ma, T., Liu, H., Chen, B. W., et al. (2019). Delivery of MiR-212 by chimeric peptide-condensed supramolecular nanoparticles enhances the sensitivity of pancreatic ductal adenocarcinoma to doxorubicin. *Biomaterials* 192, 590–600. doi: 10.1016/j.biomaterials.2018.11.035

Cleary, S. P., Gryfe, R., Guindi, M., Greig, P., Smith, L., MacKenzie, R., et al. (2004). Prognostic factors in resected pancreatic adenocarcinoma: analysis of actual 5-year survivors. *J. Am. Coll. Surg.* 198, 722–731. doi: 10.1016/j.jamcollsurg.2004.01.008

Conroy, T., Desseigne, F., Ychou, M., Bouché, O., Guimbaud, R., Bécouarn, Y., et al. (2011). FOLFIRINOX versus gemcitabine for metastatic pancreatic cancer. *N. Engl. J. Med.* 364, 1817–1825. doi: 10.1056/NEJMoa1011923

Couvreur, P., Reddy, L. H., Mangenot, S., Poupaert, J. H., Desmaële, D., Lepêtre-Mouelhi, S., et al. (2008). Discovery of new hexagonal supramolecular

nanostructures formed by squalenoylation of an anticancer nucleoside analogue. *Small* 4, 247–253. doi: 10.1002/smll.200700731

Cowan, R. W., and Maitra, A. (2014). Genetic progression of pancreatic cancer. *Cancer J.* 20, 80–84. doi: 10.1097/PPO.0000000000000011

Distler, M., Aust, D., Weitz, J., Pilarsky, C., and Grützmann, R. (2014). Precursor lesions for sporadic pancreatic cancer: PanIN, IPMN, and MCN. *Biomed Res. Int.* 2014, 1–11. doi: 10.1155/2014/474905

Dougan, S. K. (2017). The pancreatic cancer microenvironment. *Cancer J.* 23, 321–325. doi: 10.1097/PPO.0000000000000288

El-Zahaby, S. A., Elnaggar, Y. S. R., and Abdallah, O. Y. (2019). Reviewing two decades of nanomedicine implementations in targeted treatment and diagnosis of pancreatic cancer: an emphasis on state of art. *J. Control. Release* 293, 21–35. doi: 10.1016/j.jconrel.2018.11.013

Feig, C., Gopinathan, A., Neesse, A., Chan, D. S., Cook, N., and Tuveson, D. A. (2012). The pancreas cancer microenvironment. *Clin. Cancer Res.* 18, 4266–4276. doi: 10.1158/1078-0432.CCR-11-3114

Garrido-Laguna, I., and Hidalgo, M. (2015). Pancreatic cancer: from state-of-the-art treatments to promising novel therapies. *Nat. Rev. Clin. Oncol.* 12, 319–334. doi: 10.1038/nrclinonc.2015.53

Gibori, H., Eliyahu, S., Krivitsky, A., Ben-Shushan, D., Epshtein, Y., Tiram, G., et al. (2018). Amphiphilic nanocarrier-induced modulation of PLK1 and MiR-34a leads to improved therapeutic response in pancreatic cancer. *Nat. Commun.* 9:16. doi: 10.1038/s41467-017-02283-9

Glazer, E. S., Zhu, C., Massey, K. L., Thompson, C. S., Kaluarachchi, W. D., Hamir, A. N., et al. (2010). Noninvasive radiofrequency field destruction of pancreatic adenocarcinoma xenografts treated with targeted gold nanoparticles. *Clin. Cancer Res.* 16, 5712–5721. doi: 10.1158/1078-0432.CCR-10-2055

Golan, T., Khvalevsky, E. Z., Hubert, A., Gabai, R. M., Hen, N., Segal, A., et al. (2015). RNAi therapy targeting KRAS in combination with chemotherapy for locally advanced pancreatic cancer patients. *Oncotarget* 6:4183. doi: 10.18632/oncotarget.4183

Goldstein, D., El-Maraghi, R. H., Hammel, P., Heinemann, V., Kunzmann, V., Sastre, J., et al. (2015). Nab-paclitaxel plus gemcitabine for metastatic pancreatic cancer: long-term survival from a phase III trial. *JNCI J. Natl. Cancer Inst.* 107:dju413. doi: 10.1093/jnci/dju413

Gregoritza, M., and Brandl, F. P. (2015). The Diels–Alder reaction: a powerful tool for the design of drug delivery systems and biomaterials. *Eur. J. Pharm. Biopharm.* 97, 438–453. doi: 10.1016/j.ejpb.2015.06.007

Han, X., Li, Y., Xu, Y., Zhao, X., Zhang, Y., Yang, X., et al. (2018). Reversal of pancreatic desmoplasia by re-educating stellate cells with a tumour microenvironment-activated nanosystem. *Nat. Commun.* 9:3390. doi: 10.1038/s41467-018-05906-x

Handgraaf, H. J. M., Boonstra, M. C., Van Erkel, A. R., Bonsing, B. A., Putter, H., Van De Velde, C. J. H., et al. (2014). Current and future intraoperative imaging strategies to increase radical resection rates in pancreatic cancer surgery. *Biomed Res. Int.* 2014, 1–8. doi: 10.1155/2014/890230

Hingorani, S. R., Zheng, L., Bullock, A. J., Seery, T. E., Harris, W. P., Sigal, D. S., et al. (2018). HALO 202: randomized phase II study of PEGPH20 plus nab-paclitaxel/gemcitabine versus nab-paclitaxel/gemcitabine in patients with untreated, metastatic pancreatic ductal adenocarcinoma. *J. Clin. Oncol.* 36, 359–366. doi: 10.1200/JCO.2017.74.9564

Hoogstins, C. E. S., Boogerd, L. S. F., Sibinga Mulder, B. G., Mieog, J. S. D., Swijnenburg, R. J., van de Velde, C. J. H., et al. (2018). Image-guided surgery in patients with pancreatic cancer: first results of a clinical trial using SGM-101, a novel carcinoembryonic antigen-targeting, near-infrared fluorescent agent. *Ann. Surg. Oncol.* 25, 3350–3357. doi: 10.1245/s10434-018-6655-7

Hruban, R. H., Maitra, A., Kern, S. E., and Goggins, M. (2007). Precursors to pancreatic cancer. *Gastroenterol. Clin. North Am.* 36, 831–849. doi: 10.1016/j.gtc.2007.08.012

Hwang, R. F., Moore, T., Arumugam, T., Ramachandran, V., Amos, K. D., Rivera, A., et al. (2008). Cancer-associated stromal fibroblasts promote pancreatic tumor progression. *Cancer Res.* 68, 918–926. doi: 10.1158/0008-5472.CAN-07-5714

Jacobetz, M. A., Chan, D. S., Neesse, A., Bapiro, T. E., Cook, N., Frese, K. K., et al. (2013). Hyaluronan impairs vascular function and drug delivery in a mouse model of pancreatic cancer. *Gut* 62, 112–120. doi: 10.1136/gutjnl-2012-302529

Jaidev, L. R., Chellappan, D. R., Bhavsar, D. V., Ranganathan, R., Sivanantham, B., Subramanian, A., et al. (2017). Multi-functional nanoparticles as theranostic agents for the treatment & imaging of pancreatic cancer. *Acta Biomater.* 49, 422–433. doi: 10.1016/j.actbio.2016.11.053

Jaster, R., Hilgendorf, I., Fitzner, B., Brock, P., Sparmann, G., Emmrich, J., et al. (2003). Regulation of pancreatic stellate cell function *in vitro*: biological and molecular effects of all-trans retinoic acid. *Biochem. Pharmacol.* 66, 633–641. doi: 10.1016/S0006-2952(03)00390-3

Kalra, A. V., Kim, J., Klinz, S. G., Paz, N., Cain, J., Drummond, D. C., et al. (2014). Preclinical activity of nanoliposomal irinotecan is governed by tumor deposition and intratumor prodrug conversion. *Cancer Res.* 74, 7003–7013. doi: 10.1158/0008-5472.CAN-14-0572

Kiesslich, T., Berr, F., Alinger, B., Kemmerling, R., Pichler, M., Ocker, M., et al. (2012). Current status of therapeutic targeting of developmental signalling pathways in oncology. *Curr. Pharm. Biotechnol.* 13, 2184–2220. doi: 10.2174/138920112802502114

Kipps, E., Young, K., and Starling, N. (2017). Liposomal irinotecan in gemcitabine-refractory metastatic pancreatic cancer: efficacy, safety and place in therapy. *Ther. Adv. Med. Oncol.* 9, 159–170. doi: 10.1177/1758834016688816

Ko, A. H., Tempero, M. A., Shan, Y.-S., Su, W.-C., Lin, Y.-L., Dito, E., et al. (2013). A Multinational phase 2 study of nanoliposomal irinotecan sucrosofate (PEP02, MM-398) for patients with gemcitabine-refractory metastatic pancreatic cancer. *Br. J. Cancer* 109, 920–925. doi: 10.1038/bjc.2013.408

Lee, G. Y., Qian, W. P., Wang, L., Wang, Y. A., Staley, C. A., Satpathy, M., et al. (2013). Theranostic nanoparticles with controlled release of gemcitabine for targeted therapy and mri of pancreatic cancer. *ACS Nano* 7, 2078–2089. doi: 10.1021/nn3043463

Leong, H. S., Butler, K. S., Brinker, C. J., Azzawi, M., Conlan, S., Dufès, C., et al. (2019). Publisher correction: on the issue of transparency and reproducibility in nanomedicine. *Nat. Nanotechnol.* 14, 811–811. doi: 10.1038/s41565-019-0523-x

Ligorio, M., Sil, S., Malagon-Lopez, J., Nieman, L. T., Misale, S., Di Pilato, M., et al. (2018). Stromal microenvironment shapes the intratumoral architecture of pancreatic cancer. *SSRN Electron. J.* 178, 160–175.e27. doi: 10.2139/ssrn.3249464

Lu, G. H., Shang, W. T., Deng, H., Han, Z. Y., Hu, M., Liang, X. Y., et al. (2019). Targeting carbon nanotubes based on IGF-1R for photothermal therapy of orthotopic pancreatic cancer guided by optical imaging. *Biomaterials* 195, 13–22. doi: 10.1016/j.biomaterials.2018.12.025

Luo, Y., Li, Y., Li, J., Fu, C., Yu, X., and Wu, L. (2019). Hyaluronic acid-mediated multifunctional iron oxide-based MRI nanoprobes for dynamic monitoring of pancreatic cancer. *RSC Adv.* 9, 10486–10493. doi: 10.1039/c9ra00730j

Maeda, H. (2001). The enhanced permeability and retention (EPR) effect in tumor vasculature: the key role of tumor-selective macromolecular drug targeting. *Adv. Enzym. Regul.* 41, 189–207. doi: 10.1016/s0065-2571(00)00013-3

Makohon-Moore, A., and Iacobuzio-Donahue, C. A. (2016). Pancreatic cancer biology and genetics from an evolutionary perspective. *Nat. Rev. Cancer* 16, 553–565. doi: 10.1038/nrc.2016.66

Masamune, A., and Shimosegawa, T. (2009). Signal transduction in pancreatic stellate cells. *J. Gastroenterol.* 44, 249–260. doi: 10.1007/s00535-009-0013-2

Matsubayashi, H., Ishiwatari, H., Sasaki, K., Uesaka, K., and Ono, H. (2019). Detecting early pancreatic cancer: current problems and future prospects. *Gut Liver* 2019:gnl18491. doi: 10.5009/gnl18491

Mattheolabakis, G., Milane, L., Singh, A., and Amiji, M. M. (2015). Hyaluronic acid targeting of CD44 for cancer therapy: from receptor biology to nanomedicine. *J. Drug Target.* 23, 605–618. doi: 10.3109/1061186X.2015.1052072

Mattu, C., Brachi, G., and Ciardelli, G. (2018). "2 - Smart polymeric nanoparticles," in *Micro and Nano Technologies, Smart Nanoparticles for Biomedicine*, ed G. Ciofani (Elsevier), 15–29. doi: 10.1016/b978-0-12-814156-4.00002-1

Meng, H., and Nel, A. E. (2018). Use of nano engineered approaches to overcome the stromal barrier in pancreatic cancer. *Adv. Drug Deliv. Rev.* 130, 50–57. doi: 10.1016/j.addr.2018.06.014

Morris, J. P., Wang, S. C., and Hebrok, M. (2010). KRAS, Hedgehog, Wnt and the twisted developmental biology of pancreatic ductal adenocarcinoma. *Nat. Rev. Cancer* 10, 683–695. doi: 10.1038/nrc2899

Murtaugh, L. C. (2014). Pathogenesis of pancreatic cancer. *Toxicol. Pathol.* 42, 217–228. doi: 10.1177/0192623313508250

Öhlund, D., Handly-Santana, A., Biffi, G., Elyada, E., Almeida, A. S., Ponz-Sarvise, M., et al. (2017). Distinct populations of inflammatory fibroblasts

and myofibroblasts in pancreatic cancer. *J. Exp. Med.* 214, 579–576. doi: 10.1084/jem.20162024

Oluwasanmi, A., Al-Shakarchi, W., Manzur, A., Aldebasi, M. H., Elsini, R. S., Albusair, M. K., et al. (2017). Diels alder-mediated release of gemcitabine from hybrid nanoparticles for enhanced pancreatic cancer therapy. *J. Control. Release* 266, 355–364. doi: 10.1016/j.jconrel.2017.09.027

Özdemir, B. C., Pentcheva-Hoang, T., Carstens, J. L., Zheng, X., Wu, C.-C., Simpson, T. R., et al. (2014). Depletion of carcinoma-associated fibroblasts and fibrosis induces immunosuppression and accelerates pancreas cancer with reduced survival. *Cancer Cell* 25, 719–734. doi: 10.1016/j.ccr.2014.04.005

Provenzano, P. P., Cuevas, C., Chang, A. E., Goel, V. K., Von Hoff, D. D., and Hingorani, S. R. (2012). Enzymatic targeting of the stroma ablates physical barriers to treatment of pancreatic ductal adenocarcinoma. *Cancer Cell* 21, 418–429. doi: 10.1016/j.ccr.2012.01.007

Pusateri, A., and Krishna, S. (2018). Pancreatic cystic lesions: pathogenesis and malignant potential. *Diseases* 13:E50. doi: 10.3390/diseases6020050

Qi, B., Crawford, A. J., Wojtynek, N. E., Holmes, M. B., Souchek, J. J., Almeida-Porada, G., et al. (2018). Indocyanine green loaded hyaluronan-derived nanoparticles for fluorescence-enhanced surgical imaging of pancreatic cancer. *Nanomed. Nanotechnol. Biol. Med.* 14, 769–780. doi: 10.1016/j.nano.2017.12.015

Ray, P., Confeld, M., Borowicz, P., Wang, T., Mallik, S., and Quadir, M. (2019). PEG-b-poly (carbonate)-derived nanocarrier platform with PH-responsive properties for pancreatic cancer combination therapy. *Colloids Surfaces B Biointerfaces* 174, 126–135. doi: 10.1016/j.colsurfb.2018.10.069

Réjiba, S., Reddy, L. H., Bigand, C., Parmentier, C., Couvreur, P., and Hajri, A. (2011). Squalenoyl gemcitabine nanomedicine overcomes the low efficacy of gemcitabine therapy in pancreatic cancer. *Nanomed. Nanotechnol. Biol. Med.* 7, 841–849. doi: 10.1016/j.nano.2011.02.012

Rosenberger, I., Strauss, A., Dobiasch, S., Weis, C., Szanyi, S., Gil-Iceta, L., et al. (2015). Targeted diagnostic magnetic nanoparticles for medical imaging of pancreatic cancer. *J. Control. Release* 214, 76–84. doi: 10.1016/j.jconrel.2015.07.017

Rucki, A. A. (2014). Pancreatic cancer stroma: understanding biology leads to new therapeutic strategies. *World J. Gastroenterol.* 20:2237. doi: 10.3748/wjg.v20.i9.2237

Schultheis, B., Strumberg, D., Santel, A., Vank, C., Gebhardt, F., Keil, O., et al. (2014). First-in-human phase I study of the liposomal RNA interference therapeutic Atu027 in patients with advanced solid tumors. *J. Clin. Oncol.* 32, 4141–4148. doi: 10.1200/JCO.2013.55.0376

Siegel, R. L., Miller, K. D., and Jemal, A. (2018). Cancer statistics, 2018. *CA Cancer J. Clin.* 68, 7–30. doi: 10.3322/caac.21387

Singh, R., and Torti, S. V. (2013). Carbon nanotubes in hyperthermia therapy. *Adv. Drug Deliv. Rev.* 65, 2045–2060. doi: 10.1016/j.addr.2013.08.001

Smith, J. K., Chu, Q. D., and Tseng, J. F. (2015). "Pancreatic adenocarcinoma," in *Surgical Oncology* (New York, NY: Springer), 283–313. doi: 10.1007/978-1-4939-1423-4_13

Tanaka, H. Y., and Kano, M. R. (2018). Stromal barriers to nanomedicine penetration in the pancreatic tumor microenvironment. *Cancer Sci.* 109, 2085–2092. doi: 10.1111/cas.13630

Thind, K., Padrnos, L. J., Ramanathan, R. K., and Borad, M. J. (2017). Immunotherapy in pancreatic cancer treatment: a new frontier. *Ther. Adv. Gastroenterol.* 10, 168–194. doi: 10.1177/1756283X16667909

Thompson, C. B., Shepard, H. M., O'Connor, P. M., Kadhim, S., Jiang, P., Osgood, R. J., et al. (2010). Enzymatic depletion of tumor hyaluronan induces antitumor responses in preclinical animal models. *Mol. Cancer Ther.* 9, 3052–3064. doi: 10.1158/1535-7163.MCT-10-0470

Torisu, Y., Takakura, K., Kinoshita, Y., Tomita, Y., Nakano, M., and Saruta, M. (2019). Pancreatic cancer screening in patients with presumed branch-duct intraductal papillary mucinous neoplasms. *World J. Clin. Oncol.* 10, 67–74. doi: 10.5306/wjco.v10.i2.67

Tummers, W. S., Miller, S. E., Teraphongphom, N. T., Gomez, A., Steinberg, I., Huland, D. M., et al. (2018). Intraoperative pancreatic cancer detection using tumor-specific multimodality molecular imaging. *Ann. Surg. Oncol.* 25, 1880–1888. doi: 10.1245/s10434-018-6453-2

Vahrmeijer, A. L., Hutteman, M., Van Der Vorst, J. R., Van De Velde, C. J. H., and Frangioni, J. V. (2013). Image-guided cancer surgery using near-infrared fluorescence. *Nat. Rev. Clin. Oncol.* 10, 507–518. doi: 10.1038/nrclinonc.2013.123

Vassie, J. A., Whitelock, J. M., and Lord, M. S. (2017). Endocytosis of cerium oxide nanoparticles and modulation of reactive oxygen species in human ovarian and colon cancer cells. *Acta Biomater.* 50, 127–141. doi: 10.1016/j.actbio.2016.12.010

von Ahrens, D., Bhagat, T. D., Nagrath, D., Maitra, A., and Verma, A. (2017). The role of stromal cancer-associated fibroblasts in pancreatic cancer. *J. Hematol. Oncol.* 10:76. doi: 10.1186/s13045-017-0448-5

Wang-Gillam, A., Hubner, R. A., Siveke, J. T., Von Hoff, D. D., Belanger, B., de Jong, F. A., et al. (2019). NAPOLI-1 phase 3 study of liposomal irinotecan in metastatic pancreatic cancer: final overall survival analysis and characteristics of long-term survivors. *Eur. J. Cancer* 108, 78–87. doi: 10.1016/j.ejca.2018.12.007

Wason, M. S., Colon, J., Das, S., Seal, S., Turkson, J., Zhao, J., et al. (2013). Sensitization of pancreatic cancer cells to radiation by cerium oxide nanoparticle-induced ROS production. *Nanomed. Nanotechnol. Biol. Med.* 9, 558–569. doi: 10.1016/j.nano.2012.10.010

Woo, W., Carey, E. T., and Choi, M. (2019). Spotlight on liposomal irinotecan for metastatic pancreatic cancer: patient selection and perspectives. *Oncol. Targets Ther.* 12, 1455–1463. doi: 10.2147/OTT.S167590

Xie, D., and Xie, K. (2015). Pancreatic cancer stromal biology and therapy. *Genes Dis.* 2, 133–143. doi: 10.1016/j.gendis.2015.01.002

Yang, F., Jin, C., Subedi, S., Lee, C. L., Wang, Q., Jiang, Y., et al. (2012). Emerging inorganic nanomaterials for pancreatic cancer diagnosis and treatment. *Cancer Treat. Rev.* 38, 566–579. doi: 10.1016/j.ctrv.2012.02.003

Yu, B., Zhao, X., Lee, L. J., and Lee, R. J. (2009). Targeted delivery systems for oligonucleotide therapeutics. *AAPS J.* 11, 195–203. doi: 10.1208/s12248-009-9096-1

Zeiderman, M. R., Morgan, D. E., Christein, J. D., Grizzle, W. E., McMasters, K. M., and McNally, L. R. (2016). Acidic PH-targeted chitosan-capped mesoporous silica coated gold nanorods facilitate detection of pancreatic tumors via multispectral optoacoustic tomography. *ACS Biomater. Sci. Eng.* 2, 1108–1120. doi: 10.1021/acsbiomaterials.6b00111

Zhang, B., Jiang, T., Shen, S., She, X., Tuo, Y., Hu, Y., et al. (2016). Cyclopamine disrupts tumor extracellular matrix and improves the distribution and efficacy of nanotherapeutics in pancreatic cancer. *Biomaterials* 103, 12–21. doi: 10.1016/j.biomaterials.2016.06.048

Zhao, X., Li, F., Li, Y., Wang, H., Ren, H., Chen, J., et al. (2015). Co-Delivery of HIF1α SiRNA and gemcitabine via biocompatible lipid-polymer hybrid nanoparticles for effective treatment of pancreatic cancer. *Biomaterials* 46, 13–25. doi: 10.1016/j.biomaterials.2014.12.028

Zhao, X., Wang, X., Sun, W., Cheng, K., Qin, H., Han, X., et al. (2018). Precision design of nanomedicines to restore gemcitabine chemosensitivity for personalized pancreatic ductal adenocarcinoma treatment. *Biomaterials* 158, 44–55. doi: 10.1016/j.biomaterials.2017.12.015

Zhao, X., Yang, K., Zhao, R., Ji, T., Wang, X., Yang, X., et al. (2016). Inducing enhanced immunogenic cell death with nanocarrier-based drug delivery systems for pancreatic cancer therapy. *Biomaterials* 102, 187–197. doi: 10.1016/j.biomaterials.2016.06.032

Zhou, H., Qian, W., Uckun, F. M., Wang, L., Wang, Y. A., Chen, H., et al. (2015). IGF1 receptor targeted theranostic nanoparticles for targeted and image-guided therapy of pancreatic cancer. *ACS Nano* 9, 7976–7991. doi: 10.1021/acsnano.5b01288

Check for
updates

Theranostic Nanomedicine for Malignant Gliomas

Michele d'Angelo[1], Vanessa Castelli[1], Elisabetta Benedetti[1], Andrea Antonosante[1], Mariano Catanesi[1], Reyes Dominguez-Benot[1], Giuseppina Pitari[1], Rodolfo Ippoliti[1] and Annamaria Cimini[1,2]*

[1] Department of Life, Health and Environmental Sciences, University of L'Aquila, L'Aquila, Italy, [2] Department of Biology, Sbarro Institute for Cancer Research and Molecular Medicine, Temple University, Philadelphia, PA, United States

Brain tumors mainly originate from glial cells and are classified as gliomas. Malignant gliomas represent an incurable disease; indeed, after surgery and chemotherapy, recurrence appears within a few months, and mortality has remained high in the last decades. This is mainly due to the heterogeneity of malignant gliomas, indicating that a single therapy is not effective for all patients. In this regard, the advent of theranostic nanomedicine, a combination of imaging and therapeutic agents, represents a strategic tool for the management of malignant brain tumors, allowing for the detection of therapies that are specific to the single patient and avoiding overdosing the non-responders. Here, recent theranostic nanomedicine approaches for glioma therapy are described.

Keywords: theranostic nanoplatform, brain tumors, targeted therapy, drug delivery, diagnosis

THERANOSTIC TECHNOLOGY

Theranostics is the combination of the two terms "Therapeutics" and "Diagnostics," referring to technologies that include both diagnostic and therapeutic applications (**Figure 1**). The interest in personalized medicine, and thus, theranostic approaches used for individualized diagnosis and treatment are gaining increasing attention (Sun, 2010; Kelkar and Reineke, 2011; Kievit and Zhang, 2011; Ahmed et al., 2012; Wang Y. et al., 2014). This technology allows us to save time and decrease costs but, notably, also allows us to contain side effects of a single strategy (Lammers et al., 2010), obtaining better patient outcomes (Duncan, 2003; Peer et al., 2007).

Nanoplatforms (NPS) are nanoparticles combined with drug and molecular imaging probes, including metal nanoparticles, polymer-drug conjugates, polymer micelles, liposomes, and dendrimers. NPS show several advantages over conventional formulations, allowing for the conjugation or entrapment of drugs (Peer et al., 2007). Nanoparticles (NPs) are complex drug delivery systems, which can be structurally divided into the internal layer (core), and external layer (shell). Nanodimensions ensure that nanoparticles are able to increase drug solubility, mitigate cytotoxicity, and improve drug pharmacokinetic profiles. The creation of nanoplatforms, combining drugs with molecular probes, increases the drug half-life in the circulatory system, and specifically, delivers anticancer drugs to target tissues, controlling the drug release through detectors responsive to different stimuli such as pH, temperature, light, ultrasound, and enzymatic activities, thus improving the delivering of the required drug concentration to the area of interest (Tong and Cheng, 2007). By means of improving the circulating half-life, nanomedicines can accumulate in tumors through the Enhanced Permeability and Retention (EPR) effect (Golombek et al., 2018). In the last years, it has been reported that EPR varies among mouse models and patients, between tumor types of the same origin, and also among tumors and metastases of the

same patient (Harrington et al., 2001; Tanaka et al., 2017), thus explaining the heterogeneous outcomes of nanomedicine clinical trials. To overcome this issue, efforts should be focused on the use of methods that can be employed to individualize and improve nanomedicine treatments.

Despite the advantages offered by the EPR effect, the passive targeting approach offers a limited benefit in the treatment of gliomas and other CNS disorders. In these situations, the BBB remains impenetrable for different nanostructures that tend to accumulate in off-target tissues that also have vasculature gaps, such as the liver, or lymph nodes (Nam et al., 2018).

Since theranostic approaches require the use of molecular imaging tools, a combination of drug delivery systems with imaging techniques, such as computed tomography (CT), magnetic resonance imaging (MRI), optical and ultrasound (US) imaging, positron emission tomography (PET), and single photon emission computed tomography (SPECT), are currently under study. All these imaging techniques, using sensible and specific probes, can, in fact, assess drug efficacy during the drug development procedures (Cai et al., 2006; Pysz et al., 2010; Ai, 2011; Ang et al., 2014), optimizing the right choice of imaging tools and agents (Jokerst and Gambhir, 2011) and defining the best combination for specific therapeutic applications.

MULTIFUNCTIONALIZED NANOPLATFORMS

Multifunctionalized NPS are promising therapeutic approaches in cancer therapy (**Table 1**). Indeed, they offer numerous advantages over conventional agents, including specific targets, the higher ability to solubilize hydrophobic or labile drugs, lower systemic toxicity (resulting in better pharmacokinetics and higher potential to image), and better treatment and prediction of a therapeutic response. NPS utilize nanostructures, such as nanoparticles, made from soluble or colloidal aqueous solutions

and with sizes ranging between 10 and 100 nm (Bhojani et al., 2010). The small size allows them to pass via blood capillaries and reach the specific tumor cells (Bhojani et al., 2010). They have the advantages of modifying the nature and the number of linkers on and within the surface of a nanoparticle and its dimensions, thus leading to the control of the loading/releasing of the entrapped or covalently linked drugs. The NPS can also ameliorate the efficacy of current drugs or tracers, triggering a selective delivery. Among NPS, those based on nanovesicles are also biocompatible, thus increasing the maximum tolerated dose of the drug with low toxicity. This leads to an increased concentration of the agent inside the tumor and a simultaneous decrease in side effects (Liong et al., 2008; Bhojani et al., 2010). The entrapment of the drug with nanoplatforms reduces the limit for the use of poorly soluble or poorly absorbed agents by encapsulating them in the matrix of the NPS during the design and synthetic processes. Furthermore, the encapsulation prevents premature degradation of drugs or inactivation during plasma transport. Being a multidelivery system represents one of the most advantageous characteristics of NPS. They can carry imaging tracers, targeting ligands, therapeutic agents, and "cloaking" agents that avoid interference with the immune system (reviewed in Bhojani et al., 2010; Mendes et al., 2018).

Cancer researchers have shown high interest in theranostic approaches, particularly to detect and develop a solid nanosystem strategy for cancer treatment and diagnosis that can be translated into clinical practice (Cole et al., 2011).

Typical examples of the design of biocompatible nanoplatforms used as theranostic agents are based on magnetic nanoparticles, polymers, vesicles nanoparticles, and dendrimers.

Magnetic nanoparticles have been prepared using, for example, IONPs (iron oxide nanoparticles) coated with a human serum albumin. This formulation is referred as a biocompatible material for a chemotherapeutic agent, photosensitizers, and NPS (reviewed in Choi et al., 2012). Polymeric conjugates for drug delivery, biodistribution, and drug efficiency were extensively
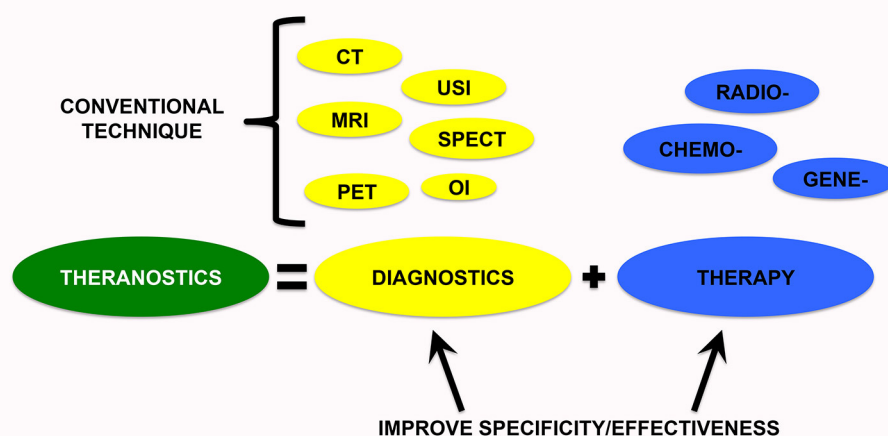

FIGURE 1 | Theranostic medicine provides new tools to improve diagnostic specificity and therapeutic effectiveness. Therefore, a nanoparticle-containing tracer can be useful to overcome the limitations of conventional diagnostic and therapeutic techniques. CT, computed tomography; MRI, magnetic resonance imaging; USI, ultrasound imaging; OI, optical imaging; PET, positron emission tomography; SPECT, single-photon emission computed tomography.

TABLE 1 | Nanoplatforms examples and their characteristics.

	Nanoplatforms	Biosafety	Size	Loading capacity	References
Magnetic Nanoparticle	DOX IONPS	Low toxicity	10–50 nm	High	Choi et al., 2012
Polymer-conjugates	DOX-GEM GADOLINIUM HPMA	Low toxicity	20–70 nm	Good	Vilos and Velasquez, 2012
Nanovesicles	β(CD) SPIO Polymeric micelles	Really low toxicity	10–70 nm	High	Liong et al., 2008; Bhojani et al., 2010
Dendrimers	asODN MNP PAMAM	Potential toxicity	10–40 nm	High	Pan et al., 2007

Different nanoplatforms and the respective biosafety, size, and loading capacity. DOX-conjugated, doxorubicin; PAMAM, poly(amidoamine); IONPs, iron oxide nanoparticles; DOX-GEM, gemcitabine (GEM), and doxorubicin (DOX); HPMA, N-2-hydroxypropylmethacrylamide; asODN, antisense oligodeoxynucleotides; MNPs, Magnetic Nanoparticles; SPIO, superparamagnetic iron oxide.

investigated (Vilos and Velasquez, 2012). Lammers et al. (2010) synthesized a simultaneous delivery of doxorubicin and gemcitabine, and they were labeled with a gadolinium HPMA (N-2-hydroxypropylmethacrylamide) copolymer to investigate the biodistribution of nanotheranostics using an MRI (Lammers et al., 2010). This investigation reported that tumor-targeted polymeric drug vectors could be utilized to deliver two different chemotherapeutic drugs to tumors concurrently (Lammers et al., 2010).

Polymeric micelles, nano core/shell structures constituted by amphiphilic copolymers, were thoroughly tested as theranostic carriers and imaging probes as well. The amphiphilic block copolymers captured the superparamagnetic iron oxide (SPIO) or Mn-SPIO nanoparticles and are employed for the MRI (Lu et al., 2009; Liu et al., 2011; Xie et al., 2011; Su et al., 2013). β-cyclodextrin (β-CD) has been successfully used to encapsulate SPIO nanoparticles and small molecule anticancer drugs (Su et al., 2013). Several multifunctional polymeric micelles for tumor drug delivery and distribution have been designed, with particular attention to the creation of a well-controlled nanostructure. The use of polymeric micelles is advantageous because they can entrap an elevated number of hydrophobic drugs and contrast agents, maintaining their hydrophilic feature as a carriers, compared to liposomes or soluble polymers. Polymeric micelles are recognized as multifunctional delivery systems that are able to maximize therapeutic efficacy (Vilos and Velasquez, 2012).

Liposomes are already approved by the FDA since they are able to incorporate drugs, such as chemotherapeutics (Al-Jamal and Kostarelos, 2011). Approved formulations are liposomal doxorubicin and pegylated liposomal doxorubicin, which show low toxicity, cardiac safety, and less alopecia, myelosuppression, nausea, and vomiting when compared to conventional anthracyclines. The difficulty in releasing the encapsulated drug in the target area is caused by a limit in the liposome system. To overcome this issue, new liposome systems have been designed that are able to induce a pH

and temperature response or the activation of certain enzymes on liposome cavities, thus improving the drug release in the targeted area (Lindner and Hossann, 2010; Wang D. et al., 2014). Recently, multifunctional theranostic nanoplatforms, using contrast agents encapsulated with liposomes, have been developed for the simultaneous diagnosis of early stage of disease and drug delivery, utilizing liposomes that encapsulate contrast agents, resulting in the creation of multifunctional NPS (Kenny et al., 2011; Na et al., 2011; Petersen et al., 2012). A theranostic nanosystem that provides the incorporation of magnetic nanoparticles inside the liposomes has been developed (Fattahi et al., 2011). Thus, multifunctional theranostic liposomes are widely used in treatment and for the detection of diseases, and they represent a valid carrier to further improve the diagnostic and therapeutic efficacy.

Furthermore, dendrimers are gaining increasing importance in the theranostic field as they can, due to their size, encapsulate several drugs or imaging tracers with high efficiency. For instance, dendrimers can bind non-covalently or covalently to chemotherapeutic drugs, imaging agents, and other biologically active targeting moieties, such as peptides, monoclonal antibodies, and folates (Boas and Heegaard, 2004; Mintzer and Grinstaff, 2011; Lo et al., 2013). The characteristic structure of dendrimers can stabilize the hydrophobic nanoparticles through the ligand exchange reaction method. Recently, multifunctional doxorubicin (DOX)-conjugated poly(amidoamine) (PAMAM) dendrimers have been developed with a specific platform for targeted chemotherapy that uses pH to release the drug to tumor cells. This multifunctional dendrimer presented excellent biocompatibility, biodistribution, and satisfactory cancer imaging results (Chang et al., 2011). Dendrimers represent promising structures for functionalization and also for conjugation with drugs (chemotherapeutics and imaging tracers) and DNA/RNA (Pan et al., 2007; Merkel et al., 2010; Zottel et al., 2019).

GLIOMAS

Glioma is a common type of tumor arising from glia-supporting neurons. About 33% of all brain tumors are gliomas and show different malignancy and differentiation grades. Symptoms depend on the area of the brain affected and by the degree of malignancy; they include headaches, nausea, or vomiting, speech difficulties, vertigo, and motor alteration. In its advanced stages, seizures may be a common manifestation. Gliomas are classified on the basis of the glial type but also on the genetic signature that predicts the outcome and the response to treatment. Gliomas are classified, according to the World Health Organization, as astrocytoma, anaplastic astrocytoma and glioblastoma, oligodendrogliomas, ependymomas, and mixed gliomas (Wesseling and Capper, 2018). Glioblastoma (GB) multiforme is the most malignant and common (more than 60%) type of primary astrocytomas (Rock et al., 2012). Despite the modern therapies to treat GB, it is still a deadly disease with an extremely poor

prognosis. Patients usually have a median survival of ∼14–15 months from the diagnosis (Thakkar et al., 2014). The standard treatment for GB is the resection of the tumor by neurosurgery, followed by radiation, and chemotherapy administration. However, these therapies are often ineffective, having a high rate of recurrence and drug resistance over time, accompanied by severe neurological deterioration of the affected patient (Silantyev et al., 2019).

The surgical approach is often not efficient due to the frequent persistence of tumoral foci; this leads to the recurrence of the disease (Alphandéry et al., 2015) thanks to the high proliferative rate and invasive behavior of GB cells. In this regard, several studies have reported the crucial role of bulk removal in increasing life expectancy and patient outcome (Silantyev et al., 2019). However, even bulk removal is not completely efficient since it is, generally, followed by relapses. For these reasons, GB is considered a not treatable disease. Temozolomide (TMZ) is currently the gold standard treatment for GB. Its metabolites form a complex with alkyl guanine alkyl transferase (O6 MGMT- DNA repair protein), leading to DNA damage; however, some patients show resistance to TMZ. Thus, many studies have reported the efficacy of the combination of TMZ with different compounds, such as curcumin, resveratrol, O6-benzylguanine, valproic acid, anti-epilectic drugs, interferon 1-β, mesenchymal stem cells, and anti-malarial drugs [extensively reviewed in Bahadur et al. (2019)], with reduced resistance and increased treatment efficacy. In particular, it has been reported that the combined administration of bone marrow-derived mesenchymal cells (MSCs), interferon β (IF-β), and TMZ significantly decreased tumor progression *in vitro* and increased the survival of patients following synergistic effects *in vivo* (Park et al., 2015). More recently, the simultaneous administration of the inducer of autophagy, sirolimus, the inhibitor of autophagy, Chloroquine, and TMZ on glioblastoma cells was investigated in order to obtain lysosome disruption and apoptotic death (Hsu et al., 2018). In the same way, several new molecules were proposed to enhance TMZ activity in glioblastoma both *in vitro* and *in vivo* (extensively reviewed in Bahadur et al., 2019).

The diagnostic tools to detect brain tumors are represented by imaging tests, mainly MRI, including different specialized MRI scan components, including functional MRI, perfusion MRI, and magnetic resonance spectroscopy. These tools help us to understand tumor size and to plan treatment. Other imaging exams may include PET, a computerized tomography (CT) scan, and a cerebral angiogram. Molecular testing of the tumor could also be recommended for the identification of specific proteins, genes, and other factors (i.e., tumor markers) distinctive to the tumor. Indeed, some biomarkers may help in determining a patient's prognosis, increasing the chance of recovery. For the final and definite diagnosis, a biopsy of the tumor's tissue is usually necessary in order for it to be analyzed by a pathologist (Piquer et al., 2014; Tandel et al., 2019).

The first occurrence in tumor transformation is not completely clarified. However, it seems that the genetic signature is different in grade II gliomas, astrocytoma, and oligodendroglioma. All tumors initially show the same invasive phenotype, making it difficult to develop a unique therapy. Progression-associated genetic modifications target cell cycle-controlling pathways and growth promoting, causing focal hypoxia, necrosis, and angiogenesis. Retinoblastoma protein (Rb) mutation was identified in 20% of malignant gliomas (Behin et al., 2003), although gliomas may also contain mutations in other molecules involved in Rb signaling, including cyclin-dependent kinase (CDK) and the cell cycle regulator cyclin-dependent kinase inhibitor 2A, multiple tumor suppressor 1 (p16^{INK4A}). Most of the anaplastic astrocytoma show homozygous mutation, deletion, and promoter hypermethylation in the INK4A/ARF locus that encodes two tumor suppressors [p16^{INK4a} and an alternate reading frame tumor suppressor, p14^{ARF} (Yamanaka, 2008)]. Moreover, it has been shown that PDGF (platelet-derived growth factor) and platelet-derived growth factor receptor (PDGFR) signaling are involved at the beginning of the progression from astrocytoma to GB. In fact, elevated levels of PDGFRα have been reported in all types of gliomas, particularly in GB. Also, gliomas induce the overexpression of other mitogens, including IGF-1 (Insulin like Growth factor) and EGF (Epidermal growth factor) as well (Wong et al., 1992; Chakravarti et al., 2002; Nicholas et al., 2006; Puputti et al., 2006; Newton, 2010). Their receptors are present as constitutively active mutant forms in gliomas (Wong et al., 1992), leading to the activation of numerous pathways, including PI3K/AKT PBK, phospholipase protein C, and RAS/mitogen-activated protein kinase. In turn, these pathways control invasion, cell proliferation, apoptosis, and differentiation processes (Schlessinger, 2000). A common alteration (20–40%) identified in glioblastoma that affects the PI3K-Akt pathway is the genetic loss or mutation of the tumor suppressor gene PTEN (Phosphatase and Tensin homolog deleted on chromosome ten). Indeed, PTEN is a key negative regulator of the PI3K/Akt pathway (Stambolic et al., 1998; Cantley and Neel, 1999). In addition, gliomas display the upregulation of angiogenic factors, such as the FGF (fibroblast growth factor), TGF (transforming growth factor), Interleukin 8 (IL-8), and Vascular-Endothelial Growth Factor (VEGF) (Benoy et al., 2004; Slettenaar and Wilson, 2006; Xiao et al., 2018). The combination of the genetic alteration of these factors triggers a malignant glioma with an aggressive phenotype and that is resistant to intensive therapies. In this tumorigenic process, glioma stem cells exert a leading role (Uchida et al., 2000; Gaya et al., 2002; Kondo et al., 2004; Gürsel et al., 2011). Since glioma stem cells are able to self-propagate, in order to avoid recurrence, it is fundamental to target specifically them (Kroonen et al., 2008). The new possibility to isolate GBM stem cells allows for new therapeutic approaches, among which are gene replacement, knockdown, or silencing (Kroonen et al., 2008). Since each GB patient shows a peculiar molecular profile, the response at radio- and chemotherapies is different. On this basis, different GB cell lines may show a different response to Cdk inhibitors (Caracciolo et al., 2012; Cimini et al., 2017).

GB, and other solid tumors as well, encounter metabolic reprogramming; thus, the tumor is able to survive in hypoxic conditions and sustain angiogenesis and hyperproliferation

(Kroemer and Pouyssegur, 2008; Tennant et al., 2009; Fidoamore et al., 2016; Antonosante et al., 2018).

In particular, tumor cells activate the glycolytic pathway, also in the presence of oxygen (Warburg effect) (Frezza and Gottlieb, 2009). Indeed, tumor cells exploit the glycolytic signaling intermediates for anabolic reactions (Gatenby and Gillies, 2004). Only the cells subjected to these alterations are able to survive in the tumor environment, suggesting the presence of a selection of those with the altered metabolic phenotype (Tennant et al., 2009). The progress in the genetic biology of gliomas, and the recent insertion of manipulable experimental models, allows for the development of effective targeted therapy.

TARGETED THERANOSTIC NANOPLATFORMS FOR BRAIN CANCER THERAPY AND IMAGING

The human brain is an extremely complicated organ, which simultaneously regulates and supervises several functions. Successful therapy in brain cancers is restricted because the administered therapeutic entity cannot reach the targeted area after systemic administration (Cheng et al., 2014), and this is the main obstacle for the transport of the therapeutic agents represented by the blood–brain barrier (BBB). The BBB consists of a physical barrier, composed by vascular endothelial cells, and is held together by tight junctions, transporters, receptors, enzymes, and the ATP-dependent, 170-kDa efflux pump P-glycoprotein (Sonali et al., 2016a,b,c). The BBB retains the passage of agents with a molecular weight >500 Da but also of the majority of small sized molecules (Wei et al., 2014; Agrawal et al., 2017a,b). ATP-binding P-gp at the same time exerts the efflux function for xenobiotics, and their strong expression inhibits the passage of substrates through the BBB. The majority of the chemotherapeutics are hydrophobic and larger in molecular size; thus, they cannot cross the BBB spontaneously. Also, chemotherapeutics are substrates of multidrug-resistant drug efflux pumps, which are active on both tumor vascular cells and the BBB (Zong et al., 2014).

Brain cancers are difficult to detect and treat during the primary stages. The diagnosis and the detection of the volume of the brain cancers are complex because an accumulation of extracellular fluid (Koo et al., 2006) surrounding the tumor region is generally present. Since the 1970s, the primary modality to treat brain cancer includes surgical resection and/or chemotherapy or radiotherapy (Koo et al., 2006).

Conventional diagnostic and therapeutic agents showed improper bio-distribution and modest pharmacokinetics, leading to insufficient dissemination into tumors (Muthu et al., 2014a,b). In addition, they are non-specific and can accumulate in healthy organs, resulting in high toxicity. To overcome these issues, the nanotheranostic approach could be very useful. Different effective nanotheranostics brain cancer therapies have been recognized, but they need further investigation (Lakka and Rao, 2008; Xie et al., 2010; Keunen et al., 2011; Fan et al., 2014; Nance et al., 2014; Arranja et al., 2017). For instance, nanoparticle-enhanced imaging of the CNS at the subcellular

level localizes more precisely the intracranial neoplasms area (**Figure 2**) (Bhojani et al., 2010). Also, nanoparticle-enhanced neuroimaging is very useful to understand physiological processes, including apoptosis, ischemia, inflammation, cell differentiation, and mitosis, representing the main tool for further research studies in neurodegenerative diseases and stroke (reviewed in Mattei and Rehman, 2015). To study physiological processes, many microscopic and macroscopic imaging modalities have been established. Microscopic methods require the invasive harvesting of tissues and imaging by cell-based assays (i.e., for apoptosis TUNEL, Annexin V, and Caspase Substrate Based Assays) (Cen et al., 2008). Macroscopic imaging modalities, by contrast, visualize apoptosis in living subjects in non-invasive modality. To date, to study these physiological processes, various *in vivo* molecular imaging technologies have been used, including Radiolabeled Small Molecular Probes, optical imaging probes, MRI agents, and multiple-modality methods. Microscopic and macroscopic imaging strategies improved the understanding of various physiological processes, or pathologies in preclinical and clinical studies (Zeng et al., 2015).

Unfortunately, the BBB still represents a limitation for nanotheranostic delivery (Wilhelm and Krizbai, 2014). To facilitate *in vitro* studies of drug delivery to the brain, promising *in vitro* BBB models have been developed based on primary or immortalized cells or on the culture of brain endothelial cells (Wilhelm and Krizbai, 2014; Helms et al., 2016). Valid models can be obtained using primary porcine brain endothelial cells and rodent co-culture models, which are characterized by low paracellular permeability and functional efflux transporters, mimicking the *in vivo* physiological complexity of the *in vivo* BBB. These include triple co-culture (brain endothelial cells with pericytes and astrocytes), dynamic, and microfluidic models, but these models are not suitable for rapid analyses. Great efforts have been made to deliver diagnostic agents and drugs into the brain. Thanks to recent advances in BBB research, new approaches have been exploited. Strategies able to pass through the BBB and reach the brain include viral vectors (characterized by high gene transfection efficiency), exosomes, brain permeability enhancers, and nanoparticles (Dong, 2018).

For example, Pilkington et al., in one of these *in vitro* BBB models, tested the properties of chitosyme nanoparticulate structures on BBB integrity, analyzing the tight junction proteins (ZO-1, occludin) and effects on the extra cellular matrix (Pilkington et al., 2014). In additional studies, paclitaxel (PTX) were constructed with a cyclic Arg-Gly-Asp (RGD) peptide as a targeting ligand to pass through the BBB by a targeting method. The nanocarriers were tested on a 3D glioma spheroid of glioma cells grown on agarose and showed targeted accumulation into tumor spheroids and excellent infiltration compared with conventional nanocarriers, suggesting a potential use in therapeutic approaches (Jiang et al., 2013). The theranostic nanosystems are combined with the targeting agent that identifies definite targets of brain cancer cells and binds to and internalizes via a specific mechanism. Several nanomaterials, including Gold Nanoparticles (AuNPs) and Quantum Dots (QDs) have intrinsic
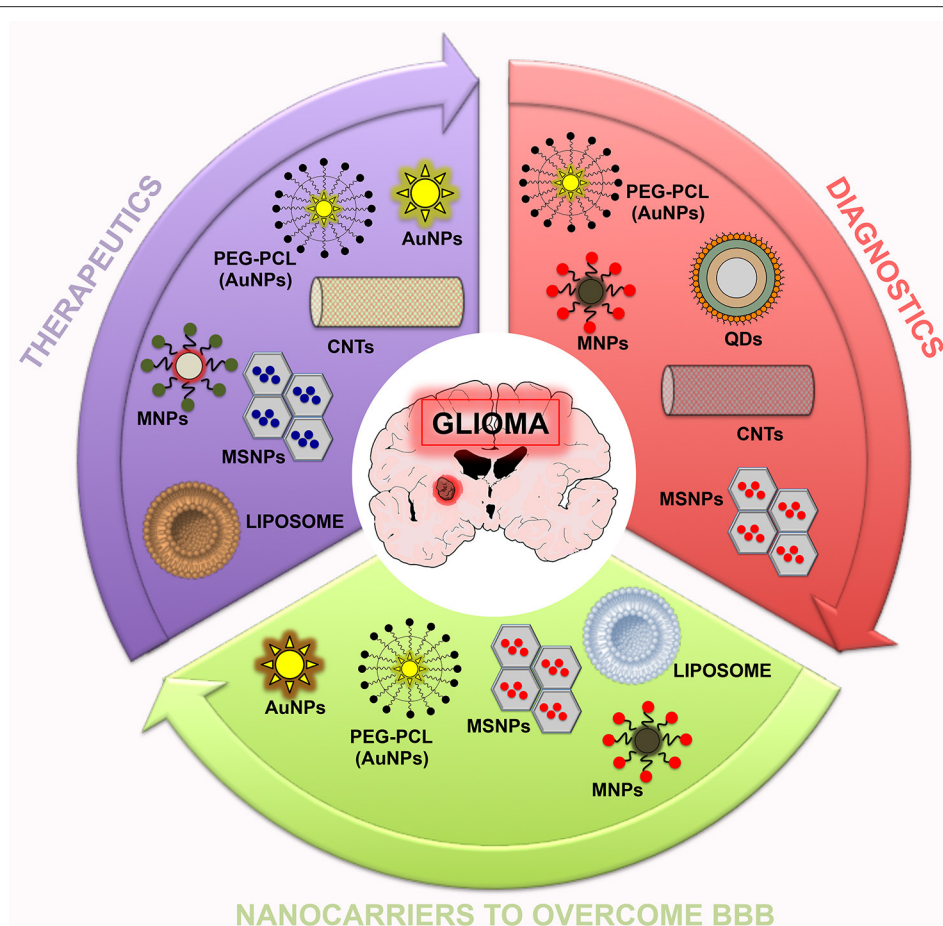
FIGURE 2 | Summary scheme of nanoparticles potentially useful in theranostic nanomedicine for glioma. In this scheme, three sets (therapeutics, diagnostics, and nanocarriers to overcome the BBB) related to the potential application of nanoparticles are reported.

diagnostic/therapeutic properties (Muthu et al., 2014a; Sonali et al., 2018).

GOLD NANOPARTICLES

Gold Nanoparticles designed from gold cores represent a new system for theranostic systems (**Table 2**). They are biocompatible and are usually prepared as spheres, wire, rods, cubes, and cages. AuNPs, like other inorganic nanoparticles, trigger oxidative stress and subsequent cytotoxic effects. The spheroidal AuNPs ultraviolet (UV) absorption is at 520 nm, while the gold nanorods absorption is in the Infrared radiation (690–900 nm). These intrinsic optical characteristic allow AuNPs to be utilized as multifarious theranostic drugs for clinical applications (Xie et al., 2010; Kumar et al., 2013). AuNPs showed a diagnostic property, tunable core size, low toxicity, surface plasmon absorption and ease of fabrication, and light-scattering properties (Fan et al., 2014). AuNPs have been widely studied; for example, Melancon et al. formulated multi-utility gold-based nanoshells with optical and magnetic activities, which were additionally conjugated with targeting moiety and studied as an approach for head and neck cancer (Melancon et al., 2011). It has

been shown that AuNPs improve the treatment of gliomas; for instance, the use of AuNPs-combined radiotherapy promoted long-term survival with respect to radiation therapy alone (Hainfeld et al., 2013; Joh et al., 2013). In another study, a theranostic system for cancer treatment, which was able to reduce the cytotoxic effect on normal cells, has been developed based on the use of gold nanoparticles surface-functionalized with a paclitaxel drug and biotin receptor. Two categories, AuNPs-4 and AuNPs-5, were investigated for their peculiar interaction with cancer cells. These nanoparticles were tested against the immortalized NIH3T3 cells, and it was suggested that the AuNPs-5 was more efficient (Heo et al., 2012). In addition, AuNPs represent an encouraging candidate for tumor margin detection, improving the surgery resection of brain cancers (Tzeng and Green, 2013). An *in-vitro* study on brain tumor cell lines showed a strong amelioration in uptake studies of targeted particles with respect to non-targeted formulations (Dixit et al., 2015b). Recently, matrix metalloproteinase-2-sensitive gold-gelatin nanoparticles were developed; RGD and octarginine were used as targeting ligands to pass through the BBB, allowing a pH-triggered release to the glioma-specific area. Indeed, it has been reported that gold nanotheranostic

TABLE 2 | Nanoparticles examples with some characteristics.

Nanoparticles	Biosafety	Size	References
Gold nanoparticles	Low cytotoxicity	2–60 nm	Fan et al., 2014
Magnetic nanoparticles	Potential cytotoxicity	7–20 nm	Alphandéry et al., 2015
Quantum dots	Potential cytotoxicity	2–50 nm	Onoshima et al., 2015
Carbon nanotubes	Potential cytotoxicity	0.4–40 nm	Wang et al., 2012
Mesoporous silica nanoparticles	Low cytotoxicity	20–25 nm	Wang et al., 2015

Different nanoparticles and the respective biosafety and size.

targeted specific tumor areas since it is able to co-localize within neovessels (Ruan et al., 2015). Gold theranostic micelles coated with polyethylene glycol-polycaprolactone (PEG-PCL) exhibited radiosensitizing efficacy for GBM therapy and can be used as a novel contrasting agent for both MRI and CT studies (Sun et al., 2016).

MAGNETIC NANOPARTICLES

Recently, Magnetic Nanoparticles (MNPs) have been introduced as potential nanocarriers in targeted drug delivery at the tumor area, having the further benefit of MRI traceability (**Table 2**). The magnetic response (iron oxide core) ameliorates the magnetic targeted delivery (Pankhurst et al., 2003; Frimpong and Hilt, 2010). Interestingly, it has been shown that intravenous administration of these particles is able to reach the cancer site in an animal model. Recently, Chertok et al. reported that magnetic nanoparticles are a useful tool for magnetically enhanced accumulation in brain tumors and for non-invasive MRI screening. This accumulation can be sharply improved with magnetic targeting, as confirmed by MRI (Chertok et al., 2008). A recent *in-vivo* study suggested the potential clinical application of these nanotheranostics since MNPs overpass the BBB in a reversible way, and the substance can reach the targeted site (Lammers et al., 2015; Tabatabaei et al., 2015). Since 2013, NanoTherm® therapy has been established as a new procedure for the focal treatment of solid tumors (Rivera Gil et al., 2010). In this procedure, magnetic nanoparticles are introduced in the tumor or in the resection cavity wall. These particles are then heated by an alternating magnetic field, determining cancer cells death. Nanoparticles are particles of iron oxide, suspended in water, with a diameter of about 15 nm. After the *in vivo* engraftment, they agglomerate and remain the tissue to be treated. An alternating magnetic field then induces the particles to generate heat. Depending on the temperatures reached in the tumor site or in individual remaining cancer cells in the resection cavity wall, and the length of treatment, cancer cells are destroyed or made more sensitive to concomitant radiotherapy or chemotherapy[1] (Alphandéry et al., 2015).

---

[1]NanoTherm® therapy. Available online at: https://www.magforce.com/en/home/our_therapy/

QUANTUM DOTS

Quantum Dots (QDs) are nanoscale (<10 nm) inorganic semiconductor nanocrystals, which represent a potential candidate for theranostic purposes (**Table 2**). They emit light which wavelength can be tuned on the basis of their shape, composition, and size. Cadmium selenide/Zinc sulfide-based QDs are the most used nanomaterials for diagnostic purposes. They have a CdSe core that is overcoated with layers of ZnS (Zhang et al., 2017). Furthermore, to gain affinity and target the cancer site, the surface of the QDs can be covalently or non-covalently conjugated with targeting probes, such as various antibodies, peptides, nucleic acids, folate aptamers, and other small molecules. One of the most suitable methods for conjugating targeting molecules on the surface of QDs is represented by the technique of avidin-biotin cross-linking (Tian et al., 2011; Onoshima et al., 2015). QDs can be conjugated with cancer cell-specific ligands, including HER2 (Ahmed et al., 2017), highly expressed in glioblastoma, CD44, proteins, antibodies, folic acid, and so on. Interestingly, QDs can be combined into paramagnetic liposomal designs containing RGD peptides and utilized as a diagnostic tool in tumor angiogenesis using MRI (Volkov, 2015). QDs in theranostic showed a clinical potential limit, due to their potential toxicity in humans (Derfus et al., 2004; Kirchner et al., 2005). To overcome this problem, further investigation is necessary to design biocompatible, excretable, surface-modified QDs (Onoshima et al., 2015).

CARBON NANOTUBES

Carbon Nanotubes (CNTs) are composed of different layers of graphene sheets, which form a cylindrical shape (**Table 2**). CNTs can be considered as allotropes of carbon with poor biocompatibility and slow biodegradation (Singh et al., 2016). CNTs are useful for theranostic applications since they can ameliorate the effect of chemotherapeutic agents and are translatable to clinical applications (Shapira et al., 2011; Singh et al., 2016). Once CNTs reach the targeted cells, they can interact with DNA and proteins, altering cellular signaling, or the mechanism of other therapeutic approaches (Ren et al., 2012; Chakrabarti et al., 2015). The intrinsic NIR light-absorption characteristic of CNTs has been exploited to eliminate tumor cells *in vitro,* whereas their NIR photoluminescence property has been utilized in cell imaging. In an interesting study, it has been reported that *i.v.* administration of single-walled carbon nanotubes (SWCNTs) as photo luminescent probes is a valid tool for *in vivo* tumor imaging, suggesting that SWCNTs could be used for theranostic applications. Moreover, CNTs are able to improve the chemotherapy effect in brain tumors (Robinson et al., 2010). In fact, recently, gold-coated surface-modified CNTs were established as optical nanotheranostic probes, which exhibited high potential as imaging tracers but had poor clinical potential due to slower biodegradation (and subsequent toxicity), as shown in *in vivo* nanotheranostic studies (Wang et al., 2012). However, CNTs may trigger adverse effects, such as lipid peroxidation, that induce inflammation and cell damage (Shapira et al., 2011; Singh et al., 2016).

MESOPOROUS SILICA NANOPARTICLES

Mesoporous Silica Nanoparticles (MSNPs) are also emerging drug delivery systems. MSNPs are thoroughly investigated and used in diagnostics because of their tunable shape and size and since their wide surface area facilitates a high drug loading (**Table 2**). Numerous drugs, including paclitaxel, camptothecin, methotrexate, colchicine, and cysteine, have been encapsulated in MSNPs. These encapsulated anticancer drugs are able to precisely cause the death of tumor cells (Gary-Bobo et al., 2012; Mamaeva et al., 2013). Thanks to the hexagonal structure, MSNPs can incorporate numerous functional components of an ideal theranostic approach in a single object, with different regions for the contrasting agent, therapeutic moiety, and biomolecular ligand. In addition, MSNPs are identified as safe materials by the FDA and are approved for evaluation in clinical studies. Scientists have utilized silica to integrate both IONPs and QDs, in order to create a hybrid with both optical and magnetic properties. MSNPs are biocompatible and biodegradable materials for nanotheranostic applications. MSNPs that dissolved silica can be absorbed by the biological system, metabolize, and be excreted through urine in the form of silicic acid or oligomeric silica species (Chen et al., 2013; Wang et al., 2015). Biomolecular targeting agents, proteins and peptides, are conjugated to the surface of MSNPs to ameliorate cancer treatment efficacy. Indeed, the surface of MSNPs was conjugated with a Tf peptide to enhance the detection of brain glioma cells (Cheng et al., 2010; Feng et al., 2016). Due to their efficient drug-loading capability, rugged nature, elevated biodegradation in the body, and diverse functionalization, MSNPs are widely used as tracers in MRIs or contrast agents in ultrasounds for accurate targeting, and they show positive results for brain cancer detection (Feng et al., 2016). In an interesting study, mesenchymal stem cells were engineered with MSNPs to treat and diagnose orthotopic glioblastomas. In particular, the intracerebral injection of engineered stem cells significantly improved the survival of rats with U87MG xenografts. This effect was concomitant with a reduction in tumor growth and proliferation and microvascular density. In GSC1 xenografts, intra-tumoral injections of Ad-hMSCs depleted the tumor cell population and induced migration of resident microglial cells (Pacioni et al., 2017). Nanotheranostics therapy was administered systemically to the mice and allowed *in vivo* imaging via MRI, NIR fluorescence, and PET; moreover, it exhibited high specificity for the glioma site (Huang et al., 2013).

NANOPARTICLES FOR GB TREATMENT

Numerous nanostructured delivery systems have been established for brain tumor delivery, and, on the basis of their composition and nature, they can be divided into organic NPS and inorganic NPS (Kumar et al., 2016; Di Martino et al., 2017). Organic NPS (i.e., liposomes, polymeric nanoparticles, lipid nanoparticles, and micelles), compared with the "free" drugs, were able to efficiently cross the BBB, with favored distribution in the brain, in both *in vitro* and *in vivo* studies (Danhier et al., 2015; Chen et al., 2016; Kuo and Cheng,

TABLE 3 | Examples of clinical trials performed using nanoparticles drugs for gliomas.

Drugs	Diseases	Phase	Clinical Trial
ABI-009 (nab-rapamycin)	Recurrent high-grade glioma; Newly diagnosed glioblastoma	II	NCT03463265
NL CPT-11 (Nanoliposomal CPT-11)	Recurrent high-grade glioma	I completed	NCT00734682
Ferumoxytol	Recurrent high-grade glioma	I	NCT00769093
9-ING-41	Glioblastoma	II	NCT03678883
Pegylated Liposomal Doxorubicine + Temozolomide	Glioblastoma And diffuse intristic pontine glioma	II completed	*NCT00944801*
SGT-53	Recurrent glioblastoma	II	NCT02340156
Myocet	Refractory or relapsed malignant glioma in children/adolescent	I	NCT02861222

Drugs, disease, and clinical trials with relative phase.

2016; Liu et al., 2016; Qu et al., 2016; Wu et al., 2016; Belhadj et al., 2017; Chai et al., 2017; Graverini et al., 2018; Jhaveri et al., 2018) (**Table 3**). The main advantages of inorganic NPS (mesoporous silica nanoparticles, gold nanoparticles, iron oxide nanoparticles, and quantum dots) are their resistance to enzymatic degradation, robustness, and interesting intrinsic characteristics (Nam et al., 2013). For the treatment of GB, different kind of NPS (lipidic, magnetic, liposomal, fluorescent, and polymeric) have already been designed in order to cross the BBB, and these take into account active, passive, and stimuli-targeting perspectives (Cheng et al., 2014; Saraiva et al., 2016; Miranda et al., 2017; Aparicio-Blanco and Torres-Suárez, 2018). Theranostic nanoparticles represent a new technological concept that provides a combination of inorganic and organic nanoparticles to acquire synergistic characteristics in a single nanoparticle, exploiting the drug delivery by organic NPS and imaging by inorganic NPS. Theranostic nanoparticles can be used to limit toxicity due to a high and invasive dosage, improving patient outcomes. Recently, a combined chemo-photothermal targeted treatment of gliomas within one nanoparticle was developed. A targeting peptide was synthesized and characterized. In particular, as a therapeutic component, Doxorubicin was chosen, and, as a drug and diagnostic delivery system, a modified mesoporous silica-coated graphene nanosheet (GSPI) was chosen. The doxorubicin-loaded GSPI-based system showed heat-stimulating, pH-responsive, and sustained release properties. The *in vitro* results were encouraging; glioma cells showed a higher rate of death and strong GSPI accumulation (Lee et al., 2011). Targeting AuNPs with two or more receptor-binding peptides for glioblastoma treatment have been established (Dixit et al., 2015a). AuNPs conjugated with peptides (EGF and transferrin) and loaded with the photosensitizer phthalocyanine 4 (Pc 4) displayed

synergistic effects in human glioma cells, concomitant with a high accumulation in the brain tumor area compared to AuNPs alone (Dixit et al., 2015a). Many *in vitro* studies reported positive effects; however, *in vivo* investigations based on theranostic NPS concepts are necessary to translate into clinical practice (Schmieder et al., 2008; Jokerst and Gambhir, 2011; Sailor and Park, 2012). *In vitro* and *in vitro* studies for GB treatment have been reported, and include gold nanoparticles, curcumin-loaded RDP-liposomes, curcumin-loaded PLGA-DSPE-PEG nanoparticles, chitosan-based nanoparticles, iron oxide nanoparticles coated with a chitosan-PEG-polyethyleneimine copolymer, hyaluronic acid conjugated liposomes, and others (Dixit et al., 2015a,b; Orunoglu et al., 2017; Zhao et al., 2018). Finally, magnetic nanoparticles and Nanotherm theranostic technology have been successfully applied in glioblastoma patients in 27 different European countries with double median survival in 59 patients (reviewed in Xie et al., 2018).

All these studies reported high efficiency against glioblastoma also in *in vivo* investigations, thus indicating a promising application in diagnosis and concomitantly in therapeutic approaches, which results from significant accumulation in the brain tumor regions. NPS are poorly investigated in clinical trials (Andronescu and Grumezescu, 2017). The main limitation for using nanotechnology to diagnose and treat cancer is due to its inability to effectively contain and regulate the activity of NPS inside the body, comprising toxicity, biodistribution, and pharmacokinetics (Wicki et al., 2015; Bregoli et al., 2016; Hare et al., 2017).

CONCLUSION AND PERSPECTIVES

In the last years, the field of "theranostic medicine" has gained increasing interest in order to improve diagnostic and therapeutic interventions by nanotechnology resources that exploit a combined approach (**Figure 1**). A nanoparticle should contain a therapeutic agent combined with a tracer to help monitor the effect of the therapy as well. Theranostic is considered a potential candidate for targeted therapy and personalized medicine because you can follow the specific behavior of each tumor concomitant with a substantial increase in the efficacy of the anticancer drugs. This monitoring during the treatment course is a non-invasive method that, through the use of theranostic strategies, allows for the implementation of the individualization of therapeutic regimens based on each patient's response.

Overall, on light of the published investigations, nanotechnology research may be a potential and valid treatment of CNS pathologies, especially brain cancers (**Figure 2**), helping to address the main issues encountered: unclear tumoral margins, neurotoxicity of adjuvant therapies, fibrosis and immunological responses to intracranial devices, vascular anastomosis, multidrug resistance, BBB blockage, and tumor cell-specificity response to pharmacological treatments. Nanotheranostics, indeed, have shown to be a valid option for malignant brain cancers. Thus, in this review, we reported that

nanotheranostics may represent a solid approach to be adopted in brain cancer management. The field of theranostics is pretty new, but considerable efforts have been made in order to develop theranostic nanoparticles for cancer therapy and targeted imaging. Advantages of theranostic nanoparticles include high biosafety, prolonged half-life into the circulatory system, concomitant loading of therapeutic and contrast agents, small size, high surface functionalization, and the ability to perform concomitantly diagnosis/monitoring and therapeutic approaches in real-time. Theranostic NPS allow a specific release of cargo in the affected site, targeting overexpressed proteins and receptors on brain cancer cells. These functions can facilitate the progress of innovative drugs in both preclinical and clinical phases.

Recently, multifunctional applications and combined approaches with personalized medicine applications have increased the hope in a successful clinical translation. Currently, as mentioned above, the only theranostic tool approved for use in the clinical treatment of GBM in Europe is NanoTherm® (Shi et al., 2017).

Overall, the goal is that multifunctional nanomedicine is an efficient, targeted *in vivo* drug delivery without systemic toxicity, and the therapeutic efficacy and the dosage can be precisely measured with low or absent invasivity.

However, in order to translate the experimental studies to clinical trials, further investigations are necessary, particularly to understand the low drug-loading capacity and to optimize the drug concentrations that reach the targeted area, and many factors need to be optimized simultaneously for the best clinical outcome.

In vitro and *in vivo* studies optimized to correctly evaluate toxicity, biodistribution, and pharmacokinetics of NPS are strongly requested to test the safety and efficacy of these nanomaterials in clinical studies. Moreover, the complexity of some nanoparticle designs and the high production costs contribute to the lower clinical uptake of NPS (Hare et al., 2017). The major efforts in the field of NPS should be directed toward bridging the gap between preclinical studies and the clinical phase.

The goal would be a better outcome for the patients thanks to the constant monitoring prior and during treatment, which allows for personalized cancer planning with predictable side effects. These multifunctional modern applications may increase a patient's life expectancy and life quality. It is highly probably that, in the near future, the field of nanotheranostics will emerge and become part of the conventional therapy and diagnostic approaches for brain cancer and other type of cancers.

AUTHOR CONTRIBUTIONS

All authors listed have made a substantial, direct and intellectual contribution to the work, and approved it for publication.

FUNDING

REFERENCES

Agrawal, P., Singh, R. P., Sonali, Kumari, L., Sharma, G., Koch, B., et al. (2017a). TPGS-chitosan cross-linked targeted nanoparticles for effective brain cancer therapy. *Mater. Sci. Eng. C Mater. Biol. Appl.* 74, 167–176. doi: 10.1016/j.msec.2017.02.008

Agrawal, P., Sonali, Singh, R. P., Sharma, G., Mehata, A. K., Singh, S., et al. (2017b). Bioadhesive micelles of d-α-tocopherol polyethylene glycol succinate 1000: synergism of chitosan and transferrin in targeted drug delivery. *Colloids Surf. B Biointerfaces* 152, 277–288. doi: 10.1016/j.colsurfb.2017.01.021

Ahmed, N., Brawley, V., Hegde, M., Bielamowicz, K., Kalra, M., Landi, D., et al. (2017). HER2-specific chimeric antigen receptor-modified virus-specific t cells for progressive glioblastoma: a phase 1 dose-escalation trial. *JAMA Oncol.* 3, 1094–1101. doi: 10.1001/jamaoncol.2017.0184

Ahmed, N., Fessi, H., and Elaissari, A. (2012). Theranostic applications of nanoparticles in cancer. *Drug Discov. Today* 17, 928–934. doi: 10.1016/j.drudis.2012.03.010

Ai, H. (2011). Layer-by-layer capsules for magnetic resonance imaging and drug delivery. *Adv. Drug Deliv. Rev.* 63, 772–788. doi: 10.1016/j.addr.2011.03.013

Al-Jamal, W. T., and Kostarelos, K. (2011). Liposomes: from a clinically established drug delivery system to a nanoparticle platform for theranostic nanomedicine. *Acc. Chem. Res.* 44, 1094–1104. doi: 10.1021/ar200105p

Alphandéry, E., Grand-Dewyse, P., Lefèvre, R., Mandawala, C., and Durand-Dubief, M. (2015). Cancer therapy using nanoformulated substances: scientific, regulatory and financial aspects. *Expert Rev. Anticancer Ther.* 15, 1233–1255. doi: 10.1586/14737140.2015.1086647

Andronescu, E., and Grumezescu, A. M. (2017). *Nanostructures for Drug Delivery*. Bucharest: Micro and Nano Technologies.

Ang, C. Y., Tan, S. Y., Lu, Y., Bai, L., Li, M., Li, P., et al. (2014). "Turn-on" fluorescence probe integrated polymer nanoparticles for sensing biological thiol molecules. *Sci. Rep.* 4:7057. doi: 10.1038/srep07057

Antonosante, A., d'Angelo, M., Castelli, V., Catanesi, M., Iannotta, D., Giordano, A., et al. (2018). The involvement of PPARs in the peculiar energetic metabolism of tumor cells. *Int. J. Mol. Sci.* 19:1907. doi: 10.3390/ijms19071907

Aparicio-Blanco, J., and Torres-Suárez, A.-I. (2018). Towards tailored management of malignant brain tumors with nanotheranostics. *Acta Biomater.* 73, 52–63. doi: 10.1016/j.actbio.2018.04.029

Arranja, A. G., Pathak, V., Lammers, T., and Shi, Y. (2017). Tumor-targeted nanomedicines for cancer theranostics. *Pharmacol. Res.* 115, 87–95. doi: 10.1016/j.phrs.2016.11.014

Bahadur, S., Sahu, A. K., Baghel, P., and Saha, S. (2019). Current promising treatment strategy for glioblastoma multiform: a review. *Oncol. Rev.* 13:417. doi: 10.4081/oncol.2019.417

Behin, A., Hoang-Xuan, K., Carpentier, A. F., and Delattre, J.-Y. (2003). Primary brain tumours in adults. *Lancet* 361, 323–331. doi: 10.1016/S0140-6736(03)12328-8

Belhadj, Z., Zhan, C., Ying, M., Wei, X., Xie, C., Yan, Z., et al. (2017). Multifunctional targeted liposomal drug delivery for efficient glioblastoma treatment. *Oncotarget* 8, 66889–66900. doi: 10.18632/oncotarget.17976

Benoy, I. H., Salgado, R., Van Dam, P., Geboers, K., Van Marck, E., Scharpé, S., et al. (2004). Increased serum interleukin-8 in patients with early and metastatic breast cancer correlates with early dissemination and survival. *Clin. Cancer Res.* 10, 7157–7162. doi: 10.1158/1078-0432.CCR-04-0812

Bhojani, M. S., Van Dort, M., Rehemtulla, A., and Ross, B. D. (2010). Targeted imaging and therapy of brain cancer using theranostic nanoparticles. *Mol. Pharm.* 7, 1921–1929. doi: 10.1021/mp100298r

Boas, U., and Heegaard, P. M. H. (2004). Dendrimers in drug research. *Chem. Soc. Rev.* 33, 43–63. doi: 10.1039/b309043b

Bregoli, L., Movia, D., Gavigan-Imedio, J. D., Lysaght, J., Reynolds, J., and Prina-Mello, A. (2016). Nanomedicine applied to translational oncology: a future perspective on cancer treatment. *Nanomedicine.* 12, 81–103. doi: 10.1016/j.nano.2015.08.006

Cai, W., Rao, J., Gambhir, S. S., and Chen, X. (2006). How molecular imaging is speeding up antiangiogenic drug development. *Mol. Cancer Ther.* 5, 2624–2633. doi: 10.1158/1535-7163.MCT-06-0395

Cantley, L. C., and Neel, B. G. (1999). New insights into tumor suppression: PTEN suppresses tumor formation by restraining the phosphoinositide

3-kinase/AKT pathway. *Proc. Natl. Acad. Sci. U.S.A.* 96, 4240–4245. doi: 10.1073/pnas.96.8.4240

Caracciolo, V., Laurenti, G., Romano, G., Carnevale, V., Cimini, A. M., Crozier-Fitzgerald, C., et al. (2012). Flavopiridol induces phosphorylation of AKT in a human glioblastoma cell line, in contrast to siRNA-mediated silencing of Cdk9: implications for drug design and development. *Cell Cycle* 11, 1202–1216. doi: 10.4161/cc.11.6.19663

Cen, H., Mao, F., Aronchik, I., Fuentes, R. J., and Firestone, G. L. (2008). DEVD-NucView488: a novel class of enzyme substrates for real-time detection of caspase-3 activity in live cells. *FASEB J.* 22, 2243–2252. doi: 10.1096/fj.07-099234

Chai, Z., Hu, X., Wei, X., Zhan, C., Lu, L., Jiang, K., et al. (2017). A facile approach to functionalizing cell membrane-coated nanoparticles with neurotoxin-derived peptide for brain-targeted drug delivery. *J. Control. Release* 264, 102–111. doi: 10.1016/j.jconrel.2017.08.027

Chakrabarti, M., Kiseleva, R., Vertegel, A., and Ray, S. K. (2015). Carbon nanomaterials for drug delivery and cancer therapy. *J. Nanosci. Nanotechnol.* 15, 5501–5511. doi: 10.1166/jnn.2015.10614

Chakravarti, A., Loeffler, J. S., and Dyson, N. J. (2002). Insulin-like growth factor receptor I mediates resistance to anti-epidermal growth factor receptor therapy in primary human glioblastoma cells through continued activation of phosphoinositide 3-kinase signaling. *Cancer Res.* 62, 200–207.

Chang, Y., Meng, X., Zhao, Y., Li, K., Zhao, B., Zhu, M., et al. (2011). Novel water-soluble and pH-responsive anticancer drug nanocarriers: doxorubicin-PAMAM dendrimer conjugates attached to superparamagnetic iron oxide nanoparticles (IONPs). *J. Colloid Interface Sci.* 363, 403–409. doi: 10.1016/j.jcis.2011.06.086

Chen, N.-T., Cheng, S.-H., Souris, J. S., Chen, C.-T., Mou, C.-Y., and Lo, L.-W. (2013). Theranostic applications of mesoporous silica nanoparticles and their organic/inorganic hybrids. *J. Mater. Chem. B* 1:3128. doi: 10.1039/c3tb20249f

Chen, Z., Lai, X., Song, S., Zhu, X., and Zhu, J. (2016). Nanostructured lipid carriers based temozolomide and gene co-encapsulated nanomedicine for gliomatosis cerebri combination therapy. *Drug Deliv.* 23, 1369–1373. doi: 10.3109/10717544.2015.1038857

Cheng, S.-H., Lee, C.-H., Chen, M.-C., Souris, J. S., Tseng, F.-G., Yang, C.-S., et al. (2010). Tri-functionalization of mesoporous silica nanoparticles for comprehensive cancer theranostics—the trio of imaging, targeting and therapy. *J. Mater. Chem.* 20:6149. doi: 10.1039/c0jm00645a

Cheng, Y., Morshed, R. A., Auffinger, B., Tobias, A. L., and Lesniak, M. S. (2014). Multifunctional nanoparticles for brain tumor imaging and therapy. *Adv. Drug Deliv. Rev.* 66, 42–57. doi: 10.1016/j.addr.2013.09.006

Chertok, B., Moffat, B. A., David, A. E., Yu, F., Bergemann, C., Ross, B. D., et al. (2008). Iron oxide nanoparticles as a drug delivery vehicle for MRI monitored magnetic targeting of brain tumors. *Biomaterials* 29, 487–496. doi: 10.1016/j.biomaterials.2007.08.050

Choi, K. Y., Liu, G., Lee, S., and Chen, X. (2012). Theranostic nanoplatforms for simultaneous cancer imaging and therapy: current approaches and future perspectives. *Nanoscale* 4, 330–342. doi: 10.1039/C1NR11277E

Cimini, A., d'Angelo, M., Benedetti, E., D'Angelo, B., Laurenti, G., Antonosante, A., et al. (2017). Flavopiridol: an old drug with new perspectives? Implication for development of new drugs. *J. Cell. Physiol.* 232, 312–322. doi: 10.1002/jcp.25421

Cole, A. J., Yang, V. C., and David, A. E. (2011). Cancer theranostics: the rise of targeted magnetic nanoparticles. *Trends Biotechnol.* 29, 323–332. doi: 10.1016/j.tibtech.2011.03.001

Danhier, F., Messaoudi, K., Lemaire, L., Benoit, J.-P., and Lagarce, F. (2015). Combined anti-Galectin-1 and anti-EGFR siRNA-loaded chitosan-lipid nanocapsules decrease temozolomide resistance in glioblastoma: *in vivo* evaluation. *Int. J. Pharm.* 481, 154–161. doi: 10.1016/j.ijpharm.2015.01.051

Derfus, A. M., Chan, W. C. W., and Bhatia, S. N. (2004). Probing the cytotoxicity of semiconductor quantum dots. *Nano Lett.* 4, 11–18. doi: 10.1021/nl0347334

Di Martino, A., Guselnikova, O. A., Trusova, M. E., Postnikov, P. S., and Sedlarik, V. (2017). Organic-inorganic hybrid nanoparticles controlled delivery system for anticancer drugs. *Int. J. Pharm.* 526, 380–390. doi: 10.1016/j.ijpharm.2017.04.061

Dixit, S., Miller, K., Zhu, Y., McKinnon, E., Novak, T., Kenney, M. E., et al. (2015a). Dual receptor-targeted theranostic nanoparticles for localized delivery

and activation of photodynamic therapy drug in glioblastomas. *Mol. Pharm.* 12, 3250–3260. doi: 10.1021/acs.molpharmaceut.5b00216

Dixit, S., Novak, T., Miller, K., Zhu, Y., Kenney, M. E., and Broome, A.-M. (2015b). Transferrin receptor-targeted theranostic gold nanoparticles for photosensitizer delivery in brain tumors. *Nanoscale* 7, 1782–1790. doi: 10.1039/C4NR04853A

Dong, X. (2018). Current strategies for brain drug delivery. *Theranostics* 8, 1481–1493. doi: 10.7150/thno.21254

Duncan, R. (2003). The dawning era of polymer therapeutics. *Nat. Rev. Drug Discov.* 2, 347–360. doi: 10.1038/nrd1088

Fan, Z., Fu, P. P., Yu, H., and Ray, P. C. (2014). Theranostic nanomedicine for cancer detection and treatment. *J. Food Drug Anal.* 22, 3–17. doi: 10.1016/j.jfda.2014.01.001

Fattahi, H., Laurent, S., Liu, F., Arsalani, N., Vander Elst, L., and Muller, R. N. (2011). Magnetoliposomes as multimodal contrast agents for molecular imaging and cancer nanotheragnostics. *Nanomedicine.* 6, 529–544. doi: 10.2217/nnm.11.14

Feng, Y., Panwar, N., Tng, D. J. H., Tjin, S. C., Wang, K., and Yong, K.-T. (2016). The application of mesoporous silica nanoparticle family in cancer theranostics. *Coord. Chem. Rev.* 319, 86–109. doi: 10.1016/j.ccr.2016.04.019

Fidoamore, A., Cristiano, L., Antonosante, A., d'Angelo, M., Di Giacomo, E., Astarita, C., et al. (2016). Glioblastoma stem cells microenvironment: the paracrine roles of the niche in drug and radioresistance. *Stem Cells Int.* 2016:6809105. doi: 10.1155/2016/6809105

Frezza, C., and Gottlieb, E. (2009). Mitochondria in cancer: not just innocent bystanders. *Semin. Cancer Biol.* 19, 4–11. doi: 10.1016/j.semcancer.2008.11.008

Frimpong, R. A., and Hilt, J. Z. (2010). Magnetic nanoparticles in biomedicine: synthesis, functionalization and applications. *Nanomedicine* 5, 1401–1414. doi: 10.2217/nnm.10.114

Gary-Bobo, M., Hocine, O., Brevet, D., Maynadier, M., Raehm, L., Richeter, S., et al. (2012). Cancer therapy improvement with mesoporous silica nanoparticles combining targeting, drug delivery and PDT. *Int. J. Pharm.* 423, 509–515. doi: 10.1016/j.ijpharm.2011.11.045

Gatenby, R. A., and Gillies, R. J. (2004). Why do cancers have high aerobic glycolysis? *Nat. Rev. Cancer* 4, 891–899. doi: 10.1038/nrc1478

Gaya, A., Rees, J., Greenstein, A., and Stebbing, J. (2002). The use of temozolomide in recurrent malignant gliomas. *Cancer Treat. Rev.* 28, 115–120. doi: 10.1053/ctrv.2002.0261

Golombek, S. K., May, J.-N., Theek, B., Appold, L., Drude, N., Kiessling, F., et al. (2018). Tumor targeting via EPR: strategies to enhance patient responses. *Adv. Drug Deliv. Rev.* 130, 17–38. doi: 10.1016/j.addr.2018.07.007

Graverini, G., Piazzini, V., Landucci, E., Pantano, D., Nardiello, P., Casamenti, F., et al. (2018). Solid lipid nanoparticles for delivery of andrographolide across the blood-brain barrier: *in vitro* and *in vivo* evaluation. *Colloids Surf. B Biointerfaces* 161, 302–313. doi: 10.1016/j.colsurfb.2017.10.062

Gürsel, D. B., Shin, B. J., Burkhardt, J.-K., Kesavabhotla, K., Schlaff, C. D., and Boockvar, J. A. (2011). Glioblastoma stem-like cells-biology and therapeutic implications. *Cancers.* 3, 2655–2666. doi: 10.3390/cancers3022655

Hainfeld, J. F., Smilowitz, H. M., O'Connor, M. J., Dilmanian, F. A., and Slatkin, D. N. (2013). Gold nanoparticle imaging and radiotherapy of brain tumors in mice. *Nanomedicine.* 8, 1601–1609. doi: 10.2217/nnm.12.165

Hare, J. I., Lammers, T., Ashford, M. B., Puri, S., Storm, G., and Barry, S. T. (2017). Challenges and strategies in anti-cancer nanomedicine development: an industry perspective. *Adv. Drug Deliv. Rev.* 108, 25–38. doi: 10.1016/j.addr.2016.04.025

Harrington, K. J., Mohammadtaghi, S., Uster, P. S., Glass, D., Peters, A. M., Vile, R. G., et al. (2001). Effective targeting of solid tumors in patients with locally advanced cancers by radiolabeled pegylated liposomes. *Clin. Cancer Res.* 7, 243–254.

Helms, H. C., Abbott, N. J., Burek, M., Cecchelli, R., Couraud, P.-O., Deli, M. A., et al. (2016). *In vitro* models of the blood–brain barrier: an overview of commonly used brain endothelial cell culture models and guidelines for their use. *J Cerebral Blood Flow Metab.* 36, 862–890. doi: 10.1177/0271678X16630991

Heo, D. N., Yang, D. H., Moon, H.-J., Lee, J. B., Bae, M. S., Lee, S. C., et al. (2012). Gold nanoparticles surface-functionalized with paclitaxel drug and biotin receptor as theranostic agents for cancer therapy. *Biomaterials* 33, 856–866. doi: 10.1016/j.biomaterials.2011.09.064

Hsu, S. P. C., Kuo, J. S., Chiang, H.-C., Wang, H.-E., Wang, Y.-S., Huang, C.-C., et al. (2018). Temozolomide, sirolimus and chloroquine is a new therapeutic combination that synergizes to disrupt lysosomal function and cholesterol homeostasis in GBM cells. *Oncotarget* 9, 6883–6896. doi: 10.18632/oncotarget.23855

Huang, X., Zhang, F., Wang, H., Niu, G., Choi, K. Y., Swierczewska, M., et al. (2013). Mesenchymal stem cell-based cell engineering with multifunctional mesoporous silica nanoparticles for tumor delivery. *Biomaterials* 34, 1772–1780. doi: 10.1016/j.biomaterials.2012.11.032

Jhaveri, A., Deshpande, P., Pattni, B., and Torchilin, V. (2018). Transferrin-targeted, resveratrol-loaded liposomes for the treatment of glioblastoma. *J. Control. Release* 277, 89–101. doi: 10.1016/j.jconrel.2018.03.006

Jiang, X., Sha, X., Xin, H., Xu, X., Gu, J., Xia, W., et al. (2013). Integrin-facilitated transcytosis for enhanced penetration of advanced gliomas by poly(trimethylene carbonate)-based nanoparticles encapsulating paclitaxel. *Biomaterials* 34, 2969–2979. doi: 10.1016/j.biomaterials.2012.12.049

Joh, D. Y., Sun, L., Stangl, M., Al Zaki, A., Murty, S., Santoiemma, P. P., et al. (2013). Selective targeting of brain tumors with gold nanoparticle-induced radiosensitization. *PLoS ONE* 8:e62425. doi: 10.1371/journal.pone.0062425

Jokerst, J. V., and Gambhir, S. S. (2011). Molecular imaging with theranostic nanoparticles. *Acc. Chem. Res.* 44, 1050–1060. doi: 10.1021/ar200106e

Kelkar, S. S., and Reineke, T. M. (2011). Theranostics: combining imaging and therapy. *Bioconjug. Chem.* 22, 1879–1903. doi: 10.1021/bc200151q

Kenny, G. D., Kamaly, N., Kalber, T. L., Brody, L. P., Sahuri, M., Shamsaei, E., et al. (2011). Novel multifunctional nanoparticle mediates siRNA tumour delivery, visualisation and therapeutic tumour reduction *in vivo*. *J. Control. Release* 149, 111–116. doi: 10.1016/j.jconrel.2010.09.020

Keunen, O., Johansson, M., Oudin, A., Sanzey, M., Rahim, S. A. A., Fack, F., et al. (2011). Anti-VEGF treatment reduces blood supply and increases tumor cell invasion in glioblastoma. *Proc. Natl. Acad. Sci. U.S.A.* 108, 3749–3754. doi: 10.1073/pnas.1014480108

Kievit, F. M., and Zhang, M. (2011). Cancer nanotheranostics: improving imaging and therapy by targeted delivery across biological barriers. *Adv. Mater. Weinheim* 23, H217–247. doi: 10.1002/adma.201102313

Kirchner, C., Liedl, T., Kudera, S., Pellegrino, T., Muñoz Javier, A., Gaub, H. E., et al. (2005). Cytotoxicity of colloidal CdSe and CdSe/ZnS nanoparticles. *Nano Lett.* 5, 331–338. doi: 10.1021/nl047996m

Kondo, T., Setoguchi, T., and Taga, T. (2004). Persistence of a small subpopulation of cancer stem-like cells in the C6 glioma cell line. *Proc. Natl. Acad. Sci. U.S.A.* 101, 781–786. doi: 10.1073/pnas.0307618100

Koo, Y.-E. L., Reddy, G. R., Bhojani, M., Schneider, R., Philbert, M. A., Rehemtulla, A., et al. (2006). Brain cancer diagnosis and therapy with nanoplatforms. *Adv. Drug Deliv. Rev.* 58, 1556–1577. doi: 10.1016/j.addr.2006.09.012

Kroemer, G., and Pouyssegur, J. (2008). Tumor cell metabolism: cancer's achilles' heel. *Cancer Cell* 13, 472–482. doi: 10.1016/j.ccr.2008.05.005

Kroonen, J., Nguyen-Khac, M. T., Deprez, M., Rogister, B., and Robe, P. (2008). [Glioblastoma, an example of translational research?]. *Rev. Med. Liege* 63, 251–256.

Kumar, A., Lee, J.-Y., and Kim, H.-S. (2016). Selective fluorescence sensing of 3,5-dinitrosalicylic acid based on pyrenesulfonamide-functionalized inorganic/organic hybrid nanoparticles. *J. Industr. Eng. Chem.* 44, 82–89. doi: 10.1016/j.jiec.2016.08.010

Kumar, A., Zhang, X., and Liang, X.-J. (2013). Gold nanoparticles: emerging paradigm for targeted drug delivery system. *Biotechnol. Adv.* 31, 593–606. doi: 10.1016/j.biotechadv.2012.10.002

Kuo, Y.-C., and Cheng, S.-J. (2016). Brain targeted delivery of carmustine using solid lipid nanoparticles modified with tamoxifen and lactoferrin for antitumor proliferation. *Int. J. Pharm.* 499, 10–19. doi: 10.1016/j.ijpharm.2015.12.054

Lakka, S. S., and Rao, J. S. (2008). Antiangiogenic therapy in brain tumors. *Expert Rev. Neurother.* 8, 1457–1473. doi: 10.1586/14737175.8.10.1457

Lammers, T., Kiessling, F., Hennink, W. E., and Storm, G. (2010). Nanotheranostics and image-guided drug delivery: current concepts and future directions. *Mol. Pharm.* 7, 1899–1912. doi: 10.1021/mp100228v

Lammers, T., Koczera, P., Fokong, S., Gremse, F., Ehling, J., Vogt, M., et al. (2015). Theranostic USPIO-loaded microbubbles for mediating and monitoring blood-brain barrier permeation. *Adv. Funct. Mater.* 25, 36–43. doi: 10.1002/adfm.201401199

Lee, J. E., Lee, N., Kim, T., Kim, J., and Hyeon, T. (2011). Multifunctional mesoporous silica nanocomposite nanoparticles for theranostic applications. *Acc. Chem. Res.* 44, 893–902. doi: 10.1021/ar2000259

Lindner, L. H., and Hossann, M. (2010). Factors affecting drug release from liposomes. *Curr. Opin. Drug Discov. Devel.* 13, 111–123.

Liong, M., Lu, J., Kovochich, M., Xia, T., Ruehm, S. G., Nel, A. E., et al. (2008). Multifunctional inorganic nanoparticles for imaging, targeting, and drug delivery. *ACS Nano* 2, 889–896. doi: 10.1021/nn800072t

Liu, G., Wang, Z., Lu, J., Xia, C., Gao, F., Gong, Q., et al. (2011). Low molecular weight alkyl-polycation wrapped magnetite nanoparticle clusters as MRI probes for stem cell labeling and *in vivo* imaging. *Biomaterials* 32, 528–537. doi: 10.1016/j.biomaterials.2010.08.099

Liu, X., Madhankumar, A. B., Miller, P. A., Duck, K. A., Hafenstein, S., Rizk, E., et al. (2016). MRI contrast agent for targeting glioma: interleukin-13 labeled liposome encapsulating gadolinium-DTPA. *Neuro-oncology* 18, 691–699. doi: 10.1093/neuonc/nov263

Lo, S.-T., Kumar, A., Hsieh, J.-T., and Sun, X. (2013). Dendrimer nanoscaffolds for potential theranostics of prostate cancer with a focus on radiochemistry. *Mol. Pharm.* 10, 793–812. doi: 10.1021/mp3005325

Lu, J., Ma, S., Sun, J., Xia, C., Liu, C., Wang, Z., et al. (2009). Manganese ferrite nanoparticle micellar nanocomposites as MRI contrast agent for liver imaging. *Biomaterials* 30, 2919–2928. doi: 10.1016/j.biomaterials.2009.02.001

Mamaeva, V., Sahlgren, C., and Lindén, M. (2013). Mesoporous silica nanoparticles in medicine–recent advances. *Adv. Drug Deliv. Rev.* 65, 689–702. doi: 10.1016/j.addr.2012.07.018

Mattei, T. A., and Rehman, A. A. (2015). "Extremely minimally invasive": recent advances in nanotechnology research and future applications in neurosurgery. *Neurosurg. Rev.* 38, 27–37; discussion 37. doi: 10.1007/s10143-014-0566-2

Melancon, M. P., Lu, W., Zhong, M., Zhou, M., Liang, G., Elliott, A. M., et al. (2011). Targeted multifunctional gold-based nanoshells for magnetic resonance-guided laser ablation of head and neck cancer. *Biomaterials* 32, 7600–7608. doi: 10.1016/j.biomaterials.2011.06.039

Mendes, M., Sousa, J. J., Pais, A., and Vitorino, C. (2018). Targeted theranostic nanoparticles for brain tumor treatment. *Pharmaceutics* 10:E181. doi: 10.3390/pharmaceutics10040181

Merkel, O. M., Mintzer, M. A., Librizzi, D., Samsonova, O., Dicke, T., Sproat, B., et al. (2010). Triazine dendrimers as non-viral vectors for *in vitro* and *in vivo* RNAi: the effects of peripheral groups and core structure on biological activity. *Mol. Pharm.* 7, 969–983. doi: 10.1021/mp100101s

Mintzer, M. A., and Grinstaff, M. W. (2011). Biomedical applications of dendrimers: a tutorial. *Chem. Soc. Rev.* 40, 173–190. doi: 10.1039/B901839P

Miranda, A., Blanco-Prieto, M. J., Sousa, J., Pais, A., and Vitorino, C. (2017). Breaching barriers in glioblastoma. Part II: Targeted drug delivery and lipid nanoparticles. *Int. J. Pharm.* 531, 389–410. doi: 10.1016/j.ijpharm.2017.07.049

Muthu, M. S., Leong, D. T., Mei, L., and Feng, S.-S. (2014a). Nanotheranostics - application and further development of nanomedicine strategies for advanced theranostics. *Theranostics* 4, 660–677. doi: 10.7150/thno.8698

Muthu, M. S., Mei, L., and Feng, S.-S. (2014b). Nanotheranostics: advanced nanomedicine for the integration of diagnosis and therapy. *Nanomedicine* 9, 1277–1280. doi: 10.2217/nnm.14.83

Na, K., Lee, S. A., Jung, S. H., and Shin, B. C. (2011). Gadolinium-based cancer therapeutic liposomes for chemotherapeutics and diagnostics. *Colloids Surfaces B Biointerfaces* 84, 82–87. doi: 10.1016/j.colsurfb.2010.12.019

Nam, J., Won, N., Bang, J., Jin, H., Park, J., Jung, S., et al. (2013). Surface engineering of inorganic nanoparticles for imaging and therapy. *Adv. Drug Deliv. Rev.* 65, 622–648. doi: 10.1016/j.addr.2012.08.015

Nam, L., Coll, C., Erthal, L., de la Torre, C., Serrano, D., Martínez-Máñez, R., et al. (2018). Drug delivery nanosystems for the localized treatment of glioblastoma multiforme. *Materials.* 11:779. doi: 10.3390/ma11050779

Nance, E., Zhang, C., Shih, T.-Y., Xu, Q., Schuster, B. S., and Hanes, J. (2014). Brain-penetrating nanoparticles improve paclitaxel efficacy in malignant glioma following local administration. *ACS Nano* 8, 10655–10664. doi: 10.1021/nn504210g.

Newton, H. B. (2010). "Overview of the molecular genetics and molecular chemotherapy of GBM," in *Glioblastoma*, ed S. K. Ray (New York, NY: Springer New York), 1–42. doi: 10.1007/978-1-4419-0410-2_1

Nicholas, M. K., Lukas, R. V., Jafri, N. F., Faoro, L., and Salgia, R. (2006). Epidermal growth factor receptor - mediated signal transduction in the development and therapy of gliomas. *Clin. Cancer Res.* 12, 7261–7270. doi: 10.1158/1078-0432.CCR-06-0874

Onoshima, D., Yukawa, H., and Baba, Y. (2015). Multifunctional quantum dots-based cancer diagnostics and stem cell therapeutics for regenerative medicine. *Adv. Drug Deliv. Rev.* 95, 2–14. doi: 10.1016/j.addr.2015.08.004

Orunoglu, M., Kaffashi, A., Pehlivan, S. B., Sahin, S., and Söylemezoglu, F., Oguz, K. K., et al. (2017). Effects of curcumin-loaded PLGA nanoparticles on the RG2 rat glioma model. *Mater. Sci. Eng. C* 78, 32–38. doi: 10.1016/j.msec.2017.03.292

Pacioni, S., D'Alessandris, Q. G., Giannetti, S., Morgante, L., Coccè, V., Bonomi, A., et al. (2017). Human mesenchymal stromal cells inhibit tumor growth in orthotopic glioblastoma xenografts. *Stem Cell Res. Ther.* 8:53. doi: 10.1186/s13287-017-0516-3

Pan, B., Cui, D., Sheng, Y., Ozkan, C., Gao, F., He, R., et al. (2007). Dendrimer-modified magnetic nanoparticles enhance efficiency of gene delivery system. *Cancer Res.* 67, 8156–8163. doi: 10.1158/0008-5472.CAN-06-4762

Pankhurst, Q. A., Connolly, J., Jones, S. K., and Dobson, J. (2003). Applications of magnetic nanoparticles in biomedicine. *J. Phys. D Appl. Phys.* 36, R167–R181. doi: 10.1088/0022-3727/36/13/201

Park, J.-H., Ryu, C. H., Kim, M. J., and Jeun, S.-S. (2015). Combination therapy for gliomas using temozolomide and interferon-beta secreting human bone marrow derived mesenchymal stem cells. *J. Korean Neurosurg. Soc.* 57, 323–328. doi: 10.3340/jkns.2015.57.5.323

Peer, D., Karp, J. M., Hong, S., Farokhzad, O. C., Margalit, R., and Langer, R. (2007). Nanocarriers as an emerging platform for cancer therapy. *Nat. Nanotechnol.* 2, 751–760. doi: 10.1038/nnano.2007.387

Petersen, A. L., Binderup, T., Jølck, R. I, Rasmussen, P., Henriksen, J. R., Pfeifer, A. K., et al. (2012). Positron emission tomography evaluation of somatostatin receptor targeted 64Cu-TATE-liposomes in a human neuroendocrine carcinoma mouse model. *J. Control. Release* 160, 254–263. doi: 10.1016/j.jconrel.2011.12.038

Pilkington, G. J., Maherally, Z., Jassam, S., Barbu, E., and Fillmore, H. (2014). An all human 3D *in vitro* model of the blood brain barrier in nanoparticle delivery and cancer metastasis studies. *Neuro-Oncology* 16:iii33. doi: 10.1093/neuonc/nou208.39

Piquer, J., Llácer, J. L., Rovira, V., Riesgo, P., Rodriguez, R., and Cremades, A. (2014). Fluorescence-guided surgery and biopsy in gliomas with an exoscope system. *Biomed Res. Int.* 2014:207974. doi: 10.1155/2014/207974

Puputti, M., Tynninen, O., Sihto, H., Blom, T., Mäenp̈äää, H., Isola, J., et al. (2006). Amplification of KIT, PDGFRA, VEGFR2, and EGFR in gliomas. *Mol. Cancer Res.* 4, 927–934. doi: 10.1158/1541-7786.MCR-06-0085

Pysz, M. A., Gambhir, S. S., and Willmann, J. K. (2010). Molecular imaging: current status and emerging strategies. *Clin. Radiol.* 65, 500–516. doi: 10.1016/j.crad.2010.03.011

Qu, J., Zhang, L., Chen, Z., Mao, G., Gao, Z., Lai, X., et al. (2016). Nanostructured lipid carriers, solid lipid nanoparticles, and polymeric nanoparticles: which kind of drug delivery system is better for glioblastoma chemotherapy? *Drug Deliv.* 23, 3408–3416. doi: 10.1080/10717544.2016.1189465

Ren, J., Shen, S., Wang, D., Xi, Z., Guo, L., Pang, Z., et al. (2012). The targeted delivery of anticancer drugs to brain glioma by PEGylated oxidized multi-walled carbon nanotubes modified with angiopep-2. *Biomaterials* 33, 3324–3333. doi: 10.1016/j.biomaterials.2012.01.025

Rivera Gil, P., Hühn, D., del Mercato, L. L., Sasse, D., and Parak, W. J. (2010). Nanopharmacy: inorganic nanoscale devices as vectors and active compounds. *Pharmacol. Res.* 62, 115–125. doi: 10.1016/j.phrs.2010.01.009

Robinson, J. T., Welsher, K., Tabakman, S. M., Sherlock, S. P., Wang, H., Luong, R., et al. (2010). High performance *in vivo* near-IR (>1 μm) imaging and photothermal cancer therapy with carbon nanotubes. *Nano Res.* 3, 779–793. doi: 10.1007/s12274-010-0045-1

Rock, K., McArdle, O., Forde, P., Dunne, M., Fitzpatrick, D., O'Neill, B., et al. (2012). A clinical review of treatment outcomes in glioblastoma multiforme–the validation in a non-trial population of the results of a randomised Phase III clinical trial: has a more radical approach improved survival? *Br. J. Radiol.* 85, e729–733. doi: 10.1259/bjr/83796755

Ruan, S., He, Q., and Gao, H. (2015). Matrix metalloproteinase triggered size-shrinkable gelatin-gold fabricated nanoparticles for tumor microenvironment

sensitive penetration and diagnosis of glioma. *Nanoscale* 7, 9487–9496. doi: 10.1039/c5nr01408e

Sailor, M. J., and Park, J.-H. (2012). Hybrid nanoparticles for detection and treatment of cancer. *Adv. Mater.* 24, 3779–3802. doi: 10.1002/adma.2012 00653

Saraiva, C., Praça, C., Ferreira, R., Santos, T., Ferreira, L., and Bernardino, L. (2016). Nanoparticle-mediated brain drug delivery: overcoming blood-brain barrier to treat neurodegenerative diseases. *J. Control. Release* 235, 34–47. doi: 10.1016/j.jconrel.2016.05.044

Schlessinger, J. (2000). Cell signaling by receptor tyrosine kinases. *Cell* 103, 211–225. doi: 10.1016/S0092-8674(00)00114-8

Schmieder, A. H., Caruthers, S. D., Zhang, H., Williams, T. A., Robertson, J. D., Wickline, S. A., et al. (2008). Three-dimensional MR mapping of angiogenesis with alpha5beta1(alpha nu beta3)-targeted theranostic nanoparticles in the MDA-MB-435 xenograft mouse model. *FASEB J.* 22, 4179–4189. doi: 10.1096/fj.08-112060

Shapira, A., Livney, Y. D., Broxterman, H. J., and Assaraf, Y. G. (2011). Nanomedicine for targeted cancer therapy: towards the overcoming of drug resistance. *Drug Resist. Updat.* 14, 150–163. doi: 10.1016/j.drup.2011.01.003

Shi, J., Kantoff, P. W., Wooster, R., and Farokhzad, O. C. (2017). Cancer nanomedicine: progress, challenges and opportunities. *Nat. Rev. Cancer* 17, 20–37. doi: 10.1038/nrc.2016.108

Silantyev, F., Falzone, L., Libra, M., Gurina, O. I., Kardashova, K. S., Nikolouzakis, T. K., et al. (2019). Current and future trends on diagnosis and prognosis of glioblastoma: from molecular biology to proteomics. *Cells* 8:863. doi: 10.3390/cells8080863

Singh, R. P., Sharma, G., Sonali, Singh, S., Kumar, M., Pandey, B. L., et al. (2016). Vitamin E TPGS conjugated carbon nanotubes improved efficacy of docetaxel with safety for lung cancer treatment. *Colloids Surf. B Biointerfaces* 141, 429–442. doi: 10.1016/j.colsurfb.2016.02.011

Slettenaar, V. I. F., and Wilson, J. L. (2006). The chemokine network: a target in cancer biology? *Adv. Drug Deliv. Rev.* 58, 962–974. doi: 10.1016/j.addr.2006.03.012

Sonali, Agrawal, P., Singh, R. P., Rajesh, C. V., Singh, S., Vijayakumar, M. R., et al. (2016a). Transferrin receptor-targeted vitamin E TPGS micelles for brain cancer therapy: preparation, characterization and brain distribution in rats. *Drug Deliv.* 23, 1788–1798. doi: 10.3109/10717544.2015.1094681

Sonali, Singh, R. P., Sharma, G., Kumari, L., Koch, B., Singh, S., et al. (2016b). RGD-TPGS decorated theranostic liposomes for brain targeted delivery. *Colloids Surf. B Biointerfaces* 147, 129–141. doi: 10.1016/j.colsurfb.2016.07.058

Sonali, Singh, R. P., Singh, N., Sharma, G., Vijayakumar, M. R., Koch, B., et al. (2016c). Transferrin liposomes of docetaxel for brain-targeted cancer applications: formulation and brain theranostics. *Drug Deliv.* 23, 1261–1271. doi: 10.3109/10717544.2016.1162878

Sonali, Viswanadh, M. K., Singh, R. P., Agrawal, P., Mehata, A. K., Pawde, D. M., et al. (2018). Nanotheranostics: emerging strategies for early diagnosis and therapy of brain cancer. *Nanotheranostics* 2, 70–86. doi: 10.7150/ntno.21638

Stambolic, V., Suzuki, A., de la Pompa, J. L., Brothers, G. M., Mirtsos, C., Sasaki, T., et al. (1998). Negative regulation of PKB/Akt-dependent cell survival by the tumor suppressor PTEN. *Cell* 95, 29–39. doi: 10.1016/S0092-8674(00)81780-8

Su, H., Liu, Y., Wang, D., Wu, C., Xia, C., Gong, Q., et al. (2013). Amphiphilic starlike dextran wrapped superparamagnetic iron oxide nanoparticle clsuters as effective magnetic resonance imaging probes. *Biomaterials* 34, 1193–1203. doi: 10.1016/j.biomaterials.2012.10.056

Sun, D. (2010). Nanotheranostics: integration of imaging and targeted drug delivery. *Mol. Pharm.* 7:1879. doi: 10.1021/mp1003652

Sun, L., Joh, D. Y., Al-Zaki, A., Stangl, M., Murty, S., Davis, J. J., et al. (2016). Theranostic application of mixed gold and superparamagnetic iron oxide nanoparticle micelles in glioblastoma multiforme. *J. Biomed. Nanotechnol.* 12, 347–356. doi: 10.1166/jbn.2016.2173

Tabatabaei, S. N., Girouard, H., Carret, A.-S., and Martel, S. (2015). Remote control of the permeability of the blood-brain barrier by magnetic heating of nanoparticles: a proof of concept for brain drug delivery. *J. Control. Release* 206, 49–57. doi: 10.1016/j.jconrel.2015.02.027

Tanaka, N., Kanatani, S., Tomer, R., Sahlgren, C., Kronqvist, P., Kaczynska, D., et al. (2017). Whole-tissue biopsy phenotyping of three-dimensional tumours reveals patterns of cancer heterogeneity. *Nat. Biomed. Eng.* 1, 796–806. doi: 10.1038/s41551-017-0139-0

Tandel, G. S., Biswas, M., Kakde, O. G., Tiwari, A., Suri, H. S., Turk, M., et al. (2019). A review on a deep learning perspective in brain cancer classification. *Cancers.* 11:E111. doi: 10.3390/cancers11010111

Tennant, D. A., Frezza, C., MacKenzie, E. D., Nguyen, Q. D., Zheng, L., Selak, M. A., et al. (2009). Reactivating HIF prolyl hydroxylases under hypoxia results in metabolic catastrophe and cell death. *Oncogene* 28, 4009–4021. doi: 10.1038/onc.2009.250

Thakkar, J. P., Dolecek, T. A., Horbinski, C., Ostrom, Q. T., Lightner, D. D., Barnholtz-Sloan, J. S., et al. (2014). Epidemiologic and molecular prognostic review of glioblastoma. *Cancer Epidemiol. Biomarkers Prev.* 23, 1985–1996. doi: 10.1158/1055-9965.EPI-14-0275

Tian, B., Al-Jamal, W. T., Al-Jamal, K. T., and Kostarelos, K. (2011). Doxorubicin-loaded lipid-quantum dot hybrids: surface topography and release properties. *Int. J. Pharm.* 416, 443–447. doi: 10.1016/j.ijpharm.2011.01.057

Tong, R., and Cheng, J. (2007). Anticancer polymeric nanomedicines. *Poly. Rev.* 47, 345–381. doi: 10.1080/15583720701455079

Tzeng, S. Y., and Green, J. J. (2013). Therapeutic nanomedicine for brain cancer. *Ther. Deliv.* 4, 687–704. doi: 10.4155/tde.13.38

Uchida, N., Buck, D. W., He, D., Reitsma, M. J., Masek, M., Phan, T. V., et al. (2000). Direct isolation of human central nervous system stem cells. *Proc. Natl. Acad. Sci. U.S.A.* 97, 14720–14725. doi: 10.1073/pnas.97.26.14720

Vilos, C., and Velasquez, L. A. (2012). Therapeutic strategies based on polymeric microparticles. *J. Biomed. Biotechnol.* 2012:672760. doi: 10.1155/2012/6 72760

Volkov, Y. (2015). Quantum dots in nanomedicine: recent trends, advances and unresolved issues. *Biochem. Biophys. Res. Commun.* 468, 419–427. doi: 10.1016/j.bbrc.2015.07.039

Wang, D., Lin, B., and Ai, H. (2014). Theranostic nanoparticles for cancer and cardiovascular applications. *Pharm. Res.* 31, 1390–1406. doi: 10.1007/s11095-013-1277-z

Wang, H., Liu, X., Wang, Y., Chen, Y., Jin, Q., and Ji, J. (2015). Doxorubicin conjugated phospholipid prodrugs as smart nanomedicine platforms for cancer therapy. *J. Mater. Chem. B* 3, 3297–3305. doi: 10.1039/C4TB01984A

Wang, X., Wang, C., Cheng, L., Lee, S.-T., and Liu, Z. (2012). Noble metal coated single-walled carbon nanotubes for applications in surface enhanced Raman scattering imaging and photothermal therapy. *J. Am. Chem. Soc.* 134, 7414–7422. doi: 10.1021/ja300140c

Wang, Y., Shim, M. S., Levinson, N. S., Sung, H.-W., and Xia, Y. (2014). Stimuli-responsive materials for controlled release of theranostic agents. *Adv. Funct. Mater.* 24, 4206–4220. doi: 10.1002/adfm.201400279

Wei, X., Chen, X., Ying, M., and Lu, W. (2014). Brain tumor-targeted drug delivery strategies. *Acta Pharm. Sin. B* 4, 193–201. doi: 10.1016/j.apsb.2014.03.001

Wesseling, P., and Capper, D. (2018). WHO 2016 classification of gliomas. *Neuropathol. Appl. Neurobiol.* 44, 139–150. doi: 10.1111/nan.12432

Wicki, A., Witzigmann, D., Balasubramanian, V., and Huwyler, J. (2015). Nanomedicine in cancer therapy: challenges, opportunities, and clinical applications. *J. Controlled Release* 200, 138–157. doi: 10.1016/j.jconrel.2014.12.030

Wilhelm, I., and Krizbai, I. A. (2014). *In vitro* models of the blood-brain barrier for the study of drug delivery to the brain. *Mol. Pharm.* 11, 1949–1963. doi: 10.1021/mp500046f

Wong, A. J., Ruppert, J. M., Bigner, S. H., Grzeschik, C. H., Humphrey, P. A., Bigner, D. S., et al. (1992). Structural alterations of the epidermal growth factor receptor gene in human gliomas. *Proc. Natl. Acad. Sci. U.S.A.* 89, 2965–2969. doi: 10.1073/pnas.89.7.2965

Wu, M., Fan, Y., Lv, S., Xiao, B., Ye, M., and Zhu, X. (2016). Vincristine and temozolomide combined chemotherapy for the treatment of glioma: a comparison of solid lipid nanoparticles and nanostructured lipid carriers for dual drugs delivery. *Drug Deliv.* 23, 2720–2725. doi: 10.3109/10717544.2015.1058434

Xiao, Q., Yang, S., Ding, G., and Luo, M. (2018). Anti-vascular endothelial growth factor in glioblastoma: a systematic review and meta-analysis. *Neurol. Sci.* 39, 2021–2031. doi: 10.1007/s10072-018-3568-y

Xie, J., Lee, S., and Chen, X. (2010). Nanoparticle-based theranostic agents. *Adv. Drug Deliv. Rev.* 62, 1064–1079. doi: 10.1016/j.addr.2010.07.009

Xie, J., Liu, G., Eden, H. S., Ai, H., and Chen, X. (2011). Surface-engineered magnetic nanoparticle platforms for cancer imaging and therapy. *Acc. Chem. Res.* 44, 883–892. doi: 10.1021/ar200044b

Xie, W., Guo, Z., Gao, F., Gao, Q., Wang, D., Liaw, B., et al. (2018). Shape-, size- and structure-controlled synthesis and biocompatibility of iron oxide nanoparticles for magnetic theranostics. *Theranostics* 8, 3284–3307. doi: 10.7150/thno.25220

Yamanaka, R. (2008). Cell- and peptide-based immunotherapeutic approaches for glioma. *Trends Mol. Med.* 14, 228–235. doi: 10.1016/j.molmed.2008.03.003

Zeng, W., Wang, X., Xu, P., Liu, G., Eden, H. S., and Chen, X. (2015). Molecular imaging of apoptosis: from micro to macro. *Theranostics* 5, 559–582. doi: 10.7150/thno.11548

Zhang, B., Yang, C., Gao, Y., Wang, Y., Bu, C., Hu, S., et al. (2017). Engineering quantum dots with different emission wavelengths and specific fluorescence lifetimes for spectrally and temporally multiplexed imaging of cells. *Nanotheranostics* 1, 131–140. doi: 10.7150/ntno.18989

Zhao, M., Zhao, M., Fu, C., Yu, Y., and Fu, A. (2018). Targeted therapy of intracranial glioma model mice with curcumin nanoliposomes. *Int. J. Nanomedicine* 13, 1601–1610. doi: 10.2147/IJN.S157019

Zong, T., Mei, L., Gao, H., Cai, W., Zhu, P., Shi, K., et al. (2014). Synergistic dual-ligand doxorubicin liposomes improve targeting and therapeutic efficacy of brain glioma in animals. *Mol. Pharm.* 11, 2346–2357. doi: 10.1021/mp500057n

Zottel, A., Videtič Paska, A., and Jovčevska, I. (2019). Nanotechnology meets oncology: nanomaterials in brain cancer research, diagnosis and therapy. *Materials.* 12:1588. doi: 10.3390/ma12101588

Corrigendum: Theranostic Nanomedicine for Malignant Gliomas

Michele d'Angelo[1], Vanessa Castelli[1], Elisabetta Benedetti[1], Andrea Antonosante[1], Mariano Catanesi[1], Reyes Dominguez-Benot[1], Giuseppina Pitari[1], Rodolfo Ippoliti[1] and Annamaria Cimini[1,2]*

[1] Department of Life, Health and Environmental Sciences, University of L'Aquila, L'Aquila, Italy, [2] Department of Biology, Sbarro Institute for Cancer Research and Molecular Medicine, Temple University, Philadelphia, PA, United States

A Corrigendum on

Theranostic Nanomedicine for Malignant Gliomas

by d'Angelo, M., Castelli, V., Benedetti, E., Antonosante, A., Catanesi, M., Dominguez-Benot, R., et al. (2019). Front. Bioeng. Biotechnol. 7:325. doi: 10.3389/fbioe.2019.00325

In the original article, we neglected to include the funder. This project has received funding from the **European Union's Horizon 2020 research and innovation programme** under the Marie Skłodowska-Curie **grant agreement No 713714** to **Reyes Dominguez-Benot**.

The authors apologize for this error and state that this does not change the scientific conclusions of the article in any way. The original article has been updated.

Check for updates

Nano-Enhanced Drug Delivery and Therapeutic Ultrasound for Cancer Treatment and Beyond

Priyanka Tharkar[1], Ramya Varanasi[1], Wu Shun Felix Wong[2], Craig T. Jin[3] and Wojciech Chrzanowski[1]*

[1] Faculty of Medicine and Health, Sydney School of Pharmacy, Sydney Nano Institute, The University of Sydney, Camperdown, NSW, Australia, [2] School of Women's and Children's Health, University of New South Wales, Sydney, NSW, Australia, [3] Faculty of Engineering, School of Electrical and Information Engineering, The University of Sydney, Sydney, NSW, Australia

While ultrasound is most widely known for its use in diagnostic imaging, the energy carried by ultrasound waves can be utilized to influence cell function and drug delivery. Consequently, our ability to use ultrasound energy at a given intensity unlocks the opportunity to use the ultrasound for therapeutic applications. Indeed, in the last decade ultrasound-based therapies have emerged with promising treatment modalities for several medical conditions. More recently, ultrasound in combination with nanomedicines, i.e., nanoparticles, has been shown to have substantial potential to enhance the efficacy of many treatments including cancer, Alzheimer disease or osteoarthritis. The concept of ultrasound combined with drug delivery is still in its infancy and more research is needed to unfold the mechanisms and interactions of ultrasound with different nanoparticles types and with various cell types. Here we present the state-of-art in ultrasound and ultrasound-assisted drug delivery with a particular focus on cancer treatments. Notably, this review discusses the application of high intensity focus ultrasound for non-invasive tumor ablation and immunomodulatory effects of ultrasound, as well as the efficacy of nanoparticle-enhanced ultrasound therapies for different medical conditions. Furthermore, this review presents safety considerations related to ultrasound technology and gives recommendations in the context of system design and operation.

Keywords: ultrasound, nanoparticles, cancer, HIFU, targeted drug delivery

INTRODUCTION

Conventionally, ultrasound has been used for imaging and diagnostic purposes. Recent technological advances, in particular in nanotechnology, opened new opportunities for ultrasound to be developed into advanced medical treatments, e.g., ultrasound triggered *in situ* drug synthesis and non-invasive surgery (Ferrara, 2008). Therapeutic ultrasound has already been demonstrated to be effective for prostate, breast and liver cancer ablation, cataract removal, uterine fibroid ablation, phacoemulsification, surgical tissue cutting, treatment of bone fractures, and transdermal drug delivery (Miller et al., 2012). Notably, ultrasound-assisted delivery of drugs has gained increasing attention in recent years as it permits spatially confined delivery of therapeutic compound into target areas, such as tumors (Zhu and Torchilin, 2013). The combination of

ultrasound and nano-drug delivery systems removes major limitations of conventional drug delivery systems, including:

– Insufficient uptake and accumulation of nanoparticles by cells (Blanco et al., 2015),
– Limited amount of drug delivered or released from nanoparticles (Du et al., 2011), and
– Targeted specific delivery of drug carrying nanoparticles.

Furthermore, the combination of ultrasound with nanoparticles has a substantial potential to enhance the efficacy of drug delivery and reduce side effects of drugs, through improved transcending of drug carrying particles through physiological barriers—a major goal for advanced drug delivery systems. These physiological barriers include endothelial lining of blood vessels (Thakkar et al., 2012), endothelium of target tissues, tight epithelial cell layers, tissue interstitium, plasma membrane of cells, diffusion through cytoplasm, and ultimately entry into the nucleus via nuclear membrane (if applicable) (Barua and Mitragotri, 2014). In addition to these, the blood–brain barrier (BBB) is a major obstacle for nanoparticle/drug penetration to the brain, which could be overcome by the use of ultrasound (Zhou et al., 2018).

BARRIERS FOR NANOPARTICLE DRUG DELIVERY TO TUMOR

Approaches for targeted delivery in cancer may involve systemic administration of chemotherapeutic agents encased in nanoparticles. They may improve the effectiveness of drug delivery and their specificity resulting in targeted drug delivery. To improve targeting, nanoparticles can also be decorated with molecules which specifically recognize and attach to cancer cells. The most commonly utilized tumor specific moieties for targeting are abnormal overexpressed receptors of the tumors. These include endothelial growth factor receptor (VEGFR), epidermal growth factor receptor (EGFR integrin receptor vascular), folate receptor (FR), and human epidermal growth factor receptor 2 (HER2) (Ko et al., 2019). The encapsulation of therapeutic drug molecules in nanoparticles can improve their bioavailability, bio-distribution, and can also improve internalization into the target cell. However, despite recent advancements in the field of nanotechnology, including functionalization with aforementioned targeting molecules, only ∼1% of nanoparticles accumulates in tumors (Wilhelm et al., 2016). Therefore, an effective treatment strategy for malignant tumors remains elusive. Very low targeting efficiency could be due to multiple physiological barriers of the tumor architecture (Rosenblum et al., 2018). The first difficulty for nanoparticles just after their intravenous administration, much before they reach the tumor microenvironment is the high chance of getting cleared by blood circulation. It can happen because nanoparticles may be opsonized by blood proteins to be later identified by the cells of the mononuclear phagocyte system (MPS) and finally cleared away from circulation. The nanoparticle populations that avoid clearance by the MPS need to diffuse out of circulation. While nanoparticles are in circulation, they need to effectively

accumulate at the endothelial lining toward the tumor micro-environment. Effective extravasation of nanoparticles through the tumor microenvironment represents the second barrier for nanoparticles. The characteristic structure of tumor tissue is distinct compared to normal tissues. The tumor structure usually have abnormal vasculature, show overexpression and presence of high density of extracellular matrix (ECM). The abnormal features of tumor are predominant reasons for inefficient delivery of nanoparticles to tumors. The ECM of tumors consist of a cross-linked network of collagen and elastin fibers, proteoglycans and hyaluronic acid that forms a cross-linked gel-like structure. The highly developed and overexpressed ECM of tumor results in significant resistance to the diffusion of therapeutic nanoparticles through the interstitium. Apart from this, high interstitial fluid pressure (IFP), which is the result of rapid proliferation of cells in a restricted area, the high permeability of tumor vasculature and absence of the lymphatic drainage system declines the force for nanoparticles to penetrate into tumors. These conditions also obstructs the transport and distribution of nanoparticles uniformly into the entire tumor volume. More importantly, the vasculature perfusion within a tumor is quite diverse, leaving several areas with poor vessel perfusion and low blood flow. The situation doubtlessly increases the distance from area over which nanoparticles must travel through to reach target cells, resulting in delivery of nanoparticles to release of therapeutic drug too far from the tumor and its microenvironment. All the distinct pathological features of the tumor profoundly retard nanoparticle delivery, accumulation, and diffusion of nanoparticles uniformly into the tumor leading to inefficient anti-tumor activity of the treatment (Sriraman et al., 2014; Zhang Y. R. et al., 2019).

To overcome the above mentioned barriers there is a need for a technique that can aid in precise delivery of drug at a tumor site and enhance penetration of nanoparticles into tumor volume. Ultrasound-assisted delivery of drug loaded nanoparticles addresses aforementioned limitations by enhancing accumulation and uptake of nanoparticles by cells, as well as by stimulation of drug release only at targeted site. These effects are achieved through various processes like sonoporosis, cavitation, and hyperthermia which occur after the interaction of ultrasound radiation concurrently with cells as well as nanoparticles. Consequently, the use of ultrasound has the potential to improve drug targeting, which in turn may reduce systemic dose of drug required for successful treatment. Therefore, ultrasound-assisted drug delivery may reduce overall treatment side effects associated with drug toxicity and non-targeted delivery (Mullick Chowdhury et al., 2017). Taken together, ultrasound-based drug delivery opens new opportunities for more effective treatments for cancer and other medical conditions.

MUCOSAL BARRIER

Mucus is a major obstacle for drug/nanoparticle delivery. Presence of mucus in lung, vagina, and bladder pose a challenge for nanoparticle delivery to the diseased area through dense

mucosal structure. For example, nanoparticle drug delivery to lung epithelium is challenging due to array of extracellular barriers such as mucociliary clearance and presence of thick mucosal coating around the tissues. In the case of cystic fibrosis a coating of infected sputum is major obstacle for delivery of the nanoparticles to the diseased area. There are a number of ways to overcome these hurdles such as the use of agents which dissolves thick mucus, viscoelastic gels, agents that break tight junctions of mucus for permission of nanoparticles efficiently to the airway epithelium. However, the above mentioned strategies to improve drug delivery through mucous are not effective (Xenariou et al., 2007). In contrast, ultrasound provides a simple and robust solution to overcome the barrier limiting extravasation of therapeutic agent/nanoparticles into mucosal tissues (Chen et al., 2017). The effect can be achieved because ultrasound is associated with energy that can disrupt the mucosal structure allowing nanoparticles to enter the tissues for local drug delivery.

Schoellhammer et al. suggested that low-frequency ultrasound could provide fast delivery of therapeutic agent to the colonic mucosa. It was first explored whether low-frequency ultrasound could improve the delivery of the drugs to the colon tissues in Franz diffusion cells. The findings of the *ex vivo* experiment revealed that treatment with low-frequency ultrasound 20 kHz was able to increase the delivery of dextran (3 kDa) labeled with texas red up to 7-times compared to control. Confocal microscopy images showed that the fluorescent dextran was uniformly diffused throughout the tissues (Schoellhammer et al., 2017). However, until now, the use of ultrasound to improve nanoparticle drug delivery thorough lung mucosal membrane has not been demonstrated. The potential use of ultrasound in transmucosal drug delivery could address the current limitation of low transmucosal nanoparticle/drug delivery for several lung, vaginal and bladder diseases. The presence of the mucus in vaginal epithelium pose an obstacle for obtaining prolonged retention, homogeneous distribution, and successful delivery of drug molecules/nanoparticles in the vaginal tract. Most particulate matter, including nanoparticles, get trapped by mucous through both adhesive and steric interactions due to mucus (Ensign et al., 2012). Mucous barriers also limits the effectiveness of conventional drug delivery systems in treating some bladder conditions including overactive bladder, interstitial cystitis, bladder cancer, and urinary tract infections (Zacchè et al., 2015). In all these situations where mucous forms a physicochemical barrier for drug or drug carrier to reach the target, ultrasound energy could be employed to improve transmucosal drug delivery.

TUMORS WITH LOW ENHANCED PERMEABILITY AND RETENTION (EPR) EFFECT

Ultrasound could be employed for improving drug delivery to the tumors with low "enhanced permeability and retention effect" (EPR). Some tumors, and typically tumors presenting with an extensive stromal compartment show suboptimal distribution of

nanoparticles within the tumor. These tumors are characterized by a dense collagen network and tight perivascular cell coverage. Therefore, the penetration of drugs and drug delivery systems (nanoparticles) into the tumor interstitium is limited. There has not been a huge success so far in developing strategies to improve low EPR of such tumors. Ultrasound could be a useful strategy for improving drug targeting to tumors with low EPR (Theek et al., 2016). Theek, Baues et al. in their study use tumor models (i.e., highly cellular A431 epidermoid xenografts and highly stromal BxPC-3 pancreatic carcinoma xenografts), which both represents relatively low levels of EPR. It was found that the liposome concentrations were increased twice in ultrasound treated tumors as compared to untreated tumors. The effect was observed because of the ability of ultrasound to induce the sonoporation effect. It enhanced the ability of liposomes to penetrate out of the blood vessels into the tumor interstitium. These findings show that ultrasound can improve the efficacy of nanomedicine in tumors treatments which has low levels of EPR.

Taken together, physiological barriers restrain the effective delivery of drugs to targeted tissues. Notably, ultrasound can be used to improve both targeting and effectiveness of drug delivery. Indeed, the ultrasound-mediated drug delivery has substantial potential to improve outcomes of many therapies. However, to move this therapeutic modality to mainstream medicine there is a need to understand effects of ultrasound treatment on cells, tissues, and extracellular matrixes. It is also necessary to understand the ultrasound beam behaviors in the context of complex hierarchical assembly of biological structures; e.g., how the ultrasound beam passes and reflects within tissues and how it interacts with different subtypes of tissues.

BIOPHYSICAL EFFECTS OF ULTRASOUNDS ON CELLS

Ultrasound beams of given frequency and intensity can induce various biophysical effects in cells or tissues that are exposed to the energy carried by the ultrasound wave. Well-known biophysical effects of ultrasound on cells are:

- Sonoporation,
- Cavitation, and
- Hyperthermia (Qin et al., 2018).

Each of the effects have different impacts on cell function and can be exploited for different therapeutic applications detailed below.

Sonoporation
Sonoporation is the process where the size of pores in the cell membrane increases as a result of mechanical impact of ultrasound radiation/energy on cell membrane molecules. Ultrasound physically disrupts the integrity of the membrane assembly causing membrane poration. Tiny pores formed in the membrane enable passive entry of drug molecules or nanoparticles into cells (**Figure 1**). Consequently, ultrasound can be used to enhance cellular internalization and accumulation of small molecules, genes, and nanoparticles.
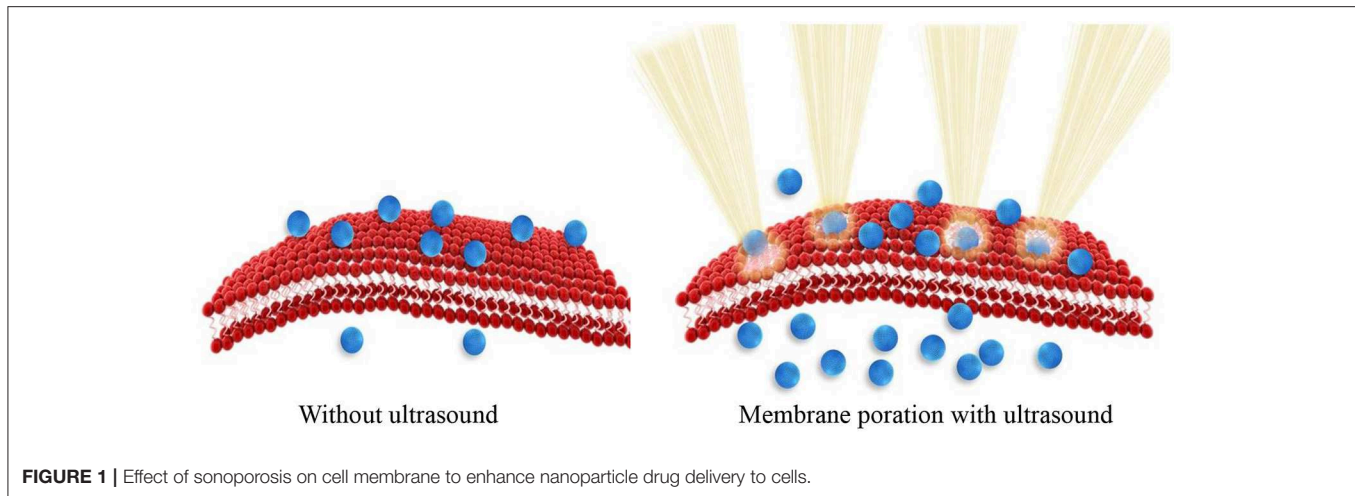
FIGURE 1 | Effect of sonoporosis on cell membrane to enhance nanoparticle drug delivery to cells.

Sonoporation can be induced in cells through the cavitation process. Cavitation is defined as tiny gas microbubbles being created, developed, vibrated (oscillated), and disintegrated (collapsed) in fluid under the influence of ultrasound radiations. Cavitation occurs for both endogenous and exogenous gas microbubbles. Endogenous gas microbubbles are naturally occurring voids in cell cytoplasm while, exogenous gas bubbles include synthetic gas bubbles, or microbubbles introduced externally in the cellular microenvironment. These comprise of spherical gas- and/or perfluorocarbon-filled cavities and are typically stabilized by a coated surfactant, phospholipid, and synthetic polymer or denatured human serum albumin. Both endogenous and exogenous microbubbles can increase the permeability of cell membranes through the formation of pores on the membrane, which leads to sonophoresis, and regarded as "cavitation induced sonoporation." Microbubbles can lead to sonoporation once certain cavitation thresholds are achieved. When ultrasound "hits" the microbubbles it induces high-frequency oscillation by absorbing ultrasonic energy. As a result, a fluid jet/shock wave is formed, leading to the perturbation of cell membrane structures. The oscillation and expansion of microbubbles exerts shear pressure on the cell membrane which also enhances permeability of the cell membrane, therefore this process makes cells more accessible to nanoparticles (**Figure 2**) (Hu et al., 2010). The drug delivery enhanced by the use of microbubbles and ultrasound is regarded as "ultrasound and microbubble (USMB) mediated drug delivery."

Fechheimer et al. (1986) demonstrated for the first time the ability of ultrasound to induce sonoporation for improved delivery of DNA to mammalian cell. In this study, the suspensions of live slime mold amoebae were exposed to ultrasound and treated with fluorescein-labeled dextran, normally impermeable to cells of its size. There was 40% increase in fluorophore uptake by the ultrasound treated cells and the concept subsequently was translated in mammalian cells for delivering DNA (Fechheimer et al., 1987; Izadifar et al., 2019).

When cells are expose to ultrasound, complex, and often synergistic physical and biochemical processes can take place which include:

1. Increase in intracellular calcium transients
2. Change in plasma membrane potential
3. Production of free radicals
4. Alteration in cell membrane fluidity.

Increase in Intracellular Calcium Transients

One of the effects of ultrasound on cell membranes is spontaneous increase in intracellular calcium transient cells (Juffermans et al., 2006; Kumon et al., 2007; Fan et al., 2010, 2012). Increased Ca^{2+} plays a vital part in cell restoration after sonoporation (Hassan et al., 2010). Moreover, calcium influx is shown to stimulate endocytosis in cells (Yang et al., 2019). The process is reversible and a number of studies have demonstrated that intracellular calcium transients have been noticed to enhance immediately and then restoring to equilibrium (Juffermans et al., 2006; Kumon et al., 2007). Juffermans's et al. showed that the increased in Ca^{2+} influx after low intensity ultrasound-exposed microbubbles cause the stimulation of BKCa channels followed by local hyperpolarization of the plasma membrane.

Change in of Plasma Membrane Potential

It is well-known that there is a direct relationship between an increase in intracellular Ca^{2+} levels, hyperpolarization and an enhanced uptake of macromolecules through the process of micropinocytosis/endocytosis (Schweizer and Ryan, 2006). These subtle cellular alterations following ultrasound exposure including hyperpolarization of cell membrane were observed when cells were treated with microbubbles. It resulted in the modulation of uptake of large therapeutic agents like plasmid DNA (Juffermans et al., 2008).

Changes in membrane potential can be observed as either hyperpolarization or depolarization of plasma membrane which are associated with sonoporation. Interestingly, it was found that the extent of sonoporation and different intensities of ultrasound can induce diverse effects on the plasma membrane potential. For instance, Wang et al. study found that when cells were treated with low intensity of ultrasound (0.64 W/cm^2), depolarization in the cell membrane potential was observed. However, when cells were treated with ultrasound of higher intensity (2.1 W/cm^2),

FIGURE 2 | Sonoporesis mediated localized drug delivery to targeted cell.
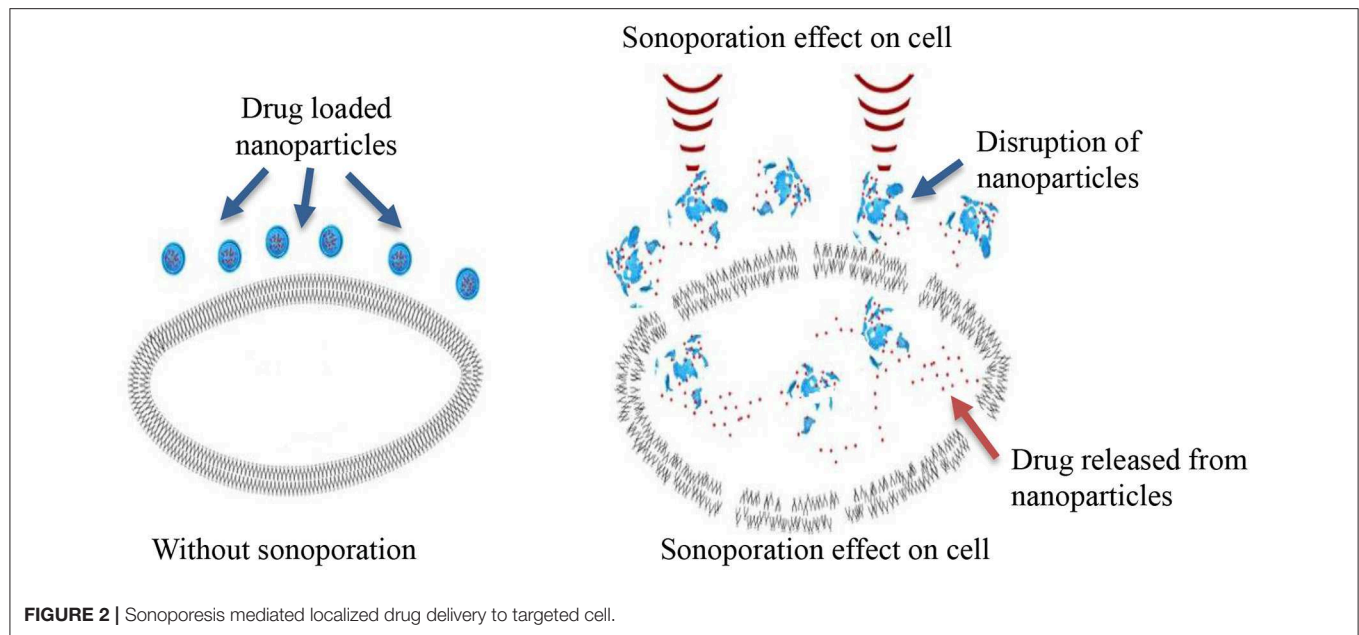
hyperpolarization of the membrane was noticed instantly after irradiation. Their study also detected that the hyperpolarization effect was reversible and returned back to the control level after 180 min (Wang S. et al., 2012).

Production of Free Radicals

It is well-established that intracellular reactive free radicals/oxygen species (ROS) are generated during ultrasound cell interaction. The production of ROS is a chemical effect of ultrasound, specifically induced by acoustic cavitation and also known as the sonochemical effect of ultrasound that results in production of ROS (Feril et al., 2008). The production of ROS during the ultrasound interaction with cells and microbubbles is a result of localized increase in temperatures and pressure of several thousand K, and several hundred atmospheres, respectively, of collapsing microbubbles. Local increase in extreme temperature and pressure leads to the decomposition/break down of water vapor into hydroxyl radicals and hydrogen atoms (Riesz and Kondo, 1992). Hydroxyl radicals can form hydrogen peroxide (H_2O_2). H_2O_2 can initiate different biochemical reactions, i.e., the cascade of production of free radicals. As a result, there is further more formation of free radicals like hydrogen peroxide, singlet oxygen, and superoxide ions. Therefore, measurement of hydroxyl radicals can be used to determine acoustic cavitation quantitatively (Riesz et al., 1990; Wang P. et al., 2012).

Intracellular production of ROS in response to ultrasound play a crucial part in the therapeutic application of ultrasound. For example, low intensity ultrasound produces free radicals that are involved in the membrane permeabilization, which can be employed for molecular delivery of drug, genes and nanoparticles. Thus, ultrasound interaction with tissues produces free radicals that contribute to the production of heat that ablates tissues, and leads to necrosis of cells. ROS can induce cell death

in tumors because of their high toxicity and more importantly they also function as signaling molecules for apoptosis in cancer (Hervouet et al., 2007).

A disadvantage of producing high levels of ROS is that can cause some adverse effects like oxidative damage to healthy cells. Other side effects includes denaturation of proteins and damage to tissues. ROS can break DNA (double- or single-strand DNA). The breakage in the DNA backbone essentially occurs between oxygen and carbon atoms, causing DNA fragmentation (Wasan et al., 1996). On one hand, ROS are essential for both cancer and normal cells for their normal function in many processes such as signal transduction (Manthe et al., 2010). Whereas, on the other hand, excessive ROS can lead to carcinogenesis in healthy cells (Ozben, 2007). Unfortunately, the exact quantity of ROS needed to induce tumor cell death is unknown (Ozben, 2007). Excessive apoptosis as a result of ROS production in normal cells can also induce autoimmune disorders, cardiovascular and neurodegenerative diseases, ischemia-reperfusion injury in healthy cells. Therefore, ROS based therapies (including ultrasound) ideally should be specifically destroying cancer cells without causing toxic/harmful effects in normal cells (Wang and Yi, 2008).

Moreover, when ultrasound is used to aid drug delivery, ROS production may decrease the potency of a drug. This is because, free radicals can alter the molecular structure/conformation of the drug, thus reduce the therapeutic effectiveness of the treatment (Zhang et al., 2010).

Alteration in Cell Membrane Fluidity

Ultrasound waves have the ability to interact with cell membranes directly or indirectly which results in changes to membrane fluidity that consequently leads to changes in cell function. Giacinto et al. demonstrated that cell membrane fluidity changes after exposure to ultrasound 1 (MHz) using conventional

therapeutic ultrasound devices. In their study it was found that the vibration modes of ultrasound can cause reversible change in cell morphology by either compression or stretching of the cell cytoskeleton. The effects were observed because the cellular membrane has a natural tendency to absorb mechanical energy from the ultrasound radiations. It causes expansion and contraction of the intramembrane space upon exposure to ultrasound (Di Giacinto et al., 2019). The transient modifications of cell morphology induced by ultrasound can also result in deformation of the plane of the lipid bilayer of the cell membrane, and the changes in the thickness of the lipid bilayer. The effect consequently can stimulate gated ion channels of the cell membrane and change the electrolyte intracellular distribution of the cells (Wiggins and Phillips, 2004).

Additionally, the membrane fluidity can reduce in reaction to lipid peroxidation. A number of reports have confirmed the reduction of membrane fluidity in different types of cell membranes after of lipid peroxidation induced by ultrasound (Kaplán et al., 2000; Solans et al., 2000; Benderitter et al., 2003). Lipid moieties inside the plasma membrane are one of the targets of ROS. Released ROS after ultrasound interaction with cells often cause lipid peroxidation of plasma membrane. Specially, polyunsaturated phospholipids present in plasma membrane are more susceptible to lipid peroxidation, because of presence of chains in their chemical structure (de la Haba et al., 2013). Lipid peroxidation of the lipids disturbs the cell membrane bilayer structure, changes membrane properties such as membrane fluidity, and also changes the physiological functions of cell membranes which ultimately contributes to cell membrane damage (Catalá, 2009, 2012).

Other effects of ultrasound includes cell body shrinkage, disruption of actin cytoskeleton organization and also cell nucleus contraction (Wang M. et al., 2018).

Cavitation

Cavitation can be utilized to further enhance the sonoporation effect, and for this purpose microbubbles (exogenous), can be introduced to the cellular microenvironment. Microbubbles are extensively used for diagnostic imaging to enhance the contrast of ultrasound images. However, during imaging ultrasound frequency and intensity is adjusted not to disrupt microbubbles, which otherwise could induce undesired side effects. Microbubbles have also been applied in drug delivery, which take benefit of the capability of ultrasound to disrupt microbubble in selected locations, thus triggering drug release on demand (Unger et al., 2004). Cavitation can be classified into two types depending on how microbubbles collapse in response to ultrasound energy, as stable, and inertial cavitation (Greillier et al., 2018).

Stable Cavitation

It is described as a non-linear, sustainable, and periodic expansion and contraction of a gas bubble. During stable cavitation, also called as non-inertial cavitation, the gas pockets present in the liquid oscillate around an equilibrium radius and can persist for long time. This means gas microbubbles can shrink and expand under the influence of ultrasound for long periods of time. The time period of microbubble oscillation lasts

until the gas content of the microbubble dissolves into the blood and it is then rapidly cleared through exhalation from the lungs (Khokhlova et al., 2015). The main application of stable cavitation is to alter vascular permeability for increased extravasation (penetration) of nanoparticles and hence improve delivery and deposition of drug/gene/nanoparticle to whole tissues (Kang and Yeh, 2012). It also results in ion channel and receptor stimulation, simultaneously, it can alter cell permeability and action potential of the cell which facilitates drug delivery to cells (Yang et al., 2019).

Inertial Cavitation

It can be defined as the violent collapse of bubbles, where microbubbles collapse instantly upon application of ultrasound (Liu D. et al., 2016). The main application of inertial cavitation is to modulate the permeability of individual cells for enhanced delivery of therapeutic agents (genes or drug) at the individual cellular platform (Liu W. W. et al., 2016). Inertial cavitation induces membrane pores of larger sizes in comparison to stable cavitation. The pore sizes can vary from hundreds of nanometers to a few micrometers (Wischhusen and Padilla, 2019). There are three possible mechanisms through which inertial cavitation can alter the permeability of subcutaneous (SC) membrane.

Modes of inertial cavitation:
A. Spherical collapse of microbubbles close to the SC membrane radiates shock waves, which has potential to disturb the SC lipid bilayers (**Figure 3A**)
B. Effect of an acoustic microjet on the SC surface. The microjet producing a region about one-tenth of the microbubble diameter influence the SC membrane without entering into the surface of the membrane. The force of the microjet may improve SC permeability by damaging SC lipid bilayers (**Figure 3B**)
C. Microjets may substantially enter into the SC and improve the SC permeability (**Figure 3C**) (Tezel and Mitragotri, 2003).

These effects are also referred as the non-thermal effect of ultrasound. Notably, in non-thermal effects of ultrasound, acoustic pressure, and velocity gradient are generated as a result of shear stress which is produced after the application of ultrasound. The shear stress suppresses the cohesive strengths within the nanoparticles and ultimately ruptures nanoparticles thus releasing their cargo at the site of action. The microjet and microstreaming events has capability to generate temperature increase as well as mechanical stresses within nanoparticle structure (**Figure 4**). In cavitation extreme stresses such as shockwaves and damaging free radicles are produced which are also responsible disruption of nanoparticles (Husseini et al., 2014).

Ultrasound-Induced Hyperthermia

Ultrasound induced hyperthermia is the rise in temperature due to the absorption of ultrasound energy by tissue as a result of mechanical compression and decompression. Some portion of the mechanical energy is utilized during friction effects and it ultimately gets transformed into heat. Ultrasound waves cause rotation or vibration molecules in the tissue and these movements results in frictional heat and local hyperthermia in
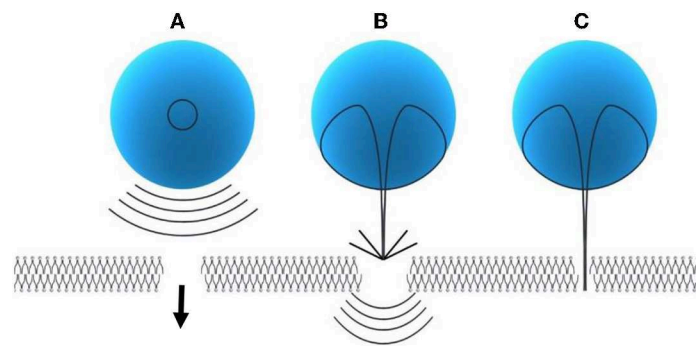
FIGURE 3 | Modes of inertial cavitation [modified from Tezel and Mitragotri (2003), reference number 59 with permission]. **(A)** Effect of spherical collapse of microbubble. **(B)** Effect of an acoustic microjet on SC membrane. **(C)** Effect of microjet entering into the SC membrane.
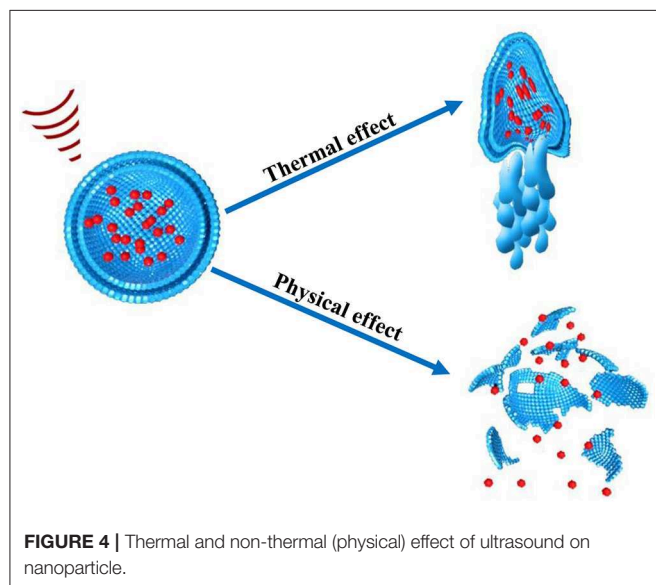

FIGURE 4 | Thermal and non-thermal (physical) effect of ultrasound on nanoparticle.

targeted tissues (Kim et al., 2008). With hyperthermia, tissue temperature rises to 40°–45°C which can be up to 60 min, the time period depends on the duration of the ultrasound treatment (Zhu et al., 2019). In general, hyperthermia is utilized in combination with other therapies such as chemotherapy and radiation therapy. Hyperthermia has been successfully used for sensitization of malignant tumors before chemotherapy to treat several types of solid tumors (Hurwitz and Stauffer, 2014).

During hyperthermia, the fluidity of the phospholipid bilayer of the cell membrane changes and results in altered, often increased, permeability of cell membrane for drugs or nanoparticles. The mild increase in temperature can also result in deformation or complete disruption by swelling of nanoparticles structure because of absorption of ultrasound energy. Nanoparticles may eventually burst which helps in enhancing release of therapeutic drug delivery at the desired sight of action. Therefore, increased temperature can act as a "trigger" at the site of action which could be exploited with nanoparticles.

Nanoparticles used for such purpose are composed of materials (typically polymers or lipids) which respond to heat, hence called as thermosensitive nanoparticles. Hence, thermosensitive nano/micro particles can be stimulated using ultrasound to enhance the targeted drug release.

For the fabrication of an ideal thermosensitive nanoparticle fundamental characteristics need to be fulfilled, they are as follows:

(i) Should comprise of phospholipids or polymers in outer structure which are sensitive to heat
(ii) Stable entrapment of therapeutic agent at body temperature
(iii) Instant and enhanced drug release after exposure to heat stimuli and
(iv) Supply of high concentration of drug to plasma while being hyperthermia treatment is applied (Liu D. et al., 2016; Garello and Terreno, 2018).

Another thermal effect of ultrasound is localized thermal ablation, which is achieved with the use of high intensity focused ultrasound (HIFU). Higher intensities of ultrasound ($>5\,\text{W/cm}^2$) are used for local heating of focused tissues for achieving ablation. It is explained in detail as following.

HIGH INTENSITY FOCUSED ULTRASOUND (HIFU)

HIFU is able to induce localized thermal ablation within the body and which is fundamentally different to hyperthermia. Hyperthermia involves heating of tissues up to 40°C, whereas HIFU irradiation induces rapid heating of targeted tissue to temperatures $>60°\text{C}$ leading to coagulative necrosis (Chu and Dupuy, 2014). For example, HIFU effectively ablates pancreatic tumors by localized heating of tissues to temperatures as high as 65°C, therefore abolishing the tumor cells completely (Ning et al., 2019). Depending on the intensity, focused ultrasound can be classified into two types: low intensity focused ultrasound (up to $3\,\text{W/cm}^2$) (LIFU) and high intensity focused ultrasound (HIFU) (over $5\,\text{W/cm}^2$). Low intensity treatments are typically used for triggering physiological responses to injury to aid healing

processes. LIFU is used to stimulate biological reactions that help in healing including: acceleration of soft-tissue regeneration and inhibiting inflammatory responses (Xin et al., 2016). Along with these applications, LIFU is applied for deep-seated tumors (Hayes et al., 2004), as it has been widely reported that low frequency ultrasound beam can propagate into deeper tissues in the body (Hayes et al., 2004).

In contrast, the purpose of HIFU treatment is to selectively destroy tissues through localized heating known as ultrasound induced thermal ablation (Hayes et al., 2004). For HIFU, a broad range of ultrasound frequencies are used from about 20 kHz up to hundreds of MHz. Frequencies less than a few hundred kHz are regarded as low frequency ultrasound, whereas frequencies equal to and higher than 1 MHz and are regarded as high frequency ultrasound (Erriu et al., 2014). In HIFU, hyperthermia results from focusing of high intensity ultrasound beam on selected areas for a certain amount of time in one area (van den Bijgaart et al., 2017). Hyperthermic cell ablation can be very precise since an ultrasound beam can be focused on a small area ∼1 mm in diameter and about 10 mm in length (Emfietzoglou et al., 2005).

In China and Korea, HIFU has been extensively utilized for the treatment of cancer and other conditions since the 1990s. More recently, National Institutes of Health (NIH) (2013) recommends HIFU as an auxiliary therapy for unresectable pancreatic ductal adenocarcinoma (PDAC) (Ning et al., 2019). There has been substantial successes with the application of HIFU for non-invasive "surgery" that allows precise ablation of solid tumors, such as breast cancer, prostate cancer, hepatocellular and pancreatic carcinoma, uterine fibroids and bone malignances (Wu, 2006). The most important benefit of HIFU is that it is less harmful than a surgical procedure. It does not require opening and cutting the body surface to access a tumor site, thus eliminating the need for anesthetics. It also minimizes surgery related biological waste, morbidity, mortality, hospital stay length, and expenses. Overall it can improve quality of life for cancer patients (Cirincione et al., 2017).

HIFU-Induced Immunomodulation

The healthy immune system has the capability to identify a broad range of pathogens and cancer cells. A compromised immune system in cancer patients is one of the primary issues which is responsible for the advancement and promotion of cancer. Cancer cells develop various "strategies" to fully escape immune surveillance (Costello et al., 1999) by releasing cytokines (with immuno-suppressive capabilities) and by depleting the tumor associated antigens (TAAs) (Lindau et al., 2013). Therefore, in order to hinder recognition by T lymphocytes (immune cells) of neoplastic cells, cancer cells down-regulate the expression of tumor antigens. Moreover, cancer cells can deactivate effector T lymphocytes by releasing immuno-suppressive cytokines (Konjević et al., 2019). The important function of anti-tumor immunity in cancer is the specific identification and destruction of cancer cells by immune system of the patient. For achieving the effect, cancer cells need to indicate tumor-associated antigens (TAAs) and produce a tumor specific immune response. Unfortunately, it doesn't happen in cancer because of a compromised immune system. Therefore, some of the immunotherapies focus on the modulation of the immune system through adoptive T cell transfer, T cell checkpoint blockade, or vaccination. These immunomodulatory strategies are rising as a potential and effective therapeutic approach with clinical benefit for cancer patients (Ayoub et al., 2019).

Interestingly, HIFU, which can induce both mechanical effects and hyperthermia, stimulates physiological responses of the immune system—immunomodulation. The effects of HIFU further extends benefits and applications of HIFU in cancer treatment. Pre-clinical and clinical research have showed that HIFU leads to modulation of long-term systemic host anti-tumor immunity (Hu et al., 2007; Wu et al., 2007; Zhou et al., 2008). HIFU-induced immunomodulation is likely to support the removal of cancer cells left at the local treatment site, thus suppressing local recurrence, and distant metastasis in cancer patients with original dysfunction of anti-tumor immunity (Cirincione et al., 2017).

The immunomodulatory function of HIFU can be explained by the following theories:

1. After HIFU-induced thermal ablation, tumor debris remains, and TAAs are released in response to the ablation. These remaining debris and released TAAs can generate hazard signal over-expression, which in combination with each other function as tumor vaccines and enhance tumor immunogenicity.
2. HIFU stimulates a Th1 type cell responses, which gives rise to substantial modulation in "cell-mediated immunity."
3. HIFU therapy works on balancing of cancer-induced immuno-suppression in the surrounding tumor environment (den Brok et al., 2004; Toraya-Brown and Fiering, 2014; Cirincione et al., 2017; van den Bijgaart et al., 2017; Yang et al., 2019; Zhu et al., 2019).

HIFU USE FOR DIFFERENT TUMOR TYPES

Uterine Fibroids

It has been discovered that cancer cells are more sensitive to heat than normal cells (Peek and Wu, 2018). For this reason, the use of ultrasound provides the opportunity for a non-invasive technique to treat various cancers of both primary solid tumors and metastatic disease. The first approved HIFU device by the FDA was in October 2004 for the treatment of uterine fibroids (Jain et al., 2018).

Uterine fibroids are among the most common tumors occurring in the female genital tract, however due to their benign nature they often grow undiagnosed for many years and cause serious health problems such as prolonged menstruation, abdominal pressure leading to pain and other obstetric complications. The standard of treatment for many years has been surgical management which leads to a full hysterectomy thus removing the choice of fertility for these women.

An evaluation of HIFU ablation for uterine fibroids in 2017 established HIFU caused considerably less morbidity than surgery with similar results with quality of life. This clinical study reported 1353 women with uterine fibroids receiving HIFU for 472 hysterectomies and 586 myomectomies (Chen et al., 2018).

Another recent study by Łozinski et al. in 2019 attempted to see the effects of HIFU treatment whilst preserving fertility. The results showed that HIFU does not impair ovarian function nor negatively effects the ability to conceive due to its minimally invasive nature. It was recommended that this therapy should only be considered as an alternative treatment until more data is established (Łozinski et al., 2019).

Such clinical studies are displaying the prospective uses of HIFU and specifically in the use of cancer treatments.

Brain Cancer

HIFU with guided systems are being heralded as a "disruptive technology" due to the possibility of overturning standard technologies used for therapy. This is because providing therapy to discrete brain targets whilst keeping an intact skull has been always been a therapeutic goal (Meng et al., 2017). In the brain, ultrasound has been used for the ablation of glioblastoma and functional neurosurgery (Bradley, 2009). Apart from ablation properties, ultrasound systems are proving advantageous in brain tumor surgery due their real time imaging and 3D-navigation properties in the head region allowing intra-operative neuro-navigation (Wei et al., 2013).

Another application of ultrasound in the treatment of brain cancers is through chemotherapy delivery. Many chemotherapies have low bioavailability in the brain and have even showed neurotoxicity due to non-specific brain uptake. Ultrasound mediated BBB disruption to administer chemotherapy has received multiple preclinical studies and a pilot trial has started to investigate the delivery of chemotherapeutic agent temozolomide (Meng et al., 2017). Further details about drug delivery across BBB below.

Breast Cancer

A predicament many surgeons currently face when removing breast tumors is their inability to visualize the tumor in determining clear margins between healthy and malignant tissue. This issue leads to higher rates of reoperation to excise the residual tumor allowing for ongoing complications. HIFU ablation with guidance using ultrasound or MRI has the potential to resolve this problem due to its non-invasive nature and ability to plan through visualization and real time monitoring (Peek et al., 2015).

Peek et al. summarizes the various HIFU devices currently in use for application in breast and outlines several clinical trials comparing ultrasound and MRI image guidance with positive results (Peek and Wu, 2018). In the 2015 meta-analysis, 46% of patients resulted in complete ablation and 30% reported near complete ablation with <10% residual tumor. The treatment times ranged between 78 to 171 min and the most common side effect of 40% was pain (Bea et al., 2018).

These results show that HIFU is a viable surgical technique for removal of breast cancer. However, the issue with long treatment times and reduction of pain is one that should be strongly considered. The HIFU technique should look at solutions to reduce adverse effects such as pain and move to larger populations of clinical trials to validate these positive results.

Pancreatic Cancer

For many pancreatic cancer patients, the time of diagnosis is already too late and inoperable due to locally advanced disease or metastasis. Ablative HIFU therapy has provided an alternate primary and palliative therapy for pancreatic cancer. Endoluminal HIFU transducers are in pre-clinical development and will allow endoscopic placement inside the stomach or duodenum to be precisely adjacent to the pancreas. This will ensure greater lesion targeting and minimizes risk of damage to soft tissue in neighboring areas (Maloney and Hwang, 2015).

Apart from ablative primary therapy HIFU is being applied for greater drug targeting as current traditional chemotherapy drugs are poorly effective in penetrating fibrotic and hypovascular stroma of pancreatic adenocarcinoma (Maloney and Hwang, 2015). Preclinical and clinical studies show the use of HIFU to deliver liposomes into pancreatic tumors applying the process of sonoporation. The study administered pancreatic cancer patients with a combination of gemcitabine and ultrasound with microbubbles causing a survival rate of 17.6 vs. 8.9 months with gemcitabine alone. The sonoporation technique indicated that HIFU can be used to enhance penetration into the pancreatic tumor interstitium (Rix et al., 2018).

Prostate Cancer

In the case of prostate cancer, HIFU has been used for treatment for a long period of time with both established systems as well as consistent developments. The HIFU transducer is placed within the rectum or urethra and the cancer is ablated via guided-HIFU therapy. Recently, this procedure is also being used for partial prostate gland ablation (Rix et al., 2018). Juho et al. evaluated the therapeutic response and complications of HIFU for patients with localized prostate cancer. The study evaluated clinical outcomes of 29 patients who received HFU as first-line treatment and results showed a 100% survival rate on the 24.6 month follow up with ~20% biochemical recurrence and similar rate for disease progression. Overall, this study confirms HIFU as an alternative therapy in patients with localized prostate cancer with a low complication at follow up in the short term (Juho et al., 2016).

Liver Cancer

It is estimated more than 80% of patients with hepatocellular carcinoma (HCC) are poor candidates for curative surgery due to advanced underlying cirrhosis. A minimally invasive method such as HIFU is gaining prominence for this reason (Maloney and Hwang, 2015). Studies of HIFU use in hepatocellular carcinoma and secondary liver metastases in human clinical trials have been published with significant promise in HIFU treatment of hepatic malignancies (Dubinsky et al., 2008).

Young et al. describes a case study of a patient with liver metastases where the tumor was not resectable and had received systemic chemotherapy. The patient was treated with a single HIFU session with complete lesion ablation under general anesthesia. The outcome of this session showed a complete remission of the metastatic liver mass (Sung et al., 2008). HIFU therapy for liver lesions remain in at early stages but may offer solutions to current therapeutic barriers (Maloney and Hwang, 2015).

ULTRASOUND INDUCED MECHANISM OF DRUG DELIVERY IN CANCER

Cancer is a leading cause of death worldwide. Systemic chemotherapy is the primary therapy used to treat various types of cancers, but it is associated with undesirable side effects and have shown unsatisfactory tumor responses. Poor tumor responses to chemotherapy arises because of major obstacles for the diffusion of anticancer drug to the tumor site. The main obstacles include the diverse and unorganized tumor vasculature, abnormal and atypical blood flow, and high interstitial pressure within the tumor tissue. It results into low and heterogeneous uptake of nanoparticles in tumor tissue which are one of the main problems for successful cancer therapy using nanoparticles. The insignificant response of tumor to therapeutic agents and nanoparticles have strongly indicated the need for developing a new strategic approach for improving targeted drug delivery to tumors and minimizing systemic side effects of the treatment at the same time.

Ultrasound has been utilized to improve the delivery of therapeutic agents for the past three decades; it includes chemotherapeutic drugs, proteins, and genes (Pitt et al., 2004). There are various ways by which ultrasound improves the efficacy of treatment, specifically by:
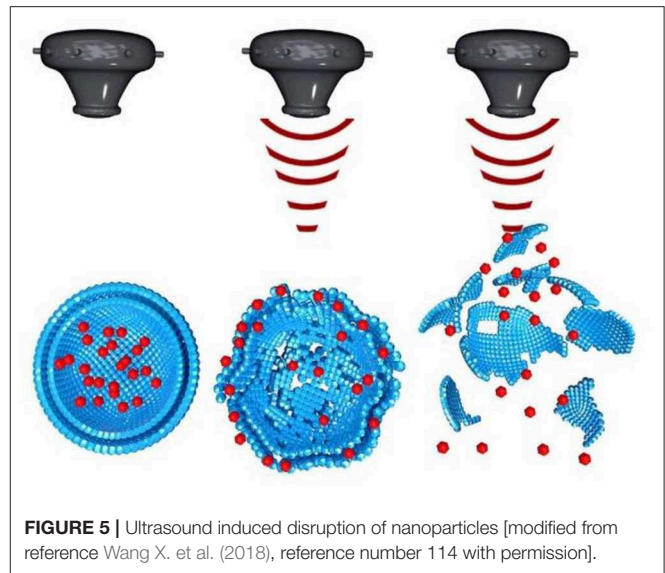
- Triggering the release of the drug from nanoparticles,
- Promoting uptake and accumulation of nanoparticle in cells,
- Enhancing the penetration of nanoparticles in tumors.

Triggering the Release of Drug From Nanoparticles at Target

The exact mechanism of how ultrasound disrupts nanoparticles and how they react to an ultrasound beam to stimulate nanoparticles is still not fully elucidated (Zhou et al., 2014). There are two possible mechanisms of disruption of nanoparticles by ultrasound i.e., thermal effect and non-thermal effects. Thermal and non-thermal mechanisms could also work as an adjunctive stimulus during drug delivery. Therefore, multi-mechanisms such as thermal and mechanical effects of ultrasound combines and act simultaneously for disruption of nanoparticles (Zardad et al., 2016). Drug delivery systems can be fabricated to react either to the increased temperature or to the mechanical effects of an ultrasound beam, or to both (Schroeder et al., 2009b).

Localized on Demand Triggered Drug Release

The universal drawback of cancer is unspecific drug delivery of chemotherapeutic drug on healthy cells. One of the distinctive characteristics of ultrasound is that it can be focused. The effect is similar to the focusing of light through a lens which can burn paper if focused for long time. In a same manner ultrasound can be focused using acoustic lens to an object in liquid medium. The focus of the ultrasound can be adjusted as small as a few cubic millimeter (Mason, 2011). This characteristic of ultrasound can be utilized for focusing an ultrasound beam electronically and with accuracy on soft tissues (such as tumor) for thermal ablation and on to nanoparticles for their disruption (**Figure 5**) to achieve localized drug delivery to tumors (Wang X. et al., 2018).

FIGURE 5 | Ultrasound induced disruption of nanoparticles [modified from reference Wang X. et al. (2018), reference number 114 with permission].

In a summary, ultrasound enables the disruption of drug carrying nanoparticles and release of drug locally at tumor sites. Therefore, the combination of ultrasound and ultrasound-sensitive nanoparticles can enhance delivery of drug from nanoparticles and selectively release drug within the focal point of ultrasound. It can synergistically reduce the amount of dosage required and facilitate selective tumor targeted drug delivery to avoid undesirable side effects on healthy cells.

Promoting Uptake and Accumulation of Nanoparticle in Cells

A major problem in cancer therapy, where drug is delivered with the help of nanoparticles, is the very low and uneven uptake of nanoparticles in tumor tissue. According to Wilhelum et al. only about 0.7% of the intravenously administered dose of nanomedicine is delivered to the tumor (Wilhelm et al., 2016). Nanoparticle uptake of the tumor can be increased if ultrasound is applied, which is attributed to the enhanced transport of nanoparticles to the tumor. Furthermore, microbubble (which are gas bubbles stabilized by coating of surfactant, polymer, or phospholipids) in combination with ultrasound can be utilized to enhance transport of nanoparticles/drug toward tumor. Upon irradiation with ultrasound, the microbubbles which are administered in the bloodstream will oscillate and induce mechanical forces on the blood vessel wall. The externally received mechanical energy from ultrasound can enhance the transport of nanoparticles and drugs across the capillary wall to enter the extracellular matrix of tumor.

Enhancing the Penetration of Nanoparticles in Tumors

The efficacy of treatment for any disease is determined by localized concentration of therapeutic agent and duration *in situ*. For instance, in cancer drug delivery into tumor tissue is achieved by penetrating through the capillary wall or through

the tumor stroma to tumor cells, resulting in tumor cell death. Unfortunately, in current chemotherapy for cancer, the localized concentration of drug within tumor is low, and the drug concentration in bloodstream is comparatively high. It leads to toxicity to healthy cells, causing unwanted side effects (Wei et al., 2019). Therefore, enhanced drug penetration in solid tumors and reduced possible side effects on healthy cells remain a major goal in cancer chemotherapy. The problem arises because of overexpression of dense extracellular matrix (ECM) by tumor cells. ECM acts as a steric barrier to transport and distribution of nanoparticles throughout the tumor (Chauhan et al., 2011). This issue can be addressed by using ultrasound, as mechanical energy associated with ultrasound physically "pushing" nanoparticles into the tumor matrix, enhancing accumulation and deeper penetration of the particles within diseased tissue. The major limitation of current drug delivery systems is that they can travel only a few μm from main blood capillary inside the tumor.

For example, nanoparticles such as liposomes fail to distribute deeper into dense tumor mass (Emfietzoglou et al., 2005). It was studied in 2006, by Dreher et al. performed expanded study on penetration of dextrans of 3.3–2,000 kDa molecular weights into solid tumors. Their study revealed that diffusion of 40–70 kDa dextrans was mostly confined to 15 μm region from the closest capillary. The permeation of 2,000 kDa dextrans was constricted to only a 5 μm from the nearby vessel wall (Dreher et al., 2006).

Kostarelos et al. (2004) also demonstrated that liposomes mainly concentrate close to the tumor vasculature, and are unable to penetrate deeper into dense tumor mass (Poh et al., 2015). Poor permeation results in inadequate exposure to antitumour therapeutics and contributes to development of chemo-resistance and increased metastasis. Ultrasound enhances the penetration of nanoparticles into tumor tissues to entirely and adequately expose tumor to therapeutics. Taken together, ultrasound-based drug delivery enhances efficacy of cancer treatment by improving the cellular uptake of nanoparticles, enhancing penetration of nanoparticles in tumor, and increasing the therapeutic delivery of the drug (by disruption of the particles on the site of action) (Hare et al., 2017).

ULTRASOUND INTERACTION WITH NANOPARTICLES

When ultrasound radiation propagates through the body, it can interact with cells and engineered nanoparticles used to deliver drugs which are circulating in the blood stream or reside in the extracellular matrix. Since the ultrasound radiation carries a substantial energy, it simultaneously interacts with cells and nanoparticles. The effects of interactions of ultrasound with nanoparticles and cells are favorable for drug delivery in cancer and synergistically enhance the effectiveness of the treatment. Moreover, ultrasound drug delivery with nanoparticles has a capability to overcome limitations associated with current cancer therapies.

Since ultrasound has the ability to interact with nanoparticles, it is possible to design drug-carrying nanoparticles that in response to ultrasound break open and release a therapeutic payload. Therefore, ultrasound can be used to trigger drug release

on demand from nanoparticles known as ultrasound-mediated drug release. Besides triggering the drug release through the disruption of the nanoparticles, ultrasound can be used to modulate intracellular pressure, as well as to induce acoustic fluid streaming, cavitation, and local hyperthermia. In fact, each of these mechanisms can be used to trigger drug release from a carrier which requires designing nanoparticles that are sensitive to one or more of these triggers (Sirsi and Borden, 2014). For example, co-polymer based nanoparticles such as ultrasound-sensitive block copolymer micelle like poly ethylene glycol (PEG) and poly propylene glycol (PPG) (Li et al., 2016) can breakdown under the influence of ultrasound to release bolus of drug precisely at the targeted tissues (Wang et al., 2009).

Since the outcomes of the interactions between ultrasound and nanoparticles are different, e.g., disruption or melting of nanoparticles (**Figure 4**), it implies that different cellular pathways will be affected by each of the interactions. It offers substantial benefit because it is possible to design nanoparticles which act on a specific pathway that is complimentary to drug action; e.g., thermosensitive nanoparticles for heat-controlled drug release. When two treatment modalities are combined it is expected that the efficacy of the treatment will be improved. For example, combination of hyperthermia, and chemotherapy leads to increased effectiveness in inducing cell apoptosis (Boissenot et al., 2017).

Furthermore, ultrasound can improve the accumulation of drug- encased nanoparticle in target tissues. The enhancement is attributed to the mechanical energy carried by ultrasound radiation that physically pushes nanoparticles within body. The physical push enhances the transport of nanoparticles toward ultrasound-exposed tissues and results in localized accumulation and increased cellular uptake of nanoparticles (Watson et al., 2012).

Types of Ultrasound-Sensitive Materials and Nanoparticles

It is well-established that ultrasound can induce the degradation of polymers to lower molecular weight. Earlier research revealed that ultrasound induce depolymerization is a non-random process. Generally, the polymer chain separation occurs mostly at the chain midpoints, and larger molecules degrade the fastest. Another noticeable characteristic of ultrasound induced degradation is that the molecular weight reduction is the result of splitting of the weakest chemical bond in the chain. Reich et al. demonstrated that ultrasound intensity of 40 W and above can substantially reduce molecular weight of poly lactic acid (PLA) and poly lactic-co-glycolic acid (PLGA), even at short treatment duration of 30 or 20 s. El-sherif et al. also reported that the high frequency ultrasound of 5–10 MHz can induce decomposition of PLGA polymer under a high frequency ultrasound. Therefore, use of ultrasound can be an effective method for designing of required polymers. The exact mechanism of ultrasonic degradation remains poorly understood. However, it is now established that the high shear fields and immediate generation of hot spots after ultrasonic cavitation are basically accountable for polymer degradation. It is also considered that at the level of cavity collapse created by ultrasound beam, friction forces and shock waves form the stresses on the surface of a polymer

TABLE 1 | Use of nanoparticles with ultrasound to enhance efficacy of the treatment.

Nanoparticle categories	Features	Reference
Micelles	• Able to preferentially accumulate in tumor cells due to enhanced permeability effect • Demonstrated use for sonodynamic therapy to generate reactive oxygen species at tumor site	Horise et al., 2019
Liposomes	• Easy preparation • Good biocompatibility • Low toxicity • Can modify surface by PEGylation to increase circulation time	Mangraviti et al., 2016
Solid lipid nanoparticles	• Can hold a high payload • Can hold both soluble and insoluble actives • Greater stability than liposomal and polymeric nanoparticles • Good biocompatibility	Özdemir et al., 2019 Sadegh Malvajerd et al., 2019
Mesoporous silica nanoparticles	• High stability • Biodegradable • Biocompatible • Can also be used as contrast agents for theranostic ultrasound applications • Can be used to sensitize tumors to effects of hyperthermia	You et al., 2016
Perfluorocarbon containing nano-/microparticle	• Nano-sized with liquid-gas phase transition • Can be used to form microbubbles to form cavitation effect with HIFU • Can be encapsulated in lipid or polymer materials	Zhang Y. et al., 2019

chain, and also into the polymer coil. It results in chain bond decomposition in large molecules in liquid (Xia et al., 2016). **Table 1** summarizes the use of nanoparticles in combination with ultrasound to enhance efficacy of the treatment.

Micelles

Micelles are self-assembled colloidal structures made up of amphiphilic molecules in an aqueous solution. They are formed by a hydrophilic outer shell and are able to avoid engulfment by the immune system (Hanafy et al., 2018), making them very useful for targeted drug delivery especially for cancer therapy. Polymeric micelles have received considerable interest due to their ability to penetrate the vasculature of tumors and have shown both high drug capacity and good efficiency in patients with malignancies of breast and lung.

Micelles sensitive to biological stimuli such as ultrasound offer a great opportunity for drug delivery as controllable systems (Hanafy et al., 2018). Recently, sonodynamic therapy with anticancer micelles and high intensity focused ultrasound was investigated in canine cancer. This study by Horise et al. was able to confirm the anticancer efficacy of their method and showed its potential to become standard therapy in human cancer (Horise et al., 2019). This study and others indicate the potential of ultrasound waves to disrupt micelle nanocarriers allowing diffusion of drugs in cancer targets.

Liposomes, e-Liposomes

Thermosensitive liposomes (TSLs) encapsulate a hydrophilic drug within a core surrounded by a lipid bilayer. TSLs take advantage of the enhanced retention and permeability effect in tumors due to their nanosize and ability to release an encapsulated drug in response to hyperthermia caused by ultrasound (Jain et al., 2018). For example, the study done by Yudina and Moonen (2012) outlines the use of doxorubicin-loaded and paclitaxel-loaded TSLs (Yudina and Moonen, 2012). The drug-loaded TSLs were externally triggered in response to

being treated with ultrasound through hyperthermia near their phase transition temperature. This study demonstrated improved effectiveness in preclinical trials for drug bioavailability and anti-tumor effect. The hyperthermia range for TSLs are ~40–45°C and it has been reported that drug delivery using TLS could be enhanced by using prolonged hyperthermia for up to 2 h (Elhelf et al., 2018).

Solid Lipid Nanoparticles (SLNs)

SLNs are an attractive means of drug delivery owing to their ability to combine the advantages of both polymeric nanoparticles and lipid structured nanoparticles such as liposomes. This is because they are suitable to hold a high payload of both soluble and insoluble actives; their size range is flexible (50–1,000 nm); greater stability compared to liposomal and polymeric nanoparticles; and are safe within the body even for an extended period due to their low toxicity. The SLN can be made to have a drug enriched core surrounded by a solid lipid shell or the shell could contain the drug and the core be made of solid lipids (Özdemir et al., 2019; Sadegh Malvajerd et al., 2019). For these reasons SLN are very suitable nanocarriers for drug targeting such as for penetrating the BBB (Sadegh Malvajerd et al., 2019).

The use of solid lipid nanoparticles with ultrasound triggered drug delivery is a novel technique. The principles of delivery with ultrasound is applicable to this category of nanoparticles. Timbe et al. describes guided ultrasound delivery of cisplatin-loaded brain penetrating nanoparticles (Timbie et al., 2017). The study hypothesized that ultrasound could enhance the efficacy of drug-loaded brain penetrating nanoparticles for the treatment of glioblastoma. The study was able to show a marked improvement of delivery and distribution when compared to the control. The novel use of ultrasound triggered SLN as nanocarriers are an attractive option and yet to be explored in great detail.

Mesoporous Silica Nanoparticles

Biocompatible mesoporous silica nanoparticles (MSNs) are inorganic nanosystems which have the ability to produce high performance molecular imaging, drug delivery and biosensors. In 2018, Wu et al. demonstrated doxorubicin encapsulated MSN could be accurately delivered into brain tumors that were concurrently triggered by focused ultrasound exposure and resulted in significant inhibition of orthotopic brain tumor progression (Wu et al., 2018). Hollow mesoporous silica nanoparticles (HMSNs) have been employed as carriers of thermos-sensitive perfluorohexane (PFH), a hydrophobic chemotherapeutic agent to act synergistically with HIFU cancer surgery (Chen et al., 2014). The mesopore channels in the shell make it possible to encapsulate and continuously release the thermosensitive PFH due to local temperature rise induced by HIFU. The procedure of fabricating PFH loaded HMSNs is to first use etching protocols to produce the HMSNs, then PFH is loaded into the pore network and inner cavities using a mild infusion procedure. After administration and exposure to HIFU, the liquid PFH is converted into small bubbles which swell and merge upon accumulation in the targeted tumor tissues (Wang X. et al., 2012). This process makes use of HIFU's mechanical and acoustic properties to enhance ablation at tumor sites.

Perfluorocarbon Containing Nano-/Microparticle

Perfluorochemicals (PFCs) are inert and highly fluorinated organic compounds that can dissolve large volumes of respiratory gases including oxygen, O_2 (Li et al., 2018). High gas solubilities of PFCs forms the foundation for an abiotic form for intravascular oxygen delivery. PFCs are characterized by a unique feature of chemical and biological inertness, and the gas contents excreted easily as a vapor by exhalation when administered in body. PFCs are intensely hydrophobic and lipophobic in nature (Riess, 2005). Therefore, PFC liquids are not soluble with aqueous phase, including blood, but they can be formulated as emulsions and can be administered into the bloodstream in a safe manner. PFC emulsion formulations are presently being tested in clinical trials as an alternative means for intravascular respiratory gas-carriers and tissue oxygenating fluids, regarded as 'blood substitutes' (Krafft and Riess, 2007; Chen et al., 2013). PFC compounds are responsive to ultrasound, it was first demonstrated by Apfel, in his pioneering work for more than two decades proving that the specifically fabricated perfluorocarbon droplets can be transformed into microbubbles after ultrasound application. Kripfgans et al. also demonstrated that micrometer-sized PFP droplets can be vaporized into gas bubbles with the application of ultrasound (1.5–8 MHz), the process is regarded as "acoustic droplet vaporization" (ADV) (Rapoport, 2012). It leads to formation of microbubbles that can act as the contrast agents for diagnostic ultrasound imaging. Perfluorocarbon can also be employed for several other biomedical applications such as lung surfactant replacement and ophthalmologic aids. Many other colloidal PFC formulations of are being tested for molecular imaging using ultrasound or magnetic resonance, and for targeted drug delivery.

MISCELLANEOUS APPLICATIONS OF THERAPEUTIC ULTRASOUND

Drug Delivery Through Blood Brain Barrier

The HIFU method involves the selective and localized disruption of the BBB to increase permeability (**Figure 6**). Typically, low frequency ultrasound waves have been employed using perfluorocarbon gas microbubbles which have been intravenously administered. The microbubbles assist in the opening of the BBB by passaging through capillaries and expand and collapse due to mechanical forces of the ultrasound. Results have shown the process is safe and the disruption to the BBB is reversible, lasting up to 4 h with no neuronal damage (Etame et al., 2012). The 2002 Mesiwala et al. study was able to successfully show that HIFU can transiently open the BBB without causing associated parenchymal damage in animal models (Mesiwala et al., 2002).

The most important consideration of HIFU in its application to BBB is that as the frequency increases the degree of tissue attenuation decreases which can lead to skull heating and distortion. The risk of tissue damage is also amplified as the degree of BBB permeability is increased. Therefore, even though an ideal frequency of 200 kHz to 1.5 MHz has been suggested for transcranial use, it is not comprehensively applicable and also depends on factors such as beam pulsing and dosage of microbubbles. Thus, considerable efforts still need to be made in establishing protocols and safety evaluations for use in BBB permeability for neurological applications (McMahon et al., 2019).

Alzheimer's Disease

As with brain tumors, overcoming the limitation the blood brain barrier could reform many central nervous system therapies including Alzheimer's disease. Alzheimer's disease treatment is currently very limited and reversing the progression of the disease is difficult. One of the principal mechanisms of this disease is the accumulation of amyloid plaques which results in loss of neurons (Chang and Chang, 2017).

A weekly study showed non-invasive opening and HIFU treatment of the BBB at targeted bilateral hippocampal areas in mice models allowed accumulation of endogenous antibodies and reduced amyloid plaques by ∼20%. This HIFU therapy exhibited a pronounced improvement of memory performance and increases in neuronal and dendritic length (Jolesz, 2014). Therefore, forthcoming studies need to be done using focused ultrasound for Alzheimer's patients.

Essential Tremor

The FDA granted approval for MR-guided focused ultrasound mediated unilateral lesioning for the treatment essential tremor (ET) in 2016. ET is a condition where current medical therapy is mostly insufficient for patients will severe and disabling tremor. Medical experience has shown reduction of tremor through targeting the ventral intermediate nucleus of the thalamus (VIM) with either sterotactic lesioning or deep brain stimulation. HIFU can be used to form a brain lesion in less invasive manner compared to surgical therapy of deep brain stimulation (Fishman, 2017).
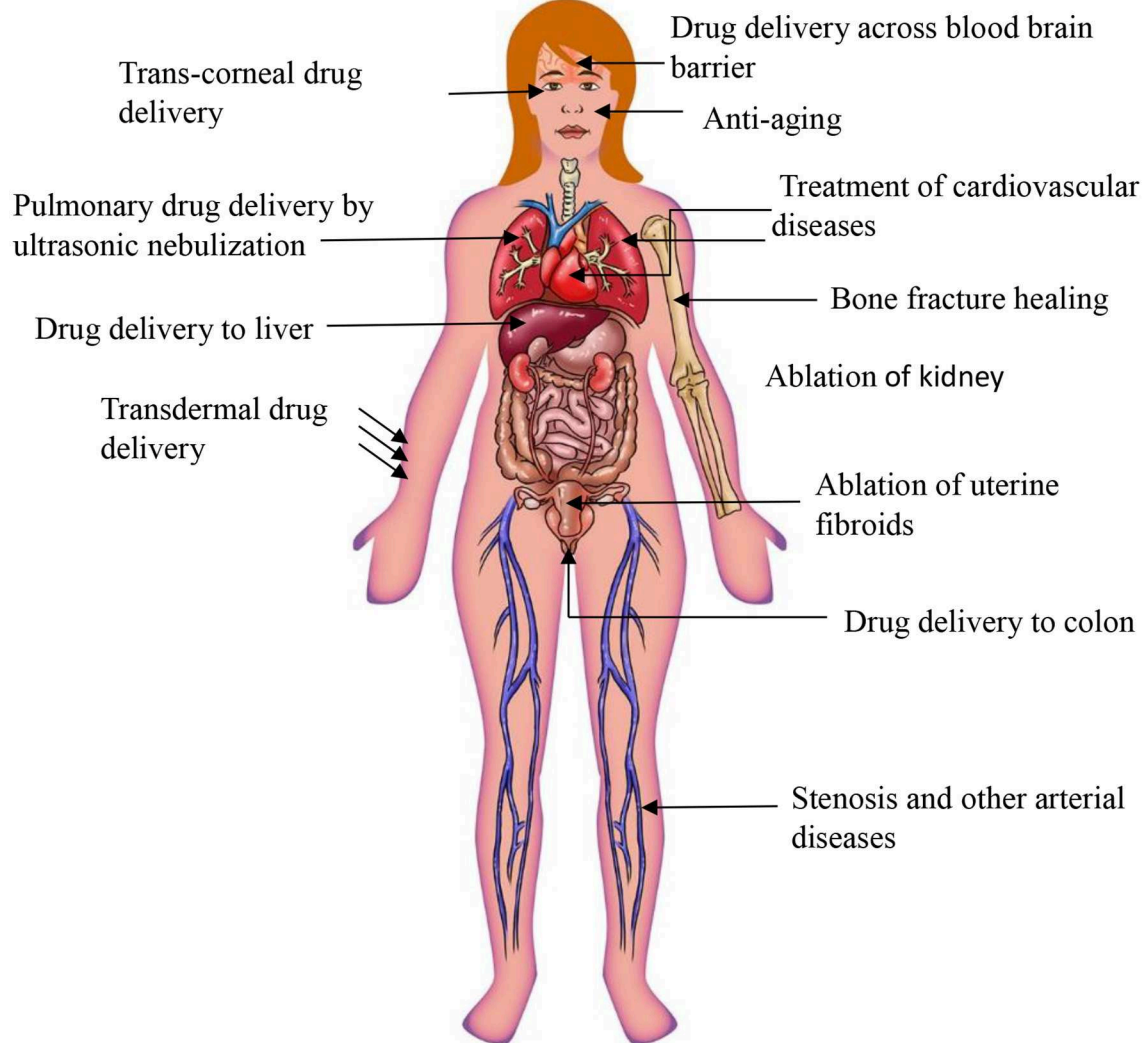
FIGURE 6 | Miscellaneous application of ultrasound.

The Elias et al. describes a randomized trial of focused ultrasound thalamotomy for ET. In this trial, 76 patients with medication-refractory ET were included and controlled using a sham procedure. The trial exhibited significantly reduced hand tremor at 3 months with tremor scores improved by 47% and this effect was perceived for 12 months through follow up. Side effects of the HIFU therapy included sensory and gait disturbances (Elias et al., 2016). This study and FDA approval have strong implications for future treatments of neurological conditions.

Parkinson's Disease

The success of MR-guided focused ultrasound has encouraged investigators to target the VIM in tremor-dominant Parkinson's disease (PD) (Lee et al., 2019). A clinical trial conducted by Bond et al. described 27 patients with tremor-dominant PD improving 62% at the 3 month assessment on a clinical

rating scale succeeding focused ultrasound thalamotomy (Bond et al., 2017). This trial confirmed the use of HIFU in ET and is considered a pilot study for HIFU use in PD. Another investigation by Martinez-Fernandez et al. investigated the safety and preliminary efficacy of MRI-guided focused ultrasound unilateral subthalamotomy in 10 patients with marked asymmetric Parkinsonism. In this study there was an improvement of 53% from baseline to 6 months in the off-medication state and an improvement of 47% in the on-medication state (Martínez-Fernández et al., 2018). Overall, the ultrasound therapy was well tolerated and modestly achieved improvement in motor features of PD. With these examples and other categories of PD there is evidence of focused ultrasound ablative therapy as an alternative to deep brain stimulation. These trials and others lay a strong foundation to more randomized controlled trials with larger cohorts to widen standard treatment options of PD.

Ultrasound for Antimicrobial Therapy

Bactericidal effect of ultrasound is very well-known (Yu et al., 2012; Kobayashi et al., 2014; Cai et al., 2017; Spiteri et al., 2017). The acoustic cavitation effect of ultrasound is believed to be involved in damaging the microorganism. The acoustic cavitation can generate mechanical forces such as shock waves, shear forces, and microjets which damage microorganisms (Ashokkumar, 2011). Another mechanism of bactericidal action of ultrasound induced cavitation is generation of a few free radicals in aqueous medium, which are OH· and H· because of the decomposition of the H_2O molecule. These radicals modulate the cellular construct of the bacteria, which results into the retardation of the bacterial action (Spiteri et al., 2017). The cavitation effect can also be employed for the prevention of biofilm formation on implant surface inside the body. In the antibiotic embedded implants, the release of antibiotic can be enhanced by exposure to ultrasound. Ultrasound radiation pressure and the stable cavitation will generate multidirectional acoustic microstreams, which in turn produce a high shear stress to increase the release and delivery of embedded antibiotic from implants surfaces (Cai et al., 2009). Low frequency focused ultrasound is a promising method to enhance the antibiotic action on bacteria as it has advantages such as capability of treating deep tissue targets without surrounding tissue damage (Cai et al., 2017). However, literature also suggests that the low intensity ultrasound alone is not effective for complete elimination of bacteria, but the combination of low intensity ultrasound and antibiotics has more potential for antibacterial activity (Yu et al., 2012).

More recently, Liu et al. demonstrated the synergistic effectiveness of sonodynamic therapy and immunotherapy (sono-immunotherapy) against one of the difficult to manipulate "methicillin-resistant *Staphylococcus aureus* (MRSA)" bacterial strain. The approach not only kills bacteria but also kills bacteria-associated virulence, therefore termed the study as "one arrow two hawks: a dual approach to eliminating bacterial infection." Their study also reported that the antimicrobial sonodynamic therapy (SDT) works with the help of sonosensitizers to produce ROS, which are highly lethal for all bacteria without causing resistance. However, a single SDT is not always effective for complete bacterial eradication. Therefore, antivirulence therapy was utilized in this study in combination with SDT. The antivirulence treatment specially deactivated bacterial pathogenicity by nullifying their virulence factors. In this way, the antvirulent technique also combats immunosuppression and preserves natural immune protection from virulence destruction. In addition, this therapy without use of antibiotic will be gentle on gut microbiota, without causing resistance to antibiotics and become less cross resistant to each other (Pang et al., 2019).

Antibacterial Chemotherapy for Biofilms

Bacterial biofilms are one of the most common reasons for contamination of various medical and biological areas. The existence of bacterial biofilm are major issues from oral biofilms in the mouth to biofilm formation on medical devices (Vyas et al., 2019). Biofilms are usually very tolerant and show resistance to conventional antimicrobial agents like antibiotics. The more complex biofilm structure as compared to single bacterial organisms poses difficulty for antimicrobials to diffuse through (Bjarnsholt, 2013; Wu et al., 2015). Within the biofilm structure, bacteria are encased in a self-produced extracellular matrix. The matrix comprises of extracellular polymeric substances (EPS) that in combination with carbohydrate-binding proteins, flagell, pili, adhesive fibers and extracellular DNA serve as a stable platform/scaffold for the three-dimensional biofilm formation. The matrix is self-sufficient, as within the matrix nutrients are trapped and water is efficiently retained. Enzymes released by the bacteria can alter the EPS make up in response to alter nutrient obtainability. Therefore, the conditions can tailor biofilm architecture to the specific environment. As a results of these favorable conditions, the structural constituents of the matrix becomes thoroughly hydrated and strong due to high tensile strength that keeps bacteria encased within the biofilm structure (Kostakioti et al., 2013). The removal of bacterial biofilm without causing damage to surrounding tissues remains the goal for ultrasound assisted therapy. The current treatments with antibiotics are not effective for removal of biofilm, as the antibiotics are effective to only metabolically active bacteria. In other words, the action of antibiotics may be antagonized by local conditions around bacterial biofilm caused by accumulation of waste products around the biofilm (Stewart and Costerton, 2001).

It has been recently proposed that the use of antimicrobials followed by physical biofilm disruption (with the help of shear stresses of ultrasound) could be an effective strategy for biofilm disruption and management (Koo et al., 2017). The mechanical energy associated with ultrasound can pull out and kill biofilms because of cavitation and acoustic streaming mechanisms associated with ultrasound. It is more effective than antimicrobial agents as it has less likelihood of developing resistance and reoccurrence of the biofilm.

DESIGN CONSIDERATIONS FOR A RESEARCH THERAPEUTIC ULTRASOUND SYSTEM

Some design considerations for a system supporting therapeutic ultrasound research are explored. These systems can be designed around a custom-designed ultrasound system or a clinical ultrasound system. Clinical systems generally have a more limited range of configuration parameters and provide less access to custom software control. In this regard, it is desirable to use a custom-designed ultrasound system purposely-built for research or a clinical system in which special access has been granted to enable more detailed control of the operating parameters. In either case, several provisions are desirable depending upon the research application. In these design considerations, we explore both *in vitro* and *in vivo* experimental conditions.

To begin, we discuss system calibration. No matter the tissue targeted, it is always beneficial to explore and validate the acoustic beam properties experimentally. It can be performed in conjunction with numerical simulations and phantom measurements. System calibration generally requires a robotic, motorized two-axis, or three-axis stage to systematically move a calibrated measurement hydrophone to record the resulting

acoustic field under specific testing conditions. In addition to system calibration, the motorized stage may also enable calibrated *in vitro* ultrasound stimulation. In this case, a petri dish may be systematically moved to ensure appropriate exposure of the target medium to the acoustic stimulation. With regard to *in vitro* vs. *in vivo* experiments, the focal depth will likely require modification, with shorter depths required for *in vitro* conditions and longer depths required for *in vivo* conditions.

We now consider transducers whose properties will be chosen for specific applications. With regard to ultrasound stimulation, often a focused beam will be desired. In this case, either a single-channel transducer with a fixed focus may be utilized or a multi-element transducer array with more flexible focus options may be used. The difference between these options should be carefully considered. The single-channel transducer will certainly be less costly, but will necessarily require relative motion of the transducer and tissue to enable movement of the focal region. A multi-element transducer array, on the other hand, enables one to move the focal region within limits by steering the acoustic beam. The offered additional flexibility may be beneficial and desirable, depending on the specific application. A further consideration with regard to transducer arrays is the geometrical configuration of the array, e.g., linear, planar or an annular ring. Planar stimulation over a relatively wider region may be especially useful for *in vitro* testing.

With regard to *in vivo* experimental conditions, it is often useful to combine either a HIFU or LIFU system with additional imaging modalities including standard ultrasound imaging. Standard ultrasound imaging enables passive cavitation imaging which may be useful for therapeutic applications involving the cavitation of microbubbles. The location of the cavitation can then be estimated. MRI-guided focused ultrasound (MRgFUS) couples magnetic resonance imaging with focused ultrasound stimulation. It enables precise targeting of the acoustic stimulation. For MRgFUS, special transducers are required which do not significantly disturb the magnetic field (Speicher et al., 2015).

Here in **Table 2**, we have summarized the ultrasound parameters like frequency and intensity for *in vivo* and *in vitro* lab studies. The studies include the application of ultrasound for disruption of nanoparticles with ultrasound and ultrasound induced sonoporation effect.

ULTRASOUND PARAMETERS

The combination of certain ultrasound parameters including frequency, intensity, mechanical index (MI), and duration of ultrasound exposure can influence the efficacy of ultrasound-mediated drug delivery.

Therapeutic Ultrasound Transducers/Devices

Ultrasound can be exposed either by using plane wave, non-focused transducers, or focused transducers. Typically, non-focused transducers are employed for achieving physical effects of ultrasound applications and for enhancing transdermal delivery by the process called as sonophoresis. Whereas, in focused ultrasound, radiations can be focused onto a very small area, which leads to an increase the intensity to a great extent and therefore named as high intensity focused ultrasound (HIFU). Focused beams are generated with specially designed spherically-curved transducers, it permits deeper permeation and deposition of energy deep inside the body (Zhang Y. R. et al., 2019). The ultrasound radiation propagates through the skin and other tissues on its way to the target over a large area creating comparatively low spatial intensities and generating no damage (Mullick Chowdhury et al., 2017). At the focus, however, intensities can be 3–4 orders of magnitude higher than at the transducer surface. Targeting of HIFU beam to specific tissues, organs and tumors may be carried out using different imaging modalities: diagnostic (B-scan) ultrasound (Xenariou et al., 2007), and magnetic resonance imaging (MRI) (Chen et al., 2017). Recent studies have also indicated that computed tomography (CT) and optical 3D tracking (Schoellhammer et al., 2017) can also be used for guiding HIFU exposures; however, these imaging modalities have not yet been incorporated into commercial HIFU devices. The advantages of using extra-corporeal HIFU exposures, for example for tumor ablation, compared to more invasive surgical procedures, are many-fold, and include limited blood loss and infection, elimination of scar formation, and a decreased risk of other complications. Tumor ablation with HIFU can also be provided on an outpatient basis, where cost and recovery times are significantly reduced in comparison to other existing techniques, such as radio frequency ablation, laser, and cryoablation (Ensign et al., 2012).

Frequency

The average ultrasound frequency utilized in drug delivery varies from kilohertz to Megahertz levels. It depends on the type of cells and the model animal selected for the particular experiment. Typically, the ultrasound frequency used for drug delivery and other therapeutic applications, is lesser than diagnostic purpose. The higher levels of frequencies may account for cavitation effect which arises from short-pulse, low-duty cycle diagnostic ultrasound (Zacchè et al., 2015). The lower ranges of ultrasound frequencies has capabilities to penetrate deeply situated tissues as they have low attenuation effect which can ensure the desired therapeutic effect without causing attenuation related side effects. The frequency range used for microbubble and ultrasound assisted treatments are also subjected to type of microbubbles used in a particular experiment. It is because the ultrasound frequency near to or equal to resonance frequency of the microbubbles enhances stable microbubble cavitation (Hu et al., 2010; Qin et al., 2018). On the other hand, high frequency has high resolution but low tissue penetration. For example, transdermal drug delivery (TDD), which includes an increase in skin permeabilization, requires ultrasound waves of 55 KHz]. Intravascular thrombus dissolution requires 2.2 MHz. Even higher level of frequencies are used for cancer therapy using hyperthermia 1–5 MHz frequency. The ultrasound frequency used for the therapeutic purposes is lower than that for diagnostic purposes (Joshi and Joshi, 2019). Lower frequencies of ultrasound covers the frequencies lower than 1 MHz, whereas, erate and

TABLE 2 | Parameters for designing of ultrasound machine for *in vivo* and *in vitro* lab studies.

	Purpose	Frequency and intensity	Ultrasonic processor	Reference	Range
A. TRIGGERED DRUG RELEASE FROM NANOPARTICLES					
1	Disruption of liposomes under mild hyperthermia (thermosensitive)	Frequency: 1.0 MHz Intensity: 1981.6 W/cm^2	Therapy Imaging Probe System, Philips Research, Briarcliff Manor, NY	Park et al., 2013	Frequency 20-kHz−7.5 MHz Intensity: 1.5–5.9 W/cm^2 up to 1981.6 W/cm^2 for hyperthermic nanoparticle disruption
2	Release of drugs from liposomes *in vivo* using LFUS. (Low Intensity focused Ultrasound)	Frequency: 20-kHz Intensity: 5.9 W/cm^2	VC400, Sonics & Materials, Newtown, CT	Schroeder et al., 2009a	
3	Mesoporoussilica composite for effective ultrasound triggered smart drug release *in vivo*	Frequency: 20–50 kHz Intensity: 1.5 W/cm^2	NA	Jafari et al., 2019	
4	Tumor-penetrating codelivery of siRNA and paclitaxel with ultrasound-responsive nanobubbles	Frequency: 1 MHz Intensity: NA	Therapeutic US system (DCT-700, WELLD, Shenzhen, China)	Yin et al., 2014	
5	Ultrasound-sensitive siRNA-loaded nanobubbles formed by hetero-assembly of polymeric micelles and liposomes	Frequency: 1 MHz, Intensity: 2.0 W/cm^2	Self-made therapeutic US system (Institute of Ultrasound Imaging, Chongqing Medical University	Yin et al., 2013	
6	PLGA nanoparticles for ultrasound-mediated gene delivery in solid tumors *in vivo*	Frequency: 7.5 MHz	Diagnostic ultrasound system 3535 (Bruel and Kjer, Denmark)	Chumakova et al., 2008	
7	Ultrasound-mediated gene transfer (sonoporation) *in vitro* and prolonged expression of a transgene *in vivo*	Frequency: 40 kHz Intensity: 1.9 W/ cm2	Sonidel SP 100 sonoporation device (Sonidel Ltd., Ireland)	Li et al., 2009	
B. SONOPORATION *in vivo*					
8	Sonoporation enhances liposome accumulation and penetration in tumors with low EPR	Frequency: 16 MHz Intensity: 0.9 W/cm^2	VisualSonics Vevo2100 imaging system (Fujifilm Sonosite, The Netherlands)	Theek et al., 2016	Frequency: 1–16 MHz Intensity: 0.4–to 2.0 W/cm^2
9	Multiparameter evaluation of *in vivo* gene delivery using ultrasound-guided, microbubble-enhanced sonoporation	Frequency: 1.4 MHz	Siemens Antares system (Siemens Health Care, Inc., Ultrasound Division, Mountain View, CA, USA)	Shapiro et al., 2016	
10	Combination of chemotherapy and photodynamic therapy for cancer treatment with sonoporation effects	Intensity: 2.0 W/cm^2	NA	Lee et al., 2018	
11	Ultrasound-responsive polymeric micelles for sonoporation-assisted site-specific therapeutic action (Wu et al., 2017)	Frequency: 1.90 MHz Intensity: 0.4 W/cm^2	Planar transducer (Institution of Applied Acoustics, Shaanxi Normal University)	Wang et al., 2013; Wu et al., 2017	
12	Epidermal growth factor receptor-targeted sonoporation with microbubbles enhances therapeutic efficacy in a squamous cell carcinoma model	Frequency: 1 MHz Intensity: 2.0 W/cm^2	Sonitron 2000 sonicator (Rich Mar Inc., Inola, OK, USA).	Hirabayashi et al., 2017	
13	Dual-targeted and pH-sensitive doxorubicin prodrug-microbubble complex with ultrasound for tumor treatment (Luo et al., 2017)	Frequency: 1 MHz Intensity: 2 W/cm^2	US system (DCT-700, WELLD, Shenzhen, China). (Yin et al., 2014)	Yin et al., 2014; Luo et al., 2017	
C. *In vitro* STUDIES					
	Sonoporation	• Less than 100 kHz, although frequencies up to 16 MHz have been investigated (ter Haar, 2007) • Achibana et al. were the first to image cells with pores by SEM after exposure to low frequency ultrasound of 255 kHz (Lentacker et al., 2014) • Low-frequency (24 kHz) (Keyhani et al., 2001)	• Intensity: 0.9–1.8 W/cm^2 (Khayamian et al., 2018) • Low acoustic intensity, consisting of 0.5, 1.0, and 1.5 W/cm^2 (Shi et al., 2017) • 1.5 W/cm^2 • 0.9W/cm^2 (Theek et al., 2016) • 0.23 W/cm^2 (Yu and Xu, 2014)	• Frequency: 3.33 kHz−16 MHz • Intensity: 0.23–1.8 W/cm^2	

(Continued)

TABLE 2 | Continued

Purpose	Frequency and intensity	Ultrasonic processor	Reference	Range
	• Ultrasonic stimulation was carried out for 2 s with frequency of 20 kHz (Khayamian et al., 2018) • 2 MHz (Helfield et al., 2017) • 1 MHz (Shi et al., 2017) • 1 MHz • 16 MHz (Theek et al., 2016) • 1-MHz (Liao et al., 2018) • 3.33 kHz (Bhutto et al., 2018) • 180 kHz (Yu and Xu, 2014)			
Disruption of nanoparticles	• 850 kHz (Stavarache and Paniwnyk, 2018) • 3.3 MHz (Papa et al., 2017) • 1 MHz (Baghbani et al., 2017)	• 3.19W (Stavarache and Paniwnyk, 2018) • 2.2 W/cm^2 (Papa et al., 2017) • 2 W/cm^2 (Baghbani et al., 2017)	• Frequency: 840 kHz−3.3 MHz • Intensity: 2–3.1 W/cm^2	
Enhancing penetration of nanoparticles through tumor (High intensity)	• 1.5 MHz (Lee et al., 2017) • 1 MHz (Wang S. et al., 2012) • 1.5 MHz (Han et al., 2017) • 3 MHz (Frazier et al., 2016) • 1.16 MHz (Zhou et al., 2016) • For liposomes in the range of 20 kHz−16 MHz (Dragicevic and Maibach, 2018)	• 5 and 20 W/cm^2 (Lee et al., 2017) • 2685 W/cm^2 (Wang S. et al., 2012) • 10 W/cm^2 (Han et al., 2017) • 816–1,411 W/cm^2 (Frazier et al., 2016) • 705–900 W/cm^2 (Zhou et al., 2016)	• Frequency: 1.5–16 MHz • Intensity: 5–2,685 W/cm^2	

high acoustic frequencies are in the range of 1–5 and 5–10 MHz, respectively (Du et al., 2011). **Table 3** summarizes the use of nanoparticles in combination with ultrasound to enhance efficacy of the treatment.

Intensity

The potential use of high intensity ultrasound (Azagury et al., 2016) is to induce ultrasound associated heating effects that alters the tissue function. Therefore, the FDA has recommended the intensity that causes the heating of tissues less than a 1°C rise in temperature (Azagury et al., 2016; Guan and Xu, 2016; Mullick Chowdhury et al., 2017). Generally, for drug delivery applications intensity range of 0.3–3 W/cm^2 is used. Higher intensities ultrasound can be employed when the pulse length (pulse cycles/ultrasound frequency) and/or pulse repetition frequency (pulses/sec) values are reduced (Joshi and Joshi, 2019).

Mechanical Index

The mechanical index (MI) of ultrasound can be explained as the peak negative pressure (in MPa) divided by the square root of center frequency (in MHz). The MI is used as an alternative variable to ultrasound intensity because they are directly proportional to the relevant acoustic pressure. Also, the MI gives an exact estimation of the produced cavitation, greater MI values induce greater cavitation activity. To circumvent undesirable thermal adverse effects in the course of ultrasound treatment, the MI in the range of 0.2 and 1.9 is used, and the FDA has a recommendation of the higher limit of the MI to 1.9 for clinical use of ultrasound to bypass direct tissue harm by ultrasound (Izadifar et al., 2019).
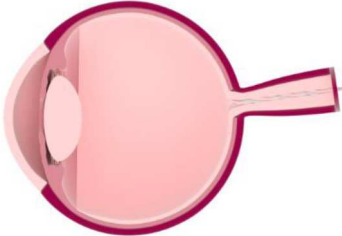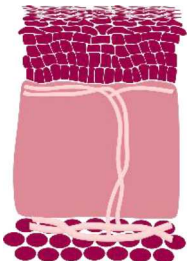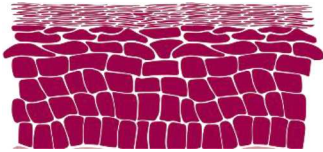
Treatment Duration

The duration of treatment in ultrasound assisted drug delivery and therapeutic ultrasound should be determined by the time required for the ultrasound to generate a desirable effect without inducing unwanted effects on the body. Moreover, the time course of ultrasound treatment in drug delivery can be influenced by other factors such as the situation and type of tissues undergoing treatment, ultrasound settings (ultrasound intensity being applied, and frequency), as well as the type of microbubbles used (if applicable) (Juffermans et al., 2006). High pressures of ultrasound waves can cause spontaneous inertial cavitation, in some cases longer treatment duration can increase the drug delivery. However, high pressures are associated with undesirable effects on body. In a similar way, for lower pressures, the duration required for stable oscillations of microbubbles should be to be contemplate for achieving the most effective drug delivery because longer treatment duration at low pressures can also induce heating effects. Therefore, the precise treatment time in every research protocol is different for different therapeutic applications, and it has to be optimized for each treatment indication (Schroeder et al., 2009b; Joshi and Joshi, 2019).
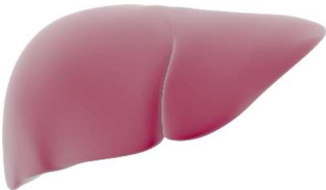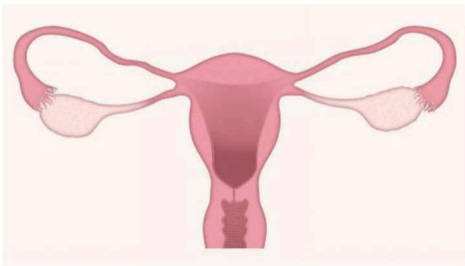
SUMMARY

Ultrasound with its tunable intensity and frequency can be utilized in a safe manner to diagnose and treat a wide range of medical conditions. It has been shown that ultrasound has an immense potential to improve cancer treatment by increasing targeting and accumulation of drugs and genes delivered to tissues (Ng and Liu, 2002; Duvshani-Eshet and Machluf, 2005;

TABLE 3 | Ultrasound frequencies used for various medical application.

Frequencies		Applications	References
>20 KHz	Audible region	NA	
19.5, 22.5, 42 KHz		Angioplasty	Siegel et al., 1994; Goyen et al., 2000; Wylie et al., 2009
20 KHz-1 GHzs		Ocular drug delivery	Zderic et al., 2002; Hariharan et al., 2017; Lafond et al., 2017
0.25–2 MHz		Drug delivery to central nervous system	O'Reilly and Hynynen, 2012
20 kHz—16 MHz		Transdermal drug delivery	Mitragotri, 2017
255 KHz—5 MHz		Gene delivery	Yu et al., 2019
1–4 MHz		Kidney stone ablation	Ikeda et al., 2016
1 MHZ		Topical delivery of hydrocartisone	
1.5 MHz—1.0 kHz		Osteoporosis	Ozdemir et al., 2008

(Continued)

TABLE 3 | Continued

Frequencies		Applications	References
≥1 MHz		Nebulizer for pulmonary drug delivery	Wiedmann and Ravichandran, 2001
20 kHz		Colon	Schoellhammer and Traverso, 2016
0·96 MHz		Liver hyperthermia	Lyon et al., 2018
0.5–2 MH		Ablation of uterine fibroids	Fan et al., 2019
<10 MHZ		Diagnosis	

Tzu-Yin et al., 2013; Mullick Chowdhury et al., 2016). Ultrasound is considered non-invasive and the ultrasound radiation can be focused onto a very small region, as small as a few millimeters. The focal point of the ultrasound beam can penetrate deep into body allowing very precise thermal ablation of tissues and the enhancement of drug delivery to a selected region during treatment (Ohmura et al., 2011; Chen and Hwang, 2013).

Furthermore, by combining ultrasound with nanoparticles, it is possible to develop on-demand drug delivery system where drug release is triggered with ultrasound energy that disrupts drug-carrying nanoparticles. A combination of ultrasound with nanoparticles to deliver drugs has already been applied for treating Alzheimer's disease, cardiovascular disease, infections and cancer (Wang et al., 2015). Ultrasound-mediated drug delivery takes advantage of the enhanced permeability of cell membrane induced by the ultrasound—sonoporation. Increased permeability permits more effective delivery of drug molecules through cell membrane and through other physiological barriers, e.g., blood brain barrier. Importantly, plasma membrane permeabilization induced by acoustic cavitation is a transient process and the membrane integrity usually returns to its original configuration within seconds (Liu et al., 1998).

Despite ultrasound technology being already in place at virtually every hospital/clinic, its use for therapeutic application has been undervalued for long time. More recently the use of ultrasound with microbubbles was approved by the Food and Drug Administration (FDA) for diagnostic applications (Mullick Chowdhury et al., 2017). Moreover, there are many ultrasound-responsive microbubbles and nanoparticle formulations that are undergoing clinical trials or have been used clinically as the ultrasound contrast agents and for the enhanced ultrasound-triggered drug release application. For example SonoVue, Definity, Optison, and Sonazoid are being utilized as an ultrasound contrast agent and ThermoDox (liposomal doxorubicin) is used to enhance temperature-triggered doxorubicin release induced by magnetic resonance high intensity focused ultrasound (Anselmo and Mitragotri, 2019). The increasing use of ultrasound with microbubbles/nanoparticles in clinics supports future clinical translation of ultrasound-enhanced nanoparticle drug delivery for improving drug delivery and drug therapy in cancer and several other medical conditions.

While there are many benefits of using ultrasound, the impact of the energy of ultrasound radiation on cell integrity raises

some concerns. Ultrasound energies higher than the cavitation threshold can disrupt the cell membrane. A high dosage of ultrasound can thermally and sonochemically induce permanent damage to lipid membranes, and cause denaturation of proteins and DNA (Domenici et al., 2013). But these perceived limitations, can be turned into therapeutic applications which include tissue hyperthermia and thermal ablation which are both used to obliterate diseased tissues.

A further limitation is that ultrasound cannot be used in all environments and there is a need to optimize the beam conditions depending on the presence of gas within tissues (e.g., lungs) which is an obstacle for propagation of ultrasound waves. The organ associated movements during the ultrasound treatment procedure is another major problem, as the continuous movements of organs cause distortion of ultrasound beam focal point. Also, while treating deep-seated tumors in the body, there is an issue with the ultrasound beam being attenuated or deflected from hard tissues during its travel to the target area. For example, in the treatment of lung cancer, the presence of both bone (ribcage) and gas may interfere with propagating ultrasound waves. Ultrasound reflection by bone or gas-containing tissue may cause collateral damage and undesired skin burns when high intensity ultrasound is used.

In summary, ultrasound has the potential to improve treatment of cancer and other medical conditions. However, more research and developments are needed for the design of a therapeutic ultrasound system considering the location of the tumor in the body. Also, a better understanding of the underlying mechanisms of the interaction of the ultrasound beam with different cell types is essential.

AUTHOR CONTRIBUTIONS

PT designed an outline for the manuscript and wrote most of the parts of the manuscript. PT also contributed toward execution of ideas for drawing all graphical pictures in the manuscript by a graphic designer. RV contributed to writing some sections of the manuscript such 'ultrasound sensitive nanoparticles', application of HIFU in different types of tumor, and application of therapeutic HIFU in central nervous system disorders. RV also contributed to proof reading of the article. CJ wrote and shared his ideas for the section about design considerations for designing of the ultrasound system for research purposes. WW proofread the manuscript. WC is the corresponding author of the manuscript, supervised, monitored the writing process time to time, and wrote add his inputs to the manuscript during the checking and correcting the manuscript. All authors reviewed the manuscript.

ACKNOWLEDGMENTS

REFERENCES

Anselmo, A. C., and Mitragotri, S. (2019). Nanoparticles in the clinic: an update. *Bioeng. Transl. Med.* 4:e10143. doi: 10.1002/btm2.10143

Ashokkumar, M. (2011). The characterization of acoustic cavitation bubbles – an overview. *Ultrason. Sonochem.* 18, 864–872. doi: 10.1016/j.ultsonch.2010.11.016

Ayoub, N. M., Al-Shami, K. M., and Yaghan, R. J. (2019). Immunotherapy for HER2-positive breast cancer: recent advances and combination therapeutic approaches. *Breast Cancer* 11, 53–69. doi: 10.2147/BCTT.S175360

Azagury, A., Amar-Lewis, E., Yudilevitch, Y., Isaacson, C., Laster, B., and Kost, J. (2016). Ultrasound effect on cancerous versus non-cancerous cells. *Ultrasound Med. Biol.* 42, 1560–1567. doi: 10.1016/j.ultrasmedbio.2016.02.005

Baghbani, F., Chegeni, M., Moztarzadeh, F., Hadian-Ghazvini, S., and Raz, M. (2017). Novel ultrasound-responsive chitosan/perfluorohexane nanodroplets for image-guided smart delivery of an anticancer agent: Curcumin. *Mater. Sci. Eng.* 74, 186–193. doi: 10.1016/j.msec.2016.11.107

Barua, S., and Mitragotri, S. (2014). Challenges associated with penetration of nanoparticles across cell and tissue barriers: a review of current status and future prospects. *Nano Today* 9, 223–243. doi: 10.1016/j.nantod.2014.04.008

Bea, V. J., Black, D., and Hunt, K. (2018). "Percutaneous ablation in the treatment of breast cancer," in *Changing Paradigms in the Management OF Breast Cancer*. ed M. Howard-McNatt (Cham: Springer International Publishing), 71–84. doi: 10.1007/978-3-319-60336-0_6

Benderitter, M., Vincent-Genod, L., Pouget, J. P., and Voisin, P. (2003). The cell membrane as a biosensor of oxidative stress induced by radiation exposure: a multiparameter investigation. *Radiat. Res.* 159, 471–483. doi: 10.1667/0033-7587(2003)159[0471:TCMAAB]2.0.CO;2

Bhutto, D. F., Murphy, E. M., Priddy, M. C., Centner, C. C., Moore Iv, J. B., and Kopechek, J. A. (2018). Effect of molecular weight on sonoporation-mediated uptake in human cells. *Ultrasound Med. Biol.* 44, 2662–2672. doi: 10.1016/j.ultrasmedbio.2018.08.008

Bjarnsholt, T. (2013). The role of bacterial biofilms in chronic infections. *APMIS* (Suppl. 136), 1–51. doi: 10.1111/apm.12099

Blanco, E., Shen, H., and Ferrari, M. (2015). Principles of nanoparticle design for overcoming biological barriers to drug delivery. *Nat. Biotechnol.* 33, 941–951. doi: 10.1038/nbt.3330

Boissenot, T., Bordat, A., Larrat, B., Varna, M., Chacun, H., Paci, A., et al. (2017). Ultrasound-induced mild hyperthermia improves the anticancer efficacy of both Taxol® and paclitaxel-loaded nanocapsules. *J. Control. Release* 264, 219–227. doi: 10.1016/j.jconrel.2017.08.041

Bond, A. E., Shah, B. B., Huss, D. S., Dallapiazza, R. F., Warren, A., and Elias, W. J. (2017). Safety and efficacy of focused ultrasound thalamotomy for patients with medication-refractory, tremor-dominant parkinson disease: a randomized clinical TrialFUS thalamotomy for medication-refractory, tremor-dominant PDFUS thalamotomy for medication-refractory, tremor-dominant PD. *JAMA Neurol.* 74, 1412–1418. doi: 10.1001/jamaneurol.2017.3098

Bradley, W. G. (2009). MR-guided focused ultrasound: a potentially disruptive technology. *J. Am. College Radiol.* 6, 510–513. doi: 10.1016/j.jacr.2009.01.004

Cai, X. Z., Chen, X. Z., Yan, S. G., Ruan, Z. R., Yan, R. J., and Xu, J. (2009). Intermittent watt-level ultrasonication facilitates vancomycin release from therapeutic acrylic bone cement. *J. Biomed. Mater. Res. Appl. Biomater.* 90, 11–17. doi: 10.1002/jbm.b.31288

Cai, Y., Wang, J., Liu, X., Wang, R., and Xia, L. (2017). A review of the combination therapy of low frequency ultrasound with antibiotics. *Biomed Res. Int.* 2017:14. doi: 10.1155/2017/2317846

Catalá, A. (2009). Lipid peroxidation of membrane phospholipids generates hydroxy-alkenals and oxidized phospholipids active in physiological and/or pathological conditions. *Chem. Phys. Lipids* 157, 1–11. doi: 10.1016/j.chemphyslip.2008.09.004

Catalá, A. (2012). Lipid peroxidation modifies the picture of membranes from the fluid mosaic model to the lipid whisker model. *Biochimie* 94, 101–109. doi: 10.1016/j.biochi.2011.09.025

Chang, W. S., and Chang, J. W. (2017). Focused ultrasound treatment for central nervous system disease: neurosurgeon's perspectives. *Biomed. Eng. Lett.* 7, 107–114. doi: 10.1007/s13534-017-0013-8

Chauhan, V., Stylianopoulos, T., Boucher, Y., and Jain, R. K. (2011). Delivery of molecular and nanoscale medicine to tumors: transport barriers and Strategies. *Annu Rev.* 2, 281–298. doi: 10.1146/annurev-chembioeng-061010-114300

Chen, H., and Hwang, J. H. (2013). Ultrasound-targeted microbubble destruction for chemotherapeutic drug delivery to solid tumors. *J. Therapeut. Ultrasound* 1, 10. doi: 10.1186/2050-5736-1-10

Chen, J., Li, Y., Wang, Z., McCulloch, P., Hu, L., Chen, W., and Fibroids (2018). Evaluation of high-intensity focused ultrasound ablation for uterine fibroids: an IDEAL prospective exploration study. *BJOG* 125, 354–364. doi: 10.1111/1471-0528.14689

Chen, J., Pan, H., Lanza, G. M., and Wickline, S. A. (2013). Perfluorocarbon nanoparticles for physiological and molecular imaging and therapy. *Adv. Chronic Kidney Dis.* 20, 466–478. doi: 10.1053/j.ackd.2013.08.004

Chen, Q., Xiao, B., and Merlin, D. (2017). Low-frequency ultrasound may improve drug penetration in colonic mucosa. *Transl. Cancer Res.* 6(Suppl 2): S276–9. doi: 10.21037/tcr.2017.03.62

Chen, Y. H., Chen, H. R., and Shi, J. L. (2014). Construction of homogenous/heterogeneous hollow mesoporous silica nanostructures by silica-etching chemistry: principles, synthesis, and applications. *Acc. Chem. Res.* 47, 125–137. doi: 10.1021/ar400091e

Chu, K. F., and Dupuy, D. E. (2014). Thermal ablation of tumours: biological mechanisms and advances in therapy. *Nat. Rev. Cancer* 14, 199–208. doi: 10.1038/nrc3672

Chumakova, O. V., Liopo, A. V., Andreev, V. G., Cicenaite, I., Evers, B. M., and Chakrabarty, S. (2008). Composition of PLGA and PEI/DNA nanoparticles improves ultrasound-mediated gene delivery in solid tumors *in vivo*. *Cancer Lett.* 261, 215–225. doi: 10.1016/j.canlet.2007.11.023

Cirincione, R., Di Maggio, F. M., Forte, G. I., Minafra, L., Bravatà, V., and Castiglia, L. (2017). High-intensity focused ultrasound– and radiation therapy–induced immuno-modulation: comparison and potential opportunities. *Ultrasound Med. Biol.* 43, 398–411. doi: 10.1016/j.ultrasmedbio.2016.09.020

Costello, R. T., Gastaut, J. A., and Olive, D. (1999). Tumor escape from immune surveillance. *Arch. Immunol. Ther. Exp.* 47, 83–88.

de la Haba, C., Palacio, J. R., Martínez, P., and Morros, A. (2013). Effect of oxidative stress on plasma membrane fluidity of THP-1 induced macrophages. *Biochim. Biophys. Acta* 1828, 357–364. doi: 10.1016/j.bbamem.2012.08.013

den Brok, M. H., Sutmuller, R. P., van der Voort, R., Bennink, E. J., Figdor, C. G., and Ruers, D. J. (2004). *In situ* tumor ablation creates an antigen source for the generation of antitumor immunity. *Cancer Res.* 64, 4024–4029. doi: 10.1158/0008-5472.CAN-03-3949

Di Giacinto, F., De Spirito, M., and Maulucci, G. (2019). Low-intensity ultrasound induces thermodynamic phase separation of cell membranes through a nucleation–condensation process. *Ultrasound Med. Biol.* 45, 1143–1150. doi: 10.1016/j.ultrasmedbio.2019.01.011

Domenici, F., Giliberti, C., Bedini, A., Palomba, R., Luongo, F., Sennato, S., et al. (2013). Ultrasound well below the intensity threshold of cavitation can promote efficient uptake of small drug model molecules in fibroblast cells. *Drug Deliv.* 20, 285–295. doi: 10.3109/10717544.2013.836620

Dragicevic, N., and Maibach, H. (2018). Combined use of nanocarriers and physical methods for percutaneous penetration enhancement. *Adv. Drug Deliv. Rev.* 127, 58–84. doi: 10.1016/j.addr.2018.02.003

Dreher, M. R., Liu, W., Michelich, C. R., Dewhirst, M. W., Yuan, F., and Chilkoti, A. (2006). Tumor vascular permeability, accumulation, and penetration of macromolecular drug carriers. *J. Natl. Cancer Inst.* 98, 335–344. doi: 10.1093/jnci/djj070

Du, J.-Z., Du, X. J., Mao, C. Q., and Wang, J. (2011). Tailor-made dual pH-sensitive polymer–doxorubicin nanoparticles for efficient anticancer drug delivery. *J. Am. Chem. Soc.* 133, 17560–17563. doi: 10.1021/ja207150n

Dubinsky, T. J., Cuevas, C., Dighe, M. K., Kolokythas, O., and Hwang, J., H. (2008). High-intensity focused ultrasound: current potential and oncologic applications. *Am. J. Roentgenol.* 190, 191–199. doi: 10.2214/AJR.07.2671

Duvshani-Eshet, M., and Machluf, M. (2005). Therapeutic ultrasound optimization for gene delivery: a key factor achieving nuclear DNA localization. *J. Control. Release* 108, 513–28. doi: 10.1016/j.jconrel.2005.08.025

Elhelf, I. A. S., Albahar, H., Shah, U., Oto, A., Cressman, E., and Almekkawy, M. (2018). High intensity focused ultrasound: the fundamentals, clinical applications and research trends. *Diagn. Interv. Imaging* 99, 349–359. doi: 10.1016/j.diii.2018.03.001

Elias, W. J., Lipsman, N., Ondo, W. G., Ghanouni, P., Kim, Y. G., and Chang, W. (2016). A randomized trial of focused ultrasound thalamotomy for essential tremor. *N. Engl. J. Med.* 375, 730–739. doi: 10.1056/NEJMoa1600159

Emfietzoglou, D., Kostarelos, K., Papakostas, A., Yang, W. H., Ballangrud, A., and Song, H. (2005). Liposome-mediated radiotherapeutics within avascular tumor spheroids: comparative dosimetry study for various radionuclides, liposome systems, and a targeting antibody. *J. Nucl. Med.* 46, 89–97.

Ensign, L. M., Tang, B. C., Wang, Y. Y., Tse, T. A., Hoen, T., and Cone, R. (2012). Mucus-penetrating nanoparticles for vaginal drug delivery protect against herpes simplex virus. *Sci. Transl. Med.* 4:138ra179. doi: 10.1126/scitranslmed.3003453

Erriu, M., Blus, C., Szmukler-Moncler, S., Buogo, S., Levi, R., Barbato, G., et al. (2014). Microbial biofilm modulation by ultrasound: current concepts and controversies. *Ultrason. Sonochem.* 21, 15–22. doi: 10.1016/j.ultsonch.2013.05.011

Etame, A. B., Diaz, R. J., Smith, C. A., Mainprize, T. G., Hynynen, K. and Rutka, J. T. (2012). Focused ultrasound disruption of the blood-brain barrier: a new frontier for therapeutic delivery in molecular neurooncology. *Neurosurg. Focus* 32, E3–E3. doi: 10.3171/2011.10.FOCUS11252

Fan, H.-J., Zhang, C., Lei, H. T., Cun, J. P., Zhao, W., and Huang, J. Q. (2019). Ultrasound-guided high-intensity focused ultrasound in the treatment of uterine fibroids. *Medicine* 98:e14566. doi: 10.1097/MD.0000000000014566

Fan, Z., Kumon, R. E., Park, J., and Deng, C. X. (2010). Intracellular delivery and calcium transients generated in sonoporation facilitated by microbubbles. *J. Control. Release* 142, 31–39. doi: 10.1016/j.jconrel.2009.09.031

Fan, Z., Liu, H., Mayer, M., and Deng, C. X. (2012). Spatiotemporally controlled single cell sonoporation. *Proc. Natl. Acad. Sci. U.S.A.* 109, 16486–16491. doi: 10.1073/pnas.1208198109

Fechheimer, M., Boylan, J. F., Parker, S., Sisken, J. E., Patel, G. L., and Zimmer, S. G. (1987). Transfection of mammalian cells with plasmid DNA by scrape loading and sonication loading. *Proc. Natl. Acad. Sci. U.S.A.* 84, 8463–8467. doi: 10.1073/pnas.84.23.8463

Fechheimer, M., Denny, C., Murphy, R. F., and Taylor, D. L. (1986). Measurement of cytoplasmic pH in Dictyostelium discoideum by using a new method for introducing macromolecules into living cells. *Eur. J. Cell Biol.* 40, 242–247.

Feril, L. B., Tachibana, K., Ogawa, K., Yamaguchi, K., Solano, I. G., and Irie, Y. (2008). Therapeutic potential of low-intensity ultrasound (part 1): thermal and sonomechanical effects. *J. Med. Ultrasonics* 35, 153–160. doi: 10.1007/s10396-008-0194-y

Ferrara, K. W. (2008). Driving delivery vehicles with ultrasound. *Adv. Drug Deliv. Rev.* 60, 1097–1102. doi: 10.1016/j.addr.2008.03.002

Fishman, P. S. (2017). Thalamotomy for essential tremor: FDA approval brings brain treatment with FUS to the clinic. *J. Therapeut. Ultrasound* 5:19. doi: 10.1186/s40349-017-0096-9

Frazier, N., Payne, A., de Bever, J., Dillon, C., Panda, A., Subrahmanyam, N., et al. (2016). High intensity focused ultrasound hyperthermia for enhanced macromolecular delivery. *J. Control. Release* 241, 186–193. doi: 10.1016/j.jconrel.2016.09.030

Garello, F., and Terreno, E. (2018). Sonosensitive MRI nanosystems as cancer theranostics: a recent update. *Front. Chem.* 6:157. doi: 10.3389/fchem.2018.00157

Goyen, M., Kröger, K., Buss, C., and Rudofsky, G. (2000). Intravascular ultrasound angioplasty in peripheral arterial occlusion. Preliminary experience. *Acta Radiol.* 41, 122–124. doi: 10.1080/028418500127345118

Greillier, P., Bawiec, C., Bessière, F., and Lafon, C. (2018). Therapeutic ultrasound for the heart: state of the art. *IRBM* 39, 227–235. doi: 10.1016/j.irbm.2017.11.004

Guan, L., and Xu, G. (2016). Damage effect of high-intensity focused ultrasound on breast cancer tissues and their vascularities. *World J. Surg. Oncol.* 14:153. doi: 10.1186/s12957-016-0908-3

Han, H., Lee, H., Kim, K., and Kim, H. (2017). Effect of high intensity focused ultrasound (HIFU) in conjunction with a nanomedicines-microbubble complex for enhanced drug delivery. *J. Control. Release* 266, 75–86. doi: 10.1016/j.jconrel.2017.09.022

Hanafy, N. A. N., El-Kemary, M., and Leporatti, S. (2018). Micelles structure development as a strategy to improve smart cancer therapy. *Cancers* 10:238. doi: 10.3390/cancers10070238

Hare, J. I., Lammers, T., Ashford, M. B., Puri, S., Storm, G., and Barry, S. T. (2017). Challenges and strategies in anti-cancer nanomedicine development: an industry perspective. *Adv. Drug Deliv. Rev.* 108:25–38. doi: 10.1016/j.addr.2016.04.025

Hariharan, P., Nabili, M., Guan, A., Zderic, V., and Myers, M. (2017). Model for porosity changes occurring during ultrasound-enhanced transcorneal drug delivery. *Ultrasound Med. Biol.* 43, 1223–1236. doi: 10.1016/j.ultrasmedbio.2017.01.013

Hassan, M. A., Campbell, P., and Kondo, T. (2010). The role of Ca2+ in ultrasound-elicited bioeffects: progress, perspectives and prospects. *Drug Discov. Today* 15, 892–906. doi: 10.1016/j.drudis.2010.08.005

Hayes, B. T., Merrick, M. A., Sandrey, M. A., and Cordova, M. L. (2004). Three-MHz ultrasound heats deeper into the tissues than originally theorized. *J. Athl. Train.* 39, 230–234.

Helfield, B. L., Chen, X., Qin, B., Watkins, S. C., and Villanueva, F. S. (2017). Mechanistic insight into sonoporation with ultrasound-stimulated polymer microbubbles. *Ultrasound Med. Biol.* 43, 2678–2689. doi: 10.1016/j.ultrasmedbio.2017.07.017

Hervouet, E., Simonnet, H., and Godinot, C. (2007). Mitochondria and reactive oxygen species in renal cancer. *Biochimie* 89, 1080–1088. doi: 10.1016/j.biochi.2007.03.010

Hirabayashi, F., Iwanaga, K., Okinaga, T., Takahashi, O., Ariyoshi, W., Suzuki, R., et al. (2017). Epidermal growth factor receptor-targeted sonoporation with microbubbles enhances therapeutic efficacy in a squamous cell carcinoma model. *PLoS ONE* 12:e0185293. doi: 10.1371/journal.pone.0185293

Horise, Y., Maeda, M., Konishi, Y., Okamoto, J., Ikuta, S., Okamoto, Y., et al. (2019). Sonodynamic therapy with anticancer micelles and high-intensity focused ultrasound in treatment of canine cancer. *Front. Pharmacol.* 10:545. doi: 10.3389/fphar.2019.00545

Hu, L., Batheja, P., Meidan, V., and Michniak-Kohn, B. B. (2010). "Iontophoretic transdermal drug delivery," in *Handbook of Non-Invasive Drug Delivery Systems,* ed V. S. Kulkarni (Boston, MA: William Andrew Publishing), 95–118. doi: 10.1016/B978-0-8155-2025-2.10004-6

Hu, Z., Yang, X. Y., Liu, Y., Sankin, G. N., Pua, E. C., and Morse, M. A. (2007). Investigation of HIFU-induced anti-tumor immunity in a murine tumor model. *J. Transl. Med.* 5, 34–34. doi: 10.1186/1479-5876-5-34

Hurwitz, M., and Stauffer, P. (2014). Hyperthermia, radiation and chemotherapy: the role of heat in multidisciplinary cancer care. *Semin. Oncol.* 41, 714–729. doi: 10.1053/j.seminoncol.2014.09.014

Husseini, G. A., Pitt, W. G., and Martins, A. M. (2014). Ultrasonically triggered drug delivery: breaking the barrier. *Colloids Surfaces B* 123, 364–386. doi: 10.1016/j.colsurfb.2014.07.051

Ikeda, T., Yoshizawa, S., Koizumi, N., Mitsuishi, M., and Matsumoto, Y. (2016). "Focused Ultrasound and Lithotripsy," IN *Therapeutic Ultrasound,* eds J. M. Escoffre and A. Bouakaz (Cham: Springer International Publishing), 113–129. doi: 10.1007/978-3-319-22536-4_7

Izadifar, Z., Babyn, P., and Chapman, D. (2019). Ultrasound cavitation/microbubble detection and medical applications. *J. Med. Biol. Eng.* 39, 259–276. doi: 10.1007/s40846-018-0391-0

Jafari, S., Derakhshankhah, H., Alaei, L., Fattahi, A., Varnamkhasti, B. S., and Saboury, A. A. (2019). Mesoporous silica nanoparticles for therapeutic/diagnostic applications. *Biomed. Pharmacother.* 109, 1100–1111. doi: 10.1016/j.biopha.2018.10.167

Jain, A., Tiwari, A., Verma, A., and Jain, S. K. (2018). Ultrasound-based triggered drug delivery to tumors. *Drug Deliv. Transl. Res.* 8, 150–164. doi: 10.1007/s13346-017-0448-6

Jolesz, F. A. (2014). Science to practice: opening the blood-brain barrier with focused ultrasound-A potential treatment for alzheimer disease? *Radiology* 273, 631–633. doi: 10.1148/radiol.14142033

Joshi, B., and Joshi, A. (2019). Ultrasound-based drug delivery systems. *Bioelectro. Med. Dev.* 2019, 241–260. doi: 10.1016/B978-0-08-102420-1.00014-5

Juffermans, L. J., Dijkmans, P. A., Musters, R. J., Visser, C. A., and Kamp, O. (2006). Transient permeabilization of cell membranes by ultrasound-exposed microbubbles is related to formation of hydrogen peroxide. *Am. J. Physiol. Heart Circ. Physiol.* 291, H1595–H1601. doi: 10.1152/ajpheart.01120.2005

Juffermans, L. J. M., Kamp, O., Dijkmans, P. A., Visser, C. A., and Musters, R. J. P. (2008). Low-intensity ultrasound-exposed microbubbles provoke local hyperpolarization of the cell membrane via activation of BKCa channels. *Ultrasound Med. Biol.* 34, 502–508. doi: 10.1016/j.ultrasmedbio.2007.09.010

Juho, Y.-C. S., Wu, T. T., Cha, L. G., Sun, H. D., Yu, S., and Kao, C. (2016). Single session of high-intensity focused ultrasound therapy for the management of organ-confined prostate cancer: a single-institute experience. *Urol. Sci.* 27, 226–229. doi: 10.1016/j.urols.2016.09.002

Kang, S. T., and Yeh, C. K. (2012). Ultrasound microbubble contrast agents for diagnostic and therapeutic applications: current status and future design. *Chang Gung Med. J.* 35, 125–139. doi: 10.4103/2319-4170.106159

Kaplán, P., Doval, M., Majerová, Z., Lehotský, J., and Racay, P. (2000). Iron-induced lipid peroxidation and protein modification in endoplasmic reticulum membranes. Protection by stobadine. *Int. J. Biochem. Cell Biol.* 32, 539–547. doi: 10.1016/S1357-2725(99)00147-8

Keyhani, K., Guzmán, H. R., Parsons, A., Lewis, T. N., and Prausnitz, M. R. (2001). Intracellular drug delivery using low-frequency ultrasound: quantification of molecular uptake and cell viability. *Pharm. Res.* 18, 1514–1520. doi: 10.1023/A:1013066027759

Khayamian, M. A., Baniassadi, M., and Abdolahad, M. (2018). Monitoring the effect of sonoporation on the cells using electrochemical approach. *Ultrason. Sonochem.* 41, 619–625. doi: 10.1016/j.ultsonch.2017.10.030

Khokhlova, T. D., Haider, Y., and Hwang, J. H. (2015). Therapeutic potential of ultrasound microbubbles in gastrointestinal oncology: recent advances and future prospects. *Therap. Adv. Gastroenterol.* 8, 384–394. doi: 10.1177/1756283X15592584

Kim, Y. S., Rhim, H., Choi, M. J., Lim, H. K., and Choi, D. (2008). High-intensity focused ultrasound therapy: an overview for radiologists. *Korean J. Radiol.* 9, 291–302. doi: 10.3348/kjr.2008.9.4.291

Ko, Y. J., Kim, W. J., Kim, K., and Kwon, I. C. (2019). Advances in the strategies for designing receptor-targeted molecular imaging probes for cancer research. *J. Control. Release* 305, 1–17. doi: 10.1016/j.jconrel.2019.04.030

Kobayashi, Y., Hayashi, M., Yoshino, F., Tamura, M., Yoshida, A., Ibi, H., et al. (2014). Bactericidal effect of hydroxyl radicals generated from a low concentration hydrogen peroxide with ultrasound in endodontic treatment. *J. Clin. Biochem. Nutr.* 54, 161–165. doi: 10.3164/jcbn.13-86

Konjević, G. M., Vuletić, A. M., Mirjačić Martinović, K. M., Larsen, A. K., and Jurišić, V. B. (2019). The role of cytokines in the regulation of NK cells in the tumor environment. *Cytokine* 117, 30–40. doi: 10.1016/j.cyto.2019.02.001

Koo, H., Allan, R. N., Howlin, R. P., Stoodley, P., and Hall-Stoodley, L. (2017). Targeting microbial biofilms: current and prospective therapeutic strategies. *Nat. Rev. Microbiol.* 15, 740–755. doi: 10.1038/nrmicro.2017.99

Kostakioti, M., Hadjifrangiskou, M., and Hultgren, S. J. (2013). Bacterial biofilms: development, dispersal, and therapeutic strategies in the dawn of the postantibiotic era. *Cold Spring Harb. Perspect. Med.* 3:a010306. doi: 10.1101/cshperspect.a010306

Kostarelos, K., Emfietzoglou, D., Papakostas, A., Yang, W. H., Ballangrud, A., and Sgouros, G. (2004). Binding and interstitial penetration of liposomes within avascular tumor spheroids. *Int. J. Cancer* 112, 713–721.

Krafft, M. P., and Riess, J. G. (2007). Perfluorocarbons: life sciences and biomedical uses dedicated to the memory of Professor Guy Ourisson, a true RENAISSANCE man. *J. Polymer Sci. Part A* 45, 1185–1198. doi: 10.1002/pola.21937

Kumon, R. E., Aehle, M., Sabens, D., Parikh, P., Kourennyi, D., and Deng, C. X. (2007). Ultrasound-induced calcium oscillations and waves in Chinese hamster ovary cells in the presence of microbubbles. *Biophys. J.* 93, L29–31. doi: 10.1529/biophysj.107.113365

Lafond, M., Aptel, F., Mestas, J. L., and Lafon, C. (2017). Ultrasound-mediated ocular delivery of therapeutic agents: a review. *Exp. Opin. Drug Deliv.* 14, 539–550. doi: 10.1080/17425247.2016.1198766

Lee, E. J., Fomenko, A., and Lozano, A. M. (2019). Magnetic resonance-guided focused ultrasound: current status and future perspectives in thermal ablation and blood-brain barrier opening. *J. Korean Neurosurg. Soc.* 62, 10–26. doi: 10.3340/jkns.2018.0180

Lee, H., Han, J., Shin, H., Han, H., Na, K., and Kim, H. (2018). Combination of chemotherapy and photodynamic therapy for cancer treatment with sonoporation effects. *J. Controlled Release* 283, 190–199. doi: 10.1016/j.jconrel.2018.06.008

Lee, S., Han, H., Koo, H., Na, J. H., Yoon, H., Y., et al. (2017). Extracellular matrix remodeling *in vivo* for enhancing tumor-targeting efficiency of nanoparticle drug carriers using the pulsed high intensity focused ultrasound. *J. Controlled Release* 263, 68–78. doi: 10.1016/j.jconrel.2017.02.035

Lentacker, I., De Cock, I., Deckers, R., De Smedt, S. C., and Moonen, C. T. (2014). Understanding ultrasound induced sonoporation: definitions and underlying mechanisms. *Adv. Drug Deliv. Rev.* 72, 49–64. doi: 10.1016/j.addr.2013.11.008

Li, F., Xie, C., Cheng, Z., and Xia, H. (2016). Ultrasound responsive block copolymer micelle of poly(ethylene glycol)–poly(propylene glycol) obtained through click reaction. *Ultrason. Sonochem.* 30, 9–17. doi: 10.1016/j.ultsonch.2015.11.023

Li, X., Sui, Z., Li, X., Xu, W., Guo, Q., Sun, J., et al. (2018). Perfluorooctylbromide nanoparticles for ultrasound imaging and drug delivery. *Int. J. Nanomed.* 13, 3053–3067. doi: 10.2147/IJN.S164905

Li, Y. S., Davidson, E., Reid, C. N., and McHale, A. P. (2009). Optimising ultrasound-mediated gene transfer (sonoporation) in vitro and prolonged expression of a transgene *in vivo*: potential applications for gene therapy of cancer. *Cancer Lett.* 273, 62–69. doi: 10.1016/j.canlet.2008.07.030

Liao, W. H., Wu, C. H., and Chen, W. S. (2018). Pre-treatment with either L-carnitine or piracetam increases ultrasound-mediated gene transfection by reducing sonoporation-associated apoptosis. *Ultrasound Med. Biol.* 44, 1257–1265. doi: 10.1016/j.ultrasmedbio.2018.02.003

Lindau, D., Gielen, P., Kroesen, M., Wesseling, P., and Adema, G. J. (2013). The immunosuppressive tumour network: myeloid-derived suppressor cells, regulatory T cells and natural killer T cells. *Immunology* 138, 105–115. doi: 10.1111/imm.12036

Liu, D., Yang, F., Xiong, F., and Gu, N. (2016). The smart drug delivery system and its clinical potential. *Theranostics* 6, 1306–1323. doi: 10.7150/thno.14858

Liu, J., Lewis, T. N., and Prausnitz, M. R. (1998). Non-invasive assessment and control of ultrasound-mediated membrane permeabilization. *Pharm. Res.* 15, 918–924. doi: 10.1023/A:1011984817567

Liu, W. W., Liu, S. W., Liou, Y. R., Wu, Y. H., Yang, Y. C., and Li, C. R. (2016). Nanodroplet-vaporization-assisted sonoporation for highly effective delivery of photothermal treatment. *Sci. Rep.* 6:24753. doi: 10.1038/srep24753

Łozinski, T., Filipowska, J., Gurynowicz, G., Zgliczynska, M., Kluz, T., Jedra, R., et al. (2019). The effect of high-intensity focused ultrasound guided by magnetic resonance therapy on obstetrical outcomes in patients with uterine fibroids – experiences from the main Polish center and a review of current data. *Int. J. Hyperther.* 36, 582–590. doi: 10.1080/02656736.2019.1616117

Luo, W., Wen, G., Yang, L., Tang, J., Wang, J., Wang, J., et al. (2017). Dual-targeted and pH-sensitive doxorubicin prodrug-microbubble complex with ultrasound for tumor treatment. *Theranostics* 7, 452–465. doi: 10.7150/thno.16677

Lyon, P., Gray, M., Mannaris, C. K., Folkes, L., Stratford, M., and Coussios, C. (2018). Safety and feasibility of ultrasound-triggered targeted drug delivery of doxorubicin from thermosensitive liposomes in liver tumours (TARDOX): a single-centre, open-label, phase 1 trial. *Lancet Oncol.* 19, 1027–1039. doi: 10.1016/S1470-2045(18)30332-2

Maloney, E., and Hwang, J. H. (2015). Emerging HIFU applications in cancer therapy. *Int. J. Hyperther.* 31, 302–309. doi: 10.3109/02656736.2014.969789

Mangraviti, A., Gullotti, D., Tyler, B., and Brem, H. (2016). Nanobiotechnology-based delivery strategies: new frontiers in brain tumor targeted therapies. *J. Control. Release* 240, 443–453. doi: 10.1016/j.jconrel.2016.03.031

Manthe, R. L., Foy, S. P., Krishnamurthy, N., Sharma, B., and Labhasetwar, V. (2010). Tumor ablation and nanotechnology. *Mol. Pharm.* 7, 1880–1898. doi: 10.1021/mp1001944

Martínez-Fernández, R., Rodríguez-Rojas, R., del Álamo, M., Hernández-Fernández, F., Pineda-Pardo, J. A., Dileone, M., et al. (2018). Focused ultrasound subthalamotomy in patients with asymmetric Parkinson's disease: a pilot study. *Lancet Neurol.* 17, 54–63. doi: 10.1016/S1474-4422(17)30403-9

Mason, T. J. (2011). Therapeutic ultrasound an overview. *Ultrason. Sonochem.* 18, 847–852. doi: 10.1016/j.ultsonch.2011.01.004

McMahon, D., Poon, C., and Hynynen, K. (2019). Evaluating the safety profile of focused ultrasound and microbubble-mediated treatments to increase blood-brain barrier permeability. *Exp. Opin. Drug Deliv.* 16, 129–142. doi: 10.1080/17425247.2019.1567490

Meng, Y., Suppiah, S., Mithani, K., Solomon, B., Schwartz, M. L., and Lipsman, N. (2017). Current and emerging brain applications of MR-guided focused ultrasound. *J. Therapeut. Ultrasound* 5:26. doi: 10.1186/s40349-017-0105-z

Mesiwala, A. H., Farrell, L., Wenzel, H. J., Silbergeld, D. L., Crum, L. A., and Mourad, P. D. (2002). High-intensity focused ultrasound selectively disrupts the blood-brain barrier in vivo. *Ultrasound Med. Biol.* 28, 389–400. doi: 10.1016/S0301-5629(01)00521-X

Miller, D., Smith, N., Bailey, M., Czarnota, G., Hynynen, K., Makin, I., et al. (2012). Overview of therapeutic ultrasound applications and safety considerations. *J. Ultrasound Med.* 31, 623–634. doi: 10.7863/jum.2012.31.4.623

Mitragotri, S. (2017). "Sonophoresis: Ultrasound-Mediated Transdermal Drug Deliverym," in *Percutaneous Penetration Enhancers Physical Methods in Penetration Enhancement*, eds N. Dragicevic and H. I. Maibach (Berlin; Heidelberg: Springer Berlin Heidelberg), 3–14.

Mullick Chowdhury, S., Lee, T., and Willmann, J. K. (2017). Ultrasound-guided drug delivery in cancer. *Ultrasonography* 36, 171–184. doi: 10.14366/usg.17021

Mullick Chowdhury, S., Wang, T. Y., Bachawal, S., Devulapally, R., Choe, J. W., and Willmann, J., K. (2016). Ultrasound-guided therapeutic modulation of hepatocellular carcinoma using complementary microRNAs. *J. Control. Release* 238, 272–280. doi: 10.1016/j.jconrel.2016.08.005

National Institutes of Health (NIH) (2013). Pancreatic Cancer Treatment (PDQ®): Treatment option overview. Bethesda, MD: National Cancer Institute, NIH.

Ng, K. Y., and Liu, Y. (2002). Therapeutic ultrasound: its application in drug delivery. *Med. Res. Rev.* 22, 204–223. doi: 10.1002/med.10004

Ning, Z., Xie, J., Chen, Q., Zhang, C., Xu, L., Song, L., et al. (2019). HIFU is safe, effective, and feasible in pancreatic cancer patients: a monocentric retrospective study among 523 patients. *Onco. Targets. Ther.* 12, 1021–1029. doi: 10.2147/OTT.S185424

Ohmura, T., Fukushima, T., Shibaguchi, H., Yoshizawa, S., Inoue, T., Kuroki, M., et al. (2011). Sonodynamic therapy with 5-aminolevulinic acid and focused ultrasound for deep-seated intracranial glioma in rat. *Anticancer Res.* 31, 2527–2533.

O'Reilly, M. A., and Hynynen, K. (2012). Ultrasound enhanced drug delivery to the brain and central nervous system. *Int. J. Hyperther.* 28, 386–396. doi: 10.3109/02656736.2012.666709

Ozben, T. (2007). Oxidative stress and apoptosis: impact on cancer therapy. *J. Pharm. Sci.* 96(9): 2181–2196. doi: 10.1002/jps.20874

Ozdemir, F., Zateri, C., and Murat, S. (2008). Evaluation of the efficacy of therapeutic ultrasound on bone mineral density in postmenopausal period. *Rheumatol. Int.* 28, 361–365. doi: 10.1007/s00296-007-0450-2

Özdemir, S., Çelik, B., and Üner, M. (2019). "Chapter 15 - Properties and therapeutic potential of solid lipid nanoparticles and nanostructured lipid carriers as promising colloidal drug delivery systems," in *Materials for Biomedical Engineering*, eds A.-M. Holban and A. M. Grumezescu (Istanbul: Elsevier), 457–505.

Pang, X., Liu, X., Cheng, Y., Zhang, C., Ren, E., Liu, C., et al. (2019) Sono-immunotherapeutic nanocapturer to combat multidrug-resistant bacterial infections. *Adv. Mater.* 31:1902530. doi: 10.1002/adma.201902530

Papa, A.-L., Korin, N., Kanapathipillai, M., Mammoto, A., Mammoto, T., Jiang, A., et al. (2017). Ultrasound-sensitive nanoparticle aggregates for targeted drug delivery. *Biomaterials* 139, 187–194. doi: 10.1016/j.biomaterials.2017.06.003

Park, S. M., Kim, M. S., Park, S. J., Park, E. S., Choi, K. S., Kim, Y. S., and Kim, H. R. (2013). Novel temperature-triggered liposome with high stability: Formulation, *in vitro* evaluation, and *in vivo* study combined with high-intensity focused ultrasound (HIFU). *J. Control. Release* 170, 373–379. doi: 10.1016/j.jconrel.2013.06.003

Peek, M. C. L., Ahmed, M., Napoli, A., ten Haken, B., McWilliams, S., Usiskin, S., et al. (2015). Systematic review of high-intensity focused ultrasound ablation in the treatment of breast cancer. *BJS* 102, 873–882. doi: 10.1002/bjs.9793

Peek, M. C. L., and Wu, F. (2018). High-intensity focused ultrasound in the treatment of breast tumours. *Ecancermedicalscience* 12, 794–794. doi: 10.3332/ecancer.2018.794

Pitt, W. G., Husseini, G. A., and Staples, B. J. (2004). Ultrasonic drug delivery–a general review. *Exp. Opin. Drug Deliv.* 1, 37–56. doi: 10.1517/17425247.1.1.37

Poh, S., Chelvam, V., and Low, P. S. (2015). Comparison of nanoparticle penetration into solid tumors and sites of inflammation: studies using targeted and nontargeted liposomes. *Nanomedicine* 10, 1439–1449. doi: 10.2217/nnm.14.237

Qin, P., Han, T., Yu, A. C. H., and Xu, L. (2018). Mechanistic understanding the bioeffects of ultrasound-driven microbubbles to enhance macromolecule delivery. *J. Control. Release* 272, 169–181. doi: 10.1016/j.jconrel.2018.01.001

Rapoport, N. (2012). Phase-shift, stimuli-responsive perfluorocarbon nanodroplets for drug delivery to cancer. *Wiley Int. Rev.* 4, 492–510. doi: 10.1002/wnan.1176

Riess, J. G. (2005). Understanding the fundamentals of perfluorocarbons and perfluorocarbon emulsions relevant to *in vivo* oxygen delivery. *Artif. Cells Blood Substit. Immobil. Biotechnol.* 33, 47–63. doi: 10.1081/BIO-200046659

Riesz, P., and Kondo, T. (1992). Free radical formation induced by ultrasound and its biological implications. *Free Radical Biol. Med.* 13, 247–270. doi: 10.1016/0891-5849(92)90021-8

Riesz, P., Kondo, T., and Krishna, C. M. (1990). Free radical formation by ultrasound in aqueous solutions. A spin trapping study. *Free Radic. Res. Commun.* 10, 27–35. doi: 10.3109/10715769009145930

Rix, A., Lederle, W., Theek, B., Lammers, T., Moonen, C., Schmitz, G., et al. (2018). Advanced ultrasound technologies for diagnosis and therapy. *J. Nucl. Med.* 59, 740–746. doi: 10.2967/jnumed.117.200030

Rosenblum, D., Joshi, N., Tao, W., Karp, J. M., and Peer, D. (2018). Progress and challenges towards targeted delivery of cancer therapeutics. *Nat. Commun.* 9, 1410–1410. doi: 10.1038/s41467-018-03705-y

Sadegh Malvajerd, S., Azadi, A., Izadi, Z., Kurd, M., Dara, T., Dibaei, M., et al. (2019). Brain delivery of curcumin using solid lipid nanoparticles and nanostructured lipid carriers: preparation, optimization, and pharmacokinetic evaluation. *ACS Chem. Neurosci.* 10, 728–739. doi: 10.1021/acschemneuro.8b00510

Schoellhammer, C. M., Lauwers, G. Y., Goettel, J. A., Oberli, M. A., Cleveland, C., and Traverso, G. (2017). Ultrasound-mediated delivery of RNA to colonic mucosa of live mice. *Gastroenterology* 152, 1151–1160. doi: 10.1053/j.gastro.2017.01.002

Schoellhammer, C. M., and Traverso, G. (2016). Low-frequency ultrasound for drug delivery in the gastrointestinal tract. *Exp. Opin. Drug Deliv.* 13, 1045–1048. doi: 10.1517/17425247.2016.1171841

Schroeder, A., Honen, R., Turjeman, K., Gabizon, A., Kost, J., and Barenholz, Y. (2009a). Ultrasound triggered release of cisplatin from liposomes in murine tumors. *J. Control. Release* 137, 63–68. doi: 10.1016/j.jconrel.2009.03.007

Schroeder, A., Kost, J., and Barenholz, Y. (2009b). Ultrasound, liposomes, and drug delivery: principles for using ultrasound to control the release of drugs from liposomes. *Chem. Phys. Lipids* 162, 1–16. doi: 10.1016/j.chemphyslip.2009.08.003

Schweizer, F. E., and Ryan, T. A. (2006). The synaptic vesicle: cycle of exocytosis and endocytosis. *Curr. Opin. Neurobiol.* 16, 298–304. doi: 10.1016/j.conb.2006.05.006

Shapiro, G., Wong, A. W., Bez, M., Yang, F., Tam, S., and Gazit, D. (2016). Multiparameter evaluation of *in vivo* gene delivery using ultrasound-guided, microbubble-enhanced sonoporation. *J. Controlled Release* 223, 157–164. doi: 10.1016/j.jconrel.2015.12.001

Shi, D., Guo, L., Duan, S., Shang, M., Meng, D., Cheng, L., et al. (2017). Influence of tumor cell lines derived from different tissue on sonoporation efficiency under ultrasound microbubble treatment. *Ultrason. Sonochem.* 38, 598–603. doi: 10.1016/j.ultsonch.2016.08.022

Siegel, R. J., Gunn, J., Ahsan, A., Fishbein, M., C., Bowes, R. J., Oakley, D., et al. (1994). Use of therapeutic ultrasound in percutaneous coronary angioplasty. Experimental *in vitro* studies and initial clinical experience. *Circulation* 89, 1587–1592. doi: 10.1161/01.CIR.89.4.1587

Sirsi, S. R., and Borden, M. A. (2014). State-of-the-art materials for ultrasound-triggered drug delivery. *Adv. Drug Deliv. Rev.* 72, 3–14. doi: 10.1016/j.addr.2013.12.010

Solans, R., Motta, C., Sola, R., La Ville, A. E., Lima, J., and Vilardell, M. (2000). Abnormalities of erythrocyte membrane fluidity, lipid composition, and lipid peroxidation in systemic sclerosis: evidence of free radical-mediated injury. *Arthritis Rheum.* 43, 894–900. doi: 10.1002/1529-0131(200004)43:4<894::AID-ANR22>3.0.CO;2-4

Speicher, D., Bartscherer, T., Becker, F. J., Jenne, J. W., Mrosk, K., and Tretbar, S. (2015). MRI compatible ultrasound transducers for simultaneous acquisition of coregistered ultrasound to MRI data. *Phys. Procedia* 70, 1002–1006. doi: 10.1016/j.phpro.2015.08.209

Spiteri, D., Chot-Plassot, C., Sclear, J., Karatzas, K. A., Scerri, C., and Valdramidis, V. P. (2017). Ultrasound processing of liquid system(s) and its antimicrobial mechanism of action. *Lett. Appl. Microbiol.* 65, 313–318. doi: 10.1111/lam.12776

Sriraman, S. K., Aryasomayajula, B., and Torchilin, V. P. (2014). Barriers to drug delivery in solid tumors. *Tissue Barriers* 2:e29528. doi: 10.4161/tisb.29528

Stavarache, C. E., and Paniwnyk, L. (2018). Controlled rupture of magnetic LbL polyelectrolyte capsules and subsequent release of contents employing high intensity focused ultrasound. *J. Drug Deliv. Sci. Technol.* 45, 60–69. doi: 10.1016/j.jddst.2018.02.011

Stewart, P. S., and Costerton, J. W. (2001). Antibiotic resistance of bacteria in biofilms. *Lancet* 358, 135–138. doi: 10.1016/S0140-6736(01)05321-1

Sung, H. Y., Cho, J. I., Kim, D. Y., Cheung, J.-Y., Han, J. K., Kim, I. S., et al. (2008). High intensity focused ultrasound therapy resulted in a complete response in a patient with advanced gastric cancer with liver metastases: a case report. *Eur. J. Gastroenterol. Hepatol.* 20, 707–709. doi: 10.1097/MEG.0b013e3282f2b136

ter Haar, G. (2007). Therapeutic applications of ultrasound. *Prog. Biophys. Mol. Biol.* 93, 111–129. doi: 10.1016/j.pbiomolbio.2006.07.005

Tezel, A., and Mitragotri, S. (2003). Interactions of inertial cavitation bubbles with stratum corneum lipid bilayers during low-frequency sonophoresis. *Biophys. J.* 85, 3502–3512. doi: 10.1016/S0006-3495(03)74770-5

Thakkar, D., Gupta, R., Mohan, P., Monson, K., and Rapoport, N. (2012). Overcoming biological barriers with ultrasound. *AIP Conf. Proc.* 1481, 381–387. doi: 10.1063/1.4757365

Theek, B., Baues, M., Ojha, T., Möckel, D., Veettil, S. K., and Lammers, T. (2016). Sonoporation enhances liposome accumulation and penetration in tumors with low EPR. *J. Controlled Release* 231, 77–85. doi: 10.1016/j.jconrel.2016.02.021

Timbie, K. F., Afzal, U., Date, A., Zhang, C., Song, J., Wilson Miller, G., et al. (2017). MR image-guided delivery of cisplatin-loaded brain-penetrating nanoparticles to invasive glioma with focused ultrasound. *J. Controlled Release* 263, 120–131. doi: 10.1016/j.jconrel.2017.03.017

Toraya-Brown, S., and Fiering, S. (2014). Local tumour hyperthermia as immunotherapy for metastatic cancer. *Int. J. Hyperther.* 30, 531–539. doi: 10.3109/02656736.2014.968640

Tzu-Yin, W., Wilson, K. E., Machtaler, S., and Willmann, J. K. (2013). Ultrasound and microbubble guided drug delivery: mechanistic understanding and clinical implications. *Curr. Pharm. Biotechnol.* 14, 743–752. doi: 10.2174/13892010146666131226114611

Unger, E. C., Porter, T., Culp, W., Labell, R., Matsunaga, T., and Zutshi, R. (2004). Therapeutic applications of lipid-coated microbubbles. *Adv. Drug Deliv. Rev.* 56, 1291–1314. doi: 10.1016/j.addr.2003.12.006

van den Bijgaart, R. J. E., Eikelenboom, D. C., Hoogenboom, M., Fütterer, J. J., den Brok, M. H., and Adema, G. J. (2017). Thermal and mechanical high-intensity focused ultrasound: perspectives on tumor ablation, immune effects and combination strategies. *Cancer Immunol. Immunother.* 66, 247–258. doi: 10.1007/s00262-016-1891-9

Vyas, N., Manmi, K., Wang, Q., Jadhav, A. J., Barigou, M., and Walmsley, A. D. (2019). Which parameters affect biofilm removal with acoustic cavitation? A Review. *Ultrasound Med. Biol.* 45, 1044–1055. doi: 10.1016/j.ultrasmedbio.2019.01.002

Wang, H., Wang, X., Wang, P., Zhang, K., Yang, S., and Liu, Q. (2013). Ultrasound enhances the efficacy of chlorin e6-mediated photodynamic therapy in MDA-MB-231 Cells. *Ultrasound Med. Biol.* 39, 1713–1724. doi: 10.1016/j.ultrasmedbio.2013.03.017

Wang, J., Pelletier, M., Zhang, H., Xia, H., and Zhao, Y. (2009). High-frequency ultrasound-responsive block copolymer micelle. *Langmuir* 25, 13201–13205. doi: 10.1021/la9018794

Wang, J., and Yi, J. (2008). Cancer cell killing via ROS: to increase or decrease, that is the question. *Cancer Biol. Ther.* 7, 1875–1884. doi: 10.4161/cbt.7.12.7067

Wang, M., Zhang, Y., Cai, C., Tu, J., Guo, X., and Zhang, D. (2018). Sonoporation-induced cell membrane permeabilization and cytoskeleton disassembly at varied acoustic and microbubble-cell parameters. *Sci. Rep.* 8:3885. doi: 10.1038/s41598-018-22056-8

Wang, P., Li, Y., Wang, X., Guo, L., Su, X., and Liu, Q. (2012). Membrane damage effect of continuous wave ultrasound on K562 human leukemia cells. *J. Ultrasound Med.* 31, 1977–1986. doi: 10.7863/jum.2012.31.12.1977

Wang, S., Shin, I. S., Hancock, H. B., Jang, H., Kim, L. S., and Dreher, M. R. (2012). Pulsed high intensity focused ultrasound increases penetration and therapeutic efficacy of monoclonal antibodies in murine xenograft tumors. *J. Controlled Release* 162, 218–224. doi: 10.1016/j.jconrel.2012.06.025

Wang, T.-Y., Choe, J. W., Pu, K., Devulapally, R., Bachawal, S. and Willmann, J. K. (2015). Ultrasound-guided delivery of microRNA loaded nanoparticles into cancer. *J. Controlled Release* 203, 99–108. doi: 10.1016/j.jconrel.2015.02.018

Wang, X., Chen, H., Chen, Y., Ma, M., Zhang, K., Li, F., et al. (2012). Perfluorohexane-encapsulated mesoporous silica nanocapsules as enhancement agents for highly efficient high intensity focused ultrasound (HIFU). *Adv. Mater.* 24, 785–791. doi: 10.1002/adma.201104033

Wang, X., Yan, F., Liu, X., Wang, P., Shao, S., Sun, Y., et al. (2018). Enhanced drug delivery using sonoactivatable liposomes with membrane-embedded porphyrins. *J. Controlled Release* 286, 358–368. doi: 10.1016/j.jconrel.2018.07.048

Wasan, E. K., Reimer, D. L., and Bally, M. B. (1996). Plasmid DNA is protected against ultrasonic cavitation-induced damage when complexed to cationic liposomes. *J. Pharm. Sci.* 85, 427–433. doi: 10.1021/js9504752

Watson, K. D., Lai, C. Y., Qin, S., Kruse, D. E., Lin, Y. C., Seo, J. W., et al. (2012). Ultrasound increases nanoparticle delivery by reducing intratumoral pressure and increasing transport in epithelial and epithelial-mesenchymal transition tumors. *Cancer Res* 72, 1485–1493. doi: 10.1158/0008-5472.CAN-11-3232

Wei, K. C., Tsai, H. C., Lu, Y. J., Yang, H. W., Hua, M. Y., Wu, M. F., et al. (2013). Neuronavigation-guided focused ultrasound-induced blood-brain barrier opening: a preliminary study in swine. *AJNR Am J Neuroradiol.* 34, 115–120. doi: 10.3174/ajnr.A3150

Wei, Y., Shang, N., Jin, H., He, Y., Pan, Y., Xiao, N., et al. (2019). Penetration of different molecule sizes upon ultrasound combined with microbubbles in a superficial tumour model. *J. Drug Target.* 20, 1–8. doi: 10.1080/1061186X.2019.1588279

Wiedmann, T. S., and Ravichandran, A. (2001). Ultrasonic nebulization system for respiratory drug delivery. *Pharm. Dev. Technol.* 6, 83–89. doi: 10.1081/PDT-100000016

Wiggins, P., and Phillips, R. (2004). Analytic models for mechanotransduction: gating a mechanosensitive channel. *Proc. Natl. Acad. Sci. U.S.A.* 101, 4071–4076. doi: 10.1073/pnas.0307804101

Wilhelm, S., Tavares, A. J., Dai, Q., Ohta, S., Audet, J., and Chan, W. C. W. (2016). Analysis of nanoparticle delivery to tumours. *Nat. Rev. Mater.* 1:16014. doi: 10.1038/natrevmats.2016.14

Wischhusen, J., and Padilla, F. (2019). Ultrasound-targeted microbubble destruction (UTMD) for localized drug delivery into tumor tissue. *IRBM* 40, 10–15. doi: 10.1016/j.irbm.2018.11.005

Wu, F. (2006). Extracorporeal high intensity focused ultrasound in the treatment of patients with solid malignancy. *Minim. Invasive Ther. Allied Technol.* 15, 26–35. doi: 10.1080/13645700500470124

Wu, F., Zhou, L., and Chen, W. R. (2007). Host antitumour immune responses to HIFU ablation. *Int. J. Hyperthermia* 23, 165–171. doi: 10.1080/02656730701206638

Wu, H., Moser, C. H.-,Wang, Z., Høiby, N., and Song, J. (2015). Strategies for combating bacterial biofilm infections. *Int. J. Oral Sci.* 7, 1–7. doi: 10.1038/ijos.2014.65

Wu, M., Chen, W., Chen, Y., Zhang, H., Liu, C., Deng, Z., et al. (2018). Focused ultrasound-augmented delivery of biodegradable multifunctional nanoplatforms for imaging-guided brain tumor treatment. *Adv. Sci.* 5:1700474. doi: 10.1002/advs.201700474

Wu, P., Jia, Y., Qu, F., Sun, Y., Wang, P., Zhang, K., et al. (2017). Ultrasound-responsive polymeric micelles for sonoporation-assisted site-specific therapeutic action. *ACS Appl. Mater. Interfaces* 9, 25706–25716. doi: 10.1021/acsami.7b05469

Wylie, M. P., McGuinness, G. B., and Gavin, G. P. (2009). Therapeutic ultrasound angioplasty: the risk of arterial perforation. An *in vitro* study. *Conf. Proc. IEEE Eng. Med. Biol. Soc.* 2009, 282–285. doi: 10.1109/IEMBS.2009.5334036

Xenariou, S., Griesenbach, U., Liang, H. D., Zhu, J., Farley, R., and Alton, E. W. (2007). Use of ultrasound to enhance nonviral lung gene transfer *in vivo*. *Gene Ther.* 14, 768–774. doi: 10.1038/sj.gt.3302922

Xia, H., Zhao, Y., and Tong, R. (2016). Ultrasound-mediated polymeric micelle drug delivery. *Adv. Exp. Med. Biol.* 880, 365–384. doi: 10.1007/978-3-319-22536-4_20

Xin, Z., Lin, G., Lei, H., Lue, T. F., and Guo, Y. (2016). Clinical applications of low-intensity pulsed ultrasound and its potential role in urology. *Transl. Androl. Urol.* 5, 255–266. doi: 10.21037/tau.2016.02.04

Yang, C., Li, Y., Du, M., and Chen, Z. (2019). Recent advances in ultrasound-triggered therapy. *J. Drug Target.* 27, 33–50. doi: 10.1080/1061186X.2018.1464012

Yin, T., Wang, P., Li, J., Wang, Y., Zheng, B., Zheng, R., et al. (2014). Tumor-penetrating codelivery of siRNA and paclitaxel with ultrasound-responsive nanobubbles hetero-assembled from polymeric micelles and liposomes. *Biomaterials* 35, 5932–5943. doi: 10.1016/j.biomaterials.2014.03.072

Yin, T., Wang, P., Li, J., Zheng, R., Zheng, B., Cheng, D., et al. (2013). Ultrasound-sensitive siRNA-loaded nanobubbles formed by hetero-assembly of polymeric

micelles and liposomes and their therapeutic effect in gliomas. *Biomaterials* 34, 4532–4543. doi: 10.1016/j.biomaterials.2013.02.067

You, Y., Wang, Z., Ran, H., Zheng, Y., Wang, D., Xu, J., et al. (2016). Nanoparticle-enhanced synergistic HIFU ablation and transarterial chemoembolization for efficient cancer therapy. *Nanoscale* 8, 4324–4339. doi: 10.1039/C5NR08292G

Yu, H., Chen, S., and Cao, P. (2012). Synergistic bactericidal effects and mechanisms of low intensity ultrasound and antibiotics against bacteria: a review. *Ultrason. Sonochem* 19, 377–382. doi: 10.1016/j.ultsonch.2011.11.010

Yu, H., and Xu, L. (2014). Cell experimental studies on sonoporation: state of the art and remaining problems. *J. Controlled Release* 174, 151–160. doi: 10.1016/j.jconrel.2013.11.010

Yu, J., Chen, Z., and Yan, F. (2019). Advances in mechanism studies on ultrasonic gene delivery at cellular level. *Prog. Biophys. Mol. Biol.* 142, 1–9. doi: 10.1016/j.pbiomolbio.2018.07.012

Yudina, A., and Moonen, C. (2012). Ultrasound-induced cell permeabilisation and hyperthermia: strategies for local delivery of compounds with intracellular mode of action. *Int. J. Hyperthermia* 28, 311–319. doi: 10.3109/02656736.2012.664307

Zacchè, M. M., Srikrishna, S., and Cardozo, L. (2015). Novel targeted bladder drug-delivery systems: a review. *Res. Reports Urol.* 7, 169–178. doi: 10.2147/RRU.S56168

Zardad, A.-Z., Choonara, Y., du Toit, L., Kumar, P., Mabrouk, M., Kondiah, P., et al. (2016). A review of thermo- and ultrasound-responsive polymeric systems for delivery of chemotherapeutic agents. *Polymers* 8:359. doi: 10.3390/polym8100359

Zderic, V., Vaezy, S., Martin, R. W., and Clark, J. I. (2002). Ocular drug delivery using 20-kHz ultrasound. *Ultrasound Med. Biol.* 28, 823–829. doi: 10.1016/S0301-5629(02)00515-X

Zhang, Y., Yong, L., Luo, Y., Ding, X., Xu, D., Gao, X., et al. (2019). Enhancement of HIFU ablation by sonosensitizer-loading liquid fluorocarbon nanoparticles with pre-targeting in a mouse model. *Sci. Rep.* 9:6982. doi: 10.1038/s41598-019-43416-y

Zhang, Y., Yu, T., and Hou, Y. (2010). "Free radicals involved in ultrasonic therapy," in *Handbook of Free Radicals: Formation, Types and Effects*, eds D. Kozyrev, V. Slutsky. 569–581.

Zhang, Y. R., Lin, R., Li, H. J., He, W. L., Du, J. Z., and Wang, J. (2019). Strategies to improve tumor penetration of nanomedicines through nanoparticle design. *Wiley Interdisc. Rev. Nanomed. Nanobiotechnol.* 11:e1519. doi: 10.1002/wnan.1519

Zhou, Q., Zhu, X. Q., Zhang, J., Xu, Z. L., Lu, P., and Wu, F. (2008). Changes in circulating immunosuppressive cytokine levels of cancer patients after high intensity focused ultrasound treatment. *Ultrasound Med. Biol.* 34, 81–87. doi: 10.1016/j.ultrasmedbio.2007.07.013

Zhou, Q. L., Chen, Z. Y., Wang, Y. X., Yang, F., Lin, Y., and Liao, Y. Y. (2014). Ultrasound-mediated local drug and gene delivery using nanocarriers. *BioMed. Res. Int.* 2014:963891. doi: 10.1155/2014/963891

Zhou, Y., Peng, Z., Seven, E. S., and Leblanc, R. M. (2018). Crossing the blood-brain barrier with nanoparticles. *J. Controlled Release* 270, 290–303. doi: 10.1016/j.jconrel.2017.12.015

Zhou, Y. Y., Wang, N., Farr, N., Zia, J., Chen, H., and Hwang, J. H. (2016). Enhancement of small molecule delivery by pulsed high-intensity focused ultrasound: a parameter exploration. *Ultrasound Med. Biol.* 42, 956–963. doi: 10.1016/j.ultrasmedbio.2015.12.009

Zhu, L., Altman, M., Laszlo, A., Straube, W., Zoberi, I., and Chen, H. (2019). Ultrasound hyperthermia technology for radiosensitization. *Ultrasound Med. Biol.* 45, 1025–1043. doi: 10.1016/j.ultrasmedbio.2018.12.007

Zhu, L., and Torchilin, V. P. (2013). Stimulus-responsive nanopreparations for tumor targeting. *Integr. Biol.* 5, 96–107. doi: 10.1039/c2ib20135f

Electrospun Nanofibers With pH-Responsive Coatings for Control of Release Kinetics

Sezin Sayin[1], Ali Tufani[1], Melis Emanet[1], Giada Graziana Genchi[2], Ozlem Sen[2], Sepideh Shemshad[1], Ece Ozdemir[1], Gianni Ciofani[2,3] and Gozde Ozaydin Ince[1,4,5*]

[1] Materials Science and Nano Engineering Department, Faculty of Engineering and Natural Sciences, Sabanci University, Istanbul, Turkey, [2] Istituto Italiano di Tecnologia, Smart Bio-Interfaces, Pontedera, Italy, [3] Department of Mechanical and Aerospace Engineering, Politecnico di Torino, Turin, Italy, [4] Sabanci University Nanotechnology Research and Application Center (SUNUM), Sabanci University, Istanbul, Turkey, [5] Center of Excellence for Functional Surfaces and Interfaces (EFSUN), Sabanci University, Istanbul, Turkey

Functional and stimuli-responsive nanofibers with an enhanced surface area/volume ratio provide controlled and triggered drug release with higher efficacy. In this study, chemotherapeutic agent Rose Bengal (RB) (4,5,6,7-tetrachloro-2′, 4′,5′,7′-tetraiodofluoresceindisodium)-loaded water-soluble polyvinyl alcohol (PVA) nanofibers were synthesized by using the electrospinning method. A thin layer of poly(4-vinylpyridine-co-ethylene glycol dimethacrylate) p(4VP-co-EGDMA) was deposited on the RB-loaded nanofibers (PVA-RB) via initiated chemical vapor deposition (iCVD), coating the fiber surfaces to provide controllable solubility and pH response to the nanofibers. The uncoated and [p(4VP-co-EGDMA)-PVA] coated PVA-RB nanofiber mats were studied at different pH values to analyze their degradation and drug release profiles. The coated nanofibers demonstrated high stability at neutral and basic pH values for long incubation durations of 72 h, whereas the uncoated nanofibers dissolved in <2 h. The drug release studies showed that the RB release from coated PVA-RB nanofibers was higher at neutral and basic pH values, and proportional to the pH of the solution, whereas the degradation and RB release rates from the uncoated PVA-RB nanofibers were significantly higher and did not depend on the pH of environment. Further analysis of the release kinetics using the Peppas model showed that while polymer swelling and dissolution were the dominant mechanisms for the uncoated nanofibers, for the coated nanofibers, Fickian diffusion was the dominant release mechanism. The biocompatibility and therapeutic efficiency of the coated PVA-RB nanofibers against brain cancer was investigated on glioblastoma multiforme cancer cells (U87MG). The coated PVA nanofibers were observed to be highly biocompatible, and they significantly stimulated the ROS production in cells, increasing apoptosis. These promising results confirmed the therapeutic activity of the coated PVA-RB nanofibers on brain cancer cells, and encouraged their further evaluation as drug carrier structures in brain cancer treatment.

Keywords: initiated chemical vapor deposition, electrospinning, controlled drug delivery, pH responsive polymers, polymer-coated nanofibers

INTRODUCTION

Implantable patches for drug delivery have gained attention in recent years. In particular, these patches are used in site-specific, targeted delivery with enhanced sustained release of drug molecules from biodegradable materials (Brown and Crawford, 2002; LaPorte et al., 2005). These devices have been developed to overcome the common challenges in drug delivery, such as achieving systematic delivery with therapeutically effective drug concentrations at the specified target. Theeuwes and Nelson (2004) developed a bilayered, patch-based device, which provided drug delivery directly to the organ surface. The biocompatible, drug-impermeable first layer acted as the drug reservoir, while the drug-permeable second layer allowed drug delivery directly to the organ. Nelson et al. (2003), on the other hand, introduced a biodegradable fiber implant for drug release, which involved three-dimensional matrices of predefined non-homogeneous patterned polymeric fibers.

Electrospun nanofibers as polymeric nanocarriers are widely used in drug delivery systems (DDS) because they have high loading and encapsulation efficiency and they can be easily produced in a cost-effective manner (Chakraborty et al., 2009; Wang et al., 2010). Blending a polymer solution with a therapeutic agent before electrospinning is the most common technique for encapsulation. The distribution of drug molecules and morphology of fibers are the main factors affecting the release behavior (Kenawy et al., 2002; Zamani et al., 2013; Tipduangta et al., 2015).

As chemotherapeutic DDS, electrospun nanofibers are promising due to high drug loading capacities. Poly(ethylene glycol)–poly(L-lactic acid) (PEG–PLLA) diblock copolymer fibers loaded with an antineoplastic drug BCNU (1,3-bis(2-chloroethyl)-1-nitrosourea) were fabricated to obtain controllable drug delivery directly to the tumor microenvironment (Xu et al., 2006). High antitumor activity for longer periods of time (72 h) was observed when the BCNU release was from the PEG–PLLA fibers whereas with pristine BCNU, loss of cytotoxic activity was observed in the same period of time due to the short half-life of the drug (Xu et al., 2006). Sharma et al. (2013) loaded insulin to poly(vinyl alcohol) PVA and sodium alginate nanofiber-based patch for anti-diabetic drug delivery. *In vivo* test of the patch on male Wistar rats showed that the drug molecules were released in their pharmacologically active states without any deterioration. In another study, for the treatment of glaucoma disease, Garg et al. (2014) used PVA and polycaprolactone (PCL) fiber mats loaded with timolol maleate and dorzolamide hydrochloride as model drugs, achieving a very high drug entrapment efficiency of ∼100%.

Although electrospun fibers are very promising with respect to drug delivery, in post-operation cancer treatment applications, controlling the initial burst release and tuning the release kinetics from fibers are the main challenges yet to be overcome (Thakkar and Misra, 2017). In order to defeat these challenges during cancer treatments, coaxial nanofibers with core-shell structures have been introduced due to their effectiveness in drug incorporation into nanofibers as reservoir-type drug delivery carriers (He et al., 2006). Recent studies include concentric spinneret electrospinning method for coaxial nanofiber formation. These core-shell nanocarriers are used mostly to control the sustained drug delivery (He et al., 2006; Zupančič et al., 2016), to release both hydrophilic and hydrophobic drugs from the same system (Oliveira et al., 2015), to enhance implant osseointegration and to prevent implant infections (Song et al., 2013), and to obtain bi-component, surface-modified, and functional graded nanofibers (Zhang et al., 2004). Another method that has been used to overcome these shortcomings is direct deposition onto nanofibers for the production of coaxial structures (Chunder et al., 2007). Layer-by-layer (LBL) deposition (Sakai et al., 2009; Li et al., 2012; Croisier et al., 2014) and vapor phase methods, such as chemical vapor deposition (CVD) (Zeng et al., 2005) are some examples.

Although studies reported have included controlled drug release from various polymeric nanofibers, stimuli-responsive and cross-linked coatings on these nanofibers have not been quite examined. In this paper, fabrication of polymeric mat with an outer coating layer for sustained release of Rose Bengal (RB) as a chemotherapeutic drug was reported. PVA polymer with RB solution was electrospun to form blend fibers. PVA is used as the polymer matrix due to its biocompatibility and biodegradable nature, leading to its wide utilization in drug delivery applications (Huang and Rhim, 1993; Taepaiboon et al., 2006; Kenawy et al., 2007; Yang et al., 2007; Jannesari et al., 2011; Bazhban et al., 2013; Li et al., 2013; Jalvandi et al., 2017). Meanwhile, RB (4,5,6,7-tetrachloro-2′,4′,5′,7′-tetraiodofluoresceindisodium) is used as the chemotherapeutic drug which is a water-soluble, photosensitive, synthetic dye used for diagnostics exhibiting cytotoxicity in various cancer types, such as brain cancer (Tserkovsky et al., 2012), colorectal cancer cells (Qin et al., 2017), melanoma and breast cancer cells (Toomey et al., 2013), and ovarian and adenovirus-transformed embryonic kidney cancer cells (Koevary, 2012). In order to provide additional functionalities to the electrospun fibers, surface of the fiber mats was coated with poly(4-vinylpyridine-co-ethylene glycol dimethacrylate) [p(4VP-co-EGDMA)], a pH-sensitive polymer, via initiated chemical vapor deposition (iCVD). iCVD is an all-dry, free-radical polymerization method that allows polymerization directly on the substrate surface, initiated by thermally decomposed radicals reacting with the monomer molecules adsorbed on the substrate (Lau and Gleason, 2006; Ozaydin-Ince et al., 2011). It is advantageous because of its conformal coating ability on high-aspect-ratio surfaces, which preserves the film thickness throughout the surface topography (Ozaydin-Ince et al., 2011; Armagan and Ince, 2015).

In the study reported here, RB release from the p(4VP-co-EGDMA)-coated PVA-RB nanofibers was investigated at different pH values, and the effect of the pH-responsive polymer coating on the release performance was studied. The degradation profiles of the nanofibers at these pH values were investigated to reveal their stability in cellular environment for their potential drug carrier activity. Moreover, the time-dependent anti-cancer activity of the coated PVA-RB nanofibers was studied on glioblastoma multiforme brain cancer cells (U87MG). The effects on cell viability were investigated as a preliminary study before exploring the therapeutic effect of the fibers via DNA

quantification by using Pico Green dye. The intracellular RB localization and conformation of the cytoskeleton structure of cells was monitored by using confocal microscopy. The intracellular stress and death mechanism of the cells were investigated to analyze their cellular response against RB exposure. The significantly decreased cell viability and increased intracellular ROS production confirmed the increased apoptosis.

MATERIALS AND METHODS

Materials

PVA (MW 85,000–124,000, 87–89% hydrolyzed, Aldrich) and Tserkovsky Bengal sodium salt (dye content ∼90%, Aldrich) were used in electrospinning for fiber synthesis. The monomer 4VP (95%, Aldrich), the cross-linker EGDMA (98%, Aldrich), and the initiator tertbutyl peroxide (TBPO, 98%, Aldrich) were used without purification. Phosphate-buffered saline (PBS, Aldrich) was utilized for the release studies.

Preparation of PVA-RB Nanofiber Mats

Ten wt% PVA solution was obtained by dissolving PVA in distilled water at 70°C and stirred continuously for 4 h. Homogeneous solution was observed after stirring overnight at room temperature, at 500 rpm. PVA-RB solution was prepared by blending 100 mg/ml RB distilled water and 10 wt% PVA solutions in RB:PVA 1:5 ratio. The loading capacity of the nanofibers was calculated to be ∼16.7%.

Electrospinning setup included syringe pump, stainless steel spinneret needle, high voltage supply, 10 × 10 cm collector, and 2 ml syringe. The distance between the needle and collector was kept at 15 cm, and the voltage was applied at 8 kV. Flow rates for both PVA and PVA-RB blend solutions were adjusted as 0.3 ml/h.

P(4VP-co-EGDMA) Coating of PVA-RB Nanofibers

P(4VP-co-EGDMA) was conformally deposited on both sides of nanofiber mats at a thickness of ∼70 nm by using iCVD.

The cross-linker EGDMA was heated to 95°C in a metal jar, and 4VP was kept at room temperature. The initiator was delivered to the system at a flow rate of 1 sccm while the flow rate of N_2 gas was 1.1 sccm. The filament and substrate temperatures were at 240 and 25°C, respectively, throughout the deposition. Reaction pressure was fixed at 600 mTorr. Flow rates of 4VP and EGDMA were 2.73 and 0.14 sccm, respectively. Si wafers were coated simultaneously as the fiber mats, to be used in ellipsometric swelling experiments. **Figure 1** shows the schematic of the coated and uncoated nanofiber mat fabrication process.

Characterization of PVA, PVA-RB, Coated PVA, and Coated PVA-RB Nanofibers

The PVA, PVA-RB, p(4VP-co-EGDMA)-coated PVA, and p(4VP-co-EGDMA)-coated PVA-RB nanofibers were imaged by field emission scanning electron microscopy (Zeiss, Leo Supra VP35) with an accelerating voltage of 4 kV. Chemical characterization of the fibers was performed by Fourier transform infrared spectroscopy (Thermo-Fisher Scientific, Nicolet iS10 FTIR) with 62 scans and the resolution of 4 cm^{-1} over the range of 800–4,000 cm^{-1}.

XPS analysis was done by using Thermo Scientific K-Alpha spectrometer by an aluminum anode (Al Kα = 1,468.3 eV) at an electron take-off angle of 90° (between the sample surface and the axis of the analyzer lens). The spectra were recorded using an Avantage 5.9 data system. The binding energy scale was calibrated by assigning the C1s signal at 284.5 eV.

Swelling behavior of the iCVD polymer film on Si wafer was investigated via a spectroscopic ellipsometer (M2000D J.A. Woollam Co. Inc.) in a liquid cell stage at room temperature at pH values of 4, 6.5, and 9. Dynamic thickness measurements were performed at 75° nominal angle of incidence within the wavelength range of 315–718 nm for 30 min. Swelling percentages were calculated by using the formula $(t − t_0)*100/t_0$, where t is the thickness of the swollen and t_0 is the thickness of the dry samples.
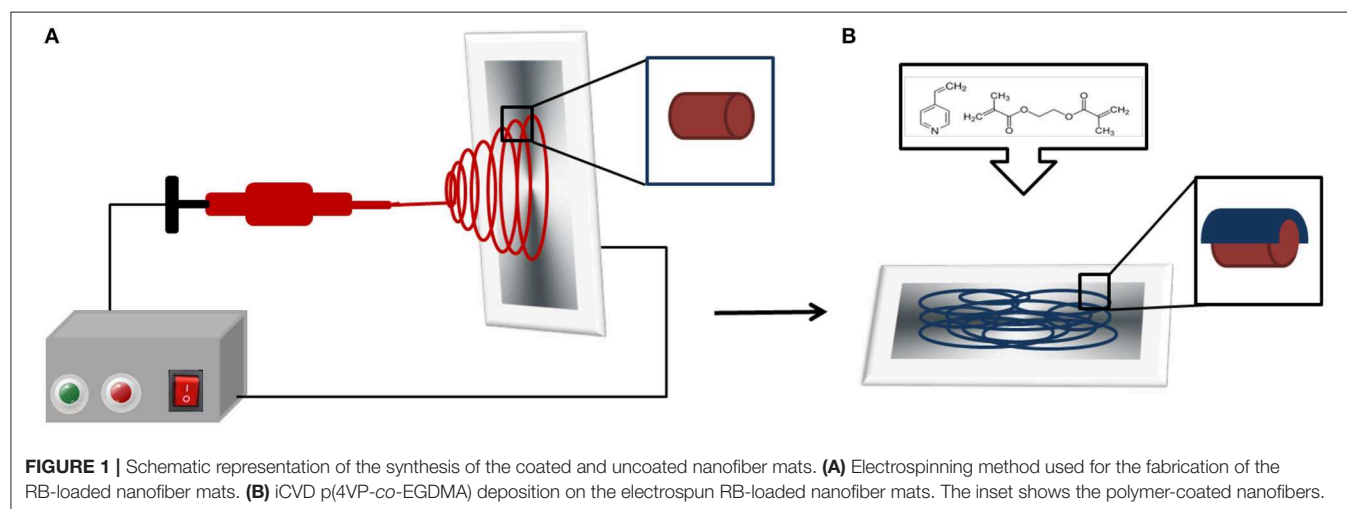

FIGURE 1 | Schematic representation of the synthesis of the coated and uncoated nanofiber mats. **(A)** Electrospinning method used for the fabrication of the RB-loaded nanofiber mats. **(B)** iCVD p(4VP-co-EGDMA) deposition on the electrospun RB-loaded nanofiber mats. The inset shows the polymer-coated nanofibers.

Degradation of PVA, PVA-RB, Coated PVA, and Coated PVA-RB Nanofibers

The degradation behavior of PVA, PVA-RB, coated PVA, and coated PVA-RB nanofibers was tested in PBS solution at several pH values (pH 4.5, 6.5, and 9) following 24 and 72 h incubation times. The morphology of the fibers was visualized by monitoring the samples using SEM (Helios Nano-Lab 600i FIB/SEM, FEI). Samples were incubated in 2-ml PBS solutions adjusted at pH 4, 6.5, and 9 for 24 and 72 h by shaking at room temperature. Following the incubations, the samples were dried under vacuum conditions for 24 h and prepared for SEM imaging. SEM imaging was carried out on samples gold-sputtered for 25 s at 60 nA, obtaining a 3 nm-thick conductive layer over the nanofibers.

Release From PVA, PVA-RB, Coated PVA, and Coated PVA-RB Nanofibers

Coated and uncoated electrospun nanofibers were cut into 1×2 cm pieces and put in 10 ml PBS solutions separately at pH 4, 6.5, and 9 and placed on a shaker for the release experiments. UV-Vis measurements were performed using NanoDrop UV-Vis spectrophotometer (Thermo Scientific NanoDrop 2000c). For each measurement, 100 µl of PBS solution was removed from the solution and replaced with fresh PBS solution in the release medium. For RB detection, the UV absorbance peak at 550 nm was used. For each release experiment, eight sets of new samples were prepared and UV-Vis measurements were repeated at least twice on each sample.

The amount of RB loaded in the nanofibers was determined by dissolving the uncoated fibers completely and measuring the RB concentration of the solution. Release percentages of the coated nanofibers were obtained by normalizing the concentration of RB released from the nanofibers by the amount loaded.

Cellular Experiments of Coated PVA and Coated PVA-RB Nanofibers

Cell Culture

U87-MG tumor cells (from ATCC) were cultured under high glucose Dulbecco's Modified Eagle's Medium, added with 10% fetal bovine serum, 2 mM L-glutamine, and 100 U/ml penicillin−100 µg/ml streptomycin (all reagents were from Sigma-Aldrich) in saturated humidity, 5% CO_2 atmosphere. Experiments were performed by seeding 30,000 U87MG cells/cm^2 in 24-well multiwell polystyrene (PS) plates and by incubating the cultures with 0.8×0.8 cm^2 coated PVA and coated PVA-RB nanofiber samples. For immunocytochemistry, cells were seeded on 0.8×0.8 cm^2 Ibidi films made hydrophilic by O_2 plasma (50 W, 25 sccm for 60 s) in a Colibrì reactor (Gambetti). Cells were exposed to nanofiber samples after overnight incubation.

Proliferation of Coated PVA and Coated PVA-RB Nanofiber-Exposed Cells

Cell proliferation was investigated by Pico Green assay (from Invitrogen) at 24 and 72 h from incubation with coated PVA and coated PVA-RB nanofiber samples. The assay enables ds-DNA quantification in solution by fluorescence measurement and requires cell lysis in a fixed volume of water (500 µl) by three cycles of freezing and thawing. To the purpose, 100 µl of working solution was mixed to 50 µl of cell lysate and to 150 µl of solution containing the PicoGreen dye. Samples were incubated in the dark for 10 min, and finally fluorescence was read with a microplate reader (Perkin Elmer Victor X3, $\lambda_{ex} = 485$ nm; $\lambda_{em} = 535$ nm).

Immunocytochemistry of Coated PVA and Coated PVA-RB Nanofiber-Exposed Cells

U87MG cells were washed with PBS with calcium and magnesium, and fixed with 4% paraformaldehyde (from Sigma-Aldrich) in PBS for 20 min at 4°C. Then, cells were again rinsed with PBS and permeabilized with 0.1% Triton X-100 (from Sigma-Aldrich) in PBS for 30 min. Specific binding sites were saturated with 10% goat serum (GS, from Thermo Scientific) in PBS for 1 h at 37°C. Then, cells were incubated with a 10% GS solution containing a rabbit polyclonal IgG primary antibody against Ki-67 (from Millipore, 1:100 diluted) for 3 h at 37°C. Samples were then rinsed four times with 10% GS (5 min each rinse), and cells were incubated with a 10% GS solution containing a goat polyclonal IgG secondary antibody (from Thermo Scientific, 1:200 diluted) and 1 µM DAPI for 45 min at 37°C. After one rinse with 0.45 M NaCl PBS and with PBS, samples underwent fluorescence imaging. The number of Ki-67 immunopositive nuclei (n) and the total number of nuclei (m) were semi-automatically counted with ImageJ software and the n/m ratio (expressed as average ± standard deviation) was calculated and plotted. For statistical reasons, 10 images at low magnification were analyzed.

Reactive Oxygen Species (ROS) and Cell Death Mechanism Detection of Coated PVA and Coated PVA-RB Nanofiber-Exposed Cells

To quantitatively assess oxidative stress, cell cultures were stained with CellROX Green reagent (from Invitrogen) at 24 and 72 h from incubation with coated PVA and coated PVA-RB nanofiber samples. To the purpose, cells were rinsed with PBS without calcium and magnesium, and suspended by 1 min incubation with 0.05% trypsin (from Sigma-Aldrich). Cell pellets were obtained with 7 min centrifugation at 1,000 g, and staining was performed for 15 min in the dark on 200 µl of cell suspension in PBS with calcium and magnesium, containing 5 µM CellRox Green reagent. To quantitatively study cell viability, cell cultures were stained with FITC Annexin V/Dead Cell Apoptosis kit (from Invitrogen) by incubating 100 µl of cell suspension in $1 \times$ annexin-binding buffer, added with 5 µl of FITC Annexin V solution and with 1 µl of 100 µg/ml of propidium iodide. Staining was performed for 15 min in the dark. Flow cytometry was conducted with CytoFLEX platform (Beckman Coulter, $\lambda_{ex} = 488$ nm; 500 nm $< \lambda_{em} < 560$ nm).

Statistical Analysis

Each experiment was carried out at least three times. Statistical analysis was carried out using an unpaired Student's t-test. The data are expressed as the mean ± standard deviation (SD).

Comparison with a *p*-value below 0.01 and 0.05 was considered statistically significant.

RESULTS AND DISCUSSION

Characterization of PVA, PVA-RB, Coated PVA, and Coated PVA-RB Nanofibers

SEM images of (a) uncoated PVA-RB nanofibers and (b) coated PVA-RB nanofibers are shown in **Figure 2**. The average diameter of pure PVA nanofibers is ∼425 ± 22 nm, whereas RB-blended PVA fibers are 523 ± 39 nm in diameter. Increased concentration in solution with RB addition resulted in larger diameters observed (Aljehani et al., 2014). The iCVD polymer coating on the fibers increased the average diameter to 587 ± 63 nm, confirming that the thickness of the polymer coating is ∼65 ± 5 nm.

As confirmed by the SEM images, the structures of the nanofibers were not damaged after the iCVD process and the

FIGURE 2 | SEM images of **(A)** uncoated PVA-RB nanofibers and **(B)** p(4VP-*co*-EGDMA)-coated PVA-RB nanofibers.

FIGURE 3 | FTIR spectra of **(a)** PVA nanofibers, **(b)** PVA-RB nanofibers, **(c)** p(4VP-*co*-EGDMA)-coated PVA-RB nanofibers, and **(d)** p(4VP-*co*-EGDMA) thin film on Si wafer. The bands at 1,597 and 1,415 cm^{-1} corresponding to the pyridine ring vibrations (indicated with asterisk) can also be observed on the coated PVA-RB nanofibers **(c)** confirming the presence of the polymer coating.

fibers could be conformally coated with the polymer layer, enabling the fabrication of p(4VP-*co*-EGDMA) coated PVA-RB nanofibers.

Swelling percentage of p(4VP-*co*-EGDMA) thin films on Si wafers was determined to be 62 ± 10% at pH 4, whereas at both pH 6.5 and pH 9, swelling was <5%, confirming the pH response of the polymer coating. The mesh sizes of the polymer coatings at pH values of 4, 6.5, and 9 were calculated as 1.16, 0.69, and 0.69 nm, respectively (**Supporting Information**). Swelling of the polymer at low pH values is attributed to the protonation of 4VP in the acidic environment, causing the chains to stretch due to electrostatic repulsion. Deprotonation of the polymer chains at high pH values, on the other hand, leads to the collapsed state observed (Li et al., 2008, Wang et al., 2013).

FTIR spectra of pure PVA, PVA-RB, and p(4VP-*co*-EGDMA)-coated PVA-RB nanofibers are shown in **Figure 3**. The absorption bands at 1,734, 1,429, and 1,091 cm^{-1} are related to the C=O double bond, CH$_2$, and C–O–C stretching modes of pure PVA nanofibers, respectively (**Figure 3a**) (Mansur et al., 2008). The bands at 1,717, 1,457, and 1,091 cm^{-1} belong to the C=O double bond, CH$_2$, and C–O–C stretching modes of PVA for RB-PVA nanofibers. Additional bands in RB-PVA blend nanofibers at 1,615 cm^{-1} belongs to the C=O double bond of carbonyl group whereas those at 1,547, 1,444, and 1,337 cm^{-1} correspond to C=C double bonds of aromatic rings (**Figure 3b**) (Dabrzalska et al., 2016). The absorption band in coated PVA-RB nanofibers at 1,719 cm^{-1} indicates CO double bond stretching of EGDMA, whereas 1,599, 1,547, and 1,417 cm^{-1} belong to pyridine ring vibration and 1,060 cm^{-1} of 4VP and 954 cm^{-1} indicate in-plane and out-of-plane CH bending of 4VP (**Figure 3c**) (Bayari and Yurdakul, 2000; Lau and Gleason, 2007), confirming the presence of the polymer coatings on the nanofibers.

X-ray photoelectron spectroscopy (XPS) was used to determine the surface composition of the PVA-RB nanofibers within 5–10 nm from the surface. **Figures 4A,B** show XPS survey scans and N1s spectrum (inset figures) of PVA-RB nanofibers without and with iCVD coating, respectively. Peaks in **Figure 4A** at 620, 532, 285, and 199 eV correspond to I3d, O1s, C1s, and Cl2p, respectively, and indicate elemental composition of PVA-RB. From the spectrum, the atomic ratios of the elements on the surface of the PVA-RB nanofibers are estimated to be 67.64% C, 31.52% O, 0.35% I, and 0.49% Cl.

According to the XPS spectrum of the polymer-coated nanofibers, depicted in **Figure 4B**, peaks at 530, 399, and 285 eV correspond to O1s, N1s, and O1s, respectively. The atomic ratios of elements on the surface of the coated nanofibers are calculated to be 73.83% C, 25.37% O, and 0.79% N. The I and Cl peaks could not be detected, possibly due to the presence of the coating. The presence of N1s peak observed only in the coated nanofibers indicates the presence of N-containing p(4VP-*co*-EGDMA) coating on the nanofiber surfaces. The low percentages can be attributed to the fact that the coatings cover mostly the nanofibers, which are closer to the surface of the mat, leaving the nanofibers below the surface uncoated. Therefore, XPS analysis confirms the presence of a polymer coating on the nanofibers exposed to the surface.
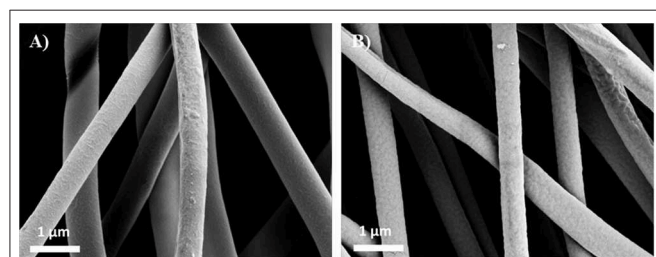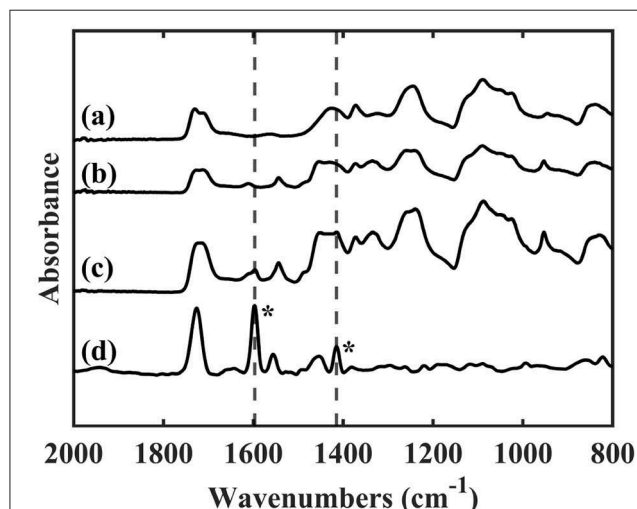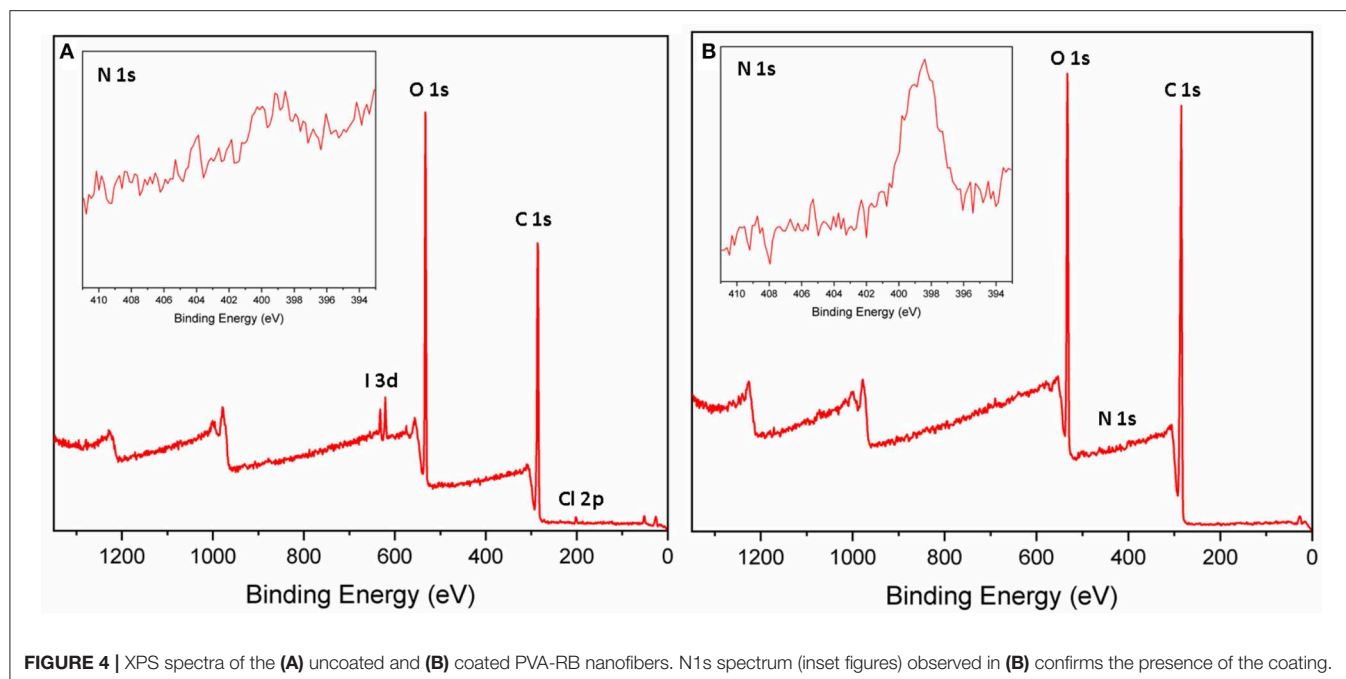
FIGURE 4 | XPS spectra of the (A) uncoated and (B) coated PVA-RB nanofibers. N1s spectrum (inset figures) observed in (B) confirms the presence of the coating.

Degradation of PVA, PVA-RB, Coated PVA, and Coated PVA-RB Nanofibers

The degradation behaviors of coated PVA and coated PVA-RB nanofibers were investigated at several pH values (4, 6.5, and 9) of PBS at increasing incubation times, as shown by SEM images (**Figure 5**). Uncoated PVA-RB and PVA nanofibers completely dissolved in <2 h at all pH values tested. Therefore, long-term stability tests were performed on the coated PVA and coated PVA-RB nanofibers. The SEM images show that the morphology of the coated PVA-RB and coated PVA nanofibers was similarly affected following the incubation.

The coated nanofibers were not stable at low pH values at incubation times longer than 12 h (**Figures 5A,D,G,J**). On the other hand, the coated nanofibers showed significantly high stability in PBS solutions at pH 6.5 (**Figures 5B,E,H,K**) and at pH 9 (**Figures 5C,F,I,L**). The pH-dependent degradation could be explained by the protonation of pyridine groups of p(4VP) at low pH values (pH 4) that lead to swelling of the p(4VP-*co*-EGDMA) coatings on the PVA nanofibers (Li et al., 2008). The swelling of the polymer coating enhanced the diffusion of the acidic solution through coating, resulting in the complete degradation of PVA nanofibers. Higher stability of the coated PVA nanofibers observed at high pH values (pH 6.5 and 9) could be attributed to the collapsed state of the polymer chains, which reduces the diffusion of the solution medium through the coating, hindering degradation of the PVA nanofibers.

Drug Release From p(4P-*co*-EGDMA)-Coated PVA-RB Nanofibers

RB release from the polymer-coated and uncoated PVA-RB nanofibers was investigated in PBS solution at pH 4, 6.5, and 9 (**Figure 6**). Release experiments from the PVA-RB nanofibers showed that more than 80% of the RB was released in 1 h with no significant dependence of the release rate on the pH of the medium (**Figure 6A**).

The kinetics of the RB release from the coated PVA-RB nanofibers, on the other hand, was strongly affected by the pH of the medium (**Figure 6B**). At all pH values, the overall release was <60% at the end of 1 h, indicating slower early time release kinetics due to the coating layer on the fibers. As the pH decreased, slower release kinetics was observed and the overall release percentages at the end of the experiments were lower at low pH. While 98% of the RB was released at the end of 6 h at pH 9, only 55% was released in 6 h at pH 4. The smaller mesh sizes of the polymer coatings at low and high pH values, compared to the size of RB molecules (hydrodynamic radius of ∼1.28 nm), indicate that the release from the uncoated or partially dissolved nanofibers dominates the release and that the release through the polymer coatings is negligible.

The fast release rates and higher release percentages of RB obtained at pH 9 compared to the release rates at lower pH values can be attributed to smaller diameters of the nanofibers due to the collapsed state of the polymer coating, which leads to the increased free volume in the electrospun mat, resulting in improved release rates. At lower pH conditions, on the other hand, the swollen polymer coating of the nanofibers reduces the free volume in the mat and entraps the RB molecules, decreasing the overall release percentages and release rates. The prolonged release observed is, thus, caused by the longer paths the RB molecules have to diffuse through due to swollen polymer.

In addition to the changes in the free volume, the electrostatic interactions between the polymer coating
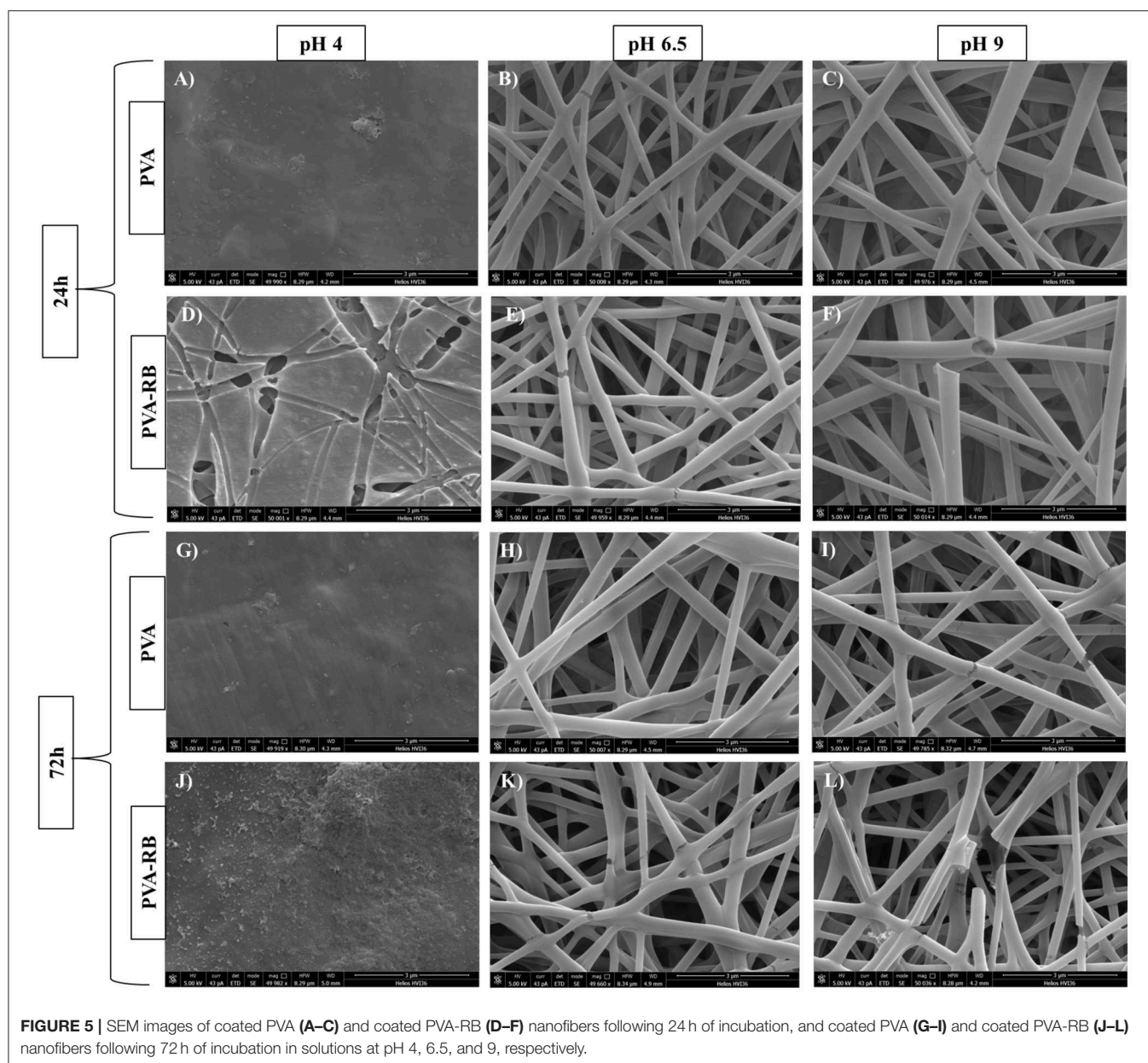
FIGURE 5 | SEM images of coated PVA **(A–C)** and coated PVA-RB **(D–F)** nanofibers following 24 h of incubation, and coated PVA **(G–I)** and coated PVA-RB **(J–L)** nanofibers following 72 h of incubation in solutions at pH 4, 6.5, and 9, respectively.

and the released RB molecules may also contribute to the pH dependence of the release profiles at early times. Protonation of pyridine groups of p(4VP), which has a pKa in the range 4.5–4.7, occurs at lower pH values, leading to an electrostatic interaction between the protonated pyridine groups and the RB molecules. This attractive interaction also contributes to the reduced release percentages observed at pH 4.

A transient behavior is observed at pH 6.5 with a faster early time release kinetics due to the collapsed polymer coating on the fibers, resulting in larger free space and shorter diffusion lengths for the dye molecules. However, overall release percentages at the end of 12 h are comparable to the release percentages at pH 4, but lower than the values obtained at pH 9.

The early time release kinetics of the polymer-coated and uncoated PVA-RB fibers were investigated using the semi-empirical Peppas model, which includes relaxation and phase changes of the polymer matrix in addition to the diffusion of the drug molecules. The Peppas model in its simplest form is given by Korsmeyer et al. (1983):

$$\frac{M_t}{M_\infty} = at^n \tag{1}$$

where M_t is the amount of drug released at time t, M_∞ is total amount of drug loaded, "a" is a constant that depends on the structure and geometry of the of drug-polymer system, and "n" is the coefficient related to the mechanism of drug release
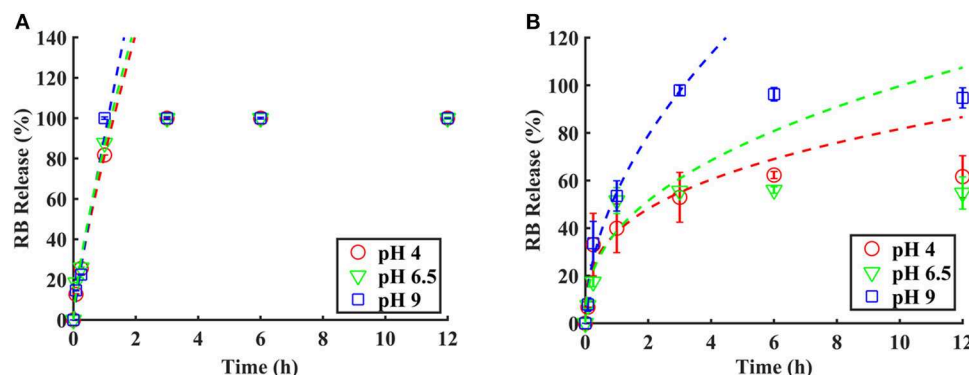
FIGURE 6 | RB release from **(A)** uncoated PVA-RB fibers and **(B)** coated PVA-RB fibers in PBS solutions at pH 4, 6.5, and 9. Data fitting was performed up to 60% of RB release using Peppas equation.

(Zamani et al., 2010; Nguyen et al., 2012; Gencturk et al., 2017). The dashed lines in **Figure 5** show the fits of Equation 1 to the early time data below 60%. The "*a*" and "*n*" values and the error R^2 obtained from the fits are given in **Table 1**.

The control experiments performed using the uncoated PVA-RB nanofibers reveal a fast-release kinetics at early times, which is not affected by the pH of the medium. The kinetic parameter "*n*" is found to be ~0.77, which indicates an anomalous transport mechanism, dominated by concentration-dependent diffusion and dissolution of the polymer. The release kinetics from the polymer-coated samples, on the other hand, reveals a pH dependent behavior. At all pH conditions, the values of "*n*" are less than the control samples, indicating that the Fickian diffusion dominates over the polymer dissolution mechanism in the coated samples (Fu and Kao, 2010). As the pH of the release medium increases, faster kinetics is observed as indicated by higher "*n*" values. Faster kinetics at high pH values can be attributed to the collapsed state of the coating, which leads to larger free volumes compared to low pH conditions.

Although Peppas model was used to fit the release data, it should be noted that the fit parameters obtained were mostly used to study the effect of the pH on the release kinetics and to comment on the dominant mechanisms, as opposed to thoroughly explaining the active mechanisms. Our system deviates from these models due to presence of an insoluble, pH-responsive polymer coating on the top and bottom layers of the mat. This coating impedes the full dissolution of the polymer nanofibers, introduces electrostatic interactions, and impacts the diffusion paths in the swollen state, thus affecting the release rate of the drug.

Cellular Response to p(4VP-*co*-EGDMA)-Coated PVA-RB Nanofibers
Immunocytochemistry of Cells Exposed to the Coated PVA-RB Nanofibers
The proliferation ability of the cells exposed to the coated PVA and coated PVA-RB nanofibers were also elucidated by

TABLE 1 | The "*a*" and "*n*" values obtained from the fit of Equation 1 to the release data of the coated and uncoated fibers.

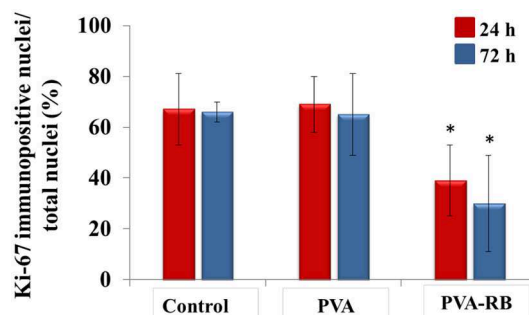|	Coated samples			Uncoated samples		
	R^2	n	a	R^2	n	a
pH 4	0.9096	0.3288	0.3829	0.9986	0.7991	0.8151
pH 6.5	0.9044	0.4110	0.3870	0.9876	0.7589	0.8693
pH 9	0.9461	0.5206	0.5503	0.9979	0.7655	0.7758

FIGURE 7 | Immunocytochemical investigation of coated PVA and coated PVA-RB exposed cells by staining with Ki67 markers at 24 and 72 h of incubation (analyzed with Student *t*-test *$p < 0.05$).

Ki67 antibody immunohistochemical staining that binds to the proliferating cell marker Ki67 antigens selectively. The results indicated that the decrease in the coated PVA nanofiber-exposed cells was insignificant while for the cells exposed to the coated PVA-RB nanofibers, cell proliferation decreased to 28% and 36% at the end of 24 and 72 h of incubations, respectively (**Figure 7**).

ROS Production in Cells Exposed to the Coated PVA-RB Nanofibers
As a defense mechanism, cells have the tendency to increase ROS production when they are exposed to foreign substances.
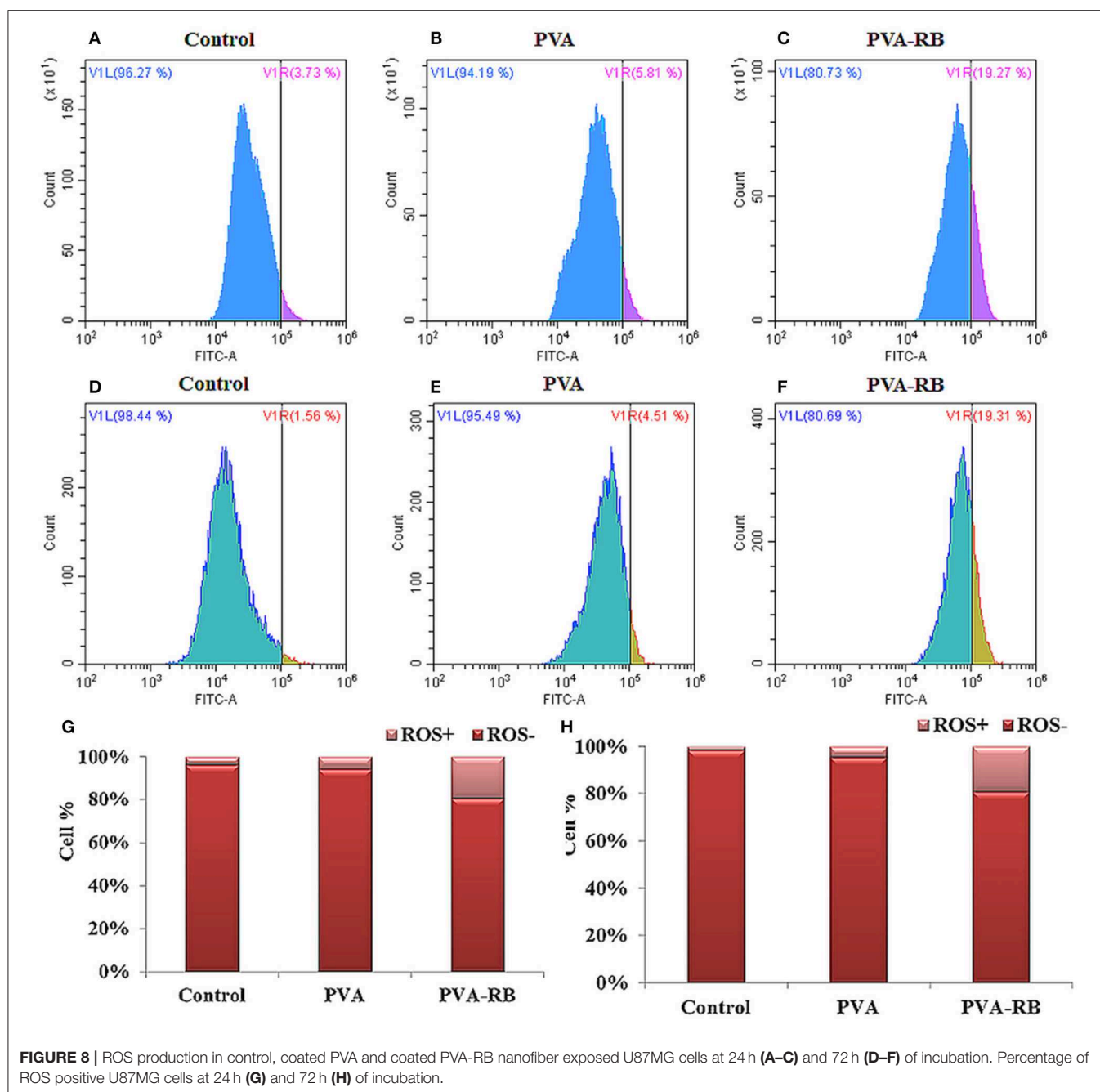
FIGURE 8 | ROS production in control, coated PVA and coated PVA-RB nanofiber exposed U87MG cells at 24 h **(A–C)** and 72 h **(D–F)** of incubation. Percentage of ROS positive U87MG cells at 24 h **(G)** and 72 h **(H)** of incubation.

The increased ROS levels in mitochondria cause cellular stress, and then stimulate further ROS production. High ROS level in the cells activates apoptosis processes due to the hindered cellular functions by damaged critical cell components, such as proteins, membrane lipids, and DNA (Murphy, 2009). In the light of the natural defense mechanism of cells, chemotherapy drugs are generally designed as ROS stimulating agents to activate apoptosis process. In this study, coated PVA-RB nanofibers were investigated comparatively to coated PVA nanofibers on U87MG brain cancer cells following 24

and 72 h of incubation, as shown in **Figure 8**. The results indicated that significant ROS level increment in coated PVA-RB fiber-exposed cells was observed (19%) after 24 and 72 h of incubation, as shown in **Figures 8C,E**, respectively. However, the ROS level of coated PVA nanofiber-exposed cells was about 5% after 24 and 72 h of incubation, as shown in **Figures 8B,D**, respectively. High levels of ROS produced in the cells exposed to the coated PVA-RB nanofibers indicated that RB induce damage in cells, as expected from chemotherapy drugs.
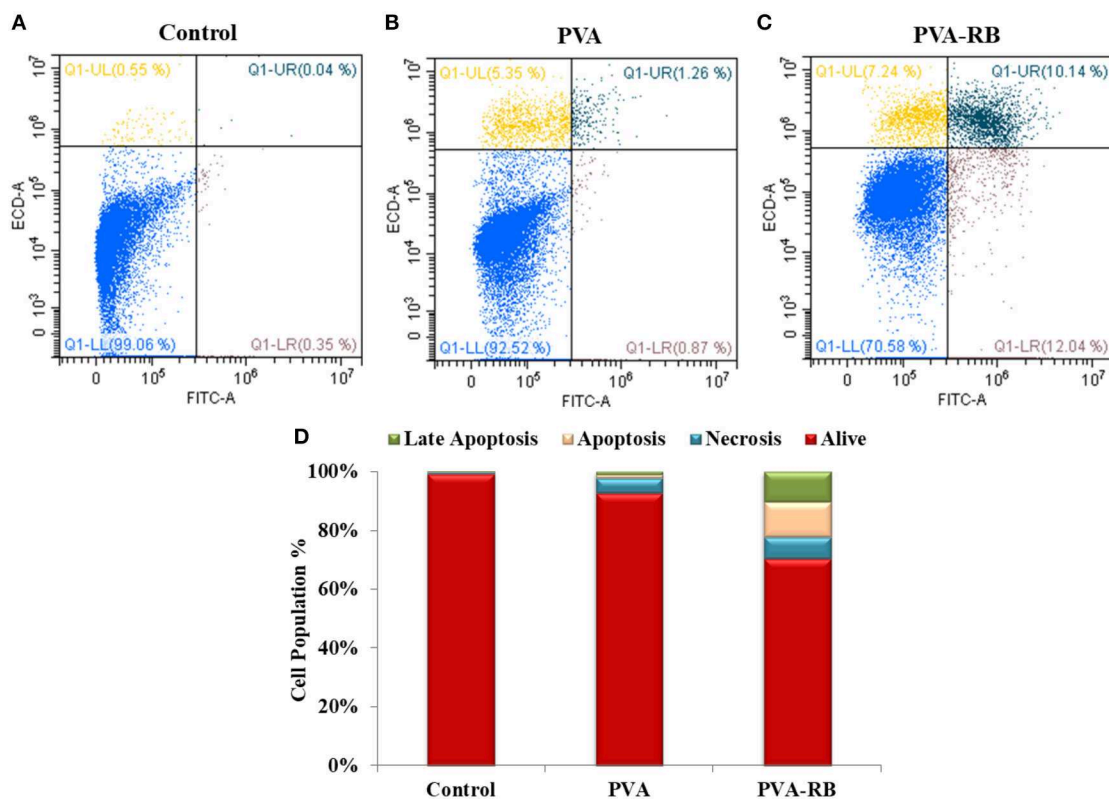
FIGURE 9 | Cell death mechanism in control **(A)**, coated PVA **(B)** and coated PVA-RB **(C)** nanofiber exposed U87MG cells at 24 h of incubation. **(D)** Percentage of living, apoptotic and necrotic cells.

Cell Death Mechanism of Cells Exposed to the Coated PVA-RB Nanofibers

The optimal *in vitro* conditions for cell death that mimic the organism were provided by Fink and Cookson (2005) to analyze the effects of structures on the death mechanism. Effects of the coated PVA-RB and coated PVA nanofibers were investigated on U87MG brain cancer cells, which were labeled with annexin-V and PI as indicators of apoptosis and necrosis, as reported in **Figure 9**.

The results showed that of all the cells exposed to coated PVA-RB nanofibers, 70% was alive, while 10, 12, and 7% of cells were in late apoptosis, apoptosis, and necrosis after 24 h of incubation, respectively (**Figure 9C**). On the other hand, 92% of the cells exposed to coated PVA nanofiber-exposed cells were alive, while 5% of the cells were in necrosis and 1% of cells were in late apoptosis after 72 h of incubation (**Figure 9B**). The results confirmed that RB-loaded nanofibers cause serious apoptotic and late apoptotic effects in glioblastoma cells, as targeted in cancer therapy applications.

CONCLUSION

A pH-responsive nanofiber mat loaded with RB was produced as a potential controlled drug delivery system for post-operational cancer treatments. A thin layer of pH-responsive cross-linked p(4VP-*co*-EGDMA) polymer was coated on PVA-RB blend nanofibers to attain pH response to the fibers and to tune

the release kinetics. The vapor-based iCVD technique was successfully employed for the conformal deposition of the polymer coating without damaging the nanofiber mat. The coating layer enabled the control of the degradation and release kinetics of the nanofibers by tuning the pH of the medium. The iCVD was demonstrated to be a successful technique to coat the nanofibers with stimuli-responsive, functional polymer films to attain additional properties to the fibers.

The therapeutic efficiency of coated PVA-RB nanofibers against brain cancer was investigated comparatively against the coated PVA nanofibers, to analyze the anti-cancer effect of RB released from the fibers. The results indicated that coated PVA-RB nanofibers selectively decreased cell proliferation and stimulated cell death in apoptotic direction by increasing ROS production in the cells at long-term incubation as desired in chemotherapeutic applications.

DATA AVAILABILITY STATEMENT

All datasets generated for this study are included in the article/**Supplementary Material**.

AUTHOR CONTRIBUTIONS

SSa designed the experiments, prepared the samples, and wrote the manuscript. AT performed the iCVD coatings and contributed to data analysis and interpretation. EO and SSh contributed to the electrospinning process and performed the

release studies. ME, GG, and OS performed the drug release studies of the nanofibers with *in vitro* cell culture experiments. GO and GC guided the study, wrote, and revised the manuscript.

SUPPLEMENTARY MATERIAL

The Supplementary Material for this article can be found online at: https://www.frontiersin.org/articles/10.3389/fbioe. 2019.00309/full#supplementary-material

REFERENCES

Aljehani, A. K., Hussaini, M. A., Hussain, M. A., Alothmany, N. S., and Aldhaheri, R. W. (2014). "Effect of electrospinning parameters on nanofiber diameter made of poly (vinyl alcohol) as determined by Atomic Force Microscopy," in *2nd Middle East Conference on Biomedical Engineering* (Doha: IEEE), 379–381. doi: 10.1109/MECBME.2014.6783283

Armagan, E., and Ince, G. (2015). Coaxial nanotubes of stimuli responsive polymers with tunable release kinetics. *Soft Matter* 11, 8069–8075. doi: 10.1039/C5SM01074H

Bayari, S., and Yurdakul, S. (2000). Fourier transform infrared and Raman spectra of 4-vinylpyridine and its transition metal (II) tetracyanonickelate complexes. *Spectrosc. Lett.* 33, 475–483. doi: 10.1080/00387010009350132

Bazhban, M., Nouri, M., and Mokhtari, J. (2013). Electrospinning of cyclodextrin functionalized chitosan/PVA nanofibers as a drug delivery system. *Chinese J. Polym. Sci.* 31, 1343–1351. doi: 10.1007/s10118-013-1309-5

Brown, C. L. III., and Crawford, N. (2002). *Iontophoresis Electroporation and Combination Patches for Local Drug Delivery to Body Tissues.* U.S. Patent No. 6,424,862. Washington, DC: U.S. Patent and Trademark Office.

Chakraborty, S., Liao, I. C., Adler, A., and Leong, K. W. (2009). Electrohydrodynamics: a facile technique to fabricate drug delivery systems. *Adv. Drug Deliv. Rev.* 61, 1043–1054. doi: 10.1016/j.addr.2009.07.013

Chunder, A., Sarkar, S., Yu, Y., and Zhai, L. (2007). Fabrication of ultrathin polyelectrolyte fibers and their controlled release properties. *Colloids Surf. B Biointerfaces* 58, 172–179. doi: 10.1016/j.colsurfb.2007.03.004

Croisier, F., Atanasova, G., Poumay, Y., and Jérôme, C. (2014). Polysaccharide-coated PCL nanofibers for wound dressing applications. *Adv. Healthc. Mater.* 3, 2032–2039. doi: 10.1002/adhm.201400380

Dabrzalska, M., Benseny-Cases, N., Barnadas-Rodríguez, R., Mignani, S., Zablocka, M., Majoral, J. P., et al. (2016). Fourier transform infrared spectroscopy (FTIR) characterization of the interaction of anti-cancer photosensitizers with dendrimers. *Anal. Bioanal. Chem.* 408, 535–544. doi: 10.1007/s00216-015-9125-0

Fink, S. L., and Cookson, B. T. (2005). Apoptosis, pyroptosis, and necrosis: mechanistic description of dead and dying eukaryotic cells. *Infec. Immun.* 73, 1907–1916. doi: 10.1128/IAI.73.4.1907-1916.2005

Fu, Y., and Kao, W. J. (2010). Drug release kinetics and transport mechanisms of non-degradable and degradable polymeric delivery systems. *Expert Opin. Drug Deliv.* 7, 429–444. doi: 10.1517/17425241003602259

Garg, T., Malik, B., Rath, G., and Goyal, A. K. (2014). Development and characterization of nano-fiber patch for the treatment of glaucoma. *Eur. J. Pharm. Sci.* 53, 10–16. doi: 10.1016/j.ejps.2013.11.016

Gencturk, A., Kahraman, E., Güngör, S., Özhan, G., Özsoy, Y., and Sarac, A. S. (2017). Polyurethane/hydroxypropyl cellulose electrospun nanofiber mats as potential transdermal drug delivery system: characterization studies and *in vitro* assays. *Artif. Cells Nanomed. Biotechnol.* 45, 655–664. doi: 10.3109/21691401.2016.1173047

He, C. L., Huang, Z. M., Han, X. J., Liu, L., Zhang, H. S., and Chen, L. S. (2006). Coaxial electrospun poly (L-lactic acid) ultrafine fibers for sustained drug delivery. *J. Macromol. Sci. B* 45, 515–524. doi: 10.1080/00222340600769832

Huang, R. Y. M., and Rhim, J. W. (1993). Modification of poly (vinyl alcohol) using maleic acid and its application to the separation of acetic acid-water mixtures by the pervaporation technique. *Polym. Int.* 30, 129–135. doi: 10.1002/pi.4990300119

Jalvandi, J., White, M., Gao, Y., Truong, Y. B., Padhye, R., and Kyratzis, I. L. (2017). Polyvinyl alcohol composite nanofibres containing conjugated levofloxacin-chitosan for controlled drug release. *Mater. Sci. Eng.* 73, 440–446. doi: 10.1016/j.msec.2016.12.112

Jannesari, M., Varshosaz, J., Morshed, M., and Zamani, M. (2011). Composite poly (vinyl alcohol)/poly (vinyl acetate) electrospun nanofibrous mats as a novel wound dressing matrix for controlled release of drugs. *Int. J. Nanomed.* 6, 993–1003. doi: 10.2147/IJN.S17595

Kenawy, E. R., Abdel-Hay, F. I., El-Newehy, M. H., and Wnek, G. E. (2007). Controlled release of ketoprofen from electrospun poly (vinyl alcohol) nanofibers. *Mater. Sci. Eng.* 459, 390–396. doi: 10.1016/j.msea.2007.01.039

Kenawy, E. R., Bowlin, G. L., Mansfield, K., Layman, J., Simpson, D. G., Sanders, E. H., et al. (2002). Release of tetracycline hydrochloride from electrospun poly (ethylene-co-vinylacetate), poly (lactic acid), and a blend. *J. Control. Release* 81, 57–64. doi: 10.1016/S0168-3659(02)00041-X

Koevary, S. B. (2012). Selective toxicity of rose bengal to ovarian cancer cells *in vitro*. *Int. J. Physiol. Pathophysiol. Pharmacol.* 4, 99–107.

Korsmeyer, R. W., Gurny, R., Doelker, E., Buri, P., and Peppas, N. A. (1983). Mechanisms of solute release from porous hydrophilic polymers. *Int. J. Pharm.* 15, 25–35. doi: 10.1016/0378-5173(83)90064-9

LaPorte, S., Haller, M., Hooper, W., Lent, M., Riff, K., Heruth, K., et al. (2005). *Implantable Medical Device and Patch System and Method of Use.* U.S. Patent Application No. 10/137,516.

Lau, K. K., and Gleason, K. K. (2006). Initiated chemical vapor deposition (iCVD) of poly (alkyl acrylates): an experimental study. *Macromolecules* 39, 3688–3694. doi: 10.1021/ma0601619

Lau, K. K., and Gleason, K. K. (2007). All-dry synthesis and coating of methacrylic acid copolymers for controlled release. *Macromol. Biosci.* 7, 429–434. doi: 10.1002/mabi.200700017

Li, D., He, Q., Yang, Y., Möhwald, H., and Li, J. (2008). Two-stage pH response of poly (4-vinylpyridine) grafted gold nanoparticles. *Macromolecules* 41, 7254–7256. doi: 10.1021/ma800894c

Li, W., Xu, R., Zheng, L., Du, J., Zhu, Y., Huang, R., et al. (2012). LBL structured chitosan-layered silicate intercalated composites based fibrous mats for protein delivery. *Carbohydr. Polym.* 90, 1656–1663. doi: 10.1016/j.carbpol.2012.07.046

Li, X., Kanjwal, M. A., Lin, L., and Chronakis, I. S. (2013). Electrospun polyvinyl-alcohol nanofibers as oral fast-dissolving delivery system of caffeine and riboflavin. *Colloids Surf. B Biointerfaces* 103, 182–188. doi: 10.1016/j.colsurfb.2012.10.016

Mansur, H. S., Sadahira, C. M., Souza, A. N., and Mansur, A. A. (2008). FTIR spectroscopy characterization of poly (vinyl alcohol) hydrogel with different hydrolysis degree and chemically crosslinked with glutaraldehyde. *Mater. Sci. Eng.* 28, 539–548. doi: 10.1016/j.msec.2007.10.088

Murphy, M. P. (2009). How mitochondria produce reactive oxygen species. *Biochem. J.* 417, 1–13. doi: 10.1042/BJ20081386

Nelson, K. D., Romero-Sanchez, A. A., Smith, G. M., Alikacem, N., Radulescu, D., Waggoner, P., et al. (2003). *Drug Releasing Biodegradable Fiber Implant.* U.S. Patent No. 6,596,296. Washington, DC: U.S. Patent and Trademark Office.

Nguyen, T. T. T., Ghosh, C., Hwang, S. G., Chanunpanich, N., and Park, J. S. (2012). Porous core/sheath composite nanofibers fabricated by coaxial

electrospinning as a potential mat for drug release system. *Int. J. Pharm.* 439, 296–306. doi: 10.1016/j.ijpharm.2012.09.019

Oliveira, M. F., Suarez, D., Rocha, J. C. B., de Carvalho Teixeira, A. V. N., Cortés, M. E., De Sousa, F. B., et al. (2015). Electrospun nanofibers of polyCD/PMAA polymers and their potential application as drug delivery system. *Mater. Sci. Eng.* 54, 252–261. doi: 10.1016/j.msec.2015.04.042

Ozaydin-Ince, G., Coclite, A. M., and Gleason, K. K. (2011). CVD of polymeric thin films: applications in sensors, biotechnology, microelectronics/organic electronics, microfluidics, MEMS, composites and membranes. *Rep. Prog. Phys.* 75:016501. doi: 10.1088/0034-4885/75/1/016501

Qin, J., Kunda, N., Qiao, G., Calata, J. F., Pardiwala, K., Prabhakar, B. S., et al. (2017). Colon cancer cell treatment with rose bengal generates a protective immune response via immunogenic cell death. *Cell Death Dis.* 8:e2584. doi: 10.1038/cddis.2016.473

Sakai, S., Yamada, Y., Yamaguchi, T., Ciach, T., and Kawakami, K. (2009). Surface immobilization of poly (ethyleneimine) and plasmid DNA on electrospun poly (L-lactic acid) fibrous mats using a layer-by-layer approach for gene delivery. *J. Biomed. Mater. Res. A* 88, 281–287. doi: 10.1002/jbm.a.31870

Sharma, A., Gupta, A., Rath, G., Goyal, A., Mathur, R. B., and Dhakate, S. R. (2013). Electrospun composite nanofiber-based transmucosal patch for anti-diabetic drug delivery. *J. Mater. Chem. B* 1, 3410–3418. doi: 10.1039/c3tb20487a

Song, W., Yu, X., Markel, D. C., Shi, T., and Ren, W. (2013). Coaxial PCL/PVA electrospun nanofibers: osseointegration enhancer and controlled drug release device. *Biofabrication* 5:035006. doi: 10.1088/1758-5082/5/3/035006

Taepaiboon, P., Rungsardthong, U., and Supaphol, P. (2006). Drug-loaded electrospun mats of poly (vinyl alcohol) fibres and their release characteristics of four model drugs. *Nanotechnology* 17, 2317–2329. doi: 10.1088/0957-4484/17/9/041

Thakkar, S., and Misra, M. (2017). Electrospun polymeric nanofibers: new horizons in drug delivery. *Eur. J. Pharm. Sci.* 107, 148–167. doi: 10.1016/j.ejps.2017.07.001

Theeuwes, F., and Nelson, T. S. (2004). *Implantable Drug Delivery Patch.* U.S. Patent No. 6,726,920. Washington, DC: U.S. Patent and Trademark Office.

Tipduangta, P., Belton, P., Fábián, L., Wang, L. Y., Tang, H., Eddleston, M., et al. (2015). Electrospun polymer blend nanofibers for tunable drug delivery: the role of transformative phase separation on controlling the release rate. *Mol. Pharm.* 13, 25–39. doi: 10.1021/acs.molpharmaceut.5b00359

Toomey, P., Kodumudi, K., Weber, A., Kuhn, L., Moore, E., Sarnaik, A. A., et al. (2013). Intralesional injection of rose bengal induces a systemic tumor-specific immune response in murine models of melanoma and breast cancer. *PLoS ONE* 8:e68561. doi: 10.1371/journal.pone.0068561

Tserkovsky, D. A., Alexandrova, E. N., Chalau, V. N., and Istomin Yu, P. (2012). Effects of combined sonodynamic and photodynamic therapies with photolon on a glioma c6 tumor model. *Exp. Oncol.* 34, 332–335.

Wang, B., Wang, Y., Yin, T., and Yu, Q. (2010). Applications of electrospinning technique in drug delivery. *Chem. Eng. Commun.* 197, 1315–1338. doi: 10.1080/00986441003625997

Wang, Y., Kozlovskaya, V., Arcibal, I. G., Cropek, D. M., and Kharlampieva, E. (2013). Highly swellable ultrathin poly (4-vinylpyridine) multilayer hydrogels with pH-triggered surface wettability. *Soft Matter* 9, 9420–9429. doi: 10.1039/c3sm51496j

Xu, X., Chen, X., Xu, X., Lu, T., Wang, X., Yang, L., et al. (2006). BCNU-loaded PEG–PLLA ultrafine fibers and their *in vitro* antitumor activity against Glioma C6 cells. *J. Control. Release* 114, 307–316. doi: 10.1016/j.jconrel.2006.05.031

Yang, D., Li, Y., and Nie, J. (2007). Preparation of gelatin/PVA nanofibers and their potential application in controlled release of drugs. *Carbohydr. Polym.* 69, 538–543. doi: 10.1016/j.carbpol.2007.01.008

Zamani, M., Morshed, M., Varshosaz, J., and Jannesari, M. (2010). Controlled release of metronidazole benzoate from poly ε-caprolactone electrospun nanofibers for periodontal diseases. *Eur. J. Pharm. Biopharm.* 75, 179–185. doi: 10.1016/j.ejpb.2010.02.002

Zamani, M., Prabhakaran, M. P., and Ramakrishna, S. (2013). Advances in drug delivery via electrospun and electrosprayed nanomaterials. *Int. J. Nanomedicine* 8, 2997–3017. doi: 10.2147/IJN.S43575

Zeng, J., Aigner, A., Czubayko, F., Kissel, T., Wendorff, J. H., and Greiner, A. (2005). Poly (vinyl alcohol) nanofibers by electrospinning as a protein delivery system and the retardation of enzyme release by additional polymer coatings. *Biomacromolecules* 6, 1484–1488. doi: 10.1021/bm0492576

Zhang, Y., Huang, Z. M., Xu, X., Lim, C. T., and Ramakrishna, S. (2004). Preparation of core– shell structured PCL-r-gelatin bi-component nanofibers by coaxial electrospinning. *Chem. Mater.* 16, 3406–3409. doi: 10.1021/cm049580f

Zupančič, S., Sinha-Ray, S., Sinha-Ray, S., Kristl, J., and Yarin, A. L. (2016). Controlled release of ciprofloxacin from core–shell nanofibers with monolithic or blended core. *Mol. Pharm.* 13, 1393–1404. doi: 10.1021/acs.molpharmaceut.6b00039

Synthesis, Functionalization, and Bioapplications of Two-Dimensional Boron Nitride Nanomaterials

Melis Emanet[†], Özlem Sen[†], Irem Çulha Taşkin and Mustafa Çulha *

Department of Genetics and Bioengineering, Faculty of Engineering, Yeditepe University, Istanbul, Turkey

Two-dimensional boron nitride nanostructures (2D-BNNs) have been increasingly investigated for their applications in several scientific and technological areas. This considerable interest is due to their unique physicochemical properties, which include high hydrophobicity, heat and electrical insulation, resistance to oxidation, antioxidation capacity, thermal conductivity, high chemical stability, mechanical strength, and hydrogen storage capacity. They are also used as fillers, antibacterial agents, protective coating agents, lubricants, boron neutron capture therapy agents, nanocarriers for drug delivery, and for the receptor phase in chemosensors. The investigations for their use in medicine and biomedicine are very promising, including cancer therapy and wound healing. In this review, 2D-BNNs synthesis and their surface modification strategies, biocompatibility, and bioapplication studies are discussed. Finally, a perspective for the future use of these novel nanomaterials in the biomedical field is provided.

Keywords: two-dimensional boron nitride nanoparticles, synthesis, functionalization, biocompatibility, bioapplication

INTRODUCTION

It is generally considered that boron nitride (BN)-based nanomaterials are not naturally formed, but the cubic crystalline boron nitrides (cBNs) are found in some rare mineral sites of Tibet and China, which suggests their natural occurrence (Du Frane et al., 2016; Yin et al., 2016). Today, most BN nanomaterials are synthesized in laboratories and are composed of an equal number of boron (B) and nitrogen (N) atoms that have specific conformations leading to different structure crystallinity (Pakdel et al., 2012). As the most stable form of BNs, hexagonal boron nitrides (hBNs) have strong covalent bonds between B-N atoms with a graphene-like structure. The 2D BN layers are held together through van der Waals interactions (Weng et al., 2016). On the other hand, in the rhomboedral (rBNs), diamond-like (cBNs), and wurzite boron nitrides (wBNs), B and N atoms are sp^3 hybridized, binding to the neighboring BN_3 tetrahedrons at different angles restraining the identical pattern of B and N atoms. The varying crystallinity in BN structures are obtained under different experimental conditions, such as temperature and pressure (Merlo et al., 2018). While hBNs and rBNs are produced at ambient pressure and at high temperature, wBNs form hBNs under high pressure at room temperature. cBNs are prepared from hBNs under high pressure at high temperature (Han, 2010).

   BN nanomaterials are the structural analogs of graphene. The main difference between BN-based nanomaterials and their C counterparts is the nature of the bonds between the atoms. The bond C-C in carbon nanomaterials has a pure covalent character, while B-N bonds present a partially ionic character due to the e^- pairs in sp^2 hybridized B-N. The

e^- pairs are more confined to N atoms owing to their high electronegativity in BN-based nanomaterials that strongly affect mechanical, optical, and electronic properties (Arenal and Lopez-Bezanilla, 2015; Jiang et al., 2015). Therefore, BN-based nanomaterials can improve thermal conductivity (Chang et al., 2005) and the mechanical (Sen and Çulha, 2015; Emanet et al., 2016) and antioxidant (Chen et al., 2004; Li et al., 2018) properties of several composites. High thermal conductivity and improved mechanical properties, including high tensile strength and elasticity, which BN-based nanomaterials can provide, are in high demand, for example for the construction of tissue-mimicking biomaterials used in transplantation (Jo et al., 2013). The finding that BN-based nanomaterials might have piezoelectric properties may allow for the generation of novel biomaterials used in tissue-engineering processing (Merlo et al., 2018). Another important property includes making BN-based nanomaterials more favorable for additives, as compared to their C counterparts, is their electrical insulation.

In recent years, BN-based nanomaterials have grasped the attention of researchers for their possible use in medical applications due to their good biocompatibility (Chen et al., 2009; Salvetti et al., 2015; Li et al., 2017) and high chemical and mechanical stability (Lahiri et al., 2011; Liu et al., 2015). In addition, their cellular internalization allowed the researchers to investigate their possible use as drug and gene carriers (Horvath et al., 2011). The therapeutic effects of boron compounds in cancer treatment also made the BN-based nanomaterials interesting structures as controlled release boron sources (Li et al., 2017). They have also been widely used in cosmetics, lubricants, insulators, and microwave-transparent materials (Jiang et al., 2015). cBNs are also called white diamonds because of their high Young's modulus compared to diamonds. They are used to cut many industrial ferrous materials, and they do not react with the related alloys, as is the case with diamonds (Han, 2010).

One-dimensional (1D) nanotubes and nanoribbons, two-dimensional (2D) nanospheres and nanosheets, and three-dimensional (3D) nanoporous BNs are typical examples of BN nanomaterials (Jiang et al., 2015). Among these nanomaterials, low dimensional nanomaterials show quantum confinement and interfacial effects compared to 3D nanomaterials. There is therefore a significant effort to use these nanomaterials with unusual physicochemical properties in novel applications (Pakdel et al., 2012). Moreover, several physical forms of the 2D nanospheres, including nanocages, nanococoons, and hollow BNs, have been synthesized, as shown in **Figure 1**, thereby providing an opportunity to choose a suitable form of 2D nanostructure for the desired applications.

In this review, synthesis methods of 2D-BNNs will be discussed first, and then their functionalization, biocompatibility, and bioapplications in drug delivery, composites, cosmetics, therapeutics, and pharmaceuticals will be discussed.

SYNTHESIS OF 2D-BNNs

The synthesis of different forms of 2D-BNNs is widely investigated in the literature, and the most relevant ones to the subject of this review are discussed here. **Table 1** shows some of the methods and experimental conditions used to synthesize 2D-BNNs. As seen, several B and N precursors were used to obtain BN-based nanomaterials with different sizes and shapes.

2D-BN nanococoons are produced through a synthesis approach typical of that followed for boron nitride nanotubes (BNNTs) using an arc discharge method already established in 2000 (Cuming and Zettl, 2000). Although this method is the easiest bulk quantity carbon nanotube production method, it was not efficient to be used for production of BN-based nanomaterials because of their non-conductive nature. To establish electrical conductivity, the use of a metal was reported in the literature (Chopra et al., 1995). However, it resulted in accumulation of high amounts of metal impurities in the synthesis environment. In the case of the 2D-BN nanococoons mentioned above, 99% elemental boron as a boron precursor, with 1% nickel and cobalt acting as a catalyst, was brought into close contact with electrodes. The synthesis procedure generated clustered nanocrystals individually coated with multi-layer graphite-like BNs. The authors managed to remove the interiors of the nanocrystal from the BN cage structures to obtain hollow BN "nanococoons."

BN spheres are one of the commonly reported structures, and the chemical vapor deposition (CVD) is a golden-standard synthesis method. For example, hexagonal BN spheres were synthesized through a two-step procedure using CVD (Wood et al., 2006). In the first step, B-N-O particles were synthesized from trimethyl borate (B(OMe)$_3$) and ammonia precursors; then, oxygen atoms were removed from spheres by heating them under an ammonia atmosphere at high temperature. Tang et al. claimed that the (OMe)$_3$BNH$_3$ complex was produced in place of removing oxygen atoms from the structure at the second step (Tang et al., 2008). Another intermediate phase was therefore introduced to produce BN spheres. The BN ceramics were formed using dehydrogenative hydrolysis from BH$_3$NH$_3$ to eliminate hydrogen. At the end, B-O impurities generated the nuclear center of BN spheres with a size range of 50–400 nm (Tang et al., 2008). In a further study, argon (Ar) gas was exploited instead of NH$_3$, allowing B-O evaporation from the inner part of nanospheres during the second phase of the synthesis to obtain hollow BN nanomaterials in a hexagonal lattice structure (Li et al., 2017).

The synthesis of nearly monodisperse 2D-hexagonal boron nitride nanoparticles (2D-BNNs) was achieved via a modified solid-state metathesis reaction route (Lian et al., 2010). In the study, sulfur was used as catalyst to produce 2D-BNNs at a relatively low temperature of 250°C. With this information on hand, the synthesis was attempted using ammonium borofluoride (NH$_4$BF$_4$), with sodium azide (NaN$_3$) used as precursors and sulfur as a catalyst. The mixture was ball milled, and then pressed at 250°C for 20 h. Finally, the product was washed with hydrochloric acid (HCl), benzene (C$_6$H$_6$), and
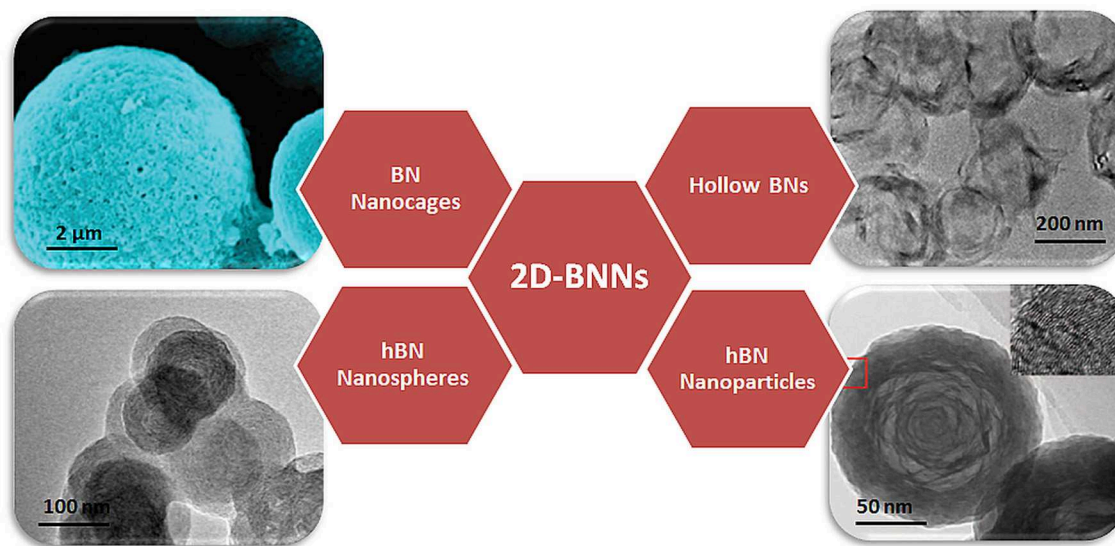
FIGURE 1 | Schematical representation of several physical forms of BN nanospheres. Reproduced with Permission from Tian et al. (2013) and Zhang et al. (2012).
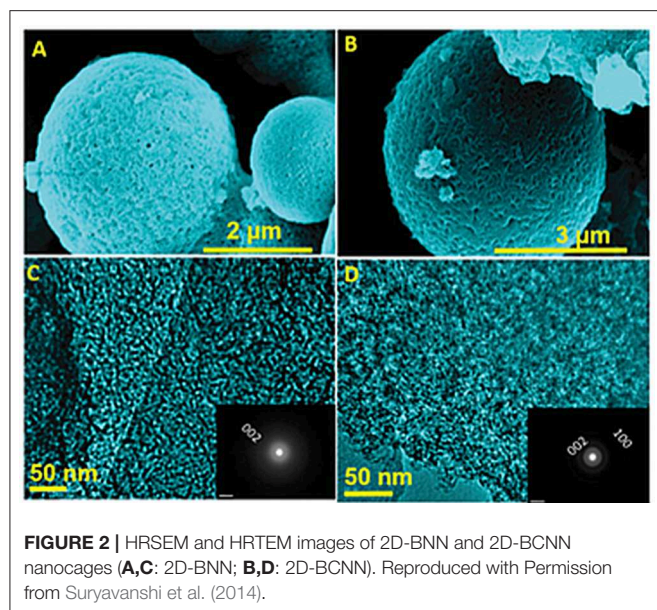
TABLE 1 | Reaction conditions and methods to produce 2D-BNNs.

Precursors	Environmental conditions	Catalyst	Methods	Purifying	Product	References
Boron-rich conducting electrodes	N_2 gas	Nickel, cobalt	Plasma-arc discharge	None	hBN Nanococoons	Cuming and Zettl, 2000
$(B(OMe)_3)$	NH_3 gas, 800–1,500°C	None	CVD	None	BN spheres	Wood et al., 2006; Tang et al., 2008
$(B(OMe)_3)$	NH_3 and Ar gas, 800–1,500°C	None	CVD	None	Hollow BNs	Li et al., 2017
NH_4BF_4 and NaN_3	N_2 gas, 250°C, 450 MPa	S	Ball milling	(HCl), C_6H_6, ddH_2O	hBN	Lian et al., 2010
H_3BO_3, $C_3H_6N_6$	NH_3 gas, 1600°C	None	CVD	None	BN	Ansaloni and Sousa, 2013
Carbon nanocages, B_2O_3	NH_3 gas, 1350-1450°C	None	Elemental substitution reaction	None	BN and BCN nanocages	Suryavanshi et al., 2014
Boron powder	NH3 gas	Fes/Fe_2O_3	TCVD	None	BN nanosheets	Ansaloni and Sousa, 2013
H_3BO_3, Colemanite, B_2O_3	NH_3 gas, 1300°C	None	CVD	None	hBN	Sen et al., 2018

deionized water to remove iron, sulfur, and water-soluble salt impurities, respectively. Nearly monodisperse 2D-BNNs, in the size range of 35–45 nm, were obtained progressing the synthesis efforts toward a high yielding low-energy state.

The ceramic structure of 2D-BNNs has become an interesting material used in cosmetic formulations to provide better lubricity and other uses, such as blocking UV radiation. Thus, their synthesis in large quantities is necessary. Addressing this issue, a two-step synthesis procedure was reported (Ansaloni and Sousa, 2013). In this procedure, first, boric acid (H_3BO_3) and melamine ($C_3H_6N_6$) solutions were prepared and mixed for 48 h. Then, their precipitate was filtered and dried at 37°C. The obtained product, $B_4N_3O_2H$ (precursor of 2D-BNNs), was first heated to

500°C, and, then, it was placed in an aluminum boat to heat at 1,600°C under ammonia gas flow for 2 h. This procedure yielded large amounts of hBN-based 2D-BNNs, and their infrared light absorption ability was very good at making these materials powerful additives for sunscreen application. The synthesis of spherical BN and BCNs was also reported. The synthesis was accomplished via an elemental substitution reaction, as shown in **Figure 2**, where carbon nanocages were used as a template, and boron trioxide (B_2O_3) was used as a boron source (Suryavanshi et al., 2014). They were mixed and heated under an NH_3 gas flow for a substitution reaction. Microspheres with a size range of 1–3 μm were formed with interconnected holes, suggesting the elemental substitution of B and N atoms in place of C atoms.

FIGURE 2 | HRSEM and HRTEM images of 2D-BNN and 2D-BCNN nanocages (**A,C**: 2D-BNN; **B,D**: 2D-BCNN). Reproduced with Permission from Suryavanshi et al. (2014).

The obtained product had a highly crystalline wall structure and uniform pore size distribution, further confirming the elemental substitution process.

Considering their biocompatibility and low cytotoxicity, BN-based nanomaterials can also be used in biological applications, including imaging. In one report, it was shown that hBN-patterned 2D-BN nanosheets had luminescent properties (Ansaloni and Sousa, 2013). They were synthesized from boron powders with NH_3 gas as precursors and FeS/Fe_2O_3 as catalysts via a thermal chemical vapor deposition (TCVD) method, and they were well-characterized, using several spectroscopic and imaging techniques to ensure the structural elucidation of the material (Ansaloni and Sousa, 2013). We also successfully synthesized hBNs with a one-step synthesis method using H_3BO_3, colemanite, or B_2O_3, as boron precursors (Sen et al., 2018). The synthesis was performed via the CVD method under ammonia gas flow at 1,300°C for 2 h. In this synthesis method, we did not use a catalyst, creating the opportunity to prepare completely pure hBNs. We also found that the boron source had an influence on their crystallinity, stability, and biodegradability in suspensions mimicking oxidative and hydrolytic degradation environments. We have concluded that an appropriate boron precursor should have been chosen depending on the target application when the crystallinity of the product is critical.

Based on the synthesis methods reported to date, it is clear that the synthesis parameters, including precursors, temperature, and pressure, are acutely important to the structure of 2D-BNNs and have a significant effect on their crystal and morphological structures. Thus, the synthesis method vs. the target application should be carefully considered. At the moment, we are not at the point where the synthesis method and the structural relationship are clearly established. More work is needed to address this point for the full benefits of these novel structures. Although a certain level of success has been achieved, a significant effort to

develop a universal approach satisfying desired product quality is necessary.

FUNCTIONALIZATION OF 2D-BNNs

Chemical Functionalization of 2D-BNNs

The functionalization of 2D-BNNs is specifically aimed at improving their applicability in biomedical applications through several routes. 2D-BNNs are composed of an equal number of sp^2 hybridized, covalently linked B and N atoms, which generate a highly stable hexagonal BN network. Differences in electronegativity in B and N atoms result in also making the structure interesting from a functionalization point of view. Electron pairs in their sp^2 hybridization are closer to N atoms due to their higher electronegativity making B atoms more electron deficient and favorable for covalent functionalization (Ikuno et al., 2007). Both N and B atoms are targeted for functionalization at the layer edges or defects. Either a hydroxyl group is attached to B or N atoms are converted to $-NH_2$ groups.

A summary of recent reports demonstrating the functionalization of 2D-BNNs and their final products is provided in **Table 2**. Despite the promising progress in the functionalization strategies, the yield is still lower than the desired target. This can perhaps be explained with the highly stable and inert chemical structure of 2D-BNNs.

In one hydroxylation study, a simple sonication in deionized water was used to generate -OH on B atoms, which was named as a "clean" method (Lin et al., 2011). The formation of hydroxyl groups was confirmed from the FT-IR spectra through the peaks that appeared at around 3,414 cm^{-1}. In another study, the formation of -OH groups on B atoms was attempted in the solution phase by forming oxygen radicals (Sainsbury et al., 2012). This procedure involves two steps; first, chemically grafting alkoxyl groups on 2D-BNNs, followed by the hydrolytic de-functionalization of the groups, using acidic solutions to obtain the hydroxyl groups. From the TGA analysis, it was found that about 4 wt% of boron atoms in the lattice were functionalized by taking the tert-butoxy groups into account. Along a BN sheet edge, the presence of four boron atoms at every nanometer was predicted, which means that sheet-edge boron atoms are 0.044% of the total atoms in the nanosheets. Since TGA analysis indicates that about 4% of boron atoms are functionalized, about two orders of magnitude difference suggest the functionalization of the center atoms of the nanosheets through the proposed oxygen radical assertion functionalization mechanism. Lee et al. proposed a scalable exfoliation process for the hydroxylation of 2D-BNNs using a ball-milling method with sodium hydroxide (Lee et al., 2015). This sodium hydroxide-assisted ball-milling process generated a higher yield (18%) of 2D-BNN hydroxylation, and they were stably dispersed in various aqueous environments that were essential for biomedical applications. In a new and interesting method, BNs with high hydroxylation degrees using thermal substitution of C atoms with boric acid substructures in graphitic carbon nitrides ($g-C_3N_4$) were prepared. The synthesized BN(OH)x (x = 0.6–0.9) was highly water soluble and porous. The suspension was prepared

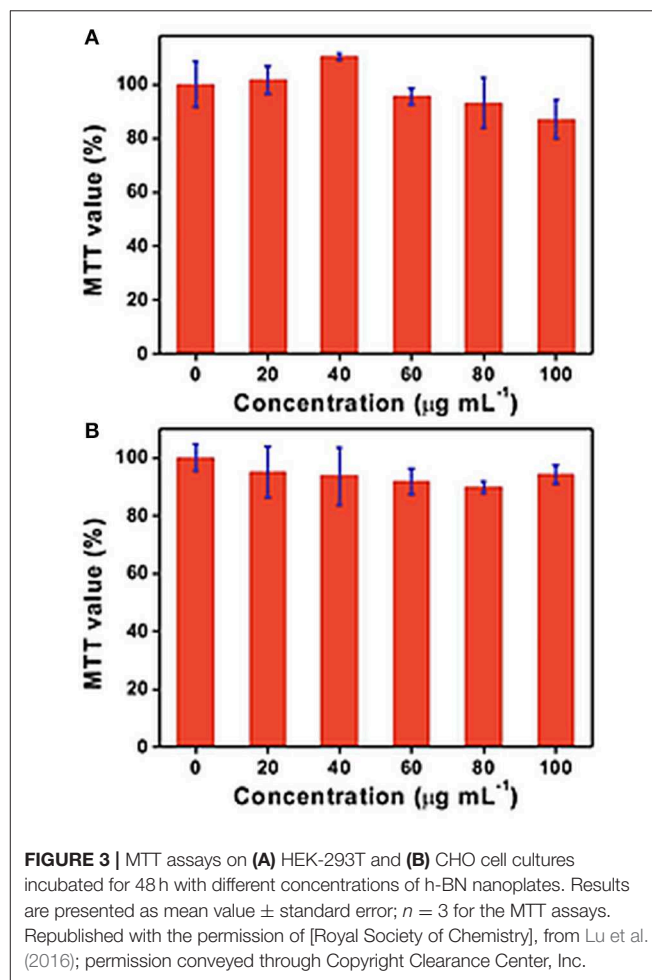**TABLE 2 |** Several functionalization approaches of 2D-BNNs.

Precursors	Chemicals	Method	Purification	Product	References
BN	ddH$_2$O	Sonication	None	BN-OH	Lin et al., 2011
BN	Alkoxyl groups	Solution phase oxygen radical functionalization	Hydrolytic defunctionalization	BN-OH	Sainsbury et al., 2012
BN	Sodium hydroxide	Ball milling method	None	BN-OH	Lee et al., 2015
BN	N$_3$C$_4$	Reverse reaction (elemental substitution reaction)	None	BN-OH	Weng et al., 2014
BN	PEG	Exfoliation	None	BN-NH$_2$	Lin et al., 2009
BN	Urea	Ball milling method	None	BN-NH$_2$	Lei et al., 2015

by dispersing it as high as 2.0 mg mL^{-1} in water, and it was stable and highly transparent (Weng et al., 2014).

Generating amine groups from N atoms in the structure of 2D-BNNs was first studied by Lin et al. by inducing the exfoliation of 2D-BNNs into some layers or monolayers to obtain electron-deficient B atoms for amine group formation through Lewis-base interactions (Lin et al., 2009). The synthesized amine group-functionalized 2D-BNNs were significantly soluble in water and common organic solvents. In another study, amine functionalization was performed by urea-assisted exfoliation of the 2D-BNNs using, once again, mechano-chemical reactions. The 2D-BNNs and urea were ball-milled under nitrogen atmosphere to generate amino groups (Lei et al., 2015).

BIOCOMPATIBILITY OF 2D-BNNs

Biocompatibility is a crucial step that should be clarified in order to identify any potential adverse effects before using nanomaterials can be used for biomedical applications. Although 2D-BNNs have been employed in biomedical applications, there is no clear consensus for their biocompatibility so far. In some studies, it has been found that the toxicity of the hBNs is dependent on cell type, dosage, and aspect ratio. In an attempt to evaluate the biocompatibility of hBNs, Lu et al. reported that the concentrations of 2D-BNNs up to 100 μg/mL with lateral size dimensions of 30–60 nm did not significantly affect the viability of HEK-293T and Chinese hamster ovary (CHO) cell lines (Lu et al., 2016). The findings were based on MTT [3-(4,5-dimethylthiazol-2-yl)-2,5-diphenyltetrazolium bromide, a tetrazole] colorimetric assay after 48 h incubation as shown in **Figure 3**. Furthermore, 2D-BNNs did not increase the apoptotic rate of both cell lines suggesting the safe use of 2D-BNNs in living systems. In another study, 2D-BNNs with average particle size of 121 nm were tested using Madin-Darby Canine Kidney (MDCK) and human normal skin fibroblast (CRL 2120) cell lines (Kivanç et al., 2018). The cell viability was assessed again using MTT, sulforhodamine B (SRB), and PicoGreen assays. The results indicated that the 2D-BNNs could be used up to 100 μg/mL on both cell lines without showing any cytotoxicity. The study concluded that 2D-BNNs could be considered potentially safe for oral care products (Kivanç et al., 2018).

FIGURE 3 | MTT assays on **(A)** HEK-293T and **(B)** CHO cell cultures incubated for 48 h with different concentrations of h-BN nanoplates. Results are presented as mean value ± standard error; $n = 3$ for the MTT assays. Republished with the permission of [Royal Society of Chemistry], from Lu et al. (2016); permission conveyed through Copyright Clearance Center, Inc.

Li et al. investigated 2D-BNNs with lateral size dimensions of 50–60 nm on androgen-sensitive LNCaP and androgen-independent DU145 prostate cancer cell lines up to 25 μg/mL with 3 and 6 days of incubations (Li et al., 2017). The cell viability was assessed using WST-8, annexin V-FITC/propidium iodide (PI), and LDH assays. It was found that 2D-BNNs crystallinity affected the B release, and this consequently decreased the cell viability at increasing concentrations and incubation times,

also inducing apoptosis. The results suggested that 2D-BNNs could be used as a novel therapeutic agent in prostate cancer treatment. Further, Mateti et al. performed MTS and 2,2-diphenyl-1-picrylhydrazyl (DPPH)-free radical assays to evaluate the cytotoxicity and biocompatibility of 2D-BNNs (Mateti et al., 2018). Micrometer-sized 2D-BNNs with a concentration of 1 mg/mL showed that they are biocompatible on the SaOS2 cell line (a human osteosarcoma cell line). However, 2D-BNNs with a concentration of 1 mg/mL and a diameter smaller than 1 μm showed lesser biocompatibility and produced ROS. Bright-field microscopy images of SaOS2 cells also supported the findings obtained from biocompatibility studies, as shown in **Figure 4**. **Figure 4C** shows that the diameter of 2D-BNNs is around 1 μm, and the thickness is around 100 nm (referring to as NS1). **Figure 4D** shows smaller 2D-BNNs with a diameter of 100 nm and a thickness of ∼3 nm (referring to NS2). **Figure 4E** shows the NP1, which has a diameter in 110 nm, and the smaller nanoparticles that have diameters in the range of 10–40 nm (referred to as NP2) were shown in **Figure 4F**. In conclusion, this study revealed that the biocompatibility of 2D-BNNs depends on structure, size, and shape, which was similar to the findings of the biocompatibility studies in the case of all other nanomaterials. Furthermore, the boron radicals that occur in the edges of the BN nanosheets could be the cause of ROS leading to cell death.

In another study, the cell viability of hBNs and water-soluble hydroxyl-functionalized hBNs (hBN-OH) that have a size range of 50–100 nm in diameter were tested on the KB (human cervix carcinoma) cells up to 500 μg/mL concentrations using an MTT assay. Even at the higher concentrations, no toxicity was observed after 24 h incubation, thereby suggesting the use of hBN-OH for imaging and *in vitro* detection applications (Nurunnabi et al., 2016).

There is a limited number of biocompatibility studies in the literature so far, and all are *in vitro*. The results of these reports are summarized in **Table 3**. In all of the studies, the 2D-BNNs are claimed to be non-toxic, but their biocompatibility clearly depends on several parameters, including cell type, dose, type of dispersion surfactant, and their lateral size dimensions. In summary, we can conclude that 2D-BNNs have no significant adverse effects on the cell proliferation, metabolism, and viability but further *in vivo* studies should be performed to reach more concrete conclusions.

BIOAPPLICATIONS OF 2D-BNNs

2D-BNNs in Drug Delivery Applications

A successful drug carrier requires the fulfillment of certain constraints, including low toxicity, flexibility, and stability in biological environments, and the successful carrying and release of drug molecules into cells at the target tissue. Numerous nanomaterials including polymeric and non-polymeric ones have been investigated for their drug carrier potentials since nanomedicine concept has been introduced. As the nature of BN based nanomaterials started to be better understood, as shown in **Table 4**, they have also been gained interest for drug delivery applications. Here, we will discuss their potential use as drug carriers in the light of reported studies so far after a brief introduction to the challenges in drug delivery.

All nanocarriers should pass through a number of biological barriers at organism and cellular levels. Therefore, an ideal carrier should have certain properties including stability, flexibility, size and shape, low toxicity and biodegradability as mentioned above for their full consideration as a nanocarrier. At the organism level, a nanocarrier should be able to carry a drug into the target region without drug leakage from the structure. Once the drug-loaded carrier reaches the target tissue, passing through the barriers, including the reticuloendothelial system (RES), at an organism level, it should trigger endocytosis pathways for cellular internalization at a cellular level, and it should then release its cargo into cells (Soma et al., 1999). Considering the properties of an ideal nanocarrier, 2D-BNNs can be good candidates through several of their unique properties, including flexibility, stability, and biocompatibility.

It is now clear that the size of the nanoparticles should be small enough to travel in the narrow blood vessels and penetrate into tumor tissue while also being large enough so as not to fenestrate into the endothelial lining (Champion et al., 2007). Therefore, spherical 2D-BNNs, in the size range of 20–200 nm, are good candidates to be used as carriers due to their biocompatible nature that allows them to interact with the hydrophobic sites of drug molecules (Emanet et al., 2017). Moreover, 2D-BNNs can be synthesized in different sizes that allow for the investigation of BNs for optimum drug loading and delivery performance.
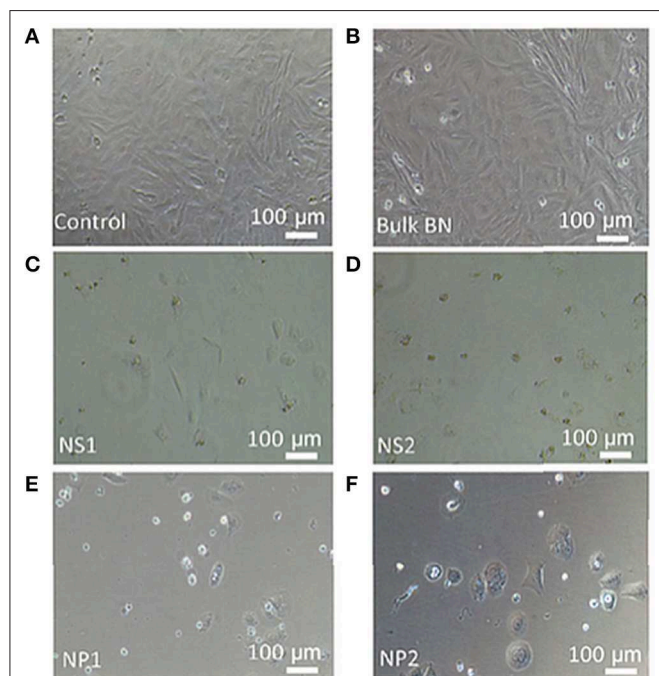

FIGURE 4 | Bright-field microscopy images of SaOS2 cells cultured in the presence of **(A)** standard culture medium (control), **(B)** bulk BN, **(C)** nanosheet NS1, **(D)** nanosheet NS2, **(E)** nanoparticle NP1, and **(F)** nanoparticle NP2. Reproduced with Permission from Mateti et al. (2018).

TABLE 3 | Cytocompatibility of 2D-BNNs on culture cell lines.

Dispersion agent	Cell lines	Toxicity assays	Incubation time	Results	References
None	HEK-293T and CHO	MTT and annexin V-FITC/PI	2 days	Nontoxic $\leq 100\,\mu g/mL$, no apoptosis	Lu et al., 2016
None	CRL 2120 and MDCK	MTT, SRB colorimetric, PicoGreen	1 or 2 days	Nontoxic $\leq 100\,\mu g/mL$ for both cell lines	Kivanç et al., 2018
None	LNCaP and DU145	WST-8, annexin V-FITC/PI, LDH	3 or 6 days	Time-dependent toxicity, induce apoptosis	Li et al., 2017
None	SaOS$_2$	MTS, DPPH assay	7 days	Size-dependent toxicity and ROS production	Mateti et al., 2018
None and hBN-OH	KB	MTT	1 days	Nontoxic $\leq 500\,\mu g/mL$	Nurunnabi et al., 2016

2D-BNNs were first used as carriers to improve immunostimulator vaccines, CpG oligonucleotides, allergy immunotherapies, and cancer and infection treatment (Zhang et al., 2012). The CpG oligonucleotides are similar to DNA motifs in bacteria that stimulate a similar immune response in the body (Pisetsky, 1996). The interaction of CpG oligonucleotides with TLR9 antigen-presenting cells activates two distinct signaling pathways, in which two transcription factors, NFκB and IRF-7, are translocated to the nucleus, thereby leading to the induction of genes encoding pro-inflammatory cytokines [interleukin (IL)-6 and IL-12] and/or type I interferons (interferon-α) (Wagner, 2002). In the study, 2D-BN nanospheres interacted with CpG oligonucleotides, and they were investigated in immunotherapy applications (Zhang et al., 2012). Due to the electrostatic repulsion between negatively charged CpG oligonucleotides and 2D-BNNs, the 2D-BNNs were first coated with peptides composed of several amino acid combinations. A 12 amino acid-long peptide with a tyrosine residue (Y) at the 8th position from the N-terminus played a crucial role in the affinity to 2D-BNNs. The peptide-bound 2D-BNNs were internalized into the cells successfully and showed no toxicity to the peripheral blood mononuclear cells. Using the peptide as a cross-linker, the CpG oligonucleotide-binding efficiency was, to 2D-BNNs, 5-fold higher than the directly binding efficiency of CpG on 2D-BNNs. Moreover, the 2D-BNNs-loaded peptide-CpG conjugates had great capacity to stimulate IL6 and TNF-α production from cells. The increased cytokine production capacity could be attributed to the higher binding capacity and strong interaction of CpG oligonucleotides to 2D-BNNs.

In a follow-up study, CpG oligonucleotides and 2D-BNNs interactions were studied after coating 2D-BNNs with positively charged chitosan to provide electrostatic attractions, as schematically shown in **Figure 5** (Zhang et al., 2013). The chitosan was chosen as low (60–120 kDa), medium (110–150 kDa), and high (140–220 kDa) molecular weights to compare the CpG oligonucleotide-binding yield to chitosan-BNNs and their immunostimulatory effects. The results indicated that the CpG oligonucleotide-binding yield was higher to the high molecular weight chitosan-coated 2D-BNNs as well as their increased cellular uptake due to the high positive charge of the structure. However, the low molecular weight chitosan-BNNs interacted with CpG created a higher immunostimulatory effect by increasing the cytokines (IL-6 and TNF-α) in TLR9 cells even more than the positive control (lipofectamine-CpGs) (Zhang et al., 2013).

In another study, the porous structure of 2D-BN nanospheres was utilized as a nanocontainer for Dox, a commonly used chemotherapeutic drug (Sukhorukova et al., 2015). The loaded Dox was stable at neutral pHs (pH 7.4) and Dox was significantly released from 2D-BNNs at low pHs (pH 4.5–5.5), suggesting that the release in the cell will be effective. Efficient cellular internalization and Dox release are two important factors qualifying the structure as a potential carrier. Moreover, the cell viability tests showed the 2D-BNN-Dox structures were highly toxic for neoplastic IAR-6-1 cancer cells (Sukhorukova et al., 2015).

Feng et al. developed a targeted drug delivery system using folic acid (FA)-conjugated 2D-BN nanospheres (Feng et al., 2016). The FA molecules were grafted on 2D-BNNs via an esterification reaction. The biocompatibility results indicated that the 2D-BNNs-FA structures were not significantly cytotoxic on HeLa cells up to 100 μg/mL. The 2D-BNNs-FA structure was loaded with Dox. The 2D-BNNs-FA/Dox complexes also had high stability at pH 7.4 while also exhibiting a high Dox release performance at low pH values (pH 5.0). Besides, the cytotoxicity results indicated that the 2D-BNNs-FA/Dox structures have a greater cytotoxic effect on HeLa cells due to the overexpressed FA receptors. Therefore, the 2D-BNNs-FA/DOX complexes were recognized as a high performance Dox internalization agent as chemotherapeutic drug for HeLa cells (Feng et al., 2016). In a follow-up study, FA molecules were conjugated to the 2D-BNNs with a three-step procedure that included FA pre-activation by N,N′-dicyclohexylcarbodiimide (DCC), BNN modification with AgNPs to provide coupling of FA to BNNPs, and their further modification with L-cysteine to provide -NH$_2$ ends (Permyakova et al., 2017). The final product was an FA-bound 2D-BNN structure (FA-Cyst-Ag/BNNs). The carboxyl-groups of FA were preactivated with DCC. Cyst, possessing a pair of cystine electrons (R–S–, Lewis base), donated its electron to the Ag+ (Lewis acid), leading to the formation of a zero-oxidation state of Ag atoms that resulted in chemically bonded Ag–S bonds via hydrocarbon chains of the cysteine. In the last stage, FA was

TABLE 4 | Bioapplications of 2D-BNNs.

2D-BN Nanomaterial	Application	Result	References
BNNS/CpG oligonucleotides	Drug delivery, immunotherapy	Show great capacity to stimulate IL6 and TNF-α production, increased cytokine production	Zhang et al., 2012
Chitosan coated BNNS/CpG oligonucleotides	Drug delivery, immunostimulatory	Higher immunostimulatory effects increasing cytokines (IL-6 and TNF-α) in TLR9 cells even more than positive control (lipofectamine-CpGs)	Zhang et al., 2013
BNNPs-Dox	Drug delivery	Efficient cellular internalization of BNNP-Dox and serious Dox release	Sukhorukova et al., 2015
BNNS-FA/Dox	Drug delivery	pH dependent Dox release, greater cytotoxic effect on HeLa cells	Feng et al., 2016
FA-Cyst-Ag/BNNPs	Drug delivery	Positive effects on cancer cell targeting	Permyakova et al., 2017
Dox-hBN	Drug delivery	pH dependent Dox release	Emanet et al., 2017
AuNPs-BNNs	Drug delivery	Attractive materials for cancer drug delivery and photodynamic therapy	Jedrzejczak-Silicka et al., 2018
2D-BN nanoparticles	Drug delivery, spectroscopic marker	Tumor cell perturbation	Gnatyuk et al., 2018
DOX@PAH-cit–BNNS	Drug delivery	Decreased cell viability in both MCF-7 and HeLa cells more than free DOX	Feng et al., 2018
BNNP/PPF	Bone tissue engineering	Enhanced mechanical strength and adsorption of collagen I protein, improved ECM deposition, cell attachment and spreading for bone grafts	Farshid et al., 2015
BNNSs/AKM scaffolds	Bone tissue engineering	Increase compressive strength and fracture toughness	Shuai et al., 2015
hBNs/gelatin ESM	Orthopedic applications, tissue engineering,	Biocompatible and biodegradable scaffolds for orthopedic applications	Nagarajan et al., 2017
OH-BNNS/PVA	Drug delivery, artificial cartilages	Controllable reinforcements in both mechanical and thermal responses	Jing et al., 2017
PEEK/hBN	Nanocomposite	Improved mechanical and thermo mechanical properties	Liu et al., 2015
hBNs-impregnated silane	Bioimplant	5-fold improvement in the corrosion resistance in simulated human body fluid even after 96 h	Al-Saadi et al., 2017
Hollow BNs	Prostate cancer treatment	More suppressive effects on tumors as compared to the PTX drugs	Li et al., 2017
hBNs	Lubricant	Better lubrication and maximum performance in LPEF	Turkoglu et al., 2005
hBNs	Lubricant	Most effective lubricant based on LFEP-lubricant concentration profile, higher concentration of hBN caused lower mechanical properties	Ugurlu and Turkoglu, 2008
BN nanoparticles	Cosmetic	Improved skin appearance by not only blurring lines and wrinkles but also providing coverage of age spots, blemishes and discolorations	Butts et al., 2007
BN fillers	Cosmetic	Enhanced filling properties and illusion about smoothness of skin by hiding the wrinkles	Newman et al., 2015
BN nanoparticles/coated with amino acids and mineral oils	Cosmetic	Improved ingredients of cosmetic product	Koshida et al., 2019
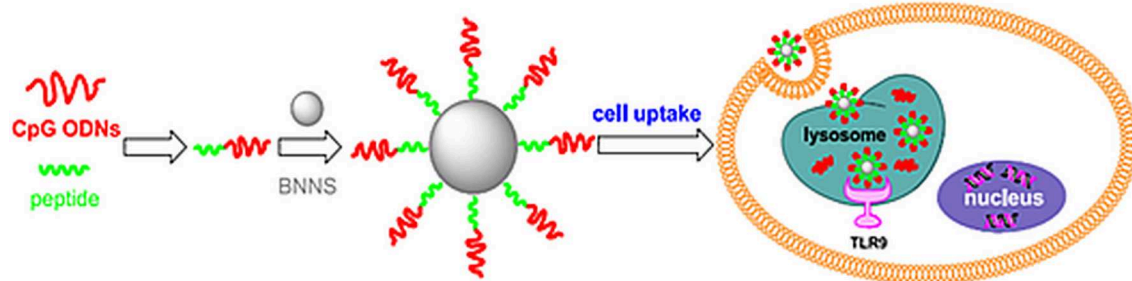
FIGURE 5 | Using a boron nitride nanosphere (BNNS)-binding peptide as a linker molecule, BNNS are able to efficiently deliver immunostimulatory CpG ODNs into cells and significantly enhance the immune response. Reproduced with Permission from Zhang et al. (2012).

grafted to the surface of BNNPs under a condensation reaction between amino groups of Cyst-Ag/BNNPs and carboxyl groups of FA using DCC. The study found that conjugating FA to the structure did not alter the targeting efficiency of FA.

In our group, hBNs were investigated as drug carriers by loading them with Dox (Emanet et al., 2017). The nature of the interaction between hBNs and Dox was non-covalent through the aromatic rings of Dox. The optimal loading was achieved at neutral and basic pH values with respect to acidic pH values. The Dox release studies indicated that the Dox-hBN conjugates were highly stable at around pH 7, while the Dox release from 2D-BNNs was triggered at low pH (pH 4).

The spectral changes of the cell membrane and cytoplasm, along with the cellular internalization of Dox-loaded 2D-BNNs, were used as a marker to monitor the cellular uptake of a nanocarrier (Gnatyuk et al., 2018). The luminescence of the 2D-BNNs-Dox was monitored using confocal microscopy to visualize the time-dependent cellular localization, as shown in **Figure 6**. The anticancer efficiency of the structure was also investigated using IR and Raman spectroscopy. The luminescent effect of the 2D-BNNs was revealed in the LNCaP cells, especially when the cells were seeded on a gold substrate. The cellular internalization was completed at the first hour of incubation and realized from the strong spectral changes in Raman spectra obtained from the membrane lipid of the cells. Then, the normalized spectral results obtained from the second hour to 10 h of study claimed the localization of the 2D-BNN in cytoplasm until nuclear internalization was completed after 10 h of incubation.

Silicka et al. investigated the drug delivery performance of gold nanoparticle-functionalized hexagonal-based 2D-BNNs (AuNP-BNNs) on L929 and MCF-7 cell lines (Jedrzejczak-Silicka et al., 2018). They found that the mitochondrial and lysosomal activities of the cells were significantly reduced at long incubation times of 48 and 72 h. They concluded that that conjugates of 2D-BNNs with AuNPs are promising materials for cancer drug delivery and are photodynamic. Feng et al. reported the development of a highly pH-responsive carrier structures using

2D-BN nanospheres for efficient drug release inside tumor cells (Feng et al., 2018). In the study, 2D-BNNs were functionalized with charge-reversal poly (allylamine hydrochloride)-citraconic anhydride (PAH-cit) following the hydroxylation and amino group modification of the 2D-BNNs. Then, the developed PAH-cit-BNNs was loaded with Dox molecules, which was 8-fold more efficient than loading free 2D-BNNs. Moreover, the DOX@PAH-cit–BNNs complexes caused a serious cell viability decrease (around 20%) in both MCF-7 and HeLa cancer cells of more than free DOX (around 40–50%) and DOX@PAH-cit (around 60–70%) structures (Feng et al., 2018).

Thus, far, all studies have aimed at understanding the potential of this novel material at a cellular level. In general, all studies found that 2D-BNNs have low cytotoxicity or are not toxic at all. The other interesting finding was the pH-dependent drug binding and release. The optimal loading was achieved at neutral and basic pHs, while low pH triggered the increased release of the drug from 2D-BNNs. This can be an important point for effective release after uptake into the cells since intracellular compartments such as lysosomes are acidic. Furthermore, the conjugation of 2D-BNNs with folate and transferrin helped the effective targeting of cancer cells. The results indicated that the model drug, Dox, also accumulated in the nucleus of the cells as desired. Moreover, increased cytokine production could be attributed to the higher binding capacity and strong interaction of CpG oligonucleotides to 2D-BNNs. This evidence strongly suggested that 2D-BNNs are a potential candidate as an effective carrier for chemotherapy and immunostimulating drugs to improve their therapeutic efficiency and to reduce their side effects.

2D-BNNs in Biomaterial Applications

BN nanostructures are used to enhance the properties of composites due to their superior mechanical properties. Their dielectric properties, allowing a composite to maintain its electrical properties, can also be advantageous (Weng et al., 2014).

Farshid et al. used 0.2 wt% BNNTs and boron nitride nanoplatelets (BNNs) to obtain biodegradable poly(propylene fumarate) (PPF) nanocomposites for bone tissue engineering (Farshid et al., 2015). The results indicated that both nanomaterials significantly enhanced the mechanical strength of the polymer and the adsorption of the collagen I protein compared to the control PPF. Moreover, the cytocompatible polymeric nanocomposites showed improved extracellular matrix (ECM) deposition, cell attachment, and spreading, suggesting the use of the developed nanocomposites as bone grafts (Farshid et al., 2015). In another study, akermanite (AKM) scaffolds were fabricated using 0.5, 1, and 1.5 wt% 2D-BN nanosheets (Shuai et al., 2015). The significant increase in both the compressive strength and fracture toughness were found when the concentration of 2D-BNNs were increased from 0.5 to 1.0 wt%. Furthermore, the cell adhesion and proliferation studies on human osteosarcoma cells (MG63) and bone marrow stromal cells (BMSCs) indicated the cytocompatibility of the scaffolds for up to 7 days, as shown in **Figure 7**. The results
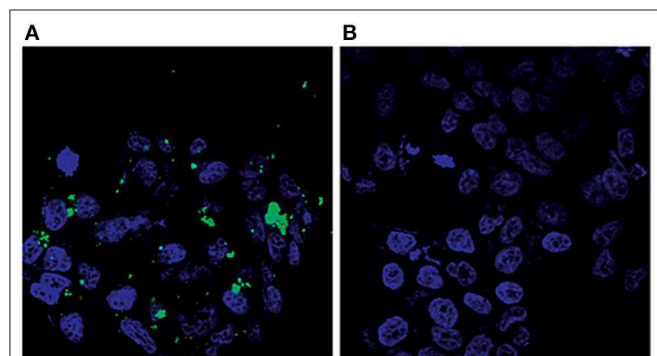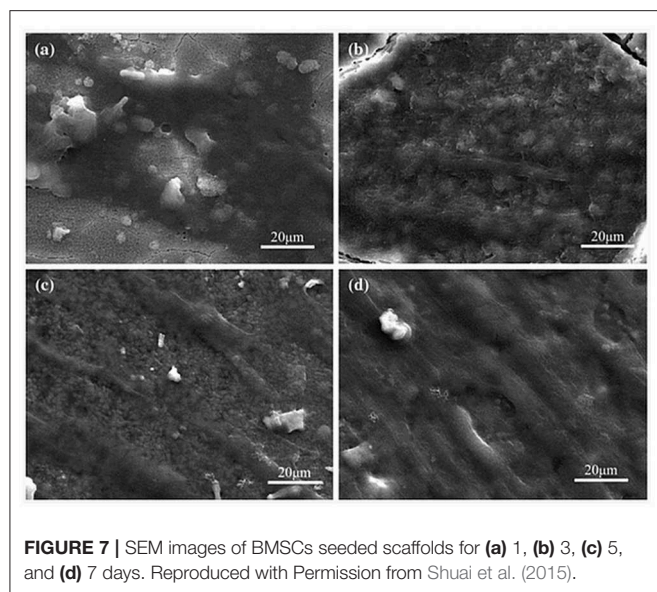

FIGURE 6 | Visualization of LNCaP cells by confocal microscopy: **(A)** cells treated with modified 2D-BN nanoparticles and **(B)** reference cells (green fluorescence: FITC, blue fluorescence: Hoechst 33258). (Gnatyuk et al., 2018): Published by The Royal Society of Chemistry.

FIGURE 7 | SEM images of BMSCs seeded scaffolds for **(a)** 1, **(b)** 3, **(c)** 5, and **(d)** 7 days. Reproduced with Permission from Shuai et al. (2015).

indicated the potential of AKM scaffolds, including 2D-BNNs, in tissue engineering.

Gelatin electrospun mats (ESM) were fabricated using 0.1, 1, and 5 wt% hexagonal 2D-BNNs to improve mechanical properties (Nagarajan et al., 2017). The effects of cell adhesion, proliferation, biocompatibility, and osteoblast gene expression on osteosarcoma cell lines showed that the ESM are biocompatible and biodegradable, and that 2D-BNNs-reinforced gelatin scaffolds can be used for orthopedic applications thanks to the improved (3-fold) Young's modulus (Nagarajan et al., 2017). Jing et al. used 0.03, 0.06, 0.09, and 0.12 wt% hydroxylated 2D-BNNs (OH-BNNs) to fabricate poly(vinyl alcohol) (PVA) hydrogels (Jing et al., 2017). In this study, changing the content of OH-BNNs provided controllable reinforcements to both mechanical and thermal responses. Furthermore, the cytocompatibility of the hydrogels was tested using MTS and live/dead assays. The results suggested that OH-BNNs/PVA hydrogels have potential in tissue engineering, drug delivery, and artificial cartilages.

The composite of 2D-BNNs (using 1, 2, 3, 4, and 5 wt%) with poly(ether-ether-ketone) (PEEK) showed improved mechanical and thermo-mechanical properties since hBNs possess a high elastic modulus, excellent lubrication properties, and good thermal conductivity (Liu et al., 2015). In another study, 2D-BNNs-impregnated silane was added into magnesium (Mg) alloys to enhance the resistance of the corrosion for bioimplant applications (Al-Saadi et al., 2017). The results showed a 5-fold improvement in corrosion resistance in simulated human body fluid even after 96 h.
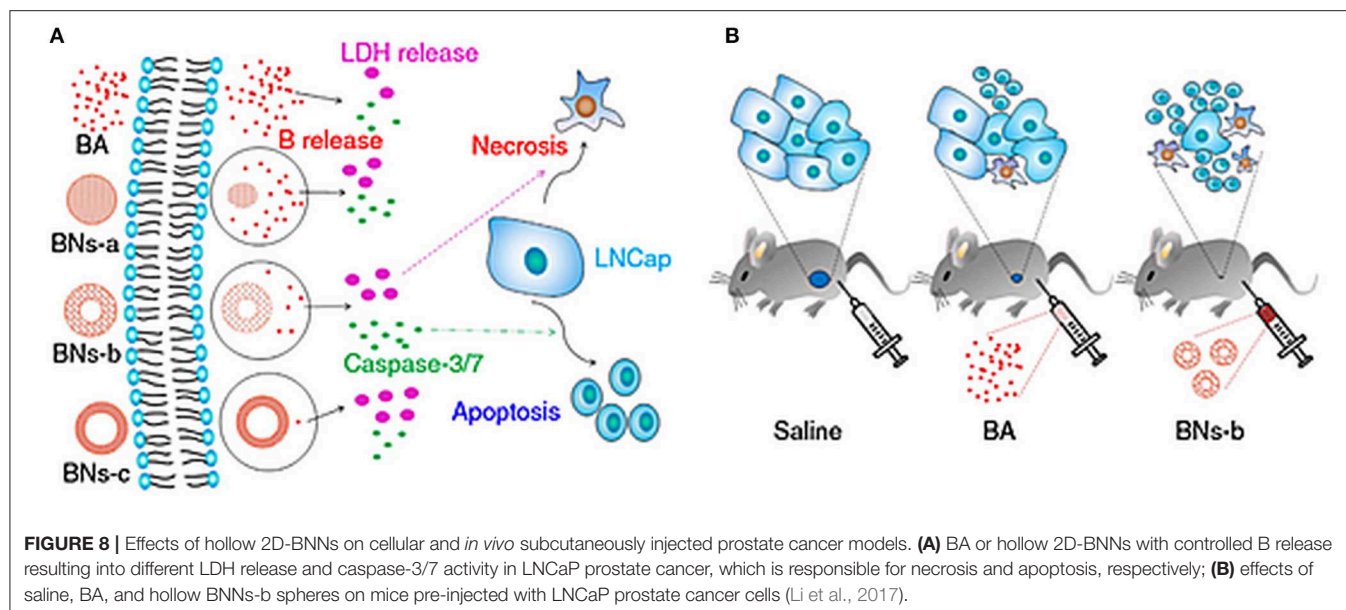
According to the results obtained from the biomaterials applications, it can be concluded that 2D-BNNs can be used as additives in nanocomposites or scaffold materials in tissue engineering and regenerative medicine since they enhance the mechanical and thermal properties of composite materials without interfering the electrical features of the polymer due to the high Young's modulus of BN nanostructures.

Therapeutic Agents

Boron-including compounds such as calcium fructoborate, borax, boric acid (BA), boronic acid, and their esters were widely studied for their potential use in cancer treatment (Hegsted et al., 1991). These studies showed that boron-including compounds have remarkable inhibitory effects on cancer cell proliferation (Korkmaz et al., 2007; Scorei and Popa, 2010). BA, as a chemical form of boron in physiological conditions, has a tendency to make ester bonds with the hydroxyl groups of organic compounds (Van Duin et al., 1984). Therefore, hydroxyl groups that include structures such as carbohydrates are good candidates for the internalization of BA into their structure (Hausdorf et al., 1988). When the complexation is performed with structurally and functionally important carbohydrates, it manipulates the presence and activity of certain biological structures (Raven, 1980). These biomolecules include diadenosine phosphates (signal nucleotide) and S-adenosylmethionine used in methylation reactions of DNA, RNA, proteins, and phospholipids (Grill and Himmelbach, 1998; Ralston and Hunt, 2001). However, the systemic administration of soluble boron compounds frustrates the therapeutic effects of the structure owing to their short half-life in organisms.

The behavior of 2D-BNNs in biological media has a great importance since they may show their desired or undesired effects through their interaction with cellular compounds. For instance, 2D-BNNs, which are used as therapeutic agents, should be flexible enough to pass through barriers of reticuloendothelial system (RES) and should be stable enough to resist early degradation. In addition, the possible role of their degradation product should be clarified from therapeutic and adverse effect perspectives. However, it is not clear what the degradation products of BN-based nanomaterials might be. There is strong evidence that they will slowly degrade in biological media (Li et al., 2017; Sen et al., 2018). Based on *ab initio* calculations of several h-BN phases and c-BN phase nanostructures, the stability of both phases changed depending on the energy differences between the stacking geometries and inter-layer spacing, which can be altered with pressure or temperature (Mosuang and Lowther, 2002). As predicted from this study, our experimental findings strongly suggest that the crystallinity has an influence on the stability of hBNs in solution, and the degradation rate changed with the crystallinity (Sen et al., 2018). The question of the degradation products remains elusive at the moment. When the structure of BN nanomaterials is considered, it is logical to assume the products are either B or N compounds. From the B atom point of view, considering BA as one of the degradation products is realistic.

In a study, three different kinds of hexagonal-based hollow 2D-BNNs, grouped depending on their degradation performance, were investigated as boron reservoirs against prostate cancer, as shown in **Figure 8** (Li et al., 2017). The low crystallinity (BNNs-a), moderate crystallinity (BNNs-b), and high crystallinity (BNNs-c) effects of structures were evaluated on androgen-dependent LNCaP prostate cancer cells. Moreover, the chemical form of boron in physiological conditions, BA,

FIGURE 8 | Effects of hollow 2D-BNNs on cellular and *in vivo* subcutaneously injected prostate cancer models. **(A)** BA or hollow 2D-BNNs with controlled B release resulting into different LDH release and caspase-3/7 activity in LNCaP prostate cancer, which is responsible for necrosis and apoptosis, respectively; **(B)** effects of saline, BA, and hollow BNNs-b spheres on mice pre-injected with LNCaP prostate cancer cells (Li et al., 2017).

was used as control owing to the degradation product of hollow 2D-BNNs. This study indicated that hollow BNNs-b spheres lead to a significantly higher fraction of apoptosis and necrosis rather than BA or with respect to the BNNs-a spheres with low crystallinity. Furthermore, hollow BNNs-b spheres and PTX drugs, commonly used drug for prostate cancer, were tested on LNCaP cell-injected male BALB/c-nu/nu mice models. The results indicated that hollow BNNs-b spheres showed more suppressive effects on tumors as compared to the PTX drugs. Besides, the hematological tests performed on hollow BNNs-b spheres injected in healthy C57/BL6 mice shows their biocompatible nature.

These progressive studies clarifying the underlying mechanism of biodegradation may provide tremendous opportunities to choose desired 2D-BNNs for targeted therapy. Moreover, in the light of the preliminary results on prostate cancer, the molecular mechanism of therapeutic efficiency should be further studied in detail to have an insight into their possible effects, not only on prostate cancer, but also on other cancer types.

Pharmaceutical Agents

In pharmaceutical applications, a variety of lubrication agents has been studied to improve physical and chemical solid drug properties. The friction between the interfaces of the drug surface and the die wall of the inner surface of the tablets must be decreased to prevent the sticking of drug to the die while enhancing the softness and tensile strength of drug tablets. Therefore, appropriate lubricants should be used to improve the fluidity, filling properties, and efficiency of drug tables (Aoshima et al., 2005). In addition, the lubricants should be biocompatible, chemically inert, sustainable, and reproducible from batch to batch, and they should not cause adverse effects on the final dosage form (Miller and York, 1988). Considering the

unique properties of 2D-BNNs, they are suitable nanostructures to be used as lubrication agents. Besides, their inertness also makes them suitable candidates for their use as lubricant agents (Wang et al., 2018).

The first study of hexagonal 2D-BNNs as lubricants was performed by Turkoglu et al. in 2005 (Turkoglu et al., 2005). The required lower punch force (LPEF) was tested on 2D-BNNs-including lubricants by comparing them with magnesium stearate (MGST), stearic acid (STAC), and glyceryl behenate (COMP). Based on the LPEF results, a better lubrication was obtained from 1% 2D-BNNs and MGST compared to the ones made from STAC and COMP. Moreover, the 2% MGST showed maximum performance in LPEF when it was mixed with 2D-BNNs that decreased LPEF to 50% as compared to only MGST-including ones (Turkoglu et al., 2005).

Later, several concentrations (0.5, 1.0, and 2.0 %) of STAC, COMP, hBN, and MGST lubricants were tested for their performance in LPEF applications (Ugurlu and Turkoglu, 2008). Tensile strengths of compacted tablets were measured by applying a diametrical load across the edge of tablets. The deformation mechanism of the tablets was also tested during compression. The study found that 2% of STAC and COMP did not decrease the LPEF as much as 0.5% of 2D-BNNs and MGST. 2D-BNNs and MGST were the most effective lubricants based on the LFEP-lubricant concentration profile. Moreover, the higher concentration of 2D-BNNs caused lower mechanical properties of tablets because of their hydrophobic character (Ugurlu and Turkoglu, 2008).

These studies showed that 2D-BNNs decreased LPEF in lubricants by improving the effects on disintegration time and tablet tensile strength, thus demonstrating their improved lubrication potential with respect to MGST. These results are encouraging for their use as lubricants in pharmaceutical applications.

Cosmetic Applications

The cosmetic research to improve product properties is growing very fast. There are many materials utilized in cosmetic products (Arraudeau et al., 2003). However, they have a tendency to accumulate in furrows and wrinkles in the skin so that it further emphasizes the wrinkles instead of showing smoother skin by hiding the wrinkles. Moreover, spherical powders, including silica, polyethylene, and polymethylmethacrylate (PMMA), are utilized as skin shiners and wrinkles hiders by blurring the appearance of skin through the use of the structure's light-scattering properties (Macchio et al., 1988; Lemperle et al., 1998; Pölloth, 2005).

The earliest use of BNs in cosmetics was reported as being a slip modifier, but it was not indicated which crystal form was used (Gottschalck and Breslawec, 2012). However, it is assumed that it is the hBN form because the pursued functionality in cosmetics corresponds to the properties of this crystal form, and BN used in cosmetics is not listed as a nanomaterial. In addition, it has been reported that the average particle size of hBNs used in cosmetics ranges from 1 to 47 mm depending on their trade names and grade (Monice et al., 2015). The assumption made by the industry was, perhaps, not due to a lack of awareness of their unique properties as nanomaterials but just because of their lubricating properties.

Based on the US Food and Drug Administration (FDA), hBNs are used in more than 650 cosmetic formulations, including lipstick, eye shadows, foundation agent, blush, shampoo, and hair conditioner, as transparent raw fillers. They enhance skin appearance by not only blurring lines and wrinkles but also by providing coverage of the age spots, blemishes, and discolorations (Butts et al., 2007). 2D-BNNs fillers are also used in cosmetic products combined with other materials, including spherical silica, PMMA, and titanium. Apart from their filling properties, it was surprising to observe that they created an illusion of smoothness on the skin by hiding the wrinkles, thereby making them promising agents in cosmetic applications (Newman et al., 2015). Moreover, the 2D-BNNs could be coated with special amino acids and mineral oils that improve the ingredients of the cosmetic product (Koshida et al., 2019).

The use of 2D-BNNs in cosmetic application is now welcomed due to their biocompatibility and transparency, which is highly desired in white formulations. Furthermore, 2D-BNNs could be easily dispersed in oily cosmetic formulations due to their hydrophobicity, and this consequently improved the formulation's homogeneity. As their properties are better understood, their use in more cosmetic products will appear.

CONCLUSION AND FUTURE PERSPECTIVES

As highlighted in this review, 2D-BNNs are considered good candidates for a wide range of biomedical and bio-related applications, such as in drug and gene delivery, biomaterials, pharmaceutics, and cosmetics, due to their excellent physicochemical properties. Considering the synthesis of 2D-BNNs, it is important to choose appropriate precursors since the structure, crystallinity, and purity of the final product strongly depends on the B precursor and catalyst. The other experimental parameters, including temperature and pressure, are important for crystallinity and product quality. Not being able to synthesize at large-scale and high-temperature requirements are still bottlenecks for their widespread use. It is clear that more research efforts should be devoted to the development of synthesis procedures at lower temperatures. The high chemical stability and hydrophobicity of the 2D-BNNs result into their poor dispersibility in aqueous media, which hinders the reliable assessment of their effects on living systems. Significant effort has therefore been dedicated to their functionalization for dispersions in physiological solutions and their interactions with other biomaterials. Moreover, biocompatibility investigations of 2D-BNNs have been performed to clarify their acceptability in biomedical applications. Although it is found that 2D-BNNs are non-toxic in *in vitro* studies, depending on the cell types, concentrations, and lateral size dimensions, *in vivo* investigations should be further performed in future studies in order to reach more concrete conclusions.

The possibility of functionalizing 2D-BNNs though their –OH or –NH$_2$ groups with a variety of molecular structures makes them suitable carriers. The short half-life of boron compounds in biological systems—caused by their fast metabolism—is a significant problem in therapeutic applications. Using 2D-BNNs in place of these compounds might be a good option in order to maintain the sustained released of boron into the biological system. The superior mechanical properties of 2D-BNNs are utilized to strengthen polymeric structures. The dispersion problem of highly hydrophobic 2D-BNNs in polymer mixtures could be overcome with their surface modifications with a suitable molecular structure. Using 2D-BNNs as additives in cosmetic products has already shown improvements in product quality and the functionalization of these novel materials to match their chemical compatibility in formulations can add another dimension for their use in cosmetics. Although the findings indicate that these nanomaterials are quite promising, researchers should put more effort into better understanding the role and behavior of BNs in a biological matrix to be able use them in biomedical applications. Finally, the establishment of a clear structure–function relationship is necessary to fully benefit from the unique properties of these novel materials in a wide range of applications.

AUTHOR CONTRIBUTIONS

ME and ÖS wrote the manuscript. IT organized the references. MÇ guided the study and revised the manuscript.

ACKNOWLEDGMENTS

REFERENCES

Al-Saadi, S., Banerjee, P. C., Anisur, M., and Raman, R. S. (2017). Hexagonal boron nitride impregnated silane composite coating for corrosion resistance of magnesium alloys for temporary bioimplant applications. *Metals* 7:518. doi: 10.3390/met7120518

Ansaloni, L. M. S., and Sousa, E. M. B. (2013). Boron nitride nanostructured: synthesis, characterization and potential use in cosmetics. *Mater. Sci. Appl.* 4, 22–28. doi: 10.4236/msa.2013.41004

Aoshima, H., Miyagisnima, A., Nozawa, Y., Sadzuka, Y., and Sonobe, T. (2005). Glycerin fatty acid esters as a new lubricant of tablets. *Int. J. Pharm.* 293, 25–34. doi: 10.1016/j.ijpharm.2004.12.007

Arenal, R., and Lopez-Bezanilla, A. (2015). Boron nitride materials: an overview from 0D to 3D (nano) structures. *Wiley Interdisc. Rev. Comput. Mol.* 5, 299–309. doi: 10.1002/wcms.1219

Arraudeau, J. P., Mellul, M., and Candau, D. (2003). *Cosmetic Composition Capable of Blurring Skin Defects.* U.S. Pat. No. 5223559.

Butts, M., Sinha, M., Genovese, S. E., and Yamada, M. (2007). *Cosmetic Compositions Comprising Sub-micron Boron Nitride Particles*, U. S. Pat. Application #:2007. 0207101.

Champion, J. A., Katare, Y. K., and Mitragotri, S. (2007). Particle shape: a new design parameter for micro- and nanoscale drug delivery carriers. *J. Control. Release* 121, 3–9. doi: 10.1016/j.jconrel.2007.03.022

Chang, C. W., Han, W. Q., and Zettl, A. (2005). Thermal conductivity of BCN and BN nanotubes. *J. Vac. Sci. Tech. B* 23, 1883–1886. doi: 10.1116/1.2008266

Chen, X., Wu, P., Rousseas, M., Okawa, D., Gartner, Z., Zettl, A., et al. (2009). Boron nitride nanotubes are noncytotoxic and can be functionalized for interaction with proteins and cells. *J. Am. Chem. Soc.* 131, 890–891. doi: 10.1021/ja807334b

Chen, Y., Zou, J., Campbell, S. J., and Le Caer, G. (2004). Boron nitride nanotubes: pronounced resistance to oxidation. *Appl. Phys. Lett.* 84, 2430–2432. doi: 10.1063/1.1667278

Chopra, N. G., Luyken, R. J., Cherrey, K., Crespi, V. H., Cohen, M. L., Louie, S. G., et al. (1995). Boron Nitride Nanotubes. *Science* 269, 966–967. doi: 10.1126/science.269.5226.966

Cuming, J., and Zettl, A. (2000). Mass-production of boron nitride double-wall nanotubes and nanococoons. *Chem. Phys. Lett.* 316, 211–216. doi: 10.1016/S0009-2614(99)01277-4

Du Frane, W., Cervantes, O., Ellsworth, G., and Kuntz, J. (2016). Consolidation of cubic and hexagonal boron nitride composites. *Diamond Relat. Mater.* 62, 30–41. doi: 10.1016/j.diamond.2015.12.003

Emanet, M., Kazanç, E., Çobandede, Z., and Çulha, M. (2016). Boron nitride nanotubes enhance properties of chitosan-based scaffolds. *Carbohydr. Polym.* 151, 313–320. doi: 10.1016/j.carbpol.2016.05.074

Emanet, M., Sen, Ö., and Çulha, M. (2017). Evaluation of boron nitride nanotubes and hexagonal boron nitrides as nanocarriers for cancer drugs. *Nanomedicine* 12, 797–810. doi: 10.2217/nnm-2016-0322

Farshid, B., Lalwani, G., Shir Mohammadi, M., Simonsen, J., and Sitharaman, B. (2015). Boron nitride nanotubes and nanoplatelets as reinforcing agents of polymeric matrices for bone tissue engineering. *J. Biomed. Mater. Res. B Appl. Biomater.* 105, 406–419. doi: 10.1002/jbm.b.33565

Feng, S., Zhang, H., Yan, T., Huang, D., Zhi, C., Nakanishi, H., et al. (2016). Folate-conjugated boron nitride nanospheres for targeted delivery of anticancer drugs. *Int. J. Nanomed.* 11, 4573–4582. doi: 10.2147/IJN.S110689

Feng, S., Zhang, H., Zhi, C., Gao, X. D., and Nakanishi, H. (2018). ph-responsive charge-reversal polymerfunctionalized boron nitride nanospheres for intracellular doxorubicin delivery. *Int. J. Nanomed.* 13, 641–652. doi: 10.2147/IJN.S153476

Gnatyuk, O. P., Dovbeshko, G. I., Yershov, A., Karakhimc, S. O., Ilchenko, O., and Posudievsky, O. Y. (2018). 2D-BN nanoparticles as a spectroscopic marker and drug delivery system with protection properties. *RSC Adv.* 8, 3040–3041. doi: 10.1039/C8RA05085F

Gottschalck, T. E., and Breslawec, H. (2012). *International Cosmetic Ingredient Dictionary and Handbook*. Washington, DC: Personal Care Products Council.

Grill, E., and Himmelbach, A. (1998). ABA signal transduction. *Curr. Opin. Plant Biol.* 1, 412–418. doi: 10.1016/S1369-5266(98)80265-3

Han, W. Q. (2010). Anisotropic hexagonal boron nitride nanomaterials: synthesis and applications. *Nanotech. Life Sci.* 3, 411–461. doi: 10.1002/9783527610419.ntls0161

Hausdorf, G., Kruger, K., Kuttner, G., Holzhutter, H. G., Frommel, C., and Hohne, W. E. (1988). Oxidation of a methionine residue in subtilisin-type proteinases by the hydrogen peroxide/borate system–an active site-directed reaction. *Biochim. Biophys. Acta* 952, 20–26. doi: 10.1016/0167-4838(88)90097-0

Hegsted, M., Keenan, M. J., Siver, F., and Wozniak, P. (1991). Effect of boron on vitamin D deficient rats. *Biol. Trace Elem. Res.* 28, 243–255. doi: 10.1007/BF02990471

Horvath, L., Magrez, A., Golberg, D., Zhi, C., Bando, Y., Smajda, R., et al. (2011). *In vitro* investigation of the cellular toxicity of boron nitride nanotubes. *ACS Nano* 5, 3800–3810. doi: 10.1021/nn200139h

Ikuno, T., Sainsbury, T., Okawa, D. C., Fréchet, J. M. J., and Zettl, A. (2007). Amine-functionalized boron nitride nanotubes. *Solid State Commun.* 142, 643–646. doi: 10.1016/j.ssc.2007.04.010

Jedrzejczak-Silicka, M., Trukawka, M., Dudziak, M., Piotrowska, K., and Mijowska, E. (2018). Hexagonal boron nitride functionalized with Au nanoparticles—properties and potential biological applications. *Nanomaterials* 8:605. doi: 10.3390/nano8080605

Jiang, X. F., Weng, Q., Wang, X. B., Li, X., Zhang, J., Golberg, D., et al. (2015). Recent progress on fabrications and applications of boron nitride nanomaterials: a review. *J. Mater. Sci. Technol.* 31, 589–598. doi: 10.1016/j.jmst.2014.12.008

Jing, L., Li, H., Tay, R. Y., Sun, B., Tsang, S. H., Cometto, O., et al. (2017). Biocompatible hydroxylated boron nitride nanosheets/poly(vinyl alcohol) interpenetrating hydrogels with enhanced mechanical and thermal responses. *ACS Nano* 11, 3742–3751. doi: 10.1021/acsnano.6b08408

Jo, I., Pettes, M. T., Kim, J., Watanabe, K., Taniguchi, T., Yao, Z., et al. (2013). Thermal conductivity and phonon transport in suspended fewlayer hexagonal boron nitride. *Nano Lett.* 13, 550–554. doi: 10.1021/nl304060g

Kivanç, M., Barutca, B., Koparal, A. T., Göncü, Y., Bostanci, S. H., and Ay, N. (2018). Effects of hexagonal boron nitride nanoparticles on antimicrobial and antibiofilm activities, cell viability. *Mater. Sci. Eng. C* 91, 115–124. doi: 10.1016/j.msec.2018.05.028

Korkmaz, M., Uzgoren, E., Bakirdere, S., Aydin, F., and Ataman, O. Y. (2007). Effects of dietary boron on cervical cytopathology and on micronucleus frequency in exfoliated buccal cells. *Environ. Toxicol.* 22, 17–25. doi: 10.1002/tox.20229

Koshida, T., Kumagai, M., and Hiwasa, S. (2019). *Hydrophilic and Highly Oil-Absorbent Boron Nitride Powder, Production Method Therefor, and Cosmetic.* U.S. Pat. No: 2014049955A20140491.

Lahiri, D., Singh, V., Benaduce, A. P., Seal, S., Kos, L., and Agarwal, A. (2011). Boron nitride nanotube reinforced hydroxyapatite composite: mechanical and tribological performance and in-vitro biocompatibility to osteoblasts. *J. Mech. Behav. Biomed. Mater.* 4, 44–56. doi: 10.1016/j.jmbbm.2010.09.005

Lee, D., Lee, B., Park, K. H., Ryu, H. J., Jeon, S., and Hong, S. H. (2015). Scalable exfoliation process for highly soluble boron nitride nanoplatelets by hydroxide-assisted ball milling. *Nano Lett.* 15, 1238–1244. doi: 10.1021/nl504397h

Lei, W., Mochalin, V. N., Liu, D., Qin, S., Gogotsi, Y., and Chen, Y. (2015). Boron nitride colloidal solutions, ultralight aerogels and freestanding membranes through one-step exfoliation and functionalization. *Nat. Commun.* 6:8849. doi: 10.1038/ncomms9849

Lemperle, G., Gauthier-Hazan, N., and Lemperle, M. (1998). PMMA-microspheres (Artecoll) for long-lasting correction of wrinkles: refinements and statistical results. *Aesthet. Plast. Surg.* 22, 356–365. doi: 10.1007/s002669900217

Li, X., Wang, X., Zhang, J., Hanagata, N., Wang, X., Weng, Q., et al. (2017). Hollow boron nitride nanospheres as boron reservoir for prostate cancer treatment. *Nat. Commun.* 6:13936. doi: 10.1038/ncomms13936

Li, Y., Yang, M., Xu, B., Sun, Q., Zhang, W., Zhang, Y., et al. (2018). Synthesis, structure and antioxidant performance of boron nitride (hexagonal) layers coating on carbon nanotubes (multi-walled). *Appl. Surf. Sci.* 450, 284–291. doi: 10.1016/j.apsusc.2018.04.205

Lian, G., Zhang, X., Zhu, L., Tan, M., Cui, D., and Wang, Q. (2010). A facile solid-state reaction route towards nearly monodisperse hexagonal boron nitride nanoparticles. *J. Mater. Chem.* 20, 3736–3742. doi: 10.1039/b920881j

Lin, Y., Williams, T. V., and Connell, J. W. (2009). Soluble, exfoliated hexagonal boron nitride nanosheets. *J. Phys. Chem. Lett.* 1, 277–283. doi: 10.1021/jz9002108

Lin, Y., Williams, T. V., Xu, T. B., Cao, W., Elsayed-Ali, H. E., and Connell, J. W. (2011). Aqueous dispersions of few-layered and monolayered hexagonal boron nitride nanosheets from sonication-assisted hydrolysis: critical role of water. *J. Phys. Chem. C* 115, 2679–2685. doi: 10.1021/jp110985w

Liu, L., Xiao, L., Li, M., Zhang, X., Chang, Y., Shang, L., et al. (2015). Effect of hexagonal boron nitride on high-performance polyether ether ketone composites. *Colloid. Polym. Sci.* 294, 127–133. doi: 10.1007/s00396-015-3733-2

Lu, T., Wang, L., Jiang, Y., and Huang, C. (2016). Hexagonal boron nitride nanoplates as emerging biological nanovectors and their potential applications in biomedicine. *J. Mater. Chem. B* 4, 6103–6110. doi: 10.1039/C6TB01481J

Macchio, R. A., Brown, I., and Tietjen, M. (1988). *Cosmetic Powder Employing Spherical Silica Particles.* U.S. Pat. No. US. 4837011A 1988.

Mateti, S., Wong, C. S., Liu, Z., Yang, W., Li, Y., Li, L. H., et al. (2018). Biocompatibility of boron nitride nanosheets. *Nano Res.* 11, 334–342. doi: 10.1007/s12274-017-1635-y

Merlo, A., Mokkapati, V. R., Pandit, S., and Mijakovic, I. (2018). Boron nitride nanomaterials: biocompatibility and bio-applications. *Biomater. Sci.* 6, 2298–2311. doi: 10.1039/C8BM00516H

Miller, T. A., and York, P. (1988). Pharmaceutical tablet lubrication. *Int. J. Pharm.* 41, 1–19. doi: 10.1016/0378-5173(88)90130-5

Monice, M., Fiume, W. F., Bergfeld, D. V., Belsito, R. A., Hill, C. D., Klaassen, D. C., et al. (2015). Safety assessment of boron nitride as used in cosmetics. *Int. J. Toxicol.* 34, 53S−60S. doi: 10.1177/1091581815617793

Mosuang, T. E., and Lowther, J. E. (2002). Relative stability of cubic and different hexagonal forms of boron nitride. *J. Phys. Chem. Solids* 63, 363–368. doi: 10.1016/S0022-3697(00)00254-7

Nagarajan, S., Belaid, H., Pochat-Bohatier, C., Teyssier, C., Iatsunskyi, I., Coy, E., et al. (2017). Design of boron nitride/gelatin electrospun nanofibers for bone tissue engineering. *ACS Appl. Mater. Interfaces* 9, 33695–33706. doi: 10.1021/acsami.7b13199

Newman, A. L., Leppla, N. L., Breyfogle, L. E., Guay, G. G., Wilson, D. E., and Zukowski, J. M. (2015). *Applied Films for Smoothing Wrinkles and Skin Texture Imperfections.* U.S. Pat. No:20150037380A1

Nurunnabi, M., Nafiujjaman, M., Lee, S. J., Park, I. K., Huh, K. M., and Lee, Y. K. (2016). Preparation of ultra-thin hexagonal boron nitride nanoplates for cancer cell imaging and neurotransmitter sensing. *Chem. Commun.* 52, 6146–6149. doi: 10.1039/C5CC10650H

Pakdel, A., Zhi, C., Bando, Y., and Golberg, D. (2012). Low-dimensional boron nitride nanomaterials. *Mater. Today* 15, 256–265. doi: 10.1016/S1369-7021(12)70116-5

Permyakova, E. S., Sukhorukova, I. V., Antipina, L. Y., Konopatsky, A. S., Kovalskii, A. M., Matveev, A. T., et al. (2017). Synthesis and characterization of folate conjugated boron nitride nanocarriers for targeted drug delivery. *J. Phys. Chem. C* 121, 28096–28105. doi: 10.1021/acs.jpcc.7b10841

Pisetsky, D. S. (1996). Immune activation by bacterial DNA: review a new genetic code. *Immunity* 5, 303–310. doi: 10.1016/S1074-7613(00)80256-3

Pölloth, C. F. (2005). Safety assessment on polyethylene glycols (PEGs) and their derivatives as used in cosmetic products. *Toxicology* 214, 1–38. doi: 10.1016/j.tox.2005.06.001

Ralston, N. V. C., and Hunt, C. D. (2001). Diadenosine phosphates and S-adenosylmethionine:novel boron binding biomolecules detected by capillary electrophoresis. *Biochim. Biophys. Acta* 1527, 20–30. doi: 10.1016/S0304-4165(01)00130-1

Raven, J. (1980). Short- and long-distance transport of boric acid in plants. *New Phytol.* 84, 231–249. doi: 10.1111/j.1469-8137.1980.tb04424.x

Sainsbury, T., Satti, A., May, P., Wang, Z., McGovern, I., Gun'ko, Y. K., et al. (2012). Oxygen radical functionalization of boron nitride nanosheets. *J. Am. Chem. Soc.* 134, 18758–71. doi: 10.1021/ja3080665

Salvetti, A., Rossi, L., Iacopetti, P., Li, X., Nitti, S., Pellegrino, T., et al. (2015). *In vivo* biocompatibility of boron nitride nanotubes: effects on stem cell biology and tissue regeneration in planarians. *Nanomedicine* 10, 1911–1922. doi: 10.2217/nnm.15.46

Scorei, R. I., and Popa, R. (2010). Boron-containing compounds as preventive and chemotherapeutic agents for cancer. *Anti Cancer Agents Med. Chem.* 10, 346–351. doi: 10.2174/187152010791162289

Sen, Ö., and Çulha, M. (2015) Boron nitride nanotubes included thermally cross-linked gelatin-glucose scaffolds show improved properties. *Colloids Surf. B* 138, 41–49. doi: 10.1016/j.colsurfb.2015.11.036

Sen, Ö., Emanet, M., and Çulha, M. (2018) One-step synthesis of hexagonal boron nitrides, their crystallinity and biodegradation. *Front. Bioeng. Biotechnol.* 6:83. doi: 10.3389/fbioe.2018.00083

Shuai, C., Han, Z., Feng, P.;,Gao, C., Xiao, T., and Peng, S. (2015). Akermanite scaffolds reinforced with boron nitride nanosheets in bone tissue

engineering. *J Mater. Sci. Mater. Med.* 26:188. doi: 10.1007/s10856-015-5513-4

Soma, C. E., Dubernet, C., Barratt, G., Nemati, F., Appel, M., Benita, S., et al. (1999). Ability of doxorubicin-loaded nanoparticles to overcome multidrug resistance of tumor cells after their capture by macrophages. *Pharm. Res.* 16, 1710–1716. doi: 10.1023/A:1018902031370

Sukhorukova, I. V., Zhitnyak, I. Y., Kovalskii, A. M., Matveev, A. T., Lebedev, O. I., Li, X., et al. (2015). Boron nitride nanoparticles with a petal-like surface as anticancer drug-delivery systems. *ACS Appl. Mater. Interfaces* 7, 17217–17225. doi: 10.1021/acsami.5b04101

Suryavanshi, U., Balasubramanian, V. V., Lakhi, K. S., Mane, G. P., Ariga, K., Choy, J. H., et al. (2014). Mesoporous BN and BCN nanocages with high surface area and spherical morphology. *Phys. Chem. Chem. Phys.* 16:23554. doi: 10.1039/C4CP04210G

Tang, C., Bando, Y., Huang, Y., Zhi, C., and Golberg, D. (2008). Synthetic routes and formation mechanisms of spherical boron nitride nanoparticles. *Adv. Funct. Mater.* 18, 3653–3661. doi: 10.1002/adfm.200800493

Tian, Y., Xu, B., Yu, D., Ma, Y., Wang, Y., Jiang, Y., et al. (2013). Ultrahard nanotwinned cubic boron nitride. *Letter* 493, 385–388. doi: 10.1038/nature11728

Turkoglu, M., Sahin, I., and San, T. (2005). Evaluation of hexagonal boron nitride as a new tablet lubricant. *Pharm. Dev. Technol.* 10, 381–388. doi: 10.1081/PDT-65684

Ugurlu, T., and Turkoglu, M. (2008). Hexagonal boron nitride as a tablet lubricant and a comparison with conventional lubricants. *Int. J. Pharm.* 353, 45–51. doi: 10.1016/j.ijpharm.2007.11.018

Van Duin, M., Peters, J., Kieboom, A., and Van Bekkum, H. (1984). Studies on borate esters 1: the pH dependence of the stability of esters of boric acid and borate in aqueous medium as studied by 11B NMR. *Tetrahedron* 40, 2901–2911. doi: 10.1016/S0040-4020(01)91300-6

Wagner, H. (2002). Interactions between bacterial CpG-DNA and TLR9 bridge innate and adaptive immunity. *Curr. Opin. Microbiol.* 5, 62–69. doi: 10.1016/S1369-5274(02)00287-4

Wang, X., Hossain, M., Wei, Z., and Xie, L. (2018). Growth of two-dimensional materials on hexagonal boron nitride (h-BN). *Nanotechnol.* 30:034003. doi: 10.1088/1361-6528/aaeb70

Weng, Q., Wang, X., Wang, X., Bandoa, Y., and Golberg, D. (2016). Functionalized hexagonal boron nitride nanomaterials: emerging properties and applications. *Chem. Soc. Rev.* 45, 3989–4012. doi: 10.1039/C5CS00869G

Weng, Q. H., Wang, B. J., Wang, X. B., Hanagata, N., Li, X., Liu, D. Q., et al. (2014). Highly water-soluble, porous, and biocompatible boron nitrides for anticancer drug delivery. *ACS Nano.* 8, 6123–6130. doi: 10.1021/nn5014808

Wood, G. L., Janik, J. F., Pruss, E. A., Dreissig, D., Kroenke, W. J., Habereder, T., et al. (2006). Aerosol synthesis of spherical morphology boron nitride powders from organoborate precursors. *Chem. Mater.* 18, 1434–1442. doi: 10.1021/cm052032x

Yin, J., Li, J., Hang, Y., Yu, J., Tai, G., Li, X., et al. (2016). Boron nitride nanostructures: fabrication, functionalization and applications. *Small* 12, 2942–2968. doi: 10.1002/smll.201600053

Zhang, H., Chen, S., Zhi, C., Yamazaki, T., and Hanagata, N. (2013). Chitosan-coated boron nitride nanospheres enhance delivery of CpG oligodeoxynucleotides and induction of cytokines. *Int. J. Nanomed.* 8, 1783–1793. doi: 10.2147/IJN.S43251

Zhang, H., Yamazaki, T., Zhi, C., and Hanagata, N. (2012). Identification of a boron nitride nanosphere-binding peptide for the intracellular delivery of CpG oligodeoxynucleotides. *Nanoscale* 4, 6343–6350. doi: 10.1039/c2nr31189e

Differential Exchange of Multifunctional Liposomes Between Glioblastoma Cells and Healthy Astrocytes via Tunneling Nanotubes

Beatrice Formicola[1†], Alessia D'Aloia[2†], Roberta Dal Magro[1], Simone Stucchi[2], Roberta Rigolio[1], Michela Ceriani[2†] and Francesca Re[1*†]

[1] School of Medicine and Surgery, University of Milano-Bicocca, Vedano al Lambro, Italy, [2] Department of Biotechnology and Biosciences, University of Milano-Bicocca, Milan, Italy

Despite advances in cancer therapies, nanomedicine approaches including the treatment of glioblastoma (GBM), the most common, aggressive brain tumor, remains inefficient. These failures are likely attributable to the complex and not yet completely known biology of this tumor, which is responsible for its strong invasiveness, high degree of metastasis, high proliferation potential, and resistance to radiation and chemotherapy. The intimate connection through which the cells communicate between them plays an important role in these biological processes. In this scenario, tunneling nanotubes (TnTs) are recently gaining importance as a key feature in tumor progression and in particular in the re-growth of GBM after surgery. In this context, we firstly identified structural differences of TnTs formed by U87-MG cells, as model of GBM cells, in comparison with those formed by normal human astrocytes (NHA), used as a model of healthy cells. Successively, we have studied the possibility to exploit U87-MG TnTs as drug-delivery channels in cancer therapy, using liposomes composed of cholesterol/sphingomyelin and surface functionalized with mApoE and chlorotoxin peptides (Mf-LIP) as nanovehicle model. The results showed that U87-MG cells formed almost exclusively thick and long protrusions, whereas NHA formed more thin and short TnTs. Considering that thick TnTs are more efficient in transport of vesicles and organelles, we showed that fluorescent-labeled Mf-LIP can be transported via TnTs between U87-MG cells and with less extent through the protrusions formed by NHA cells. Our results demonstrate that nanotubes are potentially useful as drug-delivery channels for cancer therapy, facilitating the intercellular redistribution of this drug in close and far away cells, thus reaching isolated tumor niches that are hardly targeted by simple drug diffusion in the brain parenchyma. Moreover, the differences identified in TnTs formed by GBM and NHA cells can be exploited to increase treatment precision and specificity.

Keywords: glioblastoma, liposomes, tunneling nanotubes, doxorubicin, nanoparticles, nanomedicine

INTRODUCTION

The limits of conventional therapies against tumors, in terms of effectiveness/damage ratio, lead to the development and application in clinics of different nanotechnological drugs in the last 25 years (Stupp et al., 2009). Many advancements have been achieved in this field, but different issues, such as the complexities and heterogeneity of tumor biology, still remain unsolved. Gliomas, intrinsic brain tumors, are a dissimilar group of oncological diseases for which there is currently no cure, and only very limited progress has been made in the control of the disease course over the past three decades (Westphal and Lamszus, 2011). Among gliomas, glioblastoma multiforme (GBM, also called grade IV astrocytoma) is one of the most deadly brain tumors, with a short median patient survival and a very limited response to therapies (Louis et al., 2016). In this context, many efforts are underway toward the development of new therapeutic approaches and nanomedicine seems to be one of the most promising. Nevertheless, many obstacles have not been overcome yet. GBM has a very complex pathogenesis that involves alterations of several key cellular pathways, diffuse invasiveness, and capacity to escape therapies. An important component of tumor growth is communication within cancer cells and with other cells in the microenvironments, which strengthen tumor progression and resistance to radiotherapy and chemotherapy (Broekman et al., 2018).

Normal and tumor cells exploit different communication modalities, and one of them is represented by the physical connection via tunneling nanotubes (TnTs) and microtubes (TmTs), which form a cytoplasmic continuum between cells and allow the transport of non-secretable molecules and organelles. In particular, TnTs can mediate the transfer of cellular vesicles (Rustom et al., 2004; Önfelt et al., 2006), mitochondria (Ahmad et al., 2014), lysosomes (Abounit et al., 2016), miRNAs (Thayanithy et al., 2014), single proteins (Schiller et al., 2013), and viral particles (Sowinski et al., 2008) between cells, also very distant from each other ($>100\,\mu m$ of distance). TnTs are transient transcellular channels with a diameter of 50–200 nm, a length up to several cell diameters with variable lifetimes ranging from <60 min up to many hours (Carone et al., 2015).

Lou et al. (2012a,b) firstly described the presence of TnTs in human primary tumors and in many cancer cell lines, highlighting the key role of these membranous structures in cancer cell pathogenesis and invasion. The involvement of TnTs and TmTs has also been indicated in the re-growth of GBM after surgery and in conferring resistance to chemotherapy (Moschoi et al., 2016; Weil et al., 2017). Although TnTs are not apparent in some glioma cellular models (Van der Vos et al., 2016), they may represent a new tool for bidirectional intercellular transfer of drug-loaded nanoparticles.

In this context, there are some data supporting the direct cell-to-cell transfer of nanoparticles through TnTs, and this strategy may be exploited to increase the range of drug delivery between cancer cells (Epperla et al., 2015; Sisakhtnezhad and Khosravi, 2015; Deng et al., 2018). One of the peculiarity of GBM is the presence of glioma stem cells both within the tumor bulk, which are able to reconstitute a whole tumor after surgical resection

(Fan et al., 2010; Lin et al., 2010), and in other brain regions, where minor stem-cell niches represent a pool from which new tumor cells originate (Gould, 2017). Then, targeting primary GBM with nanotherapeutics may allow the possibility to reach via TnTs isolated, infiltrating tumor cells (stem cells included) that are hardly reached by drug diffusion in the brain parenchyma.

This study aims to evaluate *in vitro* the possible intercellular transport of multifunctional liposomes (LIP) via TnTs between human primary glioblastoma cell line. We have recently designed LIP carrying doxorubicin, as an anti-cancer drug model, and dually functionalized with apoE-derived peptide and with chlorotoxin (ClTx), as GBM targeting ligands (DeBin et al., 1993; Maletínská et al., 2000; Lyons et al., 2002; Xiang et al., 2011; Ojeda et al., 2016). The ability of LIP functionalized with apoE-derived peptide (namely, mApoE) to cross the blood–brain barrier both *in vitro* and *in vivo*, was already reported (Re et al., 2011; Balducci et al., 2014; Bana et al., 2014; Dal Magro et al., 2018).

LIP trafficking via TnTs in GBM cells has not been reported yet. Moreover, we compared the heterogeneity of TnTs, in terms of structure, morphology, size, and abundance between GBM cells and human healthy astrocytes, with the aim to increase the precision and specificity of treatments.

MATERIALS AND METHODS

Materials

Cholesterol (Chol), doxorubicin (DOX), thiazolyl blue tetrazolium bromide, 4-(2-hydroxyethyl)piperazine-1-ethanesulfonic acid (HEPES), Triton X-100, ultra-low-range molecular weight marker (MW 1,060–26,600), EZBlue Gel Staining Reagent, 1,1′-dioctadecyl-3,3,3′,3′-tetramethylindocarbocyanine perchlorate (DiI probe), TRITC-phalloidin, and mouse monoclonal anti-β-tubulin antibody were purchased from Sigma Aldrich (Milan, Italy). 1,2-Distearoyl-*sn*-glycero-3-phospho-ethanolamine-*N*[maleimide(polyethyleneglycol)-2000] (mal-PEG-DSPE) and sphingomyelin from bovine brain (Sm) were purchased from Avanti Polar Lipids, Inc. (Alabaster, AL, USA). BODIPY™ FL C 12-sphingomyelin (BODIPY-Sm) was purchased from Thermo Fisher Scientific. 1,2-Distearoyl-*sn*-glycero-3-phospho-ethanolamine-*N*[(polyethyleneglycol)-2000] *n*-hydroxysuccinimide ester (NHS-PEG-DSPE) was purchased from Nanocs (Boston, USA). Ultrapure and deionized water was obtained from Direct-Q5 system (Millipore, Italy). mApoE peptide (CWG-LRKLRKRLLR, MW 1,698.18 g/mol) and ClTx (MW 4,004 g/mol) were synthetized by KareBay Biochem (Monmouth Junction, NJ, USA). Dialysis membranes (cutoff 12,000–14,000 Da) were purchased from Medicell International Ltd (London, UK). Penicillin–streptomycin (P/S) solution 100× was purchased from Euroclone (Milan, Italy); phosphate-buffered saline (PBS) 1×, collagen, trypsin/EDTA solution, and NuPAGE Bis-Tris (4–12%) were from Invitrogen. All other chemicals were of analytical grade and were obtained from either Sigma Aldrich or Merck. Alexa Fluor 488 goat anti-mouse IgG and CellTrace Far Red Dye (CT) were from Life Technologies. 3,3′-Dioctadecyloxacarbocyanine perchlorate (DiO) was from Sigma Aldrich (Milan, Italy).

Preparation of Chlorotoxin–PEG-DSPE

ClTx-lipid was prepared as described in Xiang et al. (2011) with small modifications. Briefly, 0.1 μmol of NHS-PEG-DSPE in CHCl$_3$/MeOH (2:1, vol/vol) was dried under N$_2$ to remove organic solvents. Then 5 eq (0.5 μmol) of ClTx dissolved in 10 mM of Hepes and 150 mM of NaCl pH 7.4 was added to the dried lipid. The reaction was conducted under gentle stirring for 90 min at room temperature. The resulting solution was dialyzed against MilliQ water for 2 days in a dialysis tube (molecular weight cutoff [MWCO] = 12–14,000 Da) to remove unreacted ClTx and then lyophilized overnight.

Preparation Multifunctional Liposomes

LIP were composed of sphingomyelin, cholesterol (1:1, mol/mol) added with 2.5 mol% of mal-PEG-PE, for the covalent binding of mApoE peptide, and with 0.5 mol% of BODIPY-Sm as fluorescent probe (Re et al., 2010, 2011). LIP were prepared in 10 mM of Hepes and 150 mM of NaCl pH 7.4 by extrusion procedure through polycarbonate membranes of 100-nm-diameter pores, under N$_2$. mApoE peptide was covalently attached on LIP surface by thiol–maleimide coupling, as previously described (Re et al., 2010, 2011). ClTx-lipid was added to mApoE-LIP by post-insertion technique, following the procedure previously described (Mare et al., 2018). This sample will be referred as Mf-LIP. As controls, LIP composed of sphingomyelin and cholesterol (1:1, mol/mol) were prepared in ammonium sulfate (500 mM, pH 5.5) by extrusion procedure as described above. LIP were dialyzed against 10 mM of Hepes and 150 mM of NaCl pH 7.4, overnight, and then incubated with DOX (1.5 μmol of DOX/10 μmol of total lipids) for 1 h at 65°C to allow the incorporation of DOX in the LIP core. This sample will be referred to as DOX-LIP. Mf-LIP and DOX-LIP were purified with a Sepharose G-25 fine column (25 × 1 cm) to remove unbounded and unincorporated materials.

Characterization of Multifunctional Liposomes

After purification, the amount recovered for each compound was determined by different techniques. Briefly, phospholipids content was quantified by Stewart Assay (Stewart, 1980); the amount of ClTx and mApoE on LIP surface was assessed by sodium dodecyl sulfate–polyacrylamide gel electrophoresis (SDS-PAGE). DOX loading was quantified spectrofluorometrically (λex = 495 nm; λem = 592 nm) after vesicle disruption with 0.1% Triton X-100. The DOX encapsulation yield in LIP was calculated by comparing fluorescence intensities with a previously established calibration curve of free DOX in 10 mM of Hepes and 150 mM of NaCl pH 7.4. Size and polydispersity index (PDI) were analyzed by dynamic light scattering (DLS) technique (Brookhaven Instruments Corporation, Holtsville, NY, USA). ζ-Potential was determined by using an interferometric Doppler velocimetry with the same instrument equipped with ZetaPALS device. LIP stability was measured in 10 mM of Hepes and 150 mM of NaCl pH 7.4 by observing size and PDI by DLS for 1 week.

Cell Cultures

U87-MG glioblastoma cells were purchased from American Type Culture Collection (ATCC, VA, USA) and were grown in DMEM high glucose, 10% fetal bovine serum (FBS), 1% P/S, and 1% glutamine (Tamborini et al., 2016). Normal human astrocytes (NHA), purchased from Lonza (Walkersville, Maryland, USA), were maintained in astrocyte basal medium supplemented with AGM BulletKit™. All cell lines were cultured at 37°C under a humidified atmosphere containing 5% CO$_2$.

Tunneling Nanotube Analysis by Confocal Microscopy

NHA and U87-MG cells were seeded at a density of 5×10^3 or 1.5×10^4 cells/cm^2, respectively, on porcine gelatin pretreated coverslips. One day after seeding, cells were treated for 1 or 24 h with free DOX (15 or 25 μg/ml) or with DOX-LIP (15 μg/ml of DOX and 200 nmol of total lipids) or with fluorescent-labeled Mf-LIP (200 nmol of total lipids) at 37°C in 5% CO$_2$. Untreated cells were used as a control. After treatment, cells were then left for 2 h in each culture complete medium and then stained for 20 min with 1.9 μl/ml of DiI in PBS (membrane/endocytic vesicles), or with 5 μl/ml of DiO in PBS, to label cell membranes, TnTs included, according to the manufacturer's instructions. Cells were then fixed for 8 min with 3.7% paraformaldehyde in PBS. Fluorescence images were examined with a 40× magnification on A1R Nikon (Nikon, Tokyo, Japan) laser scanning confocal microscope. Cells were carefully scored for the presence of TnTs. About 200 cells for each experiment were analyzed. TnTs were counted. Experiments were performed in triplicate. Images were analyzed by ImageJ software.

Cellular Uptake of Doxorubicin-Liposomes and Multifunctional Liposomes

U87-MG cells were seeded on a 6-well plate (5×10^3 cells/cm^2); and after 2 days of culture, cells were treated with free DOX (15 μg/ml) or LIP formulations (DOX 15 μg/ml) for 1 and 3 h. At the two different time points, free DOX and LIP formulations were removed, and the cells were washed with PBS, detached, and treated with lysis buffer (50 mM of Tris–HCl pH 7.4, 150 mM of NaCl, 2 mM of EDTA, 1% Triton X-100, 0.1% SDS, and 1 mM of DTT). Samples were centrifuged at 12,000 rpm for 15 min at 4°C and the DOX fluorescence (λex = 495 nm; λem = 592 nm) in the pellets was measured by Jasco FP-8500 spectrofluorometer. Results were expressed as DOX fluorescence in pellets/DOX fluorescence in initial sample ×100 and indicated as cell uptake (%).

High-throughput images of living U87-MG cells on a 96-well plate (3×10^4 cells/cm^2) were acquired automatically with an Operetta® High Content Imaging System (PerkinElmer, UK). After 2 days of culture, cells were treated with free DOX (15 μg/ml) or LIP formulations (DOX 15 μg/ml), and the uptake was evaluated by acquiring images at three different time points (0, 1, and 3 h). Before imaging, cells were washed three times with PBS. Images were acquired in the DOX channel and in the brightfield channel, using a 40× air objective lens and standard

instrument filters. Ten different fields were imaged in each well. The image were then analyzed by the Harmony® analysis software (PerkinElmer, UK).

Actin, Tubulin, and DAPI Staining

NHA and U87-MG cells were plated at a density of 5×10^3 or 1.5×10^4 cells/cm^2, respectively, on porcine gelatin pretreated coverslips. One day after seeding, cells were fixed for 10 min with 3.7% paraformaldehyde in PBS, permeabilized for 4 min with 0.1% Triton X-100/PBS, and finally stained with different antibodies. In particular, cells were treated with TRITC-phalloidin (1:40 in 1% BSA/PBS) for actin staining, as described previously (Ceriani et al., 2007). For tubulin staining, cells were incubated with mouse monoclonal anti-β-tubulin primary antibody (1:150 in 1% BSA/PBS) for 1 h at 37°C. Then cells were washed and incubated with the secondary antibody Alexa Fluor 488 goat anti-mouse IgG (1:200 in 1% BSA/PBS) for 45 min at 37°C.

For nuclei staining, U87-MG and NHA cells were plated on gelatin pretreated coverslips. Cells were leaved in culture complete medium for 48 h and then incubated with 15 μg/ml of free DOX for 1 h. Cells were then stained for 20 min with DiO (5 μl/ml), fixed, permeabilized, and colored with DAPI (Sigma) (1 μg/ml) for 10 min at room temperature.

Fluorescence-Activated Cell Sorting Analysis of Cell-to-Cell Liposome Transfer

U87-MG cells and NHA cells were seeded on 12-well plates at a cell density of 6.5×10^3 and 15×10^4 cells/cm^2, respectively. Three days after seeding, "donor" cells were incubated with BODIPY-Sm Mf-LIP (200 nmol of total lipids) for 1 h at 37°C, whereas "acceptor" cells were treated with CellTrace Far Red Dye (CT) at 1 μM for NHA and 10 μM for U87-MG cells for 30 min. Cells were detached, and the following co-culture between "donor" and "acceptor" cells was set up: U87-MG (donor) → NHA (acceptor); U87-MG (donor) → U87-MG (acceptor); and NHA (donor) → NHA (acceptor). Co-culture were maintained for 24 h at 37°C. Cell-to-cell transfer of Mf-LIP was assessed by fluorescence-activated cell sorting (FACS) (FACSCantoI BD Biosciences) analysis. At least 50,000 events were acquired in an operator-defined gate designed on a physical parameter (forward versus side scatter [FSC vs. SSC]) dot plot. The fluorescence intensity analysis on fluorescein isothiocyanate (FITC) (to detect BODIPY) and allophycocyanin (APC) (to detect CT) histogram was performed on a single cell gate defined on a FSC-H vs. FSC-A dot plot. The reported data refer only to the double FITC/APC-positive events among this population, representing the Mf-LIP transfer to "acceptor" cells.

Statistical Analysis

For TnT quantification, data were analyzed by Student t-test. Data were expressed as a mean ± standard error (SE). For percentage distribution of thin and thick TnTs, data were analyzed by two-way or one-way ANOVA followed respectively by Sidak's multiple comparisons test or Dunnett's *post-hoc* test.

All experiments were conducted at least in triplicate. All the analyses were performed with GraphPad Prism 8 software

(license number: GP8-1519368-RFQS-B8CB4). Differences were considered significant at $^*p < 0.05$, $^{**}p < 0.01$, and $^{***}p < 0.001$.

RESULTS

Characterization of Liposomes

The results showed that DOX-LIP displayed a diameter of 121 ± 6 nm with a PDI value of 0.098 ± 0.01; the ζ-potential was −19.32 ± 0.58 mV. Mf-LIP showed a diameter of 187 ± 5 nm with a PDI value of 0.087 ± 0.05; the ζ-potential was −14.5 ± 0.43 mV. These parameters remained constant for 1 week within the experimental error (<2.7% of variation). For both preparations, the total lipid recovery after purification was 79.5 ± 8%. For Mf-LIP, the yield of functionalization with mApoE and ClTx was 88.5
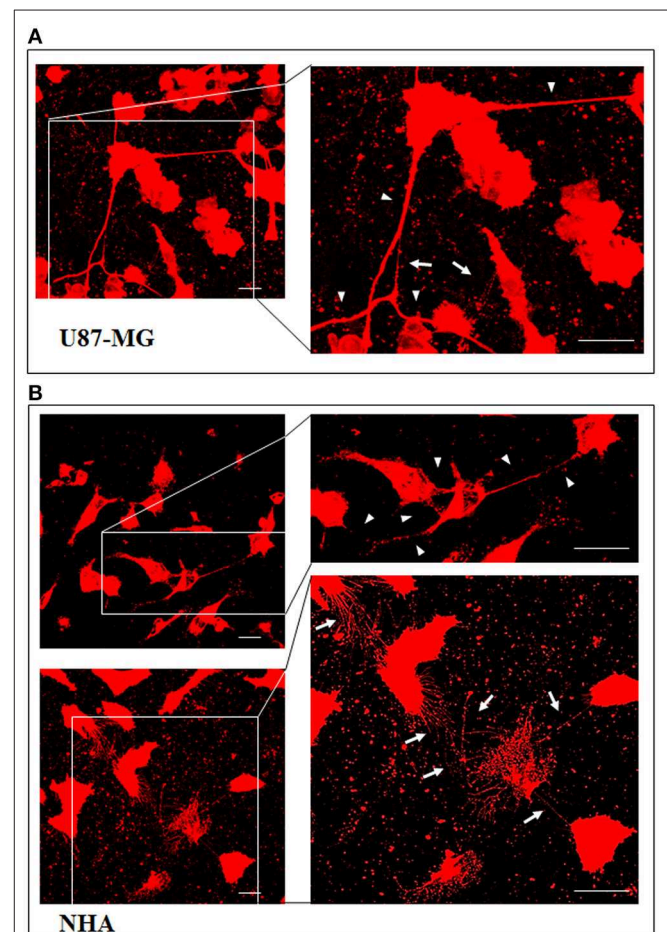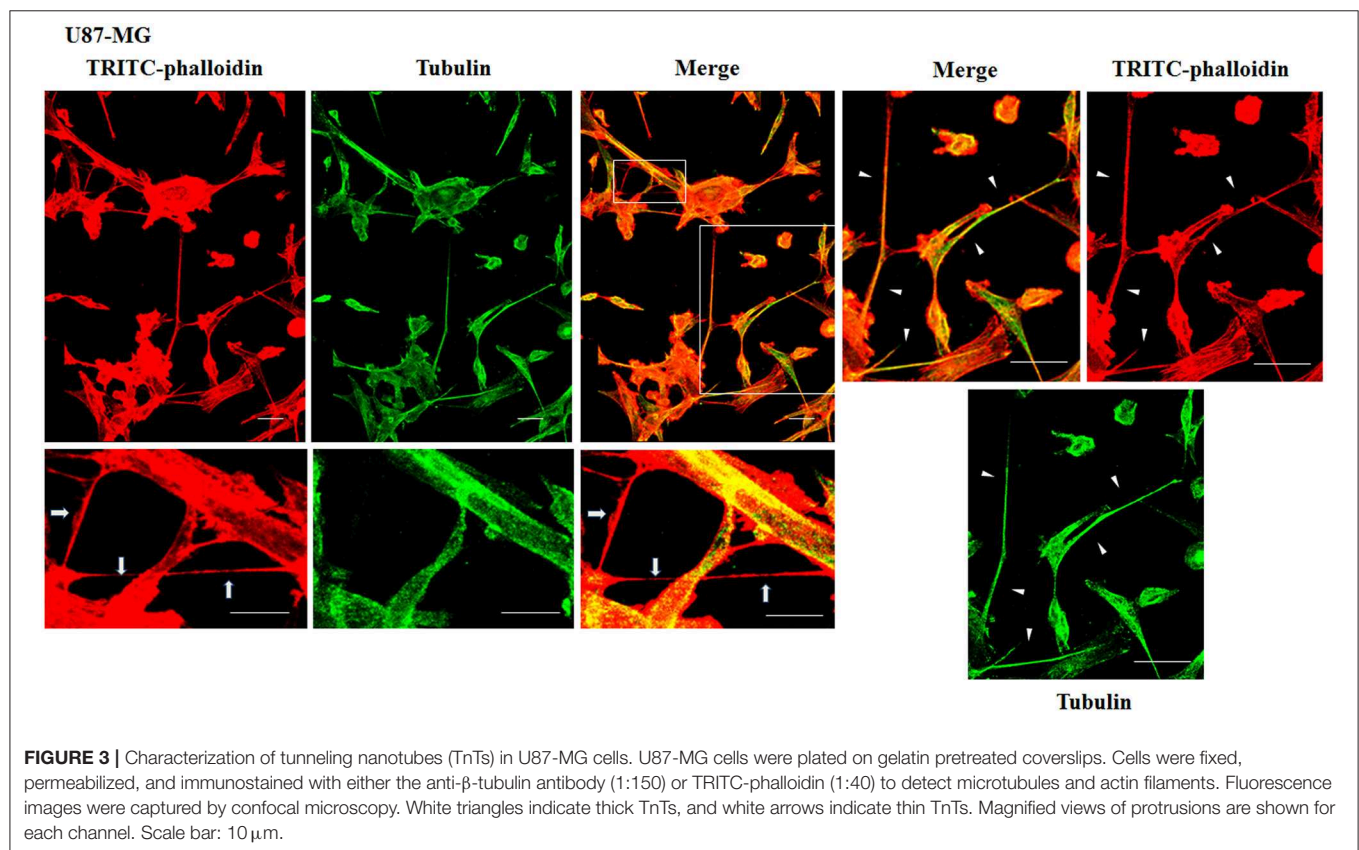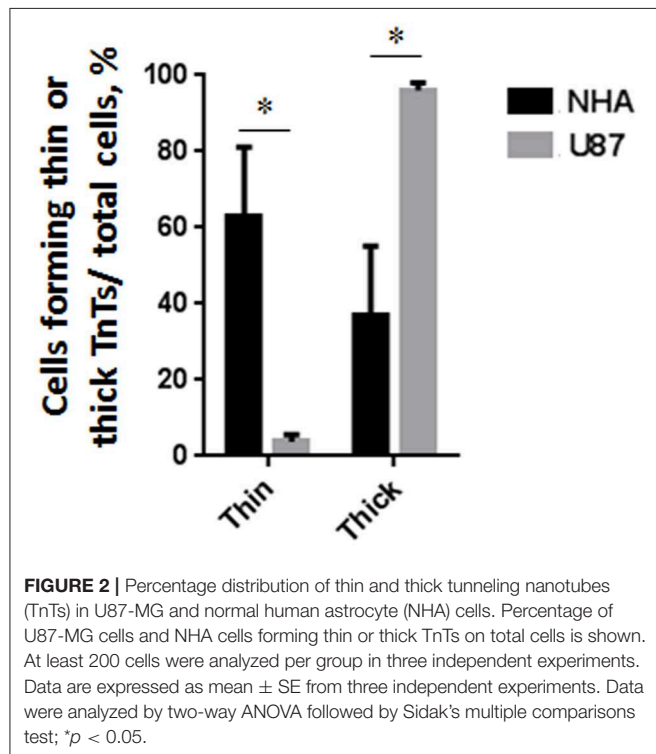

FIGURE 1 | U87-MG and normal human astrocyte (NHA) cells form thin and thick tunneling nanotubes (TnTs). U87-MG cells **(A)** or NHA cells **(B)** were plated on gelatin pretreated coverslips and then fixed and stained with 1,1′-dioctadecyl-3,3,3′,3′-tetramethylindocarbocyanine perchlorate (DiI) (1.9 μl/ml) to detect TnTs. Fluorescence images were acquired by a 40× magnification on A1R Nikon laser scanning confocal microscope. The images show the maximum projection obtained from the z-projections shown in **Figures S1, S2**. White arrows indicate thin TnTs, whereas white triangles indicate thick TnTs. Scale bar: 10 μm. Magnified views of protrusions are shown.

± 10% (corresponding to 2.2 mol% of mApoE/total lipids) and 71.2 ± 3% (corresponding to 1.42 mol% of ClTx/total lipids), respectively. For DOX-LIP, the incorporation yield of DOX was

70 ± 6%, corresponding to 80 ± 5 µg of DOX/µmol of lipids. These results derived from at least five different batches.

U87-MG Cells, Compared With Normal Human Astrocytes, Form Tunneling Nanotubes With Different Thickness

To investigate if U87-MG cells (model of GBM tumor cells) are able to form *in vitro* intercellular connections with characteristics of TnTs, and if they are different from those formed by NHA cells (model of normal healthy astrocytes), we used confocal microscopy technique and 3D reconstruction. Both cell types form protrusions connecting distant cells with characteristics of TnTs (**Figure 1**), which were not in contact with the substratum (**Figures S1, S2**). To allow for a quantitative determination, the observed membrane protrusions of about 200 cells were scored for each cell line. The results showed that the number of cells forming TnTs is comparable between U87-MG and NHA (44 ± 6.6 and 57 ± 3.5%, respectively) (**Figure S3**). Confocal images show the presence of TnTs of different thickness, very thin (≤0.7 µm, measuring a minimum of 100–200 nm) and thick (≥0.7 µm, up to 1 µm) (Gerdes et al., 2007). More interestingly, we detected significant differences in both thin and thick TnTs: U87-MG cells formed almost exclusively thick protrusions, whereas NHA formed either thin and thick TnTs (**Figure 2**). The measurement of TnT diameter by light microscopy was not accurate owing to the resolution limit. Confocal microscopy showed that some TnTs reach thicknesses of over 700 nm, which could be due to incorporation of additional components inside
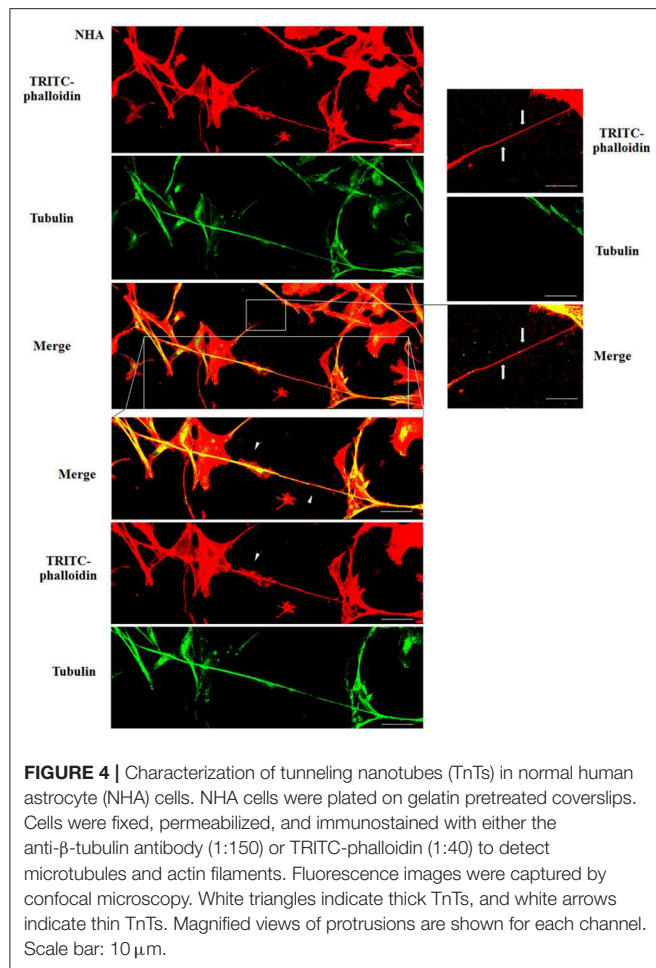

FIGURE 2 | Percentage distribution of thin and thick tunneling nanotubes (TnTs) in U87-MG and normal human astrocyte (NHA) cells. Percentage of U87-MG cells and NHA cells forming thin or thick TnTs on total cells is shown. At least 200 cells were analyzed per group in three independent experiments. Data are expressed as mean ± SE from three independent experiments. Data were analyzed by two-way ANOVA followed by Sidak's multiple comparisons test; *p < 0.05.

FIGURE 3 | Characterization of tunneling nanotubes (TnTs) in U87-MG cells. U87-MG cells were plated on gelatin pretreated coverslips. Cells were fixed, permeabilized, and immunostained with either the anti-β-tubulin antibody (1:150) or TRITC-phalloidin (1:40) to detect microtubules and actin filaments. Fluorescence images were captured by confocal microscopy. White triangles indicate thick TnTs, and white arrows indicate thin TnTs. Magnified views of protrusions are shown for each channel. Scale bar: 10 µm.

FIGURE 4 | Characterization of tunneling nanotubes (TnTs) in normal human astrocyte (NHA) cells. NHA cells were plated on gelatin pretreated coverslips. Cells were fixed, permeabilized, and immunostained with either the anti-β-tubulin antibody (1:150) or TRITC-phalloidin (1:40) to detect microtubules and actin filaments. Fluorescence images were captured by confocal microscopy. White triangles indicate thick TnTs, and white arrows indicate thin TnTs. Magnified views of protrusions are shown for each channel. Scale bar: 10 μm.

the TnTs, such as microtubules, as previously suggested (Önfelt et al., 2006).

To evaluate the presence of tubulin, typical marker for thick TnTs, and of actin, typical marker for thin TnTs (D'Aloia et al., 2018), U87-GM and NHA cells were stained with anti-tubulin fluorescent antibody and fluorescent phalloidin.

The results showed that U87-MG cells were able to form thick TnTs, which contained both actin and tubulin (**Figure 3**). NHA cells were able to form thick TnTs made of actin and tubulin, but they also established thin TnTs, which were positive only to actin staining (**Figure 4**).

Doxorubicin Treatment Induced Changes in the Tunneling Nanotube Thickness of U87-MG Cells

To evaluate the ability of U87-MG and NHA to exchange DOX via TnTs, cells were treated with two different doses of free DOX. Treatments with 25 μg/ml of DOX for 24 h induced a strong toxic effect on both cell types, hindering the image analysis (data not shown). Then, all the subsequent experiments were carried out by incubating cells with 15 μg/ml of DOX for 1 h. Analysis performed at confocal microscope showed that DOX (λex = 495 nm; λem = 592 nm) localizes principally at the nucleus

in both cell lines (**Figure 5**; **Figure S4**), as expected (de Lange et al., 1992), but it was not detectable along TnT structures. The quantitative determination of TnTs revealed that the % of cells forming TnTs was not affected by the treatment with free DOX (**Figures 6A,B**), for both the cell types used.

Comparing the thickness of TnTs, the DOX treatment on U87-MG cells induced the formation of about 80% of thin TnTs, with a strong reduction of thick TnTs (**Figure 6C**). By prolonging the incubation time up to 24 h, TnTs disappeared and U87-GM cells died (**Figure S5**).

No significant changes in TnTs thickness were detected for NHA, which remained comparable with untreated NHA (**Figure 6D**).

Multifunctional Liposomes, Compared With Normal Human Astrocytes, Were Preferentially Located in the Thickest Tunneling Nanotubes of U87-MG

The cellular uptake of Mf-LIP (LIP bi-functionalized with mApoE and ClTX) by U87-MG was evaluated by confocal microscopy and fluorescence measurements. The results showed that Mf-LIP displayed a three-fold increase of cellular uptake, compared with DOX-LIP used as a control (**Figure S6**). Both DOX-LIP and Mf-LIP were localized only in thickest TnTs (**Figures 7**, **8**). Contrarily, NHA cells were able to uptake only a small amount of DOX-LIP and Mf-LIP. Also in these cells, LIP were localized only in thick TnTs (**Figures 9**, **10**). The treatment of U87-MG cells with DOX-LIP did not affect the % of cells forming TnTs (**Figure S7A**) but strongly increased thin TnTs, with a significant reduction of thick TnTs (**Figures 11A,B**), similar to the effect exerted by free DOX.

The treatment of U87-MG and NHA cells, compared with untreated cells, with Mf-LIP did not change the percentage of thin and thick TnTs (**Figures 11C,D**). Also the treatment with Mf-LIP did not affect the % of cells forming TnTs (**Figure S7A**) neither the ratio between thin and thick TnTs (**Figures 11C,D**). No differences were detected in TnTs formed by NHA cells after incubation with DOX-LIP or Mf-LIP (**Figure S7B**; **Figures 6, 11C,D**). Finally, to evaluate the integrity of LIP inside to TnTs, double-labeled Mf-LIP (containing BODIPY-Sm and DOX) were used. As it is shown in **Figure 12**, the co-localization of both fluorescent signals was detected in TnTs from both U87-MG and NHA cells.

Multifunctional Liposomes Were Preferentially Exchanged via Tunneling Nanotubes Between U87-MG Co-cultured Cells

In order to prove the ability of cells to mutually exchange Mf-LIP, co-culture mixtures between U87-MG and NHA were set up. U87-MG or NHA cells were incubated with fluorescent-labeled Mf-LIP in order to generate Mf-LIP-loaded "donor" populations. U87-MG or NHA cells were labeled with a fluorescent cell dye to generate detectable "acceptor" populations. Then, different co-cultures of "donor" and "acceptor" cells were prepared
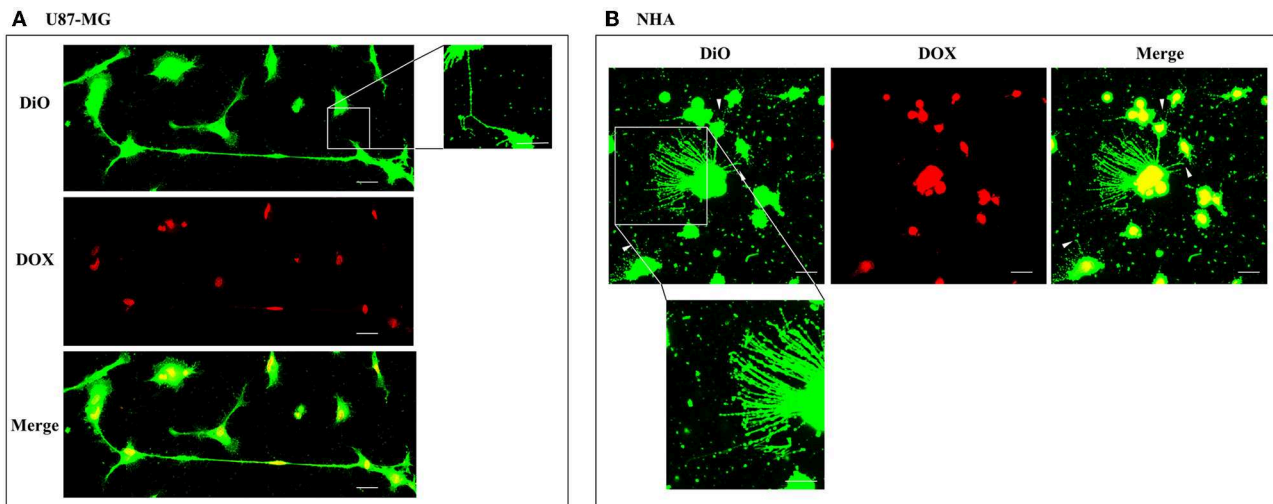
FIGURE 5 | Doxorubicin localizes into the nucleus of U87-MG and normal human astrocyte (NHA) cells. U87-MG cells **(A)** and NHA cells **(B)** were plated on gelatin pretreated coverslips, incubated with 15 μg/ml of DOX for 1 h, and then stained with 3,3′-dioctadecyloxacarbocyanine perchlorate (DiO) (5 μl/ml) to detect tunneling nanotubes (TnTs). Cells were fixed, and fluorescence images were captured with a 40× magnification on A1R Nikon laser scanning confocal microscope. White triangles indicate thin TnTs. Magnified views of thin TnT protrusions are shown. Scale bar: 10 μm. DOX = doxorubicin.
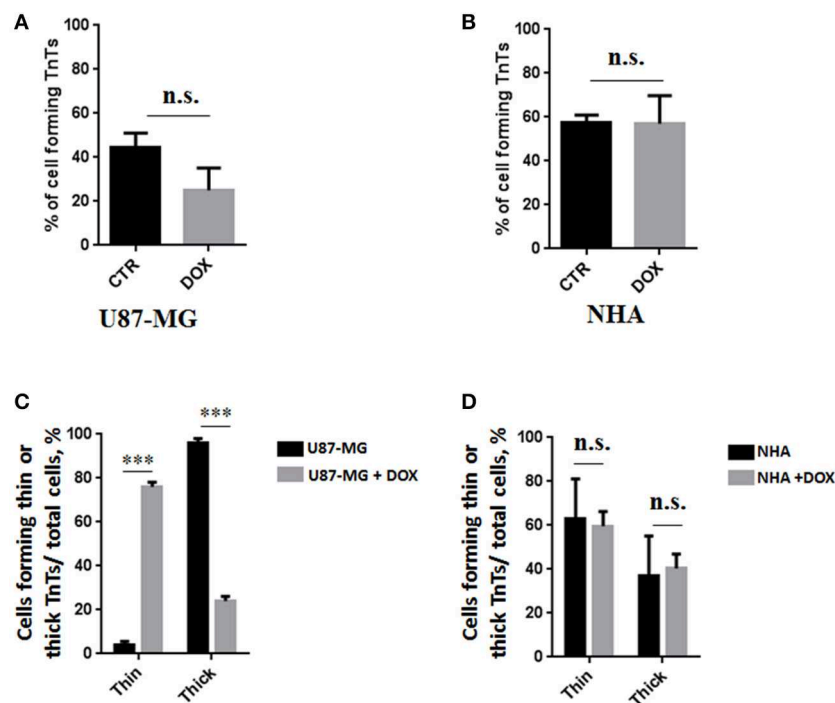
FIGURE 6 | Percentage of cells forming tunneling nanotubes (TnTs) after DOX treatment. Percentage of U87-MG cells **(A)** and normal human astrocytes (NHA) cells **(B)** forming TnTs on total cells is shown. At least 200 cells were analyzed per group in three independent experiments. Data are expressed as mean ± SE from three independent experiments. Data were analyzed by Student t-test; n.s., not significant. DOX, doxorubicin; CTR, control untreated cells. **(C,D)** Percentage distribution of thin and thick TnTs in U87-MG **(C)** and NHA **(D)** cells on total cells, after treatment with DOX. At least 200 cells were analyzed per group in three independent experiments. Data are expressed as mean ± SE from three independent experiments. Data were analyzed by two-way ANOVA followed by Sidak's multiple comparisons test; n.s., not significant; ***$p < 0.001$.

(**Figure 13A**). The cell-to-cell transfer of Mf-LIP was assessed by FACS analysis to detect the co-presence of the two fluorescent signals in the "acceptor" cells (**Figures 13B–D**).

The results showed that Mf-LIP were transferred via TnTs between NHA (donor) → NHA (acceptor) with a low rate, as demonstrated by the detection of 5 ± 0.6% of
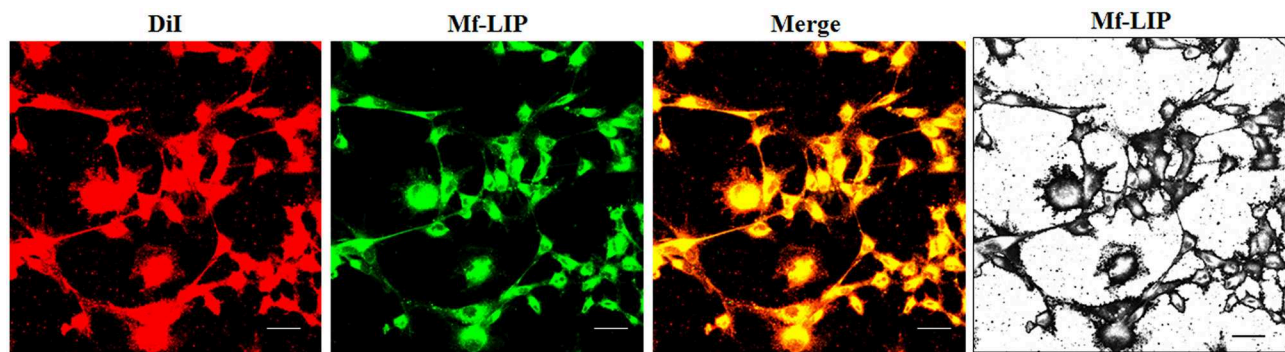
FIGURE 7 | Localization of DOX-LIP in U87-MG tunneling nanotubes (TnTs). U87-MG cells were plated on gelatin pretreated coverslips. Cells were left in culture complete medium for 48 h and then incubated with DOX-LIP (15 μg/ml of DOX and 200 nmol of total lipids) for 1 h. Cells were later stained for 20 min with 3,3′-dioctadecyloxacarbocyanine perchlorate (DiO) (5 μl/ml) and fixed, and fluorescence images were captured with a 40× magnification on A1R Nikon laser scanning confocal microscope. Black triangles indicate the DOX-LIP in thick TnTs. Magnified views of protrusions and black-and-white images are shown. Scale bar: 10 μm. DOX-LIP, liposomes embedding doxorubicin.

FIGURE 8 | Localization of Mf-LIP in U87-MG tunneling nanotubes (TnTs). U87-MG cells were plated on gelatin pretreated coverslips. Cells were left in culture complete medium for 48 h, and then cells were incubated with Mf-LIP (200 nmol of total lipids) for 1 h. Cells were later stained for 20 min with 1,1′-dioctadecyl-3,3,3′,3′-tetramethylindocarbocyanine perchlorate (DiI) (1.9 µl/ml). Cells were fixed, and fluorescence images were captured with a 40× magnification on A1R Nikon laser scanning confocal microscope. Black-and-white image is also shown. Scale bar: 10 µm. Mf-LIP, multifunctional liposomes.
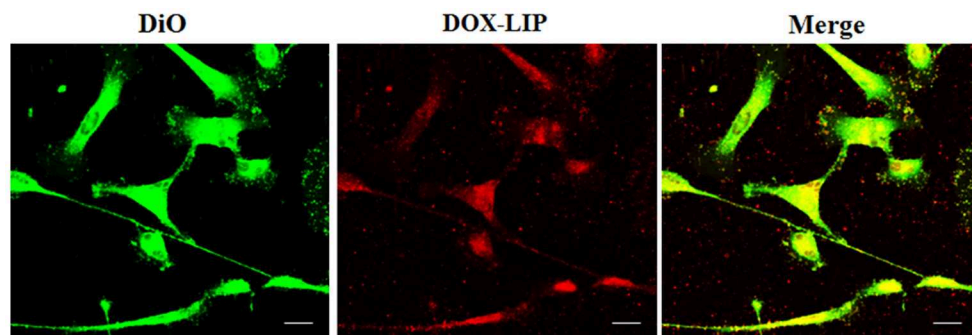
FIGURE 9 | Localization of DOX-LIP in normal human astrocytes (NHA) tunneling nanotubes (TnTs). NHA cells were seeded on gelatin pretreated coverslips. Cells were left in culture complete medium for 48 h and then incubated with DOX-LIP (15 µg/ml of DOX and 200 nmol of total lipids) for 1 h. Cells were later stained for 20 min with 3,3′-dioctadecyloxacarbocyanine perchlorate (DiO) (5 µl/ml) and fixed, and fluorescence images were captured with a 40× magnification on A1R Nikon laser scanning confocal microscope. Scale bar: 10 µm. DOX-LIP, liposomes embedding doxorubicin.

double fluorescent cells over the total cells. In comparison, the rate of Mf-LIP exchange of U87-MG (donor) → NHA (acceptor) was lower (3.8 ± 0.2% of Mf-LIP positive "acceptor" NHA).

Interestingly, the results showed that U87-MG cells were more efficient in transferring Mf-LIP between them than were U87-MG (donor) → NHA (acceptor), as demonstrated by the detection of 8.2 ± 1.5% of Mf-LIP positive "acceptor" U87-MG (**Figure 13E**).

DISCUSSION

In the context of searching more effective therapies against GBM, which remains an incurable brain tumor, we focus our attention on the cell communication. Intercellular communication plays an important role in tumor progression, invasiveness, and resistance to conventional treatments (Broekman et al., 2018). Among the different ways that cells used to exchange non-secretable messages, TnTs and TmTs are involved in the re-growth of GBM after surgery and in conferring resistance to radiotherapy and chemotherapy (Moschoi

et al., 2016; Weil et al., 2017). Starting from our expertise in the design of nanoparticles, we synthesized and characterized LIP carry doxorubicin, as an anti-cancer drug model, and dually functionalized with mApoE and with ClTx, as GBM targeting ligands (DeBin et al., 1993; Maletínská et al., 2000; Lyons et al., 2002; Ojeda et al., 2016; Formicola et al., 2019). The ability of human primary glioblastoma cell line (U87-MG), in comparison with NHA, to exchange Mf-LIP via TnTs has been investigated. Mf-LIP characterization has shown that the different batches herein prepared were highly reproducible and stable over time, with the yield of the reactions comparable with those of previously reported ones (Re et al., 2010, 2011; Formicola et al., 2019).

As it is reported in literature that TnTs are not observed in some glioma cellular models (Van der Vos et al., 2016), we checked if U87-MG cells and NHA cells herein used were able to form TnTs *in vitro*. The results showed that both types of cells were able to communicate between them by TnTs, as already reported (Zhang and Zhang, 2015; Rostami et al., 2017; Reindl et al., 2019), and the percentage of cells forming TnTs was similar between U87-MG and NHA cells.
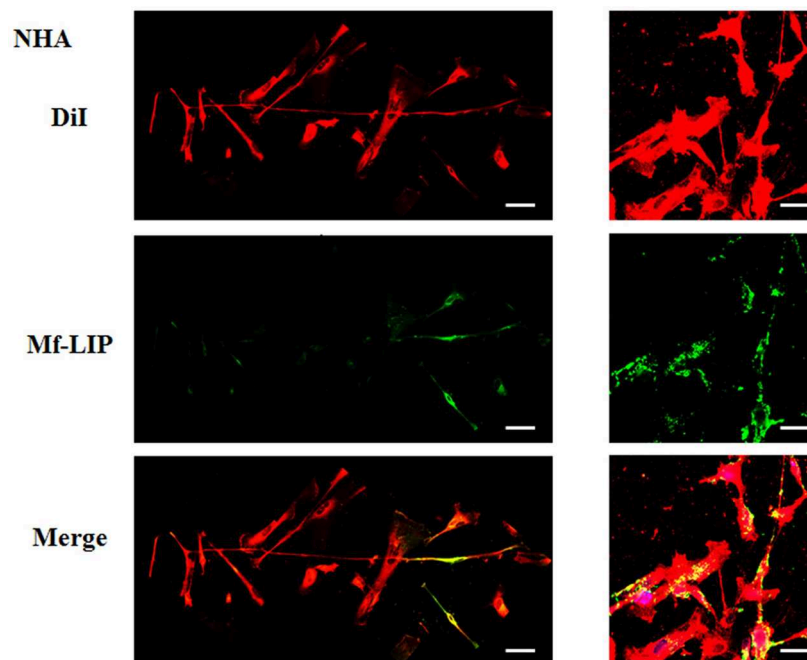
FIGURE 10 | Localization of Mf-LIP in normal human astrocytes (NHA) tunneling nanotubes (TnTs). NHA cells were plated on gelatin pretreated coverslips. Cells were left in culture complete medium for 48 h and then incubated with Mf-LIP (200 nmol of total lipids) for 1 h. Cells were later stained for 20 min with 1,1′-dioctadecyl-3,3,3′,3′-tetramethylindocarbocyanine perchlorate (DiI) (1.9 μl/ml). Cells were fixed, and fluorescence images were captured with a 40× magnification on A1R Nikon laser scanning confocal microscope. Black triangles indicate the presence of Mf-LIP in thick TnTs. Magnified views of protrusions and black-and-white images are shown. Scale bar: 10 μm. Mf-LIP, multifunctional liposomes.
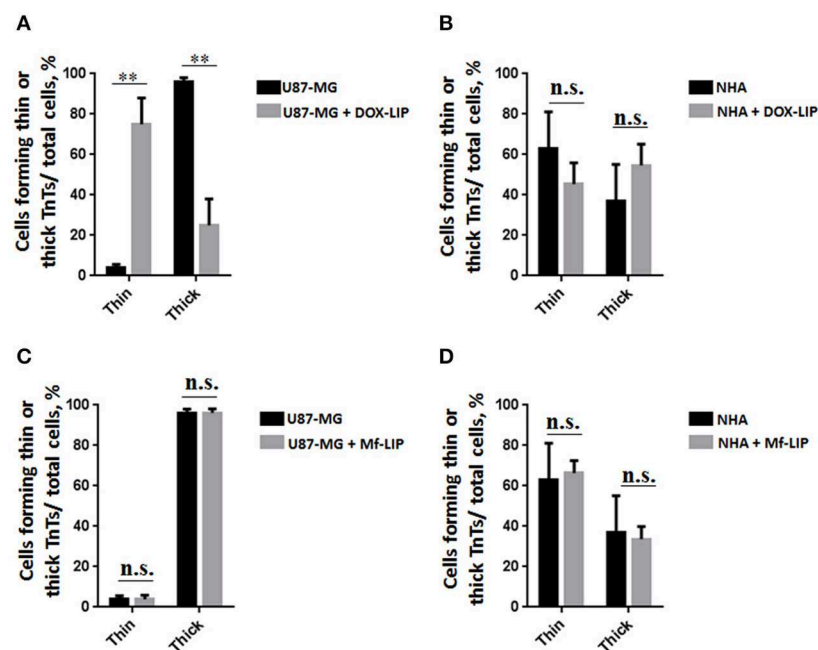
FIGURE 11 | Percentage distribution of thin and thick tunneling nanotubes (TnTs) in U87-MG and normal human astrocytes (NHA) cells after treatment with liposomes embedding doxorubicin (DOX-LIP) or multifunctional liposomes (Mf-LIP). Percentage distribution of thin and thick TnTs in U87-MG **(A)** and NHA **(B)** cells after treatment with DOX-LIP. Percentage distribution of thin and thick TnTs in U87-MG **(C)** and NHA **(D)** cells after treatment with Mf-LIP. At least 200 cells were analyzed per group in three independent experiments. Data are expressed as mean ± SE from three independent experiments. Data were analyzed by two-way ANOVA followed by Sidak's multiple comparisons test; n.s., not significant; $^{**}p < 0.01$.
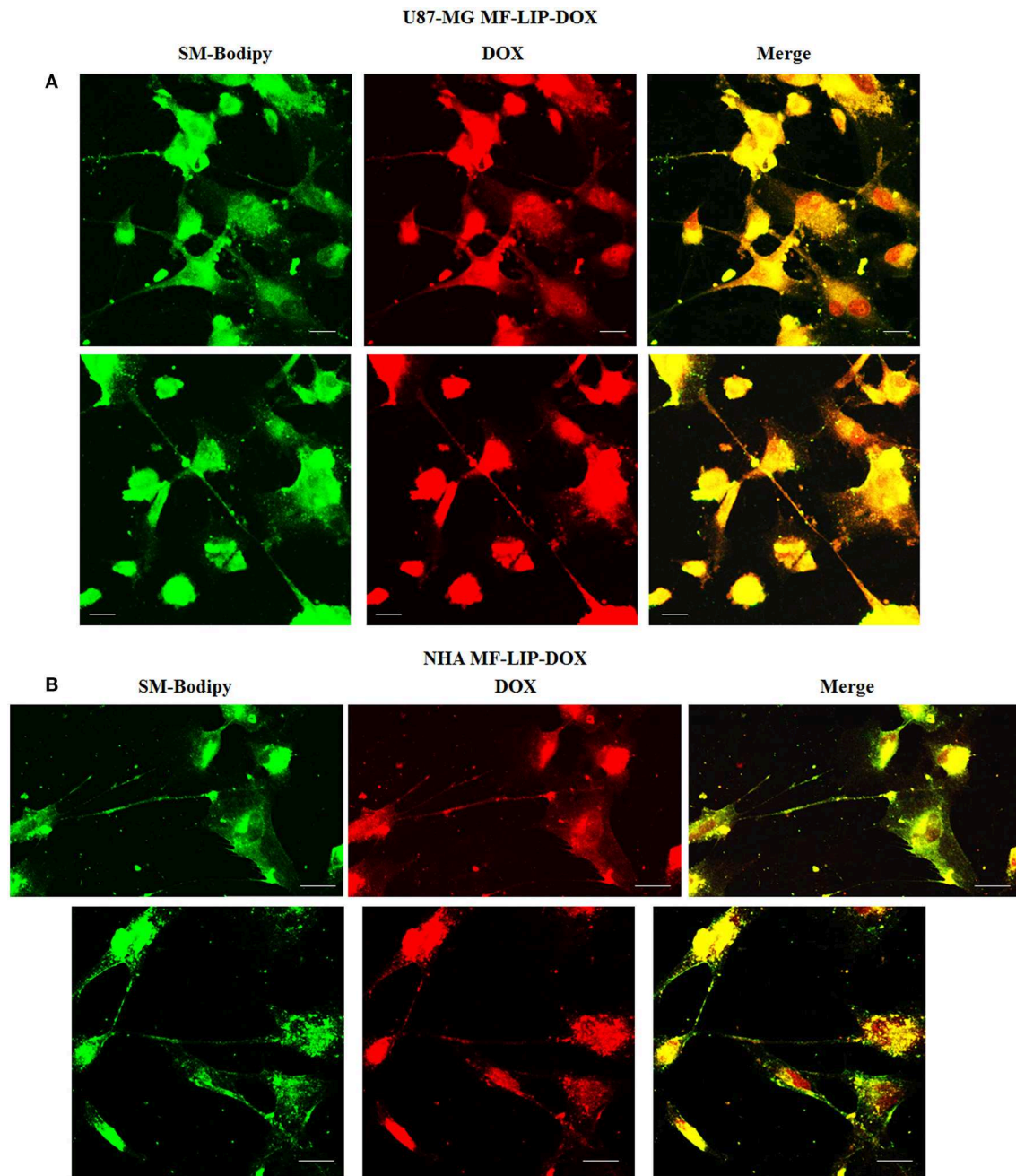
FIGURE 12 | Multifunctional liposomes (Mf-LIP) embedding doxorubicin (DOX) localized in tunneling nanotubes (TnTs) formed by U87-MG and normal human astrocytes (NHA) cells. U87-MG **(A)** and NHA **(B)** cells were plated on gelatin pretreated coverslips. Cells were left in culture complete medium for 48 h and then incubated with Mf-LIP embedding DOX (15 μg/ml of DOX and 200 nmol of total lipids) for 1 h. Cells were fixed and fluorescence images were captured with a 40× magnification on A1R Nikon laser scanning confocal microscope. Scale bar: 10 μm. BODIPY-Sm = sphingomyelin present in Mf-LIP conjugate with fluorophore BODIPY.

As TnTs have been grouped into two main classes, very thin (≤ 0.7 μm, measuring a minimum of 100–200 nm) and thick (≥ 0.7 μm, up to 1 μm; Gerdes et al., 2007), we analyzed the heterogeneity of TnTs formed by U87-MG and NHA.

Structural analysis and the comparison of the thickness of TnTs formed by these cells have shown that U87-MG cells formed almost exclusively thick protrusions, whereas NHA formed either thin or thick TnTs.

Considering that thick TnTs are more efficient in transport of molecules and organelles (Veranic et al., 2008; Mittal et al., 2019), this difference could may be exploited to increase the range of drug delivery between cancer cells. Moreover, TnTs are also classified according to their different morphology/function in
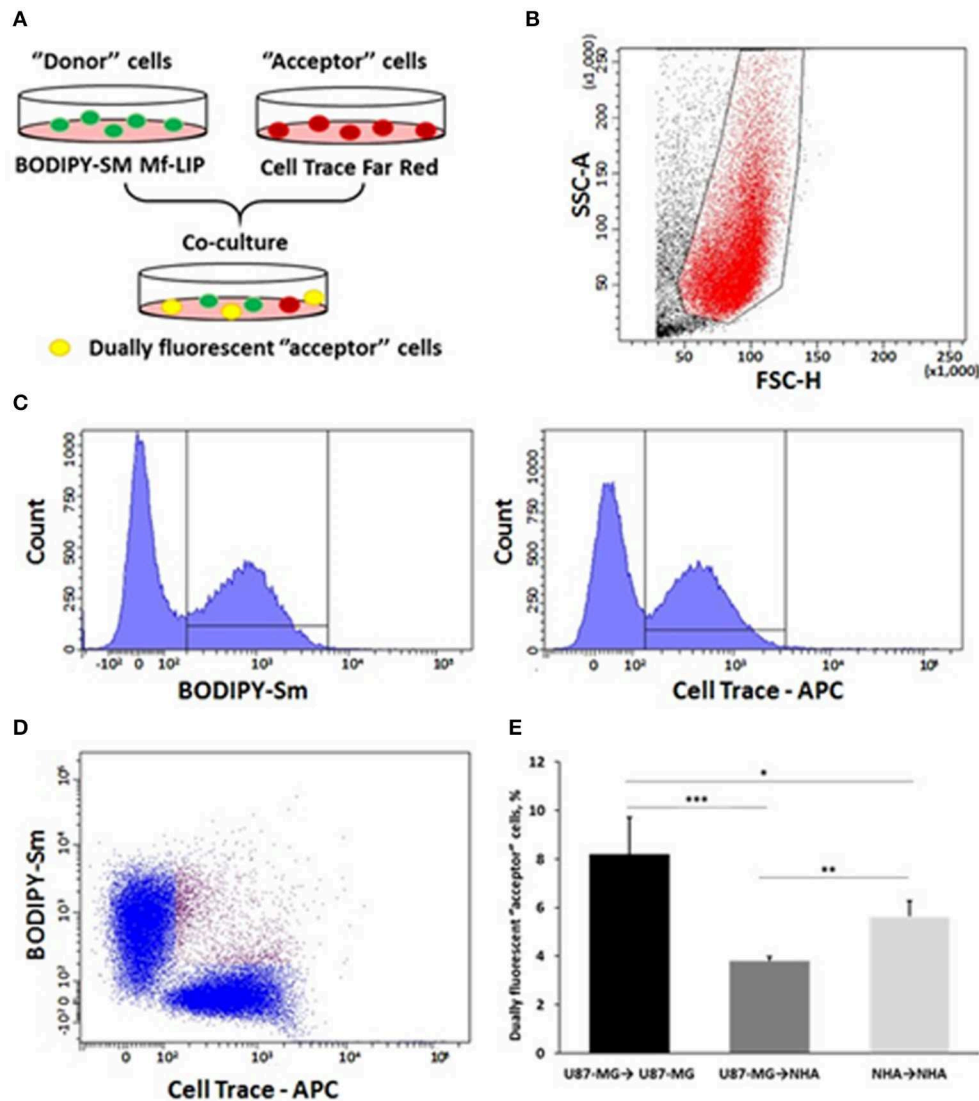
FIGURE 13 | Fluorescence-activated cell sorting (FACS) analysis of multifunctional liposomes (Mf-LIP) exchange in co-culture systems. **(A)** representative image of the experimental set-up: "donor" cells were incubated with BODIPY-Sm Mf-LIP (200 nmol total lipids) for 1 h at 37°C, whereas "acceptor" cells were treated with CellTrace Far Red Dye (CT) at 1 μM for normal human astrocytes (NHA) and 10 μM for U87-MG cells for 30 min. Cells were detached, and the following co-culture between "donor" and "acceptor" cells was set up: U87-MG (donor) → NHA (acceptor); U87-MG (donor) → U87-MG (acceptor); NHA (donor) → NHA (acceptor); and NHA (donor) → U87-MG (acceptor). Cell-to-cell transfer of Mf-LIP was assessed by FACS analysis. **(B)** The events to be analyzed (red dots) were selected on a physical parameter dot plot using an operator-defined gate. A further analysis was performed on a FSC-A vs. FSC-H dot plot to focus on the signal derived from single cells (not included). **(C)** The gated events were analyzed for fluorescence intensity on a fluorescein isothiocyanate (FITC) (BODIPY) and an allophycocyanin (APC) (Cell Trace) channel. **(D)** For each fluorescence, a single positive events' population was selected on the corresponding histograms, and the intersection highlights the double-positive events on a BODIPY vs. Cell Trace dot plot (purple dots). **(E)** Percentage of dually fluorescent "acceptor" cells that received Mf-LIP from the corresponding "donor" population. $N = 3$ independent experiments. $^*p < 0.05$; $^{**}p < 0.01$; $^{***}p < 0.001$ by Student t-test.

TnT type I, short dynamic structures, containing actin filament and engaged in exploring the surrounding microenvironment, and TnT type II, which are longer and more stable processes, containing actin and tubulin filaments and apparently involved in organelles shuttle (Veranic et al., 2008). Here, reported immunofluorescence experiments staining actin and tubulin showed that U87-MG mainly formed TnT type II, compared with NHA, which formed mostly TnT type I. Accordingly, U87-MG cells were able to better exchange Mf-LIP, as shown by the

detection of LIP-associated fluorescence in thick TnTs. Moreover, we showed that the LIP surface functionalization with mApoE and ClTx strongly increased the cell uptake by U87-MG, whereas no differences were detected with NHA in terms of LIP uptake. This suggest that the presence of these two ligands may promote a more specific targeting of cancer cells, probably owing to the overexpression of lipoprotein (LDL)-receptor by U87-MG cells (DeBin et al., 1993; Maletínská et al., 2000), which is the target ligand of mApoE peptide, and ClTx, which has been shown to

selectively bind a specific chloride channel on glioma cell surface (Lyons et al., 2002; Xiang et al., 2011; Ojeda et al., 2016).

Moreover, the encapsulation of DOX in LIP facilitates its passage through TnTs, with respect to free DOX, which remains almost exclusively localized in the nuclear region. Considering that cells physiologically produced TnTs under stress conditions (e.g., hypoxia conditions, drugs, and oxidative stress), we assessed the effect of DOX treatment on TnTs formed by U87-MG cells. The results showed that free DOX and DOX-LIP induced the formation of thin TnTs, with a strong reduction of thick TnTs, and by prolonging the incubation time, TnTs disappeared and U87-MG cells died as also shown for other cell types (Rustom, 2016). By comparing these results with those obtained in NHA cells, Mf-LIP were localized in TnTs with a little extent, and the few LIP inside in NHA's TnTs were again localized in the thick ones. This corroborates the fact that thick TnTs are mainly involved in the intercellular trafficking of drug-loaded LIP.

More appealing is that the structural difference between TnTs formed by GBM cells and NHA could be useful to design precise and specific nanotherapeutics.

As a proof-of-concept, the ability of cells to mutually exchange Mf-LIP was evaluated in different co-culture mixtures. Interestingly, the results showed that U87-MG cells were more efficient in transferring Mf-LIP between them, compared with the Mf-LIP exchange between healthy astrocytes. More excitingly, the transport of Mf-LIP via TnTs preferentially occurred from U87-MG to U87-MG, than toward NHA. This opens the possibility to exploit TnTs as drug-delivery channels, thus improving the cancer therapy. In particular, this strategy can be useful to reach isolated, infiltrating tumor cells that are hardly targeted by drug diffusion in the brain parenchyma. Nowadays, few papers are available showing the involvement of TnTs-mediated intercellular transport of nanoparticles (Kristl et al., 2013; Epperla et al., 2015; Deng et al., 2018), and none of them is dedicated to the comparison between healthy and tumor cells in nanoparticles trafficking. It is important to highlight that all the results herein reported were obtained using one GBM-derived cell line, which are not fully representative of human GBM.

For this reason, the validation of these results will be further performed on patient-derived glioblastoma cells, with stem cells included. Moreover, even with the detected TnTs connecting distant cells without being in contact with the substratum (as shown by z-stack imaging), the same analysis conducted in a 3D context could be beneficial to deeply investigate this issue.

In conclusion, the understanding of the possible intercellular delivery of nanotherapeutics cargo via TnTs can significantly influence the approaches to treat specific diseases.

DATA AVAILABILITY STATEMENT

All datasets generated for this study are included in the article/**Supplementary Material**.

AUTHOR CONTRIBUTIONS

BF performed the preparation and characterization of all liposomal formulations used. AD'A performed confocal microscopy experiments to detect TnTs. RD set up the cell culture conditions. SS performed statistical analysis of data. RR performed FACS analysis. MC and FR contributed to the data interpretation and participated in the drafting of the manuscript. FR coordinated the study, designed the experiments, and analyzed the data. All authors contributed to the paper revision, read and approved the submitted version, and agreed to be accountable for all the aspects of the work.

FUNDING

SUPPLEMENTARY MATERIAL

The Supplementary Material for this article can be found online at: https://www.frontiersin.org/articles/10.3389/fbioe.2019.00403/full#supplementary-material

REFERENCES

Abounit, S., Bousset, L., Loria, F., Zhu, S., de Chaumont, F., Pieri, L., et al. (2016). Tunneling nanotubes spread fibrillar α-synuclein by intercellular trafficking of lysosomes. *EMBO J.* 35, 2120–2138. doi: 10.15252/embj.201593411

Ahmad, T., Mukherjee, S., Pattnaik, B., Kumar, M., Singh, S., Kumar, M., et al. (2014). Miro1 regulates intercellular mitochondrial transport & enhances mesenchymal stem cell rescue efficacy. *EMBO J.* 33, 994–1010. doi: 10.1002/embj.201386030

Balducci, C., Mancini, S., Minniti, S., La Vitola, P., Zotti, M., Sancini, G., et al. (2014). Multifunctional liposomes reduce brain β-amyloid burden and ameliorate memory impairment in Alzheimer's disease mouse models. *J. Neurosci.* 34, 14022–14031. doi: 10.1523/JNEUROSCI.0284-14.2014

Bana, L., Minniti, S., Salvati, E., Sesana, S., Zambelli, V., Cagnotto, A., et al. (2014). Liposomes bi-functionalized with phosphatidic acid and an ApoE-derived peptide affect Aβ aggregation features and cross the blood-brain-barrier: implications for therapy of Alzheimer disease. *Nanomedicine* 10, 1583–1590. doi: 10.1016/j.nano.2013.12.001

Broekman, M. L., Maas, S. L. N., Abels, E. R., Mempel, T. R., Krichevsky, A. M., and Breakefield, X. O. (2018). Multidimensional communication in the microenvironments of glioblastoma. *Nat. Rev. Neurol.* 14, 482–495. doi: 10.1038/s41582-018-0025-8

Carone, C., Genedani, S., Leo, G., Filaferro, M., Fuxe, K., and Agnati, L. F. (2015). *In vitro* effects of cocaine on tunneling nanotube formation and extracellular vesicle release in glioblastoma cell cultures. *J Mol Neurosci.* 55, 42–50. doi: 10.1007/s12031-014-0365-9

Ceriani, M., Scandiuzzi, C., Amigoni, L., Tisi, R., Berruti, G., and Martegani, E. (2007). Functional analysis of RalGPS2, a murine guanine nucleotide exchange factor for RalA GTPase. *Exp. Cell Res.* 313, 2293–2307. doi: 10.1016/j.yexcr.2007.03.016

D'Aloia, A., Berruti, G., Costa, B., Schiller, C., Ambrosini, R., Pastori, V., et al. (2018). RalGPS2 is involved in tunneling nanotubes formation in 5637 bladder cancer cells. *Exp. Cell Res.* 362, 349–361. doi: 10.1016/j.yexcr.2017.11.036

de Lange, J. H., Schipper, N. W., Schuurhuis, G. J., ten Kate, T. K., van Heijningen, T. H., Pinedo, H. M., et al. (1992). Quantification by laser scan

microscopy of intracellular doxorubicin distribution. *Cytometry*. 13. 571–576. doi: 10.1002/cyto.990130604

DeBin, J. A., Maggio, J. E., and Strichartz, G. R. (1993). Purification and characterization of chlorotoxin, a chloride channel ligand from the venom of the scorpion. *Am. J. Physiol.* 264(2 Pt 1), C361–C369. doi: 10.1152/ajpcell.1993.264.2.C361

Deng, G., Wu, Z., Zhou, F., Dai, C., Zhao, J., Kang, Y., et al. (2018). Exchangeability of FITC-SiO2 nanoparticles between cancer cells increases the range of drug delivery. *J Biomed Nanotechnol*. 14, 127–138. doi: 10.1166/jbn.2018.2509

Epperla, C. P., Mohan, N., Chang, C. W., Chen, C. C., and Chang, H. C. (2015). Nanodiamond-mediated intercellular transport of proteins through membrane tunneling nanotubes. *Small* 11, 6097–7105. doi: 10.1002/smll.201502089

Fan, X., Khaki, L., Zhu, T. S., Soules, M. E., Talsma, C. E., Gul, N., et al. (2010). NOTCH pathway blockade depletes CD133-positive glioblastoma cells and inhibits growth of tumor neurospheres and xenografts. *Stem Cells* 28, 5–16. doi: 10.1002/stem.254

Formicola, B., Dal Magro, R., Montefusco-Pereira, C. V., Lehr, C. M., Koch, M., Russo, L., et al. (2019). The synergistic effect of chlorotoxin-mApoE in boosting drug-loaded liposomes across the BBB. *J. Nanobiotech.* 17, 115–122. doi: 10.1186/s12951-019-0546-3

Gerdes, H. H., Bukoreshtliev, N. V., and Barroso, J. F. (2007). Tunneling nanotubes: a new route for the exchange of components between animal cells. *FEBS Lett.* 581, 2194–2201. doi: 10.1016/j.febslet.2007.03.071

Gould, E. (2017). How widespread is adult neurogenesis in mammals? *Nat. Rev. Neurosci.* 8, 481–488. doi: 10.1038/nrn2147

Kristl, J., Plajnšek, K. T., Kreft, M. E., Janković, B., and Kocbek, P. (2013). Intracellular trafficking of solid lipid nanoparticles and their distribution between cells through tunneling nanotubes. *Eur. J. Pharm. Sci.* 50, 139–148. doi: 10.1016/j.ejps.2013.04.013

Lin, J., Zhang, X. M., Yang, J. C., Ye, Y. B., and Luo, S. Q. (2010). γ-secretase inhibitor-I enhances radiosensitivity of glioblastoma cell lines by depleting CD133+ tumor cells. *Arch. Med. Res.* 41, 519–529. doi: 10.1016/j.arcmed.2010.10.006

Lou, E., Fujisawa, S., Barlas, A., Romin, Y., Manova-Todorova, K., Moore, M. A., et al. (2012a). Tunneling Nanotubes: a new paradigm for studying intercellular communication and therapeutics in cancer. *Commun. Integr. Biol.* 5, 399–403. doi: 10.4161/cib.20569

Lou, E., Fujisawa, S., Morozov, A., Barlas, A., Romin, Y., Dogan, Y., et al. (2012b). Tunneling nanotubes provide a unique conduit for intercellular transfer of cellular contents in human malignant pleural mesothelioma. *PLoS ONE* 7:e33093. doi: 10.1371/journal.pone.0033093

Louis, D. N., Perry, A., Reifenberger, G., von Deimling, A., Figarella-Branger, D., Cavenee, W. K., et al. (2016). The 2016 World Health Organization classification of tumors of the central nervous system: a summary. *Acta Neuropathol.* 131, 803–820. doi: 10.1007/s00401-016-1545-1

Lyons, S. A., O'Neal, J., and Sontheimer, H. (2002). Chlorotoxin, a scorpion-derived peptide, specifically binds to gliomas and tumors of neuroectodermal origin. *Glia.* 39, 162–173. doi: 10.1002/glia.10083

Magro, R. D., Cox, A., Zambelli, V., Mancini, S., Masserini, M., and Re, F. (2018). The ability of liposomes, tailored for blood-brain barrier targeting, to reach the brain is dramatically affected by the disease state. *Nanomedicine* 13, 585–594. doi: 10.2217/nnm-2017-0317

Maletínská, L., Blakely, E. A., Bjornstad, K. A., Deen, D. F., Knoff, L. J., and Forte, T. M. (2000). Human glioblastoma cell lines: levels of low-density lipoprotein receptor and low-density lipoprotein receptor-related protein. *Cancer Res.* 60, 2300–2303.

Mare, R., Paolino, D., Celia, C., Molinaro, R., Fresta, M., and Cosco, D. (2018). Post-insertion parameters of PEG-derivatives in phosphocholine-liposomes. *Int. J. Pharm.* 552, 414–421. doi: 10.1016/j.ijpharm.2018.10.028

Mittal, R., Karhu, E., Wang, J. S., Delgado, S., Zukerman, R., Mittal, J., et al. (2019). Cell communication by tunneling nanotubes: Implications in disease and therapeutic applications. *J. Cell Physiol.* 234, 1130–1146. doi: 10.1002/jcp.27072

Moschoi, R., Imbert, V., Nebout, M., Chiche, J., Mary, D., Prebet, T., et al. (2016). Protective mitochondrial transfer from bone marrow stromal cells to acute myeloid leukemic cells during chemotherapy. *Blood* 128, 253–264. doi: 10.1182/blood-2015-07-655860

Ojeda, P. G., Wang, C. K., and Craik, D. J. (2016). Chlorotoxin: structure, activity, and potential uses in cancer therapy. *Biopolymers.* 106, 25–36. doi: 10.1002/bip.22748

Önfelt, B., Nedvetzki, S., Benninger, R. K. P., Purbhoo, M. A., Sowinski, S., Hume, A. N., et al. (2006). Structurally distinct membrane nanotubes between human macrophages support long-distance vesicular traffic or surfing of bacteria. *J Immunol.* 177, 8476–8483. doi: 10.4049/jimmunol.177.12.8476

Re, F., Cambianica, I., Sesana, S., Salvati, E., Cagnotto, A., Salmona, M., et al. (2010). Functionalization with ApoE-derived peptides enhances the interaction with brain capillary endothelial cells of nanoliposomes binding amyloid-beta peptide. *J. Biotechnol.* 156, 341–6. doi: 10.1016/j.jbiotec.2011.06.037

Re, F., Cambianica, I., Zona, C., Sesana, S., Gregori, M., Rigolio, R., et al. (2011). Functionalization of liposomes with ApoE-derived peptides at different density affects cellular uptake and drug transport across a blood-brain barrier model. *Nanomedicine* 7, 551–559. doi: 10.1016/j.nano.2011.05.004

Reindl, J., Shevtsov, M., Dollinger, G., Stangl, S., and Multhoff, G. (2019). Membrane Hsp70-supported cell-to-cell connections via tunneling nanotubes revealed by live-cell STED nanoscopy. *Cell Stress Chaperones* 24, 213–221. doi: 10.1007/s12192-018-00958-w

Rostami, J., Holmqvist, S., Lindström, V., Sigvardson, J., Westermark, G. T., Ingelsson, M., et al. (2017). Human astrocytes transfer aggregated alpha-synuclein via tunneling nanotubes. *J. Neurosci.* 37, 11835–11853. doi: 10.1523/JNEUROSCI.0983-17.2017

Rustom, A. (2016). The missing link: does tunnelling nanotube-based supercellularity provide a new understanding of chronic and lifestyle diseases? *Open Biol.* 6:160057. doi: 10.1098/rsob.160057

Rustom, A., Saffrich, R., Markovic, I., Walther, P., and Gerdes, H. H. (2004). Nanotubular highways for intercellular organelle transport. *Science* 303, 1007–1010. doi: 10.1126/science.1093133

Schiller, C., Huber, J. E., Diakopoulos, K. N., and Weiss, E. H. (2013). Tunneling nanotubes enable intercellular transfer of MHC class I molecules. *Hum. Immunol.* 74, 412–416. doi: 10.1016/j.humimm.2012.11.026

Sisakhtnezhad, S., and Khosravi, L. (2015). Emerging physiological and pathological implications of tunneling nanotubes formation between cells. *Eur. J. Cell Biol.* 94, 429–443. doi: 10.1016/j.ejcb.2015.06.010

Sowinski, S., Jolly, C., Berninghausen, O., Purbhoo, M. A., Chauveau, A., Köhler, K., Oddos, S., et al. (2008). Membrane nanotubes physically connect T cells over long distances presenting a novel route for HIV-1 transmission. *Nat. Cell Biol.* 10, 211–219. doi: 10.1038/ncb1682

Stewart, J. C. (1980). Colorimetric determination of phospholipids with ammonium ferrothiocyanate. *Anal. Biochem.* 104, 10–14. doi: 10.1016/0003-2697(80)90269-9

Stupp, R., Hegi, M. E., Mason, W. P., van den Bent, M. J., Taphoorn, M. J., Janzer, R. C., et al. (2009). Effects of radiotherapy with concomitant and adjuvant temozolomide versus radiotherapy alone on survival in glioblastoma in a randomised phase III study: 5-year analysis of the EORTC-NCIC trial. *Lancet Oncol.* 10, 459–466. doi: 10.1016/S1470-2045(09)70025-7

Tamborini, M., Locatelli, E., Rasile, M., Monaco, I., Rodighiero, S., Corradini, I., et al. (2016). A combined approach employing chlorotoxin-nanovectors and low dose radiation to reach infiltrating tumor niches in glioblastoma. *ACS Nano.* 10, 2509–2520. doi: 10.1021/acsnano.5b07375

Thayanithy, V., Dickson, E. L., Steer, C., Subramanian, S., and Lou, E. (2014). Tumor-stromal cross talk: direct cell-to-cell transfer of oncogenic microRNAs via tunneling nanotubes. *Transl. Res.* 164, 359–365. doi: 10.1016/j.trsl.2014.05.011

Van der Vos, K. E., Abels, E. R., Zhang, X., Lai, C., Carrizosa, E., Oakley, D., et al. (2016). Directly visualized glioblastoma-derived extracellular vesicles transfer RNA to microglia/macrophages in the brain. *Neuro Oncol.* 18, 58–69. doi: 10.1093/neuonc/nov244

Veranic, P., Lokar, M., Schütz, G. J., Weghuber, J., Wieser, S., Hägerstrand, H., et al. (2008). Different types of cell-to-cell connections mediated by nanotubular structures. *Biophys J.* 95, 4416–4425. doi: 10.1529/biophysj.108.131375

Weil, S., Osswald, M., Solecki, G., Grosch, J., Jung, E., Lemke, D., et al. (2017). Tumor microtubes convey resistance to surgical lesions and chemotherapy in gliomas. *Neuro Oncol.* 19, 1316–1326. doi: 10.1093/neuonc/nox070

Westphal, M., and Lamszus, K. (2011). The neurobiology of gliomas: from cell biology to the development of therapeutic approaches. *Nat. Rev. Neurosci.* 12, 495–508. doi: 10.1038/nrn3060

Xiang, Y., Liang, L., Wang, X., Wang, J., Zhang, X., and Zhang, Q. (2011). Chloride channel-mediated brain glioma targeting of chlorotoxin-modified doxorubicin-loaded liposomes. *J. Control Release* 152, 402–410. doi: 10.1016/j.jconrel.2011. 03.014

Zhang, L., and Zhang, Y. (2015). Tunneling nanotubes between rat primary astrocytes and C6 glioma cells alter proliferation potential of glioma cells. *Neurosci. Bull.* 31, 371–378. doi: 10.1007/s12264-014-1522-4

Optimizing the Pharmacological Properties of Discoidal Polymeric Nanoconstructs Against Triple-Negative Breast Cancer Cells

Miguel Ferreira [1†], Ilaria Francesca Rizzuti [1,2†], Anna Lisa Palange [1], Maria Grazia Barbato [1,2], Valentina Di Francesco [1,2], Martina Di Francesco [1] and Paolo Decuzzi [1*]

[1] Laboratory of Nanotechnology for Precision Medicine, Fondazione Istituto Italiano di Tecnologia, Genoa, Italy, [2] Department of Informatics, Bioengineering, Robotics and System Engineering, University of Genoa, Genoa, Italy

Fine-tuning loading and release of therapeutic and imaging agents associated with polymeric matrices is a fundamental step in the preclinical development of novel nanomedicines. Here, 1,000 × 400 nm Discoidal Polymeric Nanoconstructs (DPNs) were realized via a top-down, template-based fabrication approach, mixing together poly(lactic-co-glycolic acid) (PLGA) and poly(ethylene glycol)-diacrylate (PEG-DA) chains in a single polymer paste. Two different loading strategies were tested, namely the "direct loading" and the "absorption loading." In the first case, the agent was directly mixed with the polymeric paste to realize DPNs whereas, in the second case, DPNs were first lyophilized and then rehydrated upon exposure to a concentrated aqueous solution of the agent. Under these two loading conditions, the encapsulation efficiencies and release profiles of different agents were systematically assessed. Specifically, six agents were realized by conjugating lipid chains (DSPE) or polymeric chains (PEG) to the near-infrared imaging molecule Cy5 (DSPE-Cy5 A and DSPE-Cy5 B); the chemotherapeutic molecules methotrexate (DSPE-MTX and PEG-MTX) and doxorubicin (LA-DOX and DSPE-DOX). Moderately hydrophobic compounds with low molecular weights (MW) returned encapsulation efficiencies as high as 80% for the absorption loading. In general, direct loading was associated with encapsulation efficiencies lower than 1%. The agent hydrophobicity and MW were shown to be critical also in tailoring the release profiles from DPNs. On triple-negative breast cancer cells (MDA-MB-231), absorption loaded DOX-DPNs showed cytotoxic activities comparable to free DOX but slightly delayed in time. Preliminary *in vivo* studies demonstrated the high stability of Cy5-DPNs. Collectively, these results demonstrate that the pharmacological properties of DPNs can be finely optimized by changing the loading strategies (direct vs. absorption) and compound attributes (hydrophobicity and molecular weight).

Keywords: polymeric particles, prodrugs, drug delivery, non-spherical shape, loading and release profiles

INTRODUCTION

Nano-based pharmacotherapy deals with the safe, targeted and efficient administration of nanoparticles carrying diverse therapeutic and imaging agents for the treatment and detection of a variety of pathologies, including cancer, cardiovascular, neurological and infectious diseases (Chen et al., 2016). Man-made nanoparticles with a size ranging between a few nanometers and a few micrometers have the potential to optimize the therapeutic efficacy and imaging efficiency of small molecules and biological compounds while minimizing off-target effects (Katsube et al., 2014). Over conventional molecular agents, the encapsulation of therapeutic and imaging compounds into nanoparticles offers several key advantages (Peer et al., 2007; Ahmad et al., 2014). First, nanoparticles enable the systemic administration of agents with poor water solubility, without compromising their chemical structure and preserving their curative and contrast enhancing features. Second, nanoparticles protect delicate biological compounds, such as the various forms of nucleic acids, from a fast enzymatic degradation in blood. Third, the composition, size, shape, and surface properties of the nanoparticles can be tailored, generally, during the fabrication process, thus providing multiple tools to improve delivery to the targeted tissue while minimizing non-specific deposition in healthy, biological districts. Fourth, the release of drugs from nanoparticles can be tuned for an optimal and sustained therapeutic activity (Lu et al., 2008; Slowing et al., 2008; Agasti et al., 2009).

Traditionally, spherical nanoparticles have been extensively used for the treatment and imaging of cancer, relying on the Enhanced Permeability and Retention effect (Maeda et al., 2000). Indeed, sufficiently small nanoparticles (<200 nm) would cross the hyperpermeable tumor blood vessels (enhanced permeability) and accumulate within the tumor parenchyma due to the lack of lymphatic drainage (retention). However, clinical and pre-clinical studies are starting to demonstrate the significant variability of the EPR effect within patients and along the overall development of the disease (Natfji et al., 2017). As such, relying exclusively on the EPR effect to reach the malignant tissue may not always be a successful strategy. More recently, non-spherical particles have been proposed as an alternative drug delivery means to efficiently target the tumor microvasculature and release thereof a variety of therapeutic cargos. These non-spherical nanoparticles could take up different shapes, including rods (Huo et al., 2008), discs (Key et al., 2013), ellipsoids (Desai et al., 2018), and others (Toy et al., 2014). Within this scenario, the authors have previously demonstrated a new nanotechnological platform—the Discoidal Polymeric Nanoconstructs (DPNs). Similarly to red blood cells, DPNs tend to resist sequestration by professional phagocytic cells, such us hepatic Kupffer cells and splenic macrophages (Palomba et al., 2018). This DPN feature results in longer circulation times and increased probability to lodge within the tortuous and low perfused tumor microvasculature (Key et al., 2015).

The Discoidal Polymeric Nanoconstructs are realized with a top-down, template-based approach, where the size, shape, surface properties and mechanical stiffness can be readily and independently modulated (Key et al., 2013; Palange et al., 2017; Palomba et al., 2018). DPNs are made out of poly(lactic-co-glycolic acid) (PLGA) and polyethylene glycol (PEG) chains entangled together to form a hydrogel matrix. Indeed, given the modular fabrication strategy, other synthetic and natural polymeric materials can be used for realizing DPNs, including polycaprolactone, chitosan, hyaluronic acid, and a variety of block-copolymers. PLGA and PEG were selected for their well-known biodegradation and excretion profiles, even in human subjects (Bobo et al., 2016; Park et al., 2019). The geometrical and mechanical configurations of DPNs have been selected to enhance lodging within the malignant tissue by taking advantage of the high vascular tortuosity and low perfusion of tumor capillaries. However, as per any drug delivery system, the accumulation within the tumor microvasculature must be followed by the controlled and sustained release of therapeutic agents directly toward the diseased tissue. As such, in this work, the authors focus their efforts on characterizing and optimizing the pharmacological properties of DPNs.

Here, a systematic analysis of the loading and release for a variety of imaging and therapeutic agents encapsulated into DPNs is conducted. After characterizing the physico-chemical properties of the nanoconstructs, six different compounds are realized by conjugating directly 1,2-Distearoyl-sn-glycero-3-phosphorylethanolamine (DSPE) lipid chains or 1 kDa PEG chains with the near-infrared molecules Cy5 or the chemotherapeutic molecules methotrexate (MTX) and doxorubicin (DOX). The resulting six compounds present different molecular weights and hydrophobicity levels as compared to the original, free molecules. Then, two different loading strategies are introduced named as "direct loading" and "absorption loading." The six compounds are entrapped within the polymeric matrix of DPNs using both loading strategies, and the encapsulation efficiencies and release profiles are consequently assessed. Finally, the pharmacological and imaging properties of DPNs are documented *in vitro* on triple-negative breast cancer cells (MDA-MB-231) and *in vivo* in healthy mice, respectively.

MATERIALS AND METHODOLOGY

Materials

Silicon wafers (thickness of 525 $\pm$ 20 μm, resistivity 20–30 Ω cm, type-orient P/Bar <100>) and the Photoresist AZ 5214 E were purchased from Si-Mat silicon materials (Kaufering, Germany) and Microchemicals (Ulm, Germany), respectively. Hexamethylsilazane (Primer H.M.D.S.) was purchased from Technic. The AZ 726 MIF Developer was purchased from Merk. 1H, 1H, 2H, 2H-Perfluorooctyltrichlorosilane 97% and Methotrexate were purchased from Alfa Aesar. Sylgard 184 kit as polydimethylsiloxane (PDMS) and elastomer were purchased from Dow Coming Corp (Midland, MI, US). Doxorubicin, Poly(vinyl alcohol) (Mw 9,000–10,000, 80% hydrolyzed), Poly(DL-lactide-co-glycolide) acid (PLGA, lactide:glycolide 50:50, Mw 38,000–54,000), Poly(ethylene glycol) dimethacrylate (Mn 750) (PEG dimethacrylate), and 2-Hydroxy-40-(2-hydroxyethoxy)-2-methylpropiophenone (Photo-initiator)

were purchased from Sigma (St. Louis, MO, USA). Cyanine5 NHS ester and water-soluble sulfo-Cyanine 5 NHS ester were purchased from Luminoprobe (Hunt Valley, MD, US). All the reagents and solvents were used without further purification.

Fabrication of the Templates

A master silicon template with circular wells of ∼1,000 nm in diameter by 400 nm in thickness was realized. The geometrical pattern of the template was designed using the LASI software. An AZ5214E resist was written via a laser writer system at 405 nm (Heidelberg Instruments DWL66FS). The primer and the resist were deposited over the silicon wafer by spin coating (Sawatec) (10 s at 500 rpm and 60 s at 4,000 rpm) resulting in a final thickness of about 1,400 nm. This coating was baked on a hot plate at 110°C for 1 min and then exposed to the Direct Laser Writer working with a defocusing value of 1,700 nm and laser intensity of 0.75 mW. The substrate was developed for 4 min. The pattern was transferred to the underlying silicon substrate by deep reactive ion etching with SF_6/O_2 plasma for 60 s (Sentech SI500 Instrument GmbH RIE). The resist was removed in a piranha solution for 5 min (ratio 4:1 between sulfuric acid and hydroxide peroxide). The resulting silicon master template was imaged with Scanning Electron Microscopy (Helios Nanolab 650 Dual Beam, Fei company). A silanization step (200 μl) was also included by placing the substrate in a vacuum chamber under a nitrogen atmosphere for 1 h. Once the silicon master template was obtained, the following step required the realization of a polydimethylsiloxane (PDMS) replica. The silicon master template was fixed on a Petri dish (d = 10 cm). A solution of PDMS and curing agent was realized with a ratio 10:1. This solution was cast over the Si wafer to produce a second template presenting cylindrical pillars, which resembled the same size and shape of the wells in the original master Si template. The mixture was polymerized at 60° for 3 h. This process was repeated seven times to generate seven different PDMS templates. Then, ∼30 mg of PDMS (10:1) were poured over these replicas to form a unique structure with the size of a Petri dish (d = 15 cm). The final step required the realization of a sacrificial template of poly(vinyl) alcohol (PVA). A 5% PVA solution was deposited over the PDMS replica template to generate a third template. This presented circular wells just like the original master Si template. Upon complete drying in an oven for 3 h at 60°C, the PVA solution became a thin film and was peeled off the PDMS template.

Fabrication of Discoidal Polymeric Nanoconstructs

For the fabrication of DPNs, 30 mg of poly(lactic-co-glycolic acid) (PLGA) were dissolved in chloroform ($CHCl_3$) and mixed with 6 mg of polyethylene glycol (PEG) diacrylate and 10 μg of 2-Hydroxy-40-(2-hydroxyethoxy)-2-methylpropiophenone (photoinitiator). Thirty microgram of DSPE-Cy5 were also added to provide sufficient fluorescent optical contrast. The resulting polymeric paste was carefully deposited in the wells of the sacrificial PVA template and exposed to UV-light for polymerization. The resulting PVA film, loaded with the above polymeric paste, was immersed in water and left to stir for 3 h. This step led to the dissolution of the PVA and the release of DPNs in the aqueous solution. DPNs were eventually collected

via centrifugation and membrane filtration to remove residual fragments of PVA.

Loading of the Discoidal Polymeric Nanoconstructs

Two loading protocols were developed, namely "direct loading" and "absorption loading." In "direct loading," the imaging and/or therapeutic agents of interest were dispersed within the original polymeric paste and directly distributed in the wells of the PVA template. In "absorption loading," the collected DPNs were lyophilized to form a powder. This was eventually dispersed in an aqueous solution carrying the imaging and/or therapeutic agents of interest. Re-hydration led to the rapid absorption of the molecules within the hydrogel structure of DPNs. The concentration of DPNs, imaging agents and therapeutic molecules, the volume of the aqueous solution was systematically varied to identify optimal loading conditions.

Prodrug Synthesis

DSPE-Cyanine-5

DSPE-Cy5-A and DSPE-Cy5-B were synthesized as reported by Lee and coworkers with some modifications (Lee et al., 2017). 15 mg of DSPE-NH$_2$ were dissolved in 3 mL of dichloromethane (DCM) and 1.5 mL of MeOH. 0.98 eq of Cyanine-5 NHS ester was dissolved in 200 ml of dimethylformamide (DMF) and added to the previous solution. A catalytic amount of triethylamine (TEA) was added to the reaction and left to stir for 16 h. The resulting product was precipitated with cold diethyl ether, then washed three times with cold diethyl ether obtaining the final compound with a yield of 90%.

DSPE-Methotrexate

Fifteen milligram of DSPE-NH$_2$ were dissolved in 3 mL of dichloromethane (DCM) and 1.5 mL of MeOH. 0.98 eq of Methotrexate ester was dissolved in 200 ml of dimethylformamide (DMF) and added to the previous solution. A catalytic amount of triethylamine (TEA) was added to the reaction and was left to stir for 16 h. The intended product was precipitated with cold diethyl ether, then washed three times with cold diethyl ether getting the final product with a yield of 90%.

PEG-Methotrexate

Twenty milligram of PEG-NH$_2$ (1,000 Da) were dissolved in 3 mL of dichloromethane (DCM) and 1.5 mL of MeOH. 0.98 eq of Methotrexate was dissolved in 200 ml of dimethylformamide (DMF) and added to the previous solution. A catalytic amount of triethylamine (TEA) was added to the reaction and was left to stir for 16 h. The intended product was precipitated with cold diethyl ether, then washed three times with cold diethyl ether getting the final product with a yield of 90%.

Linoleic Acid-Doxorubicin

LA-DOX was synthesized as reported by Fernandes et al. (2016) with some modifications. Briefly, an aqueous solution of Doxorubicin hydrochloride (5 mg/mL) was neutralized with a solution of sodium bicarbonate solution (50 mg/mL). A linoleic acid solution (50 mg/mL) in ethanol was incubated with EDC/NHS (molar ratio of 3:1) for 1 h under magnetic rotation

at room temperature. The obtained solution was added drop by drop to the above mixture while stirring. After 12 h, the mixture was centrifuged (127,000 rpm, 30 min). The red pellet was washed with distilled water three times, removing the unreacted water-soluble Doxorubicin. Finally, the red pellet was collected and dried under vacuum.

DSPE-Doxorubicin

An aqueous solution of Doxorubicin hydrochloride (5 mg/mL) was neutralized with a solution of sodium bicarbonate solution (50 mg/mL). A DSPE-succinic-acid (50 mg/mL) in ethanol was incubated with EDC/NHS (molar ratio of 3:1) for 1 h under magnetic rotation at room temperature. The obtained solution was added drop by drop to the above mixture while stirring. After 12 h, the mixture was centrifuged (127,000 rpm, 30 min). The red pellet was washed with distilled water three times, removing the unreacted water-soluble Doxorubicin. Finally, the red pellet was collected and dried under vacuum.

Particle Size and Shape Characterization

The size and shape of all silicon, PDMS, and PVA templates were characterized via Scanning Electron Microscope (Helios Nanolab 650). Ultra-high resolution SEM images were acquired at high vacuum conditions after 10 nm aurum coating using a Q150T ES sputter-coater (Quorum). DPNs still embedded within the PVA templates were observed using an A1 confocal microscope (Nikon) equipped with 63× oil immersion objective. For EM characterization, a DPNs solution was dried on a carbon-copper grid and coated with 10–20 nm of carbon before Transmission Electron Microscope imaging (JEOL JEM 1011 TEM working at 100 KV). The ξ-potential was calculated using DLS (Malvern, UK).

Loading and Release Studies

To calculate the amount of drug inside DNPs, samples were lyophilized and dissolved in acetonitrile (ACN). All samples were analyzed by HPLC at 240 nm UV absorbance (Agilent 1260 Infinity, Germany). The encapsulation efficiency was defined as the percentage weight ratio between the drug amount loaded inside DPNs at the end of their preparation and the initial input amount of the drug. For the release studies, 200 μL of DPN solution was poured into Slide-A-Lyzer MINI dialysis microtube with a molecular cut off of 10 kDa (Thermo Scientific) and dialyzed against 4 L of H_2O at 37°C. For each time point, in triplicate, DPNs were collected and destroyed with ACN to release the molecule of interest. Samples were analyze depending on an HPLC (Agilent 1260 Infinity, Germany) at 340 nm UV absorbance for MTX prodrugs, and 490 nm and 646 for LA-DOX and Cy5, respectively.

Cell Culture and Viability

The human Triple-Negative Breast Cancer MDA-MB231 cell line was obtained from the American Type Culture Collection (ATCC). Cells were cultured in Eagle's minimal essential medium (EMEM) (ATCC, USA) containing 10% FBS (Gibco, Thermo Fisher Scientific, USA), 1% penicillin/streptomycin (Sigma-Aldrich, USA), under a humid atmosphere (37°C, 5% CO_2, 95% air). Upon reaching appropriate confluence, cells

were passed. Cell viability was determined via an MTT assay, which detects the reduction of MTT [3-(4,5-dimethylthiazolyl)-2,5-diphenyltetrazolium bromide] (Sigma-Aldrich, USA) by mitochondrial dehydrogenase to blue formazan product. This reflects the normal function of mitochondria and, hence, the measurement of cytotoxicity and cell viability. Briefly, 2 × 10^5 cells/well were seeded in 96-well plates and incubated at 37°C, 5% CO_2, for 24 h. Next, the medium was replaced with EMEM containing the corresponding concentrations of Doxorubicin (DOX), doxorubicin pro-drug [LA-DOX, DSPE-DOX, (LA-DOX) DPNs and (DSPE-DOX) DPNs)] (0.1–50 μM), Methotrexate (MTX) and Methotrexate prodrugs [PEG-MTX, DSPE-MTX (0–100 μM) and (DSPE-MTX) DPNs (0.01–0.5 μM)]. After 24, 48, 72, and 96 h of incubation, the MTT solution (5.0 mg/mL PBS) was added to each well and incubated at 37°C for 4 h. The resulting formazan crystals were dissolved by adding ethanol (200 μL/well), and the absorbance was read at 570 nm using a microplate reader (Tecan, CH). Controls (i.e., cells that had received no drug) were normalized to 100%, and readings from treated cells were expressed as the percentage of viability inhibition. Five replicates were considered for each data point.

Confocal Fluorescent Microscopy Imaging

Cellular uptake and intracellular localization were observed in MDA-MB-231 cells for DOX, LA-DOX, and DPNs. Briefly, 2.0 × 10^4 cells were seeded into each well of a Nunc Lab-Tek II chamber slide system (Thermo Fisher Scientific, USA) with standard culturing conditions (37°C, 5% O_2). After 24 h, the medium was removed, and cells were washed in PBS for 5 min (Thermo Fisher Scientific, USA). Cell fixation was performed using a 4% solution of paraformaldehyde (Santa Cruz Biotechnology, USA) for 5 min. Actin was stained with Alexa Fluor 488 Phalloidin (green color) (Thermo Fisher Scientific, USA), and nuclei were stained with DAPI (blue color) (Thermo Fisher Scientific, USA). Doxorubicin and DSPE-DOX DPNs were visualized in red.

In-vivo Studies

DPNs loaded with DSPE-Cy5-B were injected into week old C57B/6J female mice (Charles River). Animals were grouped in ventilated cages and able to freely access to food and water. They were maintained under controlled conditions: temperature (21 ± 2°C), humidity (50 ± 10%) and light (10 and 14 hours of light and dark respectively). The accumulation of systemically injected DSPE-Cy5-B DPNs within the different organs was assessed longitudinally by using the whole animal, near infra-red fluorescent (NIRF) imaging at 0.5, 1, 2, 6, 24 and 48 h. Also, at 48 h post-injection, the major organs were imaging ex-vivo.

RESULTS AND DISCUSSION

Fabrication and Physico-Chemical Characterization of the Discoidal Polymeric Nanoconstructs (DPNs)

A versatile fabrication strategy was used to realize polymeric nanoconstructs with controlled geometrical and mechanical features, including the size, shape, surface properties, and mechanical stiffness–*the 4S parameters*. These features can be
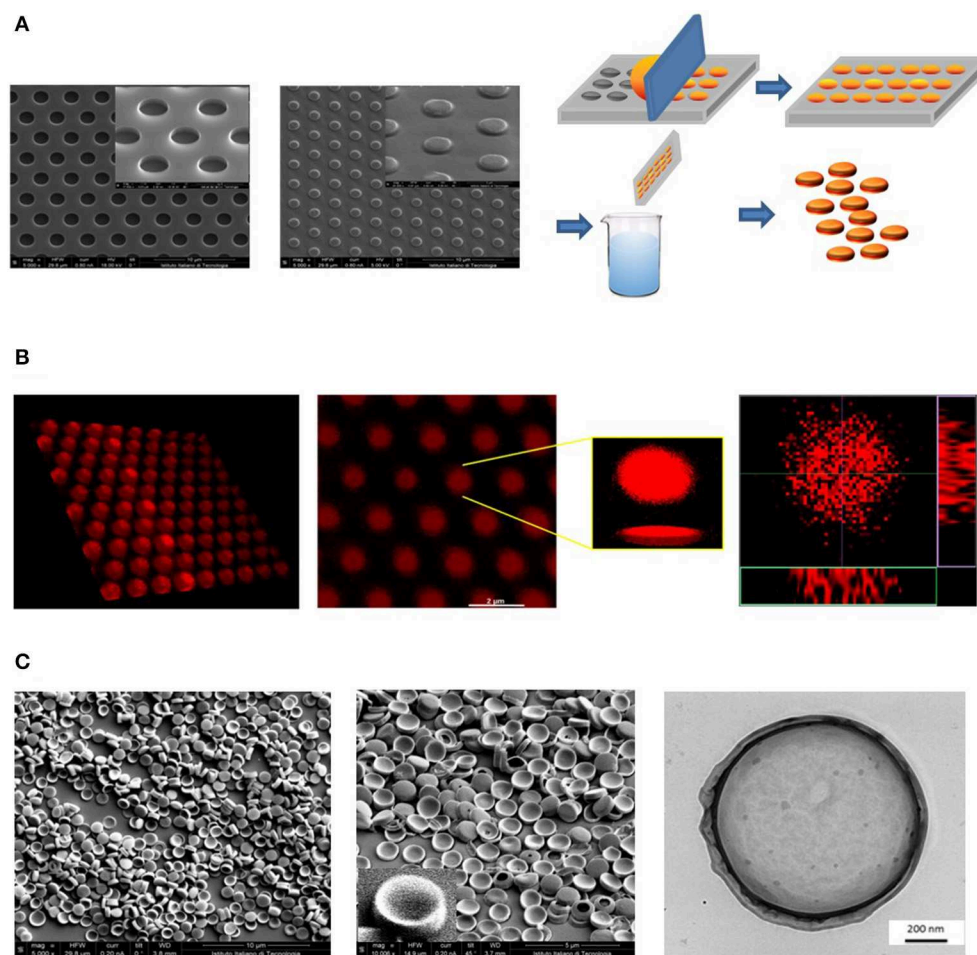
FIGURE 1 | Geometrical characterization of Discoidal Polymeric Nanoconstructs (DPNs). **(A)** Scanning electron microscope (SEM) images of the silicon templates (left); SEM images of the PDMS templates (center); schematic of the DPN fabrication steps, including loading of the PLGA/PEG polymer mixture, polymerization, sacrificial template dissolution and DPN collection (right). **(B)** Confocal microscopy images of a PVA template filled with DOX-loaded DPNs (left) and individual, 3D reconstructed DOX-loaded DPNs (right). **(C)** SEM (left) and Transmission Electron Microscopy (right) images of DPNs.

independently tuned in the fabrication process to affect the therapeutic and imaging performances, as shown by the authors and other investigators (Key et al., 2013; Palomba et al., 2018). The first step in DPNs fabrication is the realization of a master silicon template through a Direct Laser Writer lithographic process. The silicon template appears as a matrix of wells reproducing the geometry of DPNs (**Figure 1A**, left inset). Then, the silicon master template is used as a mold to realize a PDMS replica. The PDMS replica exhibits arrays of pillars with the same geometry of the wells in the silicon template. Finally, a sacrificial PVA template is obtained by replicating the PDMS template. DPNs are made out of a mixture of poly(lactic-co-glycolic acid) (PLGA), polyethylene glycol diacrylate (PEG-DA), photoinitiator (PI), and the therapeutic or imaging agent of interest. For the preparation of DPNs, the polymer mixture of PLGA, PEG-DA, and PI is directly applied and spread over the PVA template to fill the multiple wells (**Figure 1A**, right inset). This loaded template is then exposed to UV-light for the polymerization of PEG-DA chains. Eventually, the PVA film is immersed in

an aqueous solution and dissolved after stirring (**Figure 1A**, right inset) to release the DPNs. The final steps, including centrifugation and filtration, are used to remove residual PVA fragments. **Figure 1B** presents confocal fluorescent images of a PVA template loaded with a mixture of PLGA/PEG and LA-DOX. A uniform distribution of "red dots" within the structure can be appreciated. These "red dots" correspond to the DPNs before the dissolution of the PVA template and are loaded quite uniformly with LA-DOX, returning the reddish color. Finally, electron microscopy images (**Figure 1C**) show the actual geometry of DPNs that exhibits an average diameter of ∼1,250 ± 19.36 nm and a height of 469.14 ± 27.5 nm.

Loading Therapeutic and Imaging Agents Into Discoidal Polymeric Nanoconstructs (DPNs)

The dispersion of functional molecules, such as therapeutic and imaging agents, within the polymeric structure of DPNs
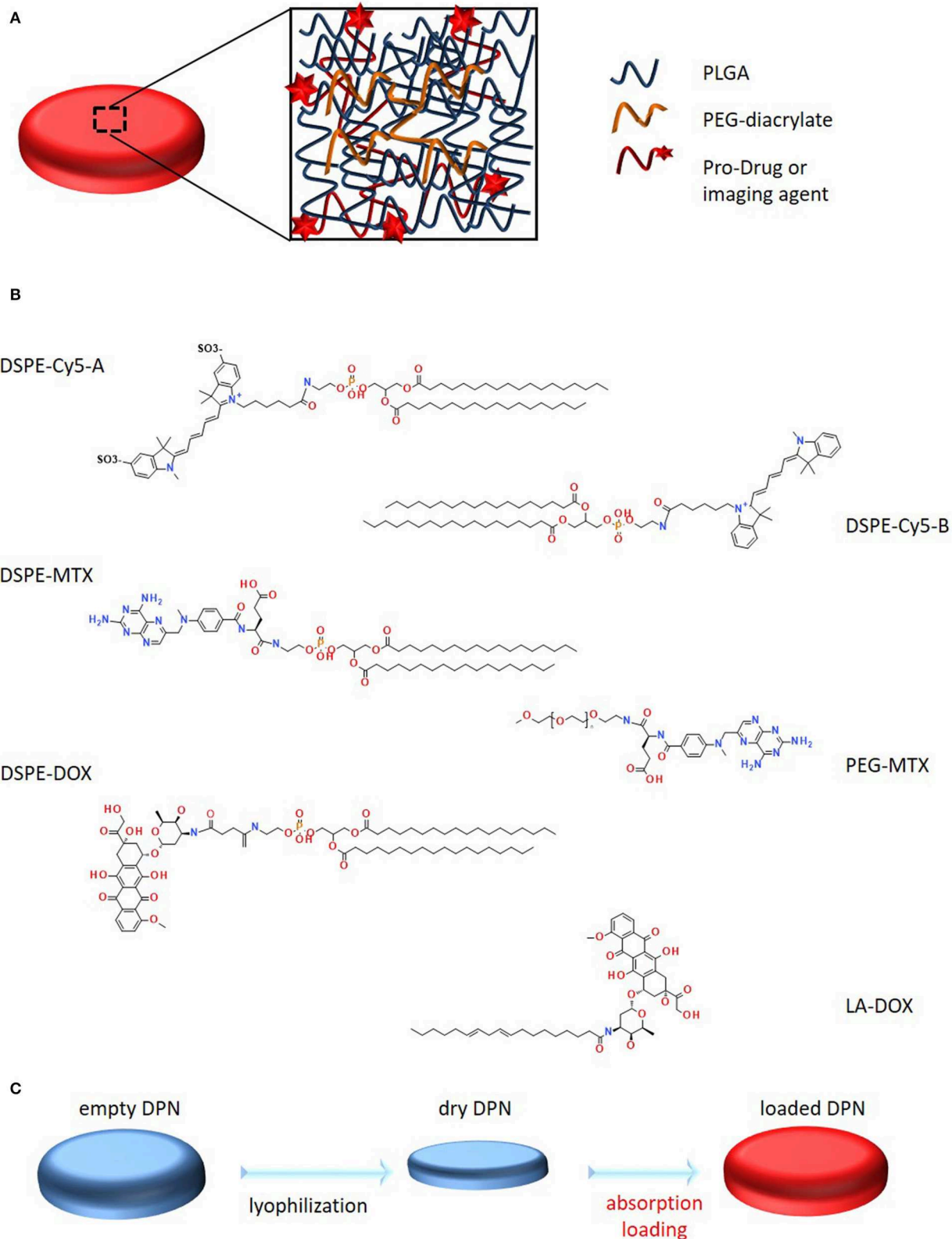
FIGURE 2 | Schematic representation of Discoidal Polymeric Nanoconstructs and prodrugs. **(A)** Schematic representation of DPNs, highlighting their porous structure and PLGA-PEG chain entanglement. **(B)** Structural representation of the six synthesized pro-drugs. **(C)** Schematic representation of the "absorption loading" method for encapsulating prodrugs into DPNs.

(**Figure 2A**) was achieved following two different strategies: a "direct method," where the agent is dissolved in the organic solvent and directly mixed with the PLGA, PEG and PI paste prior to deposition over the PVA template; an "absorption method," where the agent is dispersed in a higher concentrated water solution, which is then exposed to the lyophilized powder of DPNs. In direct loading, the agent needs to be soluble and stable in an organic solvent whereas, for the absorption method, the agent needs to be soluble in water at high concentrations without forming micellar structures. As such the proposed different loading methods can be applied to different functional agents, even sequentially.

DSPE-Cy5-A was the first compound to be loaded into the DPNs (**Figure 2B**). The Cyanine 5 (Cy5) molecule is a well-known and extensively used near infra-red molecule that can be easily detected *in vitro*, using a conventional fluorescent microscope, and *in vivo*, using a whole animal fluorescent imaging system. DSPE-Cy5-A was synthesized by reacting 1,2-distearoyl-sn-glycero-3-phosphoethanolamine-N-amino (DSPE-NH2) with Cy5 pre-activated with N-Hydroxysuccinimide (NHS) on the terminal carboxylic acid. The compound DSPE-Cy5-A resulted in being less hydrophobic than free Cy5-A. A more hydrophobic Cy5, which lacks the sulfoxide groups, increased, even more, the hydrophobicity of the compound and was used to prepare DSPE-Cy5-B (**Figure 2B**). The same protocol was used for the synthesis. Then, methotrexate (MTX) and doxorubicin (DOX) were considered. These are two chemotherapeutic molecules with different solubility properties in physiological solutions. MTX is hydrophobic whereas DOX is hydrophilic. A similar protocol as per the Cy5 was used to prepare the prodrug DSPE-MTX (**Figure 2B**). MTX was pre-activated with a mixture of DCC and NHS, before conjugation with DSPE-NH$_2$. With MTX, the hydrophobicity of the resulting compound was modulated by changing the lipid chain DSPE with PEG 1 kDa (**Figure 2B**), to increase the hydrophilicity of the resulting MTX prodrug. The synthesis protocol was the same as described above. Then, Doxorubicin (DOX) was considered, which is currently the most frequently used treatment for triple-negative breast cancer (Denard et al., 2018). In this case, the protocol to generate the DOX prodrug was modified, in that DOX has no carboxylic acid group available, but rather an amine group. Therefore, first, the hydrochloridric form of DOX was neutralized with a solution of sodium bicarbonate. Then, linoleic acid was pre-activated with EDC and NHS, and added to the solution. Given the low water solubility of the resulting compound, it was collected via precipitation. The same procedure was used for the preparation of the DSPE-DOX (**Figure 2B**), replacing the linoleic acid with the DSPE-succinic acid. After preparing all these compounds and prodrugs, the loading steps were performed.

"Direct loading" is the most straightforward procedure. The main requirement for the agent to be "direct loaded" is its solubility and stability in organic solvents, like dichloromethane (DCM), chloroform (CHCl$_3$), or acetonitrile (ACN). The compound is directly mixed with the original polymeric paste forming the DPNs and applied over the PVA template.

A drawback of this straightforward loading procedure is the low encapsulation efficiency (EE), which is due to the yielding in the preparation of DPNs and the hydrophilicity-hydrophobicity ratio of the loaded agent. As per the yielding, it should be noted that a portion of the loaded agent and polymeric paste are wasted during the deposition onto the PVA wells. As per the hydrophilicity-hydrophobicity ratio, it should be remarked that more hydrophilic compounds (lower LogP) tend to rapidly escape the DPN polymeric matrix during the purification and collection steps that occur in water.

"Absorption loading" consists in exposing a concentrated aqueous solution of the agent to lyophilized DPNs (**Figure 2C**). During the rapid re-hydration phase, DPNs avidly recall within their polymeric structure water, which was enriched with the molecules of the agent to be loaded. A fine balance between compound hydrophilicity and hydrophobicity is required for this loading strategy. Note that, after absorption, the higher molecular-weight hydrophobic prodrugs would more easily stay entrapped within the core of the DPNs as compared to their free counterparts, thus limiting their interaction with the aqueous environment.

Optimizing the "Absorption Loading" Into Discoidal Polymeric Nanoconstructs (DPNs)

Based on the above reasoning, the encapsulation efficiency (EE) into DPNs would vary for each prodrug and loading strategy. In the "direct loading," EE can be optimized by improving the filling of the wells in the PVA template and limiting the losses of polymeric paste out of the wells during the deposition phase. This optimization process is out of the scope of this work. As per the "absorption loading," three independent parameters can be systematically modified to modulate EE. These parameters are: the exposure time of the lyophilized DPNs to the aqueous solution (rehydration time); the mass of prodrug in the aqueous solution; the volume of the aqueous solution. For studying the contribution of the rehydration time, lyophilized DPNs were exposed to a 20 μL concentrated solution of 1 mg/mL DSPE-Cy5-B for 1, 3, 6, and 10 min. After exposure, water was added to the mixture followed by a centrifugation step to remove the non-absorbed DSPE-Cy5-B molecules. This was quantified via UV-Vis spectroscopy. The results showed that Cy5 loading stayed around 75% and no variation with the exposure time was observed (**Figure 3A**, left column). Also, DPNs size and ξ-potential did not change during the process demonstrating that DPNs did not suffer any significant damage induced by lyophilization and rehydration (**Figure 3A**, right column). Based on this data, 1 min of rehydration time was considered to be sufficient to load a significant amount of DSPE-Cy5-B. "Absorption Loading" is also affected by the volume of the aqueous solution and the concentration of the therapeutic agent. Therefore, after fixing the volume of DSPE-Cy5-B solution (20 μL) and the exposure time (1 min), the agent concentration was reduced from 1 to 0.9, 0.75, 0.5, and 0.25 mg/mL. Even in this case, the compound concentration did not significantly affect the loaded amount
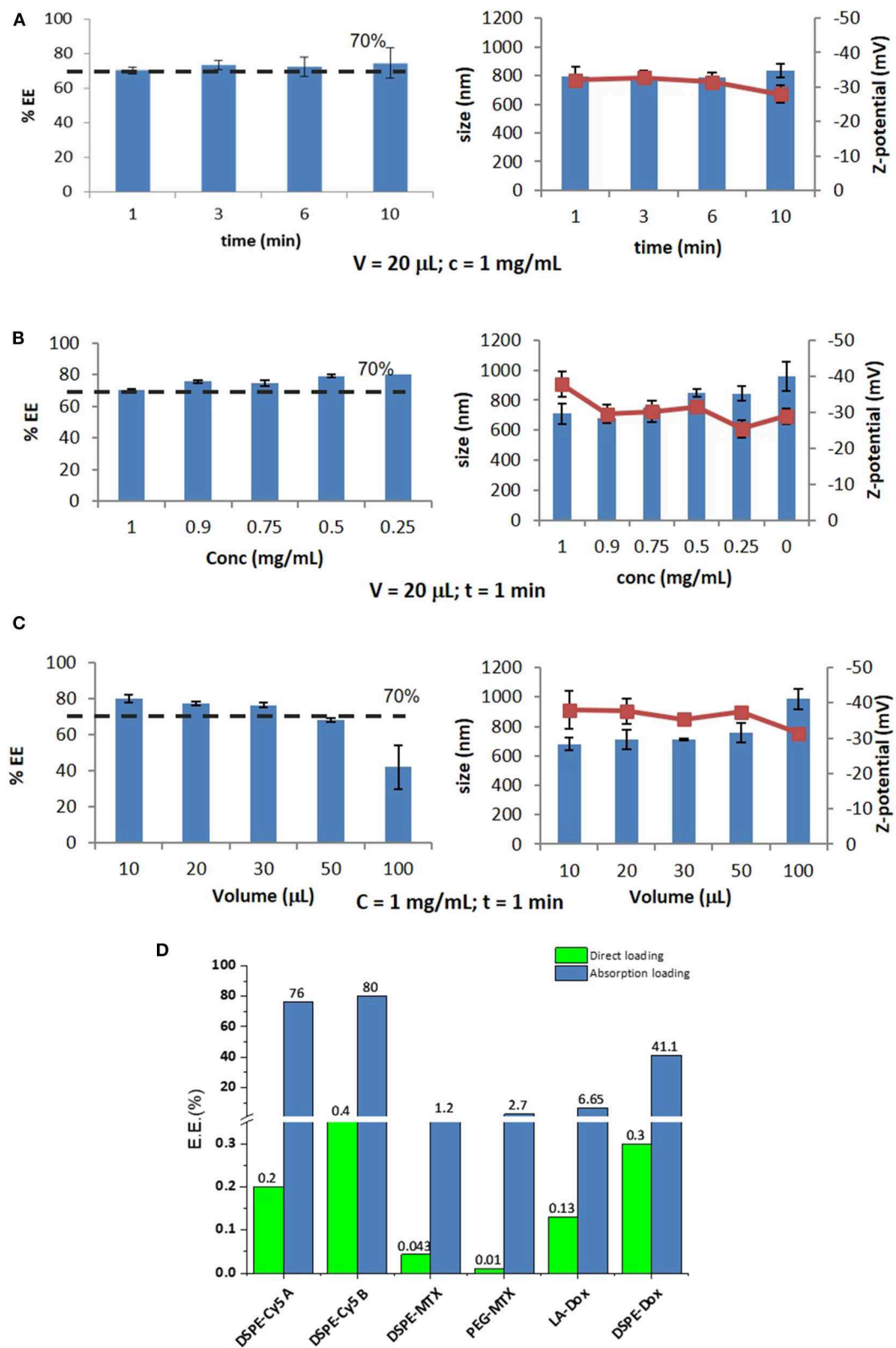
FIGURE 3 | Optimization of Absorption Loading and Encapsulation Efficiency into Discoidal Polymeric Nanoconstructs. Variation of the encapsulation efficiency and DPN size and surface ζ-potential as a function of **(A)** the rehydration time; **(B)** the pro-drug mass; and **(C)** the volume of the rehydration solution. **(D)** Encapsulation efficiencies for the six different pro-drugs and two different loading methods ("direct method"—green bars and "absorption method"—blue bars).

of DSPE-Cy5-B, which stayed around 75% (**Figure 3B**, left column). A modest change in DPNs size was observed with a decreasing concentration of the compound (**Figure 3B**, right column). At low concentrations, DPNs acquired a larger size (860 nm, at 0.25 mg/ml) compared to the higher concentrations (720 nm at 1 mg/mL). This could be related to the intercalation of the compound within the DPN polymeric matrix that would pull it toward the core resulting in a slightly smaller and more compact structure. The last independent parameter to be analyzed was the volume of rehydration. In this case, the compound concentration (1 mg/ml of DSPE-Cy5-B) and the exposure time (1 min) were fixed, whereas the volume varied between 10, 20, 30, 50, and 100 μL. Results show that with a volume increase, the loading of the DSPE-Cy5-B decreases (**Figure 3C**, left column). Indeed, lower volumes mean more DSPE-Cy5-B located in the vicinity of the DPN surface, thus leading to higher loading upon absorption. DPN size and ξ potential were not affected by the volume variation (**Figure 3C**, right column).

Summing all this data up, it can be concluded that optimal loading via absorption is achieved by minimizing rehydration volumes and maximizing the mass of the compound. Importantly, the compound should be sufficiently hydrophilic to be dispersed in water and moderately hydrophobic to stay within the DPN matrix upon exposure to the aqueous environment. Thus, for this loading strategy, it is crucial to realize prodrugs with the right hydrophilic-hydrophobic ratio and molecular weight. The bar chart in **Figure 3D** summarizes the results obtained in terms of EE for the different loading strategies and tested compounds. The DSPE-Cy5 A and B present high EE under the absorption loading strategy, reaching values as high as ~80%. Because of the DSPE derivation, these compounds are slightly less hydrophilic and have a larger molecular weight as compared to the original free molecules (Cy5 A and B). These two features favor DSPE-Cy5 loading into DPNs during the absorption phase and limit their release during the purification steps and the *in vivo* application. This ideal combination of hydrophobicity/hydrophilicity ratio and the proper molecular weight is not achieved with the MTX prodrugs. The DSPE-MTX is significantly hydrophobic, with a LogP of 13.84, and cannot be efficiently resuspended in water returning an EE = 1.2%. On the other hand, the 1 kDa PEG-MTX has a LogP of −3.31, which allows efficient resuspension in water. However, the large molecular weight of the resulting compound opposes absorption during the DPN rehydration, thus returning a moderate EE of ~3%. The beneficial effect of identifying the right hydrophobicity/hydrophilicity ratio is again demonstrated in the case of DOX. LA-DOX is significantly hydrophobic with a LogP of 6.59. This leads to an EE of ~7%, which incidentally is higher than that obtained for the more hydrophobic DSPE-MTX. Notably, DSPE-DOX has a LogP of −14.42, returning an EE of ~40%. **Figure 3D** also shows how direct loading, in the current configuration, is far less efficient than absorption loading. This data confirms that the hydrophobicity/hydrophilicity ratio and molecular weight of the prodrug are critical features to optimize loading.

Release Profiles of Prodrugs From Discoidal Polymeric Nanoconstructs (DPNs)

Release studies were conducted for all loaded prodrugs under the sink condition by exposing a known amount of DPNs to a 4 L aqueous solution. Starting with DSPE-Cy5-A (**Figure 4A**), an initial burst release was observed over the first 10 h with ~70 and 80% of the agent leaking out of DPNs for the absorption and direct methods, respectively. At 72 h, the DSPE-Cy5-A loaded via the absorption method was fully released out of DPNs as compared to a 90% release for the direct method. Indeed, the DSPE-Cy5-A suffers of a high water solubility, which would justify the observed rapid release profile. Moreover, in the absorption method, most of the DSPE-Cy5-A molecules are likely trapped near the DPN surface, which indeed facilitates their release in the surrounding aqueous environment. On the other hand, the direct loading of DSPE-Cy5-A favors its uniform distribution within the DPN polymeric matrix, thus slowing down the release rate. A different behavior is observed for the more hydrophobic compound DSPE-Cy5-B (**Figure 4B**). Over the first 10 h, only 35 and 12% of the loaded DSPE-Cy5-B are released out of DPNs for the absorption and direct methods, respectively. At 72 h, these two values become 60 and 35%, respectively. The slower release of DSPE Cy5-B as compared to DSPE Cy5-A should be ascribed entirely to the different hydrophobic/hydrophilic ratio, which is in favor of the Cy5-B compound. Notably, the direct method is still characterized by a lower release rate, likely because of the uniform distribution of the compound within the DPN polymer matrix. The release profiles for DSPE-MTX and PEG-MTX are presented in **Figures 4C,D**, respectively. Due to the different hydrophobicity level, these compounds present a different release behavior as opposed to DSPE-Cy5. The release of DSPE-MTX was characterized by an initial burst over the first 6 h with 50% of the drug being released for both loading methods. Interestingly, the release of DSPE-MTX was observed to plateau around 60% at about 24 h. A similar observation applies for PEG-MTX but only for the direct method loading. For the absorption loaded PEG-MTX, the compound leaked out of the DPN matrix in a sustained fashion over the whole period of observation. Note that DSPE-MTX is the most hydrophobic compound realized in this work and, as such, upon direct loading into DPNs, it prefers to stay associated within the PLGA/PEG matrix. This would explain the plateau observed in **Figure 4C**. Interestingly, the value of the plateau is similar for both direct loaded DSPE-MTX and 1 kDa PEG-MTX, thus confirming the importance of modulating the compound hydrophobicity. On the other hand, the absorption loaded 1 kDa PEG-MTX, which is mostly confined to the DPN surface given its high molecular weight, escapes the particle matrix just as DSPE-Cy5-B. The LA-DOX release is documented in **Figure 4E**. The release profiles for the direct and absorption loaded compound are quite similar to a moderate burst release within the first 24 h. Indeed, this initial burst was lower than for the MTX as, over the first 10 h, 55 and 50% of the LA-DOX was released via the absorption method and direct method, respectively. Then, a total of 70 and 65%
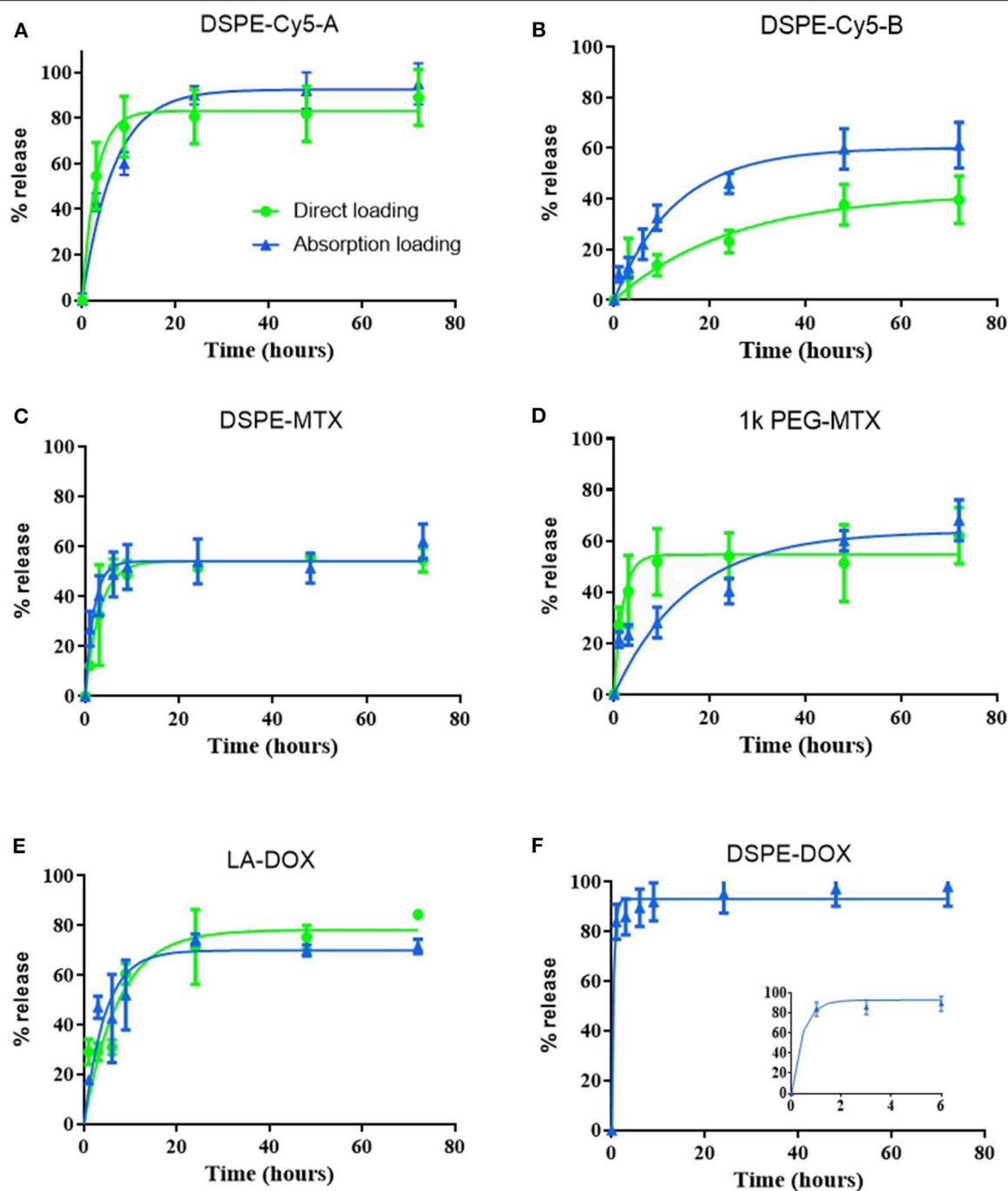
FIGURE 4 | Release profiles of the prodrugs from Discoidal Polymeric Nanoconstructs. Release profiles for **(A)** DSPE-Cy5-A; **(B)** DSPE-Cy5-B; **(C)** DSPE-MTX; **(D)** PEG-MTX; **(E)** LA-DOX; and **(F)** DSPE-DOX loaded into DPNs via the "direct method" (• green line) and the "absorption method" (▲ blue line).

LA-DOX was released at 24 h, respectively. The DSPE-DOX (**Figure 4F**) was only loaded through the absorption method, given its hydrophilicity. After the first hour, 80% of DSPE-DOX was already released out of DPNs. Note that DSPE-DOX is more soluble in water than LA-DOX, and this would explain the faster release rates documented for the first compound as compared to the second compound. This data confirms that the hydrophobicity/hydrophilicity ratio and molecular weight of the prodrugs play a critical role also in optimizing the release profiles.

Cell Viability Studies for the Prodrugs and Discoidal Polymeric Nanoconstructs

Using the MTT cell proliferation assay, the cytotoxic activity of prodrugs and DPNs was tested on MDA-MB-231 breast cancer
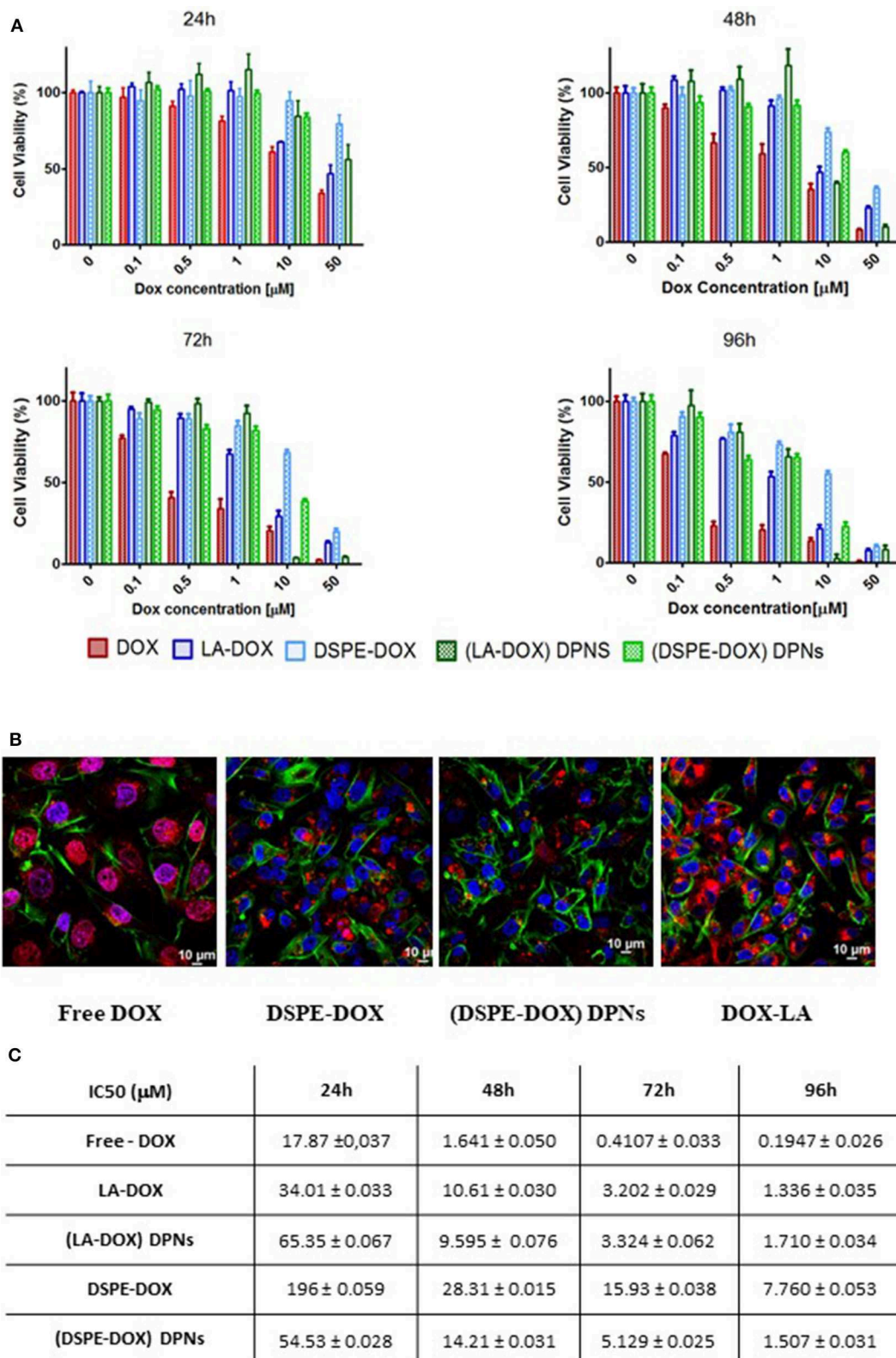
FIGURE 5 | Cytotoxic activity of DOX prodrugs and DOX-loaded Discoidal Polymeric Nanoconstructs. **(A)** Cell viability analysis of free-DOX, DSPE-DOX, DSPE-DOX DPNs, and LA-DOX at 24, 48, 72, and 96 h of incubation time on triple-negative breast cancer cells (MDA-MB-231). **(B)** Representative confocal microscopy images of free-DOX, DSPE-DOX, DSPE-DOX DPNs, and LA-DOX in MDA-MB-231 at 96 h of incubation time. **(C)** Summarizing table listing the IC50 values for free-DOX, DSPE-DOX, DSPE-DOX DPNs, and LA-DOX onto MDA-MB-231 at 24, 48, 72, and 96 h of incubation time.
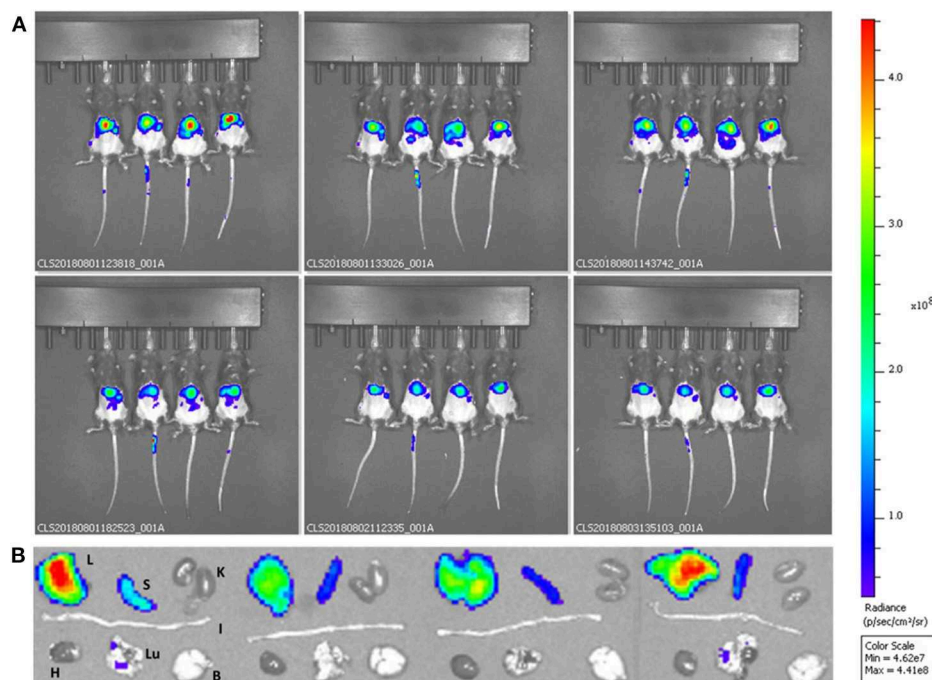
FIGURE 6 | Preliminary biodistribution studies of Discoidal Polymeric Nanoconstructs in healthy wild type C57BL/6 mice. **(A)** Whole animal optical fluorescent images at different time points post-DSPE-Cy5-DPN tail vein injection. **(B)** *Ex vivo* optical fluorescent images of harvested organs—Liver (L), Spleen (S), Kidneys (K), Intestine (I), Heart (H), Lungs (LU), and Brain (B) for DSPE-Cy5-DPNs (*n* = 4).

cells at 24, 48, 72 and 96 h (**Supplementary Figures 1A–E**). In line with the existing literature, free MTX and PEG-MTX manifested a modest cytotoxicity (Wei et al., 2019). On the other hand, DSPE-MTX presented a much lower IC50, ranging between a few tens of nanomolars to a few micromolars (**Supplementary Figures 1A–C**). However, the intrinsically low cytotoxicity of the drug together with the moderate encapsulation efficiency in DPNs return an insufficiently high cell killing activity for MTX-loaded DPNs (**Supplementary Figure 1D**). Consequently, cell viability analyses were mostly focused on DOX prodrugs and DOX-DPNs. In general, LA-DOX prodrug treatments were associated with a delayed response as compared to the free DOX. Specifically, at 24 h, the IC50 increased from 17.8 μM for the free DOX to 34.01 μM for LA-DOX (**Figures 5A–C**). This trend was documented for all tested conditions and should be ascribed to the hydrolyzation of the amide bond between DOX and oleic acid, which indeed requires times to progress. Importantly, LA-DOX DPNs were still associated with similar values of cell-killing potential. Only at 24 h, the IC50 values associated with LA-DOX DPNs were higher than for free LA-DOX (**Figure 5C**). As per DSPE-DOX, the loss in activity was even higher. At 24 h, the IC50 increased from 17.8 μM for free DOX to 196 μM for DSPE-DOX (**Figure 5C**). Even at 96 h, there was a reduction in IC50 of about 50 times as compared to DOX and 5 times as compared to LA-DOX. However, the IC50 values for the DSPE-DOX and LA-DOX loaded DPNs were documented to be quite similar at 48, 72, and 96 h of incubation time (**Figure 5C**). Similar results were

found by Sui and co-workers for free DOX and its prodrug (DOX-PEG) (Gou et al., 2013).

In order to characterize drug uptake in triple-negative breast cancer, the MDA-MB-231 cells were incubated with free DOX, prodrugs (DSPE-DOX and LA-DOX) and prodrug-loaded DPNs for 24, 48, 72, and 96 h. Representative confocal fluorescent images are provided in **Figure 5B** and **Supplementary Figures 2–5**. Both free DOX and free LA-DOX were observed to rapidly enter the cell and distribute within the cytosol around the cell nuclei. This process was also observed for the DSPE-DOX and the DPNs loaded with DSPE-DOX and LA-DOX. However, in these latter three cases, cell internalization was significantly delayed in time. In the case of DSPE-DOX, this delay should be ascribed to the lower efficiency of this prodrug in permeating through the cell membrane, as opposed to DOX and LA-DOX. In the case of prodrugs-loaded DPNs, the delay is due to the fact that, first, the prodrug would beed to be released from the nanoconstructs into the surrounding solution, and, after that, the prodrug would permeate across the cell membrane and eventually reach the cytosol (**Supplementary Figures 2–5**).

Pre-clinical Biodistribution Studies for the Discoidal Polymeric Nanoconstructs (DPNs)

DPNs directly loaded with DSPE-Cy5-B were administered into immunocompetent black mice via tail vein injection. The

accumulation of DSPE-Cy5-B DPNs in the different organs was assessed longitudinally by using a whole animal, near infra-red fluorescent (NIRF) imaging system (**Figure 6A**). Representative images were taken at 0.5, 1, 2, 6, 24, and 48 h post-tail vein injection. Also, at 48 h, the major organs, such as the liver, spleen, kidneys, heart, lungs, and brain, were harvested and imaged *ex-vivo* (**Figure 6B**). Given the absence of tumor mass or any other diseased tissues, DPNs were observed to accumulate within the abdominal cavity over time (**Figure 6A**). The lack of fluorescence signal in the bladder during the experimental observations would confirm the stable association of the DSPE-Cy5-B molecules with the structure of DPNs. However, it should be highlighted that a moderate reduction in the Cy5 signal is observed in the abdominal cavity (**Figure 6A**), which would suggest a modest but sustained release of Cy5 from DPNs in agreement with the release studies of **Figure 4B** for the directly loaded molecule. The insets of **Figure 6B** confirm that the DPN accumulation in the liver. Indeed, this was expected as liver would be the natural site of particle accumulation given the lack of any diseased tissue.

CONCLUSION

Two different loading strategies were documented to encapsulate hydrophobic and hydrophilic imaging and therapeutic compounds within the polymeric matrix of Discoidal Polymeric Nanoconstructs (DPNs). Two near-infrared imaging molecules were considered, namely Cy5-A and Cy5-B, together with two therapeutic molecules, methotrexate (MTX) and doxorubicin (DOX). The hydrophobicity/hydrophilicity ratio and molecular weight of these molecules were modulated by conjugating them directly with lipid (DSPE) and polymeric chains (PEG 1 kDa). In the "direct loading" method, the compounds were first dissolved in the polymeric paste forming the DPNs and then, together with this paste, applied to the PVA template. This approach suffered from the current sub-optimal fabrication yielding of DPNs returning encapsulation efficiencies lower than 1%. In the "absorption method," the compounds were resuspended in water at high concentrations (1 mg/ml) and dragged inside the polymeric matrix of DPNs upon rehydration. This approach required a fine-tuning between the compound hydrophobicity and molecular weight and returned encapsulation efficiencies as high as 80%. Specifically, the highest encapsulation was documented for compounds with a moderate hydrophobicity and low molecular weights. These two features were also shown to affect the release profiles of the loaded compounds. In general, direct loading was associated with lower release rates as compared to absorption loading for a given compound. This was ascribed to the fact that the compounds in the absorption loading are mostly confined in the vicinity of the DPN surface and are therefore more rapidly released into the surrounding aqueous environment. Differently, in direct loading, the compounds are uniformly distributed within the polymeric matrix. The cytotoxicity properties of MTX and DOX loaded DPNs were tested on triple-negative breast cancer cells (MDA-MB-231). As expected, it was documented a delay in the cytotoxic activity

in vitro mostly due to the hydrolyzation and release of the compounds from DPNs. Finally, in preliminary biodistribution studies, it was shown that direct loaded Cy5 compounds would stay firmly associated with DPNs during circulation and slowly leak out over an observational period of 48 h. Collectively, these results demonstrate that the pharmacological properties of DPNs can be finely tuned during the fabrication process by changing the loading strategies (direct vs. absorption) and compound properties (hydrophobicity and molecular weight). Future studies will focus more on further optimizing the loading and release conditions and pre-clinically demonstrate the therapeutic and imaging performance of this drug delivery platform in different disease models.

DATA AVAILABILITY STATEMENT

The datasets generated for this study are available on request to the corresponding author.

ETHICS STATEMENT

All animal experiments were performed at the Italian Institute of Technology (IIT) animal facility according to the guidelines established by the European Communities Council Directive (Directive 2010/63/EU of 22 September 2010) and approved by the National Council on Animal Care of the Italian Ministry of Health. All efforts were made to minimize animal suffering and to use the minimal number of animals required to produce reliable results.

AUTHOR CONTRIBUTIONS

MF performed all the loading and release experiments, and fabricated the particles. IR fabricated and characterized the particles. AP fabricated the particles and performed the *in vivo* experiments. MB, VD, and MD performed all the cell viability studies. PD designed the experiments, wrote the manuscript, and oversaw all the research activities. All authors have discussed the results and read the manuscript.

of the paper. The authors acknowledge the precious support provided by the Nikon Center, the Material Characterization Facility, the Electron Microscopy, and Nanofabrication facilities at the Italian Institute of Technology.

REFERENCES

Agasti, S. S., Chompoosor, A., You, C. C., Ghosh, P., Kim, C. K., and Rotello, V. M. (2009). Photoregulated release of caged anticancer drugs from gold nanoparticles. *J. Am. Chem. Soc.* 131, 5728–5729. doi: 10.1021/ja900591t

Ahmad, Z., Shah, A., Siddiq, M., and Kraatz, H. B. (2014). Polymeric micelles as drug delivery vehicles. *RSC Adv.* 4, 17028–17038. doi: 10.1039/C3RA47370H

Bobo, D., Robinson, K. J., Islam, J., Thurecht, K. J., and Corrie, S. R. (2016). Nanoparticle-based medicines: a review of fda-approved materials and clinical trials to date. *Pharm. Res.* 33, 2373–2387. doi: 10.1007/s11095-016-1958-5

Chen, G., Roy, I., Yang, C., and Prasad, P. N. (2016). Nanochemistry and nanomedicine for nanoparticle-based diagnostics and therapy. *Chem. Rev.* 116, 2826–2885. doi: 10.1021/acs.chemrev.5b00148

Denard, B., Jiang, S., Peng, Y., and Ye, J. (2018). CREB3L1 as a potential biomarker predicting response of triple negative breast cancer to doxorubicin-based chemotherapy. *BMC Cancer* 18:813. doi: 10.1186/s12885-018-4724-8

Desai, P., Venkataramanan, A., Schneider, R., Jaiswal, M. K., Carrow, J. K., Purwada, A., et al. (2018). Self-assembled, ellipsoidal polymeric nanoparticles for intracellular delivery of therapeutics. *J. Biomed. Mater. Res. A* 106, 2048–2058. doi: 10.1002/jbm.a.36400

Fernandes, R. S., Silva, J. O., Monteiro, L. O. F., Leite, E. A., Cassali, G. D., Rubello, D., et al. (2016). Doxorubicin-loaded nanocarriers: a comparative study of liposome and nanostructured lipid carrier as alternatives for cancer therapy. *Biomed. Pharmacother.* 84, 252–257. doi: 10.1016/j.biopha.2016.09.032

Gou, P., Liu, W., Mao, W., Tang, J., Shena, Y., and Su, M. (2013). Self-assembling doxorubicin prodrug forming nanoparticles for cancer chemotherapy: synthesis and anticancer study *in vitro* and *in vivo*. *J. Mater. Chem. B* 1, 284–292. doi: 10.1039/C2TB00004K

Huo, Z., Tsung, C. K., Huang, W., Zhang, X., and Yang, P. (2008). Sub-two nanometer single crystal Au nanowires. *Nano Lett.* 8, 2041–2044. doi: 10.1021/nl8013549

Katsube, T., Wajima, T., Yamano, Y., and Yano, Y. (2014). Pharmacokinetic/pharmacodynamic modeling for concentration-dependent bactericidal activity of a bicyclolide, modithromycin. *J. Pharm. Sci.* 103, 1288–1297. doi: 10.1002/jps.23897

Key, J., Aryal, S., Gentile, F., Ananta, J. S., Zhong, M., Landis, M. D., et al. (2013). Engineering discoidal polymeric nanoconstructs with enhanced magneto-optical properties for tumor imaging. *Biomaterials* 34, 5402–5410. doi: 10.1016/j.biomaterials.2013.03.078

Key, J., Palange, A. L., Gentile, F., Aryal, S., Stigliano, C., Di Mascolo, D., et al. (2015). Soft discoidal polymeric nanoconstructs resist macrophage uptake and enhance vascular targeting in tumors. *ACS Nano* 9, 11628–11641. doi: 10.1021/acsnano.5b04866

Lee, A., De Mei, C., Fereira, M., Marotta, R., Yoon, H. Y., Kim, K., et al. (2017). Dexamethasone-loaded polymeric nanoconstructs for monitoring and treating inflammatory bowel disease. *Theranostics* 7, 3653–3666. doi: 10.7150/thno.18183

Lu, J., Choi, E., Tamanoi, F., and Zink, J. I. (2008). Light-activated nanoimpeller-controlled drug release in cancer cells. *Small* 4, 421–426. doi: 10.1002/smll.200700903

Maeda, H., Wu, J., Sawa, T., Matsumura, Y., and Hori, K. (2000). Tumor vascular permeability and the EPR effect in macromolecular therapeutics: a review. *J. Control. Release* 65, 271–284. doi: 10.1016/S0168-3659(99)00248-5

Natfji, A. A., Ravishankar, D., Osborn, H. M. I., and Greco, F. (2017). Parameters affecting the enhanced permeability and retention effect: the need for patient selection. *J. Pharm. Sci.* 106, 3179–3187. doi: 10.1016/j.xphs.2017.06.019

Palange, A. L., Palomba, R., Rizzuti, I. F., Ferreira, M., and Decuzzi, P. (2017). Deformable discoidal polymeric nanoconstructs for the precise delivery of therapeutic and imaging agents. *Mol. Ther.* 25, 1514–1521. doi: 10.1016/j.ymthe.2017.02.012

Palomba, R., Palange, A. L., Rizzuti, I. F., Ferreira, M., Cervadoro, A., Barbato, M. G., et al. (2018). Modulating phagocytic cell sequestration by tailoring nanoconstruct softness. *ACS Nano* 12, 1433–1444. doi: 10.1021/acsnano.7b07797

Park, K., Skidmore, S., Hadar, J., Garner, J., Park, H., Otte, A., et al. (2019). Injectable, long-acting PLGA formulations: analyzing PLGA and understanding microparticle formation. *J. Control. Release* 304, 125–134. doi: 10.1016/j.jconrel.2019.05.003

Peer, D., Karp, J. M., Hong, S., Farokhzad, O. C., Margalit, R., and Langer, R. (2007). Nanocarriers as an emerging platform for cancer therapy. *Nat. Nanotechnol.* 2, 751–760. doi: 10.1038/nnano.2007.387

Slowing, I. I., Vivero-Escoto, J. L., Wu, C. W., and Lin, V. S. (2008). Mesoporous silica nanoparticles as controlled release drug delivery and gene transfection carriers. *Adv. Drug Deliv. Rev.* 60, 1278–1288. doi: 10.1016/j.addr.2008.03.012

Toy, R., Peiris, P. M., Ghaghada, K. B., and Karathanasis, E. (2014). Shaping cancer nanomedicine: the effect of particle shape on the *in vivo* journey of nanoparticles. *Nanomedicine* 9, 121–134. doi: 10.2217/nnm.13.191

Wei, C. W., Yu, Y. L., Chen, Y. H., Hung, Y. T., and Yiang, G. T. (2019). Anticancer effects of methotrexate in combination with alphatocopherol and alphatocopherol succinate on triplenegative breast cancer. *Oncol. Rep.* 41, 2060–2066. doi: 10.3892/or.2019.6958

Advantages of publishing in Frontiers

OPEN ACCESS
Articles are free to read
for greatest visibility
and readership

FAST PUBLICATION
Around 90 days
from submission
to decision

HIGH QUALITY PEER-REVIEW
Rigorous, collaborative,
and constructive
peer-review

TRANSPARENT PEER-REVIEW
Editors and reviewers
acknowledged by name
on published articles

Frontiers
Avenue du Tribunal-Fédéral 34
1005 Lausanne | Switzerland

Visit us: www.frontiersin.org
Contact us: info@frontiersin.org | +41 21 510 17 00

REPRODUCIBILITY OF RESEARCH
Support open data
and methods to enhance
research reproducibility

DIGITAL PUBLISHING
Articles designed
for optimal readership
across devices

FOLLOW US
@frontiersin

IMPACT METRICS
Advanced article metrics
track visibility across
digital media

EXTENSIVE PROMOTION
Marketing
and promotion
of impactful research

LOOP RESEARCH NETWORK
Our network
increases your
article's readership